

BEYOND GRAPHENE: MONOLAYER TRANSITION METAL
DICALCOGENIDES, A NEW PLATFORM FOR SCIENCE

Carl Hugo Naylor

A DISSERTATION

in

Physics & Astronomy

Presented to the Faculties of the University of Pennsylvania

in

Partial Fulfillment of the Requirements for the

Degree of Doctor of Philosophy

2017

Supervisor of Dissertation

A.T. Charlie Johnson, Professor, Department of Physics & Astronomy.

Graduate Group Chairperson

Ravi Sheth, Professor, Department of Physics & Astronomy.

Dissertation Committee

Marija Drndic, Fay R. and Eugene L. Langberg Professor, Department of Physics & Astronomy.

Cherie Kagan, Stephen J. Angello Professor, Department of Electrical & Systems Engineering.

Mark Trodden, Fay R. and Eugene L. Langberg Professor and Chair, Department of Physics & Astronomy.

Robert W. Carpick, John Henry Towne Professor and Chair, Department of Mechanical Engineering & Applied Mechanics.

BEYOND GRAPHENE: MONOLAYER TRANSITION METAL DICHALCOGENIDES, A NEW
PLATFORM FOR SCIENCE

COPYRIGHT

2017

Carl Hugo Naylor

This work is licensed under the
Creative Commons Attribution-
NonCommercial-ShareAlike 3.0
License

To view a copy of this license, visit

<https://creativecommons.org/licenses/by-nc-sa/3.0/us/>

*This work is dedicated to my loving fiancé Mandy; my devoted parents Peter and Vicky;
and my inspiring siblings Adam, Alice, Bruno, and Peter Jack.*

ACKNOWLEDGMENT

It is my pleasure to acknowledge here all those who were instrumental in my doctoral education.

First and foremost, I would like to thank my PhD advisor: Professor A. T. Charlie Johnson. Charlie, you were instrumental throughout my years at the University of Pennsylvania. Thank you for providing me continuous guidance, support, and trust, without which I would not be where I am today. Your scientific knowledge, leadership, and passion for the field equals some of the greatest scientists of this era. Under your mentoring, I was able to thrive and develop unique skills and knowledge that have enabled me to become a better scientist and person in today's society.

Secondly, I would like to thank all my collaborators and or peers at the University of Pennsylvania. Former PhD students: Dr. Nicholas J. Kybert and Dr. Mitchell B. Lerner. You both took me under your wings when I joined the lab, and taught me the ins and outs of experimental research within nanotechnology. You both quickly became more than mentors to me; you have become and will remain some of my closest friends. William M. Parkin, a graduate student peer and a close friend from Professor Drndic group that I frequently consulted on many experiments. Will, you were instrumental in most of the work performed in this thesis, your extended understanding of electron microscopy and general scientific knowledge is truly remarkable. Thank you for being my right-hand man in many of my publications, and for your support throughout my thesis. Dr. Ganghee Han and Dr. Zhaoli Gao, former postdoctoral students in the lab.

Your knowledge on the synthesis of materials by chemical vapor deposition is unmatched and have enabled me to thrive in this field, thank you. William Zhou, a very promising graduating Senior. Thank you for assisting me on many projects; your scientific potential and sense of humor will lead you to unimaginable achievements. It was an honor to have mentored you during your undergraduate years. Anthony T. Chieco, a graduate student peer and a close friend from Professor Durian's group. Thank you for keeping me sane and on track during our lunch breaks and for the general discussions we've had where you've helped me see pass the everyday lab issues. I would like to thank previous and current postdoctoral, graduate and undergraduate students of the Johnson group: Dr. John Qi, Dr. Eric Datolli, Dr. Jinglei Ping, Dr. Qicheng Zhang, Dr. Mengqiang Zhao, Dr. Madeline Diaz, Dr. Pedro Ducos, Sung Ju Hong, Hojin Kang, Ramya Vishnubhotla, Christopher Kehayias, Ram Gona, Amey Vrudhula, Alexander Hunt IV, Jeremy Yodh and Camilla Schneier. I would like to thank Professor Marija Drndic, Professor Robert Carpick, Professor James Kikkawa, Professor Andrew Rappe, Professor David Srolovitz, Professor Ritesh Agarwal, Professor Ertugrul Cubukcu, Professor Cherie Kagan, and their respective students, for all the wonderful collaborations and discussions that lead to scientific breakthroughs. I would like to thank Noah Clay and the staff at the Singh Center for Nanotechnology for their assistance in many of my work. I would also like to thank my graduate student classmates: William Parkin, Anthony Chieco, Michele Kim, Nathan Lourie, Steven Gilhool, Zachariah Addison, Eric Wong, Wei-Shao Wei, Sara Stanchfield, Rob Fletcher, Tom Dodson, and Sang Hoon Chong, for all the comradery throughout graduate school classes, and throughout the past five years.

I would like to thank my family. Mum and Dad. Thank you for your unconditional love and support in the past twenty-eight years. Living so far from home can be daunting at times, but you made it easier with the Skype calls, the Whatsapp messages, and the Philly visits. Everything I have achieved today was made possible because of your hard work, your sacrifices and your commitment to all your children, and for that I am eternally grateful. My siblings: Adam, Alice, Bruno, and Peter Jack. Thank you for inspiring me every day to be better - Adam, with your passion, Alice, with your fearlessness, Bruno, with your determination, and Peter Jack, with your enthusiasm. You are the best brothers and sister I could ask for, and I know I can always seek your guidance in times of need.

Finally, I need to thank my fiancé Mandy. And our little dog Penny. You both make all the troubles and difficulties of the lab disappear as I walk through the door. Mandy, you are my inspiration, you are the love of my life, thank you for supporting me every day through the good times and bad, thank you for the love you give me, thank you for taking this journey with me, without you none of this would have been possible, thank you.

ABSTRACT

BEYOND GRAPHENE: MONOLAYER TRANSITION METAL DICHALCOGENIDES, A NEW PLATFORM FOR SCIENCE

Carl Hugo Naylor

A.T. Charlie Johnson

Following the isolation of graphene in 2004, scientists quickly showed that it possesses remarkable properties. However, as the scientific understanding of graphene matured, it became clear that it also has limitations: for example, graphene does not have a bandgap, making it poorly suited for use in digital logic. This motivated explorations of monolayer materials “beyond graphene”, which could embody functionalities that graphene lacks. Transition metal dichalcogenides (TMDs) are leading candidates in this field. TMDs possess a wide variety of properties accessible through the choice of chalcogen atom, metal atom and atomic configuration (1H, 1T, and 1T’). Similar to graphene, monolayer TMDs may be produced on a small scale through mechanical exfoliation, but useful applications will require development of reliable methods for monolayer growth over large areas. In this thesis, I report our group’s recent progress in the chemical vapor deposition (CVD) of high quality, large area, monolayer TMDs under a 1H atomic configuration, which were integrated into high-quality biosensor arrays. These devices were incorporated in a flexible platform and were used for electronic read out of binding events of molecular targets in both vapor and liquid phases. I also report

our findings on the CVD growth of monolayer TMDs in the 1T' atomic configuration and measurements of their physical properties. 1T' TMDs have been labeled the holy grail of materials due to theoretical predictions that they are 2D topological insulators; however they remain relatively unexplored due to the difficulty of monolayer growth and their lack of stability in air. Through careful passivation techniques, we were able to stabilize the as-grown monolayer 1T' TMD flakes and perform the first characterizations on the structure. Lastly, in-plane 2D TMD heterostructures are promising material systems that combine the unique properties of each TMD. I discuss our results on the synthesis and study of 1H TMD heterostructures and unique 1H/1T' TMD heterostructures. TMDs, with its many different accessible physical properties, coupled with the large variety of applications, have been classified as the leading nanomaterials in the realm “beyond graphene”.

TABLE OF CONTENTS

ACKNOWLEDGMENT IV

ABSTRACT..... VII

LIST OF FIGURES XI

CHAPTER I. Overview of Thesis..... 1

CHAPTER II. Fundamental Properties of Materials, from Bulk to Monolayer..... 8

2.1 Overview of solid state physics9

 2.1.1 Atomic arrangement of solids9

 2.1.2 Atomic interactions within a solid11

 2.1.3 Metal, insulators and semiconductors14

 2.1.4 Band theory16

 2.1.5 Free electron and Kronig-Penney model.....20

2.2 “Traditional” monolayer materials26

 2.2.1 Graphene26

 2.2.2 Hexagonal boron nitride.....31

2.3 Beyond graphene: transition metal dichalcogenides33

 2.3.1 Overview of transition metal dichalcogenides33

 2.3.2 The 1H phase39

 2.3.3 The 1T phase.....44

 2.3.4 The 1T’ phase47

2.4 Other materials beyond graphene.....51

CHAPTER III. Experimental Methods 54

3.1 Isolating monolayer material.....55

3.2 Characterization techniques.....60

 3.2.1 Atomic force microscopy60

 3.2.2 Raman spectroscopy64

 3.2.3 Electron microscopy69

 3.2.4 Three terminal measurements74

CHAPTER IV. 1H-MoS₂, from Synthesis to Applications 90

4.1 1H-MoS₂ synthesis.....91

 4.1.1 Large area growth of monolayer 1H-MoS₂ flakes by CVD91

 4.1.2 Large area 1H-MoS₂ transfer95

 4.1.3 Seeded growth of highly crystalline molybdenum disulfide monolayers at controlled locations97

4.2 1H-MoS₂ sensors.....111

 4.2.1 Scalable production of molybdenum disulfide-based biosensors111

4.2.2 Understanding the large electrical responses from MoS ₂ vapor sensors	126
4.2.3 Universal biosensor	141
4.2.4 Flexible devices	151
4.3 Miscellaneous experiments performed on 1H-MoS₂	155
4.3.1 Band alignment and minigaps in monolayer MoS ₂ -Graphene van der Waals heterostructures	155
4.3.2 Electrical tuning of exciton-plasmon polariton coupling in monolayer MoS ₂ integrated with plasmonic nanoantenna lattice	174
4.3.3 Optomechanical enhancement of doubly resonant 2D optical nonlinearity	190
 CHAPTER V. 1H-WS₂, 1H TMD Heterostructure, 1H-MoSe₂ & 1H-WSe₂	202
5.1 1H-WS₂.....	203
5.1.1 Synthesis of 1H-WS ₂	203
5.1.2 Monolayer WS ₂ nanopores for DNA translocation with light-adjustable sizes	206
5.2 1H-MoS₂/1H-WS₂ heterostructure.....	229
5.3 1H-MoSe₂ and 1H-WSe₂	231
 CHAPTER VI. 1T'-MX₂, Unexplored Monolayer Materials	233
6.1 1T'-MoTe₂.....	234
6.1.1 Monolayer single-crystal 1T'-MoTe ₂ grown by chemical vapor deposition exhibits weak antilocalization effect.....	234
6.1.2 Intrinsic phonon bands in high quality monolayer T' molybdenum ditelluride	252
6.2 1T'-WTe₂.....	270
6.2.1 Large-area synthesis of high-quality monolayer 1T'-WTe ₂ flakes	270
6.3 1H /1T' heterostructures.....	295
6.3.1 Synthesis and physical properties of monolayer transition metal dichalcogenide 1H/1T' heterostructures	295
 CHAPTER VII. Summary, Future Work and Conclusion.....	319
7.1 Summary of 1H-MX₂ materials.....	319
7.2 Summary of 1T'-MX₂ materials.....	322
7.3 Summary of TMD heterostructures	324
7.4 Future work and conclusion	325
 BIBLIOGRAPHY	329

LIST OF FIGURES

Figure 2.1.1. Schematic of atoms in different crystal arrangements	10
Figure 2.1.2.1. Schematic of covalent bond	11
Figure 2.1.2.2. Schematic of ionic bond.....	12
Figure 2.1.2.3. Schematic of metallic bond	13
Figure 2.1.2.4. Van der Waals force between graphene layers in bulk graphite	13
Figure 2.1.4.2. Filling of the energy levels for increasing amount of Au atoms	18
Figure 2.1.4.3. Energy diagram for a metal, semiconductor and insulator	18
Figure 2.1.4.4. Energy diagram for n-type and p-type semiconductor	19
Figure 2.1.5.1. The Kronig-Penney model	21
Figure 2.1.5.2. Solution to the Kronig-Penney (KP) and free electron model.....	22
Figure 2.1.5.3. Repeated zone scheme	23
Figure 2.1.5.4. Band diagram for a bulk semiconductor to a 0D quantum dot semiconductor	25
Figure 2.1.5.5. Variation of density of states as dimensionality of the system is reduced	25
Figure 2.2.1.1. Graphene	26
Figure 2.2.1.2. Graphene stacking arrangements	27
Figure 2.2.1.3. Band structure of graphene.....	29
Figure 2.2.1.4. Beyond graphene.....	30
Figure 2.2.2.1. Ball and stick model of hBN.....	31
Figure 2.3.1.1. Ball and stick model of a monolayer MX ₂ material under a 1H atomic configuration	33
Figure 2.3.1.2. Periodic table highlighting the metal and chalcogen atoms that make MX ₂	35
Figure 2.3.1.3. D band filling of different TMD groups and summary of the electrical properties.....	36
Figure 2.3.1.4. Ball and stick model of the 1H, 1T and 1T' phase of TMDs	38
Figure 2.3.2.1. Ball and stick mode of 1H-MX ₂	39
Figure 2.3.2.2. A _{1g} ¹ and E _{2g} ¹ vibrational modes for 1H-MX ₂ materials	40
Figure 2.3.2.3. Band diagram of 1H-MX ₂ and table summarizing the bandgaps for 1H and 2H-MX ₂	41
Figure 2.3.2.4. Tunable bandgap in 1H-MX ₂	42
Figure 2.3.3.1. Ball and stick model of the 1T-MX ₂	44
Figure 2.3.3.2. Electrostatic force microscopy phase image and high resolution transmission electron microscopy image of 1H-MoS ₂ and 1T-MoS ₂	45
Figure 2.3.3.3. In-situ observation of phase transformation from 1H-MoS ₂ to 1T-MoS ₂	46
Figure 2.3.4.1. Ball and stick model of the 1T' phase	47
Figure 2.3.4.2. Theoretical predictions of QSH in monolayer 1T'-MX ₂	48
Figure 2.3.4.3. Theoretical prediction of phase transformation from 1H-MX ₂ to 1T'-MX ₂ induced by strain in the MX ₂ lattice	49
Figure 2.3.4.4. Artistic representation of the encapsulation of monolayer 1T'-MX ₂ using graphene	50
Figure 2.4.1. Black Phosphorous.....	52
Figure 2.4.2. Mxenes.....	53
Figure 3.1.1. Mechanical exfoliation.....	56
Figure 3.1.2. Liquid exfoliation.....	56
Figure 3.1.3. Molecular beam epitaxy.....	57
Figure 3.1.4. Chemical vapor deposition.....	59
Figure 3.2.1.1. Schematic of AFM measurement.....	60
Figure 3.2.1.2. Schematic of photodiode with the laser deflection for AFM	61
Figure 3.2.1.3. AFM images of various CVD grown samples	63
Figure 3.2.2.1. Raman spectrum of graphene	65
Figure 3.2.2.2. Raman spectrum of MoS ₂ with thickness dependence	66
Figure 3.2.2.3. Raman mapping of 1T'-WTe ₂	67
Figure 3.2.2.4. TERS on 1H-MX ₂ /1T'-MoTe ₂ heterostructure	68
Figure 3.2.3.1. Schematic of a SEM and TEM.....	69
Figure 3.2.3.2. Schematic of the interaction in the SEM and TEM.....	70
Figure 3.2.3.3. Electron microscope images	71

Figure 3.2.3.4. Dark Field TEM image of 1H-MoS ₂ /1T'-MoTe ₂ heterostructure with SAED of 1T'-MoTe ₂ and 1H-MoS ₂ regions respectively	72
Figure 3.2.3.5. High angle annular dark field STEM image of a 1H-MoS ₂ /1T'-MoTe ₂ heterostructure	73
Figure 3.2.4.1.1. Qualitative description of a MOSFET device	75
Figure 3.2.4.1.2. Band diagram of MOS	76
Figure 3.2.4.1.3. Band diagram of FET	78
Figure 3.2.4.2.1. Schematic of a three terminal device	79
Figure 3.2.4.2.2. CAD design for SEM	80
Figure 3.2.4.2.3. Mask for photolithography	82
Figure 3.2.4.2.4. Photolithography exposure modes	82
Figure 3.2.4.2.5. Outline for photolithography process	83
Figure 3.2.4.2.6. E-beam lithography and photolithography	84
Figure 3.2.4.3.1. IV _g curve for different semiconductors	85
Figure 3.2.4.4.1. Artistic representation of chemical binding on nanomaterials	87
Figure 3.2.4.4.2. Qualitative description of the ChemFET and the influence it has on a MOSFET device ..	88
Figure 3.2.4.4.3. IV _g curves of MoS ₂ as it undergoes a local chemical gating effect	89
Figure 4.1.1.1. Optical image showing the chip layout before 1H-MoS ₂ growth	91
Figure 4.1.1.2. Schematic of the 1H-MoS ₂ growth setup	92
Figure 4.1.1.3. Optical microscopy images of a 1H-MoS ₂ growth	93
Figure 4.1.1.4. Characterization of the CVD grown 1H-MoS ₂	94
Figure 4.1.2.1. Schematic representation of the 1H-MoS ₂ transfer process using KOH	95
Figure 4.1.2.2. Optical photograph capturing the KOH etching step	96
Figure 4.1.3.1. Schematic of the growth process for MoS ₂ using patterned molybdenum sources	99
Figure 4.1.3.2. Pattern growth of MoS ₂	102
Figure 4.1.3.3. AFM and optical analysis of pattern growth MoS ₂ flakes	104
Figure 4.1.3.4. Transmission electron micrographs and electron diffraction data of monolayer MoS ₂	106
Figure 4.1.3.5. Device fabrication and I-V measurement of MoS ₂ devices	107
Figure 4.2.1.1. MoS ₂ growth and devices	115
Figure 4.2.1.2. Physical characterization of MoS ₂	117
Figure 4.2.1.3. Electrical characteristics of MoS ₂ devices	118
Figure 4.2.1.4. MoS ₂ structure and functionalization schematic	120
Figure 4.2.1.5. Electrical signatures of protein-target binding	122
Figure 4.2.2.1. Scalable arrays of MoS ₂ vapor sensors.	130
Figure 4.2.2.2. Initial MoS ₂ vapor responses	132
Figure 4.2.2.3. MoS ₂ TLM device	134
Figure 4.2.2.4. Intrinsic and contact resistance responses	136
Figure 4.2.3.1. Schematic of the universal biosensor	143
Figure 4.2.3.2. Fabrication steps for hBN/MoS ₂ heterostructures	145
Figure 4.2.3.3. CVD growth of monolayer hBN films	146
Figure 4.2.3.4. Bubble transfer method	147
Figure 4.2.3.5. Three terminal measurements on 50 hBN/MoS ₂ heterostructure FETs	147
Figure 4.2.3.6. Electrical signature of target binding events for the universal biosensor	149
Figure 4.2.4.1. Next generation of smart flexible systems	151
Figure 4.2.4.2. Schematic of layout for the flexible MoS ₂ FETs using graphene as back gate	152
Figure 4.2.4.3. Scalable flexible MoS ₂ FETs	154
Figure 4.3.1.1. Structural and electronic properties of a MoS ₂ /graphene heterostructures	158
Figure 4.3.1.2. Raman characterization of MoS ₂ /graphene heterostructures	163
Figure 4.3.1.3. High-resolution XPS of MoS ₂ /graphene heterostructures	165
Figure 4.3.1.4. Band alignment diagram of MoS ₂ /graphene obtained from XPS measurement	167
Figure 4.3.1.5. ARPES measurements on MoS ₂ /graphene heterostructures	170
Figure 4.3.1.6. Electronic structure of MoS ₂ /graphene heterostructures	172
Figure 4.3.2.1. Electrical tuning of monolayer MoS ₂ coupled with plasmonic nanodisk array configured in a field-effect transistor geometry	178

Figure 4.3.2.2. Tuning of exciton-plasmon coupling between the lattice-LSP modes to both neutral (A^0) and charged (A^-) excitons via gate voltage	180
Figure 4.3.2.3. Coupled Oscillator Model fitting of the evolution of the exciton-plasmon coupling under different electron doping conditions	184
Figure 4.3.2.4. Gate-voltage dependent exciton-plasmon coupling in three different silver nanodisk arrays with different exciton-LSP detuning values	186
Figure 4.3.3.1. Optomechanically reconfigurable frequency doubling device	192
Figure 4.3.3.2. Voltage tuning of the cavity resonances	194
Figure 4.3.3.3. Doubly resonant second harmonic generation measurements	197
Figure 5.1.1.1. 1H-WS ₂ growth	204
Figure 5.1.1.2. 1H-WS ₂ characterization	205
Figure 5.1.2.1. Characterization of WS ₂ flakes	209
Figure 5.1.2.2. Photoluminescence study of monolayer WS ₂ flakes	211
Figure 5.1.2.3. Change in PL due to beam exposure and nanopore drilling	213
Figure 5.1.2.4. Fabrication and characterization of WS ₂ nanopore devices	216
Figure 5.1.2.5. Double stranded DNA translocation through WS ₂ nanopores	218
Figure 5.1.2.6. Optical activity of WS ₂ nanopores in 1M KCl solution	220
Figure 5.2.1. MoS ₂ WS ₂ heterostructure	230
Figure 5.3.1. Characterization of the 1H-MSe ₂	232
Figure 6.1.1.1. MoTe ₂ growth	239
Figure 6.1.1.2. Characterization of MoTe ₂ flakes by XPS and Raman spectroscopy	241
Figure 6.1.1.3. MoTe ₂ TEM characterization	244
Figure 6.1.1.4. Stability computation using first-principals	246
Figure 6.1.1.5. Electrical measurements of monolayer 1T'-MoTe ₂	247
Figure 6.1.2.1. Optical microscope, AFM and dark TEM images of 1L-T'-MoTe ₂	256
Figure 6.1.2.2. Schematics of light-polarization and crystal-orientation resolved Raman spectroscopy	258
Figure 6.1.2.3. The intensity angular dependences of the 9 Raman-active modes of 1L-T'-MoTe ₂	262
Figure 6.1.2.4. Raman spectra of degraded 1L-T'-MoTe ₂	264
Figure 6.1.2.5. Spectral evolution of samples with 1L-T'-MoTe ₂	267
Figure 6.2.1.1. 1T'-WTe ₂ growth	275
Figure 6.2.1.2. 1T'-WTe ₂ characterization	277
Figure 6.2.1.3. TEM characterization of 1T'-WTe ₂	280
Figure 6.2.1.4. Degradation of 1T'-WTe ₂ in air	282
Figure 6.2.1.5. Surface structure of monolayer 1T'-WTe ₂	286
Figure 6.2.1.6. Electrical data of monolayer 1T'-WTe ₂	288
Figure 6.3.1.1. 1H/1T' growth	301
Figure 6.3.1.2. Characterization of 1H/1T' heterostructure flakes	303
Figure 6.3.1.3. Characterization by Transmission Electron Microscopy	308
Figure 6.3.1.4. Effects of the composition, elastic misfit strain, and out-of-plane bending on the interface structure and growth morphology	314
Figure 6.3.1.5. Electrical responses from the 1T'/1H/1T' structure	315
Figure 7.1.1. Summary of 1H-MX ₂	321
Figure 7.2.1. Summary of 1T'-MX ₂	323
Figure 7.3.1. Summary of TMD heterostructures	324
Figure 7.4.1. 1H-WSe ₂ /1T'-WTe ₂ heterostructure	325
Figure 7.4.2. 1H-WSe ₂ /1H-MoS ₂ heterostructures, a p/n junction	326
Figure 7.4.3. 1T-TaS ₂	326
Figure 7.4.4. Potential applications with TMDs	327
Figure 7.4.5. TMDs	328

CHAPTER I.

Overview of Thesis

Nanomaterials have had tremendous impact in today's technologies and will continue to further impact tomorrow's technologies. Potential applications of nanomaterials include biosensing, energy storage, next generation quantum computing, and many more; hence, an apparent need to research novel nanomaterials. To study monolayer materials, scientists preferentially result to mechanical exfoliation from bulk materials; however, mechanical exfoliation offers small amounts of monolayer material and thus is not a scalable method for industrial applications.

Graphene, one of the most studied nanomaterial throughout the past decade, offers a large range of properties that are accessible in the monolayer form. Graphene is reported to be the strongest material ever tested,^{1,2} it is biocompatible,³ and possesses high electron mobility due to massless-like charge carriers.^{4,5} Despite its remarkable qualities, graphene lacks key property essential to the semiconducting industry: a bandgap. The bandgap enables the tuning of the electrical resistivity of a material from an "on" state to an "off" state; this tuning capability is key for digital logic devices. Consequently, new materials are being explored that possess the qualities that graphene lacks. These next generation of nanomaterials belong to the realm "beyond graphene".

The goal of this doctoral thesis is to develop a reliable synthesis method for a subset of next generation nanomaterials called transition metal dichalcogenides (TMDs).

Growth was performed by chemical vapor deposition (CVD) and material characterization was accomplished with a variety of tools that include spectroscopy, microscopy, and three terminal electrical measurements. These nanomaterials were incorporated into innovative applications such as biosensors. Biosensors offer the ability to detect low concentrations of chemical and biological targets that have potential applications as early stage diagnostics of diseases or general healthcare monitoring systems. TMD devices can be used for a wide variety of applications, such as military, medical, and leisure activities. To further realize these applications, the TMD devices were incorporated onto flexible substrate that could potentially be incorporated into fabric.

In Chapter 2 of this thesis, I will provide a short review of essential solid state physics knowledge necessary for the full understanding of this thesis. To this extent, I will discuss the different atomic arrangements and interactions involved within a solid and the key differences between a metal, an insulator, and a semiconductor. By utilizing the free electron model, the Kronig-Penney model, and band theory, I will explain the origin of the different properties within solids and the outcome that they have on the electronic structure of monolayer materials. I will follow this discussion with the introduction of “traditional” monolayer materials, graphene and hexagonal boron nitride (hBN), which motivated the exploration for next generation nanomaterials. This will lead us to the introduction of TMDs and specifically the group 6 metal TMDs, followed by detailed differentiation between the 3 possible atomic configurations for monolayer TMDs: the 1H phase, the 1T phase, and the 1T' phase. Each phase has an impact on the

intrinsic properties of the monolayer TMD. I will also highlight other emerging nanomaterials “beyond graphene”, such as phosphorene and MXenes.

Chapter 3 will review the experimental methods that were essential in synthesizing, characterizing and evaluating the overall quality of our 2D materials. I will highlight how one can isolate a 2D material, either through exfoliation or by direct synthesis, such as CVD. I will detail the different characterization techniques (microscopy and spectroscopy) involved in the exploration of the 2D TMDs. Atomic force microscopy enables the careful characterization of the topography and height of the nanomaterials. Raman spectroscopy provides a fingerprint of the atomic vibration frequencies, identifying the compounds present and their atomic configuration. Electron microscopy (scanning, tunneling, and aberration corrected) offers valuable direct imaging of the nanomaterial’s surface. Three terminal measurements give an estimation of the overall electronic quality of the nanomaterial. I will discuss how three terminal measurements are manufactured, explain the principle behind the measurements (utilizing the previous band theory discussion), provide examples of three terminal measurements on different nanomaterials, and explain the mechanism behind the local chemical gating effect. The local chemical gating effect plays a fundamental role in biosensing, which will be discussed in Chapter 4.

In Chapter 4, I will discuss our group’s work with the most common TMD to date, 1H molybdenum disulfide (1H-MoS₂). I will report our synthesis method by CVD of high quality, large area, monolayer 1H-MoS₂. 1H-MoS₂ is directly synthesized on a silicon/silicon-dioxide (Si/SiO₂) substrate by the reaction between an ammonium

heptamolybdate source (Mo feedstock) and sulfur vapor (S feedstock). This growth method offers large areas of monolayer single crystal 1H-MoS₂ flakes that can be transferred onto any desirable substrate (e.g. pre-patterned photolithography devices for scalable 1H-MoS₂ devices). The amount of 1H-MoS₂ flakes and the growth location can be predetermined with the seeded growth method. Seeded growth method utilizes small Mo sources that are positioned at predetermined locations where the resulting 1H-MoS₂ flake grows. Due to the highly efficient growth process for dense monolayer 1H-MoS₂ flakes, we were able to incorporate the MoS₂ into many innovative applications such as biosensors. I will report our work on a scalable 1H-MoS₂ biosensor that was functionalized to detect small traces of opioids (painkillers). Opioid overdose accounts for over 30,000 deaths a year in the United States (US).^{6,7} There are an estimated 250 million prescriptions for opioids handed out per year in the US, which is equivalent to one prescription per adult living in the US.^{6,7} These statistics highlight the urgent need to understand the interactions opioids have with our bodies. The 1H-MoS₂ opioid biosensor is a first step towards helping medical doctors prescribe the accurate amount of painkillers. The 1H-MoS₂ devices were also electrically measured in the presence of vapor analytes. The intriguingly high responses of the 1H-MoS₂ flakes to small traces of vapor analytes suggest a more complex interaction mechanism than solely the 1H-MoS₂ surface with the analytes. By transmission line measurements, we identified that changes in electrode-MoS₂ contact resistance play an important role in the responses to vapor analytes. In addition, I will discuss how we manufactured a universal biosensor utilizing monolayer hBN films. By synthesizing large areas of monolayer hBN by CVD, we transferred the hBN on top of the scalable 1H-MoS₂ devices, ergo creating a 1H-

MoS₂/hBN heterostructure. This heterostructure can be functionalized independently of the underlying 1H-MoS₂ since the functionalization chemistry depends solely on the top hBN layer, thus turning the 1H-MoS₂/hBN heterostructure into a universal biosensor. These devices were incorporated onto flexible/bendable substrates. Flexible devices are necessary for wearable and portable electronics. We transferred the 1H-MoS₂ flakes onto a flexible substrate made with kapton, creating scalable flexible 1H-MoS₂ devices that can be utilized for biosensing applications and much more. Finally, in this chapter, I will highlight the recent work performed by some of our collaborators with our high quality synthesized monolayer 1H-MoS₂. This work includes the band alignment and mini-gaps in monolayer MoS₂-graphene van der Waals heterostructures, electrical tuning of exciton-plasmon polariton coupling in monolayer MoS₂ integrated with plasmonic nanoantenna lattice, and optomechanical enhancement of doubly resonant 2D optical nonlinearity.

Chapter 5 will highlight additional monolayer 1H materials that were synthesized by our CVD method. I will discuss the synthesis of 1H-WS₂, 1H-MoSe₂, and 1H-WSe₂. Each 1H TMD has unique properties that differentiates it from its 1H TMD counterpart. For instance, 1H-WS₂ possess high photoluminescence due to large exciton binding energy, and 1H-WSe₂ is the only TMD known to be an intrinsic p-type semiconductor. By our efficient growth method, we are able to explore all of the different metal group 6 1H TMDs and utilize them in different applications. I will discuss the work performed on monolayer WS₂ nanopores for DNA translocation with light-adjustable sizes. Finally, I will discuss our work on the combination of 1H TMDs to form in-plane heterostructures.

In-plane heterostructures offer the prospect of uniting the unique properties of each TMD into one material, for this reason they are currently heavily explored. For example, 1H-WS₂ has a larger bandgap than 1H-MoS₂ and thus emits light at a different energy. But when synthesizing in-plane monolayer 1H-MoS₂/1H-WS₂ heterostructures, we are able to obtain a material that has specific regions with either bandgap value. By fluorescence measurements we were able to specifically choose which region of the heterostructure emits light (either the 1H-MoS₂ or the 1H-WS₂).

In Chapter 6 we will shift our focus towards monolayer 1T' TMDs. Monolayer 1T' materials are unexplored due to their high instability in air and the difficulty of synthesizing monolayer materials in the 1T' phase. Indeed, mechanical exfoliation of bulk 1T' TMDs down to the monolayer form has been proven challenging, as the resulting monolayer material decayed during the exfoliation process. I will show that the direct synthesis of monolayer 1T' TMDs is possible. I will discuss monolayer single-crystal 1T'-MoTe₂ grown by chemical vapor deposition which exhibits a weak antilocalization effect. This will be followed by a discussion of the intrinsic phonon bands in high quality monolayer 1T'-MoTe₂. This synthesis is not limited to the molybdenum-containing TMDs and was applied to the tungsten compounds as well, with the large-area synthesis of high-quality monolayer 1T'-WTe₂ flakes. As mentioned previously, in-plane heterostructures of TMDs with similar atomic configurations are currently being explored. We were able to synthesize a unique in-plane heterostructure combining two different atomic configurations (1H and 1T'). I will also detail the

synthesis and properties of monolayer transition metal dichalcogenide 1H/1T' heterostructures in this chapter.

A summary of the work discussed in this thesis can be found in Chapter 7. I will highlight our results of the TMDs grown in the 1H and 1T' phase as well as their potential applications. I will also summarize the work performed on the various in-plane TMD heterostructures. Finally, I will discuss the outlook for TMDs including potential hurdles that need to be overcome for technological applications and future work that will begin in our lab over the next few years.

CHAPTER II.

Fundamental Properties of Materials, from Bulk to Monolayer

The properties of materials derive from their intrinsic atomic arrangement and bonds. Metals, insulators and semiconductors are all made of atoms, however they differ in their electronic band structure. These properties can be altered when the size, width or height is changed. In the monolayer form, new physics appears and materials exhibit fascinating and unique properties.

In this Chapter, I will first give a brief overview of solid state physics. I will then introduce the “traditional materials”, such as graphene and hexagonal boron nitride, and detail why materials research is expanding in the field “beyond graphene”. I will introduce transition metal dichalcogenides (TMDs), highlighting their many exciting properties in the monolayer form that can be altered by exchanging the combination of elements or by modifying the atomic configuration. Finally, I will briefly highlight other promising 2D materials currently being explored in the realm “beyond graphene”.

2.1 Overview of solid state physics

2.1.1 Atomic arrangement of solids

Atoms in a solid can arrange themselves in three possible configurations: monocrystalline, polycrystalline and amorphous.^{8,9}

Monocrystalline (or single crystal) is a periodic arrangement of the atoms in all three directions of space (or two directions for monolayer) in the material.^{8,9} The lattice is continuous throughout the entire sample with no discontinuities or grain boundaries (figure 2.1.1). A high quality material tends to be single crystal as the presence of defects or grain boundaries can cause electrical resistivity to increase (or conductivity to decrease).¹⁰ Scientists synthesizing large areas of monolayer materials try to achieve these large areas of single crystals to reduce the amount of grain boundaries that can reduce the overall performance.

Polycrystalline solids are made of many monocrystalline grains.^{8,9} These grains are randomly oriented with respect to each other and are of variable sizes. When two grains merge they form a grain boundary (figure 2.1.1), which is the location of chemical impurities in the material.¹¹ As detailed above, grain boundaries decrease the electrical performance of the material.¹⁰ Grain boundaries are also a preferential site for the precipitation of new phases from the solid and the onset of corrosion.¹² A grain boundary can be used as a seed location site for the growth of a different material around the original crystal (please see sections 5.2 and 6.3 for more details on in-plane heterostructures).^{13,14}

Amorphous material (non-crystalline) refers to a material that has no atomic arrangement for short distances, it lacks long range order (figure 2.1.1).^{8,9} Due to the nature of chemical bonding however, amorphous materials have some short range order. Amorphous films, such as few nm of SiO₂ are very important in semiconductor technology as they represent the insulator (oxide) in the metal-oxide-semiconductor field-effect transistor (MOSFET) device (please see section 3.2.4 for more information regarding MOSFET technology).

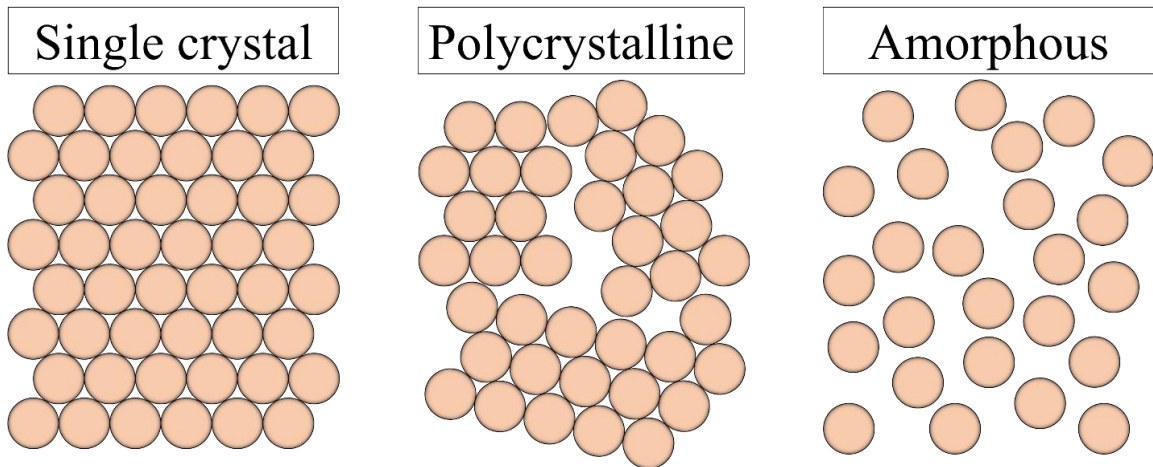


Figure 2.1.1. Schematic of atoms in different crystal arrangements. Single crystal, the atoms are in a periodic order all across the material. Polycrystalline, grain boundaries between different regions of single crystal. Amorphous, no order.

2.1.2 Atomic interactions within a solid

Atoms constitute a solid and can interact in many ways. There are four predominant bonds that are used to explain phenomena observed throughout this thesis: covalent bond, ionic bond, metallic bond and van der Waals forces.

Covalent bond is a strong, directional bond that results from the sharing of peripheral electron pairs between 2 atoms in order to satisfy noble gas configuration.^{8,9} Examples of covalent bonding can be seen in figure 2.1.2.1. A coordinate covalent bond, also known as a dative bond, is when the 2 electrons that form the covalent bond are brought in from the same atom.

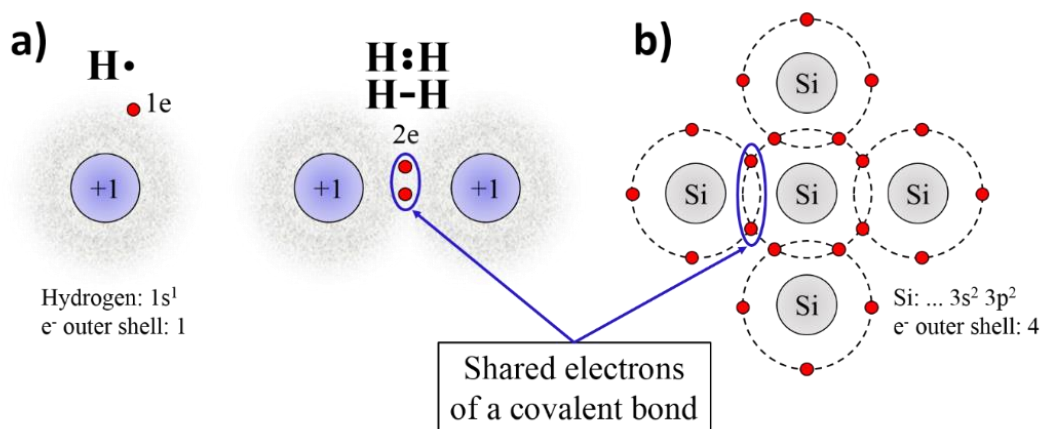


Figure 2.1.2.1. Schematic of covalent bond. a) Covalent bond for H₂. b) Covalent bond for Si.

Ionic bond is a strong, directional bond, which is the result of a complete transfer of electrons between atoms known as an electrovalence.^{8,9} When two oppositely charged ions interact (an anion and a cation), the extra electron on the anion will transfer to the cation in order for both atoms to have filled outer shells. Figure 2.1.2.2 is an example of ionic bond with sodium chloride. Sodium's atomic configuration is: 1s²2s²2p⁶3s¹. It has 2

electrons on first shell, 8 on second shell and 1 on the outer shell. Chlorine's atomic configuration is $1s^2 2s^2 2p^6 3s^2 3p^5$. It has 2 electrons on first shell, 8 on second shell and 7 on the outer shell. The chlorine will take the extra electron off the sodium to fill its outer shell, creating sodium chloride through this ionic bond.

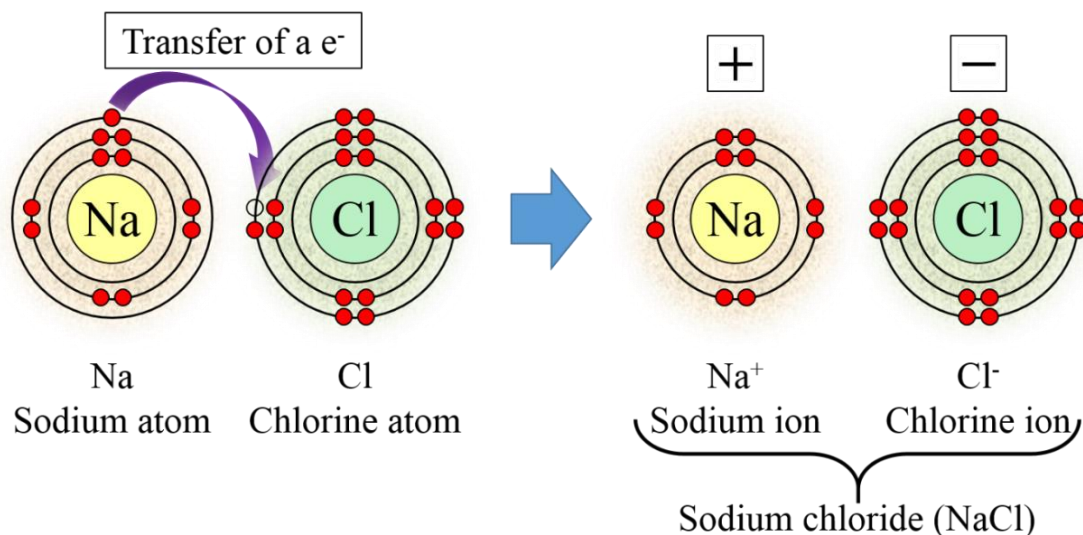


Figure 2.1.2.2. Schematic of ionic bond. Sodium and chlorine will come together to make sodium chloride.

Metallic bond is a strong, non-directional, strongly polarized bond that is the outcome from the attraction of free valence electrons in a lattice of positively charged metal ions.^{8,9} Whereas the electrons in a covalent or ionic bond are fixed, the electrons involved in metallic bonds can delocalize creating a sea of electrons. It is this sea of electrons that contributes to the high electrical conductivity of metals. Figure 2.1.2.3 is an example of metallic bonds creating a sea of electrons. For example gold (Au), a known metal, filling the molecular orbitals we obtain the electronic configuration: $[\text{Xe}] 4f^{14} 5d^{10} 6s^1$, $6s^1$ is only half full and represents the free electron.

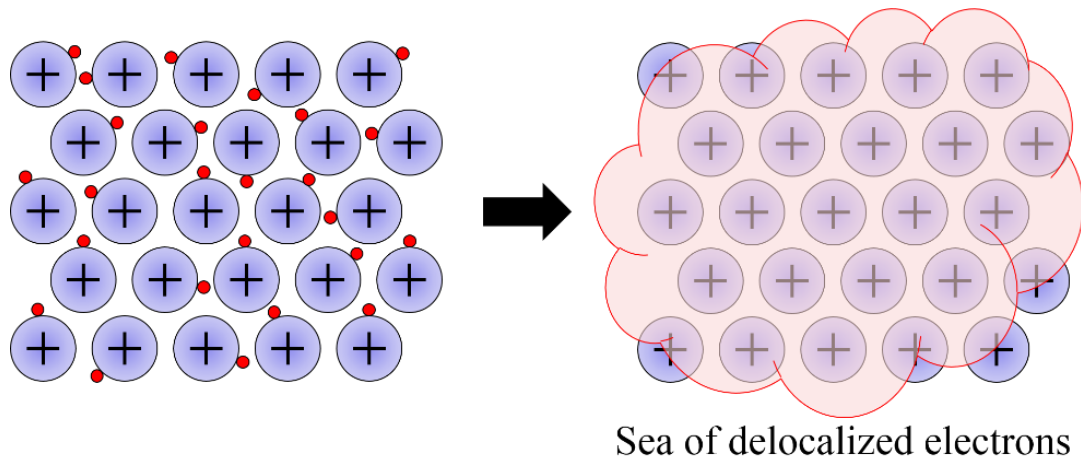


Figure 2.1.2.3. Schematic of metallic bond. In a lattice of metallic bonds, the electrons are delocalized creating a sea of electrons.

Van der Waals force is a weak, attractive force, it is the driving force keeping the stacked monolayer sheets together in a bulk material.¹⁵ For example, graphite is many layers of graphene held together by weak van der Waals forces (figure 2.1.2.4).

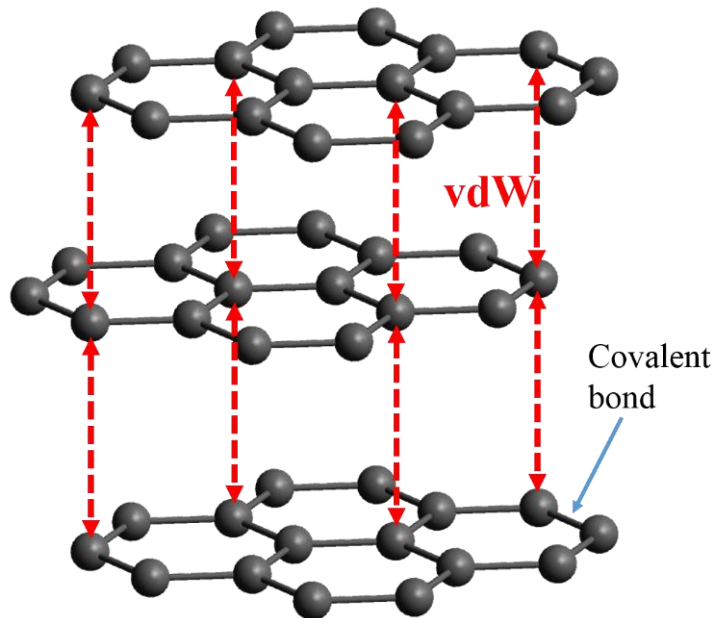


Figure 2.1.2.4. Van der Waals force between graphene layers in bulk graphite.

2.1.3 Metal, insulators and semiconductors

Metals (M), insulators or oxide (O) and semiconductors (S) are vital in the MOS field effect transistor (MOSFET) technology (please see section 3.2.4 for details on MOSFET devices) used throughout this thesis to estimate the quality of a 2D material.

Metals are good electrical and thermal conductors, this originates from their outer delocalized electrons that we described in the previous section 2.1.2 (metallic bond).^{8,9} The delocalized electrons are a sea of highly mobile electrons. Without an electric field, there is a random motion of the electrons. An electric field can be generated through an applied potential U across the material, $\vec{E} = -\vec{\nabla}U$. The electric field will generate a coulomb force $\vec{F} = q\vec{E}$ that will make the electrons move and this will make a current appear. The resistivity of metals are on the order of $\rho \sim 10^{-6} \Omega\cdot\text{cm}$.

Insulators, which include oxides such as SiO_2 , are not conductors of electricity. Their internal electric charges do not flow freely. By applying an electric field no current can be measured. However no insulator is perfect and by applying a very large electric field there is a small number of mobile charges that can carry current. When a massive electric field is applied, the electric field will tear electrons away from the atoms.¹⁶ This is known as the breakdown voltage and is the origin of gate leaks in a MOSFET device (discussed in section 3.2.4). Insulators have very high resistivity $\rho \gg \text{M}\Omega\cdot\text{cm}$.

Semiconductors are materials where the conduction properties can be tuned.^{8,9} Semiconductors are named based on their position in the periodic table, for example Si is called a group IV whereas GaAs is called a III-V semiconductor. There are two types of

semiconductors, intrinsic and extrinsic.^{8,9} Intrinsic semiconductors are materials that are perfect semiconductors in their single crystal form (e.g. pure Si). Extrinsic semiconductors are doped materials, adding impurities will induce various conduction properties. It can be n-doped or p-doped depending on the charge carrier (please see section 2.1.4 for further details). Furthermore, thin film semiconductor material can be dictated from an on to an off state by an induced electric field (this is as MOSFET device that will be discussed further in section 3.2.4). The resistivity of semiconductors is $10^{-3} \leq \rho \leq 10^3 \Omega \cdot \text{cm}$. In contrast to a metal, as the temperatures increase, the conductivity increase (decrease of resistance).^{8,9} The tuning of the electrical resistivity is an incredible feature that makes high quality semiconductors a large area of research in academic and industrial settings.

2.1.4 Band theory

Band theory of solids highlights the key differences between a conductor, insulator and a semiconductor.

As we discussed in the previous section 2.1.2, metallic bonds contain free valence electrons in the lattice.^{8,9} One gold (Au) atom has an electronic configuration: ...6s¹, meaning it has one free electron on a molecular orbital 6s¹ and the other levels are full. Based on quantum molecular orbital theory, when this Au atom is brought in close range with another Au atom their 6s orbitals will overlap and they will share a pair of electrons between those two orbitals.^{8,9} From quantum mechanics we know energies are quantized (fixed values), the orbitals will combine making a new molecular orbital with a lower in energy called σ -bonding orbital and a higher energy called σ^* -antibonding orbital (figure 2.1.4.1).^{8,9} The electrons will fill the lower energy state giving a filled σ -bonding orbital and an empty σ^* -antibonding orbital (figure 2.1.4.1).

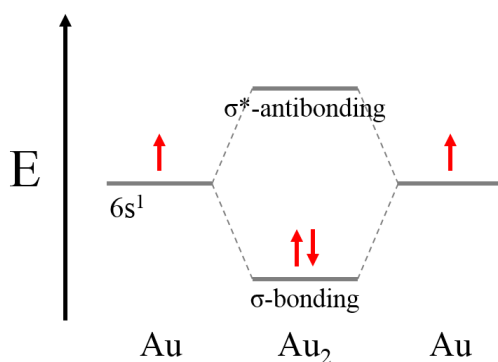


Figure 2.1.4.1. Schematic of orbital overlap.

When additional Au atoms are brought in, more energy levels are created, the energy levels will start to get closer together due to the Paul exclusion principle.^{8,9,17}

When n Au atoms are present, with n on the order of Avogadro constant (6.022×10^{23}), the energy levels are very compact (figure 2.1.4.2). These levels are so close that they are referred to as bands, with the σ -bonding orbitals the valence band E_V and the σ^* -antibonding orbitals the conduction band E_C . In figure 2.1.4.2, the bands are so close that an electron can easily jump up and down to different levels within a band with minimal amount of thermal energy, when an electron reaches the E_C band electrical current is observed. The highest occupied electron state at 0 K is called the Fermi energy, however in systems with thermal fluctuations we refer to a Fermi level (E_F). It is the energy level with a 50% probability of being occupied at finite temperature T .^{8,9,18} The probability that a given available electron energy state with energy E will be occupied at a given temperature is defined by the Fermi function $f(E)$ (derived from Fermi-Dirac statistics)^{8,9,18}:

$$f(E) = \frac{1}{e^{\frac{(E-E_F)}{kT}} + 1}$$

This equation dictates that at ordinary temperatures, most of the levels up to the Fermi level E_F are filled, and that relatively few electrons have energies above the Fermi level. The position of E_F with respect to the E_C and E_V bands is the defining criteria between a metal, insulator and semiconductor.

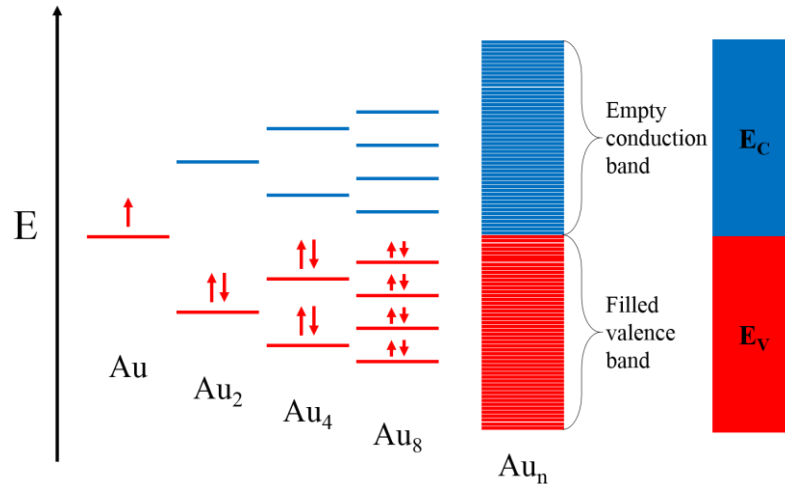


Figure 2.1.4.2. Filling of the energy levels for increasing amount of Au atoms.

For a metal, E_F is located in the band (figure 2.1.4.3). The electrons can enter E_C with minimal energy and we obtain high current. Thus the outer electrons are said to be “free” and will move under an electric field as described in section 2.1.3.

For an insulator, there is a large gap between E_C and E_V preventing electrons from entering E_C therefore preventing any conduction. E_F is far from the bands (figure 2.1.4.3). If a massive electric field is applied electrons could potentially be extracted as explained in section 2.1.3, however this is called the breakdown voltage and to be avoided.

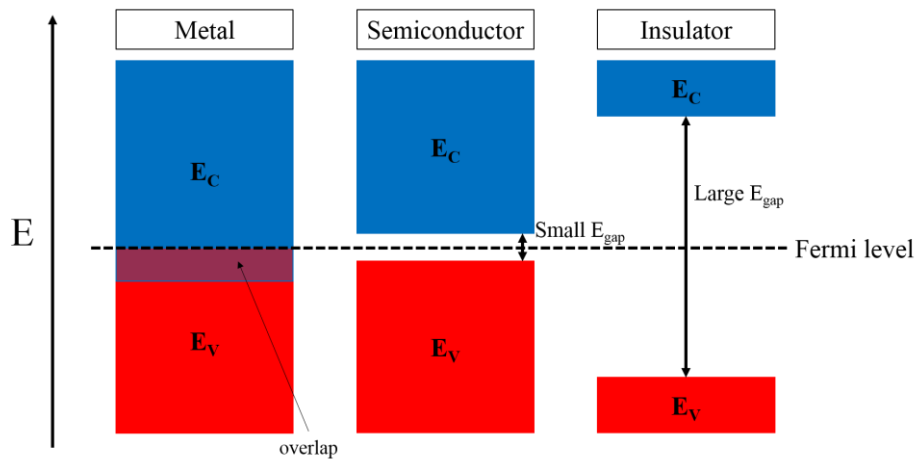


Figure 2.1.4.3. Energy diagram for a metal, semiconductor and insulator.

For a semiconductor, the gap between E_C and E_V is small and therefore E_F is close to the bands (figure 2.1.4.3). Only a small amount of energy is necessary to induce conduction. We classify semiconductors into two categories, n-type and p-type. For a n-type semiconductor E_F is closer to E_C and leads to preferential electron conduction, for a p-type semiconductor E_F is closer to E_V and leads to preferential hole conduction (figure 2.1.4.4).^{8,9} By doping the material, E_F can be moved closer or further away from the bands making it easier or harder to conduct. For example Si is a known semiconductor, however a highly p-doped Si (p^{++} -Si) acts like a metal as E_F is low in the E_V band. By controlling E_F you can dictate whether the semiconductor conducts or not. In MOSFET technologies, where thin film semiconductors are used (MOSFET operation is discussed in further detail in section 3.2.4), E_F can be controlled under an electric field making the semiconductor act as an on/off switch. Semiconductors are extremely promising and vital materials in today's technologies, they are present in all our electronics and billion dollar companies such as Intel make processors based of nm size semiconductors.

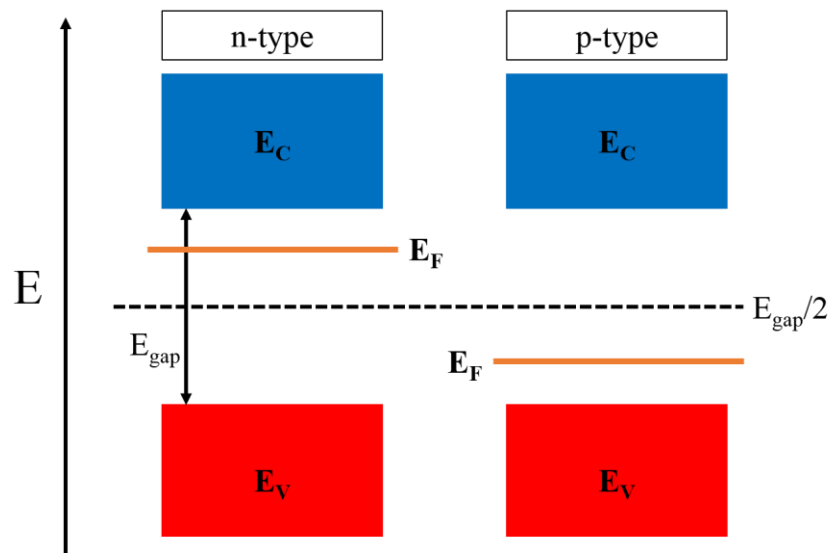


Figure 2.1.4.4. Energy diagram for n-type and p-type semiconductor.

2.1.5 Free electron and Kronig-Penney model

To explain the appearance of the bandgaps in a band diagram, we must first describe the free electron model.^{8,9,17} To simplify the model we will assume a 1D system.

Starting with the time independent Schrödinger equation:

$$\frac{-\hbar^2}{2m} \frac{d^2\Psi(x)}{dx^2} + V(x)\Psi(x) = E\Psi(x)$$

A metal of length L, for $0 < x < L$ we have $V(x) = 0$, outside the metal $V(x) = \infty$ (infinite well). This is model makes sense since in section 2.1.2 we explained why a metal has a sea of delocalized electrons. The equation simplifies and becomes:

$$\begin{aligned} \frac{-\hbar^2}{2m} \frac{d^2\Psi(x)}{dx^2} &= E\Psi(x) \\ \frac{d^2\Psi(x)}{dx^2} + \frac{2mE}{\hbar^2} \Psi(x) &= 0 \\ \frac{d^2\Psi(x)}{dx^2} + k^2\Psi(x) &= 0 \end{aligned}$$

Solving this equation gives a traveling wave, $\Psi(x) = A_+e^{ikx} + A_-e^{-ikx}$. The energy is

$E = \frac{\hbar^2 k^2}{2m}$ and yields a parabolic E vs K, this is the solution to the free electron model. The

metal has a length L and sets the boundary conditions $\Psi(0) = \Psi(L) = 0$ to our wave

function. Solving gives restrictions on k, where $k = \frac{n\pi}{L}$ and yields the solution

$\Psi_n(x) = \sqrt{\frac{2}{L}} \sin\left(\frac{n\pi x}{L}\right)$ where $n = 1, 2, 3, \text{ etc.}$ Therefore $E_n = \frac{\hbar^2 n^2 \pi^2}{2mL^2}$ giving us discrete

energy levels. L (10^{-3} m) is large compared to the lattice spacing a (10^{-10} m), when plotting E vs k on a small scale such as $n\pi/a$, the discrete states for a free electron will look like a solid line.

In semiconductors there is no sea of electrons and the electrons “feel” the coulombic potential of the lattice $V(x)$. The potential $V(x)$ is caused by ions in the periodic structure of the crystal creating an electromagnetic field, therefore the electrons are subject to a regular potential inside the lattice and $V(x) \neq 0$.^{8,9,17} This coulombic potential of the lattice is the reason behind the gap opening. The Kronig-Penney (KP) model demonstrates that a simple one-dimensional periodic potential yields energy bands as well as energy bandgaps.^{8,9,17,19} An illustration of the KP periodic potential can be found in figure 2.1.5.1.

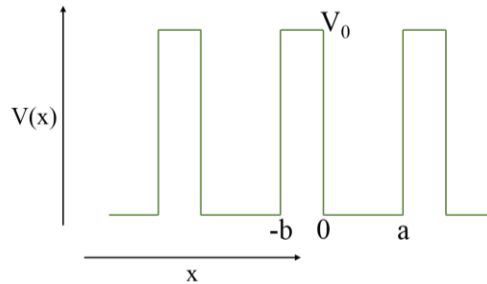


Figure 2.1.5.1. The Kronig-Penney model.

For simplified use, the potential barrier is a delta function with area $V_0 b$ at $x=a$ and repeated with a period of a . Details solving the KP model can be found in the reference.¹⁹ As b tends to 0 we obtain the following solution:

$$\cos(ka) = P \frac{\sin(\beta a)}{\beta a} + \cos(\beta a) , \text{ with } \beta = \frac{\sqrt{2mE}}{\hbar} \text{ and } P = \frac{mV_0 b a}{\hbar^2}$$

Solving this equation numerically gives an $E(k)$ relation that resembles a parabola except only specific ranges of energies are valid solutions and therefore allowed states,

while others are not (figure 2.1.5.2 red curve). If we set $V(x) = 0$, we obtain our parabolic free electron model described above (figure 2.1.5.2 green curve). The effect of the periodic barriers has led to gaps in the energy spectrum where the traveling wave has become a standing wave. The values for the plot in figure 2.1.5.2 were found using an available software from reference.²⁰

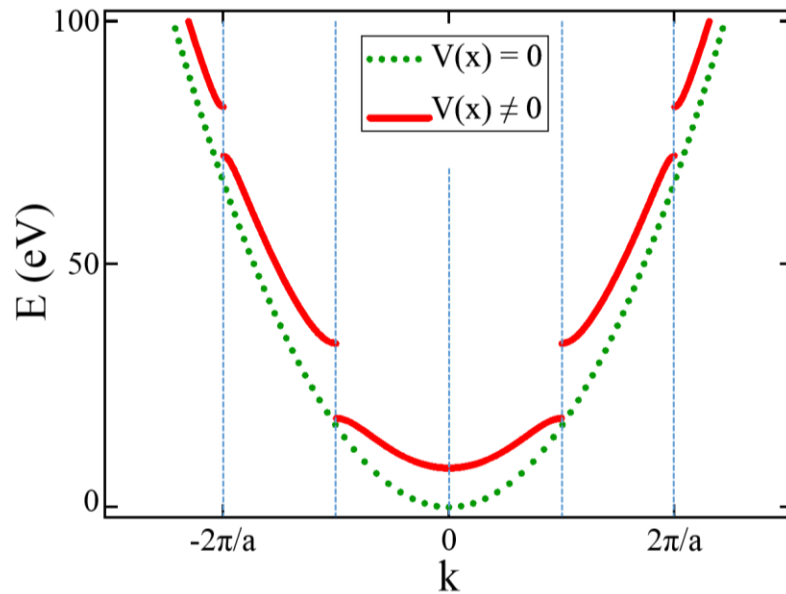


Figure 2.1.5.2. Solution to the Kronig-Penney (KP) and free electron model, plotted in extended zone scheme for entire reciprocal lattice.

An alternate way to think about the opening of the bandgaps, is in term of Bragg planes and diffraction. Bragg planes originates from the reciprocal lattice and represents the periodicity of the structure (similar to our periodic potential in the KP model).^{8,9} The Fourier transform in direct space of a lattice yields the reciprocal lattice and provides information with the periodicity of the structure in reciprocal unit. A 1D lattice of spacing a in direct space becomes $1/a$ in reciprocal space, and in k space becomes $2\pi/a$. The reciprocal lattice vector occurs by interval of $2\pi/a$ from the choice of origin. A Bragg plane is the perpendicular bisector to a valid reciprocal lattice vector.^{8,9} The

perpendicular bisector to our reciprocal lattice vector will occur at intervals of π/a . In our k space energy spectrum we insert Bragg plane lines at intervals of π/a (dashed blue line in Figure 2.1.5.2). When a free electron (green curve in figure 2.1.5.2) touches a Bragg plane line, conditions for diffraction are satisfied and diffraction will occur.^{8,9} At the intersection, the traveling wave becomes a standing wave and this is forbidden due to Bloch theorem.^{8,9} Consequently the k value corresponding to the standing wave is prohibited. E vs k will get distorted near the diffraction condition and forbidden values will occur at the Bragg lines, yielding the red curve in figure 2.1.5.2. Using Bragg planes is an alternative way to visualize the band openings.

Figure 2.1.5.2 reveals the opening of gaps in the energy diagram, however there are other ways of representing this plot. The choice of origin was selected for our convenience and is somewhat arbitrary, so therefore we can select the reciprocal lattice point $2\pi/a$ as our origin. Shifting the plot by $\pm n2\pi/a$, the curves will build giving us a repeated zone scheme, figure 2.1.5.3a.

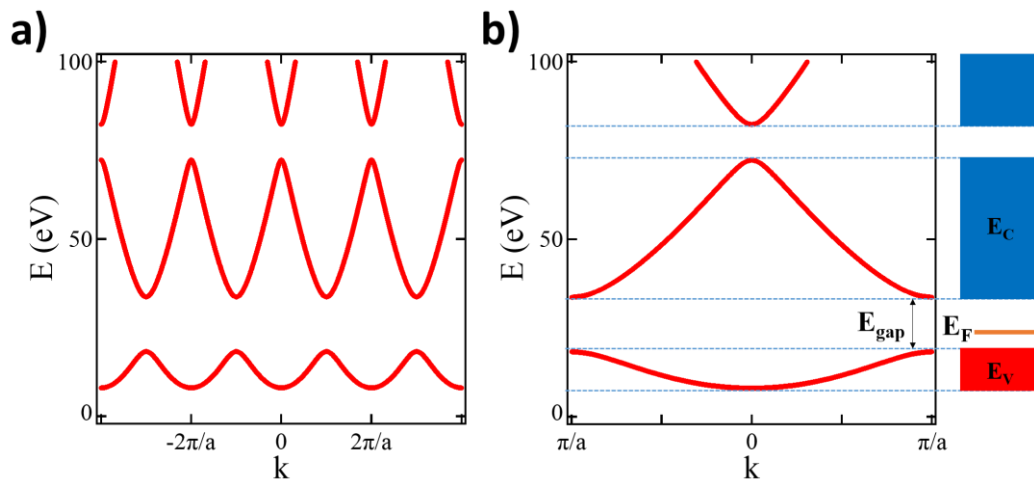


Figure 2.1.5.3. Repeated zone scheme. a) Reciprocal lattice. b) First Brillouin zone.

If we look solely at the region described as the first Brillouin zone. The Brillouin zone is a defined cell in the reciprocal space, it represents a region in space that you can access without crossing a single Bragg plane.^{8,9} The first Brillouin zone is defined from $-\pi/a$ to $+\pi/a$, the second Brillouin zone is defined from $-2\pi/a$ to $-\pi/a$ and π/a to $2\pi/a$. If we plot the energy diagram for the first Brillouin zone we obtain figure 2.1.5.3b and all the information in the repeated zone scheme is now present in the first Brillouin zone due to symmetry. All the conclusions made from inspecting the first Brillouin zone will actually be representative of the conclusion across the entire lattice in a periodic structure. This image can be drawn in terms of block diagram similar to section 2.1.4. As described in section 2.1.4, categorizing the material is dependent on the position of the fermi level (E_F). If the energy gap (E_{gap}) is small and E_F is located in the gap, this defines a semiconductor. If the E_{gap} is big we will have an insulator. No gap (free electron model) or large doping that results in E_F located in the band would yield a metal.

The most important consequence of the periodic potential is the formation of small bandgap at the boundary of the Brillouin zone.

Reducing material dimensions (L_x , L_y , L_z) to small length scales gives rise to novel chemical and physical material properties. The key differences between bulk and a 0D is the quenching of the band diagram and yielding fewer energy levels (figure 2.1.5.4). A direct example for this is the semiconductor molybdenum disulfide (MoS_2) that will be described in Chapter IV, in bulk form (3D) MoS_2 has a bandgap of 1.2 eV whereas in monolayer form (2D) it is 1.8 eV.²¹

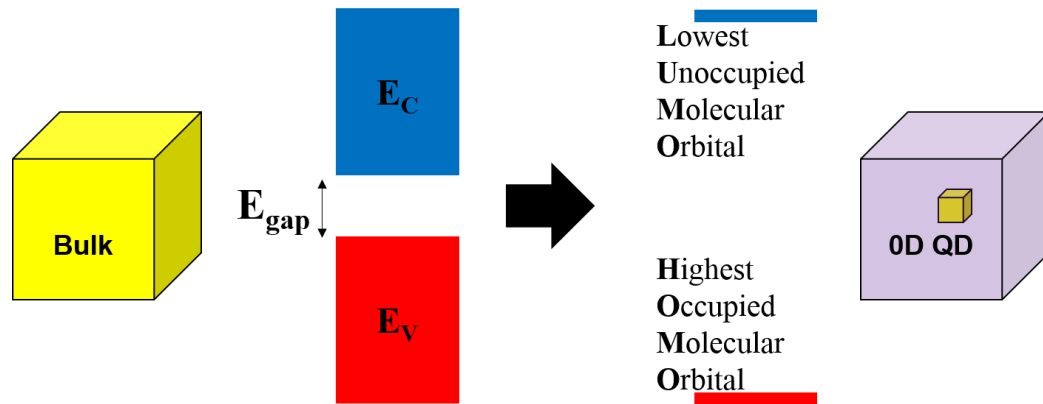


Figure 2.1.5.4. Band diagram for a bulk semiconductor to a 0D quantum dot semiconductor. (Figure was modified from Professor Cherie Kagan ESE525 lecture).

This confining is illustrated in the density of states (DOS) of a material, the DOS changes with dimensionality (figure 2.1.5.5). The DOS of a system describes the number of states per interval of energy, at each energy level, that are available to be occupied.^{8,9}

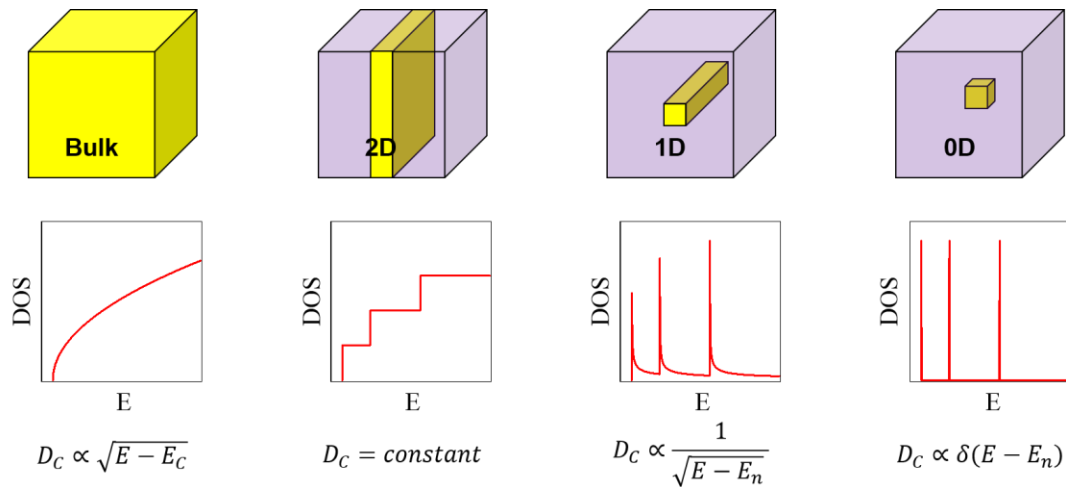


Figure 2.1.5.5. Variation of density of states as dimensionality of the system is reduced. (Figure was modified from Professor Cherie Kagan ESE525 lecture).

The DOS explains why novel physics appear when one shrinks the dimensions of a system. You modify the energy diagram of a material, confine the electrons with physical barriers, and have direct influence on the charge carriers in the system that contribute to the electrical conductivity.

2.2 “Traditional” monolayer materials

2.2.1 Graphene

Fundamental properties of graphene

The term graphene was first used in 1987 to describe one sheet of graphite.²² Graphene is a two dimensional allotrope of carbon atoms tightly packed in a hexagon network (figure 2.2.1.1).²³ Each hexagon is made of 6 carbon atoms, referred to as a honeycomb lattice. Each carbon atom in the honeycomb lattice has four bonds, one σ -bond with each of its three carbon neighbors (separated by a length $a = 1.42 \text{ \AA}$ and an angle of 120°) and one π -bond that is oriented out-of-plane.²³ The σ -bond is made of a combination of hybridized orbitals ($2s$, $2p_x$ and $2p_y$) or sp^2 .²³ The π -bond refers to the remaining p_z orbital and determines the low-energy electronic structure of graphene.²³ The unit cell of graphene (figure 2.2.1.1) contains two carbon atoms referred to A and B. The basis vectors of the unit cell are written as:

$$a_1 = a \left(-\left(1 + \cos\left(\frac{\pi}{3}\right)\right), \sin\left(\frac{\pi}{3}\right) \right) \quad a_2 = a \left(1 + \cos\left(\frac{\pi}{3}\right), \sin\left(\frac{\pi}{3}\right) \right)$$

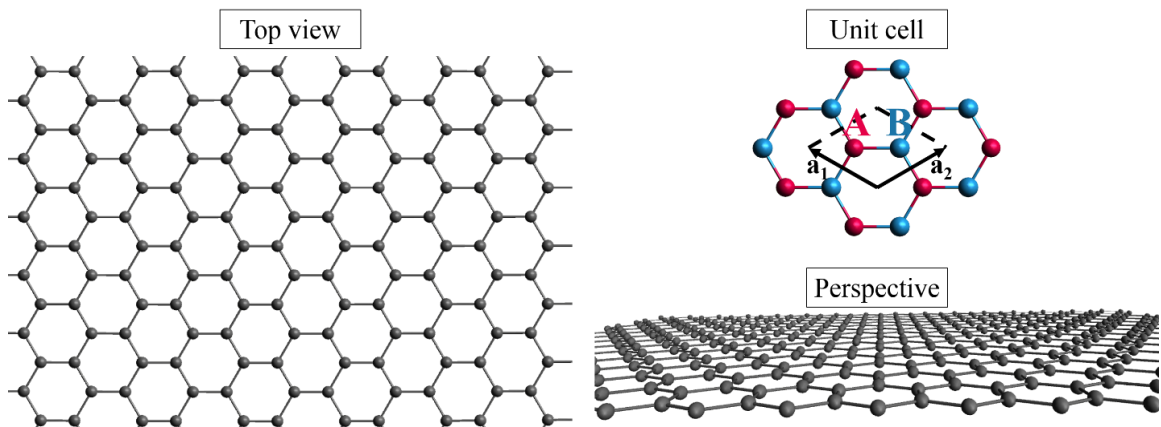


Figure 2.2.1.1. Graphene.

When sheets of graphene are stacked together forming bi-layer, tri-layer or few layer graphene and are electronically coupled, we refer to the stacking order in terms of the A and B atoms.²⁴ As shown in figure 2.2.1.2, when the A of the first layer is aligned with the B atom of the second layer we refer to it as AB stacking. If a third layer is stacked on top of an AB stacking there are multiple configurations possible. Most common stacking of tri-layer graphene are: the A atom of the third layer aligns with the AB atoms creating an ABA stacking (Bernal-stacking),²⁴ or the center of the honeycomb lattice of the third layer aligns with AB atoms making an ABC stacking (rhombohedral-stacking)²⁴ figure 2.2.1.2. The layers are held together by a weak van der Waals forces.¹⁵

The layer number and quality of graphene can be estimated by Raman (section 3.2.2) and three terminal measurements (section 3.2.4). Raman will provide us with a vibrational fingerprint of our material, whereas the three terminal measurement will give us valuable information on the charge carrier mobility.

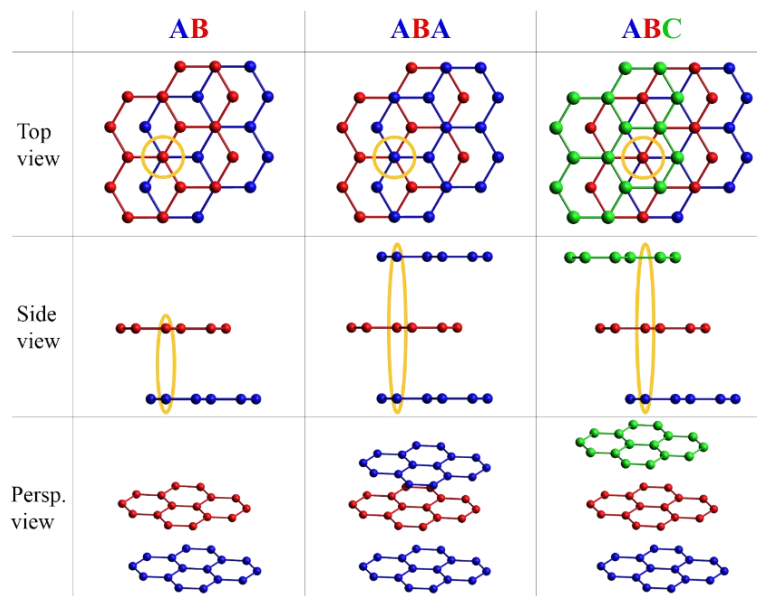


Figure 2.2.1.2. Graphene stacking arrangements.

Graphene was first isolated in 2004 by Andre Geim and Konstantin Novoselov at the University of Manchester using mechanical exfoliation (please see section 3.1 for more details regarding mechanical exfoliation).²⁵ Their work complimented theoretical descriptions of its composition, structure, and properties. Scientists are now able to synthesis large area of high quality graphene by chemical vapor deposition (CVD) (please see section 3.1 for details), which has enabled extended studies on this fascinating material.²⁶ Graphene is reported to be the strongest material ever tested with an intrinsic tensile strength of 130 GPa and a Young's modulus (stiffness) of 1 TPa ($1.5 \cdot 10^8$ psi).^{1,2} Graphene maintains excellent carrier mobility when being deformed showing mechanical robustness that makes it ideal for flexible devices (see section 4.2.4 where graphene was incorporated onto a flexible substrate).²⁷ Graphene is biocompatible and possesses a high surface to volume ratio due to its monolayer form, making it an effective biosensor.³ It has unique electrical properties that will be discussed in the following section.

Electrical properties of graphene

As discussed in the previous section, graphene possesses a honeycomb lattice carbon network.²³ The carbon atoms in the lattice are held together by σ -bonds, however each carbon atom also possesses a π -bond that is oriented out-of-plane.²³ This p_z orbital or “ π ” orbital determines the low energy state of graphene. Each unit cell has 2 carbon atoms (as described in figure 2.2.1.1) and therefore has 2 π -bonds. The π -bonds hybridize together to form the π -band and π^* -bands.²³ These bands are responsible for most of graphene's notable electronic properties and can be thought of as bonding (the lower energy valence band E_V) and anti-bonding (the higher energy conduction band E_C) in our

semiconductor illustration in section 2.1.4. The gap between the bonding (E_V) and anti-bonding (E_C) closes at the corners of the Brillouin zone, or K points (see figure 2.2.1.3a).^{4,28,29} This is why graphene is referred to as a zero bandgap semiconductor. The pi-band dispersion are approximately linear at the K point (also referred to as the Dirac point), instead of the typical parabolic bands for a semiconductor,^{4,28,29}

$$E = \hbar * v_F * |k|$$

where \hbar is Planck's constant h divided by 2π , v_F is the Fermi velocity in graphene (measured at approximately 10^6 ms^{-1} , 300 times smaller than the speed of light), and k is the wave vector measured at the K point (figure 2.2.1.3b). A linear dispersion describes a particle with a kinetic energy vastly exceeding their rest mass energy (e.g. photons, neutrinos). Graphene owes its remarkable electron mobility (higher than any other measured material to date) to the quasi-massless nature of the charge carriers.^{4,28,29} For comparison, carrier mobility of various materials are shown in figure 2.2.1.3c. Suspended graphene has a mobility recorded up to $10^6 \text{ cm}^2\text{V}^{-1}\text{s}^{-1}$.^{30,31} Extrinsic carrier scattering by substrate phonons limits graphene's room temperature mobility to $20,000 \text{ cm}^2\text{V}^{-1}\text{s}^{-1}$.^{32,33} On average, CVD grown graphene exhibits a mobility of about $10^5 \text{ cm}^2\text{V}^{-1}\text{s}^{-1}$.

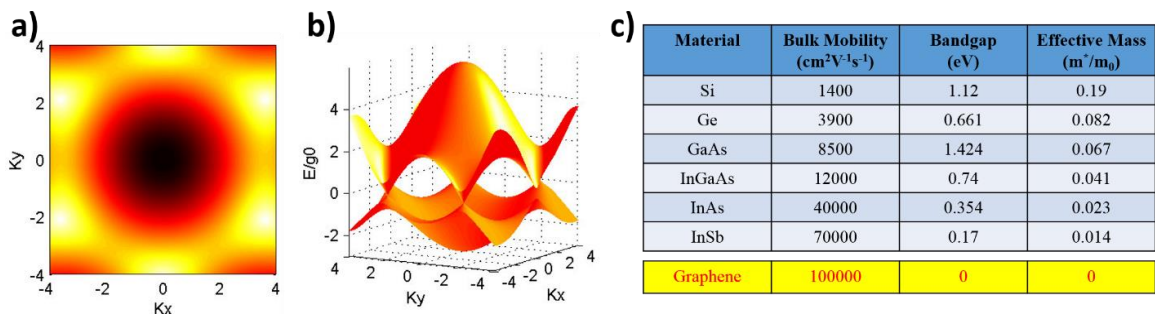


Figure 2.2.1.3. Band structure of graphene. a) The graphene Brillouin zone. Six points where the conduction and valence bands meet, the K and K' points are indicated in white. b) Linear dependence of the electron energy at the K and K' points. c) Mobility values of various materials.

In summary, graphene is a zero gap semiconductor, with a linear E vs k (unlike traditional 2D electron system which have parabolic bands) and charge carriers with zero effective mass. It has tremendous electrical properties that make it very promising for next generation devices. However graphene's lack of a bandgap is the reason scientists are exploring the field "beyond graphene" at rapid pace (figure 2.2.1.4).³⁴⁻⁴⁵ The bandgap is essential for on/off state in a transistor. The bandgap is also vital for the emission or absorption of light. A true 2D semiconductor would have high on/off ratio, reasonable values of mobility and large photoluminescence.

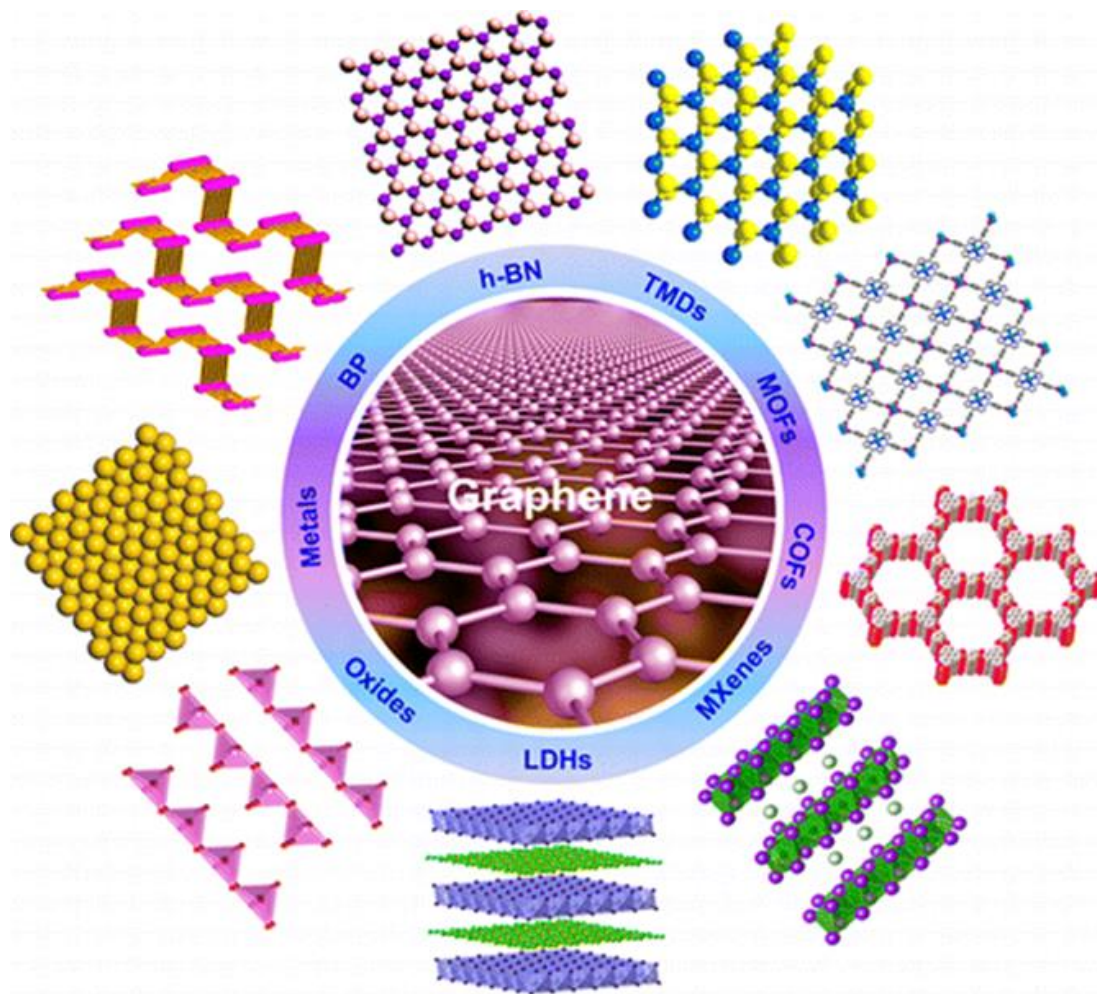


Figure 2.2.1.4. Beyond graphene.⁴⁵

2.2.2 Hexagonal boron nitride

Hexagonal boron nitride (hBN) possess a honeycomb lattice similar to that of graphene, however instead of carbon atoms it is made of alternating boron and nitrogen atoms (figure 2.2.2.1).⁴⁶ The boron and nitrogen atoms are tightly held together by covalent bonds and the layers are held together by a weak van der Waals force.⁴⁶ hBN can be produced in bulk form similar to graphite and reduced down to monolayer using mechanical exfoliation (details regarding mechanical exfoliation can be found in section 3.1). Scientists are currently trying to synthesis monolayer hBN by CVD, however the quality is still lacking (please see section 4.2.3 about our CVD growth process for hBN). The lattice constant of hBN is 2.5 \AA ,⁴⁷ approximately 1.7% larger than that of graphene. It is a well-known insulator, referring back to section 2.1.4, indicating that it possesses a large bandgap that doesn't permit the current flow of the charge carriers. hBN owes its 5.2 eV bandgap⁴⁶ to the different onsite energies of the boron and nitrogen atoms.

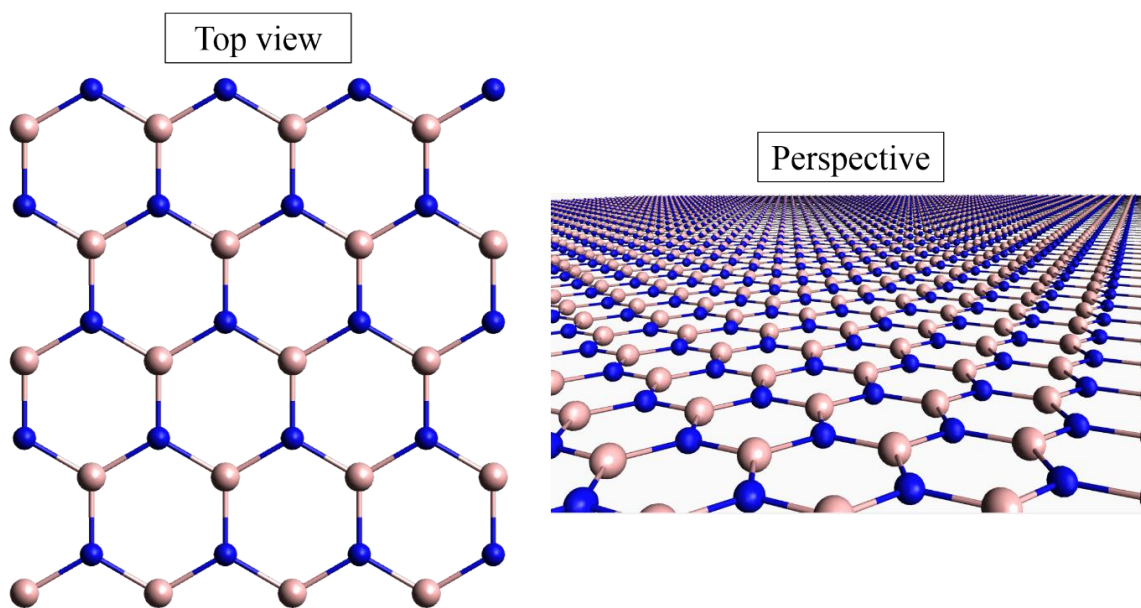


Figure 2.2.2.1. Ball and stick model of hBN.

Due to its large bandgap, hBN is commonly used as a passivation material. hBN is relatively inert due to the somewhat ionic in-plane bonding, and should be free of dangling bonds and surface charge traps.⁴⁸⁻⁵¹ hBN deposited on top of any given material will passivate it from the environment. Because of its insulating properties, hBN will have no ill effect on the electrical properties of the underlying material. In fact, the electrical properties of a material capped by hBN will yield higher results as the material is no longer subject to degradation or reactions with O₂ and H₂O molecules.

With a lattice similar to that of graphene, hBN is known to complement graphene very well. As discussed in the previous section 2.2.1, suspended graphene has a mobility recorded at 10⁶ cm²V⁻¹s⁻¹.^{30,31} However due to the extrinsic carrier scattering by the substrate phonons, graphene's room temperature mobility is measured at 20,000 cm²V⁻¹s⁻¹. By utilizing hBN as the substrate instead of the traditional SiO₂, the mobility values of the graphene are reported at 60,000 cm²V⁻¹s⁻¹, which is three times higher than on SiO₂.³³ Because of the honeycomb lattice and overall structure configuration similarity, the surface chemistry between hBN and graphene are comparable. A pi-pi stacking chemistry enables direct functionalization of the surface of graphene or hBN. Details of the surface chemistry of hBN can be found in the section 4.2.3 with a direct application towards a "universal biosensor".

Its large bandgap and its high complementarity to other 2D materials (e.g. graphene) is why hBN has been extensively exfoliated and studied.^{33,48,52,53} However there is a real need for large area synthesis of high quality monolayer hBN to enable further studies and incorporate hBN into future technologies.

2.3 Beyond graphene: transition metal dichalcogenides

2.3.1 Overview of transition metal dichalcogenides

Transition metal dichalcogenides (TMDs) are an extremely promising class of materials in the field “beyond graphene”. TMDs, also referred to as MX_2 materials, are made of metal atoms (M) sandwiched on either side by chalcogen atoms (X). The properties of the MX_2 material are dependent on the choice of metal, chalcogen atom and the atomic configuration.^{35–37,42,44} Figure 2.3.1.1 is an artistic representation of a monolayer MX_2 under a 1H atomic configuration, the metal atoms are colored in turquoise and the chalcogen atoms in yellow. Layers of monolayer MX_2 can be stacked to form bulk MX_2 . The height of monolayer MX_2 is approximately 6-7 Å and can be recorded by atomic force microscopy (AFM) (please see section 3.2.1 regarding details on AFM measurements).

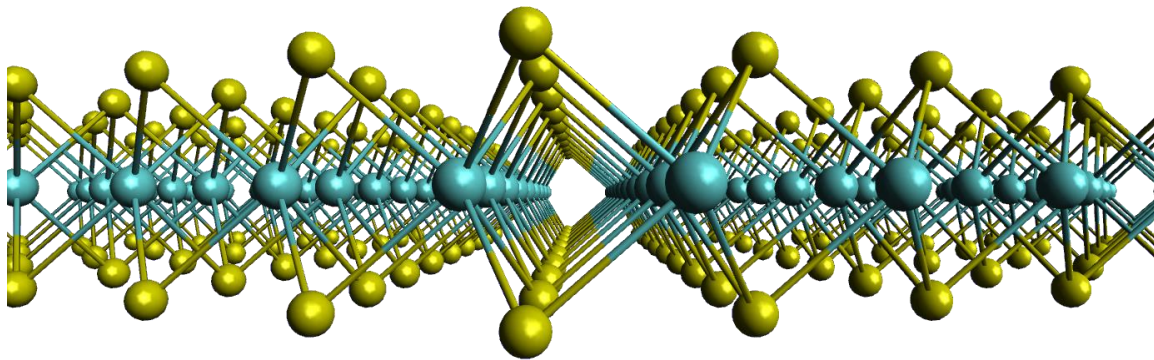
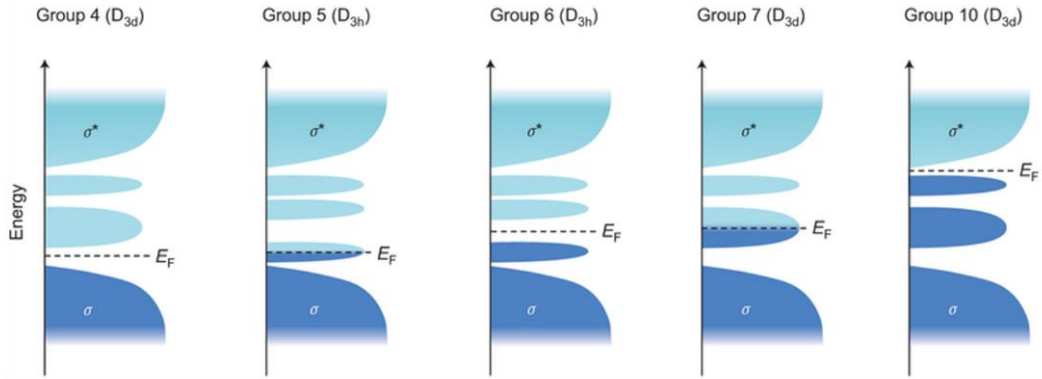


Figure 2.3.1.1. Ball and stick model of a monolayer MX_2 material under a 1H atomic configuration.

Each metal atom in the MX_2 coordinate covalently bonds to 6 chalcogen atoms (3 on either side), and each chalcogen atom bonds respectively to 3 metal atoms. Consider the example of molybdenum disulfide (MoS_2). The electronic configuration of sulfur (S)

is [Ne] $3s^2 3p^4$ and molybdenum (Mo) is [Kr] $4d^5 5s^1$, therefore they each have 6 electrons that can contribute to the binding. The Mo will donate 2 electrons to each of 2 S atoms, becoming Mo^{4+} (2 electrons left) sandwiched in between 2 S^{-2} (S now has 8 electrons and a noble gas configuration). Each S will bind to 3 molybdenum atoms by coordinate covalent bonds using 6 of the 8 available electrons and enable a stable MoS_2 structure (please see section 2.1.2 on information regarding coordinate covalent bonds). This attachment will leave a pair of electrons on the outer of shell of the S atom. This electron pair can be utilized for the surface functionalization of MoS_2 . In section 4.2.1 we will use this electron pair for coordinate covalent bonding to Ni^{2+} that enables the creation of a MoS_2 biosensor.

In a similar story to graphite that was used as pencil lead for many years prior to the discovery of graphene, bulk TMDs have been extensively used as a lubricant for engines due to the weak van der Waals interaction between each MX_2 layer resulting in low friction properties and robustness.⁵⁴ In the monolayer form however, 2D MX_2 exhibit numerous fascinating properties such as a semiconductor, topological insulator, and many more.^{37,41,55–66} In contrast to graphene that possess a set of defined properties, with TMDs we have access to a whole library of properties that can be chosen depending on your choice of metal and chalcogen atom from the periodic table. A periodic table can be found in figure 2.3.1.2, the metal atoms have been highlighted in various colors depending on their group (blue, green, red, yellow and purple), whereas the chalcogen atom are in orange.



Transition metal	Chalcogen	Electrical/Magnetic properties (MX ₂)
Ti, Hf, Zr	S, Se, Te	Semiconducting. Diamagnetic
V, Nb, Ta	S, Se, Te	Narrow band metals or semimetals, superconducting.
Mo, W	S, Se, Te	S, Se: semiconducting. Te: semimetallic
Tc, Re	S, Se, Te	Small-gap semiconductor
Pd, Pt	S, Se, Te	S, Se: semiconducting. Te: metallic

Figure 2.3.1.3. D band filling of different TMD groups and summary of the electrical properties.³⁵

Mo or W combined with S or Se will make semiconductors whereas with Te it will make semimetals (however we will discover that these properties can be altered by modifying the atomic configuration). This group of MX₂ materials are very interesting in the academic and industrial setting. The semiconducting MX₂ materials have good electronic properties and exhibit countless other features such as tunable bandgap and high photoluminescence.^{21,34–45,57,64} The semiconductor industry is very attracted to the semiconducting TMDs as they search for an alternative to silicon (Si) in their transistor devices. Large corporations such as Intel work on reducing the size of the Si MOSFET (see section 3.2.4 on details regarding MOSFET), however the scaling limits are caused by materials and device structure rather than hard quantum limits. The Si layer becomes difficult to uniformly dope when the dimensions are reduced below 20 nanometers, there is also leakage from neighboring devices. Therefore there is a real need to find an

alternative to Si and monolayer semiconducting TMDs are a potential candidate. For these multiple reasons, semiconducting MX_2 materials have become a highly explored material since the first semiconducting MX_2 flake was mechanically exfoliated to the monolayer form a couple years ago (please see section 3.1 regarding details on mechanical exfoliation). Scientists are currently trying to synthesis high quality monolayer semiconducting MX_2 flakes by chemical vapor deposition (CVD) (please see section 3.1 regarding details on CVD method). In order to estimate the quality of the CVD grown semiconducting TMD, three terminal measurements are performed to study and characterize their electrical properties (please see section 3.2.4 regarding details on three terminal measurement).

Scientists have recently discovered that alternating the atomic configuration of the MX_2 will alter the electronic properties of the TMDs,^{61,67-71} this technique is known as a phase transformation. There are three possible atomic configurations (three phases) for monolayer MX_2 : the 1H, 1T and 1T'. Figure 2.3.1.4 shows a ball and stick model revealing each configuration. Aberration correct transmission electron microscopy (ACTEM) as well as Raman spectroscopy is the characterization technique utilized in identifying the atomic configuration (please see section 3.2.2 and 3.2.3 regarding details on ACTEM and Raman). We will now refer to monolayer MX_2 materials as 1H- MX_2 , 1T- MX_2 and 1T'- MX_2 depending on which atomic configuration they are in. In the bulk or multilayer they will be referred to as 2H- MX_2 . The following sections will highlight the key differences between each phase.

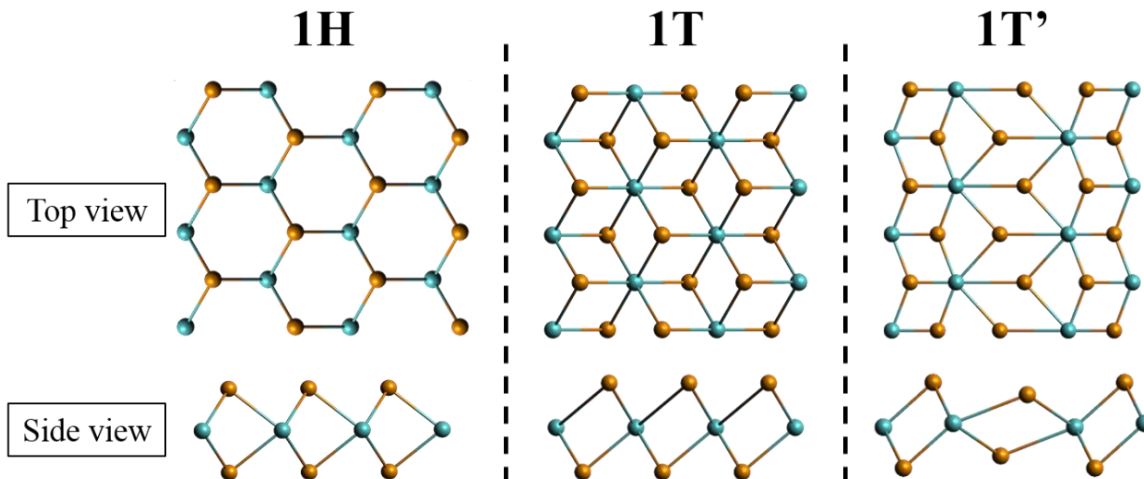


Figure 2.3.1.4. Ball and stick model of the 1H, 1T and 1T' phase of TMDs.

There is a real need for synthesizing large area, high quality, monolayer MX_2 flakes in various phases. Throughout this thesis, I will highlight our growth results by CVD of monolayer TMDs in different atomic configurations. I will discuss some of the intriguing phenomena occurring within these TMDs as well as potential applications such as biosensing. Some of these atomic configurations, such as the 1T', were believed to be unstable and unachievable in the monolayer form. However we were able to synthesis the first monolayer 1T' flakes and perform characterizations on this unique phase.^{58,59}

With the wide set of different metal and chalcogen atoms that form a TMD, coupled with the 3 possible atomic configurations, yield a tremendous amount of MX_2 combinations all with their unique properties. TMDs have a potential broad impact in various applications such as the semiconductor industry, quantum computing, water filtration, energy storage, solar cells, light emission diodes, piezoelectric, and many more.^{44,72-75} TMDs truly are a leading candidate in the field “beyond graphene”, and scientists are only just discovering some of the countless properties TMDs have to offer.

2.3.2 The 1H phase

The 1H phase of MX_2 materials is the most studied to date. A schematic of the atomic configuration can be found in figure 2.3.2.1. In the 1H configuration, the metal and chalcogen atoms are alternating and arranged in a honeycomb like structure (top view), however they are not on the same plane unlike graphene and hBN (side view). In 1H- MX_2 the chalcogen atoms are aligned, so viewed from above the underlying chalcogen atom is hidden. The 1H phase is the most common atomic configuration in the MX_2 materials, it is the configuration predominant in the family of semiconducting MX_2 .

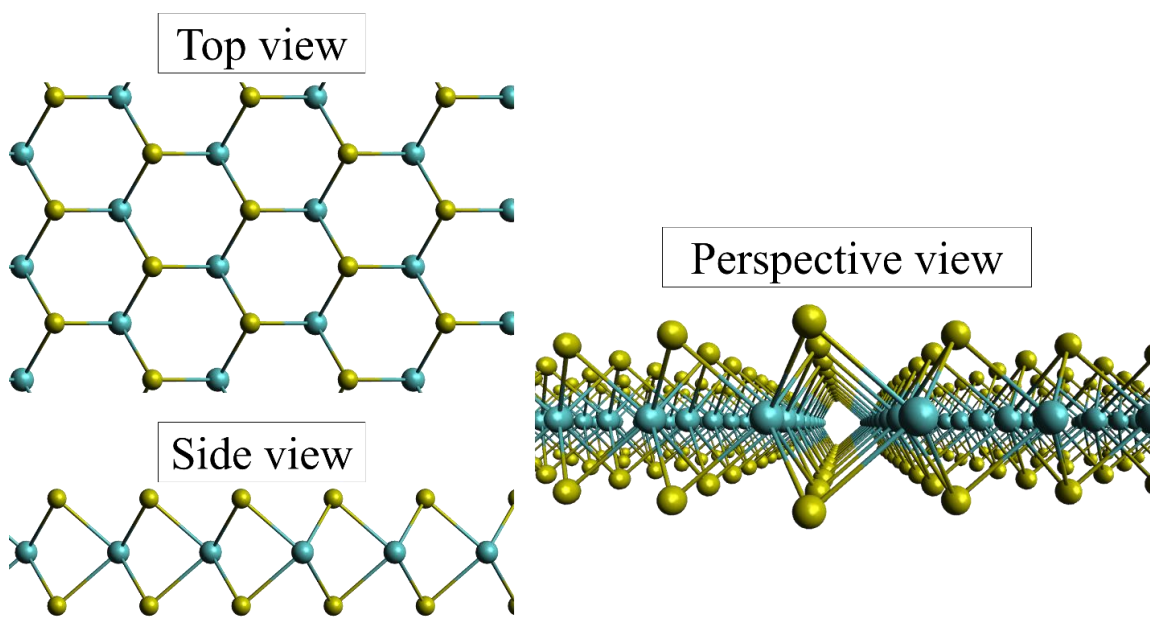


Figure 2.3.2.1. Ball and stick mode of 1H- MX_2 .

To differentiate a 1H- MX_2 material from another, we rely on Raman spectroscopy (please see section 3.2.2 regarding Raman spectroscopy and more details on its operation). Raman spectroscopy provides us with a vibrational fingerprint of our material; it is a rapid way to characterize the 1H- MX_2 material. 1H- MX_2 possess many

phonon vibration modes, however 2 are dominant and are used to identify the layer number and the elements: the E_{2g}^1 and A_g^1 peak (figure 2.3.2.2). Each 1H-MX₂ will have different positions for the E_{2g}^1 and A_g^1 peak as each metal or chalcogen will have different atomic size which will translate into the phonon vibration. If we have multiple layers (2H-MX₂) this will move the position of the peaks, the E_{2g}^1 will redshift and A_g^1 peak will blueshift (stiffening).^{21,76-78} Strain and doping can also effect the position of the peaks (please see section 6.3 regarding doping of 1H-MX₂).^{79,80} The Raman intensity and peak position is dependent on the layer number and elements present. Raman can serve as a credible tool for characterizing the 1H-MX₂ material.

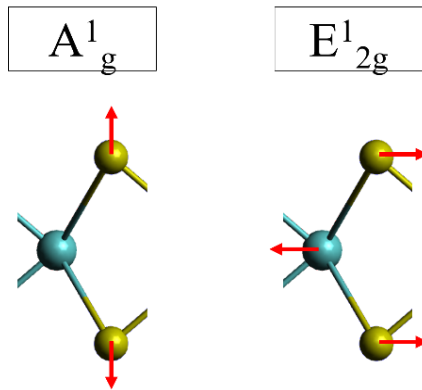


Figure 2.3.2.2. A_g^1 and E_{2g}^1 vibrational modes for 1H-MX₂ materials.

1H-MX₂ possess a bandgap and are semiconductors, a quality that graphene lacks. The bandgaps are different for each 1H-MX₂ material but the energy values are located in the visible range. Figure 2.3.2.3 is inspired from reference⁸¹ and represents the calculated band diagram for each 1H-MX₂ combination. The calculations were performed with the Perdew-Burke-Ernzerhof and spin-orbit coupling (red line), including the GW corrected band edges (blue dashed line). As seen in the figure, the bandgap energies (E_{gap}) are different for each 1H-MX₂ combination. Please notice in figure 2.3.2.3 that 1H-MoTe₂

and 1H-WTe₂ are semiconductors in this 1H phase, in the previous figure 2.3.1.3 we claimed that they would be semimetals, this a clear indication that the electrical properties of the MX₂ materials can be altered with the atomic configuration. The table in figure 2.3.2.3 summarizes the energy gaps for the group 6 1H-MX₂ and 2H-MX₂, we notice that the E_{gap} changes from multilayer (2H) to monolayer (1H). This highlights an incredible quality of TMDs, they possess a tunable bandgap.^{21,41,63,82-84} The bandgap can be tuned when reducing the number of layers, this is due to the constrictions and changes happening in the energy diagram.

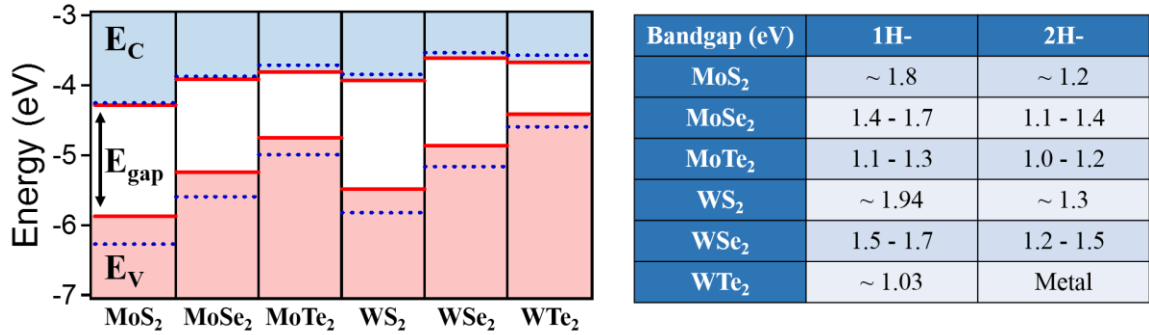


Figure 2.3.2.3. Band diagram of 1H-MX₂ and table summarizing the bandgaps for 1H and 2H-MX₂.

Figure 2.3.2.4a is the calculated energy diagram for 2H-MoS₂ in k-space as we reduce the layer numbers to monolayer (1H-MoS₂). Figure 2.3.2.4a was modified from a figure in reference.³⁷ In bulk (2H-MoS₂), the lowest energy level at the conduction band and the highest energy level in the valence band are not aligned, this is called an indirect bandgap. In monolayer (1H-MoS₂), the levels are aligned and we have a direct bandgap. The difference between a direct and indirect bandgap is highlighted in figure 2.3.2.4b. For a direct bandgap (1H-MoS₂), when an electron and hole pair (exciton) align they can recombine and emit a photon (hν) with an energy equal to E_{gap}. For an indirect bandgap

(2H-MoS₂), a phonon must be first emitted to align the electron and hole pair in k-space, then this is followed by the recombination and emission of a photon. The probability of a phonon followed by a photon is very low, therefore by changing the layer number we are tuning the bandgap and modulating the light emission. The exciton binding energy in MX₂ materials are very high which leads to intense photoluminescence. Another quality is that 1H-MX₂ materials have inequivalent valleys in the k-space electronic structure with an extra valley degree of freedom (figure 2.3.2.4a).^{56,85,86} This new degree of freedom can lead to new physics termed “valleytronics”, as manifested by polarized photoluminescence in monolayer 1H-MoS₂ and the valley Hall effect.^{56,85–89} These qualities makes 1H-MX₂ materials very attractive for optic applications and research.

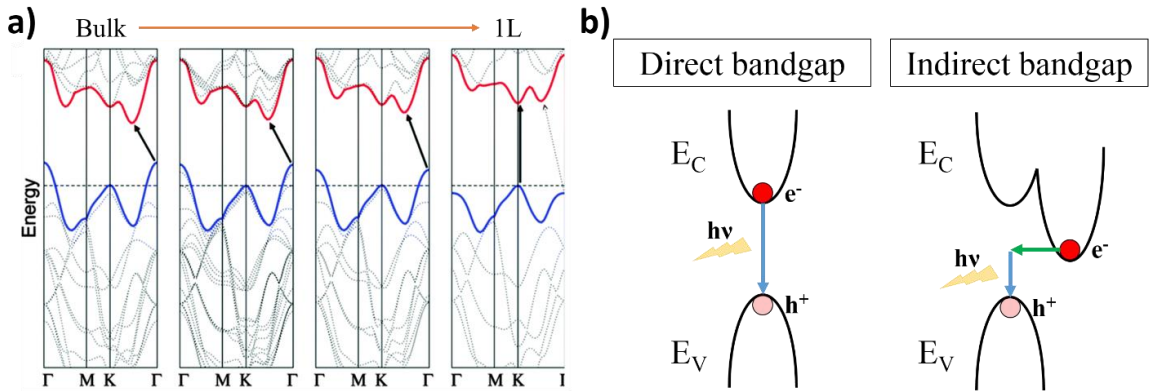


Figure 2.3.2.4. Tunable bandgap in 1H-MX₂. a) Changes in the energy diagram from 2H-MoS₂ to 1H-MoS₂.³⁷ b) Schematic of light emission process for direct and indirect bandgap.

The variety of bandgaps accessible with 1H-MX₂ materials is truly remarkable. The electronic properties of the semiconducting 1H-MX₂ is dependent on the position of the Fermi level (E_F). Please see section 2.1.4 regarding difference between n-type and p-type semiconductors. Most of the 1H-MX₂ are n-type semiconductors apart from 1H-WSe₂ the only known p-type semiconductor.^{90,91} The 1H-MX₂ have reasonable values of

mobility and high on/off ratio in MOSFET structure (see section 3.2.4 regarding MOSFET).^{41,62,92-94} The high value of these numbers are essential for the potential impact 1H-MX₂ can make in the semiconducting industry.

A potential application for monolayer 1H-MX₂ is biosensing. In the monolayer form 1H-MX₂ have high surface to volume ratio, therefore a large fraction of atoms are exposed on the materials surface and the charge carriers will be influenced by the chemistry on the surface (please see section 3.2.4.4 regarding local chemical gating effect). We were able to create a biosensor with 1H-MoS₂,⁷⁴ details regarding a scalable 1H-MoS₂ biosensor can be found in section 4.2.1.

In order to study 1H-MX₂ materials we need to achieve monolayer 1H-MX₂. Details regarding techniques used to obtain monolayer materials can be found in section 3.1. 1H-MX₂ materials were first mechanically exfoliated after graphene in 2004. However there is a real need for large area, monolayer and high quality 1H-MX₂ materials for industrial and educational research. This has led to a surge in the synthesis of 1H-MX₂ materials by chemical vapor deposition (CVD). To date, 1H-MoS₂ and 1H-WS₂ are the most synthesized and studied^{41,48,62,77,95} however there is a need to improve the quality of the synthesized material. 1H-MoSe₂ and 1H-WSe₂ are less common and still being explored. 1H-MoTe₂ and 1H-WTe₂ are only theoretically studied in the monolayer 1H phase. We will highlight in Chapter IV and Chapter V the high quality and large growth of our synthesized 1H-MoS₂, 1H-WS₂, 1H-MoSe₂ and 1H-WSe₂. The high quality of our synthesized material has led to numerous publications.^{74,96-111}

2.3.3 The 1T phase

A schematic of the 1T phase can be seen in figure 2.3.3.1. In the 1T phase, the top layer of chalcogen atoms have shifted with respect to the bottom, exposing all the chalcogen atoms (top view). This phase is very unique and phase transforming 1H-MX₂ materials into 1T-MX₂ material will alter the electric properties. For example, 1H-MoS₂ is a semiconductor whereas 1T-MoS₂ is a metal. Research groups are interested in heterostructures of 1H-MoS₂/1T-MoS₂ in order to study possible novel properties that would result from the combination of both phases. The 1T phase has been explored in TaS₂ and MoS₂. In this thesis I will discuss the group 6 metals, so for details on TaS₂ please see section 7.4. There are two known methods to induce a phase transformation from 1H-MoS₂ to 1T-MoS₂, by chemical treatment or by thermal annealing in an electron microscope with atom intercalation.^{69,70,112}

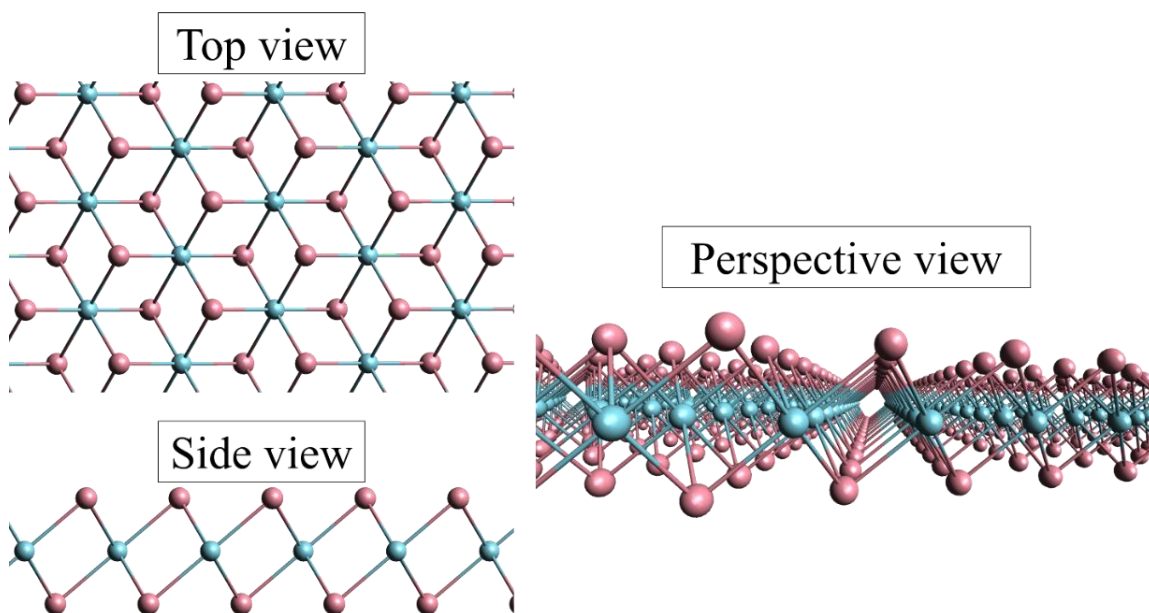


Figure 2.3.3.1. Ball and stick model of the 1T-MX₂.

Phase transformation of 1H-MoS₂ to 1T-MoS₂ induced by chemical treatment was first reported by Chhowalla *et al.* using an organolithium chemical method.^{69,70} By electron beam (e-beam) lithography, they expose the edges of a 1H-MoS₂ flake while the center of the flake remains passivated by an e-beam polymer. The flake is then inserted in n-butyllithium solution, only the edges of the flake will see the chemical as the center of the flake is protected. After several hours, the flake is retrieved and the unexposed PMMA is removed. Electrostatic force microscopy (EFM) phase image of a monolayer MoS₂ can be seen in figure 2.3.3.2. EFM is an alternative to atomic force microscopy (AFM) described in section 3.2.1, EFM will reveal regions of different electrical conductivity. In the EFM image, we clearly see two different regions highlighting the metallic 1T-MoS₂ and the semiconducting 1H-MoS₂. An aberration corrected transmission electron microscope (ACTEM) image can be seen in figure 2.3.3.2, ACTEM gives an atomic image of the boundary between the 1H-MoS₂ and 1T-MoS₂. This method is very effective in inducing a phase transformation from 1H to 1T, however n-butyllithium is pyrophoric which makes scalability of this technique an issue.

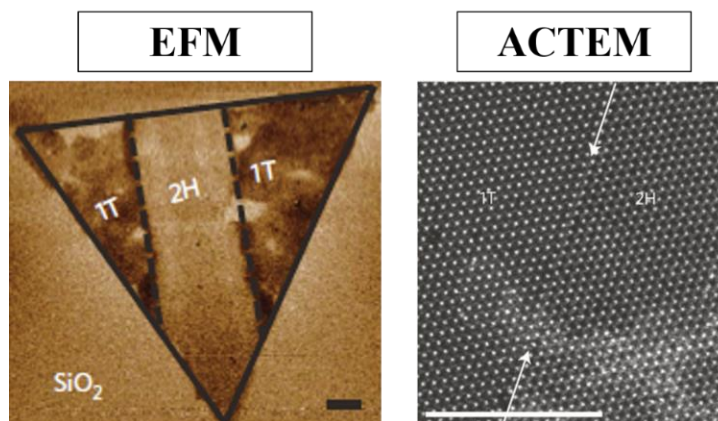


Figure 2.3.3.2. Electrostatic force microscopy phase image and high resolution transmission electron microscopy image of 1H-MoS₂ and 1T-MoS₂, scale bars are 1 μ m and 5 nm respectively.⁶⁹

An alternative approach to inducing a phase transformation is by Rhenium (Re) intercalation and thermal annealing.¹¹² A group has shown that by first doping a 1H-MoS₂ flake with Re, one induces Re defects in the 1H-MoS₂ crystal lattice figure 2.3.3.3a. The flake is inserted in an electron microscope and thermally annealed. The thermal activation energy can be reached to induce a phase transformation from 1H-MoS₂ to 1T-MoS₂ (figure 2.3.3.3abcd). Figure 2.3.3.3efgh is a simplified schematic illustration. Figure 2.3.3.3 was the first in-situ thermal activation of a phase transformation from 1H-MoS₂ to 1T-MoS₂.

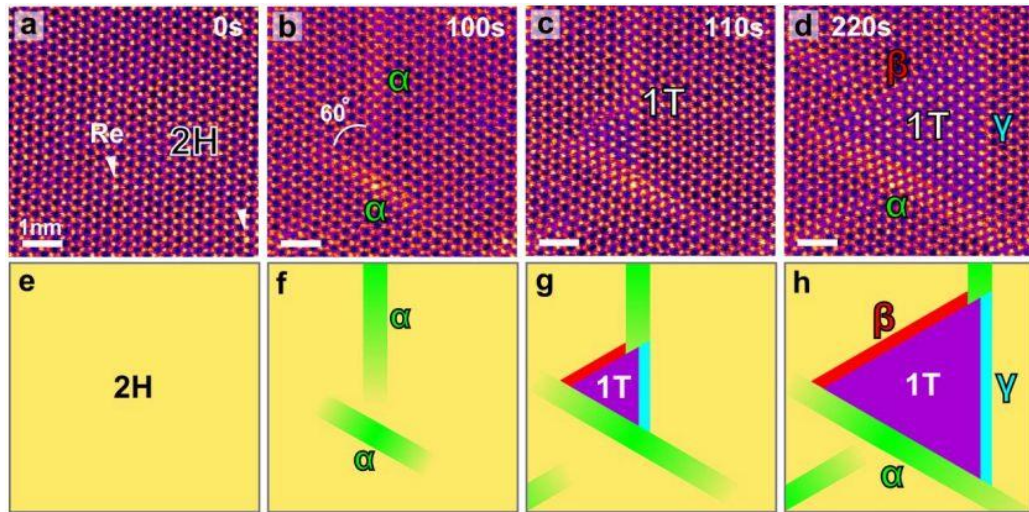


Figure 2.3.3.3. In-situ observation of phase transformation from 1H-MoS₂ to 1T-MoS₂.¹¹²

All the experiments presented were performed on mechanically exfoliated 1H-MoS₂, no group has reported the phase transformation of a CVD grown 1H-MoS₂ to 1T-MoS₂. Furthermore, no group has successfully synthesized by CVD a monolayer MX₂ in the 1T phase. This highlights the difficulty of synthesizing materials in an alternate phases than the traditional 1H phase.

2.3.4 The 1T' phase

A schematic of the 1T' phase can be found in figure 2.3.4.1. The 1T' phase is a distorted 1T phase. Starting from the 1T phase, if one strained the unit cell on either side, one would isolate a line of chalcogen atoms. The isolated chalcogen has been highlighted in red in the top view image of figure 2.3.4.1 and is the signature of 1T'-MX₂.⁶¹

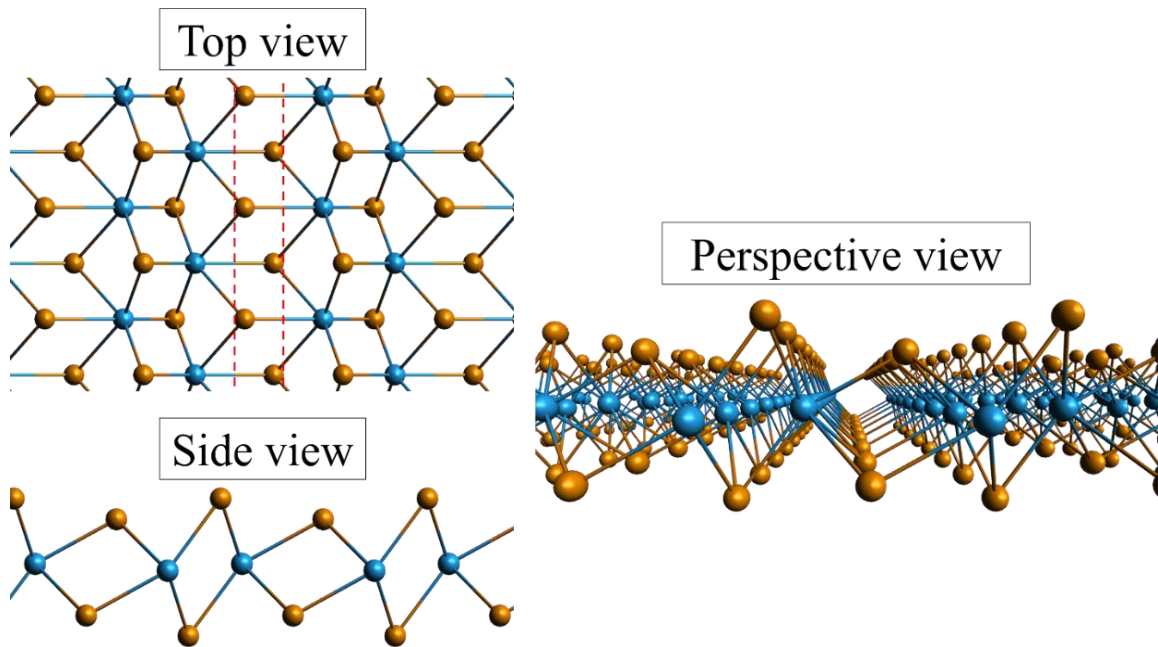


Figure 2.3.4.1. Ball and stick model of the 1T' phase.

Theoretically, the 1T' TMDs are fascinating and have been acclaimed the “holy grail” of materials. A groups has recently shown by first principle calculations that a quantum spin hall (QSH) effect is present in monolayer 1T'-MX₂.⁶¹ QSH insulators have an insulating bulk but conducting edge states that are topologically protected from backscattering by time-reversal symmetry.^{113–115} 1T'-MX₂ materials could therefore provide an alternative route to quantum electronic devices such as quantum computing. Figure 2.3.4.2a shows the theoretically predicted edge density of states, we can see that

the material is conducting at the edge because of the connection at the Γ point. Figure 2.3.4.2b is the theoretically predicated local density of states at Γ point as a function of distance away from the edge (L_y). A sharp peak is present in the bandgap at the edge of the flake and decays at a length of ~ 5 nm away from the edge. Indicating that $1T'$ - MX_2 will conduct along the edges of the flake but not in the center. Theoretical predictions also highlight that $1T'$ - MX_2 would be suitable for innovative transistor structures that can be switched *via* a topological phase transition rather than conventional carrier depletion.⁶¹ Indeed, first principle calculations demonstrate that the QSH edge channels in the “on” state can be rapidly switched off via a topological phase transition by applying a vertical electric field. A van der Waals heterostructure topological field-effect transistor, made of hBN and $1T'$ - MX_2 , was simulated to show the feasibility of the device (figure 2.3.4.2c).⁶¹

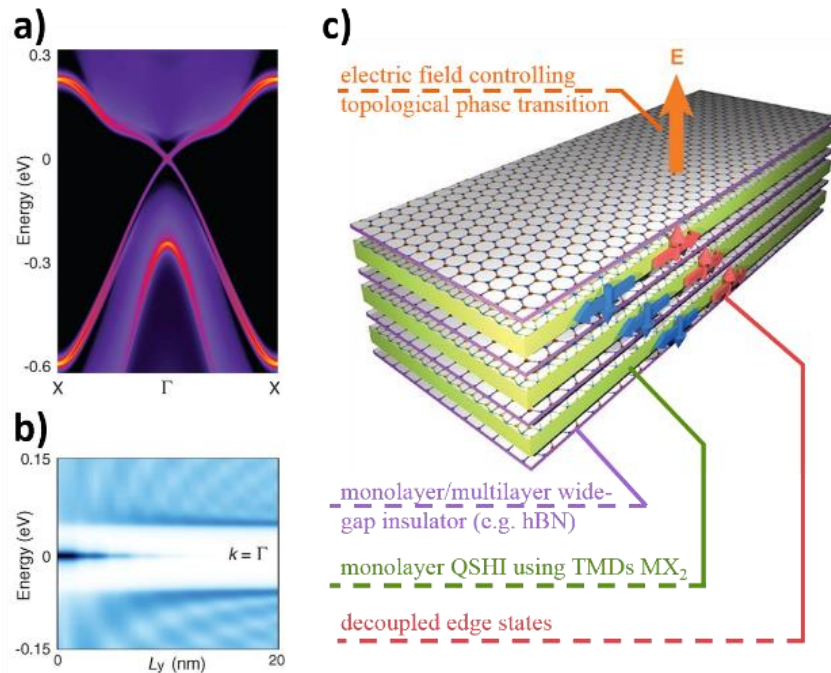


Figure 2.3.4.2. Theoretical predictions of QSH in monolayer $1T'$ - MX_2 . a) Edge density of states. b) Local density of states at Γ point as a function of distance away from the edge (L_y). c) Schematic of van der Waals heterostructured topological field-effect transistor.⁶¹

There is a real need for monolayer 1T'-MX₂ materials to enable studies on this fascinating phase. Unlike phase transformation from 1H-MX₂ to 1T-MX₂, 1H-MX₂ to 1T'-MX₂ is challenging. Theoretical prediction reveal the large amount of strain that is necessary to be applied along the unit cell axis of the TMD to induce a phase transformation from 1H to 1T' for all MX₂ materials (figure 2.3.4.3).⁶⁸ For example, extensive amount of strain would be necessary to induce a phase transformation from 1H-MoS₂ to 1T'-MoS₂. However, we notice that MoTe₂ and WTe₂ would require minimum or no strain to induce a phase transformation from 1H to 1T'. Theoretical prediction indicate that WTe₂ should automatically be found in bulk in the 1T' phase.

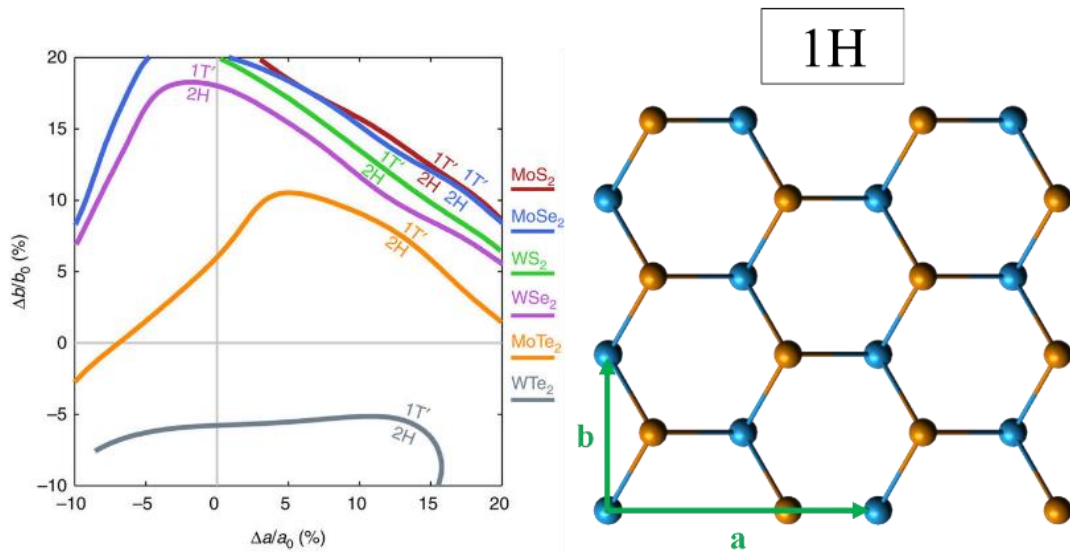


Figure 2.3.4.3. Theoretical prediction of phase transformation from 1H-MX₂ to 1T'-MX₂ by strain.⁶⁸

Experimentally, monolayer 1T' TMDs have not been explored. Few groups report the study of bulk or few layers of 1T'-WTe₂ materials. They were able to mechanically exfoliate bulk 1T'-WTe₂ down to a few layers but never to monolayer form due to the high instability in air of 1T'-MX₂ (please see section 3.1 for information on mechanical exfoliation process). Their findings on few layers 1T'-WTe₂ are truly remarkable. Few

layers $1T'$ -WTe₂ would possess extensive properties such as superconducting behavior, large non-saturating magnetoresistance, weak antilocalization effect and many more.^{55,60,61,65,66} But no one has achieved or isolated a monolayer $1T'$ flake because of its fast decaying time in air and rarity. There is a real need for scientists to isolate monolayer $1T'$ -MX₂ flake to enable research on some of the fascinating theoretically predicated properties monolayer $1T'$ -MX₂ has to offer. I will reveal how we were able to produce the first monolayer $1T'$ TMDs, with the synthesis of $1T'$ -MoTe₂ and $1T'$ -WTe₂ (please see Chapter VI). We solved its rapid decaying time by utilizing graphene as a passivation layer, this lead to the first atomic images of monolayer $1T'$ -MX₂ (figure 2.3.4.4).

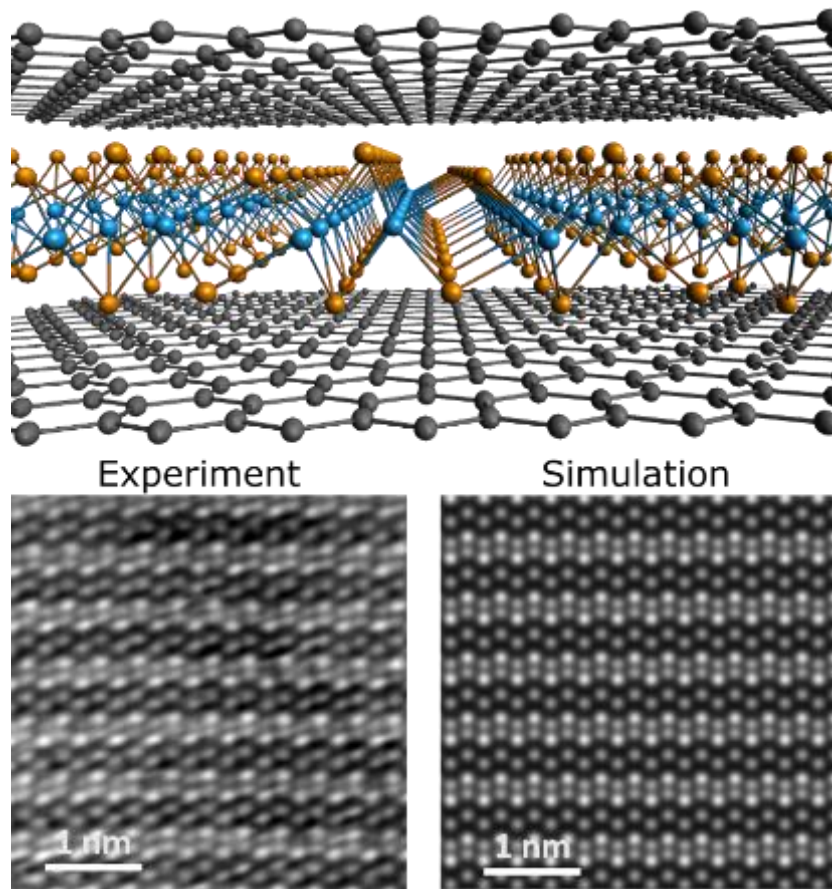


Figure 2.3.4.4. Artistic representation of the encapsulation of monolayer $1T'$ -MX₂ using graphene. AC-TEM images of monolayer $1T'$ -MX₂, experimental results in excellent agreement with simulation.

2.4 Other materials beyond graphene.

The field beyond graphene is not limited to TMDs, there are many other materials currently being explored. In this section, I plan to briefly summarize these materials.

Black phosphorus, phosphorene

In the same concept of stacking graphene layers form graphite, stacking phosphorene layers form black phosphorus (BP). BP and phosphorene have attracted tremendous amount of attention in the past couple years. They are one of few p-type semiconductors and have a tunable bandgap dependent on the layer number similar to 2H-MX₂ TMDs. In 2H-MoS₂ the bandgap can be tuned between 1.2eV (bulk) and 1.8eV (monolayer). In BP it can be dialed up from 0.3 to 2.0 eV.¹¹⁶ However unlike 2H-MoS₂ and some other TMDs, there is no direct to indirect bandgap transition. In other words, both monolayer phosphorene and multi-layer BP have a direct gap. This large range of bandgap values makes BP and phosphorene a very promising material for optics and electronics. BP hole mobility has been reported at 1000 cm²V⁻¹s⁻¹ and on/off ratio of 10⁴.¹¹⁷ Interestingly, black phosphorus properties are dependent on the direction of the crystal, this is due to an intrinsic, strong in-plane anisotropy.^{118,119} Its atomic arrangement can be seen in figure 2.4.1. However BP is very unstable and will decay within a few hours.^{120,121} BP reacts with the oxygen and water present in the atmosphere, therefore proper passivation is necessary. Groups have successfully grown bulk BP by chemical vapor transport, keeping it isolated in a quartz tube and inserting the tube in a glove box. In the glove box, BP can be exfoliated down to phosphorene and properly passivated against air. To date, no group has reported the successful synthesis of phosphorene.

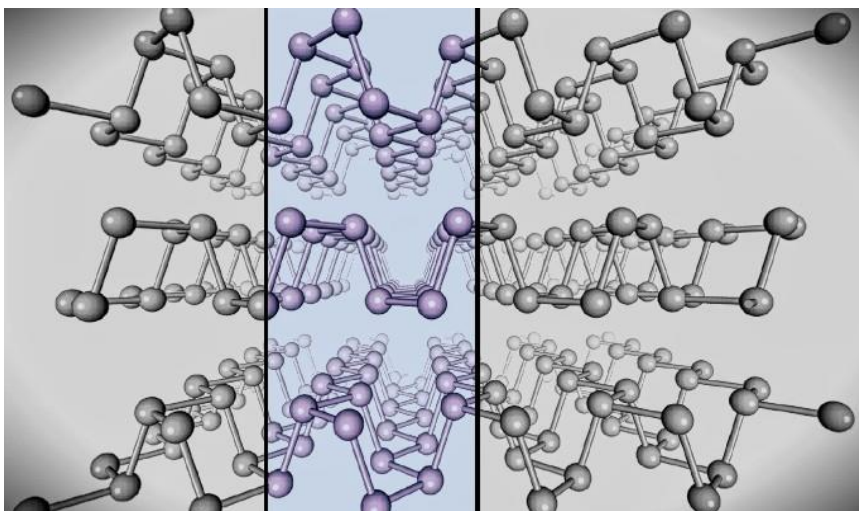


Figure 2.4.1. Black Phosphorus.¹²²

MXenes

MXenes are a new class of 2D nanomaterials that are attracting a tremendous amount of attention due to their potential broad impact. MXenes consist of few atoms thick layers of transition metal carbides, nitrides, or carbonitrides (figure 2.4.2).¹²³ These atoms are organized into a layered hexagonal structure with P63/mmc symmetry by strong metallic, ionic, and covalent bonds, where M (transition metals) layers are nearly closed packed and X (C and/or N) atoms fill octahedral sites. What defines each MXene is the composition and the surface termination. There are hundreds of theoretical combinations of MXenes possible, and to date ~20 have been synthesized since their discovery in 2011.^{123–127} They include metals and semiconductors. The semiconductors have a tunable bandgap when decreasing the layer number, similar to H-MX₂ TMDs.^{128,129} However the most appealing aspect of MXenes is the hydrophilicity. MXenes are conductive while hydrophilic, and can be considered as conductive graphene oxide or hydrophilic graphene.¹²⁸ MXenes have been defined as the product of metals and

ceramic, which has triggered the label “conductive clay”. Benefiting from the 2D morphology, excellent conductivity, and the involvement of transition metals, MXenes exhibit promising charge storage properties based on redox reaction and intercalation.¹²⁸ Besides, unlike graphene where binding polymer nanocomposites to the surface is an issue due to the few functional groups available, MXenes have a tunable surface termination enabling many functional groups which yields much stronger polymer nanocomposite attachment. Due to these amazing features, MXenes are expected to be excellent hosts for a variety of applications such as energy storage applications (Li-ion batteries and supercapacitors), water purification, gas sensors, and more.^{130–132}

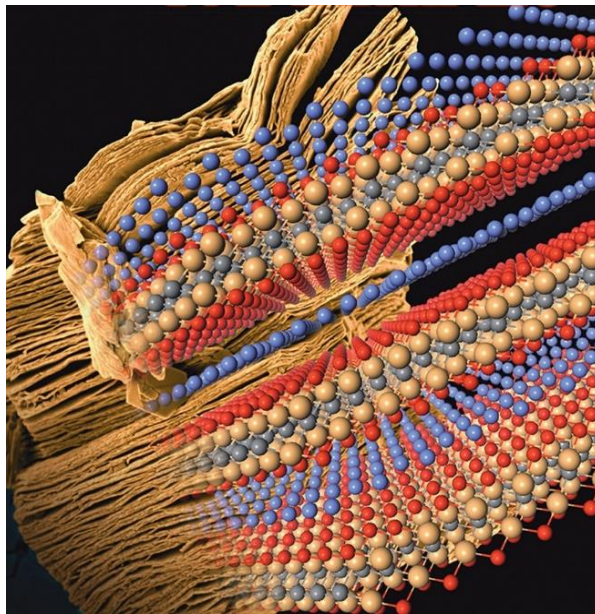


Figure 2.4.2. MXenes.¹³³

Scientists have been exploring the field “beyond graphene” at rapid pace. TMDs, BP and MXenes are promising materials with unique capabilities that make them appealing. With a vast range of possible applications, the synthesis of high quality and large area monolayer phosphorene, MXenes and TMDs have become a top priority.

CHAPTER III.

Experimental Methods

In order to evaluate the quality of a material, scientists rely on various characterization techniques. These techniques are extremely valuable as they represent the first step in quantifying and understanding the properties of a given material. Each technique will provide specific information on the structure and properties and will compliment a previous technique. As we further characterize the material, we will be able to paint a clearer picture of its quality and underlying intrinsic properties.

In this Chapter, I will first demonstrate how scientists can obtain monolayer materials. Methods of production include exfoliation from a bulk source or by direct synthesis. I will follow-up by describing characterizations tools that are used throughout this thesis. These tools can be categorized in three areas: spectroscopy, microscopy and three terminal electrical measurements. Spectroscopy measurements will provide us information on the chemical composition, composition variation, crystallographic structure, and optoelectronic properties of the materials. Microscopy measurements will provide us information on the sample's structure with valuable direct imaging approaches. Three terminal electrical measurements will reveal the charge carrier mobility and will help define the overall crystallinity.

3.1 Isolating monolayer material

To study materials in the monolayer form, one needs to isolate high quality monolayer material. There are multiple methods to obtain materials in the monolayer form. Some bulk materials are native element minerals on earth (e.g. graphite) and are reduced down to the monolayer form, others are directly synthesized using novel techniques and advanced equipment.

Mechanical exfoliation is the most common method for reducing bulk material down to the monolayer form. The “scotch tape method” was first developed by Andre Geim and Konstantin Novoselov at the University of Manchester in 2004, using a piece of tape to successfully isolate graphene.²⁵ They were able to characterize and study isolated graphene for the first time in history. This discovery led them to the Nobel Prize in Physics in 2010 "for groundbreaking experiments regarding the two-dimensional material graphene".¹³⁴ The “scotch tape method” is a technique currently used worldwide that has enabled the study of countless materials in the monolayer and few layer form. “Scotch tape method” requires a piece of tape, bulk material and the substrate onto which one wishes to deposit the monolayer material. The method consists on wrapping the tape around the bulk material and peeling it back and forth multiple times to separate the layers of the material from their weak van der Waals interaction. The tape is then pressed on the substrate and gently heated to release the material from the tape onto the substrate. The tape is then removed and the substrate is studied under an optical microscope. Small regions of monolayer material can be observed on the substrate (figure 3.1.1). The isolated monolayer region is of very high quality but very small. This

method is exceptional for the initial characterization and study of novel nanomaterials, however the sparse monolayer region makes this process non-scalable for any future application.



Figure 3.1.1. Mechanical exfoliation. Mechanical exfoliation of graphene using scotch tape method.¹³⁵

Liquid exfoliation offers large amounts of monolayer material. A bulk material is inserted into a solvent, the solvent intercalates in the layers of the bulk material and through an agitation (ultra-sonication) the solvent separates the layers (figure 3.1.2).¹³⁶ The shearing of the layers in the bulk material results in the abundance of monolayer and few layers in the solvent. A droplet of the solution is deposited onto the substrate and large amounts of monolayer material can be found (figure 3.1.2). This method offers large amounts of monolayer material, however the quality of the monolayer material has degraded due to surface contamination and structural distortion.

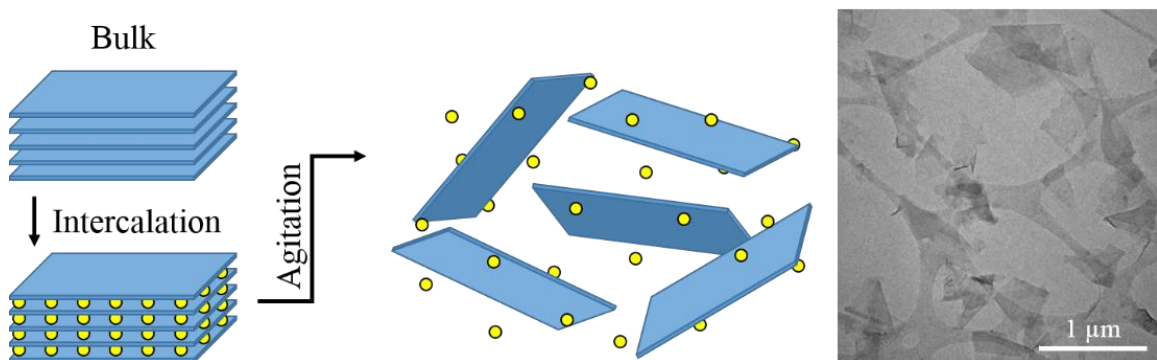


Figure 3.1.2. Liquid exfoliation. Few layer graphene by shear exfoliation in liquids.¹³⁶

Molecular beam epitaxy (MBE) was invented at the Bell labs and enables the direct deposition of single crystal thin-films.¹³⁷ MBE consists of a chamber with a stage and effusion cells (figure 3.1.3). A growth substrate is placed on the stage and the effusion cells are filled with the natural elements of the material we wish to synthesize. The system is pumped down to low pressure and the effusion cells are slowly heated until the compound in the cell begins to sublime. By using a shutter we can control which compounds reaches the substrate. Due to the long mean free path of the atoms, they do not interact with each other until reaching the surface.¹³⁷ By controlling the deposition rate and the temperature of the substrate, the gaseous elements impinging on the surface of the substrate may be adsorbed and thin-film single crystal material will grow. This growth technique requires the careful optimization and control of all parameters. The resulting material quality is very high, however it will have different thickness across the substrate and achieving solely monolayer material from MBE can be very challenging.

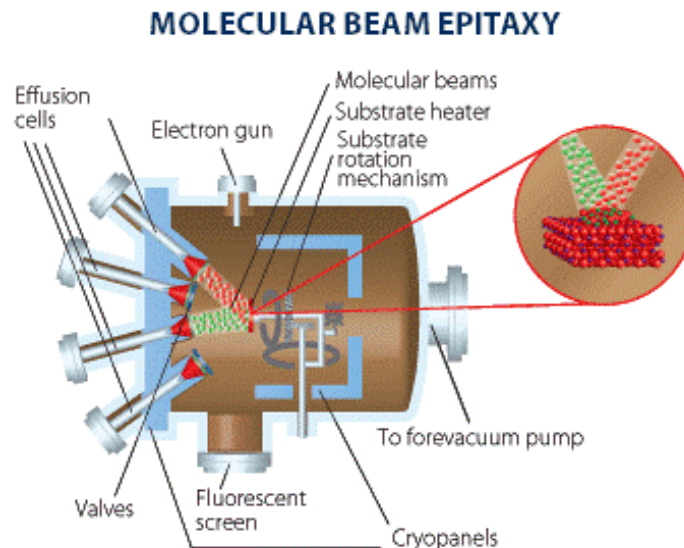
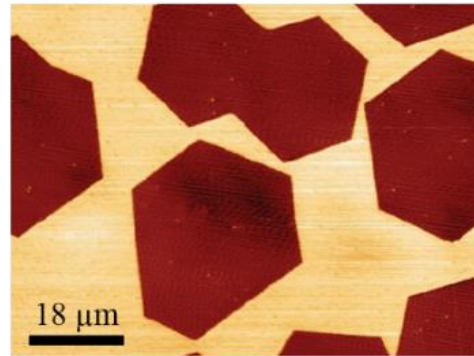


Figure 3.1.3. Molecular beam epitaxy.¹³⁸

Chemical vapor deposition (CVD) enables the direct synthesis of monolayer material on a substrate, and is the technique predominantly used throughout this thesis. The process involves a growth substrate positioned in the center of a furnace which is ramped up to high temperatures under gases and precursors, and the material starts to grow on the substrate. After careful optimization of all the growth parameters in a 1 inch CVD furnace, monolayer single crystal flakes can grow across the substrate. Figure 3.1.4 shows the growth results of monolayer single crystal graphene flakes. By increasing the size of the furnace, larger monolayer growth regions can be achieved. Using a 4 inch CVD system, graphene can be grown across large areas (figure 3.1.4 middle). With a roll to roll process, scientists can synthesize huge sheets of graphene (figure 3.1.4 bottom).¹³⁹ Scientists are currently optimizing Metal-Organic CVD (MOCVD) processes for wafer scale monolayer 1H-MoS₂.¹⁴⁰ The larger the furnace, the more challenging it is to achieve high quality, homogenous monolayer growth. Small deviations from the growth recipe will either result in no growth or in multilayer growth. Therefore all recipes undergo careful optimization processes and rigorous checking to maintain the high quality growth. The materials grown can be transferred from the growth substrate to a different substrate (e.g. TEM grid) through etching or bubble transfer (please see section 4.1.2 and 4.2.3 on transfer techniques). Transfers can lead to contaminations which would degrade the quality of the material.¹⁴¹ The large amount of good quality monolayer material synthesized, the reproducibility between each growth and the ability to dabble at new and unexplored materials make CVD a reliable process for exploring new and exciting 2D nanomaterials.

1 inch CVD



4 inch CVD



Roll to roll CVD

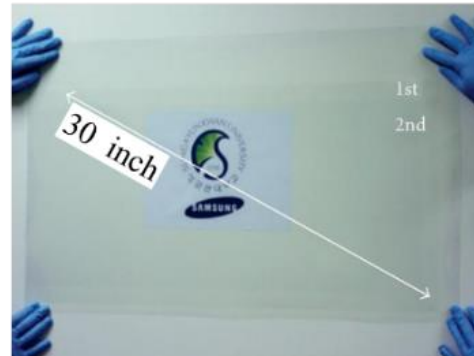


Figure 3.1.4. Chemical vapor deposition. 1 inch CVD growth of single crystal graphene flakes. 4 inch CVD growth of large area graphene, hydrophobicity on the surface indicates the presence of carbon. Roll to roll chemical vapor deposition for scalable graphene growth.¹³⁹

3.2 Characterization techniques

3.2.1 Atomic force microscopy

Atomic force microscopy (AFM) enables the careful characterization of the surface of nanomaterials with nanometer (nm) resolution. AFM relies on the attractive and repulsive forces between a mechanical probe (AFM tip) and the substrate. AFM has three major abilities: force measurements, manipulation and imaging. Force measurements can be performed at a specific location on the substrate. It entails measuring the forces between the probe and the sample as a function of their mutual separation. Manipulation involves directly displacing or stimulating the sample using the AFM tip. Imaging relies on guiding the AFM tip along the surface of the sample using a precise piezoelectric controller and recording the height changes of the probe due to the intramolecular forces the tip undergoes with the sample (figure 3.2.1.1). Imaging yields a 3 dimensional topographic image of the surface of the sample with resolution of nanometer size features, well below the diffraction limit of light.

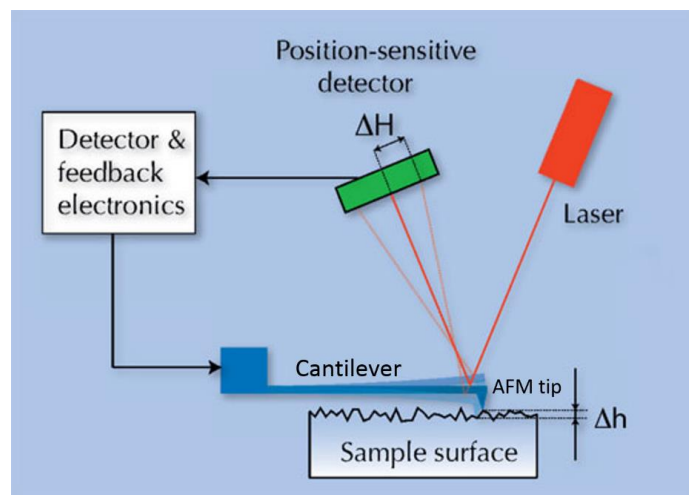


Figure 3.2.1.1. Schematic of AFM measurement.

AFM imaging relies on a laser monitoring the displacement of the AFM tip during its interaction with the sample. The laser is reflected off the top surface of the cantilever and is then captured by a four quadrant photodiode. When the AFM tip is displaced the laser position deviates from its original position on the photodiode (figure 3.2.1.2a), this shift is converted into a voltage difference that is returned to the feedback electronics. To maintain a constant interaction force between the tip and surface, the feedback loop moves the cantilever using the piezoelectric controllers and returns the laser to the center of the photodiode. The voltage required to do so gives a measure of surface height at that location. A topographic image of the surface over a scanned area is then created with nm scale resolution. The image resolution is dependent on the radius of the AFM tip. Typical resolution is below 1nm (figure 3.2.1.2b shows a typical AFM tip).

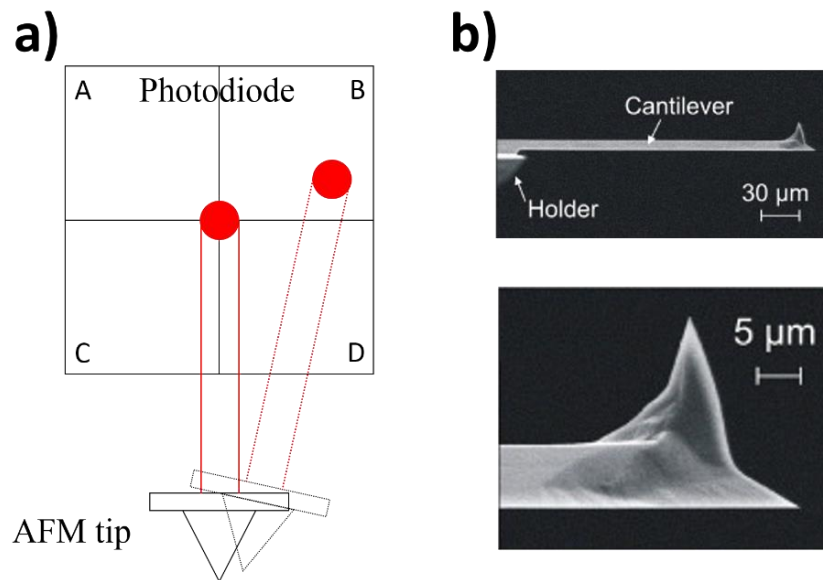


Figure 3.2.1.2. a) Schematic of photodiode with the laser deflection. b) SEM image of an AFM tip.¹⁴²

There are three methods for AFM imaging: contact, non-contact and tapping mode. In contact mode, the tip contacts the surface with a set point normal force kept

constant during the scan, the AFM tip is dragged across the sample that could potentially damage the surface of the sample. Non-contact mode requires the AFM tip to hover over the sample at a distance of 50-150 Å and monitors the weak attractive van der Waals forces between the tip and sample. There is a loss in resolution using this technique. In tapping mode, the tip is driven across the sample close to its resonant frequency (50-500 kHz) and the amplitude of oscillations is kept constant while the tip intermittently enters the repulsive regime. Parameters of the cantilever oscillation, in particular the phase and amplitude of oscillation, can give information on the properties of the surface including stiffness and attractive force.¹⁴³ Throughout this thesis, AFM measurements were performed using tapping mode, unless specified otherwise.

Using the tapping mode of the AFM, we are able to scan the height and study the surface topography of our CVD grown materials. When characterizing materials such as graphene (figure 3.2.1.3a) and MoS₂ (figure 3.2.1.3b), a profile scan indicates the material has a height of around 0.8 nm confirming the monolayer height. We are also able to study protein attachment to the surface of MoS₂ and study the chemical binding. Figure 3.2.1.3c reveals specific protein attachment to the MoS₂ surface whereas the SiO₂ substrate remains clean. AFM can also reveal nm scale buckling at the interface of two CVD grown materials that have different lattice constants. Figure 3.2.1.3d is an AFM image of a CVD grown 1H-MX₂/1T'-MX₂ heterostructure. High resolution scanning reveals buckling in the 1H-MX₂ region that matches theoretical computations (please see section 6.3 for further information on this buckling mechanism).

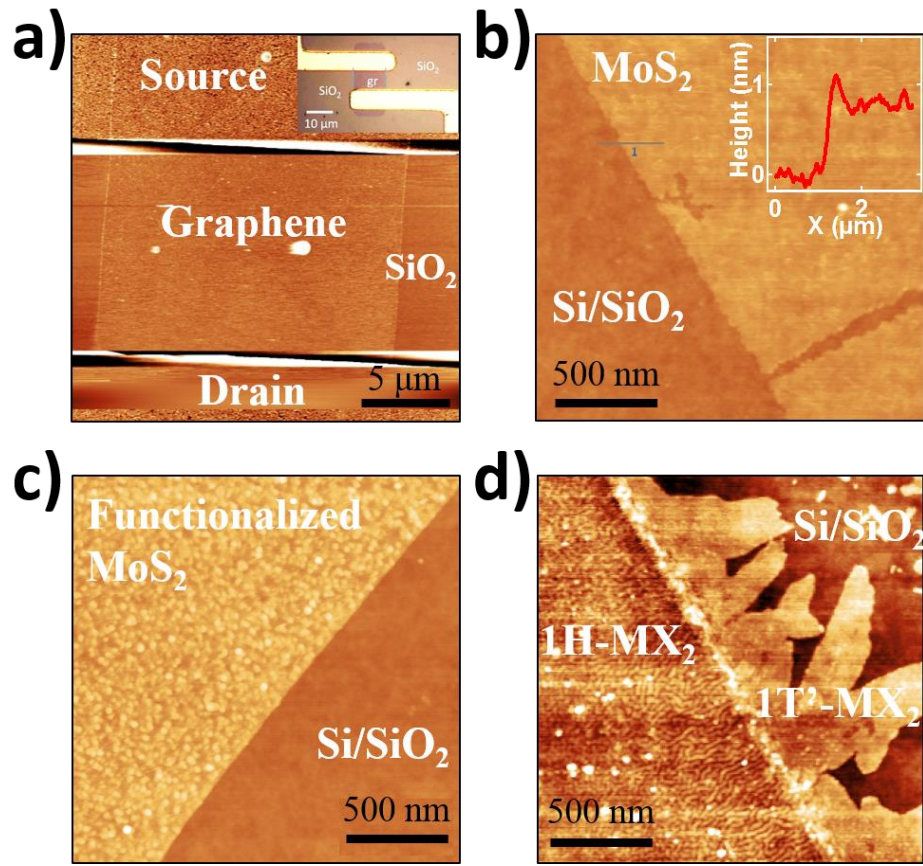


Figure 3.2.1.3. AFM images of various CVD grown samples. a) AFM of graphene device with embedded image of the device. b) AFM image of CVD grown MoS₂ with embedded high profile scan revealing monolayer height. c) AFM image of functionalized MoS₂ revealing specific binding to MoS₂ region and not to Si/SiO₂. d) AFM image of CVD grown 1H-MX₂/1T'-MX₂ revealing buckling mechanism in 1H region.

AFM is a powerful tool in the field of nanotechnology that not only permits the study of the height of nanomaterials but also the surface morphology as it undergoes chemical transformations or topological strains. AFM is used heavily throughout the remainder of this work as a premier surface characterization technique.

3.2.2 Raman spectroscopy

Raman spectroscopy is a technique that provides us with a vibrational fingerprint of our material. Light emerging from a laser source inelastically scatters off the material and is recorded by a CCD camera. The energy of the scattered photon is shifted from its original value due to the interaction the laser has with the molecular vibration of the material (phonons). The energy difference between the incident and scattered photon is plotted as Raman shift in wavenumbers (cm^{-1}) using the following equation, where $\Delta\omega$ is the Raman shift, λ_{inc} is the incident and λ_1 is the shifted wavelength in nanometers.

$$\Delta\omega (\text{cm}^{-1}) = \left(\frac{1}{\lambda_{\text{inc.}}(\text{nm})} - \frac{1}{\lambda_1(\text{nm})} \right) * 10^7$$

Due to the weak interaction the laser has with these modes, there is a need to filter the intense unwanted Rayleigh scattered light. Rayleigh scattering is light scattered at the incident wavelength. A notch filter is used to eliminate all reflected light at the incident wavelength, leaving us solely with the vibrational fingerprint of our material. The intensity of the signal is proportional to $\lambda_{\text{inc}}^{-4}$, thus the choice of laser is crucial in distinguishing the vibrational modes. Using an infrared laser (800-1000 nm) results in a decrease of scattering intensity compared to green laser (532 nm). However different wavelengths work better for different systems and materials. Red or near-infrared (600-830 nm) lasers are used for fluorescence suppression; blue or green lasers are used for inorganic materials and resonance Raman experiments (e.g. CNTs) and enhanced Raman scattering; UV lasers are used for resonance Raman on biomolecules (e.g. DNA) and fluorescence suppression.¹⁴⁴ In this thesis, a green laser (532 nm) was used unless otherwise specified.

The Raman shifts enable molecular identification and atomic configuration distinction, but also provide us with information on the quality and the height of our nanomaterials. In graphene, the G band, D band and 2D (or G') band are the three peaks identified in graphitic carbon located at 1582 cm^{-1} , 1350 cm^{-1} and $2500\text{-}2800\text{ cm}^{-1}$ respectively (figure 3.2.2.1).¹⁴⁵ The G-band and D-band are associated with the sp_2 and sp_3 hybridized bonds, whereas the 2D band is a second-order two-phonon process related to the phonons near the K point in k-space.¹⁴⁵ Analysis of height, width and position of these 3 peaks provides us information on the quality, layer thickness and doping level of the graphene. For instance, high quality monolayer graphene, the D/G ratio should be less than 0.05 and the 2D/G ratio ~ 2 ratio.¹⁴⁶⁻¹⁴⁹

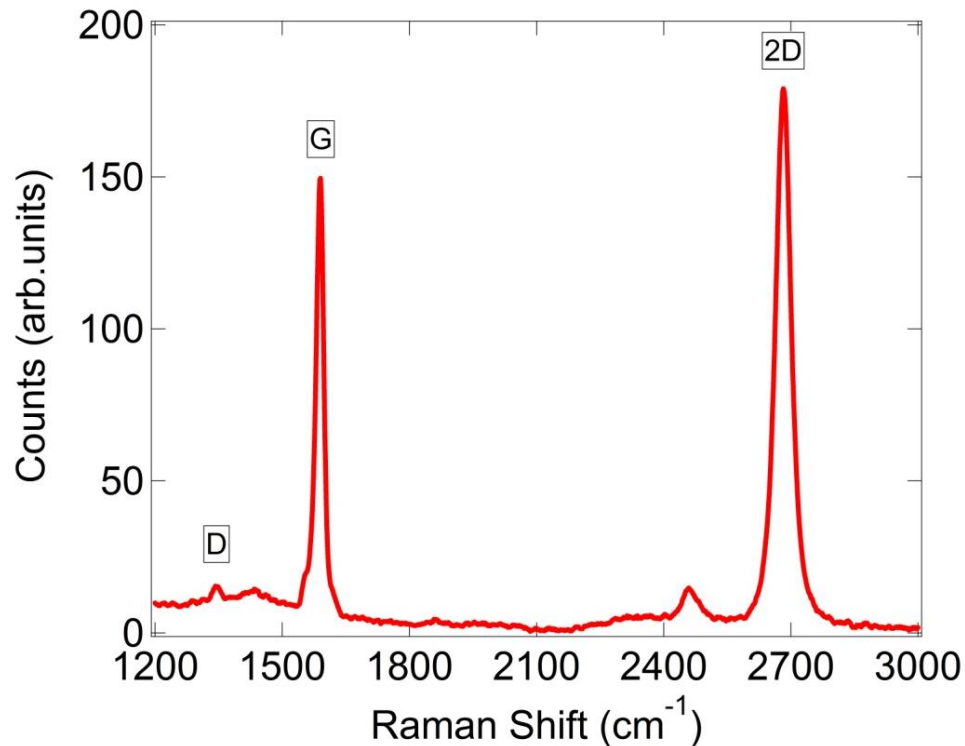


Figure 3.2.2.1. Raman spectrum of graphene.

In TMDs the separation between vibrational modes provides us with a direct estimate of the layer number. 1H-MoS₂ has predominantly 2 vibrational modes, the E¹_{2g} and A_{1g} modes which correspond to the in-plane and out-of-plane vibrations, located at 384 cm⁻¹ and 403 cm⁻¹ respectively. For bulk MoS₂, the E¹_{2g} redshifts to 382 cm⁻¹ and the A_{1g} blueshifts to 408 cm⁻¹ (figure 3.2.2.2). The separation of the E¹_{2g} and A_{1g} peaks therefore increases with increasing layer number from 19 cm⁻¹ in monolayer MoS₂ to 26 cm⁻¹ in bulk.^{21,77,78}

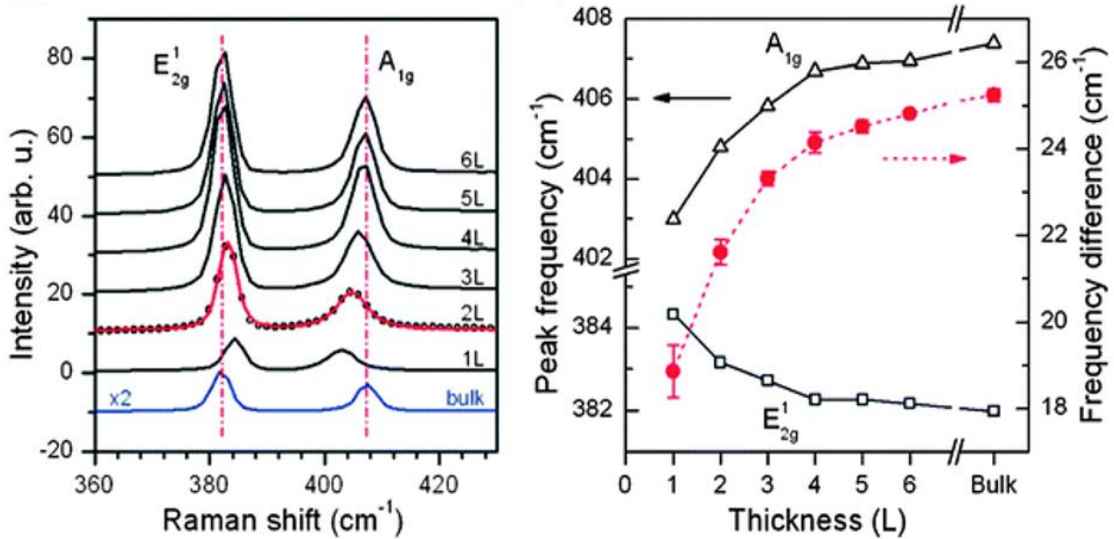


Figure 3.2.2.2. Raman spectrum of MoS₂ with thickness dependence.⁷⁷

Raman mapping enables the careful mode mapping of an entire flake, revealing the intensity and peak positions in specific physical locations on a flake. This enables the careful characterization of different layers within one flake. For instance monolayer 1T'-WTe₂ has 2 known vibrational modes, the in-plane A⁷₁ and A⁹₁ that contains in-plane and out-of-plane phonon vibrations.^{150,151} In bilayer, the A⁷₁ mode does not shift, whereas the A⁹₁ mode redshifts by ~ 1.5 cm⁻¹. The Raman mapping of the A⁹₁ mode for 1T'-WTe₂ in figure 3.2.2.3 clearly reveals this redshift in wavenumbers from monolayer to bilayer.

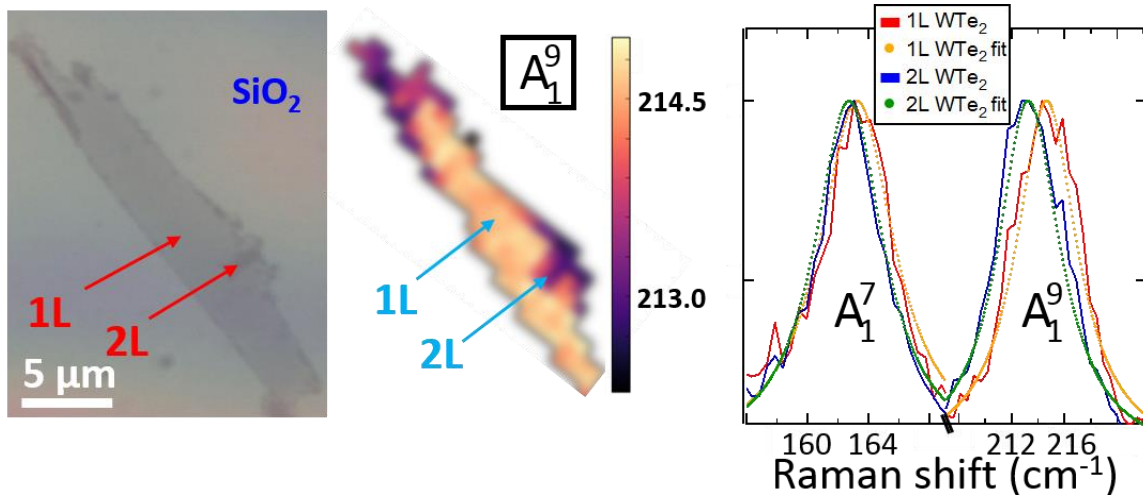


Figure 3.2.2.3. Raman mapping of 1T'-WTe₂. Revealing shift of A₁⁹ mode for monolayer to bilayer.

Due to the large spot size of the Raman laser ($\sim\mu\text{m}^2$) it may be challenging to obtain the vibrational modes in smaller regions. By placing an AFM tip on the substrate and focusing the laser on the AFM tip, one can perform Tip Enhanced Raman Spectroscopy (TERS). In TERS, the Raman scattering occurs at the end of the atomically thin tip. TERS enables the mapping of nanometer-sized areas with high resolution. For instance in 1H-MX₂/1T'-MoTe₂ heterostructures, the 1T'-MoTe₂ region is very small ($<\mu\text{m}^2$) and normal Raman mapping cannot differentiate this unique region. By performing TERS along the heterostructure, one can clearly identify both regions of the heterostructure and associate the correct vibrational modes (figure 3.2.2.4).

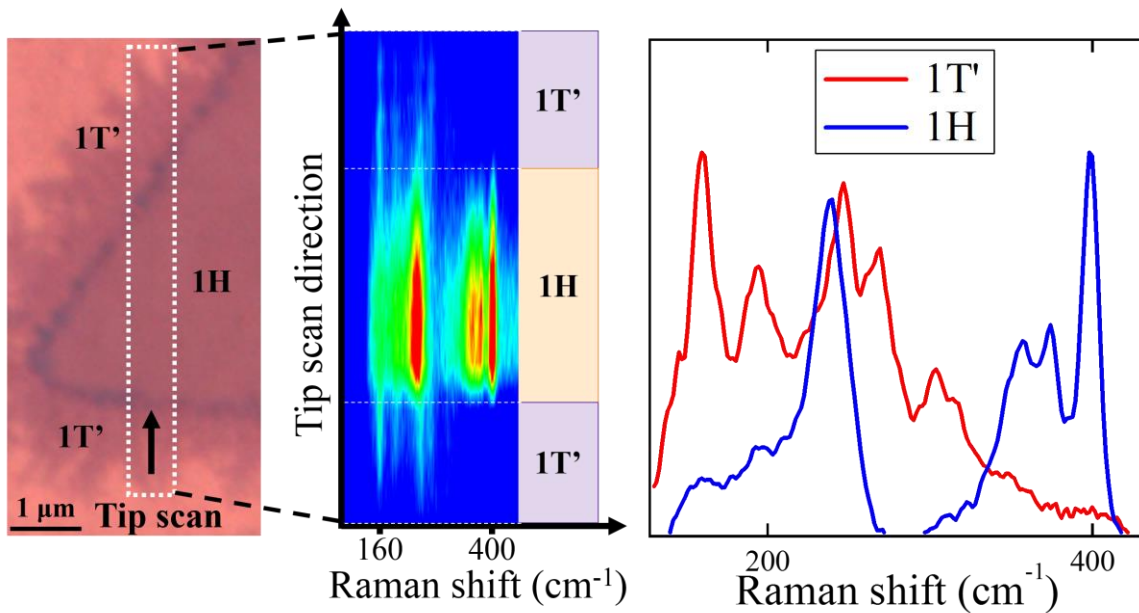


Figure 3.2.2.4. TERS on 1H/1T' heterostructure. Raman spectrum indicates 2 distinct regions in agreement with the in-plane monolayer heterostructure.

Raman spectroscopy is a quick, powerful and non-destructive tool that enables the careful characterization of our CVD grown material. It provides us with molecular identification, information on the atomic configuration, quality, height and doping of our materials.

3.2.3 Electron microscopy

Electron microscopy such as scanning electron microscopy (SEM) or transmission electron microscopy (TEM) offer much higher resolution than traditional optical microscopes. Electrons are emitted from a gun (thermal or field emission) and accelerated towards the sample that we wish to characterize. Electron microscopes owe their high resolution to the small de Broglie wavelength:

$$\lambda = \frac{h}{\sqrt{2m_0eU(1 + \frac{eU}{2m_0c^2})}}$$

where h is Planck's constant, m_0 is the rest mass of the electron, c is the speed of light and eU is the energy of the electron. The electron wavelength of a 50 keV e-beam writing system is 0.0054 nm, but this resolution is limited by lens aberrations. The configuration difference between SEM and TEM is the placement of the detector with respect to the sample: for a SEM it is placed above whereas for a TEM it is below (figure 3.2.3.1).

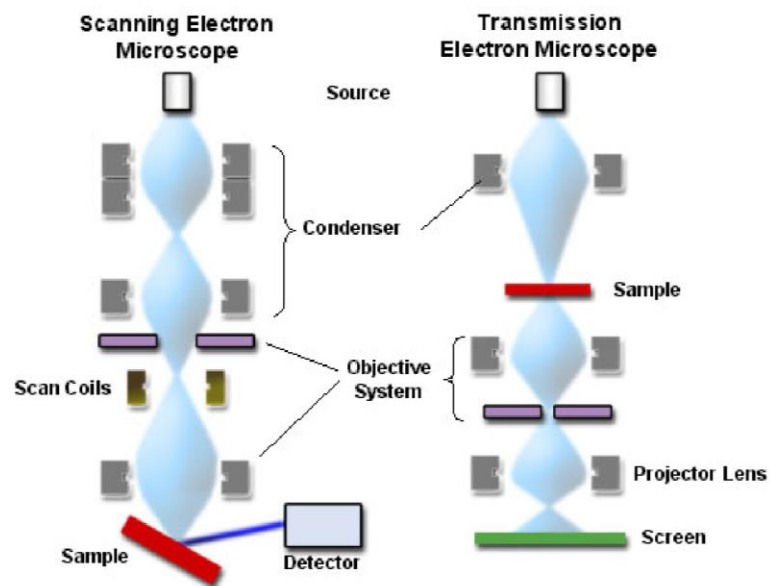


Figure 3.2.3.1. Schematic of a SEM and TEM. (Figure is from Professor Kagan ESE525 lecture).

For SEM, the electrons interact with atoms in the sample and several signals are produced that contain information about the topography and composition of the sample's surface (figure 3.2.3.2). The secondary electrons (SE) provides us with the topography, the backscattered electrons (BSE) with the chemical compositional (Z-contrast) and X-rays the chemical makeup (inner shell electrons) of our sample. The SE are captured by a detector and an image displaying the topography of the surface is created. SEM is operated at lower accelerating voltage (5 – 50 kV) than TEM (80 – 200 kV) which results in the sample being less damaged, however much higher resolution can be achieved through TEM. Figure 3.2.3.3 shows a SEM image of a CVD grown 1H-MoS₂ directly on Graphene/Cu foil.

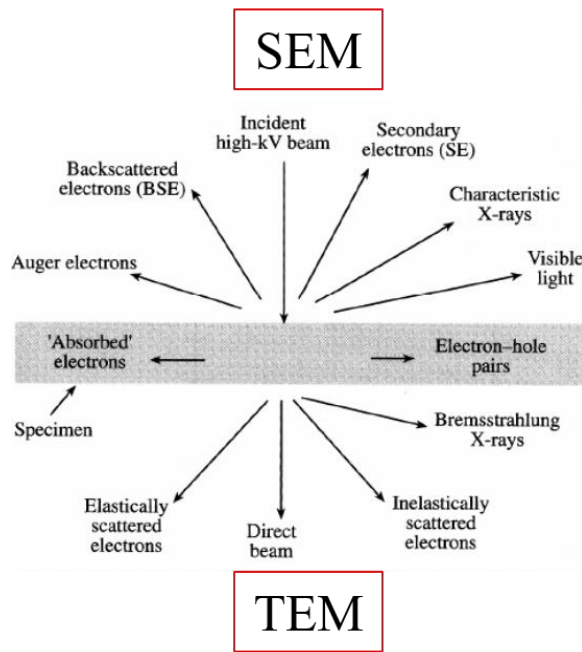


Figure 3.2.3.2. Schematic of the interaction the electrons have with sample in the SEM and TEM. (Figure is from Professor Kagan ESE525 lecture).

For TEM, the electrons are accelerated towards thin samples and are transmitted through. In order for the electrons to solely traverse the thin sample and not a thick

substrate that could block the imaging, the sample is transferred onto holey carbon grids or thin SiN membrane. The electrons interact with the sample as it passes through and an image is formed from these interactions (figure 3.2.3.2). Imaging can be done in either bright field or dark field mode. Bright field includes the main unscattered beam and the imaging is done by the occlusion and absorption of electrons in the sample. Regions with no material appear bright whereas thick or higher atomic number regions appear dark. Figure 3.2.3.3 shows a bright field image taken of a 1H-MoS₂/1T'-MoTe₂ heterostructure. It is hard to identify the heterostructure due to the lack of contrast but one can see the triangular region characteristic of the 1H-MoS₂. Dark field image excludes the main beam, the intensity of the image is lower and it requires longer exposure times, however the contrast is much higher. In contrast to bright field, regions with no material appear dark whereas thicker and higher atomic number regions appear bright. Due to the high contrast, this imaging mode is used for identification of defects or different atoms on a surface. Figure 3.2.3.3 shows a dark field image taken of a 1T'-MoTe₂, one can clearly identify the rectangular flake spanning across the holey carbon grid.

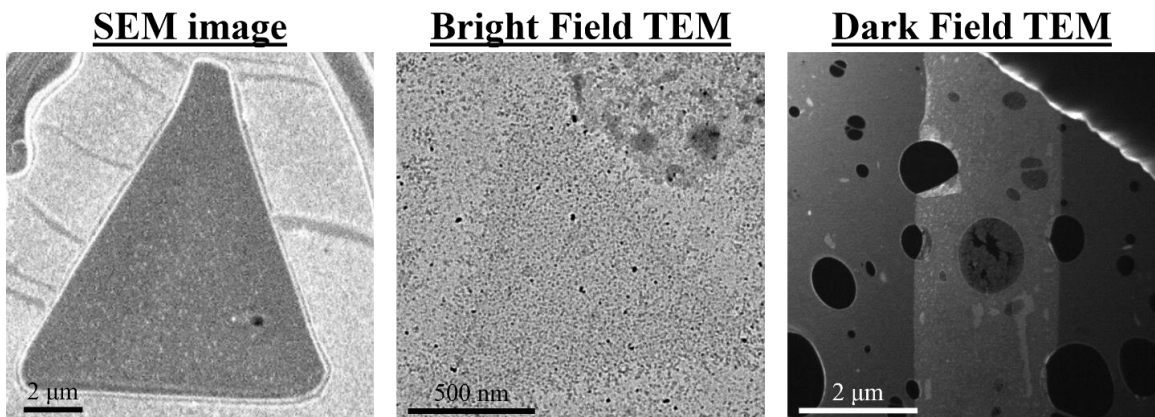


Figure 3.2.3.3. SEM image of 1H-MoS₂ grown on Graphene/Cu foil. Bright Field TEM image of 1H-MoS₂/1T'-MoTe₂ heterostructure. Dark Field TEM image of 1T'-MoTe₂.

A Selected Area Diffraction (SAED) image can be generated through the elastically scattered electrons in the TEM. The image holds information about the space group symmetries, crystal length and orientation. Figure 3.2.3.4 is an SAED image of 1H-MoS₂ and 1T'-MoTe₂ clearly highlighting the differences in the atomic configuration of the underlying materials.

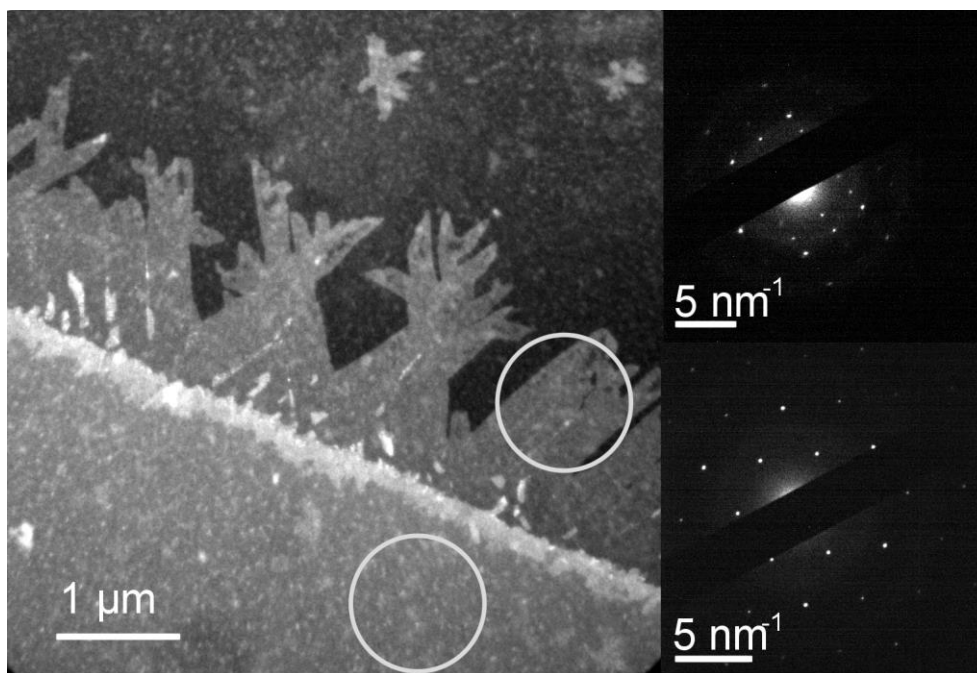


Figure 3.2.3.4. Dark Field TEM image of 1H-MoS₂/1T'-MoTe₂ heterostructure with SAED of 1T'-MoTe₂ and 1H-MoS₂ regions respectively.

For TEM, the electrons travel through many lenses to create an end image. The spherical and chromatic aberrations caused by going through these lenses reduce the overall resolution of the system. Modern TEM include aberration correctors to resolve this issue, by adding lenses in the column and increasing the stage stability so that resolutions below 1 angstrom can be achieved.^{152,153} Therefore, TEM offers atomic resolution imaging that is essential to having visual confirmation of the atomic arrangement and atomic elements present in our sample. Figure 3.2.3.5 is a high angle

annular dark field STEM image of a 1H-MoS₂ and 1T'-MoTe₂ heterostructure taken by aberration corrected TEM (ACTEM). The image shows a distinct separation between both regions, in the top region we can identify the hexagonal lattice that is characteristic of the 1H phase and in the bottom region we recognize the isolated Te chain specific of the 1T' phase (please see section 2.3 for more details on 1H and 1T' phase). The intensity of the atoms is proportional to the atomic number squared (Z^2), therefore we can easily identify the bright Te atoms ($Z = 52$) from the dim S atoms ($Z = 16$).

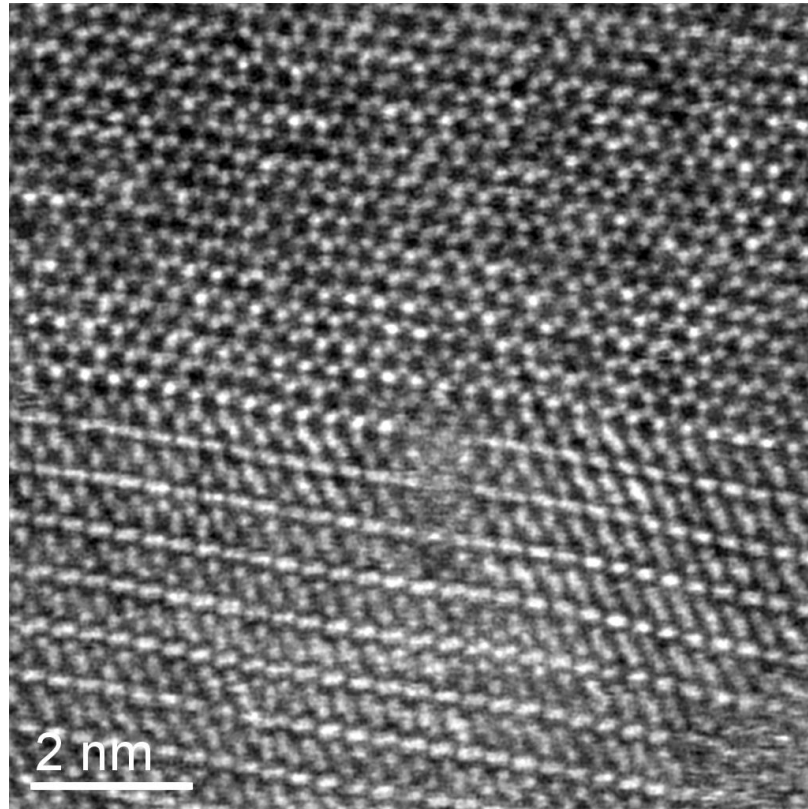


Figure 3.2.3.5. High angle annular dark field STEM image of a 1H-MoS₂/1T'-MoTe₂ heterostructure highlighting the distinction between two different atomic configuration.

Electron microscopy are state of the art imaging systems that offer resolution down to the atomic level. These tools are essential for the careful characterization and understanding of our samples.

3.2.4 Three terminal measurements

3.2.4.1 Principle of a MOSFET device

Three terminal measurements under a metal-oxide-semiconductor-field-effect-transistor (MOSFET) configuration enable the study of the electrical properties of our nanomaterials. The electrical properties are one of the core characteristics of a nanomaterial and a defining criteria when evaluating the quality of the CVD grown material. Devices can be manufactured by photolithography or e-beam lithography on a Si/SiO₂ substrate. Both methods will be described in the following section. The nanomaterial is contacted by source and drain electrodes across which a constant bias is applied. A voltage is applied to the underlying highly p-doped Si substrate. The 300 nm SiO₂ dielectric layer ensures a capacitive coupling to the nanomaterial channel (figure 3.2.4.1.1). The external field alters the Fermi level in the nanomaterial and thus modulates the source-drain current. Please note that throughout this thesis a dielectric of 300 nm SiO₂ is used, unless stated otherwise.

Figure 3.2.4.1.1 shows qualitative description of the effects arising in a semiconducting channel when a voltage is applied to the gate. When a positive voltage is applied to the gate an electric field is created. The electric field pushes away the holes and attracts the electrons creating a conductive electron channel between the source and drain. However to paint a clearer picture it is essential to understand this phenomena in terms of energy bands. We will discuss the effects the applied gate voltage has on the

band diagram in the metal oxide semiconductor (MOS) junction, and the effect the applied field has on our transistor (FET).

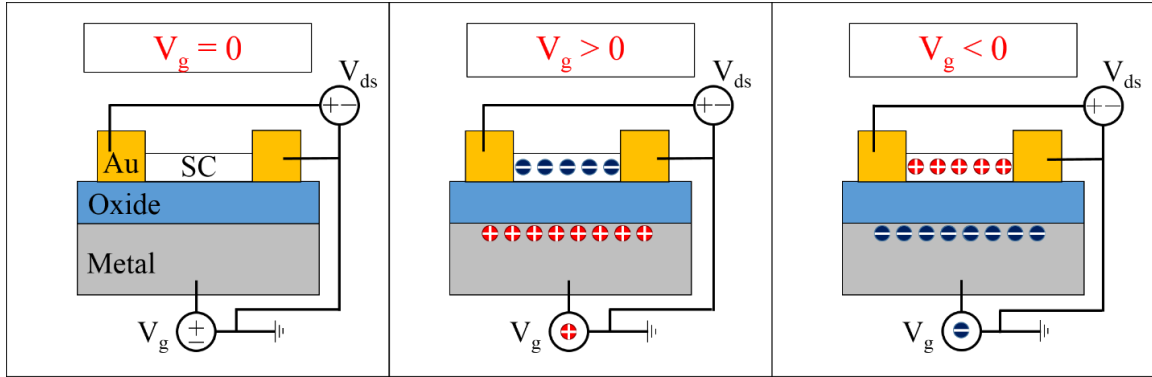


Figure 3.2.4.1.1. Qualitative description of a MOSFET device. The schematic shows the accumulation of charges in the semiconductor due to an electric field resulting from a voltage applied to the gate.

The energy diagram of the MOS setup for an n-type semiconductor at different applied gate voltages to the metal is shown in figure 3.2.4.1.2. As detailed in the previous section 2.1.4, a metal (labeled as the grey region) does not have a bandgap and its Fermi energy (E_F) sits at the top of the conduction band. E_F describes the highest occupied state in a system at 0K.^{8,9,18} The metal has a work function labeled as (ϕ_M). The work function refers to the minimum quantity of energy that is required to extract an electron into vacuum. An insulator (or oxide) has a very large bandgap ($E_{\text{Gap}} > 6\text{eV}$), the insulator is labeled as the blue region. A semiconductor has a small bandgap ($E_{\text{Gap}} < 5\text{eV}$), and an n-type semiconductor has an E_F closer to the conduction band (E_C) than the valence band (E_V) leading to a preferential conduction of electrons over holes. A semiconductor has a work function labeled as (ϕ_S) and the electron affinity labeled as (X_S). When no voltage is applied to the gate ($V_g = 0$) the E_F of the metal and semiconductor align and the system is at equilibrium, this is labeled flatband. When a positive gate voltage is applied ($V_g > 0$), the E_F of the metal decreases pushing the left side of the figure down, and this effect

causes a band bending in the semiconducting region. The band bending is the result of the electric field created by the back gate voltage which decreases the E_C and E_V energies of the semiconductor electrons near the insulator. As shown in figure 3.2.4.1.2, the conduction and valence band both start to bend downwards towards the metal. At the interface of the semiconductor and insulator, E_F is now much closer to E_C making the semiconductor more n-type than before at the interface. This band bending enables an accumulation of majority carriers (electrons) in the n-type semiconductor and since we are using nanomaterials this will effectively take place over the whole area. For a negative applied gate voltage ($V_g < 0$), the opposite effect occurs. The E_F of the metal increases, causing the bands in the semiconducting region to bend upwards. This bending increases the separation between the E_C and E_F of the semiconductor at the interface. This band bending will cause a depletion of electrons at the interface. If a very large negative gate voltage is applied ($V_g \ll 0$), the bending of E_V could reach the E_F causing an accumulation of holes, this is called an inversion.

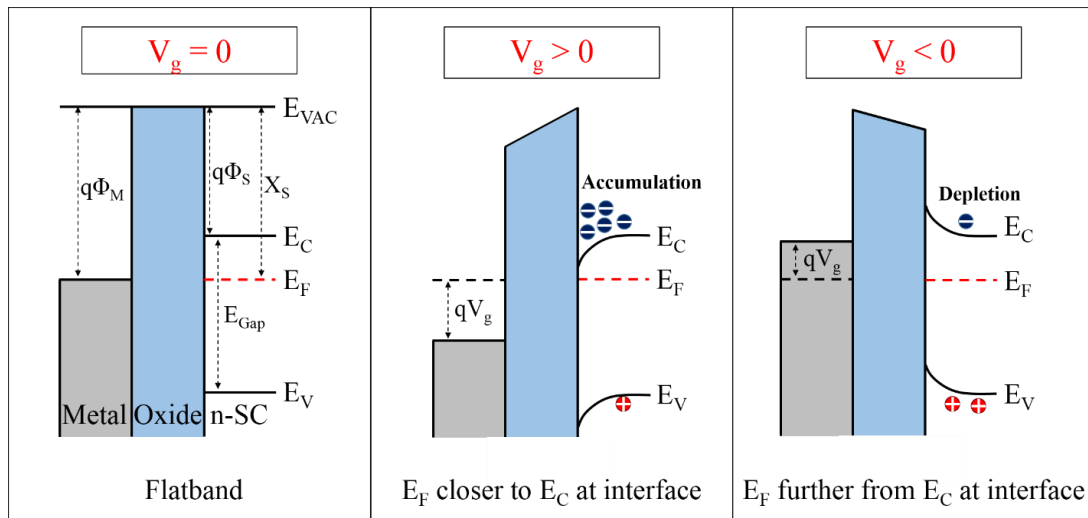


Figure 3.2.4.1.2. Band diagram of MOS. Schematic of band bending with the accumulation or depletion of charges due to an applied voltage on the gate.

With this new understanding we can study the band diagram of our field effect transistor (FET). The n-type semiconductor is contacted by gold (Au) and chromium (Cr) electrodes (figure 3.2.4.1.1 and figure 3.2.4.1.3). At equilibrium ($V_g = 0$) and at $V_{ds} = 0$ the E_F of the Cr metal and the semiconductor align. However, due to the different work functions between the Cr and semiconductor, a band bending arises which causes the appearance of a barrier (Schottky barrier) between them. A Schottky barrier is an electrostatic depletion layer at the interface between the metal and semiconductor that the electrons need to overcome to access the channel. By choosing an adequate metal with a work function compatible with the semiconductor, Schottky barriers can be avoided. For n-type devices, low work function metals that have proven to be effective (e.g. scandium (3.5 eV) and erbium (3.0 eV)).¹⁵⁴⁻¹⁵⁶ However, low work function metals have disadvantages such as they suffer from oxidation that cause transistor degradation and low yield. Larger work function metals are more stable in air and do not suffer from oxidation (e.g. Au (5.1eV), palladium (5.12 eV) and platinum (5.65eV)).¹⁵⁴⁻¹⁵⁶ To prevent delamination from the SiO_2 surface they are combined with adhesions layers of oxidizing metals such as Cr and titanium. For illustration, in figure 3.2.4.1.3 we contacted the semiconducting channel with Cr, creating a Schottky barrier. When $V_{ds} > 0$, the source rises above the drain causing a tilt in the diagram and enabling a preferential current direction. At $V_g = 0$, there is some electron drift. Some electrons tunnel through or leap the barrier and enable conduction. At $V_g > 0$, E_F moves closer to E_c and the Schottky barrier becomes smaller and thinner. This enables high conduction of electrons through the channel. When $V_g < 0$, E_F is far from E_c and the Schottky barrier is high, this will cause no conduction of electrons through the channel. As detailed in the previous

paragraph, if a high enough $V_g \ll 0$ is applied, it is possible to create an inversion in the channel, however experimentally the dielectric layer will most likely break down first causing gate leaks through the channel. Please recall that an n-type semiconductor is used for all the portrayed scenarios; for a p-type semiconductor the mechanism of operation is flipped.

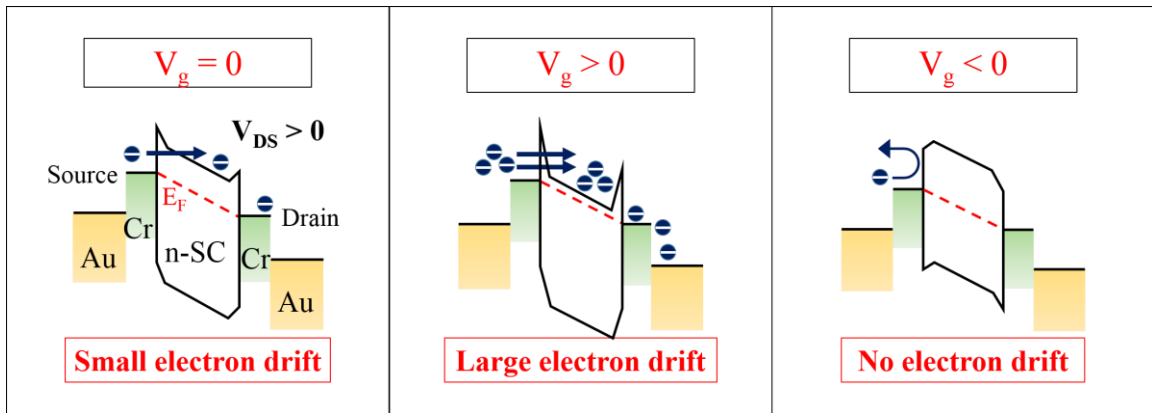


Figure 3.2.4.1.3. Band diagram of FET. The schematic shows the current flow for an FET at various applied gate voltages and the modulation of the Schottky barrier.

In summary, an applied voltage to the gate can dictate the current level throughout the 2D semiconducting channel by modulating the E_F , enabling on/off states in the semiconductor. These on/off states make FETs very important for technological applications and high on/off ratio semiconductors such as 1H-MoS₂ very promising candidates for next generation electronics. Three terminal measurements conducted on graphene (zero gap semiconductor), 1H-MoS₂ (n-type semiconductor) and CNTs (p-type semiconductor) will be presented in a following section.

3.2.4.2 Device fabrication

Two methods enable the creation of a three terminal device (figure 3.2.4.2.1): electron beam lithography (e-beam) and photolithography. E-beam lithography relies on electrons scanning an electron-sensitive resist (e.g. C4 PMMA), while photolithography relies on ultraviolet photons scanning a light-sensitive photoresist (e.g. S1813). Both methods allow the manufacturing of sub-micron size features on a substrate.

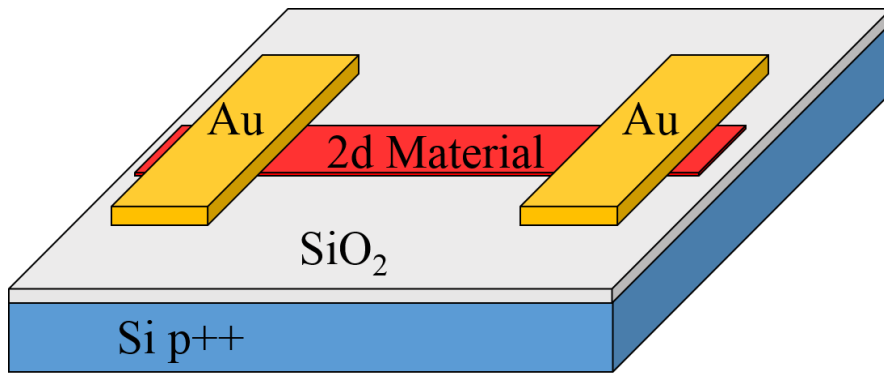


Figure 3.2.4.2.1. Schematic of a three terminal device.

E-beam lithography.

A highly p doped Si/SiO₂ substrate is spin coated with an electron sensitive resist (C4 PMMA) at 3000 rpm for 60 seconds. The substrate is baked at 150 °C for 2 min to harden the resist. It is then inserted into a scanning electron microscope (SEM). In the SEM, a LaB₆ filament emits electrons through a thermionic emission process and the electrons are accelerated at 30 kV towards the substrate. Using magnetic fields, the electron beam is directed to write a pattern on the substrate; the pattern is determined by a predesigned CAD file. The areas of the resist that have been scanned by the electrons become soluble in the organic solvent MIBK. The exposure length and power is

dependent on the minimum size feature we wish to realize: lower current (55 pA) and slow scan times will be used for sub-micron size features. The substrate is extracted from the SEM and developed for 5 seconds in a 1:1 MIBK:IPA solution followed by a 10-second rinse in IPA; the features of the CAD design are now defined on the substrate which is ready for metal deposition (figure 3.2.4.2.2).

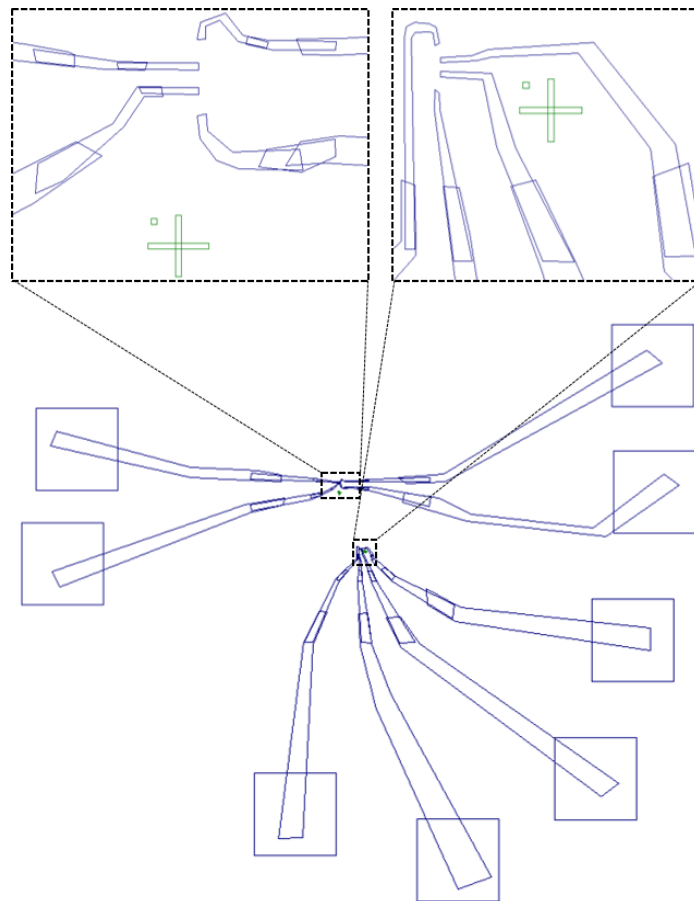


Figure 3.2.4.2.2. CAD design for SEM. E-beam writing design for a four probing contact, the green cross is acting as an alignment marker and is 20 μm in length.

Photolithography

A highly p doped Si/SiO₂ 4 inch wafer is spin coated with the 1st layer of positive photoresist PMGI at 4000 rpm for 45 seconds and baked at 210 °C for 5 min. This is

followed by a 2nd layer of positive photoresist S1813 spin coated at 5000 rpm for 45 seconds and baked at 100 °C for 2 min. The initial PMGI is used a sacrificial layer in this bilayer photolithography process and will protect the underlying material or substrate. The wafer is then inserted into a Mask Aligner accompanied by a pre-made mask with a specific design. The goal of the mask is to protect regions of the wafer from the UV light whereas the unprotected regions are exposed to the UV light which break down the polymer chain of the photoresist making it soluble in the organic solvent MF319. A typical mask for photolithography used throughout this thesis can be found in figure 3.2.4.2.3. There are three exposure modes: contact, proximity and projection (figure 3.2.4.2.4). In contact mode the mask is in direct contact with the substrate which can cause damage to the wafer and mask, in proximity mode the mask is at a small distance from the substrate protecting the sample but this comes with a sacrifice in resolution, in projection mode lenses are used between the mask and the substrate which enables higher resolution. Each exposure mode is governed by the minimum feature size (MFS):

$$\begin{aligned}
 \textit{Contact mode: MFS} &= \sqrt{d\lambda} \\
 \textit{Proximity mode: MFS} &= \sqrt{(d + g)\lambda} \\
 \textit{Projection mode: MFS} &= k_1 \frac{\lambda}{NA}
 \end{aligned}$$

where λ is the wavelength of the incoming photons, d is the resist thickness, g is the gap between the mask and substrate, NA is the numerical aperture and k_1 is a “technology constant”. Throughout this thesis the photolithography devices were made using contact mode unless specified otherwise. The UV light is emitted from a lamp at 1000 W, an exposure dose of 80 mJ/cm² and a 5 second exposure time. The substrate is developed in MF319 for 30 seconds followed by 60 seconds in DI water. The exposed channels are

now visible on the wafer and are ready for metal deposition. It should be noted that this process describes a positive photoresist; negative photoresists also exist, whereby the unexposed regions are removed by the developer. However, negative photoresists were not employed in any experiments described in this thesis.

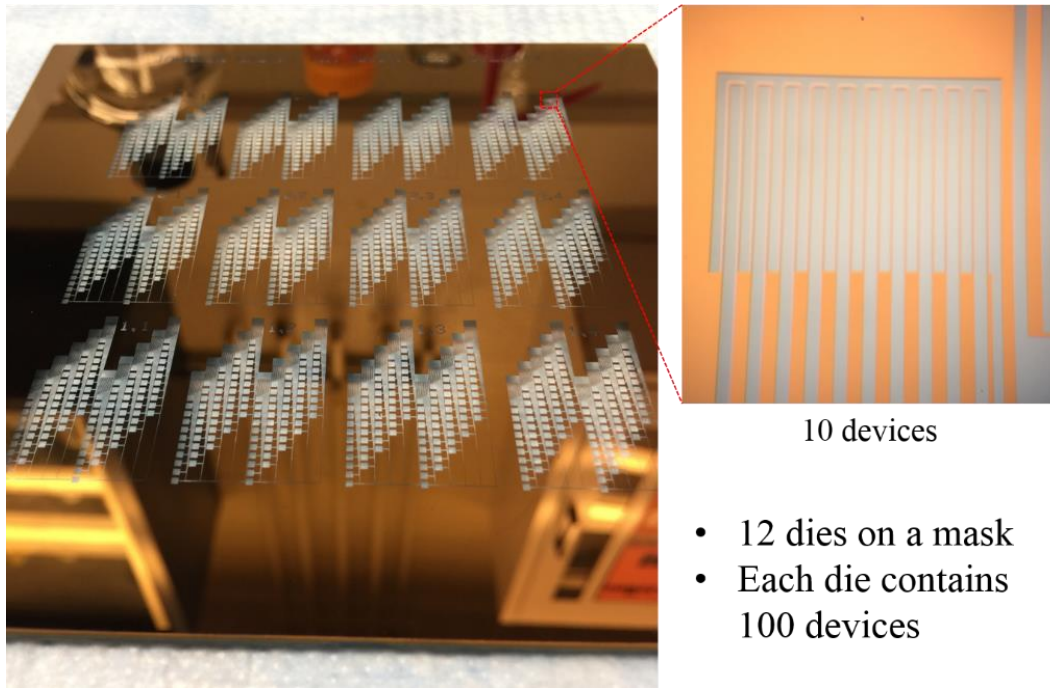


Figure 3.2.4.2.3. Mask for photolithography. Typical photolithography mask, mask consists of 12 dies, each die contains multiple interdigitated source drain figures yielding 100 devices per die.

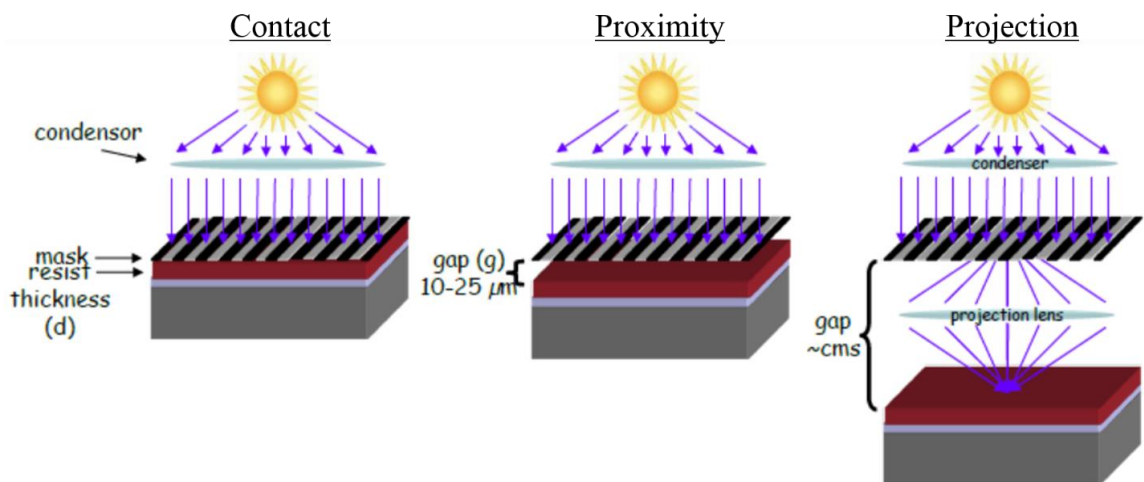


Figure 3.2.4.2.4. Photolithography exposure modes. (Figure from Professor Kagan ESE525 lecture).

Following the photolithography or e-beam lithography process, metal contacts are deposited into the visible channels. The substrate is inserted into a thermal evaporator where metals (e.g. 5 nm Cr/ 40 nm Au) are evaporated onto the substrate. The initial Cr layer enables better adhesion of the Au to the substrate. The substrate is retrieved from the evaporator and inserted into a solvent for lift-off. For photolithography, the sample is inserted into an 1165 bath (an organic solvent) for 12h then followed with a 1h acetone bath and 1h IPA bath. For e-beam lithography, the sample is inserted into an acetone bath for 12h followed with a 1h IPA bath. Once the lift-off is complete the samples are dried with a N₂ gun and the devices are ready for use. An illustration of the photolithography process is shown in figure 3.2.4.2.5.

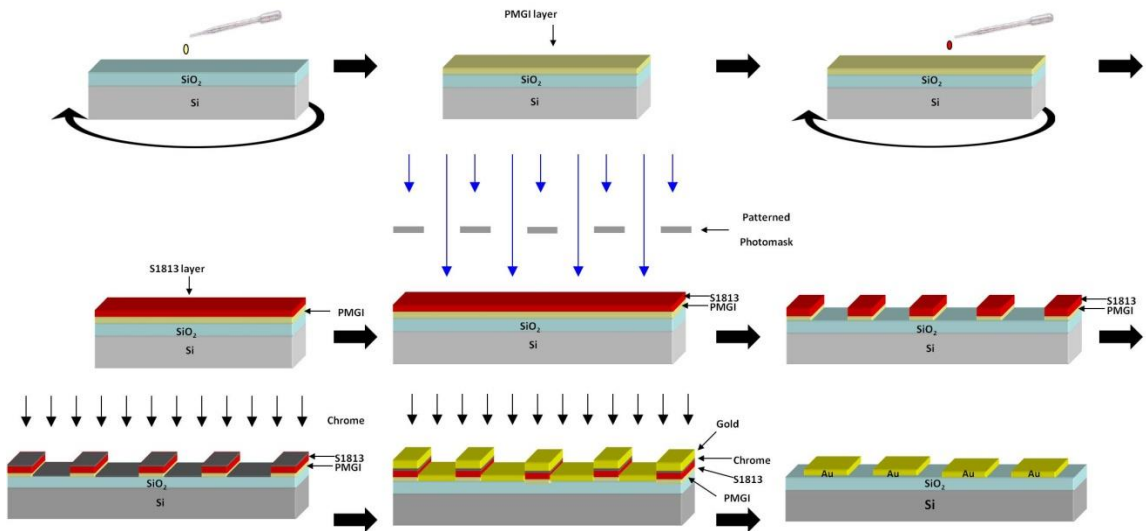


Figure 3.2.4.2.5. Outline for photolithography process. In order: deposition of positive photoresist PMGI and spin coating, baking, deposition of positive photoresist S1813 and spin coating, baking, exposure to UV light, developing using MF319, evaporating initial chrome layer, evaporating gold layer and finally liftoff.

Three terminal devices made by e-beam lithography and photolithography can be found in figure 3.2.4.2.6. As previously mentioned, e-beam lithography enables the contact of a unique flake allowing only the creation of few devices but with high

precision. In figure 3.2.4.2.6 devices were made on a Si/SiO₂ chip after CVD growth by e-beam lithography so that we can avoid certain regions and contact flakes at specific locations. By photolithography we contact many flakes, this method permits the manufacturing of many devices in a scalable format. As seen in figure 3.2.4.2.6, many 1H-MoS₂ flakes overlap the source drain creating many contact regions for one device, hundreds of devices are made across a small chip.

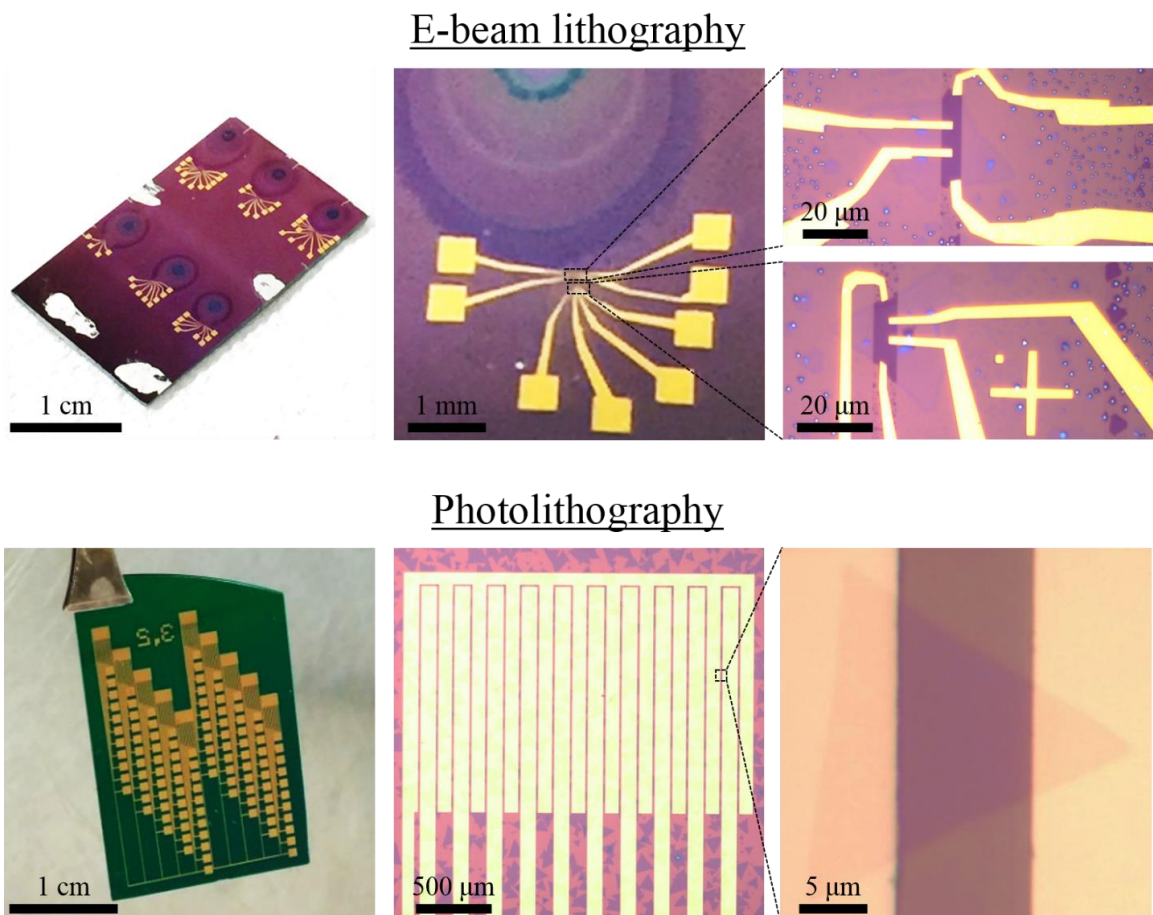


Figure 3.2.4.2.6. E-beam lithography and photolithography. E-beam lithography contacts unique flakes at specific location creating only few devices. Photolithography contacts many flakes making scalable devices.

3.2.4.3 Three terminal measurements and mobility calculation

Figure 3.2.4.3.1 shows a three terminal measurement performed in ambient atmosphere and temperature on CVD synthesized 1H-MoS₂, graphene and CNTs. The current vs. gate voltage (I_{V_g}) plot of 1H-MoS₂ reveals an n-type semiconductor with the off state at $V_g < 0$ and the on state at $V_g > 0$. CNTs are p-type semiconductors; we therefore presume opposite behavior from the 1H-MoS₂. Graphene is a zero gap semiconductor and as such we do not observe an off state but a Dirac cone. All curves show a hysteresis effect: the current in the forward sweep does not overlap with the back sweep. Hysteresis is attributed to residual electric fields induced near the material by the gate voltage sweep, identified as charge traps in the silicon oxide layer or adsorbed impurities on the material surface. Charge traps in the silicon oxide layer fill during the forward gate sweep resulting in a different electrostatic environment on the return sweep.^{157–159} Inserting the 1H-MoS₂ device under vacuum significantly reduces hysteresis in the I_{V_g} curves. Vacuum reduces the amount of adsorbed impurities on the monolayer surface, therefore fewer molecules can be polarized to induce a residual electric field.

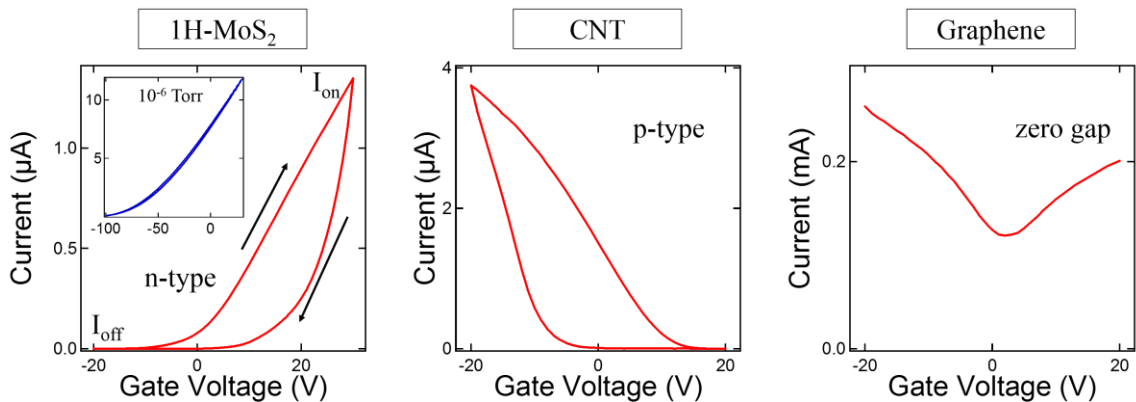


Figure 3.2.4.3.1. I_{V_g} curve for different semiconductors. I_{V_g} for 1H-MoS₂ in air (red) and in vacuum (blue) with an applied V_{ds} of 1V, for CNT a applied V_{ds} of 0.1V, for graphene a applied V_{ds} of 0.1V.

From the IV_g curve of a semiconductor we can extract 2 important characteristics that are vital in evaluating the quality of the CVD grown material: mobility and the on/off ratio. Graphene lacks the on/off ratio, its quality is therefore evaluated on the V_g value of the Dirac point and carrier mobility. The carrier mobility can be estimated using:¹⁶⁰

$$\mu_{FE} = \frac{L}{W} * G_m * \frac{1}{C_i} * \frac{1}{V_{ds}}$$

where L is the channel length, W is the channel width, G_m is the transconductance, C_i is insulator capacitance per unit area and V_{ds} the applied bias. μ_{FE} reflects not only the intrinsic properties of the channel material but also sources of contact resistance such as Schottky barriers. C_i and G_m can be estimated using the following equations:

$$C_i = \frac{C}{A} = \frac{\epsilon_0 * \epsilon_r}{d} \quad ; \quad G_m = \frac{\delta I}{\delta V_g}$$

ϵ_0 is the permittivity of vacuum ($8.85 * 10^{-12}$ F/m), ϵ_r is the relative dielectric constant (3.9 for SiO_2), d is the thickness of dielectric material. δI is extracted for a specific δV_g in our IV_g curve. The mobility of the CVD grown graphene device shown in figure 3.2.4.3.1 is measured at $2020 \text{ cm}^2\text{V}^{-1}\text{s}^{-1}$ and the Dirac point is identified at 2V. These values are comparable to that of exfoliated graphene showing the tremendous progress made in the CVD synthesis of high quality graphene. The carrier concentrations in 1H-MoS₂ are much lower than in graphene, leading to much lower conductance and lower mobility. Reported mobility values for 1H-MoS₂ range in the $0.1\text{-}30 \text{ cm}^2\text{V}^{-1}\text{s}^{-1}$ with on/off ratio as high as 10^8 .^{41,48,62,95,161,162} The mobility of the CVD grown 1H-MoS₂ device shown in figure 3.2.4.3.1 is measured at $10 \text{ cm}^2\text{V}^{-1}\text{s}^{-1}$ and the on/off ratio is estimated at 10^6 . The mobility values for the CVD grown 1H-MoS₂ show the high quality synthesized material and is fast approaching the reported values for exfoliated material.^{163,164}

3.2.4.4 Local chemical gating effect

The local chemical gating effect is a term that is referenced throughout the biosensing sections of this thesis. It involves 2D materials and a chemical gating effect happening on the surface of the nanomaterial (figure 3.2.4.4.1). In the previous section, we described how our 2D materials is greatly influenced by the electric field generated from the gate. However the gate is not the only option to generate an electric field. Charged chemicals can also have the same effect as the gate on the conducting channel, causing the 2D material to function as a chemical field effect transistor (ChemFET).¹⁶⁵

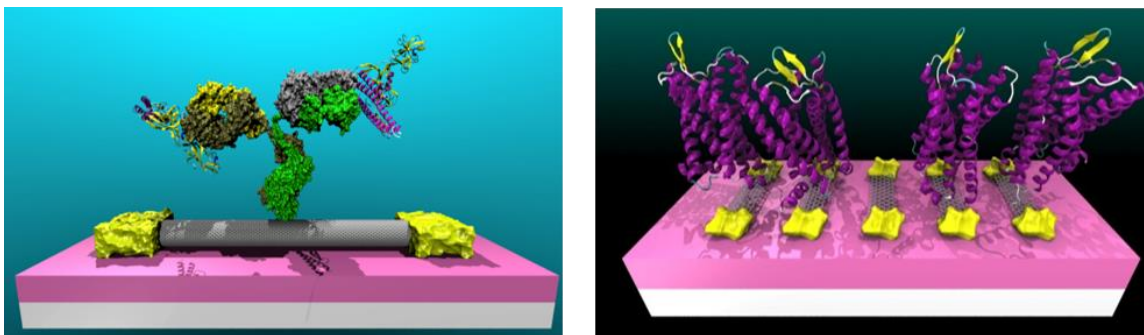


Figure 3.2.4.4.1. Artistic representation of chemical binding on nanomaterials. Chemical binding for CNT and graphene.

Figure 3.2.4.4.2 is a qualitative description of the ChemFET and the effect adsorbed molecules/ions have on the MOSFET device. Starting with our previous schematic of an n-type semiconductor MOSFET (step 1), a bias is applied across the nanomaterial and a positive gate voltage induces negative charges in the channel leading to conduction in our nanomaterial. The surface of the nanomaterial is then functionalized making the nanomaterial specific to a target (step 2). The target is introduced and binds to the surface of the nanomaterial due to the functionalized surface (step 3). This approach resembles a key and keyhole model where only a specific target binds to the surface and

nothing else. The target is charged and at a distance d (\sim nm) from the conducting channel, and the two are separated by air that acts as a dielectric. Referring back to the capacitance equation, the capacitive coupling between the target and the nanomaterial becomes non negligible and the target creates a local electric field. This field induces charges in our conducting channel that effectively change the overall current level. For our example, let us assume the target in step 3 is negatively charged, the negative charges induce positive charges in our MOSFET. The positive charges pair with the negative charges present in the MOSFET and reduce the current level in our channel (step 4).

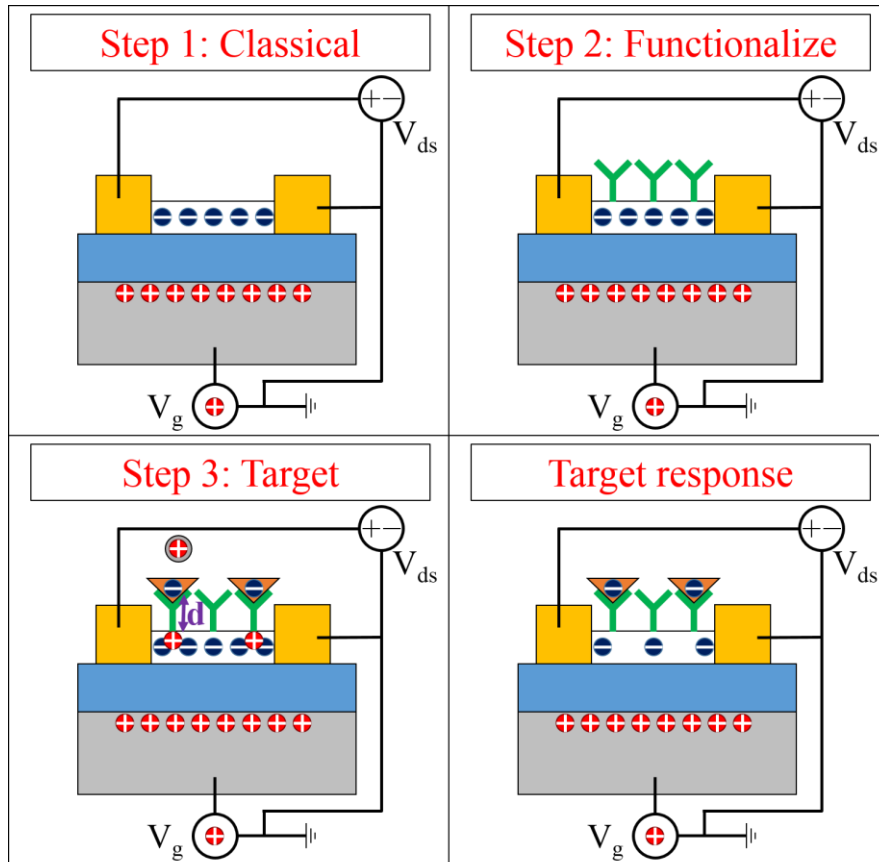


Figure 3.2.4.4.2. Qualitative description of the ChemFET and the influence it has on a MOSFET device. Step 1, classical n-type MOSFET device. Step 2, the surface of conducting channel is functionalized. Step 3, charged targets are introduced and bind to the surface resulting in a local chemical gating effect, the ChemFET induces charges in the conducting channel of the MOSFET. Step 4, decrease in current level in the MOSFET due to the ChemFET.

An example of the ChemFET having a direct effect on the conduction level in a MOSFET can be seen in figure 3.2.4.4.3. Figure 3.2.4.4.3 is an I_{V_g} curve of 1H-MoS₂ (n-type semiconductor) as it undergoes the same procedure described in figure 3.2.4.4.2. The functionalization curve does not differ from the raw original MoS₂. The target is applied and the current level dramatically drops by an amount Δ , showing clear evidence that the target has had an effect on the overall free charge concentration in the channel through the local chemical gating effect. For biosensing, it is these changes of current that we monitor throughout the sensing, by exposing the channel to different concentrations of target and reading out the changes in current Δ . By plotting the changes in current Δ as a function of target, we identify a clear relation between the two that is fitted by a Hill Langmuir equation.^{166–168} The Hill Langmuir equation will be described in section 4.2.1.

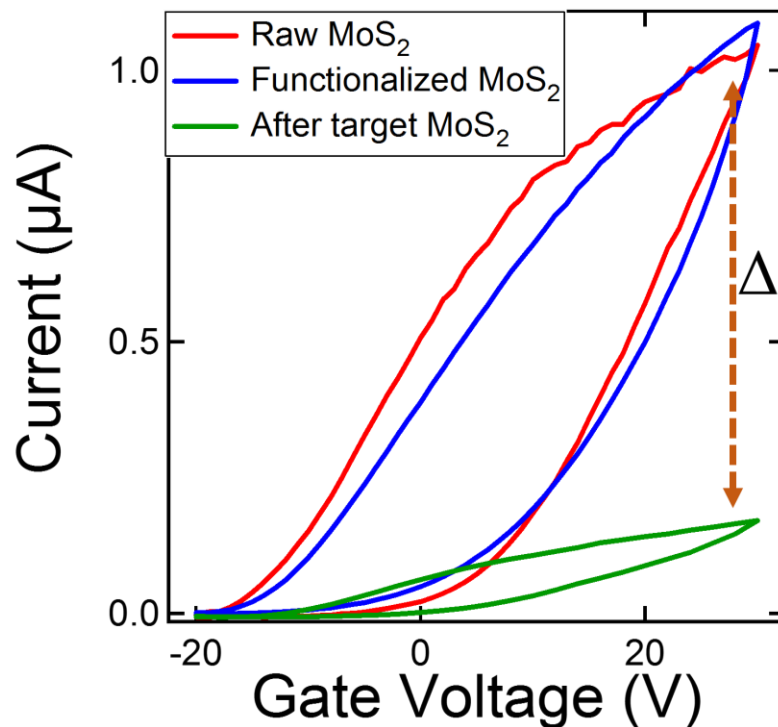


Figure 3.2.4.4.3. I_{V_g} curves of MoS₂ as it undergoes a local chemical gating effect. Raw MoS₂ (red curve), functionalized MoS₂ (blue curve), after the target (green curve).

CHAPTER IV.

1H-MoS₂, from Synthesis to Applications

Monolayer 1H- molybdenum disulfide (1H-MoS₂) is the most studied transition metal dichalcogenide (TMD) to date. It possesses reasonable values of charge carrier mobility, high on/off ratios, a tunable bandgap, high photoluminescence, and many more properties that scientists continuously discover.

In this Chapter, I will detail our synthesis approach for high quality monolayer 1H-MoS₂ flakes and how we were able to control the exact growth nucleation site through a patterning technique. The high quality of the flakes we synthesized have been reported in a number of publications. I will reveal the transfer procedure to remove the as-grown flakes from the growth substrate. This transfer technique enabled the manufacturing of scalable 1H-MoS₂ field effect transistors that led to multiple applications, notably in sensing. I will then discuss our work on a MoS₂ biosensor that can detect low levels of opioids in buffer; how we understood the large responses associated with MoS₂ vapor sensors; the manufacturing of a universal biosensor; and the incorporation of these sensors on flexible substrates. Finally, I will report the work of multiple groups we collaborate with, presenting their unique and fascinating results on our synthesized monolayer 1H-MoS₂ flakes.

4.1 1H-MoS₂ synthesis

4.1.1 Large area growth of monolayer 1H-MoS₂ flakes by CVD

Monolayer 1H-MoS₂ flakes are grown by chemical vapor deposition (CVD) method on a Silicon/Silicon-dioxide (Si/SiO₂) substrate. A 1% sodium cholate growth promoter is initially applied on a Si/SiO₂ substrate. Sodium cholate promotes monolayer growth by increasing the surface adhesive energy relative to the adatom cohesive energy.^{58,59,98,169} We then apply micro-droplets of a saturated aqueous solution of ammonium heptamolybdate (AHM) on the corners of the growth substrate; the AHM acts as the molybdenum (Mo) feedstock. The growth substrate is then inserted into the center of the furnace. We place a Si/SiO₂ chip containing 25 mg of sulfur (S) upstream at a distance of 17 cm from the growth substrate. The chamber is then flushed for 5 min under a constant flow of 500 standard cubic centimeter per minute (sccm) of ultra-high purity nitrogen (N₂). An optical image before 1H-MoS₂ growth is shown in figure 4.1.1.1.

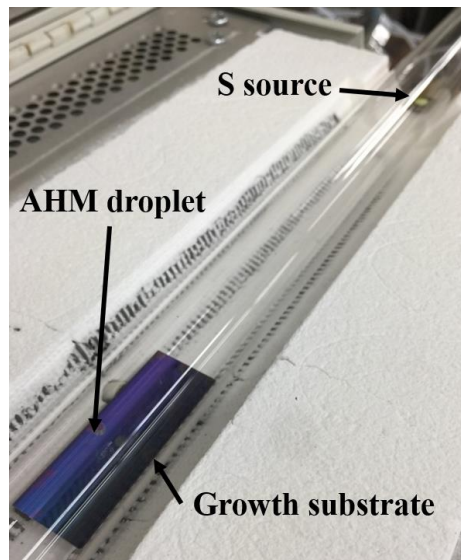


Figure 4.1.1.1. Optical image showing the chip layout before 1H-MoS₂ growth.

The furnace is ramped up to 750 °C at a rate of 70°C/min under a constant flow of 500 sccm of N₂. The S source, conveniently placed upstream, reaches a temperature of 150 °C and starts sublimating. S atoms are then carried to the growth substrate by the N₂ carrier gas. On the growth substrate, the S atoms encounter the Mo atoms, causing monolayer 1H-MoS₂ flakes to grow. After a 30 min growth time, the furnace is rapidly cooled and the growth substrate is retrieved. A schematic of the growth process can be found in figure 4.1.1.2.

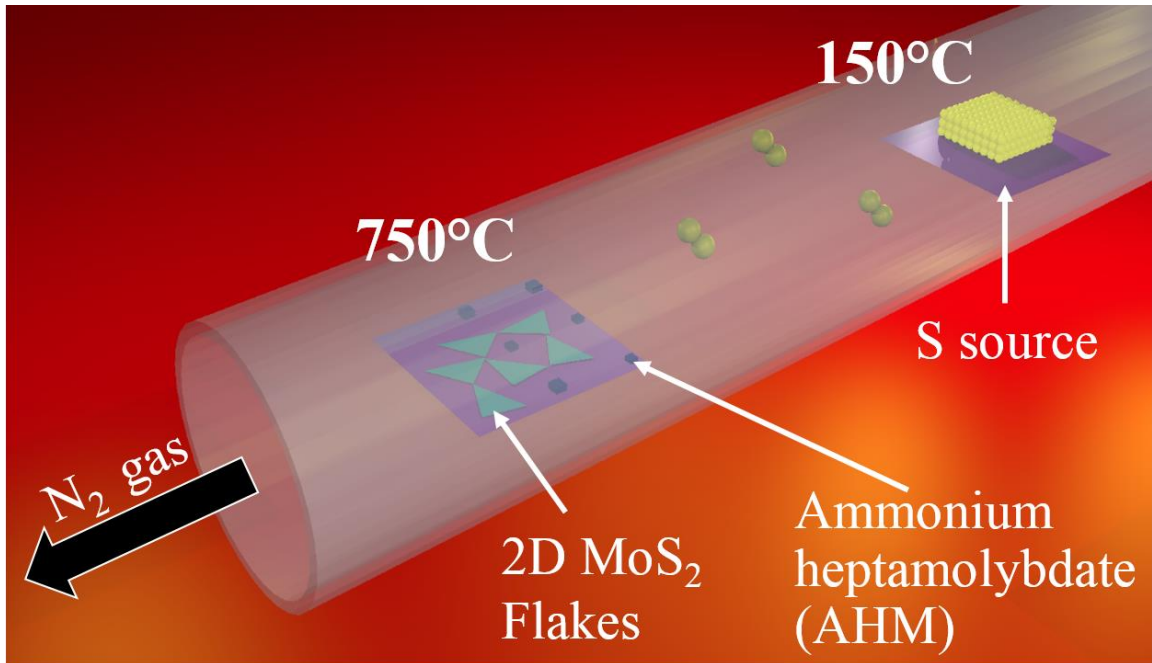


Figure 4.1.1.2. Schematic of the 1H-MoS₂ growth setup.

Optical microscopy images of a high quality growth can be found in figure 4.1.1.3. In figure 4.1.1.3 we can see the diffusion of the AHM droplets on the growth substrate and at higher magnification we can see high quality monolayer 1H-MoS₂ flakes have grown from the AHM micro-droplets. A careful optimization of all the parameters is necessary to obtain the synthesis of dense, high quality, monolayer 1H-MoS₂ flakes. For

instance, if the S source is positioned further upstream it will not reach the required temperature for sublimation, resulting in no growth. If the S source is placed closer to the growth substrate it will not sublimate at the correct rate, the latter would yield small multilayer 1H-MoS₂ flakes. A careful analysis of all the parameters and their implications is done during the optimization of the growth process. Once the optimized parameters are found, the growth process becomes very reproducible.

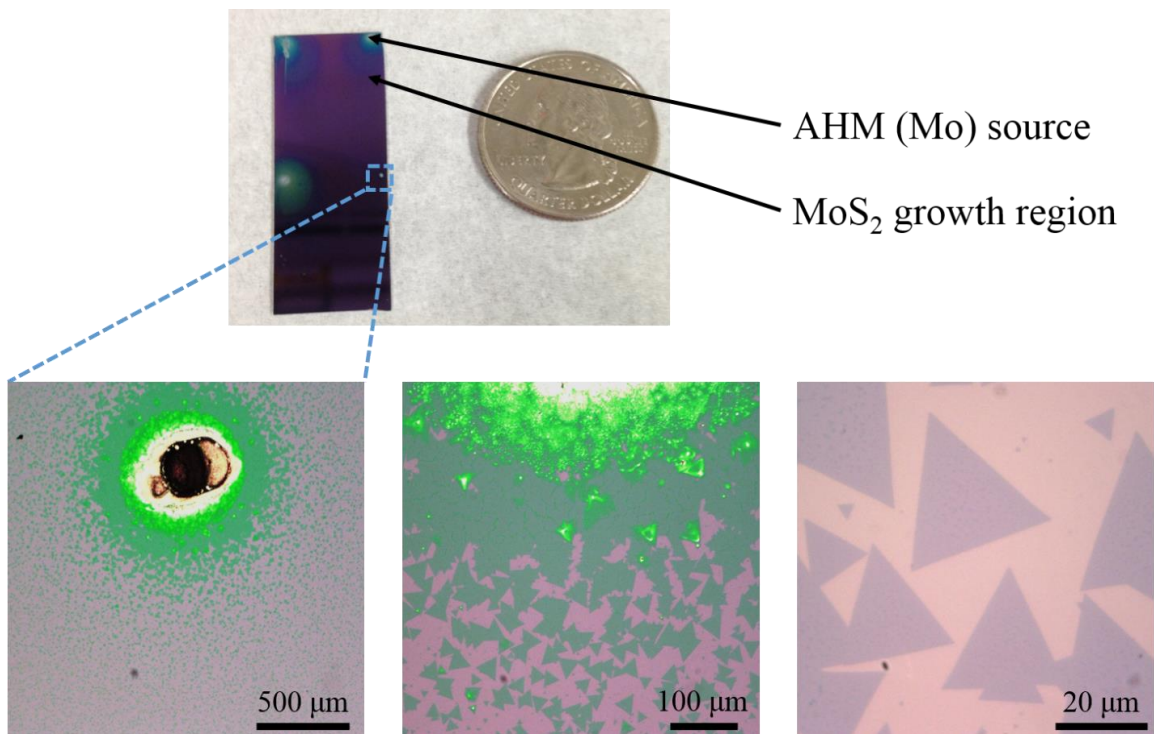


Figure 4.1.1.3. Optical microscopy images of a 1H-MoS₂ growth. Results reveal high quality monolayer 1H-MoS₂ grown throughout the growth substrate.

After growth, the monolayer 1H-MoS₂ flakes are carefully characterized by Raman, atomic force microscopy (AFM), and Aberration Corrected Scanning Transmission Electron Microscopy (ACSTEM) to confirm the monolayer height and the quality of the 1H-MoS₂ flakes (figure 4.1.1.4).

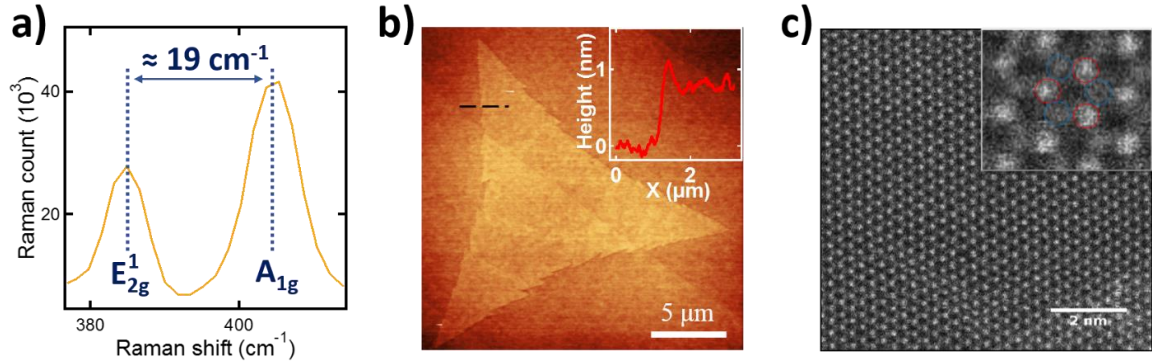


Figure 4.1.1.4. Characterization of the CVD grown 1H-MoS₂. a) Raman results. b) Atomic Force microscopy scan. c) High-angle annular dark field images.

Raman peaks reveal the E_{2g}¹ and A_{1g} peaks spacing of 19 cm⁻¹ (figure 4.1.1.4a.), in agreement with previous reports of monolayer 1H-MoS₂.^{21,77,78} AFM height scan confirms the monolayer height of 0.8 nm (figure 4.1.1.4b), in agreement with previous reports of monolayer TMDs.^{62,74,170,171} ACSTEM images reveal the 1H phase and low defect density (figure 4.1.1.4c). In the ACSTEM images we can also correctly identify the S and Mo atoms as the high-angle annular dark field (HAADF) image intensity is proportional to the square of the atomic number (Z). These results are in agreement with previous reports and with section 3.2.

4.1.2 Large area 1H-MoS₂ transfer

CVD grown 1H-MoS₂ flakes are transferred onto various substrates by potassium hydroxide (KOH) etching (e.g. carbon grid for TEM imaging, or devices made by photolithography for electrical measurements). KOH is a known etchant for Si and SiO₂ and is widely used due to its non-toxicity, fast etch rate and affordability.¹⁷² The transfer process follows the steps highlighted in figure 4.1.2.1.

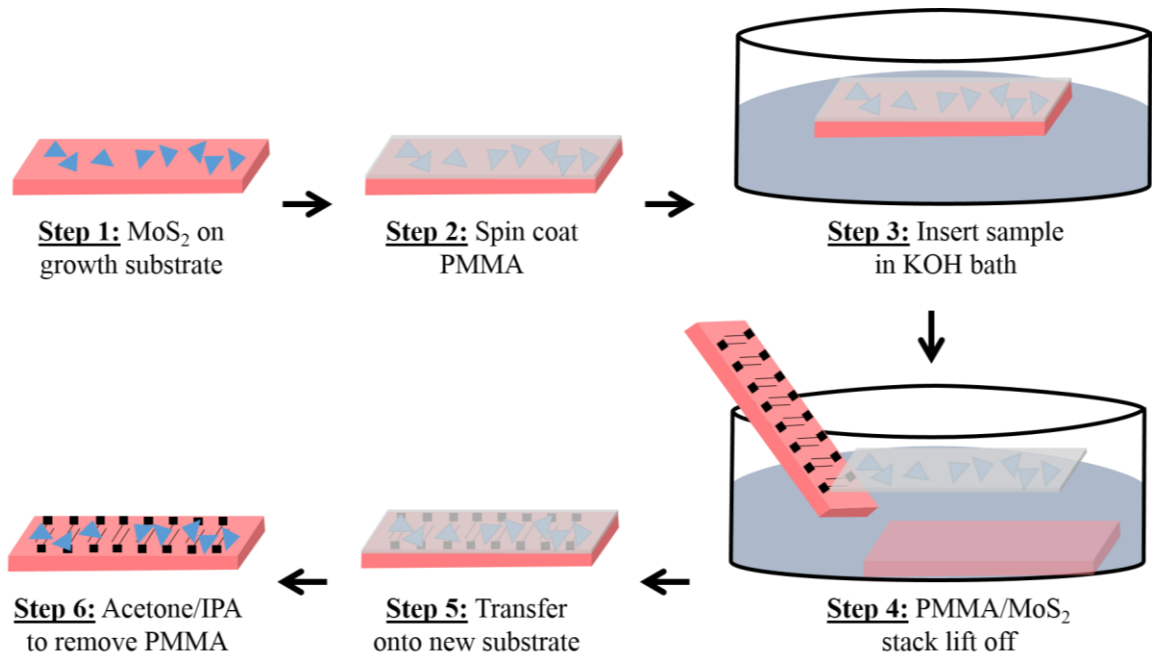


Figure 4.1.2.1. Schematic representation of the 1H-MoS₂ transfer process using KOH.

The sample is first retrieved from the CVD furnace and examined to confirm the presence of MoS₂ flakes on the growth substrate (step 1). C4 PMMA is then spin coated on the substrate at 3000 rpm for 60 seconds (step 2) creating a PMMA/MoS₂ stack. The sample is then set afloat in a 1M KOH bath (step 3); the corners of the substrate are in contact with the etchant and the etching begins along the edges. As seen in figure 4.1.2.2 the PMMA/MoS₂ stack remains afloat throughout the etching process until KOH has

completely etched the top layer of SiO₂ atoms, releasing the PMMA/MoS₂ stack from the growth substrate (step 4). The PMMA/MoS₂ stack is then transferred through 2 *deionized water (DI) baths* using a piece of polyethylene terephthalate (PET) to remove KOH residue. It is then scooped onto the new substrate (step 5) and left to dry for 1h. The sample is then baked at 100°C for 20 seconds to promote a better adhesion between the 1H-MoS₂ flakes and the new substrate. The sample is inserted into an acetone bath for 12h to fully remove the top PMMA layer, this is followed with a 1h isopropanol (IPA) bath to remove any acetone residue (step 6). The sample is retrieved and gently dried with a N₂ gun. Through this method we were able to successfully transfer the MoS₂ flakes off the growth substrate and onto any arbitrary substrate with minimal flake tearing and PMMA residue.

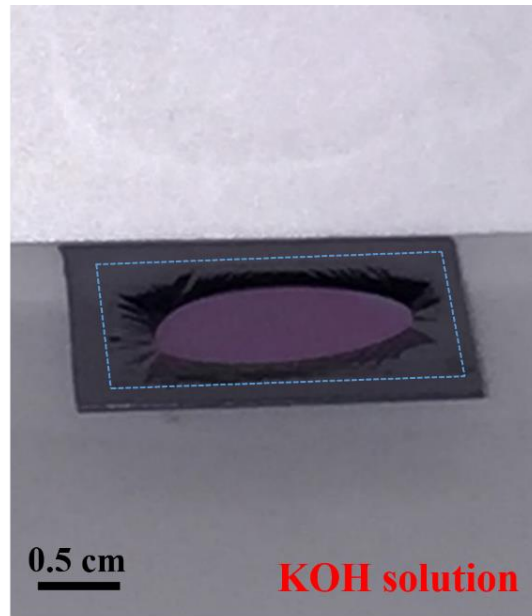


Figure 4.1.2.2. Optical photograph capturing the KOH etching step. The edges of the PMMA have been highlighted in blue.

4.1.3 Seeded growth of highly crystalline molybdenum disulfide monolayers at controlled locations

The results presented in this section have also appeared in the publication “Seeded Growth of Highly Crystalline Molybdenum Disulphide Monolayers at Controlled Locations”, Gang Hee Han, Nicholas J. Kybert, Carl H. Naylor, Bum Su Lee, Jinglei Ping, Joo Hee Park, Jisoo Kang, Si Young Lee, Young Hee Lee, Ritesh Agarwal, A. T. Charlie Johnson, Nature Communications, 2015, 6 6128.

Abstract

Monolayer transition metal dichalcogenides are materials with atomic structure complementary to graphene but diverse properties, including direct energy band gaps that make them intriguing candidates for optoelectronic devices. Various approaches have been demonstrated for the growth of molybdenum disulphide (MoS₂) on insulating substrates, but to date growth of isolated crystalline flakes has been only at random locations. Here we use patterned seeds of molybdenum source material to grow flakes of MoS₂ at predetermined locations with micrometre-scale resolution. MoS₂ flakes are predominantly monolayers with high material quality, as confirmed by atomic force microscopy, transmission electron microscopy, and Raman and photoluminescence spectroscopy. Since the monolayer flakes are isolated at predetermined locations, transistor fabrication requires only a single lithographic step. Device measurements exhibit carrier

mobility and on/off ratio that exceed $10 \text{ cm}^2\text{V}^{-1}\text{s}^{-1}$ and 10^6 , respectively. The technique provides a path for in-depth physical analysis of monolayer MoS₂ and fabrication of MoS₂-based integrated circuits.

Introduction

The presence of an intrinsic direct energy bandgap in molybdenum disulphide (MoS₂) monolayers makes this two-dimensional material of both fundamental and technological interest.^{62,173–177,177–180} Several synthetic methods have been reported, including sulphiding of Mo thin film,¹⁸¹ and annealing of ammonium tetrathiomolybdate (ATM), which has both Mo and S components.¹⁸² One promising technique is the growth of MoS₂ flakes by chemical vapour deposition (CVD) of molybdenum trioxide (MoO₃) and solid sulphur, which can yield highly crystalline, predominantly monolayer material.^{95,169,183–185} However, this method typically leads to growth of MoS₂ flakes in uncontrolled locations on the substrate, which limits its utility for many applications. Control over the position of MoS₂ flakes on oxidized silicon has been reported through the use of stamping¹⁸⁶ and masking¹⁸⁷ techniques, but neither of these allowed for the creation of large (tens of micrometres) monolayer domains at predetermined locations with micrometre-scale resolution. Substrate patterning has been used to control nucleation and growth of crystalline flakes of two-dimensional topological insulator materials on mica,¹⁸⁸ but it remains unclear whether this approach can be generalized to MoS₂ on oxidized silicon. Seeding techniques that allow growth at defined locations are

well established for graphene,^{189,190} and equivalent approaches for MoS₂ synthesis are highly desirable.

Here we report the use of lithographically patterned islands of MoO₃ or ammonium heptamolybdate (AHM) as seed material for the growth of crystalline MoS₂ monolayers at pre-defined locations on oxidized silicon substrates. MoS₂ grown by this approach shows many favourable characteristics, e.g., high crystallinity; excellent optical properties, including a direct band gap, as indicated by photoluminescence and reflection measurements; and carrier mobility ca. 10 cm²V⁻¹s⁻¹. Because the method enables control over the location of discrete MoS₂ flakes, integration into device structures is straightforward using optical lithography, with no need for an etching step. Although some applications may require further study to achieve control over the precise shape and size of the MoS₂ flakes, the methodology presented here opens a path towards scalable production of high quality devices and circuits based on MoS₂ and other transition metal dichalcogenides.

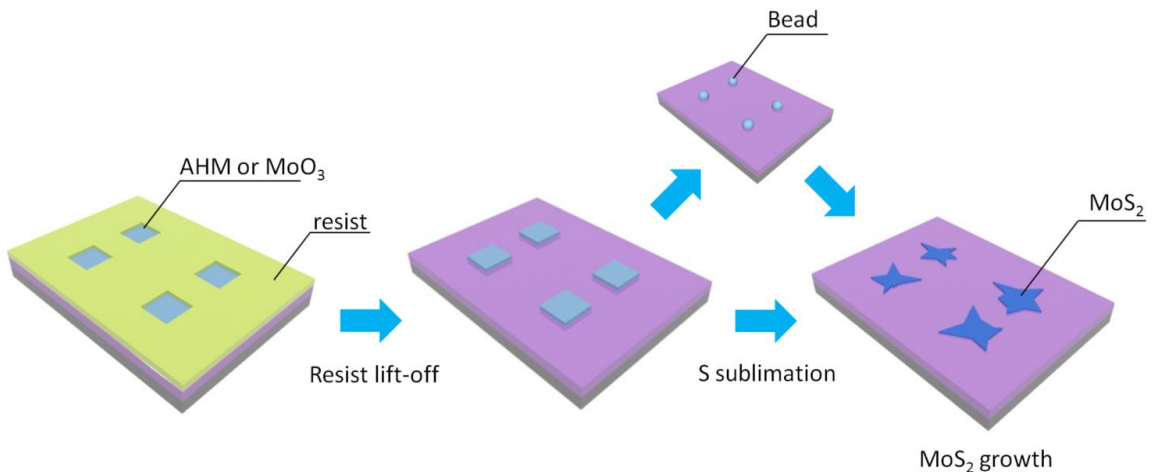


Figure 4.1.3.1. Schematic of the growth process for molybdenum disulfide using patterned molybdenum sources. An array of square wells is patterned in a conventional lithographic resist. The wells are filled by spin-coating with ammonium heptamolybdate ((NH₄)₆Mo₇O₂₄·4H₂O, AHM)

solution or thermal evaporation of molybdenum trioxide (MoO_3). The resist is removed in a lift-off process. Water droplets are condensed onto the AMH or MoO_3 by reducing the sample temperature to below the dew point using a Peltier cooler. The AMH or MoO_3 is solubilized and forms spherical beads upon drying. MoS_2 flakes are then synthesized by sublimation of solid S in a nitrogen environment in a tube furnace.

Results

Growth process. Figure 4.1.3.1 is a schematic of the MoS_2 growth process (see the Methods section and Supplementary Fig. 1 for details). The process begins with patterning of an array of square windows, typically 5 - 10 μm on a side, by e-beam or optical lithography. Next, molybdenum-containing seed material is deposited into the windows, either by thermal evaporation of MoO_3 or by spin-casting of a saturated solution of AHM in water. The AHM solution collects in the square wells but there is almost no deposition of AHM on the resist layer, which is not wet by the solution. Spin coating of AHM has advantages of speed, simplicity, and requiring no equipment beyond a standard spin coater. The resist and unwanted molybdenum source material are removed in a standard lift-off step.

At this point, the molybdenum-containing seed particle has a shape that depends upon the relative humidity and other details of the deposition process. To improve the uniformity of the seed shape and subsequent MoS_2 growth, an aggregation step is performed (see Supplementary Figs. 2 and 3) where the sample temperature is reduced to below the dew point using a Peltier cooler. Due to the hygroscopic nature of MoO_3 and AHM, water collects on the surface of the seed, which is transformed into a spherical-cap shape. This reduces the surface area of the seed particles and makes them more

uniform, leading to more efficient and reproducible MoS₂ growth. This step ensures that the seed particle is sufficiently thick to not be consumed by evaporation during the heat-up phase of the growth process. This step is essential when AHM is used as the molybdenum source, since it is quite thin when initially deposited (~ 50 nm, see Supplementary Fig. 2). In contrast, the aggregation step improves the growth reproducibility but is not required when evaporation is used to deposit a MoO₃ seed of thickness approximately 150 nm or greater. The aggregation step is followed by an annealing step at 300 °C in a nitrogen atmosphere, which converts AHM to MoO₃.^{186,187}

The next step in the process is chemical treatment of the SiO₂ surface, which has been shown to facilitate growth of MoS₂. For example, it was reported that MoS₂ growth was promoted when the SiO₂ surface was coated with materials that contain carbon ring structures that persist at the MoS₂ growth temperature, e.g., perylene-3,4,9,10-tetracarboxylic dianhydride, perylene-3,4,9,10-tetracarboxylic acid tetrapotassium salt,¹⁸⁴ or reduced graphene oxide.^{183,184} These materials promote monolayer growth by increasing the surface adhesive energy relative to the adatom cohesive energy.¹⁶⁹ We achieved excellent results by first preparing the surface with an oxygen plasma treatment and then spin-casting onto the substrate an aqueous solution of 0.1 – 1 % sodium cholate (SC), which contains multiple carbon ring structures.

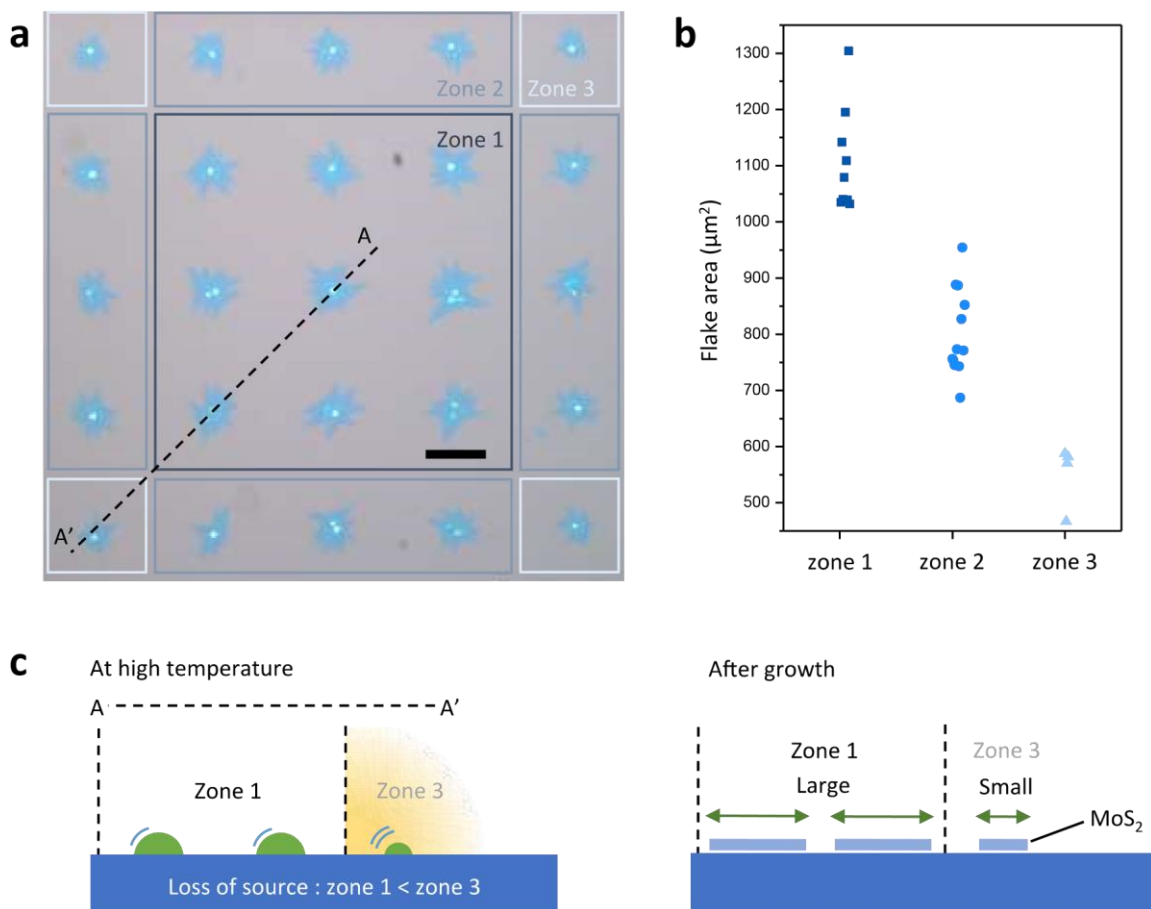


Figure 4.1.3.2. Growth of molybdenum disulphide (a) 5 x 5 array of flakes of monolayer MoS₂ grown by chemical vapour deposition. Scale bar is 50µm. Different growth zones, with different average size of the flakes (see panel (b)), are indicated by outlining: dark blue (zone 1), blue (zone 2) and light blue (zone 3). (b) Areas of individual flakes for Zone 1, 2 and 3 in panel (a). Large (500 – 1300 µm²) flakes of crystalline, monolayer MoS₂ (with small multilayer regions) were grown from the seed particles. The size of the flakes is largest in zone 1 and smallest in zone 3. (c) Schematic illustrating the proposed mechanism underlying the observation that the growth process results in larger MoS₂ flakes in the interior of the array and smaller flakes towards the edges.

For MoS₂ growth, the sample was placed in the middle of the furnace, and 20 - 50 mg of solid sulphur was placed at the upstream end. The entire growth process, including temperature ramp, growth, and cooling, was conducted under a nitrogen flow of 700 sccm. The use of patterned molybdenum source material resulted in the growth of an array of triangular/spike shaped flakes of monolayer MoS₂ (Figs. 4.1.3.2a, 4.1.3.3a-b). The flakes were comprised of multiple crystalline domains of MoS₂, as analysed

below (see Fig. 4.1.3.4). The majority of the flake region consisted of monolayer MoS₂, with small regions of multi-layer MoS₂ and/or residual seed material observed at the centre of the flake. It was found that the formation of multilayer regions could be suppressed by optimizing the dimensions of the growth seed (see Supplementary Fig. 4). The structure is consistent with a model where growth is initiated at multiple points on the MoO₃ seed to produce MoS₂ crystallites that eventually merge into a larger, faceted structure. For additional data in support of this picture, see Supplementary Fig. 5. Although the sizes and locations of the flakes were primarily determined by the array of the growth seeds, it was consistently observed that flakes that grew at the edge of the array were markedly smaller than those that grew in the middle. This is presumed to reflect diffusion of source material as the furnace temperature was increased that led to shrinkage of seed particles on the edge of the array. Particles in the centre of the array are more replenished than those at the edges due to the larger number of neighbouring particles. Once sulphur sublimation and transport into the furnace occurs, the larger source particles at the centre of the array grow larger MoS₂ flakes than the smaller source particles at the edges. In some experiments, small, triangular, presumably singlecrystal MoS₂ flakes were observed to grow in the regions between the MoO₃ seeds (data not shown). This occurred during growths that were at higher temperature compared to the samples shown in Figs 4.1.3.2a and 4.1.3.3a, and where sulphur was introduced at a later time. Presumably these conditions allowed for evaporation of Mo from the growth seed, which then reacted with the injected sulphur to form MoS₂ crystallites in regions between the seeds.

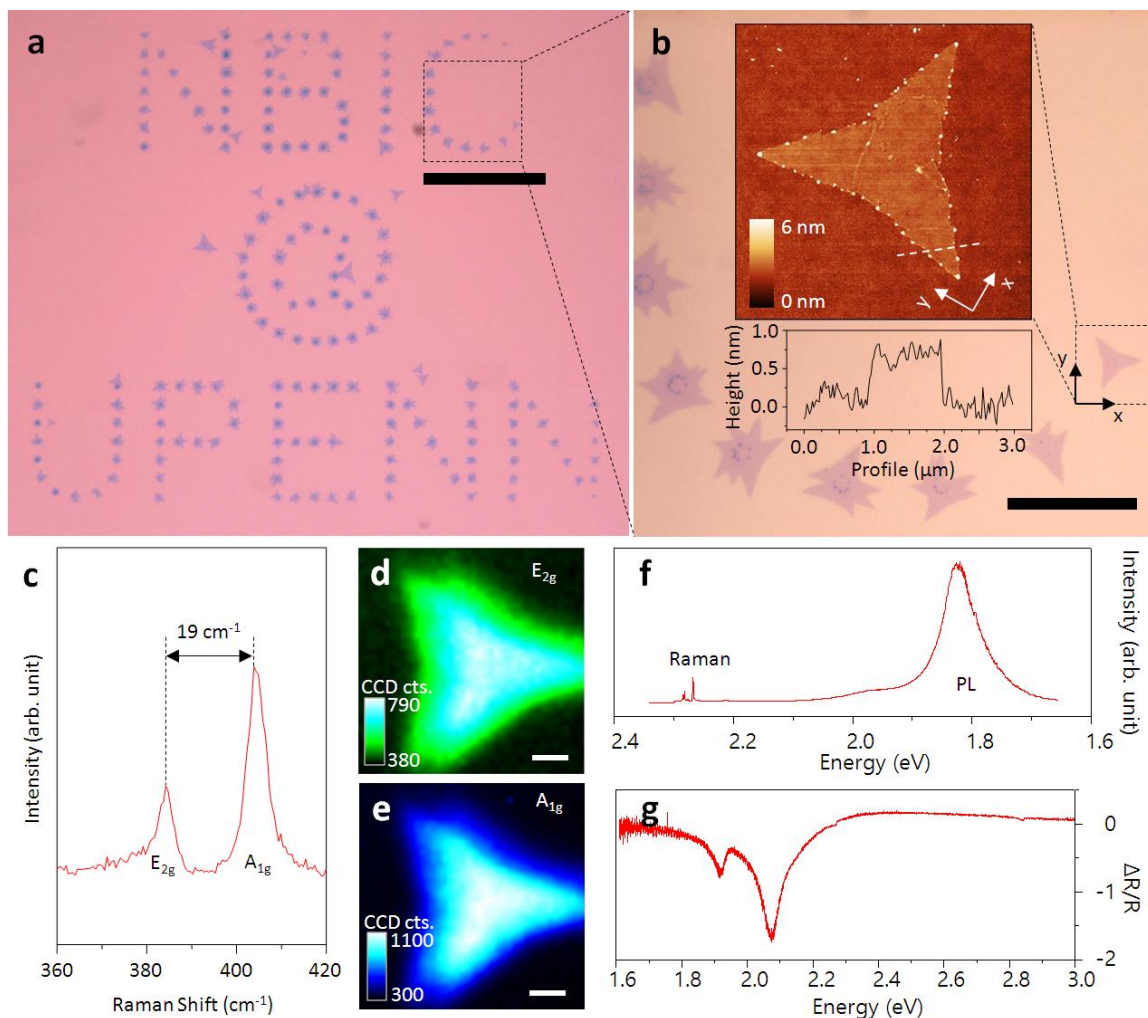


Figure 4.1.3.3. AFM and optical analysis of MoS₂ flakes (a) Optical micrograph of MoS₂ flakes grown at locations that form NBIC @ UPENN. Scale bar is 100 μm . (b) Selected area (dashed square in panel (a)) at higher magnification. Scale bar is 20 μm . Inset: AFM image of selected MoS₂ flake (dashed square). Scan image is 10 x 10 μm^2 . (c) Raman signal from the flake shows the E_{2g} and A_{1g} peaks with a spacing (19 cm^{-1}) characteristic of monolayer MoS₂. (d-e) 2D Raman maps for the E_{2g} mode (panel (d)) and A_{1g} mode (panel (e)). Scan images are 10 x 10 μm^2 . (f) Photoluminescence (PL) spectrum for the flake shows strong emission associated with the A and B excitation. at 1.83 eV and 1.97 eV, respectively. Strong PL is characteristic of monolayer MoS₂ and is absent in multilayer films. (g) Differential reflectance spectrum showing the A and B exciton features.

Structural and optical property measurements. To demonstrate the versatility of the growth technique, we synthesized a set of monolayer MoS₂ flakes to spell out the acronym for the Nano-Bio Interface Center at the University of Pennsylvania,

‘NBIC@UPENN’ (Fig. 4.1.3.3a). The centre-to-centre spacing between adjacent seeds was ca. 15 μm . Atomic force microscopy (AFM) was used to confirm that the height of a typical flake was 0.7 nm (Fig. 4.1.3.3b, inset; additional line scan data is provided in Supplementary Fig. 6. AFM images of other representative monolayer flakes of MoS₂ are provided in Supplementary Fig. 7), as expected for monolayer MoS₂.^{77,184,185,191,192} The Raman spectrum of the monolayer region of the flakes (Fig. 4.1.3.3c) showed the expected peak spacing of 19 cm^{-1} between the E_{2g} and A_{1g} modes. Raman mapping (Figs. 4.1.3.3d-e) was used to confirm that the Raman spectrum was uniform over the monolayer region as well as distinct from the spectra associated with multilayer regions and the substrate.^{77,191,193} (Maps of Raman peak positions are also shown in Supplementary Fig, 8). We performed photoluminescence (PL) and reflection measurements to confirm that the existence of a direct band gap, which is known to be characteristic of monolayer MoS₂.^{41,63,64,194} Peak features associated with the A (1.83 eV in PL and 1.91 eV in reflection measurement) and B (1.97 eV in PL and 2.07 eV in reflection measurement) excitons were also observed (Figs. 4.1.3.3f-g), confirming that the MoS₂ grown by the seeded CVD process shows the same characteristics as monolayer material fabricated by mechanical exfoliation.¹⁹⁵

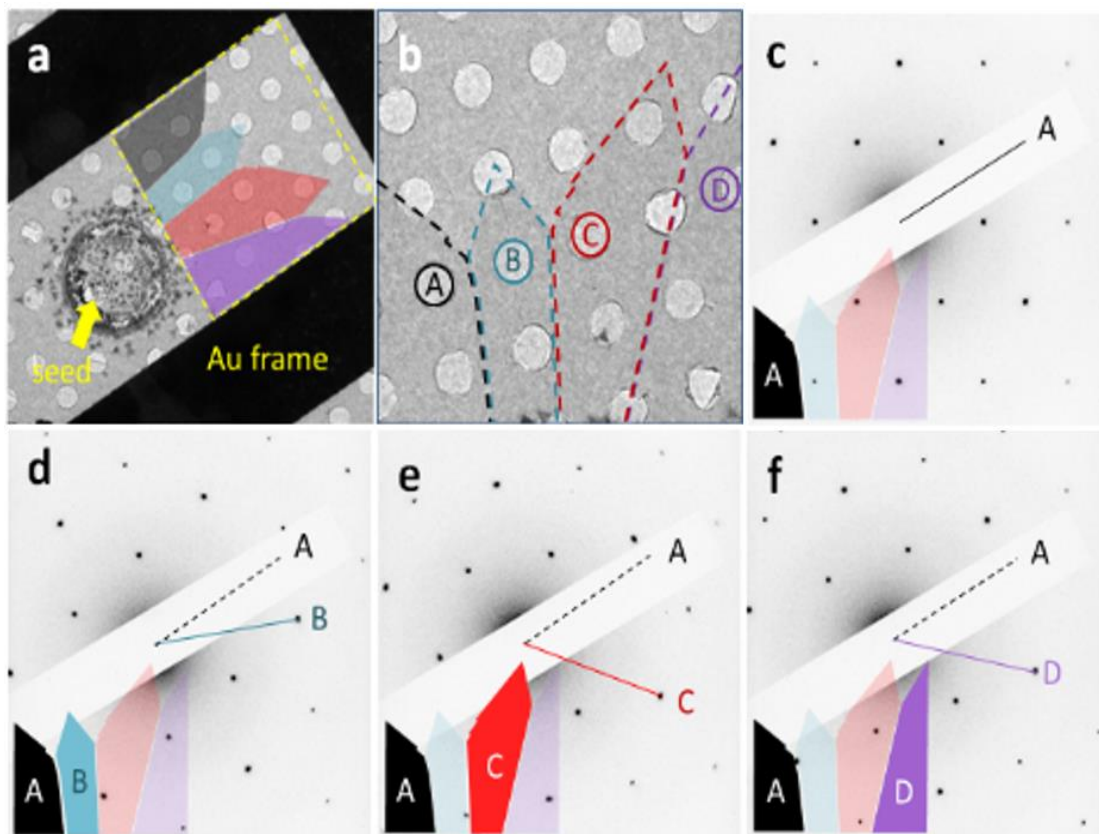


Figure 4.1.3.4. Transmission electron micrographs and electron diffraction data (a) Monolayer MoS₂ regions are coloured grey, light blue, red, and purple (top-bottom) according to their crystallographic orientation. The black regions are parts of a gold frame used to prevent tearing during the transfer process (see main text and Supplementary Fig. S6). Triangular shaped multilayer MoS₂ flakes were formed in the seed region, indicated by the yellow arrow. The 1- μ m holes in the TEM grid serve as the scale bar. (b) Bright field (BF) image from the square region outlined by a dashed white line in panel (a). (c-f) Electron diffraction data from the regions labelled A-D in panel (b).

Sample crystallinity was further characterized with bright-field imaging and selected-area electron diffraction (SAED) measurements conducted in the transmission electron microscope (TEM). A gold grid was first patterned onto a MoS₂ flake to prevent tearing of the flake when it was transferred onto a TEM grid covered by a carbon membrane with 1- μ m diameter holes (Fig. 4.1.3.4a and Supplementary Fig. 9). To minimize damage to the sample, imaging and SAED were conducted using an accelerating voltage of 80 kV. The TEM bright-field images are shown in Figs. 4.1.3.4a-

b. Triangular shaped multi-layer MoS₂ flakes were observed very close to the seed particle, possibly due to limited diffusion of the source during the growth time. Further from the seed, flower-petal-like monolayer MoS₂ regions were observed (dashed square in Fig. 4.1.3.4a and Fig 4.1.3.4b; see Supplementary Fig. 10 for the raw image used to create Fig. 4.1.3.4b and an atomic resolution image of a monolayer MoS₂ flake). The crystalline structure of the MoS₂ was investigated by SAED. Using the intensities of the first and/or second order diffraction spots,^{196,197} the flower-petal-like structures were identified as monolayer MoS₂ (see Supplementary Fig. 11). Individual single-crystal MoS₂ domains, labelled (a)-(d) in Fig. 4.1.3.4b, were distinguished by the orientations of the diffraction spots in SAED (Fig 4.1.3.4c-f). The data indicate that each domain is well crystallized and their orientations are uncorrelated.

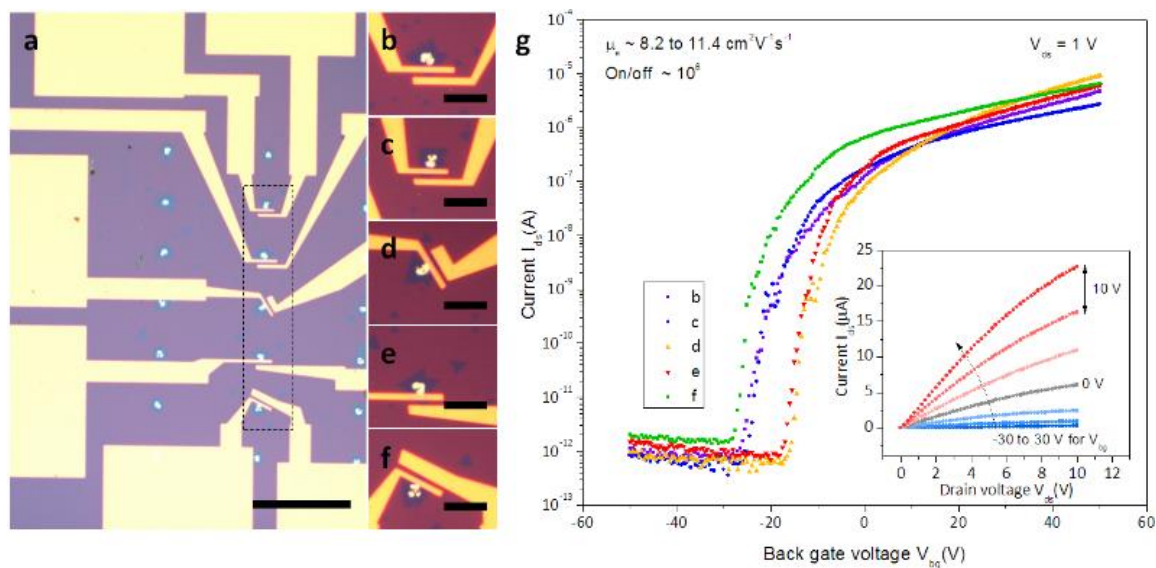


Figure 4.1.3.5. Device fabrication and I-V measurement (a) Optical micrograph of devices that were fabricated from MoS₂ grown by the patterned seed technique. Scale bar is 100 μm . (b-f) Higher magnification images of the rectangular region indicated in panel (a). Scale bar is 20 μm . (g) I-V_g characteristics for the devices in panels (b-f). Inset: I_{ds}-V_{ds} characteristics at several back gate voltages.

Fabrication and measurement of electronic devices An etch step is typically used to define individual devices from a continuous layer of material, which creates the risk of degrading a two-dimensional material as well as added processing cost. In contrast, the patterned growth approach to monolayer MoS₂ outlined here has the advantage of enabling direct fabrication of multiple devices (Figs. 4.1.3.5a) and (4.1.3.5b-5f), without the need for etching. To demonstrate process compatibility with conventional manufacturing, an array of MoO₃ growth seeds was patterned by e-beam lithography, and MoS₂ monolayer flakes were synthesized as described above. Since the MoS₂ flakes were grown at known, pre-patterned locations, it would be straightforward to align an electrode pattern to the MoS₂ flakes, with no need for a separate etch step. After fabrication of the electrodes, the sample was annealed at 150 °C at 10⁻⁵ Torr for 1h. Figure 4.1.3.5g shows the I-V_g characteristics for a set of devices prepared using this approach, measured at a pressure of 40 mTorr. Device mobilities were between 8.2 and 11.4 cm²V⁻¹s⁻¹ and the on/off ratios were in excess 10⁶ comparable to earlier best reports for exfoliated MoS₂ monolayers.^{95,185,195,196}

Discussion

In summary, we have developed a novel patterned growth method for flakes of highly crystalline monolayer MoS₂, where molybdenum-containing growth seeds (AHM or MoO₃) are defined using conventional lithographic methods. This technique should be generalizable to the growth of any layered transition metal dichalcogenide (LTMD), and

it creates a pathway to controllably tailor the size and position of the material. Control of growth parameters enables synthesis of high quality, crystalline, monolayer MoS₂ with electrical and optical properties comparable to exfoliated material. The process enables straightforward fabrication of integrated circuits without the need for a separate etch step. The work represents an important advance towards scalable production of high quality LTMD-based devices and circuits. An ongoing challenge to the field is patterned growth of monolayer, single-crystalline domain MoS₂ at predefined locations.

Methods

Preparation of patterned molybdenum sources. 5 x 5 arrays of 5- μ m square windows were prepared by electron-beam or photolithography. A 7 x 7 array of 3- μ m square windows was used for the experiment that resulted in the growth of exclusively monolayer MoS₂ flakes (see Supplementary Fig. S4). Molybdenum-containing source material was then deposited by either spin coating (1000 rpm for 30 sec, followed by 3000 rpm for 10 sec) with a saturated solution of ammonium heptamolybdate (AHM, product number A674, Fisher Scientific) in deionized water or thermal evaporation of 150-nm thick molybdenum trioxide (MoO₃, product number 203815, Sigma-Aldrich). The resist was removed using acetone followed by isopropyl alcohol, and the sample was then blown dry with compressed nitrogen gas. An aggregation step was then performed to obtain regular beads of the source material. While monitoring the sample under an optical microscope, the substrate was cooled until the hygroscopic AHM or

MoO₃ absorbed water, forming droplets at the seed locations. As the temperature was increased back to room temperature, the water evaporated, leaving behind rounded, uniform, beads of AHM or MoO₃ as shown in Supplementary Fig. S2. Samples were then annealed at 300 °C for 20 min in a flow of 500 sccm of nitrogen gas (99.999% purity). To promote MoS₂ growth, the sample was treated with oxygen plasma (65W, 300 mTorr, 2 min) and then spin-coated (3000 rpm, 1 min) with a surfactant solution (0.1 – 1 % solution of sodium cholate in deionized water).

Growth process. Samples with patterned growth seeds were placed into a 1-inch CVD furnace with a 25-mg solid sulphur source (part number 213292, Sigma-Aldrich) at the upstream end. The furnace temperature was increased to 750 °C at a ramp rate of 70 °C/min under a nitrogen (99.999%) flow of 700 sccm. The temperature was held constant for 20 min during the MoS₂ growth phase, and the system was then rapidly cooled to room temperature. It was noted that the sulphur source started to melt when the temperature in the middle of the furnace was ca. 650 °C.

Device fabrication and current-voltage measurements. After growth of monolayer MoS₂ flakes from patterned growth seeds, electron beam lithography was used to define an electrode pattern that was aligned to the growth sites. The electrode metallization consisted of 1 nm Cr and 30 nm Au deposited by e-beam evaporation. After metallization, devices were annealed for 60 min at 150 °C at a pressure of 10⁻⁵ Torr. Current-voltage measurements were conducted at room temperature under a vacuum of 40 mTorr.

4.2 1H-MoS₂ sensors

4.2.1 Scalable production of molybdenum disulfide-based biosensors

The results presented in this section have also appeared in the publication “Scalable Production of Molybdenum Disulfide-Based Biosensors”, Carl H. Naylor, Nicholas J. Kybert, Camilla Schneier, Jin Xi, Gabriela Romero, Jeffery G. Saven, Renyu Liu, A.T. Charlie Johnson, ACS Nano, 2016, *10* (6) pp 6173–6179.

Abstract

We demonstrate arrays of opioid biosensors based on CVD-grown molybdenum disulfide (MoS₂) field effect transistors (FETs) coupled to a computationally redesigned, water soluble variant of the μ -opioid receptor (MOR). By transferring dense films of monolayer MoS₂ crystals onto prefabricated electrode arrays, we obtain high quality FETs with clean surfaces that allow for reproducible protein attachment. The fabrication yield of MoS₂ FETs and biosensors exceeds 95%, with an average mobility of 2.0 cm²V⁻¹s⁻¹ (36 cm²V⁻¹s⁻¹) at room temperature under ambient (in vacuum). An atomic length nickel-mediated linker chemistry enables target binding events that occur very close to the MoS₂ surface to maximize sensitivity. The biosensor response calibration curve for a synthetic opioid peptide known to bind to the wild type MOR indicates binding affinity that matches values determined using traditional techniques and a limit of detection ~ 3 nM (1.5 ng/mL). The combination of scalable array fabrication and rapid, precise binding readout

enabled by the MoS₂ transistor offer the prospect of a solid-state drug testing platform for rapid readout of the interactions between novel drugs and their intended protein targets.

Nanomaterials such as carbon nanotubes and graphene have great promise for biosensing applications due to their environmentally sensitive electronic properties and all-surface geometries that result in enhanced sensitivity to target binding events.¹⁹⁸ Nanomaterial-protein hybrid devices have been shown to be sensitive to conformational changes of a single protein,¹⁹⁹ and nano-bio hybrid devices have been used to detect cancer biomarker proteins²⁰⁰ and other small molecule targets²⁰¹ at femtomolar concentrations. It has been suggested that two-dimensional materials that are intrinsic semiconductors with an energy band gap (*e.g.* MoS₂) may exhibit better performance than graphene for this application.^{202,203} However, reproducible, high-yield fabrication processes are necessary for this emerging technology.

Approaches have been established to couple proteins to nanomaterials by linker chemistries that target exposed amino acid residues. For example, amine sites are common on the exterior of proteins, which enables chemistries that link carbon nanotubes or graphene to almost any protein *via* amide bond formation.^{204–206} However, in order to increase device-to-device reproducibility and lower detection thresholds, linker chemistries that provide control over the site of the chemical bond to the protein can be beneficial. In particular, poly-histidine tags (histags), which are routinely used to enable purification of recombinant proteins, have been targeted for this purpose.^{207–210}

Here we present an approach to fabrication of large arrays of biosensors based on field effect transistors (FETs) derived from molybdenum disulfide (MoS_2) grown by chemical vapor deposition (CVD). We introduce a nickel ion-mediated surface functionalization scheme for attachment of recombinant proteins *via* a histidine tag directly to the MoS_2 surface, without the need for deposition of an oxide layer on top of the FET channel.²⁰³ The linker chemistry is compact, ensuring that target binding events occur close to the MoS_2 surface. Since signal transduction in FET biosensors is dominated by electrostatic interactions,²¹¹ this should lead to enhanced sensitivity, especially in ionic solutions (*e.g.* bodily fluids,) where the Debye length can be on the scale of a few nanometers.²¹²⁻²¹⁵ The biosensors used here are based on a computationally redesigned water-soluble variant of the human mu-opioid receptor (MOR), referred to as wsMOR, which has structural properties similar to that of the wild-type receptor and comparable opioid affinities.^{216,217} The wsMOR- MoS_2 biosensors are used to readout the binding of DAMGO ([D-Ala², N-MePhe⁴, Gly-ol]-enkephalin), a synthetic opioid peptide with high specificity for the native MOR. The wsMOR affinity inferred from the biosensor data agrees with results for the native MOR based on conventional analytical techniques. The array fabrication method outlined here is scalable, yielding sensitive devices that provide quick, accurate readout of receptor binding. The work opens a path towards multiplexed arrays of MoS_2 -based biosensors for many applications, for example, a drug testing platform that would allow for rapid readout of the interactions between novel drugs and their intended protein target in a solid-state test bed.

Results and Discussion

Recently developed methods for CVD growth of monolayer MoS₂^{98,181,218} offer prospects for devices and systems beyond the exploratory work enabled by mechanical microexfoliation.^{212,213} Indeed, due to the small size and low areal density of monolayer flakes achieved through microexfoliation, a reliable large-area growth process for dense monolayer MoS₂ flakes is essential for scalable fabrication. In a typical CVD process, sulfur sublimated from a solid source is introduced into the furnace along with a molybdenum source such as molybdenum oxide^{95,184} or ammonia heptamolybdate,⁹⁸ and triangular monolayer flakes of MoS₂ nucleate and grow directly on the substrate. Although the mobility of MoS₂, typically 1-50 cm²V⁻¹s⁻¹,^{25,98,192} is lower than that of graphene, the presence of a 1.8 eV direct bandgap for monolayer MoS₂⁴¹ provides the devices with on/off ratios as large as 10⁷^{98,192} and strong photoluminescence.^{63,98,219} These properties make MoS₂ promising for photonic and optoelectronic applications including vapor sensors,^{220,221} solar cells,^{222,223} optical modulators^{180,224} and valleytronics.²²⁵

For these experiments, MoS₂ samples were grown *via* CVD in a 1” quartz tube furnace (Fig 4.2.1.1a). Microliter droplets of saturated ammonia heptamolybdate solution were dried onto the corners of a 2 cm x 8 cm Si/SiO₂ growth substrate that had previously been coated with a layer of sodium cholate (1% solution spin coated 4000 rpm for 60 sec). Sodium cholate is a known growth promoter, acting to increase diffusion of the molybdenum source by increasing the surface adhesive energy relative to the adatom cohesive energy.⁹⁸ The growth substrate was placed in the center of the furnace and

heated to 800 °C at a rate of 70 °C min⁻¹. A 25-mg sulfur pellet was placed on a piece of silicon and positioned upstream in the furnace at a distance of 16 cm from the growth substrate, such that its temperature was approximately 150 °C, sufficient for the pellet to melt and evaporate slowly. A flow of 500 sccm N₂ carried the sulfur vapor into the furnace during a 30 min growth period. After growth, the sample was rapidly cooled by cracking open the furnace and sliding it downstream with respect to the 1" quartz tube.

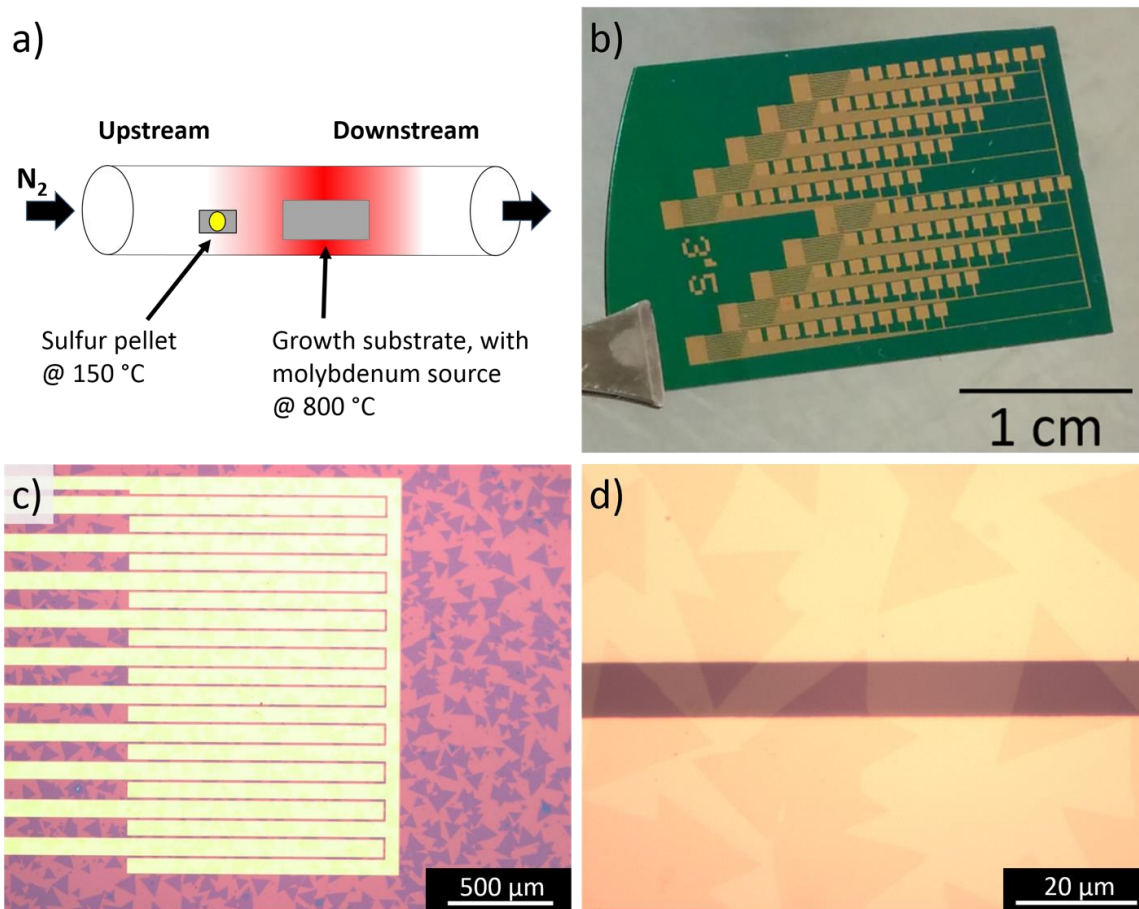


Figure 4.2.1.1. MoS₂ growth and devices. a) Schematic of the CVD growth setup. b) Photograph of the electrode array chip onto which MoS₂ is transferred. Each of ten columns of contact pads leads to a cluster of interdigitated electrodes, one of which is shown in panel c. c) Optical micrograph showing interdigitated electrodes corresponding to a set of 10 sensors. The dark purple regions are monolayer MoS₂. d) Higher magnification optical micrograph showing how multiple triangular, crystalline monolayer MoS₂ flakes span the electrodes.

The growth process leaves the Si/SiO₂ surface decorated with triangular crystals of monolayer MoS₂. The sensor array fabrication process is designed to minimize the need for lithography and etching steps that can contaminate and degrade the samples. To that end, we transferred the randomly grown MoS₂ flakes onto prefabricated electrodes by releasing the samples from the growth substrate with a polymer backing layer.¹⁸¹ This was accomplished by spin-coating PMMA onto the sample, which was then placed in a bath of 1 M KOH to slowly etch the SiO₂ surface and release the PMMA/MoS₂ layer from the substrate. The floating PMMA/MoS₂ layer was then transferred into successive water baths for cleaning and finally scooped onto a target substrate that had prefabricated arrays of metal contacts, defined using photolithography (Fig. 4.2.1.1b-d). The sample was dried, and the PMMA was removed with an acetone spray, followed by an acetone bath. The electrode design used individual source fingers, interdigitated with a common drain electrode. The effective device area of 10 μm (channel length) x 2 mm (channel width) ensured that many MoS₂ flakes spanned each electrode pair, leading to a device yield exceeding 90% and good reproducibility of device electrical properties (see below). Each die contained 100 devices, arranged as ten sets of ten devices, where each set could be addressed independently for chemical functionalization and testing of analyte responses (Fig. 4.2.1.1c).

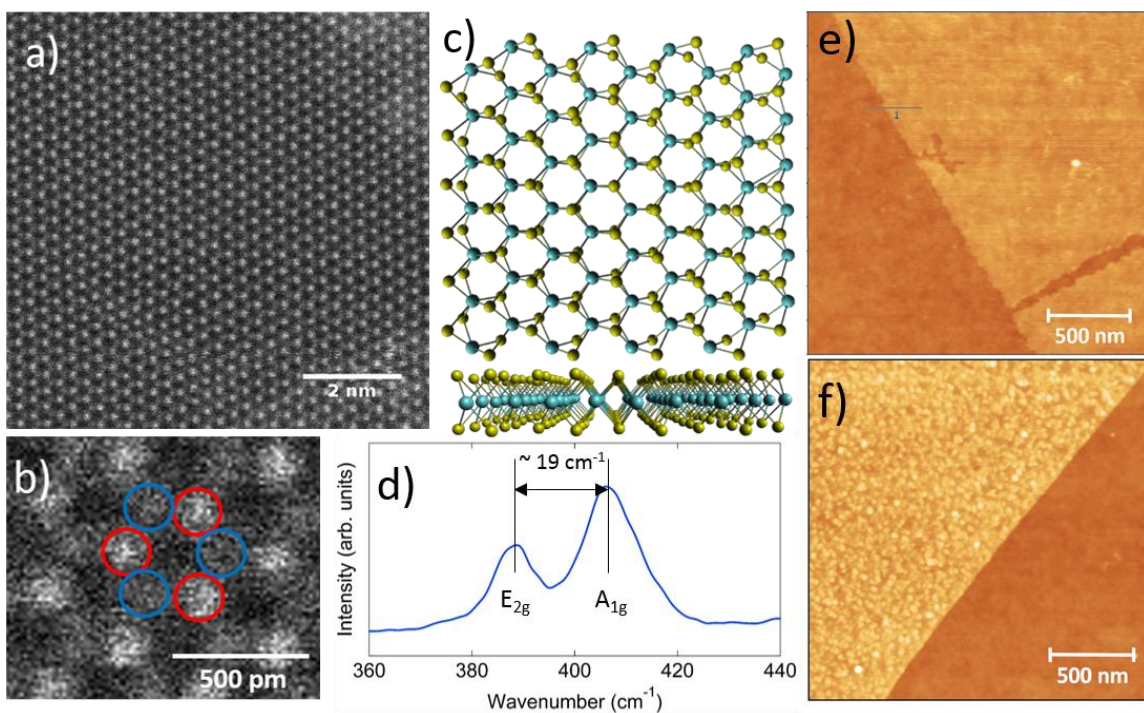


Figure 4.2.1.2. Physical characterization of MoS₂. a) Aberration-corrected TEM image shows the honeycomb lattice expected for MoS₂. b) Higher magnification image shows brightness differences for the Mo and S sites. c) Ball-and-stick model for monolayer MoS₂, consistent with the TEM data in panels a and b. d) Raman spectrum of the MoS₂ film shows positions and separation of the E_{2g} and A_{1g} Raman peaks consistent with monolayer MoS₂. e) Atomic Force Microscope (AFM) topographic image reveals a pristine surface, 0.8 nm in height before functionalization. f) AFM topographic image after functionalization shows dense coverage with 2-3 nm high features, consistent with coverage of proteins bound with the Ni²⁺-histidine linker.

The material was characterized after transfer by aberration corrected TEM (ACTEM), Atomic Force Microscopy (AFM), and Raman spectroscopy. ACTEM showed the expected hexagonal lattice, with different brightness for the molybdenum and sulfur sites, reflecting their different atomic numbers (Fig. 4.2.1.2a,b). AFM (Fig. 4.2.1.2e) revealed that the film was clean and uniform with thickness ~ 0.8 nm, consistent with monolayer MoS₂.⁷⁷ Raman spectroscopy showed the expected E_{2g} and A_{1g} MoS₂ intraband vibrational modes, separated by 19 cm⁻¹ (Fig. 4.2.1.2d),^{77,191} as expected for monolayer MoS₂.^{221,223} Together, these experiments confirm that the MoS₂ samples are highly crystalline with very high monolayer content.

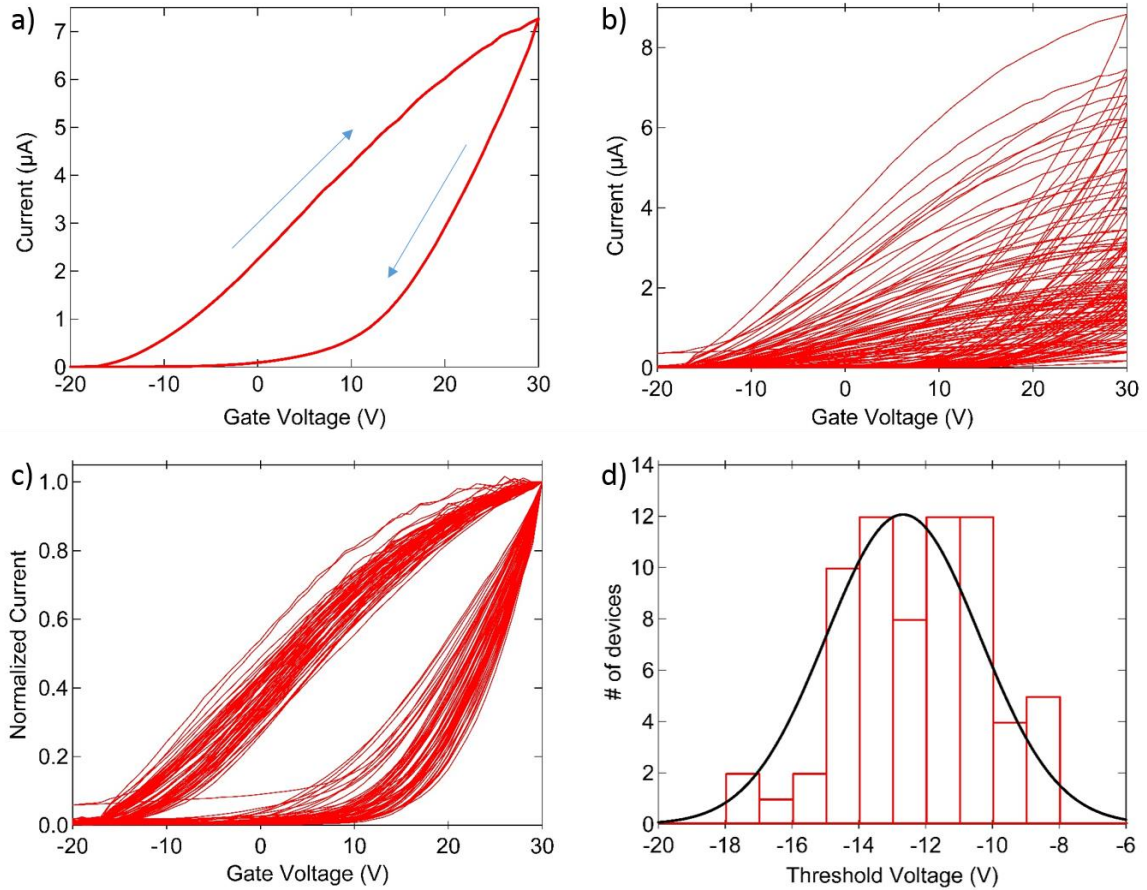


Figure 4.2.1.3. Electrical characteristics of MoS₂ devices. a) Typical I-V_g characteristic, showing on/off ratio as large as 10⁶ and device hysteresis, ascribed to surface charge injection. b) I-V_g characteristics for 70 devices in an array measured under ambient. c) Curves from panel b normalized to the on-state current. The collapse of the data suggests that device variation is due primarily to variation in the number of MoS₂ flakes contacted. d) Histogram of turn-on voltages for a set of 70 devices.

Current-back gate voltage (I-V_G) measurements conducted under ambient conditions showed the expected n-type behavior of MoS₂, with hysteresis ascribed to adsorbed water²²⁶ and substrate charge traps.²²⁷ Figure 4.2.1.3a shows the I-V_G of a device comprised of ~ 15 individual MoS₂ crystalline flakes. By summing the active area of the individual crystals that span the electrodes to derive the effective length and width of the channel, we estimate the field effect mobility to be 1.9 cm²/V-s. Measurements in vacuum, however, showed greatly increased conductivity and inferred field effect

mobility. Across a set of 18 devices measured under ambient and then again at a pressure of 10^{-6} Torr, the average mobility increased from $1.2 \text{ cm}^2/\text{V-s}$ to $36 \text{ cm}^2/\text{V-s}$, while the on-state current increased by a factor of approximately 50 (data not shown). This enhancement is ascribed to removal of atmospheric adsorbates that suppress conduction through the MoS_2 and/or limit the mechanical contact between the MoS_2 and the underlying electrodes. Fig. 4.2.1.3b shows $I-V_g$ curves for 70 devices on a single chip, measured under ambient. The yield is over 95% (68/70 functioning devices), and device properties are highly reproducible once the curves are normalized by their respective on-state currents (Fig. 4.2.1.3c). Based on this observation, differences in on-state currents across devices are assumed to reflect primarily variation in the number of MoS_2 flakes spanning the electrodes. A histogram of threshold voltages shows a tight distribution, with $\sim 75\%$ of the devices having a turn-on voltage in the range -16 V to -10 V .

Previous studies^{203,228} of MoS_2 -based biosensors have utilized a top dielectric layer as the binding surface for protein functionalization. Disadvantages of this approach include fabrication complexity and the fact that the target-binding event is necessarily remote from the transistor channel, which is expected to reduce the sensitivity of the device. Here we instead relied upon direct binding of the protein to the MoS_2 , using nickel ions that bind to the histidine tag of the recombinant protein as a well-defined anchoring site. A similar surface functionalization approach was previously used to attach ligands to MoS_2 nanoparticles in order to alter their solubility.²²⁹ The protein functionalization process begins by incubating the MoS_2 FET array in 5 mM NiCl_2 solution so that Ni^{2+} ions form coordinate covalent bonds with a trio of sulfur atoms in

the top layer of the MoS₂. These ions are then available to bind to nickel chelating agents, such as histidine residues,^{207,209} nitrilotriacetic acid,²⁰⁷ ethylene diamines²³⁰ or nickel porphyrins.²³¹ The resulting MoS₂-protein hybrid structure is shown schematically in Fig. 4.2.1.4b-c. The histidine tag has been used as an anchor site in other biosensor systems, including those based on carbon nanotube²⁰⁷ and graphene²⁰⁹ FETs. These earlier functionalization schemes relied upon nitrilotriacetic acid to bind Ni ions, resulting in a ~ 2 nm-thick linker layer.²⁰⁹ The MoS₂ functionalization scheme presented here is a simple one-step surface chemistry that results in an extremely short linker. This is expected to ensure strong electrostatic coupling of target binding events to the MoS₂ channel and should render the devices robust against screening that occurs for measurements in ionic liquids.

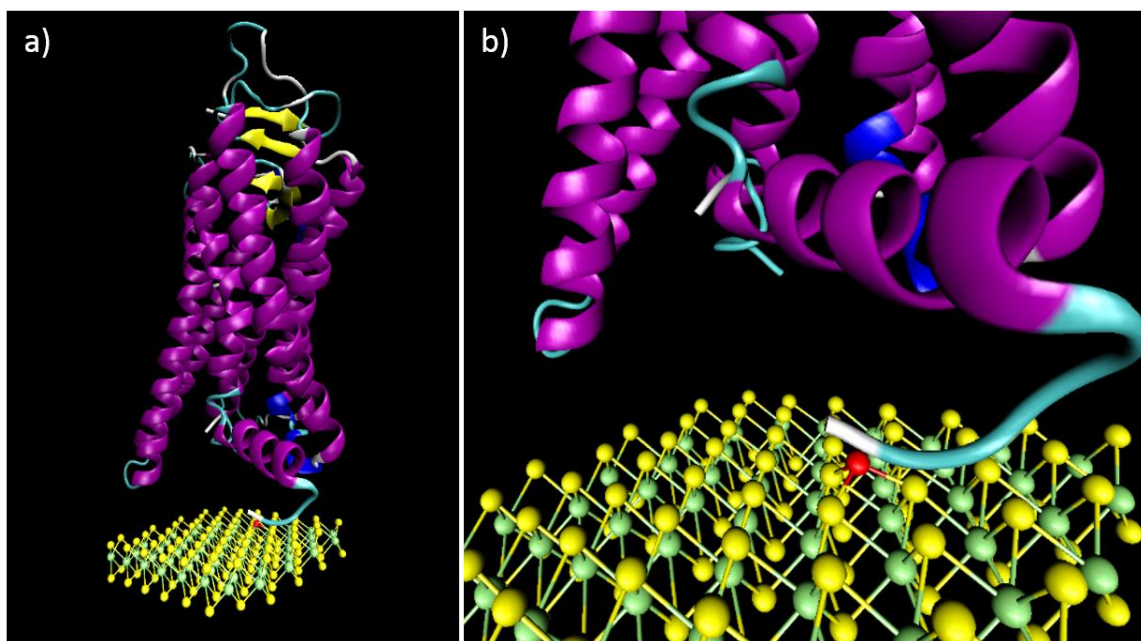


Figure 4.2.1.4. MoS₂ structure and functionalization schematic. Sulfur atoms are shown in yellow, molybdenum in green. The nickel ion used as a protein linker is shown in red. The MOR protein is made of seven connected α -helices, and C-terminus and N-terminus tails that contribute to the protein function. The histidine tag region is shown in white.

Experiments were based upon a computationally redesigned, water-soluble variant of the human μ -opioid receptor (MOR),^{216,217} referred to as wsMOR. The redesigned variant of the MOR used in this experiment was expressed in *E. coli* and purified using standard techniques,²¹⁷ without the need for a membrane, or membrane surrogate such as a nanodisc.^{207,232} Physiologically, the native MOR is involved in pain and reward recognition pathways, and it has high affinity for endogenous and exogenous opioids such as heroin, morphine, β -endorphin, enkephalin, and β -funaltrexamine. The wsMOR has been previously used in a graphene biosensor construct, where its affinity for the drug target naltrexone was confirmed.²⁰¹ For this work we used a different target [D-Ala², N-MePhe⁴, Gly-ol]-enkephaline (Sigma Aldrich), DAMGO, the synthetic opioid peptide analogue to enkephalin. Natural enkephalins are endogenous opioid pentapeptides involved in pain perception, cognitive functions, affective behaviors and locomotion.²³³ Experiments were based on solutions of DAMGO diluted in deionized water to concentrations in the pM- μ M range.

AFM was used to examine the surface morphology of the same MoS₂ flake before and after protein attachment. Before functionalization, the surface of the flake was uniform and nearly featureless (Fig. 4.2.1.2e). After chemical treatment based on a 10 μ M solution of wsMOR, AFM revealed a nearly uniform layer of 2-3 nm high features (density $\sim 330/\mu\text{m}^2$), consistent with the size of the 46 kDa wsMOR (Fig. 4.2.1.2f). The SiO₂ surface remained very smooth, indicating that wsMOR does not adsorb non-specifically on the surface but instead is preferentially bound to Ni ions on the MoS₂.

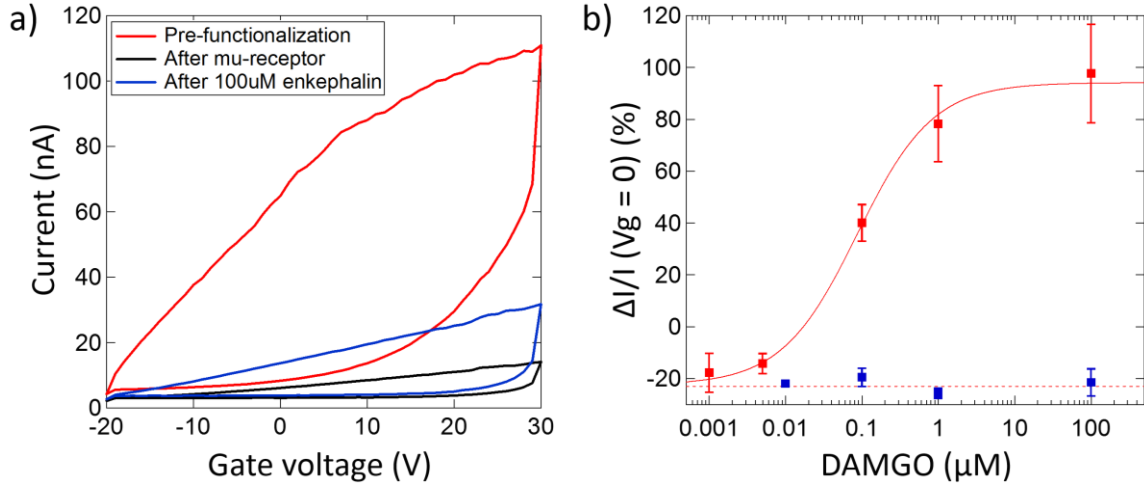


Figure 4.2.1.5. Electrical signatures of protein-target binding. a) Current-gate voltage characteristics of an as-fabricated FET, the FET biosensor after wsMOR functionalization, and the biosensor after exposure to the target DAMGO. The biosensor conductivity increases upon exposure to DAMGO, which is taken as the sensor response. b) Response *versus* concentration characteristic for the biosensor (red markers) and negative control experiment where the wsMOR functionalization step was omitted (blue markers). The biosensor calibration curve is well described by a model based upon the Langmuir-Hill isotherm (red curve). The error bars represent the standard deviation of the mean.

After wsMOR attachment, the device on-state conductance typically dropped by ~ 70 % (Fig. 4.2.1.5a), attributed to depletion of electron carriers due to the binding chemistry and increased carrier scattering due to the presence of the Ni^{2+} ions and bound wsMOR. The devices were then exposed to the target DAMGO in DI water. Based on the trends in the data (Fig. 4.2.1.5a), the sensor response is reported as the percent increase in on-state current (upper branch of the I - V_G characteristic) at $V_G = 0\text{V}$, measured before and after the introduction of the target DAMGO. The response-vs-concentration curve shows a sigmoidal shape that is well fit by a model based on the Langmuir-Hill equation for ligand-receptor binding at equilibrium:

$$\frac{\Delta I}{I_0} = A \frac{c^n}{K_a^n + c^n} + Z,$$

where C is the DAMGO concentration, A is the response when all binding sites are occupied, K_a is the concentration that yields half the maximum response, Z is an offset response to pure water, and n is the Hill coefficient, describing cooperativity and other effects. For this data set, $A = 117 \pm 17 \%$, $K_a = 87 \pm 39 \text{ nM}$ and $n = 0.87 \pm 0.23$, and $Z = -23 \pm 4 \%$. A Hill coefficient near $n = 1$ suggests non-cooperative binding for this system. From standard measurements performed by others,²³⁴ DAMGO is known to bind to the wild type MOR with an affinity in the range of tens of nM, consistent with the value found through the fitting procedure. The close agreement between our results and affinity measurements from more traditional techniques demonstrates that the affinity of the reengineered membrane protein for this target is comparable to that of the wild type, and that this chemical recognition functionality is retained after surface immobilization, enabling sensitive, rapid readout of the target concentration with this device construct. We performed a negative control experiment to test whether DAMGO is exclusively reacting with the wsMOR. In the control experiment the wsMOR functionalization step was omitted, and MoS₂ FET devices were tested against DAMGO solutions at various concentrations as described in the Methods section. The measured responses were identical for all DAMGO concentrations tested and statistically indistinguishable from biosensor responses to pure DI water (Fig. 4.2.1.5b). This negative control experiment demonstrates that specific binding of DAMGO to the wsMOR is essential for the observed sensor responses.

Conclusion

In summary, we have demonstrated wafer-scale, high-yield fabrication of monolayer MoS₂-based biosensors based upon CVD growth and direct protein functionalization of the MoS₂ surface. The chemical recognition functionality of the computationally redesigned receptor protein is retained when it is immobilized and read out electronically, and the inferred binding affinity is comparable to that found using other measurement techniques. The combination of this reproducible, high-yield fabrication method and versatile linker chemistry should be suitable for the construction of multiplexed biosensor arrays appropriate for simultaneous detection of multiple targets in complex fluids. With further understanding of the relationship between conformational changes induced by target binding and sensor output signals, this approach might also enable construction of a solid-state device useful for understanding the interactions between other molecular targets and novel engineered receptor variants.

Methods/Experimental

Fabrication of field effect transistor arrays. Fabrication of FET arrays is based upon traditional photolithography methods. A highly p-doped Si/SiO₂ wafer with 300nm of oxide is first baked at 200C for 1h to remove residual H₂O on the surface. A layer of polymethylglutarimide (PMGI) is spin coated at 4000 RPM for 45 seconds and then baked at 210C for 5 min. Then a layer of photoresist (Shipley Microposit S1813) is spin coated at 5000 RPM for 45 seconds and baked at 100C for 2 min. Photoexposure is

performed according to manufacturer instructions using a mask with 12 chip dies each containing 100 devices. Devices are arranged in ten sets of ten devices, and the device area is 10 μm (channel length) x 2 mm (channel width). The sample is then developed for 45 seconds in Microposit developer MF 319, and a contact metallization of 5nm Cr and 40nm Au is deposited by thermal evaporation. The wafer is then immersed in an acetone bath for 12h, followed by an isoproponol bath for 1h. The wafer is then blown dry with compressed N_2 . A large-area MoS_2 monolayer film is then transferred onto the contact electrode array as explained in the main text.

Protein Functionalization. The protein functionalization process begins by pipetting a 5 mM NiCl_2 solution onto the surface of the chip, which is allowed to incubate in a humid atmosphere for 1h. The sample is then immersed in a deionized (DI) water bath for 5min, transferred into a second DI water bath for 20min, and then blown dry using compressed N_2 . A 10 μM solution of wsMOR is pipetted onto the array and incubated in a humid atmosphere for 1h. The array is then immersed in DI water bath for 5 min and blown dry. For testing of sensor responses, solutions of DAMGO in DI water at various concentrations are pipetted on the sets of 10 sensor devices that make up the array and allowed to incubate in a humid atmosphere for 30min. This is followed by a 2min DI water bath blow drying with N_2 . Each set of 10 devices is exposed to a different concentration of DAMGO, so a single array may be used to test sensor responses to as many as 10 different DAMGO concentrations in a single experiment.

4.2.2 Understanding the large electrical responses from MoS₂ vapor sensors

The results presented in this section are being prepared in a manuscript for publication “Understanding the large electrical responses from MoS₂ vapor sensors”, Carl H. Naylor, Yu Ren Zhou, Christopher Kehayias, Nicholas J. Kybert, A. T. Charlie Johnson.

Abstract

Monolayer Molybdenum Disulfide (MoS₂) is an attractive 2D material due to its promise for use as highly sensitive sensors. We have developed a reliable Chemical Vapor Deposition (CVD) growth process for growing dense monolayer MoS₂ flakes. By utilizing one growth and traditional photolithography methods, thousands of MoS₂ devices are made with a > 95% yield. The MoS₂ devices show high responses to small traces of vapor analytes and there is a need to better understand vapor-MoS₂ interactions. Transmission Line Measurements (TLM) was used to determine the effects of the analytes on the contact resistance and on the intrinsic resistivity of the MoS₂ flake. This study provides an insight into the interaction mechanisms between the analyte molecules and the highly sensitive MoS₂ devices.

Two-dimensional materials, such as graphene and the transition metal dichalcogenides (TMDs), have attracted a tremendous amount of attention over the past

decade.^{34,40,235} Molybdenum Disulfide (MoS_2), the most commonly studied TMD,^{95,236,237} is composed of three-atom thick layers held together by van der Waals forces, each consisting of a layer of molybdenum atoms sandwiched between sulfur atoms. The material has attractive mechanical properties,²³⁸⁻²⁴¹ with an elastic modulus approximately equal to that of graphene and an out-of-plane bending modulus roughly five times that of graphene. It also exhibits interesting electronic properties,^{63,192,242} with reasonable values of carrier mobility, high on/off ratio, and a band gap that can change from an indirect gap of 1.2 eV in the bulk to a direct gap of 1.8 eV in the monolayer. Monolayer MoS_2 can be produced through various methods, most commonly mechanical exfoliation or direct growth by chemical vapor deposition (CVD). Monolayer MoS_2 can be synthesized by CVD using a silicon oxide substrate patterned with microcrystals of Molybdenum Dioxide (MoO_3) seeds and sulfur vapor.^{98,243} To date, there are a variety of growth methods to produce high quality monolayer MoS_2 ^{95,140,169,184,239} and these growth methods have been able to produce other TMDs²⁴⁴⁻²⁴⁶ and in various atomic phases.⁵⁹

Monolayer MoS_2 is an excellent candidate for use as a sensor since every atom in the structure is exposed to the external environment.^{74,203} The electrical responses of mechanically exfoliated MoS_2 exposed to organic vapors such as TEA, tetrahydrofuran (THF), acetone and methanol were first examined and revealed increasing electrical resistivity with increasing concentration of organic vapor.²²¹ The electrical resistivity of CVD grown MoS_2 changed by 2-3 orders when exposed to the gases NO_2 and NH_3 , with appreciable changes in resistivity for as low as 20 ppm NO_2 and 1 ppm NH_3 .²²⁰ A theoretical study showed that inorganic gases such as NO and NO_2 undergo electron

transfer when adsorbed to the MoS₂ surface, thus implying a change in electrical resistivity when MoS₂ is exposed to gases.²⁴⁷ However to date, there have been no published reports on scalable methods for creation of MoS₂ vapor sensors and no investigations of the relative effect these molecules may have on the MoS₂-Au contacts.

Here we report a scalable method to enable simultaneous fabrication of multiple MoS₂ vapor sensors. Very large changes in MoS₂ electrical characteristics were observed upon introduction of chemical vapors, suggesting that this scalable approach to monolayer MoS₂ retains the excellent chemical sensing properties of the material. We also used the Transmission Line Method measurement to independently determine the effect of the chemical vapors on the bulk material and the metal contacts to the MoS₂.

MoS₂ growth and scalable vapor sensor fabrication

Monolayer single crystal MoS₂ flakes were grown directly on a 300nm SiO₂ substrate through CVD deposition in a Lindberg/Blue 1 inch atmospheric pressure furnace. A pretreatment of the growth substrate was used to obtain high quality material.^{74,169} A 1% solution of sodium cholate, a well-known MoS₂ growth promoter, was spin-coated onto the substrate at 4000 rpm for 60 seconds. The sodium cholate increases the surface adhesive energy relative to the adatom cohesive energy which encourages the growth of monolayer flakes.^{59,98,169} A drop of ammonium heptamolybdate (AHM) was then applied to the corners of the growth substrate. The substrate was placed in the center of the furnace, and a second chip containing 25mg of Sulfur was placed

upstream in the furnace at a distance of 17cm from the growth substrate. A constant flow of 500sccm of Nitrogen (99.999% purity) acting as the carrier gas was applied throughout the growth process. The furnace was ramped to 800°C at a rate of 70°C.min⁻¹. At 300°C the AHM droplet is converted to MoO₃ through thermal decomposition. Once the system achieves the growth temperature, the upstream Sulfur chip reaches a temperature of 150°C, which is sufficient to create sulfur vapor. After a 25 minute growth time, the furnace was rapidly cooled. The substrate was retrieved and high quality monolayer MoS₂ flakes were found over the entire growth substrate (fig. 4.2.2.1a top). The MoS₂ was characterized by Raman spectroscopy and atomic force microscopy (AFM) (figure 4.2.2.1b). AFM revealed a height of approximately 0.8 nm and Raman spectroscopy a separation of approximately 19 cm⁻¹ between the E_{2g}¹ and A_{1g} peaks, both consistent with the growth of monolayer MoS₂ flakes, as detailed in earlier reports.^{95,106,191}

Monolayer flakes were then transferred from the growth substrate onto an array of prefabricated electrodes. First, the growth substrate was cut into several pieces, each with a high density of monolayer MoS₂ flakes. A layer of PMMA (C4 Microchem) was spin-coated onto each piece and set afloat in a 1 M KOH solution. The KOH solution gently etched the SiO₂ surface, releasing the PMMA/MoS₂ stack from the growth substrate and setting it afloat on the solution. To clean off KOH residue, the PMMA/MoS₂ stack was transferred through two deionized water baths using a polyethylene terephthalate (PET) substrate. The stack was then transferred onto a prefabricated electrode array, which had been made using photolithography. The electrodes were composed of individual source fingers interdigitated with a common drain electrode to ensure contact to the MoS₂ flakes

(fig. 4.2.2.1a bottom). The effective device area is $10\ \mu\text{m}$ (channel length) \times $2\ \text{mm}$ (channel width). This design and transfer methods resulted in many flakes being contacted, leading to high current and high yield of devices. Each die contained 100 field effect transistors (FETs) arranged as ten sets of ten devices.

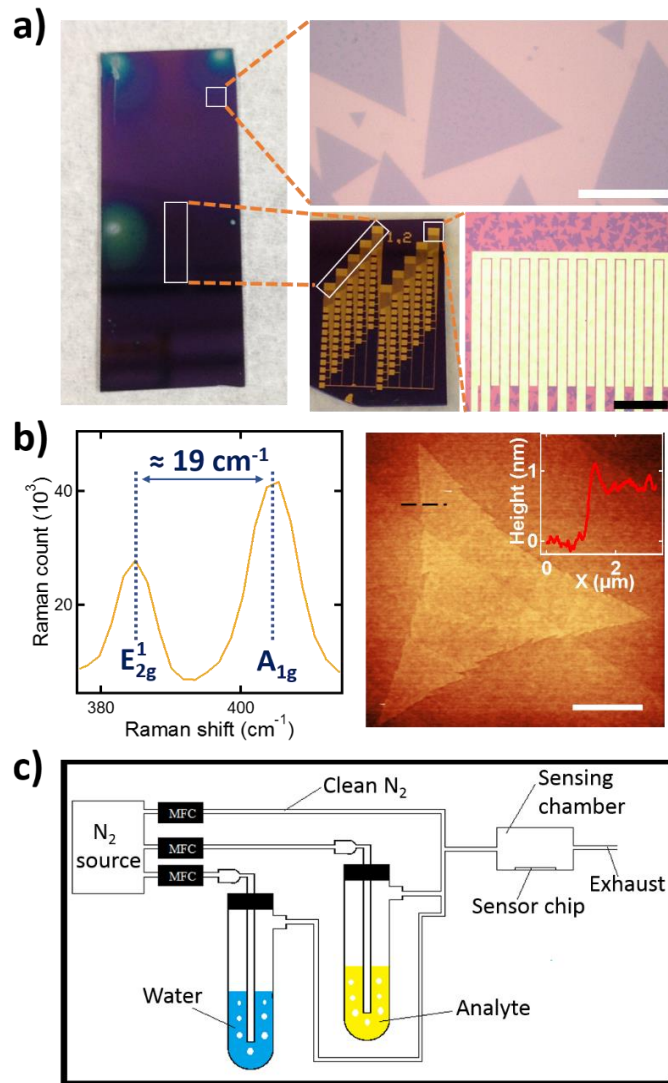


Figure 4.2.2.1. Scalable arrays of MoS₂ vapor sensors. a) Photograph of a MoS₂ growth and device fabrication. The scale bars are $20\ \mu\text{m}$ and $500\ \mu\text{m}$ respectively. b) Raman spectroscopy and AFM scan reveal monolayer thickness of MoS₂ flakes. c) Schematic of the vapor sensing setup.

A die with 100 MoS₂ FETs was mounted in the sensing chamber. A schematic diagram of the measurement setup is shown in figure 4.2.2.1c. N₂ carrier gas (99.999%

purity) was flowed through three streams, each controlled by mass flow controllers. One stream flowed through a water bubbler to give saturated water vapor, one through an analyte (test chemical) bubbler to produce a flow of saturated analyte vapor, and the third stream was pure N₂ gas. The three streams were mixed and flowed into the sensing chamber. The second stream could be switched to flow either through the analyte bubbler or through an empty bubbler. In this way experiments could be conducted with constant total flow (1500 sccm) and constant relative humidity (33%). Electrical measurements were performed on the devices as they are exposed to various concentrations of different analytes.

Electric current responses through the MoS₂ devices is plotted as a function of time in figure 4.2.2.2a as the MoS₂ is exposed in increasing amounts of saturated Propionic Acid vapor (0.04 to 1.3 vol%) at $V_g = 30V$. A crude average of the devices is presented in figure 4.2.2.2b. The responses of carbon nanotubes to increasing amount of propionic acid (1.3 vol% to 33 vol%) are presented in figure 4.2.2.2c. The MoS₂ devices respond with a negative change in current to the propionic acid. This inversion is expected since MoS₂ is an n-type semiconductor and CNTs are p-type, a deprotonation of the Propionic Acid is believed to be the cause of these responses. The percentage change in current of MoS₂ at *low* concentrations is much greater than the percentage change in current for functionalized carbon nanotubes at *high* concentrations (figure 4.2.2.2d).²⁴⁸ The data reveals that the electrical properties of MoS₂ are affected by even the smallest concentrations of organic vapor. These observations suggest that MoS₂ has the potential to be an excellent sensor.

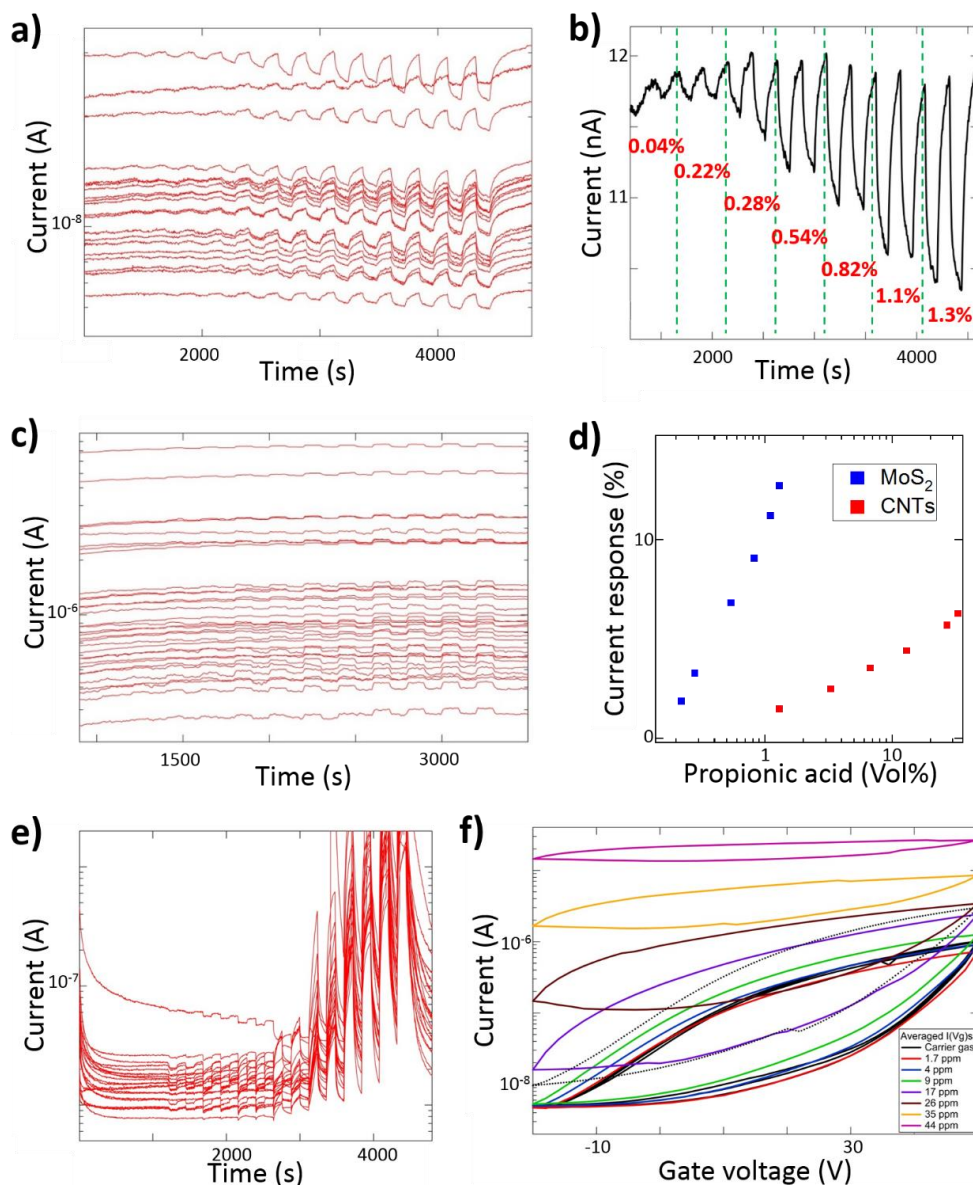


Figure 4.2.2.2. Initial MoS₂ vapor responses. a) 23 MoS₂ devices showing responses to propionic acid vapor with increasing analyte concentration from 0.04vol% to 1.3vol%. b) Crude average of the devices showing up to 14% increase for as little as 1.3vol% of propionic acid. c) 35 CNT devices showing responses to propionic acid vapor with increasing analyte concentration from 1.3vol% to 33vol%. d) MoS₂ vs CNT, current changes for increasing propionic acid vapor. e) MoS₂ devices response to increasing DMMP vapor from 0.2vol% to 6vol%. f) Gate voltage sweeps at different DMMP analyte concentrations.

We then introduced dimethyl methyl phosphonate (DMMP) vapor into the chamber. The MoS₂ dramatically reacts to the DMMP vapor analyte. As we increase the vol% of analyte flowing into the chamber, the electrical responses absurdly increase as

seen in figure 4.2.2.2e. Up to an order of magnitude increase in MoS₂ electrical conductivity is observed upon exposure to 6vol% at V_g=30V. In contrast to Propionic Acid, DMMP is more neutral and no protonation nor deprotonation should be happening. To understand these responses, we performed field sweeps under a constant vapor analyte vol% with V_{ds}=1V across the device (fig. 4.2.2.2f). We notice that the off state current dramatically increases with increasing DMMP concentration. This increase in off state level would indicate large changes in the contact resistance rather than the MoS₂. Therefore, it is possible that the DMMP is not only interacting with the intrinsic MoS₂ but the large changes could be due to the MoS₂ contact resistance. The measurements shown in figure 4.2.2.2 do not provide any insight into the mechanism of interaction between the MoS₂ sensor device and organic molecules. Specifically, there is no information about whether the molecules are interacting with the monolayer MoS₂ or the MoS₂-Au contact. We performed a transmission line measurements (TLM) to determine the interaction mechanisms between various organic molecules and the MoS₂ devices.

TLM study

TLM is used to study the Au-MoS₂ contact resistance and MoS₂ intrinsic resistivity. Metal electrode contacts are constructed and each pair of electrodes is separated by different lengths (x₁, x₂, x₃, etc.). The total resistance between each pair is measured at constant bias. Resistance vs. separation is plotted and a linear function is fitted to the data. The resistance is equal to $R(x) = R_{contact} + R_{intrinsic} = R_{contact} + \frac{\rho x}{A}$,

where ρ is the intrinsic electrical resistivity of the semiconductor and A is the cross-section area of the sample. The y-intercept ($x = 0$) shows the contact resistance R_{contact} , while the slope $\frac{\rho}{A}$ is proportional to the intrinsic resistivity. TLM is used to monitor the changes in contact resistance and intrinsic resistivity when the monolayer MoS_2 is exposed to the various organic vapors, providing insight into the interaction mechanisms of molecules with the sensor. If molecules interact with the Au-MoS_2 contact, the contact resistance will change causing a shift of the y-intercept. If molecules interact with the monolayer MoS_2 , the intrinsic resistance will change, causing a shift in slope. Eight electrode separations, ranging from $0.5 \mu\text{m}$ to $20 \mu\text{m}$, are used for this experiment. The electrodes were made by e-beam lithography and the electrode configuration is shown in figure 4.2.2.3a. Large monolayer single crystal MoS_2 flakes are transferred onto the TLM grid using the previously described technique.

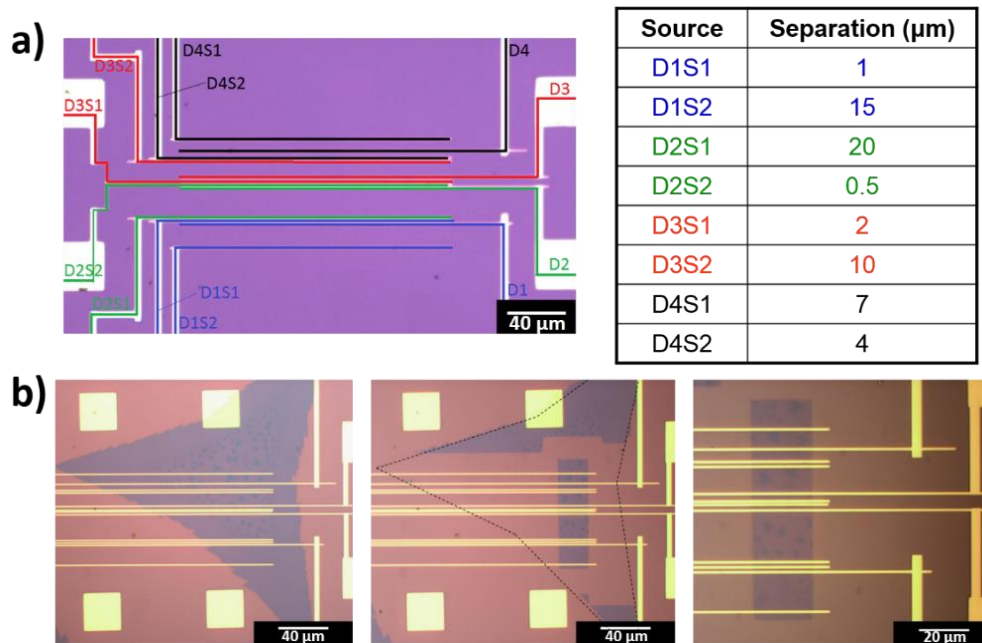


Figure 4.2.2.3. MoS_2 TLM device. a) TLM device pattern performed by ebeam lithography. b) Large MoS_2 flake transferred onto TLM device and resized into rectangle.

The width of the MoS₂ flake must be kept constant across all electrodes, requiring the flake to be resized into a rectangle. This was accomplished by first spin-coating a layer of PMMA onto the devices and using electron beam lithography to define a rectangular region. The devices were then etched by oxygen plasma, destroying the monolayer MoS₂ that was left exposed. After etching, the device was placed in acetone for 24 hours to remove PMMA residue followed by a 1h IPA bath and then gently dried with N₂ gun. A reshaped rectangular MoS₂ flake is shown in figure 4.2.2.3b.

Contact resistance and resistivity decrease with increasing gate voltage in air and vacuum. The contact resistance decreases because as we increase the gate voltage, we are decreasing the Schottky barrier height. For the range of gate voltages tested, contact resistance ranges on the order of 100 kΩ in air and 1 kΩ in vacuum. The vacuum values are two orders of magnitude smaller than contact resistance in air, possibly because vacuum enhances physical contact between MoS₂ and gold and because vacuum causes evaporation of impurities at the contact. These values are in agreement with previous contact resistance studies of MoS₂.²⁴⁹ Placing the MoS₂ devices in vacuum also improves electron mobility by a factor of 30 and significantly reduces hysteresis in the I-V_g curves. Electron mobility improves because impurities adsorbed onto the MoS₂ surface (e.g. water molecules) which interfere with the monolayer's electrical properties are removed by the vacuum. Hysteresis is caused by residual dipole fields induced near the monolayer flake by the gate voltage sweep, which changes the effective gate voltage seen by the monolayer. By reducing adsorbed impurities on the monolayer, fewer molecules could be polarized to induce the residual electric fields, thereby reducing the amount of hysteresis.

Results and discussion

The MoS₂ TLM device is tested against DMMP, Propionic Acid and Ammonia vapors. During each sensing run, a constant bias and gate voltage is applied to each separation. The contact resistance and intrinsic resistivity of the MoS₂ are then studied for various analyte concentrations and at different applied gate voltages.

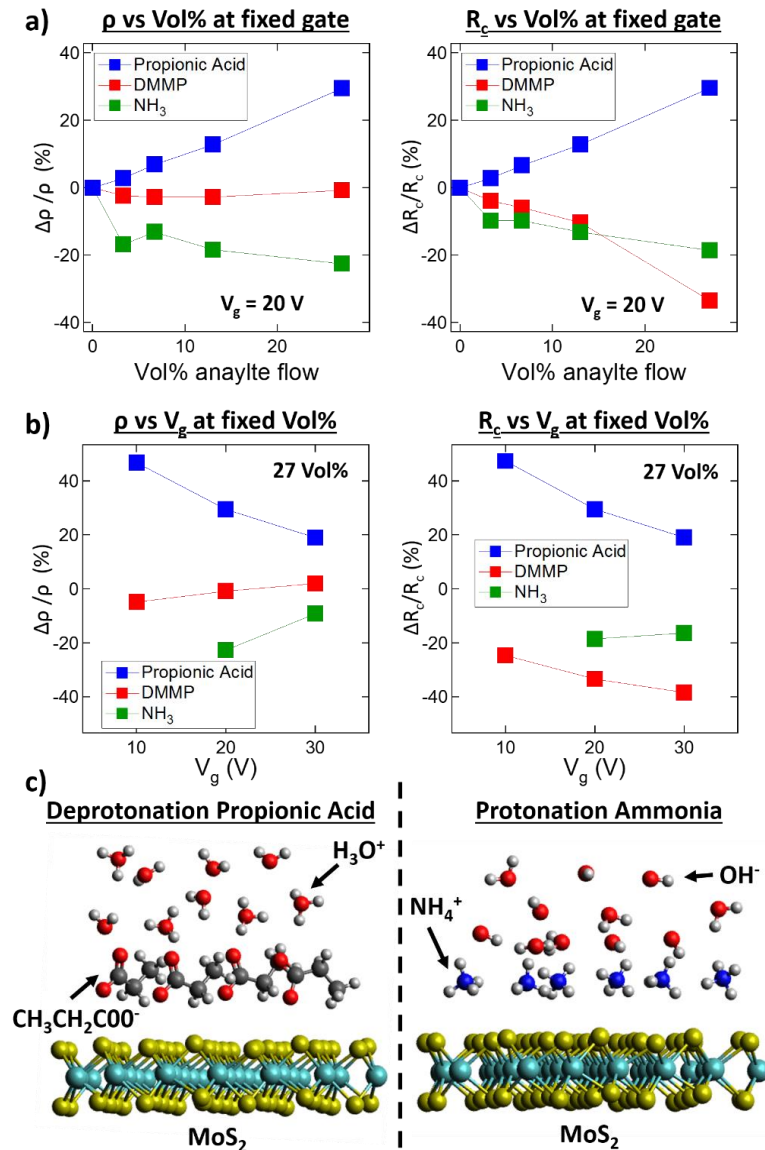


Figure 4.2.2.4. Intrinsic and contact resistance responses. a) Changes in intrinsic resistivity and contact resistance for MoS₂ device under increasing concentration of Propionic Acid, DMMP and

Ammonia for $V_g = 20V$. b) Changes in intrinsic resistivity and contact resistance for MoS₂ device under increasing gate voltage with a fixed concentration of Propionic Acid, DMMP and Ammonia. c) Schematic of deprotonation and protonation on top of MoS₂ channel for Propionic acid and Ammonia respectively.

From figure 4.2.2.4a, we identify that Propionic Acid and Ammonia are interacting with both the intrinsic MoS₂ flake and the gold-MoS₂ contact. For Propionic Acid, the intrinsic resistivity and contact resistance increase by up to 30% (at $V_g = 20$ V). Ammonia displays the opposite trend, the intrinsic resistivity and contact resistance decrease by 20% (at $V_g = 20$ V). Propionic Acid and Ammonia adsorbing onto the MoS₂ device are acting in opposite ways. These results would suggest a chemical gating effect due to deprotonation and protonation at the surface of the MoS₂ flake. Propionic Acid is a proton donor while Ammonia is a proton acceptor in aqueous solution. That is, Propionic Acid loses a proton to form the negative Propionate ion, while Ammonia gains a proton to form the positive NH₄⁺ (Ammonium) ion. A thin layer of water is present on the surface of the MoS₂ device due to the water vapor flow into the sensing chamber, facilitating proton transfer reactions of the analytes. Propionic acid and Ammonia are believed to be undergoing the following reactions for deprotonation and protonation: $CH_3CH_2COOH + H_2O = CH_3CH_2COO^- + H_3O^+$ and $NH_3 + H_2O = NH_4^+ + OH^-$. The associated product ions from the Propionic Acid and Ammonia then adsorb to the surface of the device. An illustration of the proposed interaction mechanism is shown in figure 4.2.2.4b. Negative ions adsorbed on the monolayer surface decrease the electric potential near the monolayer surface, causing the same effect as a negative gate voltage. Therefore, increasing the Propionic Acid concentration produces a larger amount of negative ions on the surface of the flake, decreasing the effective gate voltage and decreasing the current.

The converse is true for interactions with Ammonia, positive ions adsorbing on the monolayer increase the electric potential. Therefore, increasing ammonia concentration has the same effect as increasing gate voltage which results in increased current.

When decreasing the applied gate voltage, the fraction changes in intrinsic and contact resistance are amplified for Propionic Acid and Ammonia (figure 4.2.2.4b). At 27 vol% Propionic Acid, the intrinsic and contact resistance change drops from 50% at $V_g = 10$ V to 20% at $V_g = 30$ V. The amplified change of intrinsic resistivity decreases with increasing gate voltage is explained by the n-type nature of monolayer MoS₂, since carrier concentration increases with increasing gate voltage. Larger carrier concentration causes MoS₂ to behave more like a metal, meaning that adsorbed ions (which change effective gate voltage) have a smaller effect on electrical properties. While for the contact resistance, it is suggested that a Schottky (electron potential energy) barrier between gold and MoS₂ whose height decreases with increasing electric field intensity from the gate voltage. The Schottky barrier is higher at lower gate voltages, meaning that adsorbed analytes could produce a greater change on barrier height.

In figure 4.2.2.4a, it is apparent that DMMP is not interacting with the intrinsic resistivity of the MoS₂. DMMP is a more stable analyte than Propionic acid and Ammonia, so neither protonation nor deprotonation is expected. However, the contact resistance decreases by up to 40% at $V_g = 20$ V when the MoS₂ device is exposed to 27% DMMP vapor. Also, in contrast to above, decreasing the applied gate voltage diminishes the fraction decrease in contact resistance (figure 4.2.2.4b). At 27 vol% DMMP, the contact resistance change increased from 25% at $V_g = 10$ V to 40% at $V_g = 30$ V. A

possible explanation for these results is charge transfer rate between DMMP and the gold-MoS₂ contact. As the gate voltage increases, we are decreasing the height of the Schottky barrier, but we are also inducing an increase in the rate of charge transfers from the DMMP to the gold-MoS₂ contact. This suggests formation of a second Schottky barrier between DMMP and MoS₂, a barrier higher than the gold-MoS₂ Schottky barrier at the gold-MoS₂ interface region. While the gold-MoS₂ Schottky barrier acts essentially ohmic at high gate voltages, the DMMP-MoS₂ barrier does not flatten at high gate voltages. The amount of charge transfer increases with increasing gate voltage due to the decrease in barrier height, and continues to increase even at high gate voltage. From the decrease in contact resistance with increasing gate voltage, it is clear that the majority carrier concentration in MoS₂ is larger near the contacts. Because MoS₂ exhibits n-type behavior, the decrease in contact resistance is caused by addition of electrons, meaning that electron transfer must occur from the DMMP molecules to the MoS₂. The molecular structure of DMMP shows that each oxygen atom contains two lone pairs of electrons. Because the lone pair electrons have higher energy than electrons in bonding orbitals, their transfer to MoS₂ involves a much lower energy barrier. Therefore, it is most likely that the lone pair electrons in oxygen atoms are transferred into MoS₂.

Conclusion

We developed a CVD process for synthesizing monolayer MoS₂ flakes using a solid AHM molybdenum target and gaseous sulfur source with a silicon wafer growth

substrate. From this efficient growth process we achieved a method for scalable MoS₂ FETs for vapor sensing. Initial vapor sensing of Propionic Acid, Ammonia and DMMP reveal enticing results. Up to an order of magnitude increase in electrical conductivity was observed when the devices were exposed to 6 vol% saturated DMMP vapor. By TLM method, we explored the effect the analytes have on the intrinsic resistance of the MoS₂ and the contact resistance between the MoS₂ and electrodes. We discovered that a deprotonation and protonation effect is occurring on the MoS₂ surface for Propionic Acid and Ammonia. The DMMP molecules, however, interact almost exclusively at the contact. We hypothesize that charge transfers at the contact are responsible for the high current responses in DMMP vapors.

We believe that our comprehensive study explains the mechanisms involved in the sensing of various analytes, painting a clearer picture in the large responses observed for our scalable MoS₂ vapor sensor. Paving the way for more studies on the promising vapor sensing properties of this “beyond graphene” candidate.

4.2.3 Universal biosensor

The results presented in this section are currently being prepared in a manuscript for publication “Universal biosensor”, Carl H. Naylor,* Ramya Vishnubhotla,* Abigail Lee, Camilla Schneier, A. T. Charlie Johnson.

Two dimensional (2D) materials such as graphene and the transition metal dichalcogenides (TMDs), are promising for sensor applications due to their outstanding electrical and thermal properties, high tensile strength, and biocompatibility.^{1–3,27,74,203,238–241,250,251} Many nano-biosensor concepts require chemical functionalization of the 2D material with a biomolecule (e.g., antibody, engineered antibody, single-stranded DNA oligomer, etc.).^{74,250,252–255} However 2D materials, and especially the TMDs, have different chemical composition and atomic configurations, giving them different surface chemistries. Direct functionalization of the surface may therefore require very different chemical treatment, increasing the complexity of nano-biosensor design. By utilizing a hexagonal boron nitride (hBN) layer we have resolved this issue, creating a universal, highly-scalable, back-gated biosensor fabrication process that can be applied to any given 2D material.

hBN is a chemically inert insulating material, and application of this layer will not degrade the properties of the underlying 2D material, in fact it has been reported that it enhances the electrical properties.^{33,48} Stacking monolayer hBN on top of a 2D TMD brings several advantages. First, it has been predicted that biosensors based on

semiconducting 2D materials with a finite energy band gap (e.g. MoS₂) will have lower detection limits than biosensors based on graphene, where the energy band gap is zero.^{202,203} Second, some TMD materials degrade on exposure to atmosphere (e.g., 1T'-MoTe₂ and 1T'-WTe₂), and the hBN layer will suppress this process. The hBN layer can further protect the 2D material from the chemistry steps that follow. In this experiment, we report a 99% “survival” rate of devices after functionalization steps. Third, monolayer hBN allows the use of pyrenebutyric acid N-hydroxysuccinimide ester (pyrene-NHS) as a linker molecule, independent of the identity of the underlying 2D material.

We applied this new methodology to the creation of MoS₂/hBN biosensors in a field effect transistor (FET) geometry. Arrays of MoS₂/hBN FETs were treated with a pyrene linker molecule and then functionalized with single-strand DNA (ssDNA) to yield a high quality biosensor for DNA hybridization. By incorporating monolayer hBN on top of the MoS₂ we were able to perform functionalization chemistry that was previously not possible on MoS₂ due to its atomic configuration. The heterostructure biosensor was highly sensitive and selective. This approach could be used for any 2D material, providing a universal pathway towards biosensor fabrication.

Experimental details

Attractive noncovalent bonding between hexagonal atomic rings is referred to as π - π stacking, due to the presence of π bonds.^{23,46} Graphene for instance processes a hexagonal structure. When graphene is used in biosensing, the most common approach is

to functionalize the surface using pyrene-NHS.²⁵⁶ Pyrene-NHS also possesses these hexagonal rings and will Pi-Pi stack to the surface of the graphene. Once the pyrene-NHS step is linked, multiple chemistry steps are now possible to functionalize the surface for a specific target (figure 4.2.3.1a). hBN also possesses these hexagonal rings (figure 4.2.3.1b), therefore the pyrene-NHS chemistry is also applicable to hBN. MoS₂ and other TMDs do not possess an in plan hexagonal structure as they are a 3 layered material (transition metal sandwiched on either side by chalcogen atoms). Therefore the pyrene-NHS chemistry is not applicable to MoS₂. However, by utilizing the insulating and passivating properties of hBN, pyrene-NHS chemistry could be performed on the surface of an hBN/MoS₂ heterostructure (Figure 4.2.3.1c). This technique is not limited to MoS₂, stacking monolayer hBN on top of any 2D material would yield similar results, ergo creating a universal biosensor.

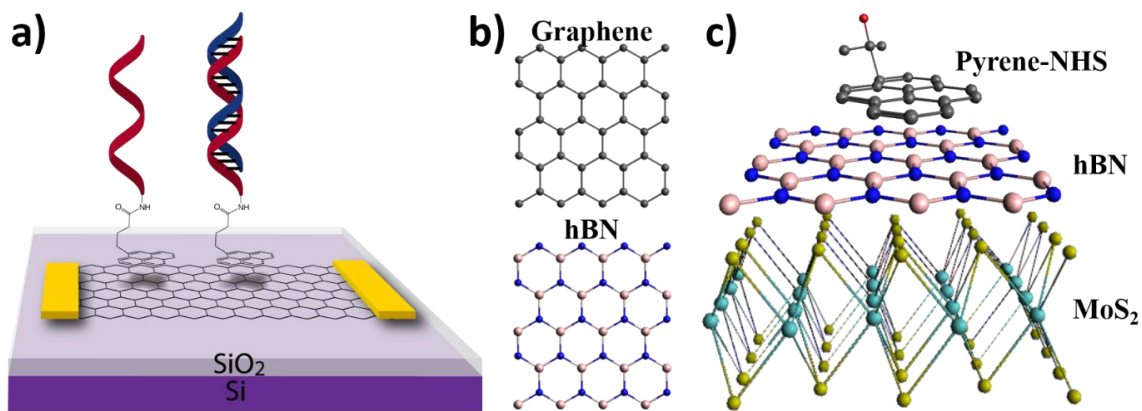


Figure 4.2.3.1. Schematic of the universal biosensor. a) Traditional pyrene-NHS chemistry on graphene.²⁵⁷ b) Ball and stick model comparing graphene and hBN in top view. c) Universal biosensor schematic.

Monolayer MoS₂ flakes are grown on a Si/SiO₂ by chemical vapor deposition (CVD) in a 1 inch furnace. A 2 cm x 8 cm Si/SiO₂ chip is spin coated with a 1% sodium cholate solution at 4000 rpm for 60 seconds. Sodium cholate is a known growth promoter

for MoS₂, it increases the diffusion of the molybdenum source by increasing the surface adhesive energy relative to the adatom cohesive energy.^{58,59,98,169} Microliter droplets of a saturated solution of ammonia heptamolybdate are dried onto the corners of the substrate. The growth substrate is then inserted into the center of the furnace. A chip containing 25mg of sulfur is positioned upstream at a distance of 17 cm from the growth substrate. The furnace is flushed with 500 sccm of N₂ for 5 minutes. The furnace is then ramped up to 800°C at a rate of 70°C.min⁻¹ under the constant N₂ flow. The sulfur chip located upstream will reach a temperature of 150°C and start sublimating. After a 30 minute growth time, the furnace is rapidly cooled and MoS₂ flakes have grown across the substrate.

The MoS₂ flakes are transferred by KOH method onto prefabricated photolithography made devices (figure 4.2.3.2 step 1). The growth substrate is spin coated with a polymethyl methacrylate (PMMA) layer at 3000 rpm for 60 seconds. The sample is then placed in a 1M KOH bath, the edges of the chip are exposed to the solution which enables a slow etch of the SiO₂ layer. Once the etching of the SiO₂ is complete, the PMMA/MoS₂ stack will be released from the substrate and will float above the solution. The floating PMMA/MoS₂ stack is transferred through two successive DI water baths to clean off any KOH residue. The PMMA/MoS₂ stack is aligned onto the premade devices and dried with N₂ gun. The devices are inserted into an acetone bath for 12h to dissolve the PMMA layer, followed with a 1h IPA bath and dried by N₂ gun. The MoS₂ flakes will span across the interdigitated source drain fingers of the devices, enabling scalable arrays of MoS₂ FETs (figure 4.2.3.2 step 2).

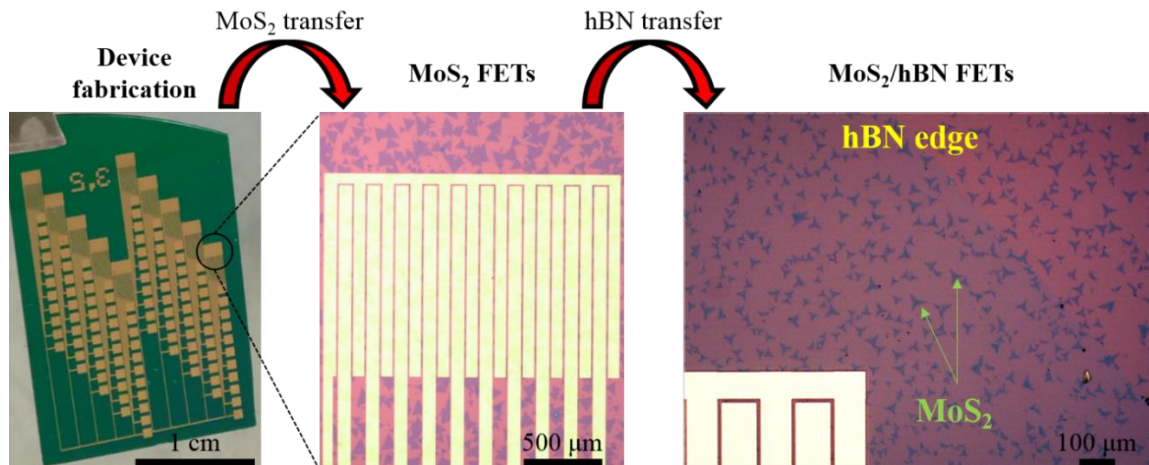


Figure 4.2.3.2. Fabrication steps for hBN/MoS₂ heterostructures.

Monolayer films of hBN are grown on a copper foil substrate in a 1inch CVD furnace. A copper foil substrate is inserted into the center of the furnace and accompanied upstream with a solid ammonia borane source (figure 4.2.3.3a). The ammonia borane source is located approximately 20 cm from the edge of the furnace. The foil is heated up to 1050°C at 70°C/min and annealed at this temperature for 15 minutes under a constant flow of 50 sccm H₂ and 500 sccm Ar. The H₂ is then lowered to 20 sccm and the hBN pellet is brought to within 7.5 cm of the furnace (figure 4.2.3.3b). This proximity to the heat of the furnace causes the solid borane-ammonia pellet to sublime. After 12 minutes, the pellet is moved back to its original position, the Ar flow is increased to 1000 sccm and the H₂ flow is set to 10 sccm. The furnace is cooled down to below 100°C and the copper foil substrate containing monolayer hBN films is retrieved.

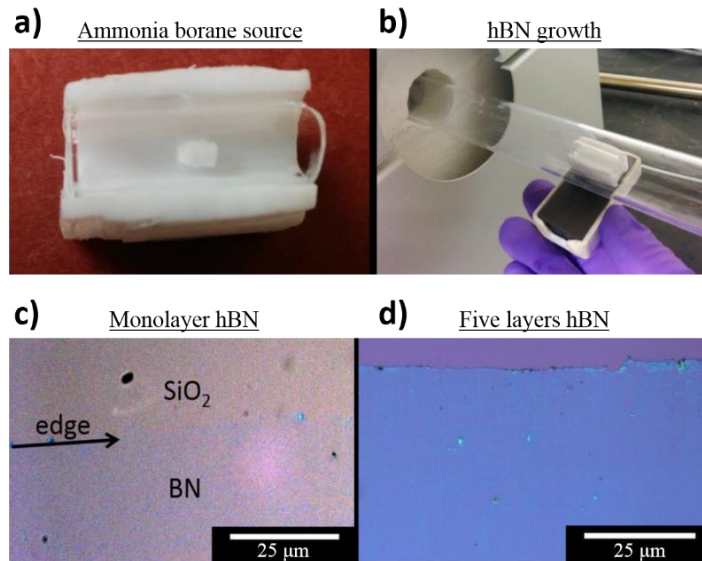


Figure 4.2.3.3. CVD growth of monolayer hBN films. a) Ammonia borane source. b) Sliding mechanism for the ammonia borane source. c) Transferred monolayer hBN on a SiO₂ substrate. d) Five stacked transferred layers of hBN on a SiO₂ substrate.

The monolayer hBN on the copper foil is transferred off the copper foil by “bubble transfer method” (figure 4.2.3.4). The hBN-copper growth substrate is spin coated with a layer of PMMA at 3000rpm for 60sec and baked at 120°C for 2 minutes to ensure good adhesion between the hBN and PMMA. The PMMA/hBN film is then detached from the copper foil by an electrolysis process in a sodium hydroxide (NaOH) solution. The film is transferred through a series of DI water baths to remove NaOH residue. The PMMA/hBN stack can then be transferred onto any given substrate. Figure 4.2.3.3c is one layer of hBN transferred onto a SiO₂ substrate, figure 4.2.3.3d is up to five layers of hBN on SiO₂. The PMMA/hBN is transferred on top of the prefabricated MoS₂ FETs (figure 4.2.3.2 final step). The stack is air-dried overnight and then baked at 150°C for 2 minutes. The PMMA layer is removed by an acetone bath for 10 minutes. The substrate is then sprayed with IPA for 30 seconds and dried with a N₂ gun. Through this method we have achieved scalable hBN/MoS₂ FETs (figure 4.2.3.2).

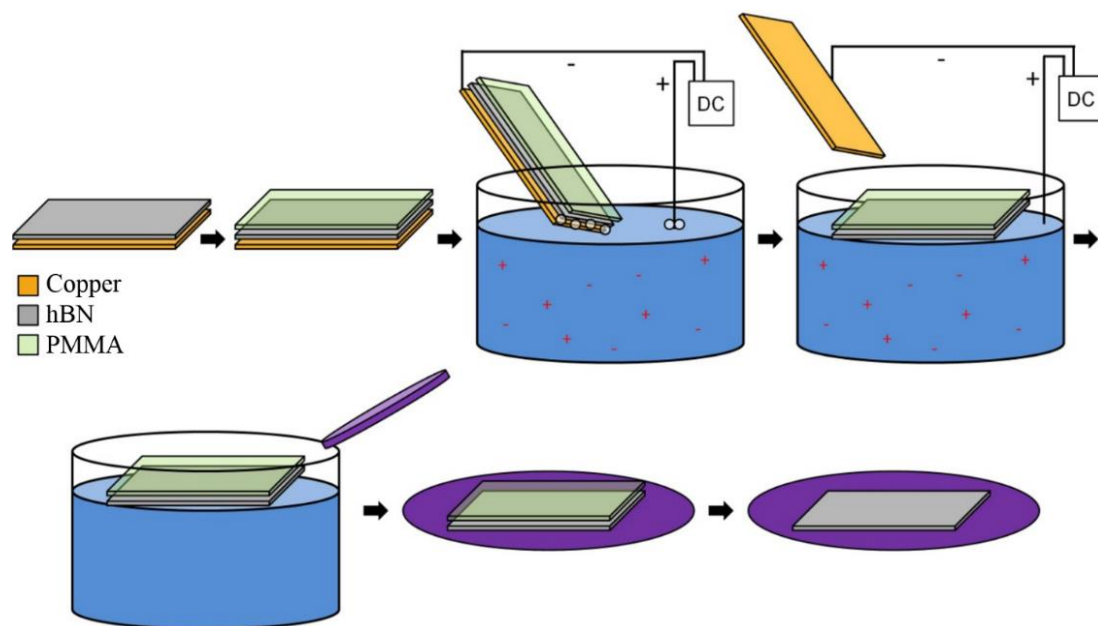


Figure 4.2.3.4. Bubble transfer method.

The MoS₂/hBN device yield exceeds 90%, with good reproducibility of electrical properties across the chip. Each die contains 100 devices, arranged as ten sets of ten, each set could be addressed independently for chemical functionalization and testing of analyte responses. Figure 4.2.3.5 is the electrical responses of 50 hBN/MoS₂ FETs.

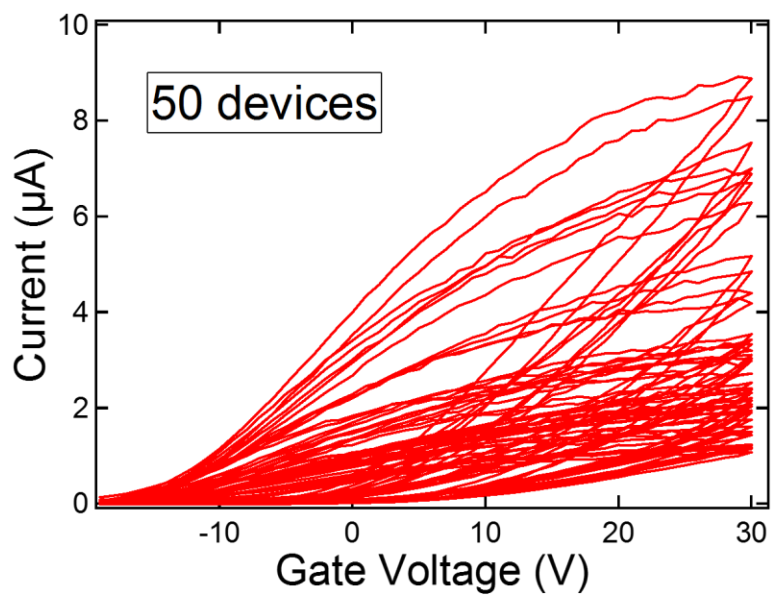


Figure 4.2.3.5. Three terminal measurements on 50 hBN/MoS₂ heterostructure FETs.

Devices were incubated in a solution of 2mg of pyrene-NHS in 25 mL of dimethyl formamide (DMF) for 20 hours. Figure 4.2.3.1c is a ball and stick model showing the MoS₂/hBN heterostructure after the pyrene-NHS step. Following the pyrene-NHS attachment, devices were soaked in a 1μM solution of probe DNA for 2 hours. The pyrene-NHS acts as a linker molecule, with the pyrene moiety bound to the hBN and the NHS group allows a strand of 5'-aminated ssDNA (referred to as "probe" DNA) to bind to the pyrene group so that the DNA is immobilized on the hBN surface. At this point, the devices were electrically characterized to provide a sensor baseline before the detection step. For the detection step, different concentrations of DNA (complementary target) in deionized water were pipetted onto different regions of devices and then allowed to conjugate for 30 min in a humid environment. The devices were electrically characterized once again to obtain the sensor response.

The sensor response was determined using the current-backgate voltage characteristic. After the chemistry steps, the on state current will shift for different applied gate voltages. This shift in current level will be directly proportional the chemistry happening on the surface of the hBN. Encouragingly, there were no changes in current level after the pyrene-NHS and probe DNA attachment (Figure 4.2.3.6a blue and red curve). This is a direct indication that the MoS₂ (acting as the "sensing" material) is completely passivated from the chemistry happening on the surface of the hBN. When introducing the complementary strand of DNA, there is a clear shift in the on state current level (Figure 4.2.3.6a green curve). As the concentration of the complementary ssDNA target decreased, so did the changes in current (Figure 4.2.3.6b). The sensor response to

pure DI water is shown by the blue line in Figure 4.2.3.6b. The lowest concentration of ssDNA tested was 1 nM and this can clearly be distinguished from the response of the DI water level. The data was fitted using the Hill-Langmuir equation (red dotted line in Figure 4.2.3.6). The detection limit is below 1nM and entering the pM range, making this sensor comparable to graphene in sensitivity²⁵⁷ and extremely promising in the field of biosensing. There was a 99% “survival” rate of the FET heterostructures through the chemistry steps, clearly showing the perfect encapsulation of the underlying material. By incorporating hBN on the surface of a material, the atomic arrangement and elements of the underlying material become irrelevant. Chemistry steps for functionalization are dependent on the top hBN layer whereas the underlying material is solely used for the detection by local chemical gating effect. By stacking hBN on top of any given material, a universal biosensor is made.

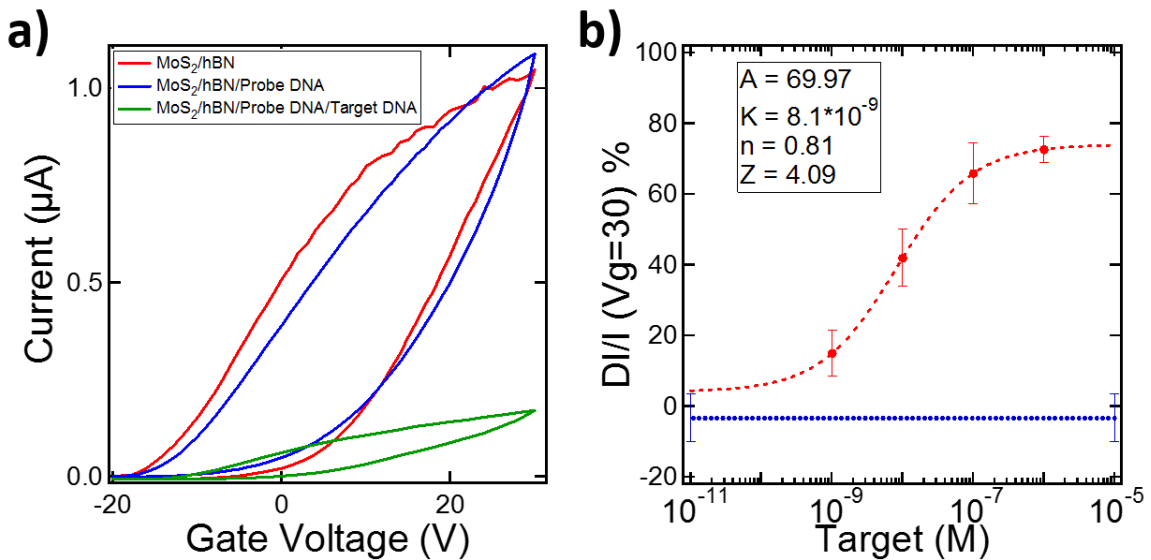


Figure 4.2.3.6. Electrical signature of target binding events for the universal biosensor. a) Three terminal measurements of the heterostructure after each chemistry step. b) Response *versus* concentration characteristic for the biosensor (red markers). Response of the biosensor to DI water (blue curve). The biosensor calibration curve is well described by a model based upon the Langmuir-Hill isotherm (red curve).

In summary, we have demonstrated the feasibility of creating a universal biosensor involving hBN films. Large monolayer MoS₂ flakes were grown by CVD and transferred onto prefabricated electrodes. CVD grown monolayer hBN film were then transferred on top of the devices to isolate the MoS₂ from the environment, enabling the creation of MoS₂/hBN FETs. The FET devices were then functionalized with pyrene-NHS, which binds to the surface of the hBN via pi-pi stacking. The pyrene-NHS acts as a linker molecule to a probe ssDNA, the probe ssDNA was then used to detect the complementary DNA strand. Electrical responses reveal a clear attachment of the target DNA and low detection limits. The hBN film also perfectly encapsulated the scalable devices with a 99% “survival” rate following the experiment. This technique provides an alternative pathway, to resolving the difficulties involved in the chemistry steps for functionalizing a 2D material. By incorporating hBN films on the surface of any given 2D material, irrelevant of its atomic configuration and composition, the local chemistry steps will remain consistent. This universal biosensor could lead to dramatic changes in the way scientists approach functionalization schemes for biosensors, which could potentially lead to real impacts in health care monitoring systems.

4.2.4 Flexible devices

Current and future technologies will rely on electronic systems being based on flexible substrates, making devices wearable and practical for everyday use (figure 4.2.4.1). These devices include sensors that can read out hydration levels or bendable phones that can fold into one's pocket. Therefore, there is a large interest in incorporating these novel and promising nanomaterials onto flexible substrates.

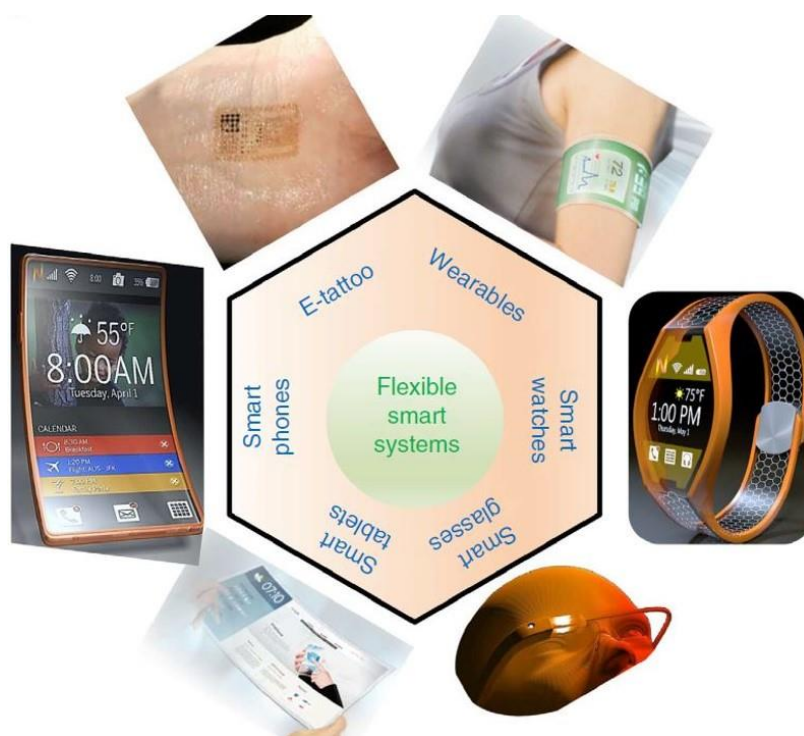


Figure 4.2.4.1. Next generation of smart flexible systems.²⁵⁸

We have successfully manufactured scalable flexible 1H-MoS₂ Field Effect Transistors (FETs) using a kapton substrate, graphene back gate and hafnium oxide (HfO₂) dielectric. Kapton is the most commonly used substrate for flexible systems, due to its large range of temperature stability (−269 °C to +400 °C), electrical insulation capabilities and low-cost.²⁵⁹ We incorporated graphene as the back gate due to

graphene's biocompatibility, high electrical conductance and because of our established and efficient CVD growth process for large scale high quality graphene.^{201,260} HfO₂ was utilized as the dielectric layer due to its reproducible deposition by Atomic Layer Deposition (ALD) and intrinsic high-K dielectric properties. A schematic of the flexible device layout can be seen in figure 4.2.4.2.

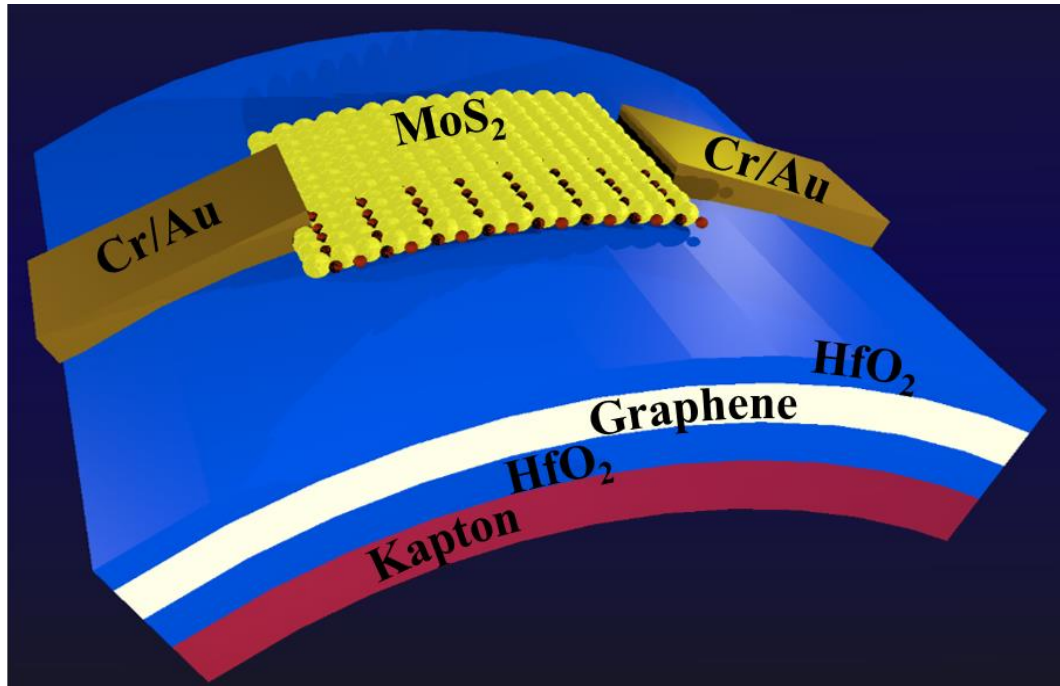


Figure 4.2.4.2. Schematic of layout for the flexible MoS₂ FETs using graphene as back gate.

A 4 inch wide and 50 μm thick piece of kapton is applied to a Si wafer by Polydimethylsiloxane (PDMS). The kapton tends to recoil during the photolithography processing steps, therefore by sticking it to the wafer avoids such displacements. PDMS withstands the high temperature baking and does not leave residue on the back of the kapton, making it ideal for this scenario. PDMS is spin coated at 500 rpm for 60 sec onto a Si wafer, inserted into an oven and cured at 80 $^{\circ}\text{C}$ for 20 min. The kapton is then carefully pressed onto the PDMS/Si wafer and sticks to it through van der Waals forces.

At the end of the device fabrication the kapton sheet can be gently peeled off the wafer. The kapton is then inserted into the ALD chamber and a 20 nm HfO₂ layer is first deposited at 150 °C onto the kapton. This initial HfO₂ layer acts as the spine of our flexible device and will stop the kapton tape from expanding and shrinking during future processing. CVD grown graphene is then transferred by bubble transfer onto the HfO₂/kapton (please see section 4.2.3 for information about bubble transfer). Graphene is then patterned to create only gate channels that will be directly under the device. Polymethylglutarimide (PMGI) is spin coated at 4000 rpm for 45 sec onto of the graphene/HfO₂/kapton and baked at 125 °C for 5 min. Shipley 1813 (S1813) is then spin coated on top at 5000 rpm for 45 sec and baked at 100 °C for 2 min. The PMGI is designed to act a sacrificial layer in the photolithography processing. The non-desirable graphene regions are exposed by UV light and developed for 30 seconds by MF319. The undesirable graphene is then plasma etched at 80W for 30 seconds with 1.25 Torr of O₂, leaving us with a patterned graphene back gate. The graphene/HfO₂/kapton stack is then inserted the ALD and a 60 nm HfO₂ layer is deposited at 150 °C. By using alignment markers and following the same photolithography process discussed above, Au/Cr contacts are deposited over the HfO₂ dielectric layer and aligned on top of the graphene channel. CVD grown MoS₂ is then transferred on top of the devices by KOH etching (please refer to section 4.1.2 for details regarding KOH etching). The scalable flexible MoS₂ device can be seen in figure 4.2.4.3a, the optical photograph displays the flexibility and stability of the final product. Figure 4.2.4.3b gives a virtual top view image of the patterned graphene back gate. An optical micrograph in figure 4.2.4.3c reveals the MoS₂ flakes spanning across the Au/Cr contacts. We also notice a slight color contrast along

the edges of the device revealing the graphene back gate. Three terminal field effect transistor measurements were performed on the scalable MoS₂ FETs (figure 4.2.4.3d). Electrical data reveals n-type semiconducting behavior with high on/off ratio (10⁶) and reasonable values of mobility (1cm²V⁻¹s⁻¹).

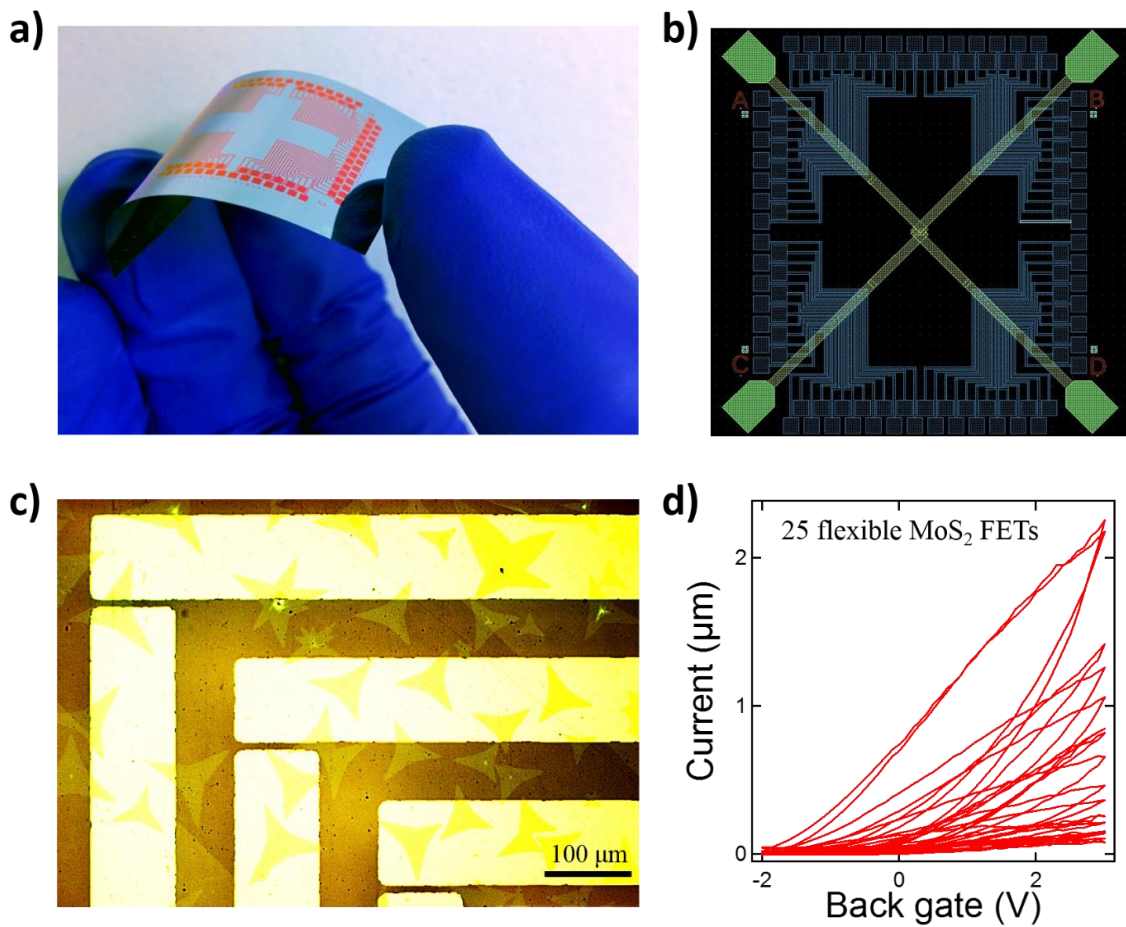


Figure 4.2.4.3. Scalable flexible MoS₂ FETs. a) Optical photograph of scalable flexible devices with Al as gate electrode. b) CAD design of mask revealing pattern graphene back gate. c) Optical micrograph showing MoS₂ flakes spanning across source/drain electrode and the graphene back gate. d) Electrical measurement of 25 flexible MoS₂ FETs.

We have successfully created scalable flexible MoS₂ FETs on a kapton substrate with a biocompatible graphene back gate. These devices are currently being converted into biosensors.

4.3 Miscellaneous experiments performed on 1H-MoS₂

4.3.1 Band alignment and minigaps in monolayer MoS₂-Graphene van der Waals heterostructures

The results presented in this section have also appeared in the publication “Band Alignment and Minigaps in Monolayer MoS₂-Graphene van der Waals Heterostructures”, Debora Pierucci, Hugo Henck, Jose Avila, Adrian Balan, Carl H. Naylor, Gilles Patriarche, Yannick J. Dappe, Mathieu G. Silly, Fausto Sirotti, A. T. Charlie Johnson, Maria C. Asensio, and Abdelkarim Ouerghi, Nano Letters, 2016, 16, 4054–4061.

Abstract

Two-dimensional layered MoS₂ shows great potential for nanoelectronic and optoelectronic devices due to its high photosensitivity, which is the result of its indirect to direct band gap transition when the bulk dimension is reduced to a single monolayer. Here, we present an exhaustive study of the band alignment and relativistic properties of a van der Waals heterostructure formed between single layers of MoS₂ and graphene. A sharp, high-quality MoS₂-graphene interface was obtained and characterized by microRaman spectroscopy, high-resolution X-ray photoemission spectroscopy (HRXPS), and scanning high-resolution transmission electron microscopy (STEM/HRTEM). Moreover, direct band structure determination of the MoS₂/graphene van der Waals heterostructure monolayer was carried out using angle-resolved photoemission spectroscopy (ARPES), shedding

light on essential features such as doping, Fermi velocity, hybridization, and band-offset of the low energy electronic dynamics found at the interface. We show that, close to the Fermi level, graphene exhibits a robust, almost perfect, gapless, and n-doped Dirac cone and no significant charge transfer doping is detected from MoS₂ to graphene. However, modification of the graphene band structure occurs at rather larger binding energies, as the opening of several miniband-gaps is observed. These miniband-gaps resulting from the overlay of MoS₂ and the graphene layer lattice impose a superperiodic potential.

The recent rise of a large family of 2D materials, with unique electronic and optical properties, has opened exciting prospects for new devices based on so-called “van der Waals (vdW) heterostructures”. The latter are only a few atoms thick and are expected to exhibit new properties and functionalities that cannot be achieved using bulk materials. Indeed, 2D materials can be considered as “exposed” two dimensional electron gases, whose properties can be dramatically influenced by noncovalent coupling to low-dimensional adsorbates. So far, most studies have focused on heterostructures based on graphene, boron nitride, and transition metal dichalcogenides,²⁶¹ obtained from mechanical exfoliation or chemical vapor deposition (CVD) growth.^{33,44,262–266} In particular, graphene, a 2D semimetal with extremely high carrier mobility but no bandgap and monolayer MoS₂, a direct bandgap semiconductor with good carrier mobility, are highly promising building blocks for future nanoelectronics.^{224,267} Heterojunctions interfacing different 2D materials would enable so-called van der Waals epitaxy, in

which the lattice-matching condition in traditional epitaxy is drastically relaxed, allowing the formation of a wide range of 2D/2D, 2D/bulk heterostructures.²⁶⁸ In these vdW heterostructures, each material maintains its individual electronic properties due to the weak interactions between the layers. One of the key parameters in the design of a heterojunction is the determination of the band offset.^{263,269–271} This offset is defined as the difference between the tops of the valence bands in the case of a semiconductor junction, and as the difference between the Fermi level and the top of the valence band in the case of a (semi) metal/semiconductor heterostructure. The band offset is critical for many properties such as quantum confinement and chemical activity. Moreover, as in the case of 3D materials, designing heterostructure devices based on 2D materials requires accurate band offset parameters across the different materials. In the case of 3D semiconductor junctions, thermal equilibrium implies that the chemical potential is the same on both sides of the interface, meaning that the Fermi levels have to be aligned. Charge transfer from one side to the other establishes this situation. Due to the low densities of free carriers in semiconductors, the screening process at the interface involves band bending, with the formation of depletion or accumulation layers. In the case of a 2D system in vertical stacking, this model needs to be revised. Indeed, the very low dimensionality of these systems (just a few Å thick) prohibits the formation of a depletion region. Consequently, the issue of band alignment in these systems is still not completely understood and little explored.

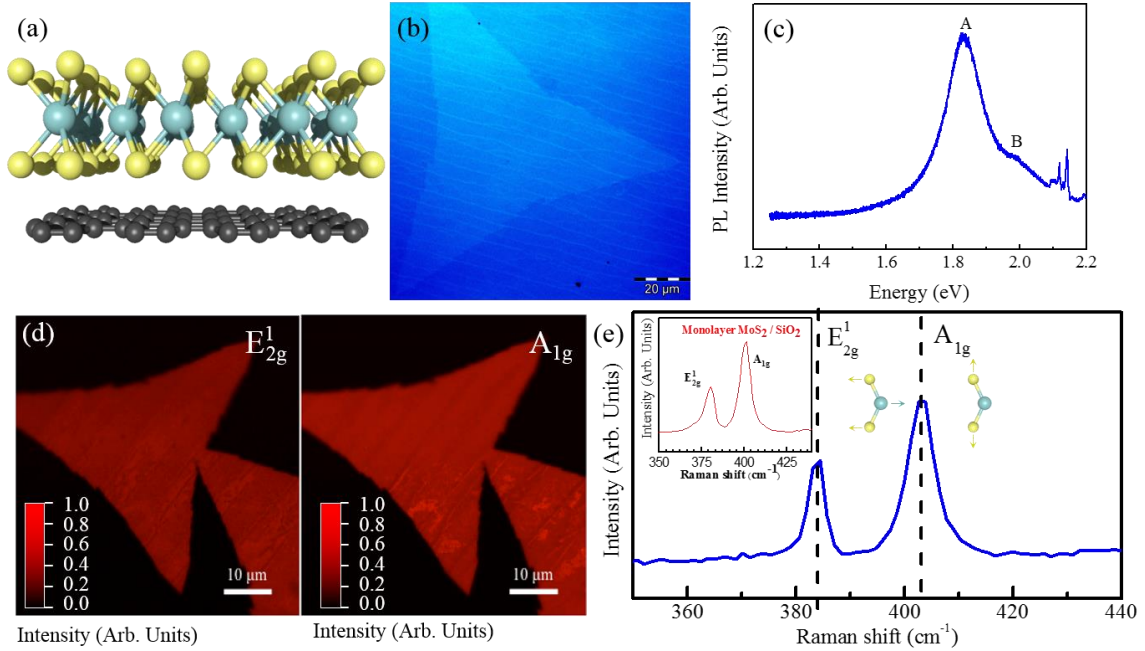


Figure 4.3.1.1. Structural and electronic properties of a MoS₂/graphene heterostructure: (a) Schematic structure of one MoS₂ monolayer on a graphene underlayer, (b) typical optical image of the MoS₂ transferred onto the epitaxial graphene layer (the contrast has been adjusted in order to improve the visibility of the flake), (c) photoluminescence (PL) spectrum of MoS₂/graphene heterostructures (in insert the PL spectrum of MoS₂/SiO₂ sample for comparison), (d) micro-Raman maps of peak intensity of the E_{2g}¹ and A_{1g} modes of MoS₂ on epitaxial graphene, and (e) averaged Raman spectrum of MoS₂ on epitaxial graphene from the map in panel d.

Recently, the band structure of single- and bilayer MoS₂ was studied using ARPES, focusing mostly on their bandgap values, with relatively little attention to their band offsets.²⁷² Previously, Diaz et al. investigated the band alignment between CVD derived monolayer graphene and bulk MoS₂.²⁶⁹ However, due to the quantum confinement effect, the physical properties of monolayer MoS₂ are very different compared to their MoS₂ bulk counterparts, and therefore the band alignment of a single layer of MoS₂ is expected to show important differences. Especially, 1 ML MoS₂ presents a rather unconventional and peculiar electronic band structure. While bulk MoS₂ is typically an indirect gap (IG) semiconductor with a band gap of ~1.29 eV,²⁷³ a single layer MoS₂ behaves as a direct-gap (DG) semiconductor with a band gap of ~1.8

eV.^{83,274,275} So far, the band alignment of monolayer MoS₂ and n-doped graphene/SiC(0001) is completely unknown. In this study, large-scale MoS₂ monolayers were successfully fabricated using a CVD method on SiO₂.⁹⁸ By transferring large-scale monolayer MoS₂, we were able to create MoS₂/graphene heterostructures. To explore the electronic properties of these heterostructures, it was vital to understand both the interfacial band alignment and interaction of these 2D materials. We therefore studied the electronic structure of 1 ML MoS₂ on graphene using high resolution X-ray photoemission spectroscopy (HRXPS) and angle-resolved X-ray photoemission spectroscopy (ARPES). Using STEM and Raman spectroscopy we also demonstrated the high interface quality of this vdW heterostructure.

Graphene may be a suitable material to combine with alternative vdW solids due to its lack of dangling bonds, chemical inertness, and the ability to remain intact under high stress.^{38,235} We obtained the MoS₂/graphene heterostructure by transferring monolayer MoS₂ onto graphene, which was formed by annealing a 4H-SiC(0001) substrate (see Materials and Methods) (Figure 4.3.1.1a). Large-scale MoS₂ monolayer flakes (~20 to ~100 μm) were created by CVD on oxidized silicon substrate (see Materials and Methods and ref).⁹⁸ Monolayer MoS₂ flakes were then easily identified by their optical contrast with respect to the substrate (Figure S1a) and confirmed by micro-Raman spectroscopy (Figure S1b). The shape of the MoS₂ flakes is not perfectly triangular but presents cusps with 3-fold symmetry, irrespective of their size. This is probably due to the growth process starting with small triangular flakes, the apex of which then acts as active nucleation sites for a sequence of intersecting triangles

developing in this particular shaped triangular monolayer.²⁷⁶ In addition to the MoS₂ monolayer, we occasionally observed the growth of a second layer of MoS₂ on top of some monolayer flakes. After the transfer of MoS₂ onto graphene, an annealing process at T = 300 °C for 30 min in UHV (base pressure better than P ~ 10⁻¹⁰ mbar) was used to further clean the surface and interface of the MoS₂/graphene heterostructure. The shape of the flakes and their huge size was not modified after the transfer. The optical micrograph in Figure 4.3.1.1b shows large (lateral size about 100 μm) flakes of MoS₂ on the graphene layer. For the following experiments, the monolayer coverage was estimated to be around 30% of the total area of the sample.

Figure 4.3.1.1c shows the photoluminescence (PL) spectrum for monolayer MoS₂ on graphene. The strong peak observed at 1.83 eV arises from the direct interband recombination at the K-point of the Brillouin zone of the photogenerated electron–hole pairs; the weaker shoulder at about 2 eV is attributed to the energy split of the valence band spin–orbit coupling of MoS₂.^{41,63,277} This value is in agreement with the theoretical expected value for monolayer (ML) MoS₂, indicating the absence of high strain in the MoS₂/graphene heterostructure.⁸⁰ The intensity of the two characteristic Raman peaks of MoS₂ in the wavenumber range between 300–450 cm⁻¹ is mapped in Figure 4.3.1.1d. These two Raman features correspond to the in-plane vibration (E_{2g}¹) and the out-of-plane (A_{1g}) of Mo and S atoms.^{77,191} The average Raman spectrum obtained from the map on the MoS₂ flake is represented in Figure 4.3.1.1e. The Raman shift Δ ~ 19 cm⁻¹ confirms the monolayer structure of the CVD transferred MoS₂.^{77,191} Comparing the Raman spectrum of the as-grown MoS₂ on SiO₂ (insert in Figure 4.3.1.1e) with the

spectrum of the MoS₂/graphene heterostructure, we noticed an upshift (of about 4 and 3 cm⁻¹, respectively) and a narrowing (full width at half-maximum (fwhm) as a result of a Lorentzian fitting, is about ~3 cm⁻¹ smaller) of the A_{1g} and E¹_{2g} Raman features. This is explained by the fact that when the MoS₂ is transferred to the graphene, due to the weak van der Waal forces at the interface, the existing lattice strain between MoS₂ and SiO₂ related to the different thermal expansion coefficients during the growth of the MoS₂ flakes, is released.²⁷⁸ The results of this tensile strain release were observed in the upshift of the E¹_{2g} peak.^{80,278–280} The A_{1g} mode showed weaker strain dependence than the E¹_{2g} one, meaning that the observed shift in this case can be attributed to a signature of the existence of a van der Waals interaction between MoS₂ and graphene⁷⁷ (although a possible charge transfer from MoS₂ to graphene under illumination cannot be excluded^{79,109,281}). The presence of this shift was very important to ensure a good quality of interface, as shown by Zhou *et al.*²⁷⁹ In fact, as opposed to the SiO₂ substrate, as the graphene layer is free of dangling bonds and impurity, it played a critical role in the formation of an atomic and abrupt interface with MoS₂. This effect was also reflected in the narrowing of the Raman peaks.²⁸²

Figure 4.3.1.2a compares the Raman spectra of pristine graphene (black line) and the MoS₂/graphene heterostructure (red line) in the wavenumber range of 300–2800 cm⁻¹. The three main typical structures expected of graphene are present on both spectra, superimposed on the second-order Raman bands originating from the SiC substrate:²⁸³ (i) the D band (defect-induced mode), (ii) the G band (in-plane vibration mode), and (iii) the 2D band (two-phonon mode). The high quality of the graphene underlayer is indicated by

the low intensity of the D peak ($\sim 10\%$ of the G peak intensity). Moreover, after the MoS₂ transfer, the intensity of the D peak did not increase, showing the good structural quality of the MoS₂/graphene heterostructure.

The quality of the interface between graphene and MoS₂ was analyzed using STEM cross-section measurements (Figure 4.3.1.2b). This cross-sectional view was observed along the (11–20) SiC zone axis. STEM images reveal the thickness of the MoS₂ and graphene layers and the detailed interface structure of the MoS₂/graphene. As observed in the figure, the heterostructure was composed of MoS₂ and graphene monolayers. The MoS₂ layer was atomically flat and showed a continuous film. The interlayer separation between the graphene underlayer and the MoS₂ flake was about $3.4 \pm 0.1 \text{ \AA}$. This interlayer distance was in good agreement with that for bulk graphite^{284,285} or a vdW heterostructure.^{286,287} This means that a very sharp interface was obtained between the graphene and MoS₂ without contamination or PMMA residues. Also, the quality of the interface was shown by the energy-dispersive X-ray spectroscopy (EDX) study, where the elemental distribution of S and Mo in a selected area of the ML MoS₂ on graphene, was mapped (Figure 4.3.1.2c and 4.3.1.d). The EDX images demonstrate a high crystalline and continuous film of MoS₂, in which the Mo and S atomic range could be identified. Indeed, a sharp vertical interface between the MoS₂ and graphene layers is visible. The intensity of the Mo and S maps across the interface also shows that the sharpness of the interface is within 0.1 nm, corresponding to the spatial resolution of EDX elemental mapping.

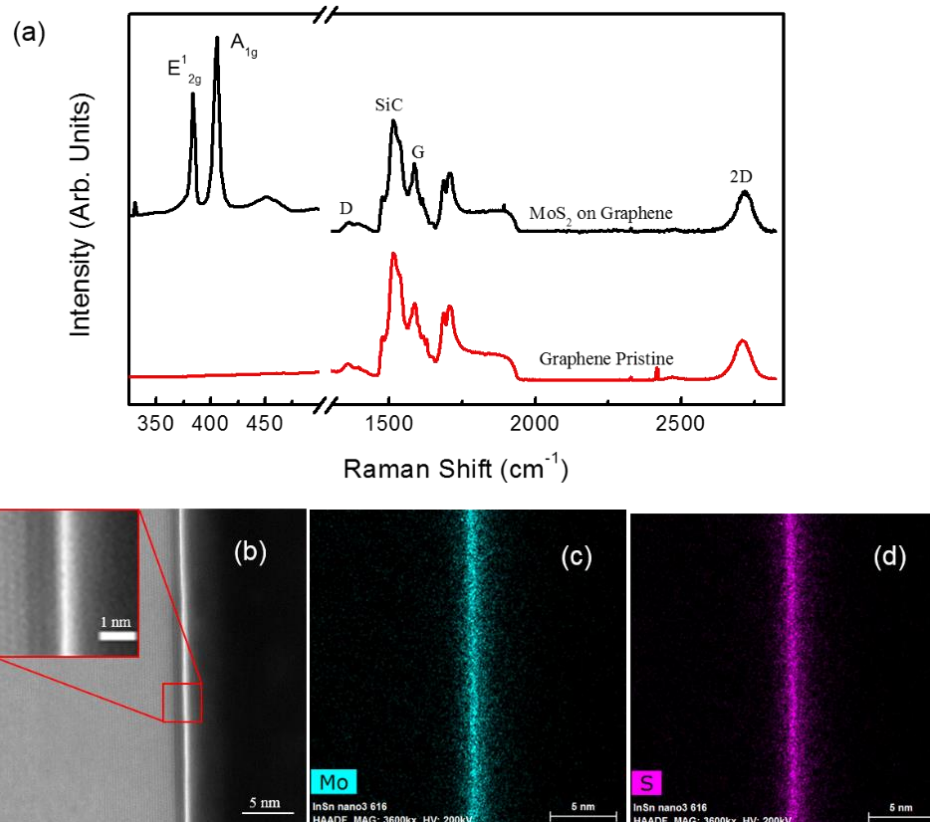


Figure 4.3.1.2. (a) Raman spectra in the wavenumber region between 300 and 2800 cm^{-1} of pristine graphene (black data) and graphene capped with MoS_2 (red data), (b) Bright-field scanning transmission electron microscopy (STEM) image of MoS_2 /graphene heterostructure, (c, d) EDX elemental maps showing the spatial distribution of Mo and S, respectively.

Local analysis using STEM was coupled with a macroscopic technique such as HR-XPS in order to ensure the quality of the interface of the sample on a large scale. High-resolution spectra recorded under surface sensitive conditions ($h\nu = 340 \text{ eV}$) for C 1s, Si 2p, Mo 3d, and S 2p are shown in Figure 4.3.1.3. The spectra were analyzed using the curve fitting procedure described in Methods. The experimental data points are displayed as dots. The solid line is the envelope of fitted components.

The C 1s spectrum (Figure 4.3.1.3a) shows the conventional deconvolution expected for monolayer graphene on $\text{SiC}(0001)$.^{288–290} This is characterized by three main components attributed to the (SiC) substrate at binding energy $\text{BE} = 283.9 \text{ eV}$, the

graphene layer (G) at BE = 284.7 eV, and the buffer layer at 285.3 eV (IL). The Si 2p doublet (Figure 3b) was reconstituted with a $2p_{1/2}:2p_{3/2}$ ratio of 0.5 and a spin-orbit splitting of 0.6 eV.²⁹¹ This is characterized by a main Si 2p $3/2$ component at 101.5 eV (SiC bulk), a small shoulder at a higher binding energy (102.1 eV) attributed to Si atoms at the interface between the bulk and the buffer layer, and a component at a lower binding energy (100.9 eV). This latter is due to the Si clusters formed when the Si-C bonds were broken during the graphitization process.^{292,293} The C 1s and Si 2p spectra presented no modifications induced by the MoS₂ transfer process (pristine spectra are shown in Figure S2 (a) C1s and (b) Si 2p, respectively). This confirmed that the transfer process did not induce contamination of the graphene underlayer and that a perfect vdW MoS₂/graphene heterostructure was formed. This was also confirmed by the Mo 3d and S 2p peak deconvolution, which presented the standard MoS₂ stoichiometry. The Mo 3d peak (Figure 4.3.1.3c) was reconstituted with a $3d_{3/2}:3d_{5/2}$ ratio of 0.66 and a spin-orbit splitting of 3.10 eV.²⁹⁴ The peak at a binding energy of 229.9 eV was attributed to Mo $3d_{5/2}$ for Mo⁴⁺ in a sulfur environment.²⁹⁵ The small peaks at lower binding energies corresponded to defective/substoichiometric MoS₂ with sulfur vacancies (inside or at the edge of the flake).^{295,296} Moreover, the weight of this component (between 5 and 15% of the whole Mo 3d spectrum) is not really representative of a single flake, in fact due to the large X-ray beam size (~100–150 μm diameter), extended regions were probed enclosing probably flakes with different size or more defective MoS₂ region. The small shoulder at 226.9 eV was the sulfur 2s peak. For the S 2p, a $2p_{1/2}:2p_{3/2}$ ratio of 0.5 and a spin-orbit splitting of 1.19 eV was used.²⁹⁴ The component at a binding energy of 162.7 eV corresponded to the S 2p $3/2$, as expected for divalent sulfide ions (S²⁻) in MoS₂.^{277,295} The

peak at a lower binding energy (152.8 eV) was the signature of the Si 2s from the SiC substrate (Figure 4.3.1.3d). These values of BE for the Mo 3d and S 2p indicated an intrinsic n-type doping of the MoS₂.²⁹⁷ In both spectra, the signature of no other bonds were present^{295,298–301} (i.e., oxygen or carbon), which corroborated the absence of any interdiffusion and contamination between the MoS₂ and graphene layers.

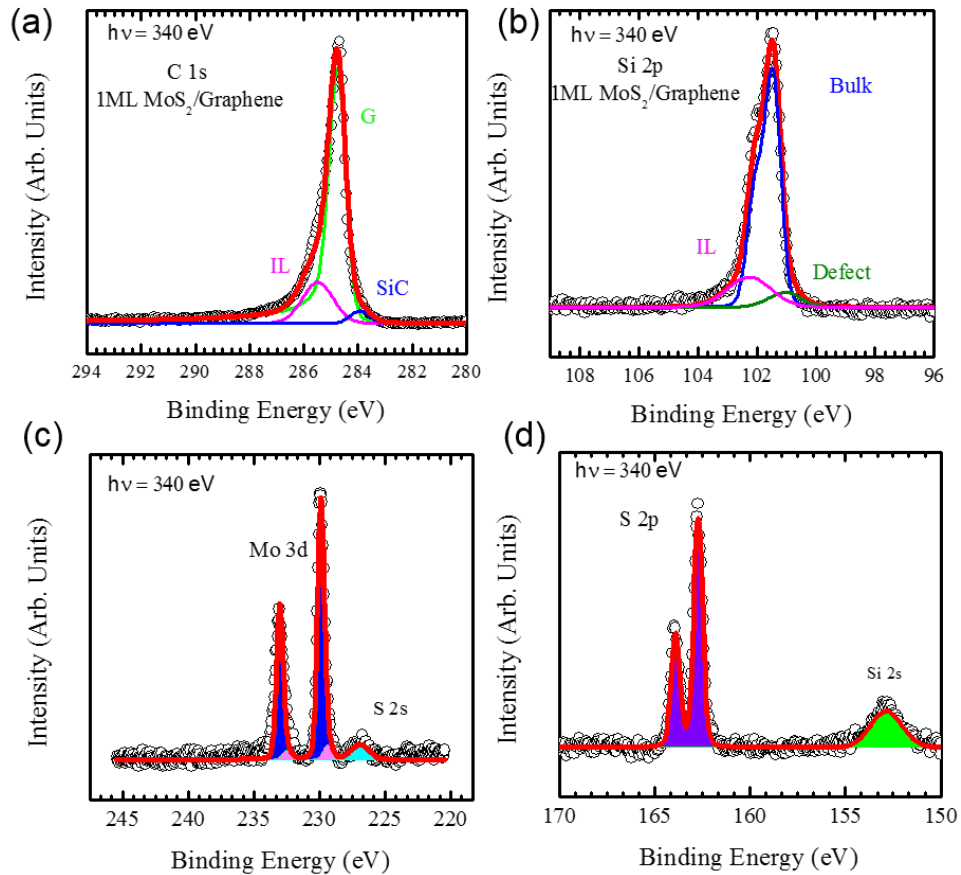


Figure 4.3.1.3. High-resolution XPS of MoS₂/graphene heterostructures: (a) C 1s core level, (b) Si-2p core level, (c) Mo 3d, and (d) S 2p, respectively, at $h\nu = 340$ eV. XPS measurements were performed at $\phi = 45^\circ$ emergency angle with respect to the sample normal.

To gain insight into the electronic structure of the MoS₂/ graphene interface, the MoS₂ valence band maximum and the total work function were measured. The angle integrated photoemission spectra of the valence band for the pristine graphene and MoS₂

graphene heterostructure over the full BZ were measured with a photon energy of 350 eV (Figure S3). Compared to pristine graphene, the MoS₂/graphene heterostructure presented new structures in the valence band spectrum (between 2 and 4 eV) due to MoS₂. Generally speaking, in the case of MoS₂, the measured valence band was derived from hybridization of Mo 4d and S 3p.²⁷⁴ For a photon energy of 350 eV, the calculated atomic photoionization cross section³⁰² for Mo 4d was almost twice the one of S 3p. Therefore, the new components appearing in the valence band spectrum were mostly due to the Mo 4d. From the intersection of the linear extrapolation of the leading edge of the valence band spectrum with the baseline, we could locate the position of the valence band maximum (VBM) for the MoS₂ in the heterostructure, VBM = 1.40 ± 0.05 eV. We also determined the total work function ϕ of the heterostructure via the measurement of the secondary electron (SE) edge. The position of the cutoff (E_k^{cutoff}) was measured by extrapolating the edge of the peak to the zero baseline, as shown in Figure S3 (right side). The position of the Fermi level ($E_{F(\text{polarized})}$) was determined by fitting the leading edge of the graphene underlayer, at the same photon energy and under the same experimental conditions (Figure S3b, left). The work function of the MoS₂/graphene heterostructure is given by:

$$\phi = h\nu + E_k^{\text{cutoff}} - E_{F(\text{polarized})} = 4.30 \pm 0.05 \text{ eV}$$

In addition, the optical band gaps of the bilayer MoS₂/ graphene was determined to be 1.83 eV using photoluminescence measurements, as shown before (Figure 4.3.1.1c). It should be noted that, by probing the quasiparticle band structure by STM/STS, the band gap was 2.0 eV, which was larger than the optical band gap,

considering the binding energy for an exciton.³⁰³ On the basis of these results, we constructed a band diagram of the MoS₂/graphene heterostructure (Figure 4.3.1.4). In this vertical heterostructure formed from one layer of a semimetal (graphene) and one layer of a semiconductor (MoS₂), the traditional Schottky barrier expected for 3D materials was not present. The small thickness of 1 ML of MoS₂ (only 6.5 Å) prohibited the possibility of forming a depletion region, which was here replaced by what is called a van der Waals gap.^{304,305}

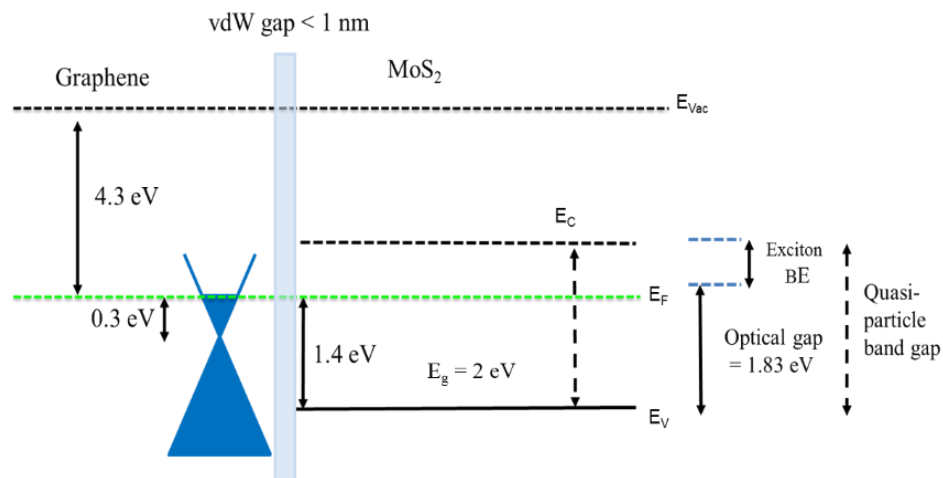


Figure 4.3.1.4. Band alignment diagram of MoS₂/graphene obtained from XPS measurement. The value of the optical band gap is obtained from the PL measurement in Figure 1c, and the value of the quasi particle band gap is obtained from ref.³⁰³

In order to clearly highlight the interaction between the MoS₂ and graphene layers, ARPES measurements were carried out. Figure 4.3.1.5 shows ARPES constant energy (CE) maps in panels a, b, and c, measured at the Fermi level, 0.3 and 1 eV binding energies, respectively. The six unambiguous Dirac cones at the K high symmetry points of the heterostructure reciprocal space confirmed the metallic electronic character of the interface dominated by the π^* bands of the epitaxial graphene, close to the Fermi level. Moreover, the classical interface generating diffraction spots of the primary band of

graphene was still present,³⁰⁶ also indicating that the interface between graphene and the buffer layer is not contaminated. These structures were reflected in π graphene band replicas, as shown in Figure 4.3.1.5d, where the Fermi surface was coupled in a 3D plot with the band structure of the MoS₂/graphene heterostructure. The single and robust Dirac cone at the six identical K high symmetry points (at $k_{\parallel} = 1.703 \text{ \AA}^{-1}$) confirmed that the graphene monolayer at the heterostructure preserved the Dirac linear dispersion and the massless relativistic character of the graphene carriers close to the Fermi level. The π bands of graphene determine a Fermi velocity $v_F \sim 1.1 \times 10^6 \text{ m/s}$ and an n-doping close to $9 \times 10^{12} \text{ cm}^{-2}$. As in the case of pristine graphene on SiC(0001) (Figure S4), the Dirac point was located at about 0.3 eV below the Fermi level (Figure S5). This indicates that there was no significant charge transfer from MoS₂ to graphene. Corroborating the case of pristine graphene, a new structure was present at the Γ point of the Brillouin zone (BZ), which is the signature of the MoS₂ valence band. As expected for a monolayer MoS₂, only one band was present^{272,307–310} at the Γ point. Moreover, in our experiments, we found in one area (Figure 4.3.1.6a) that, although the graphene π band preserved its linearity and the absence of a gap opening at the k point (i.e., same values of Fermi velocity v_F and n-type doping), at a higher binding energy with respect to the Dirac point, small band gap openings were present (Figures S6 and S7). These features are shown by red dashed lines in the second derivative of the ARPES map in Figure 4.3.1.6b. Different hypothesis can be proposed to explain the appearance of these minigaps. It is known that the interaction of graphene with a substrate can modify its electronic structure. In particular, in the case of graphene on metal substrates, several regions of different arrangements of carbon atoms above the metal substrate can be found, inducing a

buckling on graphene (i.e., a not constant interlayer distance). The nature of the buckling and then the distance between the graphene layer and the metal substrate depends on the type of underlying metal and the interaction between these two interfaces. When only a weak interaction is present^{311–315} (i.e., with Pt, Ir, and Cu), the graphene layer is located at minimum distance of about 3.3–3.6 Å from the metal surface, and the linear dispersion at the Dirac point is preserved. When the interaction between graphene and the substrate is stronger, the graphene layer's minimum distance from the metallic surface is reduced to about 2.1 Å (i.e., with Ni, Rh, Ru).^{316–319} In this case, an hybridization between the carbon and metal atoms leads to a loss of the linear dispersion of graphene bands.³²⁰ However, it has been shown that the electronic properties of graphene can be restored by the intercalation of noble metal atoms, which reduce the hybridization between the metal d-orbitals and the graphene π bands.³²¹ Even though the intercalation of noble metals increases the distance of the graphene layer from the substrate to 3.47 Å, an effect of possible hybridization is still present on the graphene band structure in the form of mini band gaps at a higher binding energy with respect to the Fermi level.³²² This effect was also observed by Batzill et al. in the case of graphene on a bulk MoS₂ substrate.³²³ The authors explain the presence of the small gap on the π band of graphene due to the hybridization of the bands by the out-of-plane orbital character of MoS₂ with the graphene π band. Nevertheless, they say that the specific rotation of the graphene grains does not significantly affect the band gaps.³²³ In our case, the distance between 1 ML of MoS₂ and graphene was 3.4 Å, so we can expect that the hybridization process could be present, as was the case for Batzill et al. However, differently from their study, the

minigaps on the π band of graphene were not visible on all the flakes, but only for a particular mismatch angle between MoS₂ and graphene.

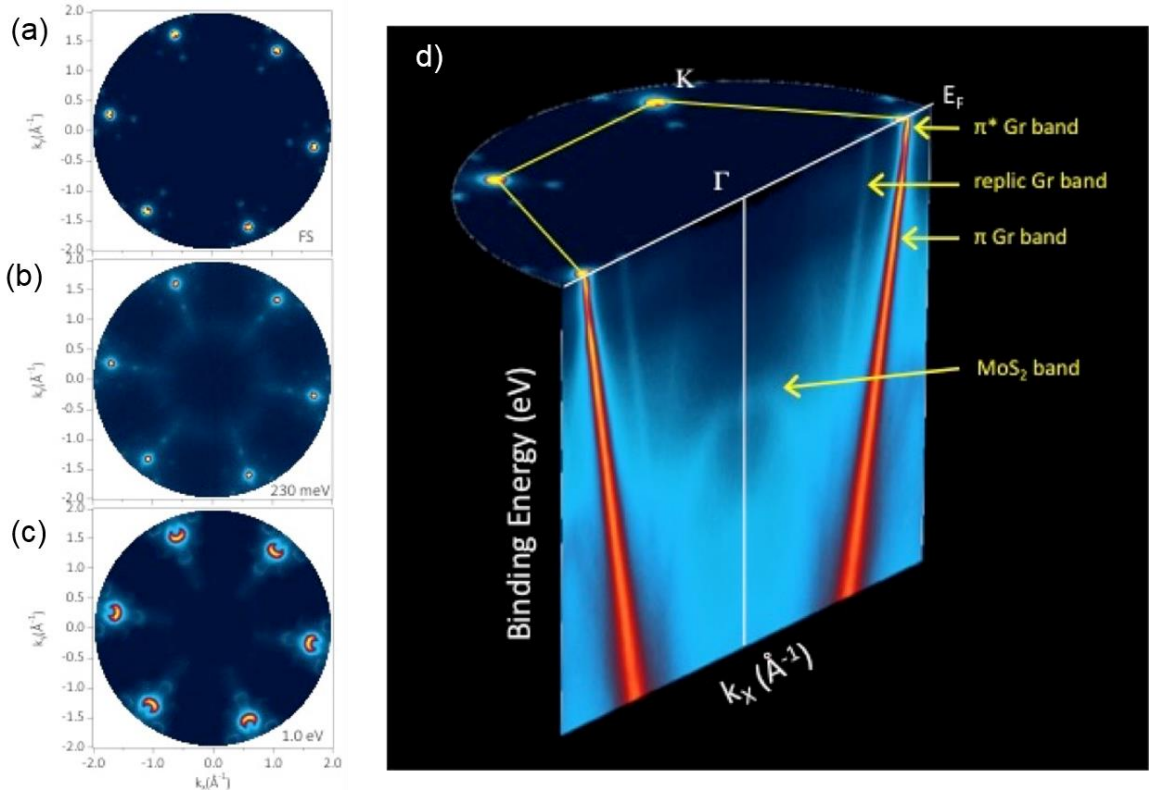


Figure 4.3.1.5. (a–c) ARPES constant energy (CE) maps measured at the Fermi level (a), 0.3 eV (Dirac point) (b), and 1 eV (c) binding energies, respectively. (d) 3D Fermi surface and band structure of MoS₂/graphene heterostructure ($h\nu = 100$ eV).

This means that the respective orientations of the two 2D layers play a role in this phenomenon. In this respect, Pletikoscic et al. studied the electronic structure of graphene on Ir (111) by ARPES.³¹² The authors underlined that, due to the lattice mismatch between graphene and Ir, a moiré superstructure was formed. This periodic perturbation introduced a superlattice potential, which gave rise to the opening of moiré-induced minigaps in the π band of graphene. In our heterostructure formed from 1 ML of MoS₂ on epitaxial graphene on SiC, two moiré superstructures can be formed. The first one is due to the SiC underlayer. In fact, in the case of epitaxial graphene on SiC(0001), due to the

reconstruction of the SiC interface beneath the graphene, a quasi-periodic moiré (6×6) hexagonal superstructure is formed with a periodicity of about 2 nm.³²⁴ However, the presence of mini-band gaps on the π band of graphene has never been observed in our pristine graphene²⁹⁰ or on common epitaxial graphene on SiC(0001).²⁹² The second possible superstructure is due to the lattice mismatch ($\delta \sim 28\%$), together with a possible misalignment of the two lattices between the graphene underlayer and the MoS₂, as already seen for graphene/h-BN.^{325,326} Following Yankowitz et al., we can define the primitive moiré lattice period for this hexagonal superstructure as³¹⁴

$$\lambda = \frac{(1 + \delta)a}{\sqrt{2(1 + \delta)(1 - \cos \phi) + \delta^2}}$$

where a is the graphene lattice constant and ϕ the relative rotation angle between the two lattices. This periodic perturbation introduces a superlattice potential that acts on graphene's charge carriers^{325,327} and generates the observed mini gap openings at the supercell Brillouin zone (SBZ) boundary at energies $E = \pm \frac{\hbar v_F G}{2}$ given by the reciprocal superlattice vector $G = \frac{4\pi}{\sqrt{3}\lambda}$ (where v_F is the Fermi velocity and \hbar the Planck's constant divided by 2π). As expected for this model no band gap opening was present at the graphene's Dirac point³²⁷ (Figure 4.3.1.6a). Then, from the energy value of the first mini-gap ($E = -3.55$ eV) obtained from Figure 6b and using the value obtained for the Fermi velocity of $v_F \sim 1.1 \times 10^6$ m/s, we could determine the relative rotation angle between the MoS₂ flake and the graphene, which is about 6° (Figure 4.3.1.6c). For this angle, we obtained a super structure with a period of 0.74 nm, as shown in Figure 6d. We briefly discussed the interaction between graphene and MoS₂ in this heterostructure. The

MoS₂/graphene heterostructure presented a lattice mismatch of about 28%, or the so-called moiré patterns, characterized by the rotation angle between the two layers (about 6°). These patterns provide a periodic potential to graphene and lead to a band gap opening at a higher energy relative to the graphene neutrality point. These minigaps often give rise to interesting phenomena.³²⁷ However, the Dirac cone at the six K high symmetry points confirm that the graphene monolayer in this heterostructure preserved the Dirac linear dispersion and the massless relativistic character of the graphene carriers close to the Fermi level in agreement with pristine graphene.

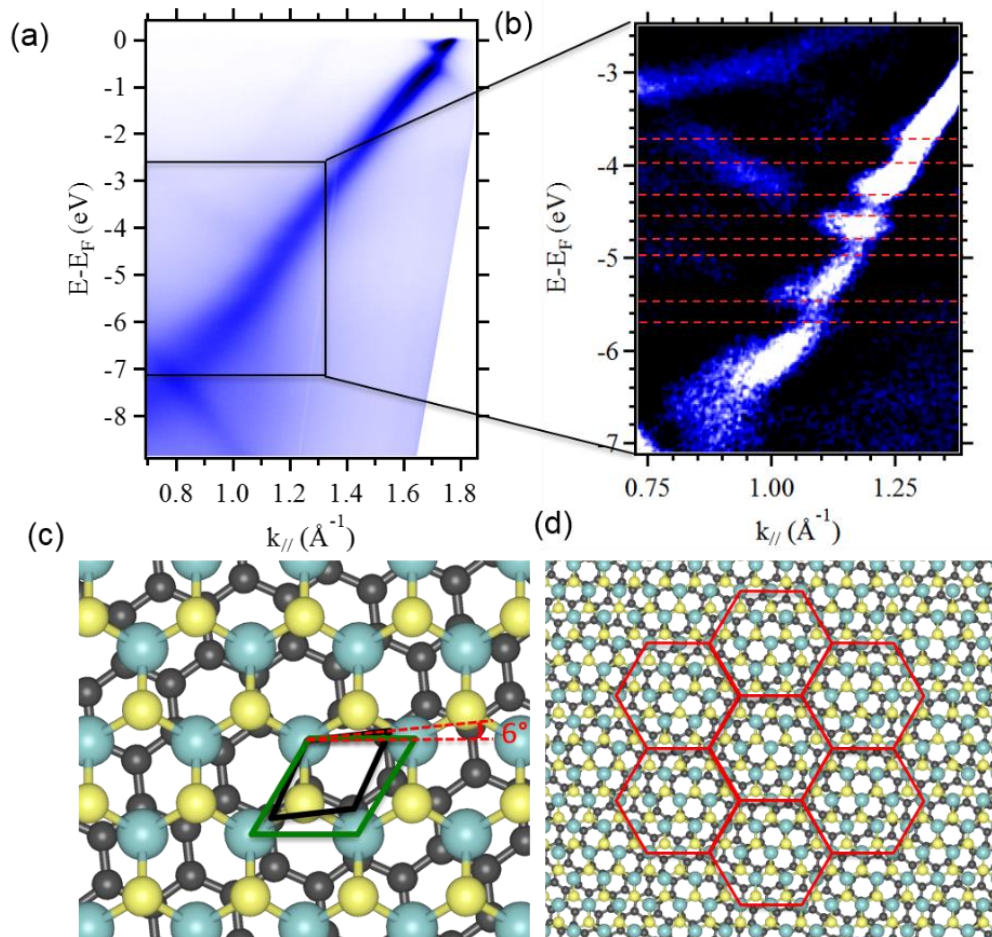


Figure 4.3.1.6. Electronic structure of MoS₂/graphene heterostructures: (a) ARPES spectrum of monolayer MoS₂ thin films on graphene at $h\nu = 100$ eV, (b) second-derivative spectra of panel a to

enhance the visibility of the bands. The red dashed lines indicate the miniband gap, (c) diagram of MoS₂ on epitaxial graphene twisted by 6°, (d) primitive moiré lattice period for this MoS₂/graphene hexagonal superstructure.

In summary, for the first time we have demonstrated that, with a transfer process, we obtained a high-quality vdW MoS₂/ graphene junction. The homogeneity, large area, and high quality of the sample are confirmed by optical and microRaman imaging. The STEM measurement shows that the interlayer separation is about 3.4 ± 0.1 Å nm between the graphene underlayer and the monolayer MoS₂ flake, and the MoS₂ layers are atomically flat. The high- resolution XPS measurements also show the absence of any interdiffusion and contamination between MoS₂ and graphene layers and suggest that the MoS₂ exhibits n-type behavior. Finally, the direct measurement of the electronic properties of this vdW heterostructure was investigated using HR-XPS and ARPES. Using XPS, we achieved for the first time the band alignment of both MoS₂ and epitaxial graphene monolayers. ARPES measurements showed that the Fermi velocity of graphene remained intact in comparison with pristine graphene. Finally, we demonstrate the formation of miniband gaps in the π band of monolayer epitaxial graphene. These miniband gaps can be associated with a periodic moiré pattern between graphene and MoS₂ and then to band anticrossing at the Brillouin zone edge of the new superperiodicity, which appear when bands with derivatives of the same sign are renormalized by an extra potential.

4.3.2 Electrical tuning of exciton-plasmon polariton coupling in monolayer MoS₂ integrated with plasmonic nanoantenna lattice

The results presented in this section are currently under review for publication “Electrical tuning of exciton-plasmon polariton coupling in monolayer MoS₂ integrated with plasmonic nanoantenna lattice”, Bumsu Lee[†], Wenjing Liu[†], Carl H. Naylor, Joohee Park, Stephanie Malek, Jacob Berger, A.T. Charlie Johnson and Ritesh Agarwal, Science, 2017.

Abstract

Active control of light-matter interactions in semiconductors is critical for realizing next generation optoelectronic devices, with real-time control of the system’s optical properties and hence functionalities via external fields. The ability to dynamically manipulate optical interactions by applied fields in active materials coupled to cavities with fixed geometrical parameters opens up possibilities of controlling the lifetimes, oscillator strengths and the relaxation properties of a coupled exciton-photon (or plasmon) system. Here, we demonstrate electrical control of exciton-plasmon coupling strengths between strong and weak coupling limits in a two-dimensional semiconductor integrated with plasmonic nanoresonators assembled in a field-effect transistor device by electrostatic doping. As a result, the energy-momentum dispersions of such an exciton-plasmon coupled system can be altered dynamically with applied electric field by modulating the

excitonic properties of monolayer MoS₂ arising from many-body effects. In addition, evidence of enhanced coupling between charged excitons (trions) and plasmons was also observed upon increased carrier injection, which can be utilized for fabricating fermionic polaritonic and magnetoplasmonic devices. The ability to dynamically control the optical properties of a coupled exciton-plasmonic system with electric fields demonstrates the versatility of the coupled system and offers a new platform for the design of optoelectronic devices with precisely tailored responses.

Introduction

Mono- and few-layered two-dimensional (2D) transition metal dichalcogenide (TMDC) semiconductors have been receiving great attention due to their very unique attributes originating from strong two-dimensional confinement and inadequate dielectric screening along with new potential applications including ultra-thin optoelectronic devices, exciton-polariton formation at high temperature, and spin-valley devices.^{42,328,329} The strongly confined 2D excitons in monolayer TMDC semiconductors lead to several interesting optical features such as large exciton binding energy³³⁰⁻³³³ and oscillator strength,^{334,335} and the observation of higher-order excitations such as charged excitons (trions).^{336,337} The optical properties of 2D excitons can be significantly altered when coupled to an external cavity, leading to enhancement of spontaneous emission rate and lasing in the weak exciton-photon coupling regime, and the formation of exciton-polaritons in the strong coupling regime.^{101,102,338-347} Various types of optical cavities

including distributed Bragg Reflectors (DBRs),^{339,345,347} photonic crystals³⁴¹ and plasmonic nanoresonators^{101,102,338,340,342–344,346} have been utilized to manipulate the optical properties of 2D excitons, demonstrating weak, intermediate and strong coupling regimes. Among different cavity types, plasmonic nanoantenna arrays offer unique opportunities for tailoring light-matter interactions in 2D materials with geometric compatibility, strong optical confinement as well as their ease of integration, which is also compatible with electrical injection or gating device configuration. Furthermore, plasmonic lattices depending on the lattice geometry allows for tunable and intense resonances originating from localized surface plasmons (LSPs) coupled to the lattice dispersion known as “surface lattice resonances” or “lattice-LSP” modes.^{348,349} The lattice-LSPs are propagating modes with strong electric fields, and relatively high quality factors in comparison to LSP resonances from individual (uncoupled) nanoparticles. Recently, monolayer molybdenum disulfide (MoS₂) integrated with plasmonic nanoantenna lattice has shown large enhancements of the Raman scattering and photoluminescence in the weak coupling regime,¹⁰¹ Fano resonances in the intermediate coupling range¹⁰¹ and normal mode splitting with the formation of exciton-plasmon polaritons in the strong coupling regime.^{102,340}

On the other hand, owing to the atomically thin nature and the associated significantly reduced screening of the charge carriers, monolayer TMDC semiconductors provide unique platforms for electrically controlling their optoelectronic properties, via electrostatic doping in a field-effect transistor (FET) geometry. As a result, novel findings have been reported including the modulation of exciton binding energies,^{350,351}

observation of charged trions,^{336,339} and valley-contrast second-harmonic generation.³⁵² Here, by configuring the plasmonic lattice-monolayer MoS₂ system in an FET device geometry, we demonstrate active control of the coupling strengths between the MoS₂ excitons and lattice-LSP resonances, with continuous and reversible transition between the strong and weak exciton-plasmon coupling regimes achieved by electron injection or depletion in the active MoS₂ monolayer. Furthermore, under certain doping conditions, evidence of enhanced coupling between negatively charged excitons (trions) and plasmons was also observed, which are *fermionic* exciton-plasmon polaritons that can provide a novel platform for quantum optics. Therefore, we demonstrated that the spin classification of the exciton-plasmon system can be switched back and forth between bosonic (neutral exciton-plasmon) and fermionic (trion-plasmon) polaritonic states by simply applying an external electric field to the system.

Results

To fabricate the optoelectronic device (Fig. 4.3.2.1A), monolayer MoS₂ was grown directly on Si/SiO₂ substrate by chemical vapor deposition⁹⁸ followed by the fabrication of source and drain electrodes and silver plasmonic nanodisk arrays (see Materials and Methods). A 285 nm-thick thermally grown SiO₂ layer sandwiched between MoS₂ and highly doped Si substrate produces a metal-oxide-semiconductor FET with a capacitance of ~12 nF/cm². Charge carriers are injected or depleted from the electrical contacts depending on the gate electrostatic potential (V_G) with respect to MoS₂.

For example, a V_G of ~ 100 V can lead to a carrier density of $\sim 8 \times 10^{12}/\text{cm}^2$ in the MoS₂ monolayer, estimated from the capacitance of the device. As a result, the chemical potential (Fermi level) of MoS₂ can be altered by ~ 50 meV depending on the carrier density. Figure 1B shows a typical transconductance curve obtained from a MoS₂ FET device, displaying *n*-type channel performance. The plasmonic lattice cavities were fabricated with the diameters of the silver nanodisks varied between 110 and 140 nm, with a constant thickness of 50 nm and with a lattice parameter of $a \times b = 460$ nm \times 460 nm. These cavity geometries allow tuning the LSP energies near the MoS₂ excitonic region to enable strong exciton-plasmon coupling.¹⁰² To characterize the evolution of the coupling between the MoS₂ excitons and lattice-LSPs, the dispersions of the coupled MoS₂-plasmonic lattice system were measured by a home-built angle-resolved setup³⁵³ while tuning the gate voltage (see Materials and Methods).

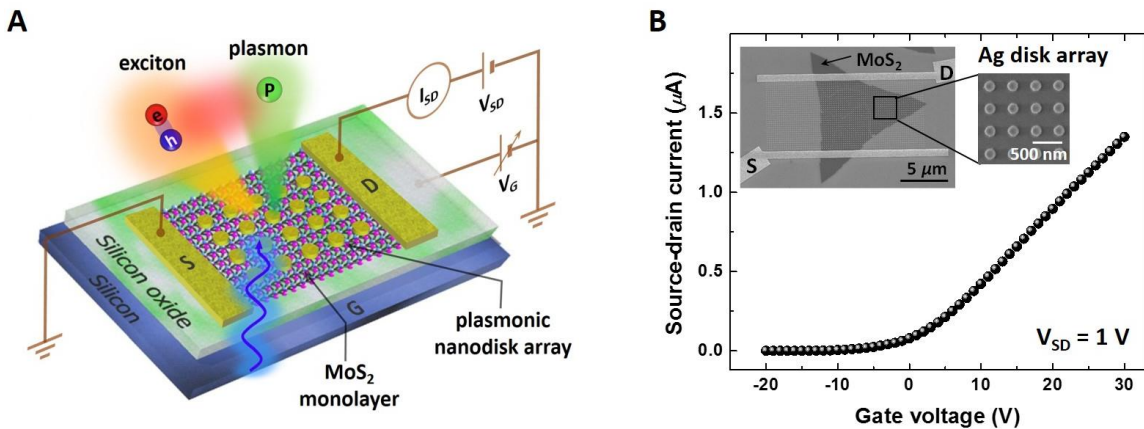


Figure 4.3.2.1. Electrical tuning of monolayer MoS₂ coupled with plasmonic nanodisk array configured in a field-effect transistor geometry. (A) Schematic diagram of the MoS₂ monolayer-plasmonic lattice system integrated with an FET device which enables carrier injection and depletion. (B) Typical transconductance data obtained from a MoS₂ FET device. Inset: SEM images of the MoS₂-plasmonic lattice FET device.

The angle-resolved differential reflectance spectra ($\Delta R/R = (R_{\text{sample}} - R_{\text{substrate}})/R_{\text{substrate}}$) measured at 77 K for MoS₂ monolayer integrated with silver nanodisk array with disk diameters, $d = 110$ nm are presented in figures 4.3.2.2A-C at three representative gate voltages. The lattice was carefully designed to tune the LSP mode of the nanodisks nearly in resonance with the A excitons to allow maximum exciton-plasmon coupling.¹⁰² As a result, strong coupling of the lattice-LSP modes to both the neutral excitons (A⁰) and negatively charged excitons (trions, A⁻) was observed at different applied voltages, leading to the formation of their own discrete polariton branches. At $V_G = 0$ V (Fig. 4.3.2.2A), the system's dispersion shows an anti-crossing behavior near the MoS₂ A exciton state (yellow (green) dashed-lines express the positions of A⁰ (A⁻) excitons in Fig. 4.3.2.2A-C), indicating strong coupling between the MoS₂ excitons and lattice-LSPs; When a gate bias was applied, significant changes in the angle-resolved spectra were observed (Fig. 4.3.2.2B and C). Upon sweeping the V_G from 0 to 80 V, the anti-crossing gradually disappeared in the dispersion curves, indicating that the strong A exciton-lattice LSP coupling was gradually changed to weak coupling upon carrier injection. Interestingly, starting from $V_G = 40$ V (Fig. 4.3.2.2B and C), new spectral features show up near 650 nm, which matches the A⁻ exciton (trion) resonance, implying the appearance of the trion state and their strong coupling with the lattice-LSP modes upon carrier injection.

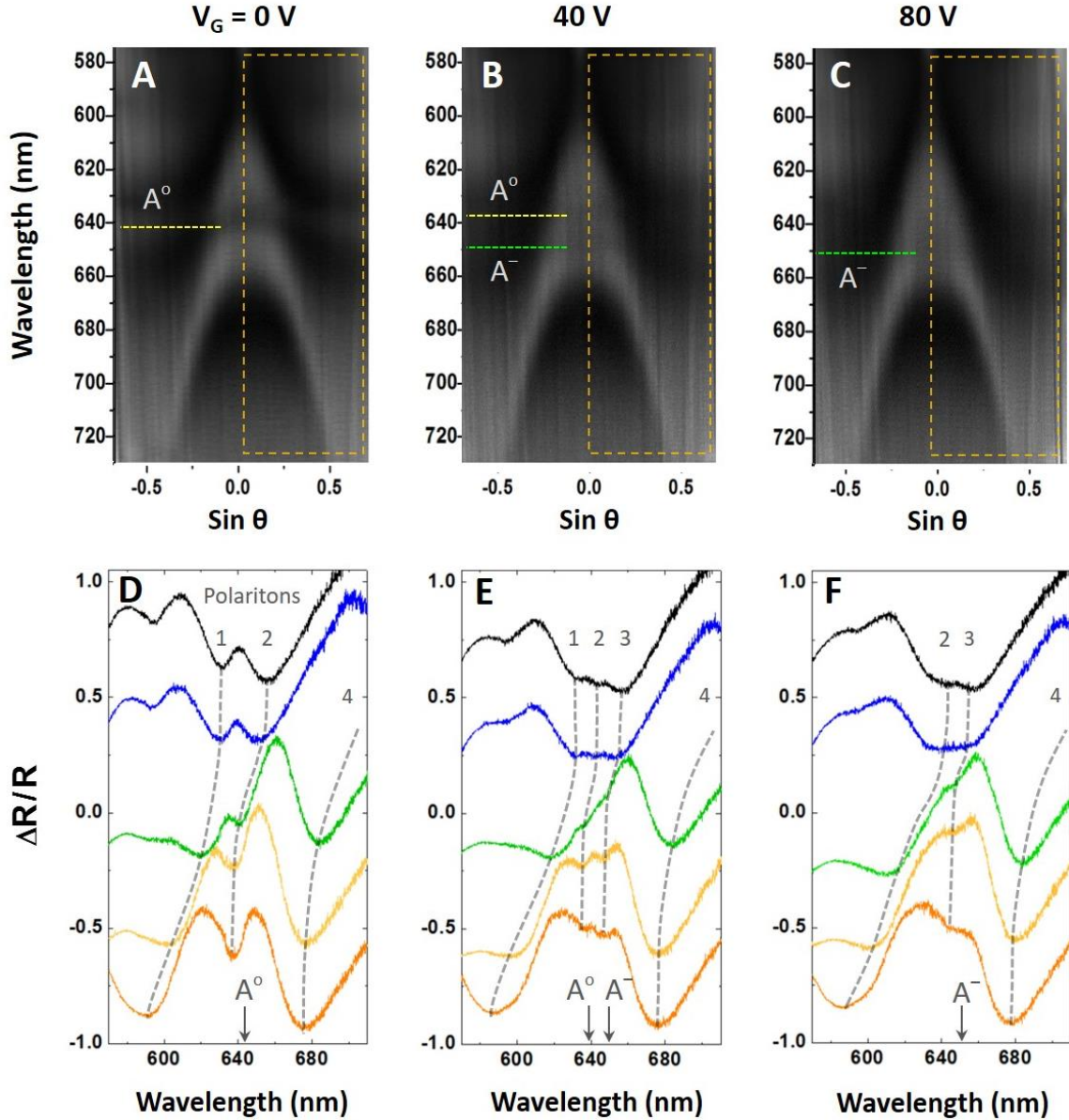


Figure 4.3.2.2. Tuning of exciton-plasmon coupling between the lattice-LSP modes to both neutral (A°) and charged (A^-) excitons via gate voltage. (A-C) Angle-resolved $\Delta R/R$ spectra at three different gate voltages ($V_G = 0, 40$ and 80 V), showing A° and A^- exciton-plasmon coupling. (D-F) Line cuts extracted from the orange dashed rectangular area of the angle-resolved spectra at each gate voltage in (A-C). Evolution of the system's eigenmodes are shown by grey-dashed lines. The positions of uncoupled A° and A^- excitons are indicated as arrows. The $\Delta R/R$ spectra are offset for clarity. Lattice constant is $(a \times b) = (460 \text{ nm} \times 460 \text{ nm})$.

Figure 4.3.2.2D-F show a series of $\Delta R/R$ line-cuts extracted at different angles from the individual angle-resolved spectra (Fig. 4.3.2.2A-C, orange-dashed rectangular areas) at $V_G = 0, 40$, and 80 V. Positions of uncoupled A° and A^- exciton resonances of

bare MoS₂ are also indicated as arrows in Fig. 2D-F. These $\Delta R/R$ spectra show clearly resolved exciton-plasmon polariton dispersions originated from both A⁰ and A⁻ exciton-plasmon coupling at different gate voltages. At $V_G = 0$ V, distinct polariton branches resulting from strong A⁰ exciton-plasmon coupling can be observed, as indicated by the gray-dashed lines in Fig. 4.3.2.2D. The strong A⁰ exciton-plasmon coupling and the absence of the spectral features of A⁻ excitons indicate that the sample was lightly doped. As the carrier concentration increased upon applying a positive $V_G = 40$ V, new polariton mode (~650 nm) corresponding to A⁻ exciton-plasmon coupling appeared in the $\Delta R/R$ spectra (Fig. 4.3.2.2B and E), accompanied by a slight blue-shift of the preexisting polariton branches. Upon increasing V_G to 80 V (Fig. 4.3.2.2C and F), the polariton modes originating from A⁰ exciton-plasmon coupling vanished while the A⁻ (trion) polariton gained oscillator strength, resulting in more enhanced reflection features and mode splitting, which suggests that the system changed progressively from strong A⁰ exciton-plasmon coupling to enhanced A⁻ exciton-plasmon coupling regime with increasing carrier concentration. These experiments demonstrate that plasmon coupling to the excitonic resonances can be finely tuned between the weak and strong coupling limits via electric control of charge carrier density in the active medium of 2D semiconductors. In addition, the possibility of creating trion-plasmon polaritons, a unique type of fermionic light-matter hybrids, in which the spin structure of the trion can effectively couple to the plasmon, can enable a new class of magnetoplasmonic systems.

In order to quantitatively characterize the observed tuning phenomena of the exciton-plasmon coupling, the angle-resolved spectra were fitted to a coupled oscillator

model (COM) to calculate the exciton-plasmon coupling strengths as a function of V_G , as shown in figure 4.3.2.3 (see Supplementary Materials). The COM fitting results are in excellent agreement with the experimental data, capturing all the features of the recorded dispersions over large wavelength and angle ranges at different applied V_G (a set of full angle-resolved $\Delta R/R$ simulation images are also presented in the Supplementary Materials). The V_G -dependent exciton-LSP coupling strengths are presented in Fig. 4.3.2.3F, while the exciton-diffractive order coupling strengths were found to be nearly negligible in this device (See Supplementary Materials for all the matrix elements obtained from COM fitting). At $V_G = 0$ V, only the A^0 exciton-plasmon strong coupling was observed in the reflectance spectrum, as indicated by clear anti-crossing behaviors of the dispersion curves (Figs. 4.3.2.2D and 4.3.2.3A) with a coupling strength of 63 meV. As the carrier concentration increased upon applying positive V_G , the A^0 exciton state displayed a slight blue shift in its energy (yellow dashed-lines in Fig. 4.3.2.3A-E) and linewidth broadening in the $\Delta R/R$ spectra attributed to many-body effects upon carrier doping³⁵¹ (see also Supplementary Materials). As a result, it gradually decoupled from the lattice-LSP modes, and eventually disappeared in the dispersion spectra. Upon increasing the positive gate voltage, an additional polariton branch emerged (Fig. 4.3.2.3B), resulting from the splitting of the initial polariton branch 2 at the A^- exciton state, indicating A^- -plasmon coupling. With a further increase in V_G (Fig. 4.3.2.3B-D), the new polariton branch 2 progressively blue shifted, suggesting increased mode splitting between the polariton branches 2 and 3 near the A^- state (increase in A^- plasmon coupling), and decreased mode splitting between polariton branches 1 and 2 near the A^0 state (decrease in A^0 plasmon coupling). At $V_G = 80$ V (Fig. 4.3.2.3E), the polariton

branches 1 and 2 merged into one branch, which indicates that the coupling between A^0 excitons and the lattice-LSP modes vanished, owing to the collapse of their oscillator strengths under high doping conditions. The evolution in the exciton-plasmon coupling strengths is simulated by the COM fitting. Upon applying positive V_G , the A^0 exciton-LSP coupling strength undergoes a large change from 63 meV to almost zero, while the coupling between trions and lattice-LSP modes gradually increased with increased doping and reached a maximum coupling strength of 42 meV at $V_G = 80$ V, caused by a partial transition of the oscillator strengths from neutral excitons to negatively charged trions. At intermediate V_G (Fig. 4.3.2.3C), the observed polariton modes originated from both the A^- (lower energy) and A^0 (higher energy) excitons indicated by gray arrows. The lower value in the maximum coupling strength of A^- excitons can be explained by their weaker oscillator strengths than A^0 excitons. However, given that the typical oscillator strengths of trions found in 2D quantum wells or bulk materials are more than an order of magnitude lower than that of the neutral excitons,^{337,354} this finding is intriguing since the magnitude of the coupling strength of trions with plasmons is comparable to neutral exciton-plasmon coupling, which further illustrates the enhanced interaction between excitons and charged carriers due to significantly reduced screening and large overlap between electron and hole wave functions from their extreme 2D confinement.³⁴¹ In control experiments (see Supplementary Materials), reflectance spectra of bare monolayer MoS₂ FET device also revealed a decrease (increase) of the oscillator strength of the A^0 (A^-) exciton transition upon electrostatic doping and only a very small shift of their resonance energies due to many-body effects.^{350,351} These results are consistent with

our observation of the evolution of the exciton-plasmon coupling with increased doping, as will be discussed later in more detail.

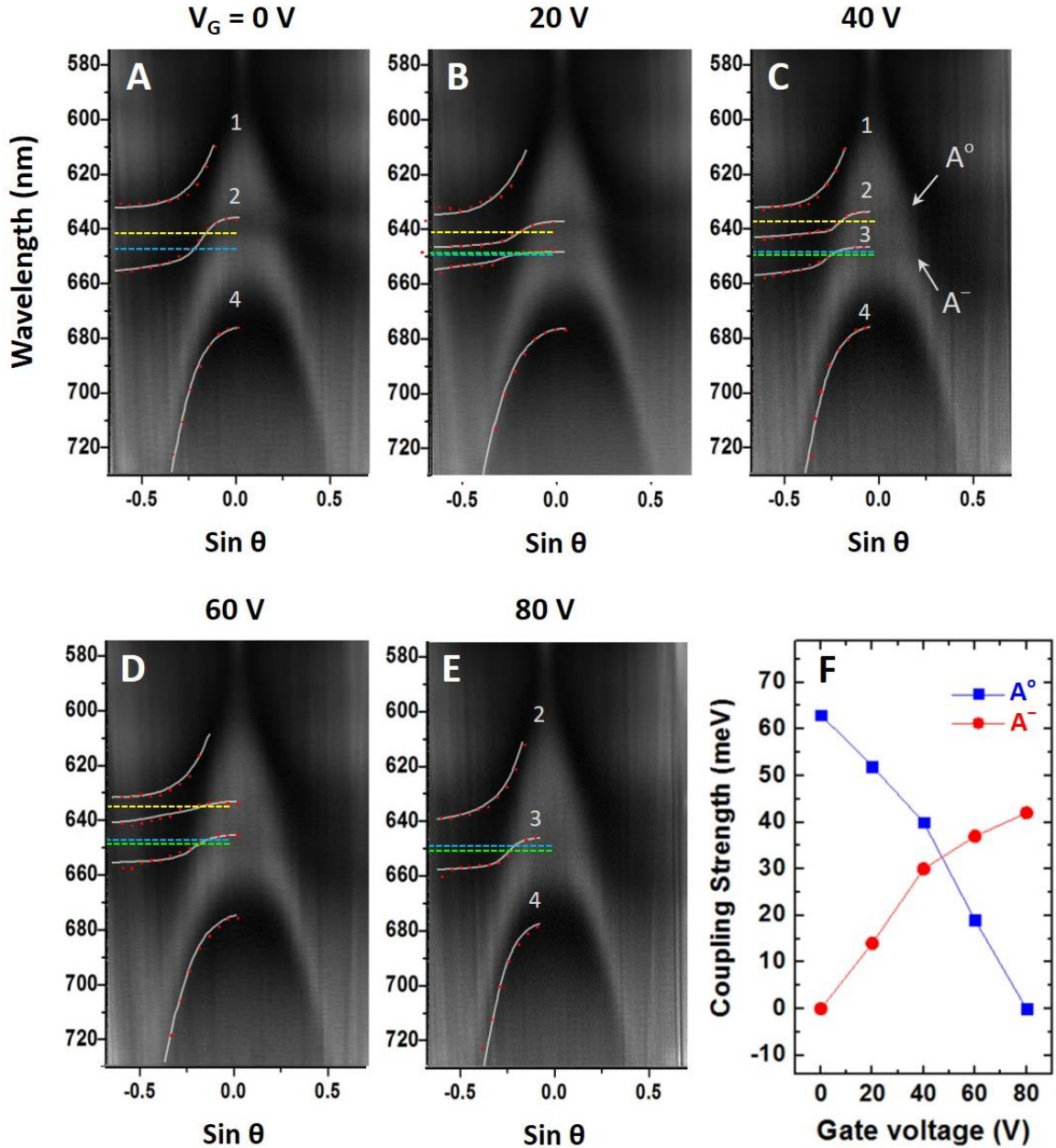


Figure 4.3.2.3. Coupled Oscillator Model fitting of the evolution of the exciton-plasmon coupling under different electron doping conditions. (A-E) Angle-resolved $\Delta R/R$ spectra and the corresponding coupled oscillator model (COM) fits at different gate voltages. At $V_G = 40$ V, polariton modes are observed from both A° and A^- excitons as indicated in (C). The positions of uncoupled A° and A^- excitons, and LSP resonances are indicated as yellow-, green- and blue-dashed lines,

respectively in (A-E). (F) Calculated coupling strengths between LSP and both A^0 and A^- excitons obtained from the COM as a function of the gate voltage.

To further study the modulation of light-matter coupling of the system and its active control via external fields, measurements were carried out on nanodisk arrays with different disk diameters ($d = 120$ and 140 nm) patterned on the same large area MoS_2 monolayer. LSP resonances arising from different sized silver disks resulted in different coupling strengths with A^0 and A^- excitons (Fig. 4.3.2.4) due to different LSP-exciton detuning.¹⁰² Unlike the previous device with the LSP in resonance with the A^- exciton ($d = 110$ nm, Fig. 4.3.2.3 and 4.3.2.4A-C), these two lattices have their LSP resonances more detuned from the excitonic region at 670 nm and 685 nm (blue-dashed lines in Fig. 4.3.2.4F-H and K-M) respectively. Especially, the 685 nm mode is largely detuned from the excitonic region with > 150 meV detuning. The tuning of the mode dispersions (Fig. 4.3.2.4F-H and K-M) with different V_G was observed in both devices, with qualitatively similar trends (Fig. 4.3.2.3I and N) as observed for the device in Fig. 4.3.2.3 and Fig. 4.3.2.4A-D. However, the exciton-plasmon coupling strengths of the array with LSP in resonance with the excitons ($d = 110$ nm) were significantly higher than the array with detuned LSP resonance ($d = 140$ nm) at the same V_G . The different LSP resonances in these two different arrays not only quantitatively changed the exciton-plasmon coupling strengths, but more importantly, altered the nature of the exciton-plasmon coupling of the system. Figure 4.3.2.4E, J and O show a series of line-cuts obtained at different V_G , extracted from the angle-resolved spectra of the three arrays at the angles where the lattice-LSP modes have zero detuning with the A^0 exciton ($\sin\theta = 0.34, 0.32,$ and 0.27 for $d = 110, 120$ and 140 nm, respectively). For $d = 110$ and 120 nm devices (Fig. 4.3.2.4E

and J), evolution of the exciton-plasmon dispersion indicated by grey-dashed lines with V_G suggests that the system changed progressively from strong A^0 exciton-plasmon coupling to strong A^- exciton-plasmon coupling regime. In contrast, the $d = 140$ nm device (Fig. 4.3.2.4O) showed two polariton modes observed at $V_G = 0$ V gradually merged into one broad dip with increasing V_G , indicating that the system evolved from strong to weak coupling regime. These results, consistent with other similar devices, also provide more insights about design strategies for obtaining precisely tailored optoelectronic responses in 2D polaritonic devices.

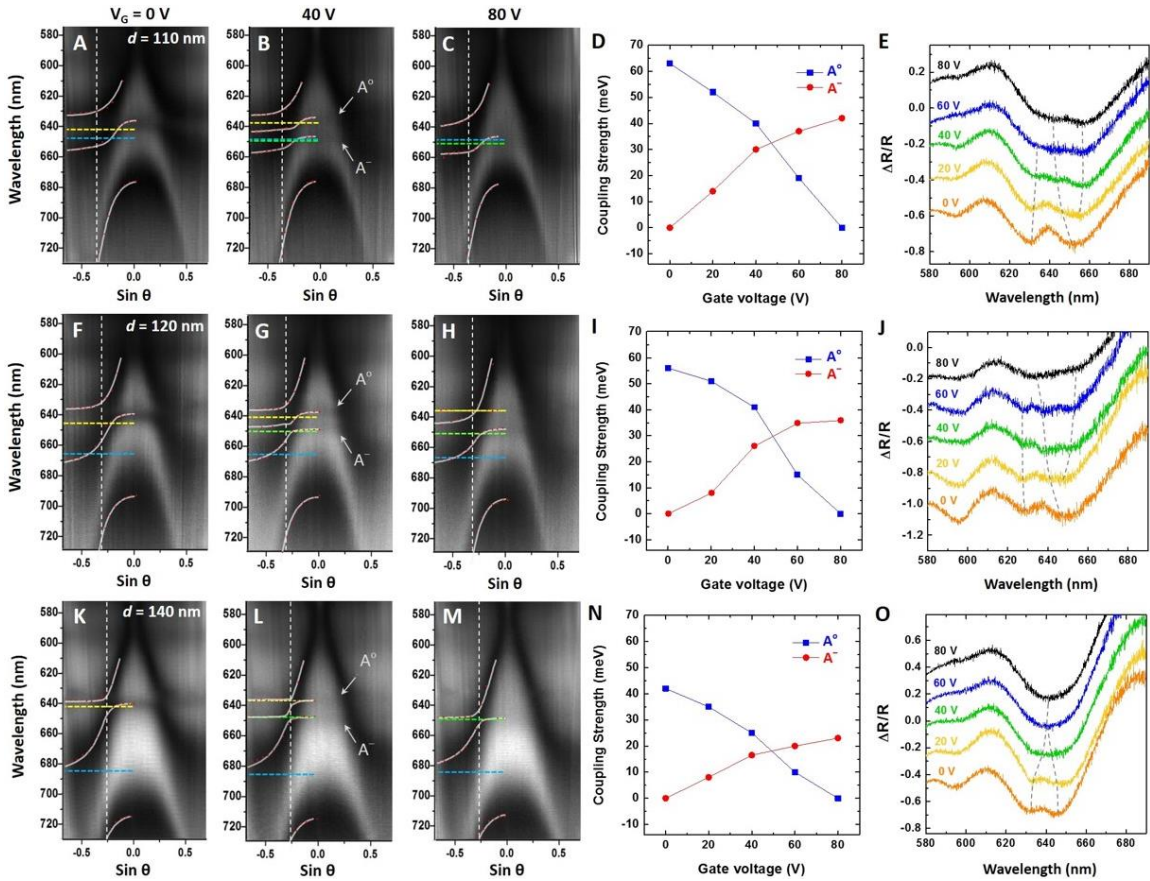


Figure 4.3.2.4. Gate-voltage dependent exciton-plasmon coupling in three different silver nanodisk arrays with different exciton-LSP detuning values. (A-C) $d = 110$ nm. (F-H) $d = 120$ nm (K-M) $d = 140$ nm. The positions of uncoupled A^0 and A^- excitons, and LSP resonances are indicated as yellow-, green- and blue-dashed lines, respectively. (D,I,N) Comparison of the exciton-plasmon coupling strengths between LSPs and both A^0 and A^- excitons obtained from the COM as a function of the

gate voltage. (E,J,O) Line cuts (vertical white-dashed lines, $\sin\theta = 0.34$ in (A-C), $\sin\theta = 0.32$ in (F-H), and $\sin\theta = 0.27$ in (K-M), respectively) from the angle-resolved spectra at different V_G . Grey-dashed lines in (E), (J) and (O) trace the evolution of the system's eigenstates upon carrier doping. The $\Delta R/R$ spectra are offset for clarity. Lattice constants of all devices are $(a \times b) = (460 \text{ nm} \times 460 \text{ nm})$.

Discussion

Enhanced many-body effects are one of the unique characteristics of highly confined TMDC monolayers even at moderate doping levels, which can be easily achieved from Si/SiO₂ back-gated FET devices.^{331,337,350,351} Greatly reduced screening due to the lack of large bulk polarization leads to enhanced Coulomb interaction and scattering process, which, along with phase-space filling (Pauli blocking) effect, influences the exciton oscillator strength and binding energy.^{350,351,355} The increased charge carrier concentration under positive electrostatic gating results in the reduction of the A^o oscillator strength due to exciton bleaching, giving rise to weaker interactions between excitons and plasmons, which drives the system towards weak coupling regime. On the contrary, the depletion of charge carriers makes MoS₂ more intrinsic, resulting in stronger exciton-plasmon coupling. Thus, in TMDC monolayers, continuous and reversible switching between strong and weak exciton-plasmon coupling regimes can be achieved in response to the variation of charge carrier concentration (Fermi level shift), which can be easily controlled by external fields, owing to the unique attributes of the 2D excitonic systems.

In summary, we demonstrated active control of the coupling strengths between 2D MoS₂ excitons and plasmonic lattices integrated in an FET device, via charge carrier

injection/depletion. Continuous and reversible transition between the strong and weak exciton-plasmon coupling regimes was achieved by tuning the gate voltage. Furthermore, we also showed that the trion resonances could also couple with the lattice plasmons at high electron doping concentration, showing their own dispersion properties. Our work demonstrates that unique opportunities exist in 2D monolayer semiconductors to electrically control light-matter interactions, owing to the lack of bulk polarization in these ultrathin materials, which reduces carrier screening, and hence leads to extraordinarily strong exciton oscillator strengths and binding energies, as well as enhanced many body effects. Electrical control of light-matter interactions in photonic devices is very attractive for designing modulators, switches, sensors, and other functional polaritonic devices. Furthermore, stronger trion-plasmon coupling can be an attractive platform for studying the strongly coupled spin and plasmon systems, i.e., *magnetoplasmons*, in which the combination of plasmonics and magnetism can enable the control of plasmonic properties by magnetic fields, giving rise to novel magneto-optical responses in these class of materials.

Materials and Methods

MoS₂ growth and device fabrication. Monolayer MoS₂ flaks were grown on Si/SiO₂ substrate (285 nm thick SiO₂ layer) via chemical vapor deposition (CVD) method. Silver nanodisk array and the source and drain electrodes were patterned directly on the as-grown MoS₂ substrate by electron beam lithography, followed by the deposition

of 50 nm silver by electron-beam evaporation. More detailed information for both MoS₂ growth and fabrication of the plasmonic nanostructures and electrical contacts have been described in references.^{98,101,102} The device (on the substrate) was then attached to a chip carrier with electrical pins designed for our optical microscopy cryostat (Janis ST-500) and the sample electrodes were connected to electrical pads of the chip carrier by wire-bonding for the electrical measurements.

Optical and electrical measurements. Angle-resolved reflectance spectra were acquired from our home-built angle-resolved optical setup. The setup configuration and the detailed information about the measurements are described elsewhere in our previous study.^{102,353} For electrical measurements, two Keithley 2400 voltage sources were used to apply the source-drain bias and the gate voltage, and the channel current was recorded through Keithley 6517 electrometer.

4.3.3 Optomechanical enhancement of doubly resonant 2D optical nonlinearity

The results presented in this section have also appeared in the publication “Optomechanical Enhancement of Doubly Resonant 2D Optical Nonlinearity”, Fei Yi, Mingliang Ren, Jason C. Reed, Hai Zhu, Jiechang Hou, Carl H. Naylor, A. T. Charlie Johnson, Ritesh Agarwal, and Ertugrul Cubukcu, *Nano Letters*, 2016, 16, 1631–1636.

Abstract

Emerging two-dimensional semiconductor materials possess a giant second order nonlinear response due to excitonic effects while the monolayer thickness of such active materials limits their use in practical nonlinear devices. Here, we report 3300 times optomechanical enhancement of second harmonic generation from a MoS₂ monolayer in a doubly resonant on-chip optical cavity. We achieve this by engineering the nonlinear light-matter interaction in a microelectromechanical system enabled optical frequency doubling device based on an electrostatically tunable Fabry–Perot microresonator. Our versatile optomechanical approach will pave the way for next generation efficient on-chip tunable light sources, sensors, and systems based on molecularly thin materials.

Nonlinear optical materials have made possible a plethora of wavelength tunable coherent light sources crucial in many applications extending from bioimaging to laser machining. Recent studies on monolayer crystals of molybdenum disulfide (MoS_2) that lack inversion symmetry have confirmed that they possess a giant second order nonlinear optical response.^{352,356–361} However, the subnanometer interaction length available for light-matter coupling in two-dimensional MoS_2 crystals limits their overall nonlinear conversion efficiency and prevents them from being considered in practical applications.³⁶⁰

Using photonic structures to resonantly control and enhance interaction of light with MoS_2 monolayers appears to be a logical step for their use in optoelectronics applications.^{339,362,363} Optical resonators have been implemented for enhancing linear processes such as the photoluminescence from MoS_2 .^{342,343,364–366} However, to maximize the enhancement of second harmonic generation (SHG) the nonlinear nature of the light matter interaction necessitates a doubly resonant optical cavity scheme, where both the fundamental wave (FW) and the second-harmonic wave (SHW) are simultaneously resonant.^{367–371} This double resonance scheme requires delicate on-chip reconfiguration of the cavity modes reminiscent of phase matching in bulk crystals. With this in mind, we have devised an integrated optomechanical frequency doubling device with a chemical vapor deposition (CVD) grown monolayer MoS_2 as the active nonlinear material. This microelectro-mechanical system (MEMS) enabled optical device can be electrostatically reconfigured to enhance nonlinear light generation by more than 3 orders of magnitude. The device is based on a voltage controlled widely tunable micro-

Fabry–Perot (FP) cavity that consists of a spectrally selective dielectric distributed Bragg reflector (DBR) mirror and a voltage deformable silver mirror fabricated on a silicon nitride membrane as shown in Figure 4.3.3.1a. Figure 4.3.3.1b shows the multilayer stack arrangement used in our calculations for the field enhancement by the cavity and the DBR mirror consists of alternating layers of silicon nitride and oxide.

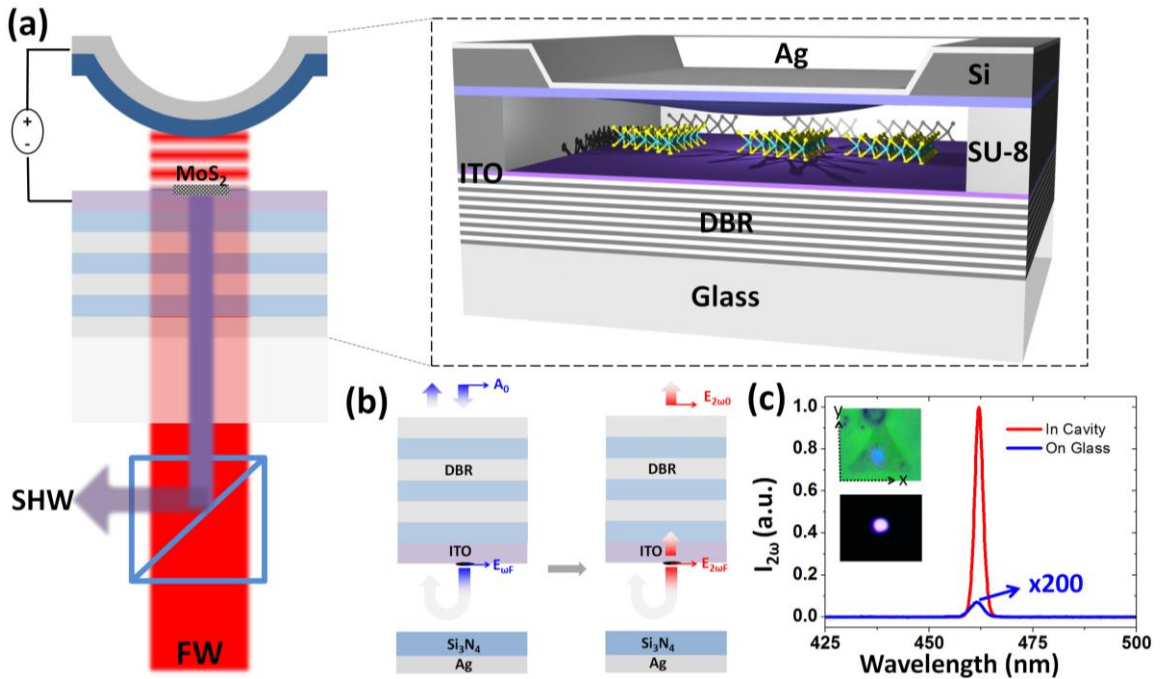


Figure 4.3.3.1. Optomechanically reconfigurable frequency doubling device. (a) Schematic of the device structure formed by the dielectric mirror on a glass substrate and a silver mirror on a suspended membrane. The silver mirror on suspended nitride membrane can be deformed by electrostatic force across the silver layer and the ITO layer, enabling the reconfiguration of the cavity. FW, fundamental wave; SHW, second harmonic wave. (b) The multilayer stack models used to calculate the cavity enhancement of the fundamental wave excitation (left) and the second harmonic wave output (right), respectively. (c) The second harmonic wave signal generated from the MoS₂ flake inside the cavity (red solid line) and the MoS₂ flake on a glass substrate (blue solid line) flake. Here the pump wavelength is 925 nm and the tuning voltage is 20 V. The insets show the spot of the second harmonic wave generated from the MoS₂ flakes in the cavity under bright (top) and dark (bottom) fields. The x-axis is defined along one of triangle sides of a CVD grown MoS₂, which is the zigzag direction. Therefore, the nonzero nonlinear coefficients are $\chi^{(2)} = \chi^{(2)}_{yyy} = -\chi^{(2)}_{yxx} = -\chi^{(2)}_{xxy} = -\chi^{(2)}_{xyx}$. In this work, we only focus on $\chi^{(2)}_{yyy}$.

The nonlinear light-matter interaction is engineered by optomechanical tuning of the FP cavity length. This in turn controls the intracavity optical field strengths on the

MoS₂ monolayer integrated directly on the DBR mirror designed to be highly reflective in the fundamental and second harmonic wave regions. The transparency window between these two regions allows us to clearly identify the triangular MoS₂ monolayer crystals from the backside of the glass substrate under the optical microscope (inset in Figure 4.3.3.1c). The length of integrated FP cavity can be reconfigured by applying a voltage between the metal-coated free-standing top mirror and the indium tin oxide (ITO) layer embedded in the DBR mirror as a transparent electrode (Figure 4.3.3.1a). The red solid line in Figure 4.3.3.1c shows the measured SH output intensity generated by the MoS₂ monolayer inside the doubly resonant cavity. The blue solid line shows the reference SH signal generated from a monolayer MoS₂ flake on a glass substrate. On the basis of this configuration, we have observed a very bright spot of SHW (~462 nm) from an individual MoS₂ monolayer that stood inside the cavity and was excited by FW at 925 nm (inset of Figure 4.3.3.1c). The normalized conversion efficiency is measured to be $1.62 \times 10^{-8}/W$ (red line of Figure 4.3.3.1c), which is >5000 times larger than the previous literature³⁶¹ and ~3300 times stronger than that from a typical MoS₂ monolayer on glass (blue line of Figure 4.3.3.1c). Moreover, we observed that the SHG signal from MoS₂ in the doubly resonant cavity has a narrower linewidth compared to SHG signal from MoS₂ on the glass substrate and this is ascribed to the cavity enhancement. In order to gain insights on this significant phenomenon, we characterized the optomechanical tuning properties of the fabricated device. We measured the linear optical response of FP cavity under different tuning voltages to determine spectral position of the resonance modes. Figure 4.3.3.2a,b shows plots of the voltage dependence of spectral reflectance at the center of the device near fundamental wave and SH wave regions, respectively. It can

be seen that the resonant wavelengths of the two optical modes in the fundamental wave region (marked as M1 and M2 in Figure 4.3.3.2a) are blue-shifted due to the decreasing cavity length by electrostatic deflection of the deformable membrane mirror. With a tuning voltage of 25 V corresponding to a 535 nm change in cavity length, M1 resonance wavelength blueshifts by 70 nm. From this blueshift, we determined the corresponding cavity length reduction, that is, mechanical deflection of the membrane, by matching the measured data with the optical transfer matrix method (TMM) calculations^{372,373} (see Figure S2).

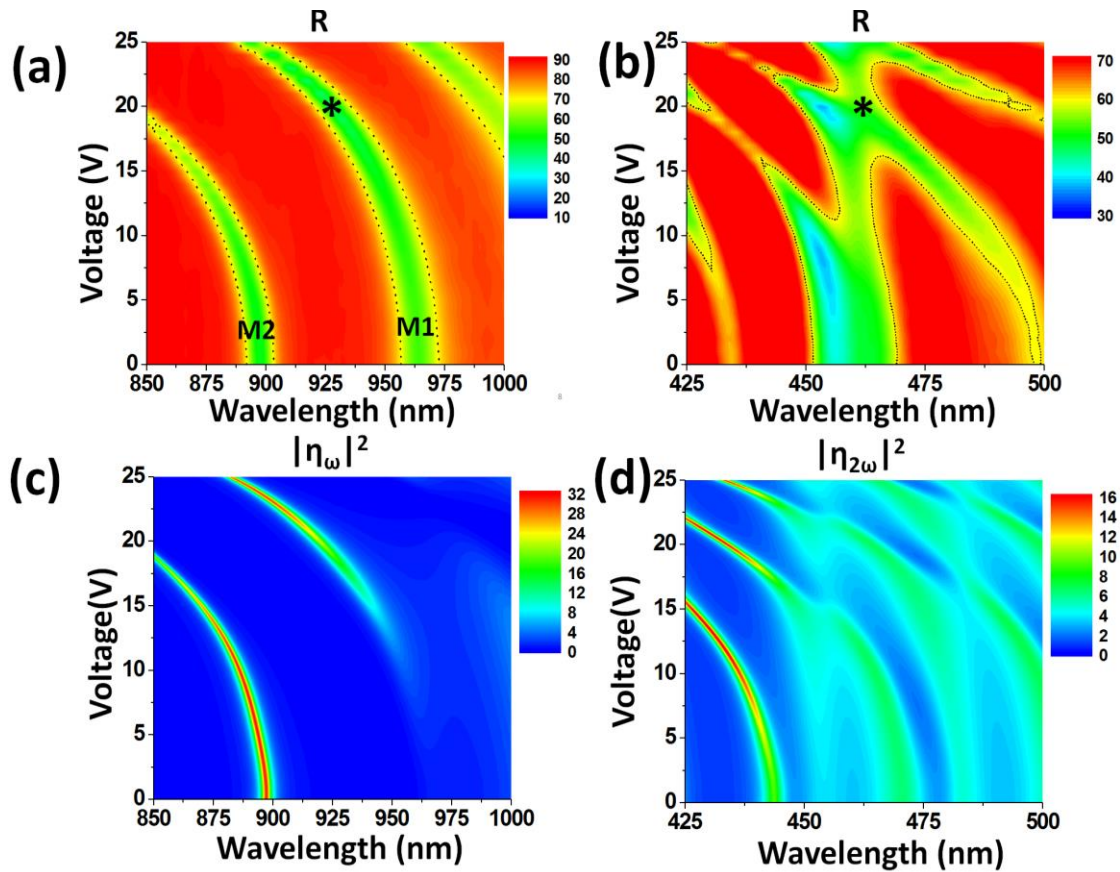


Figure 4.3.3.2. Voltage tuning of the cavity resonances. Voltage dependence of the spectral reflectance near the input fundamental (a) and output second harmonic frequencies (b), at the center of the device. The two FP cavity modes near the fundamental pump frequency region are labeled as M1 and M2. * indicates a region where a double resonance is expected. (c,d) The simulated voltage dependence of the power enhancement factors for the fundamental and the second harmonic waves.

Having characterized the far-field linear response of the doubly resonant FP cavity, we need to estimate the near-field strength in the cavity to determine the nonlinear response. For this purpose, we theoretically investigate the enhancement of the second harmonic generation in the monolayer MoS₂ inside the FP cavity. We assume that the complex amplitude of the radiated second harmonic wave from a nonlinear monolayer flake $S_F(2\omega)$ in response to a harmonic electric field of angular frequency ω and complex amplitude $E_F(\omega)$ is given by³⁷⁴ $S_F(2\omega) = \eta_F \times E_F(\omega) \times E_F(\omega)$, where $\eta_F = 4 \mu_0 \omega^2 \chi^{(2)}$ is the nonlinear constant of the monolayer and $\chi^{(2)}$ is the second order nonlinear susceptibility in the plane of the material. To account for the resonant enhancement effect in the FP cavity for the fundamental wave, we define the field enhancement factor for the fundamental wave as the ratio of the fundamental electric field $E_F(\omega)$ built up at the MoS₂ monolayer to the incident field $A_0(\omega)$ from outside the cavity, $\eta_\omega = E_F(\omega)/A_0(\omega)$. Figure 4.3.3.2c shows the calculated intensity enhancement factor of the fundamental wave (defined as $|\eta_\omega|^2$) as a function of wavelength and voltage (see Supporting Information for the details of calculation). It can be seen that the resonant wavelengths of the cavity modes can be blue-shifted through voltage tuning while the enhancement factor $|\eta_\omega|^2$ can be tuned up to 30 times. Similar to the fundamental wave, the radiated second harmonic wave also builds up in the resonant cavity. We define the field enhancement factor $\eta_{2\omega}$ for the second harmonic wave as the ratio of the output electric field $S_0(2\omega)$ at the second harmonic frequency to the radiated second harmonic electric field from the MoS₂ flake $S_F(2\omega)$: $\eta_{2\omega} = S_0(2\omega)/S_F(2\omega)$.

Figure 4.3.3.2d shows that the intensity enhancement factor for the second harmonic wave $|\eta_{2\omega}|^2$ can also be tuned by changing the cavity length. The total power enhancement factor by the cavity is then characterized by $|\eta_{2\omega}|^2 \times |\eta_{\omega}|^4$. Because the intracavity power is proportional to the quality factor, this result is consistent with calculations from coupled mode theory for doubly resonant cavities under critical coupling conditions.^{374,375} In this case, the nonlinear output power qualitatively scales with $(Q_{\omega})^2 \times (Q_{2\omega})$, where Q_{ω} and $Q_{2\omega}$ are the quality factors for the fundamental and second harmonic waves, respectively.^{374,375} Our TMM calculation predicts that the total second harmonic output power can be enhanced above 3500 times through voltage tuning the cavity to attain double resonance. This maximum enhancement corresponds to the case where both the fundamental and second harmonic waves are spectrally tuned with two cavity modes, that is, double resonance condition.

To test our theoretical predictions, we experimentally characterized the nonlinear conversion efficiency of the fabricated device. For excitation, we use transform limited pulses with a duration of 140 fs. For different tuning voltages, we scan the pulse center wavelength in the 850–1000 nm window corresponding to the region where the micro-FP cavity supports fundamental wave resonances. This allows us to map the overall optomechanical power enhancement factor of SHG that is the ratio between SHG signals from a MoS₂ monolayer in our cavity device and from a typical MoS₂ monolayer on a glass, as shown in Figure 4.3.3.3a. The measured data agree well with the theoretical results (see Figure S6). For a pump wavelength of 925 nm and a tuning voltage of 17 V, the measured maximum enhancement is 3300 times larger than the SHG from a

monolayer on a glass substrate. This set of parameters corresponds to the doubly resonant cavity case as shown in Figure 4.3.3.3b, where the fundamental and second harmonic wavelengths overlap spectrally with two separate cavity resonances. It can be seen that the traces for cavity resonances near the fundamental and second harmonic frequencies intersect in that region when a 17 V tuning bias is applied unlike the mismatched case for 0 V. This is reminiscent of phase matching for copropagating beams in bulk birefringent nonlinear materials. For other combinations of tuning voltage and fundamental wavelength, the nonlinear enhancement is not significant. Singly resonant coupling is also observed when only the fundamental wavelength is resonant with M1 and the second harmonic wavelength is spectrally mismatched from a cavity mode. Similarly, when the fundamental wavelength follows M2, the enhancement is 30× weaker due to lack of a double resonance condition.

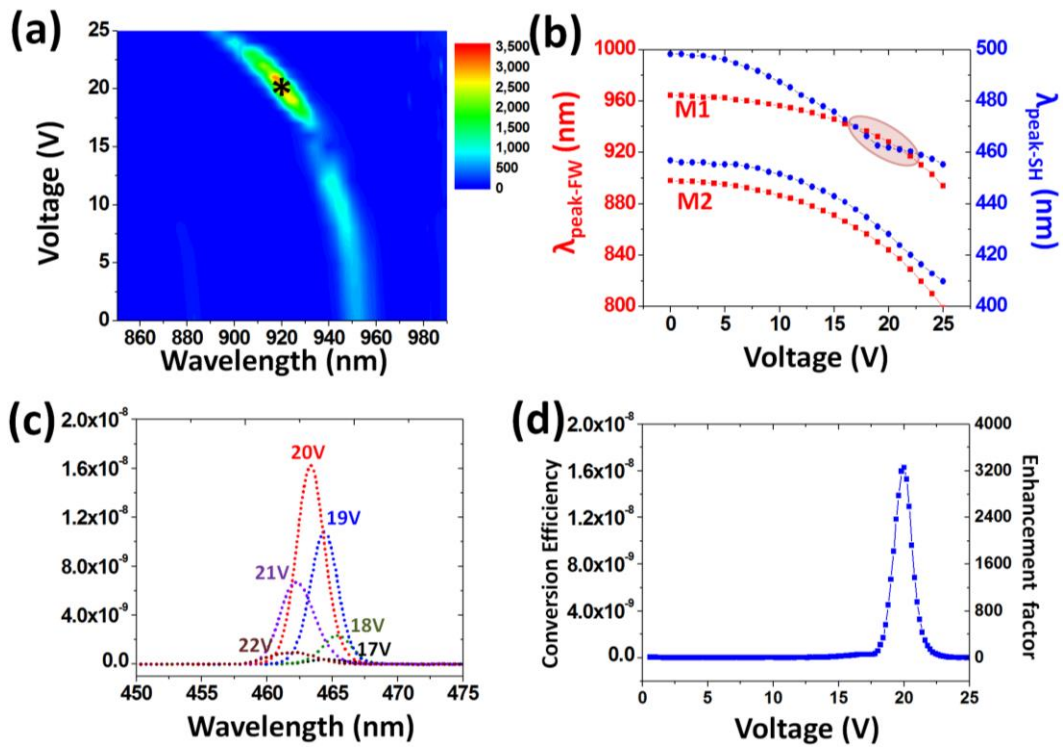


Figure 4.3.3.3. Doubly resonant second harmonic generation measurements. (a) The measured voltage dependence of the total output SHG power enhancement factor normalized to a monolayer on glass substrate. (b) The voltage dependence of the peak FP resonance wavelengths (traces from Figure 4.3.3.2a,b) in the fundamental (red lines) and the corresponding second harmonic (blue lines) wave regions. The crossing points in the oval between the blue and red curves indicate a double resonance region. (c) The evolution of the optical spectrum of the second harmonic wave as a function of the tuning voltage. The output peak wavelength is tunable due to the resonances narrower than the spectral pulse width of the fundamental wave fixed at 930 nm. (d) The measured voltage dependence of the total power enhancement factor and the power conversion efficiency for a pump wavelength of 930 nm. The inset shows the measured output SHG signal that is quadratically proportional to the input power.

We also characterized the absolute conversion efficiency ($P_{2\omega}/P_{\omega}^2$, see Methods) of the second harmonic generation. Figure 4.3.3.3c shows the evolution of the optical spectrum of the second harmonic wave as a function of the tuning voltage. The output SHG peak wavelength can be tuned slightly by voltage because the cavity modes are spectrally narrower than the incident fundamental pulse width (Figure S5). Our unique nonlinear device configuration also allows us to dynamically control the output of this frequency doubler with voltage. Figure 4.3.3.3d plots the voltage dependence of the measured power conversion efficiency and enhancement factor when the fundamental wave is fixed at 930 nm.

On the contrary, the light-matter interactions in this device can be completely turned off by an applied voltage that detunes the fundamental cavity resonance from the pump. This enables the full optomechanical control of the SHG output intensity for a given input wavelength and optical power. Also, the SHG signal is switched from ON state at 20 V to completely OFF state at 22.5 V, indicating the very efficient tuning capability of our cavity (40% per volt). Because of the capacitive nature, this frequency doubler will not consume any energy for static switching operations. The inset in Figure 4.3.3.3d shows the SHG output power as a function of the input pump power for the

double resonance condition from which we calculate the power conversion efficiency to be $1.62 \times 10^{-8}/W$, which is 5000 larger than reported value measured from MoS₂ flake on a Si/SiO₂ (280 nm) substrate.³⁶¹ The measured modulation cutoff frequency for this proof-of-concept-device was 200 Hz limited by the driving electronics (see Figure S4). These devices can be modulated resonantly at much higher frequencies if driven at one of the acoustic resonances supported by the membrane mirror.³⁷⁶

In summary, we demonstrated optomechanical enhancement of effective nonlinear optical response in monolayer MoS₂ crystals in a versatile nonlinear device platform based on doubly resonant optical cavities. This on-chip voltage controlled frequency doubling device can address the short nonlinear interaction lengths in emerging two-dimensional materials. We envision that our strategy of on-chip nanoscale opto-electromechanical integration will lead to next generation tunable nonlinear light sources and devices.

Methods.

Sample Preparation. The DBR was fabricated by plasma-enhanced chemical vapor deposition (PECVD, Oxford PlasmaLab 100) on a glass slide after 10 min sonication cleaning in acetone and IPA. Layer stacking of DBR first consists of eight pairs of 130 nm SiNx/130 nm SiOx thin film deposition. Then a layer of ~50 nm ITO was deposited on top as-fabricated DBR structure by DC magnetron sputtering (Explorer 14) under 5 mTorr at 450 W with Ar/O₂ ratio as 100:3. The refractive indices of the ITO

and the PECVD SiN_x and SiO_x thin films are characterized using Filmmetrics F40. A 1.5 μm thick SU-8 layer is then spin-coated and patterned on top of the ITO layer as the spacer. A commercially available silicon nitride window with 100 nm thick membrane bonded on top of the SU-8 spacer through commercially available adhesive (cyanoacrylate). The backside of the membrane is precoated with a 50 nm of silver layer at the backmirror through e-beam evaporation. Electrical contacts to the MEMs capacitor are through the silver layer and the ITO layer, respectively.

MoS₂ Growth. Single crystal MoS₂ flakes were grown directly on a 300 nm SiO₂/Si substrate by chemical vapor deposition. A 1% sodium cholate solution is initially spin coated onto the SiO₂ substrate to help promote a growth region. A microdroplet of a saturated solution of ammonium heptamolybdate (AHM) is deposited onto the corner of the substrate. The AHM will act as the molybdenum feedstock. The substrate is placed in the center of a 1 in. Lindberg blue furnace and 25 mg of solid sulfur (part number 213292, Sigma-Aldrich) is placed upstream at a distance of 18 cm from the growth substrate. Nitrogen at 700 sccm is flown through the chamber and the temperature of the furnace is ramped up to 800 C; the sulfur pellet is heated up to 150 °C. After a 30 min growth, the furnace is then stopped and rapidly cooled to room temperature. The growth substrate is retrieved and MoS₂ flakes were grown across the SiO₂ substrate.

Characterization of the Optomechanical Resonant Cavity. We first measured the voltage-dependent spectral reflectance of the FP-cavity at the center of the device using Filmmetrics F40. The corresponding voltage controlled cavity length is then determined by fitting the simulated spectral reflectance (by transfer matrix method) with the

measured spectral reflectance. We then simulated the voltage controlled mechanical deflection of the silver-coated silicon nitride membrane in the MEMs capacitor using the electromechanics module in COMSOL 4.4 and compared it with the voltage controlled cavity length determined by the spectral reflectance measurement to predict the pull-in voltage of the MEMs capacitor.

Characterization of Optomechanically Enhanced 2D Nonlinearity. A femtosecond-pulsed Ti:sapphire laser (Chameleon), tuned from 680 to 1000 nm with ~ 140 fs pulse width and 80 MHz repetition rate, was focused onto individual flakes through the DBR mirror by means of a home-built microscope equipped with a $10\times$, 0.25 NA objective (Nikon). The average excitation power of ~ 2 mW (FW) was used to excite SHG from the MoS₂ flakes. The SHG signals were imaged by a cooled charge-coupled device and measured by a spectrometer (Acton) with a spectral resolution of 0.1 nm. The external normalized conversion efficiency is defined as $P_{2\omega}/P_{\omega}^2$ where P_{ω} is the peak power of FW illuminated upon the DBR mirror while $P_{2\omega}$ is the peak power of generated SHW coming out from the cavity. The reported conversion efficiency (e.g., $1.68 \times 10^{-8}/\text{W}$) has considered the system collection efficiency,³⁷⁷ including transmission/reflection coefficient of each optical elements. The measured power enhancement factor is defined as the SH power from the cavity normalized to the SH power from the MoS₂ monolayer on a glass substrate.

CHAPTER V.

1H-WS₂, 1H TMD Heterostructure, 1H-MoSe₂ & 1H-WSe₂

1H-tungsten disulfide (1H-WS₂), 1H-molybdenum diselenide (1H-MoSe₂), 1H-tungsten diselenide (1H-WSe₂), and 1H-heterostructures are alternative materials under the 1H atomic configurations that are less explored compared to their 1H-MoS₂ counterpart. They are semiconductors but possess properties that differ from 1H-MoS₂. 1H-WS₂ has a larger band gap and stronger photoluminescence than 1H-MoS₂. 1H-WSe₂ is the only known p-type transition metal dichalcogenides (TMD). Heterostructures of multiple TMDs are enticing, because of the possibility of combining different properties of each material.

In this Chapter, I will report our synthesis approach for monolayer 1H-WS₂ flakes. I will discuss the work performed by a collaborating group, involving the fabrication of nanopores in a suspended monolayer 1H-WS₂ flake for DNA translocations. I then will show our recent success with the synthesis of in-plane monolayer heterostructures with 1H-MoS₂/1H-WS₂. Due to their different bandgaps, each material emits light at different energies upon electronic excitation and this was demonstrated by photoluminescence measurements. Finally, I will discuss our recent results with the Se-containing chalcogenides with the synthesis of 1H-MoSe₂ and 1H-WSe₂.

5.1 1H-WS₂

5.1.1 Synthesis of 1H-WS₂

1H-WS₂ is the second most studied transition metal dichalcogenide (TMD) to date after 1H-MoS₂. As previously discussed in section 2.3, WS₂ has tremendous optical properties that make it very sought after in the optics community, such as large photoluminescence. The synthesis of high quality 1H-WS₂ flakes is imperative in order to capture some of its fascinating properties. WO₃ evaporates at a higher temperature than MoO₃, and W is heavier than Mo so doesn't diffuse as quickly on the surface; this makes the synthesis of high quality 1H-WS₂ challenging. We are able to grow high quality 1H-WS₂ flakes by Chemical Vapor Deposition (CVD) through two different tungsten (W) source approaches: through direct deposition of WO₃ or through an ammonium metatungstate hydrate (AMT) micro-droplet.

Direct deposition of WO₃ on a Silicon/Silicon-dioxide (Si/SiO₂) substrate is done by thermal evaporation. 2 bars of WO₃ source are evaporated on the growth substrate as illustrated in figure 5.1.1.1. This configuration was found to be optimal for the synthesis of 1H-WS₂ flakes. The growth substrate is then spin coated with a 2% sodium cholate solution at 4000 rpm for 60 seconds. Sodium cholate is a known growth promoter that increases the surface adhesive energy relative to the adatom cohesive energy, enabling diffusion of atoms on the surface.^{58,59,98,169} For the AMT solution approach, the Si/SiO₂ substrate is first spin coated with the 2% sodium cholate solution and then micro-droplets of a 3.1 mM solution of AMT are applied to the corners of the Si/SiO₂ chip. Either of

these two W source approaches yield growth of 1H-WS₂ flakes and they both follow the same growth process. The growth substrate is inserted into the center of the furnace accompanied with a 25 mg sulfur (S) source conveniently placed upstream. The furnace is ramped up to 800°C at a rate of 70°C/min under a constant flow of 700 standard cubic centimeter per minute (sccm) of ultra-high purity nitrogen gas (N₂), the S source reaches 150°C and start sublimating. Following a similar schematic that can be found in Chapter IV for the 1H-MoS₂ growth figure 4.1.1.2, 1H-WS₂ starts to grow from the W sources. After a 30 minute growth time, the furnace is rapidly cooled and the growth substrates are retrieved. Optical micrograph images of the growth results can be found in figure 5.1.1.1.

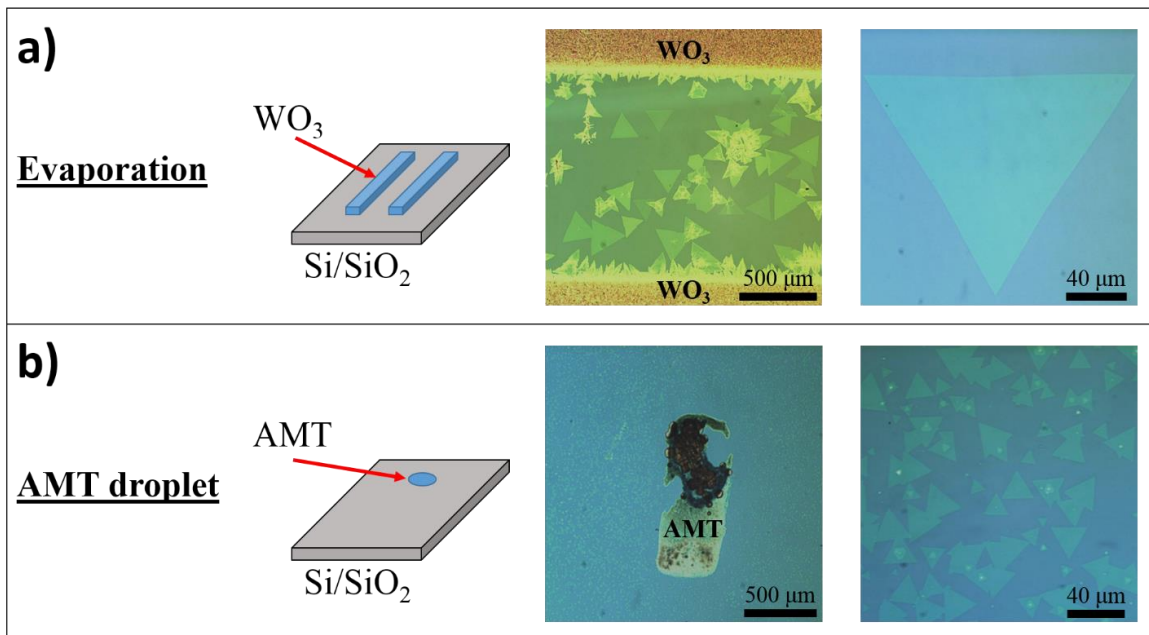


Figure 5.1.1.1. 1H-WS₂ growth. a) Growth through evaporation method, optical micrograph reveals large monolayer 1H-WS₂ flakes but also multilayer. b) Growth through AMT micro-droplet, optical micrograph reveals dense small monolayer 1H-WS₂ flakes.

The 1H-WS₂ flakes grown through evaporation of WO₃ bars can be seen in figure 5.1.1.1a. These flakes are single crystal and very large domain (100-500 μm), however there is a mixture of multilayer and monolayer flakes. The quality of the monolayer

flakes grown through this source are very high however the growth reproducibility is low, which makes growth through WO_3 source non-practical.

The 1H- WS_2 flakes grown through the AMT microdroplet can be seen in figure 5.1.1.1b. The flakes are single crystal and have reasonable domain size (20-50 μm). The growth produces predominantly monolayer 1H- WS_2 flakes of reasonable quality, and the growth is very reproducible. The high reproducibility and large monolayer regions of 1H- WS_2 flakes make this method very attractive. Flakes from both growth methods were characterized by Raman and atomic force microscopy (AFM) and no differences were observed. The Raman reveals an E^1_{2g} peak and a A_{1g} peak at 352 cm^{-1} and 417 cm^{-1} respectively (figure 5.1.1.2a), the inter-distance of the peaks is measured at 66 cm^{-1} and the amplitude of A_{1g} is smaller than the E^1_{2g} peak in agreement with reports for monolayer 1H- WS_2 .^{378–380} The peak inter-distance reduces from 70 cm^{-1} for bulk 1H- WS_2 to 66 cm^{-1} for monolayer, and the amplitude of the A_{1g} is higher than the E^1_{2g} peak for bilayer and above. AFM measurements reveal a height of 0.8 nm confirming the monolayer height of our material (figure 5.1.1.2b).

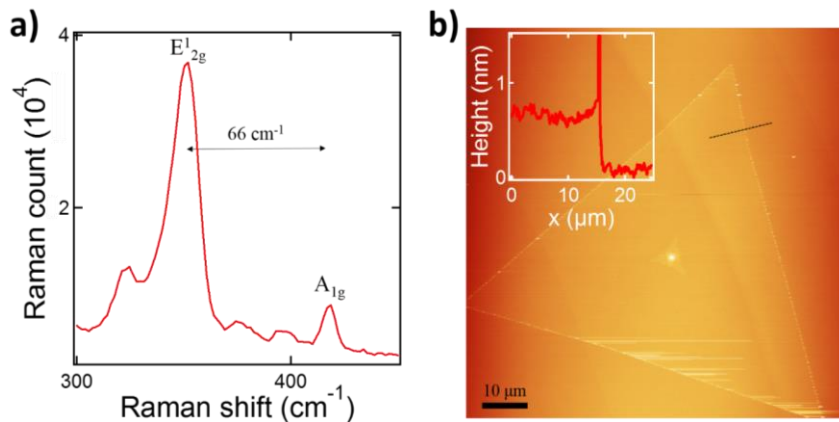


Figure 5.1.1.2. 1H- WS_2 characterization. a) Raman spectroscopy of 1H- WS_2 revealing A_{1g} and E^1_{2g} . b) AFM image of large 1H- WS_2 flake, with embedded height profile.

5.1.2 Monolayer WS₂ nanopores for DNA translocation with light-adjustable sizes

The results presented in this section have also appeared in the publication “Monolayer WS₂ Nanopores for DNA Translocation with Light-Adjustable Sizes”, Gopinath Danda, Paul Masih Das, Yung-Chien Chou, Jerome T. Mlack, William M. Parkin, Carl H. Naylor, Kazunori Fujisawa, Tianyi Zhang, Laura Beth Fulton, Mauricio Terrones, Alan T. Charlie Johnson, and Marija Drndić, ACS Nano, 2017, 11, 1937–1945.

Abstract

Two-dimensional materials are promising for a range of applications, as well as testbeds for probing the physics of low-dimensional systems. Tungsten disulfide (WS₂) monolayers exhibit a direct bandgap and strong photoluminescence (PL) in the visible range, opening possibilities for advanced optoelectronic applications. Here we report the realization of two-dimensional nanometer size pores in suspended monolayer WS₂ membranes, allowing for electrical and optical response in ionic current measurements. A focused electron beam was used to fabricate nanopores in WS₂ membranes suspended on silicon-based chips and characterized using PL spectroscopy and aberration-corrected high-resolution scanning transmission electron microscopy (AC-HRSTEM). It was observed that the PL intensity of suspended WS₂ monolayers is ~10-15 times stronger when compared to substrate-supported monolayers, and low dose scanning transmission electron

microscope (STEM) viewing and drilling preserves the PL signal of WS₂ around the pore. We establish that such nanopores allow ionic conductance and DNA translocations. We also demonstrate that under low-power laser illumination in solution, WS₂ nanopores grow slowly in size at an effective rate of ~0.2-0.4 nm/s, thus allowing for atomically-controlled nanopore size using short light pulses.

Nanopore sensors based on two-dimensional (2D) materials such as graphene, molybdenum disulfide (MoS₂) and boron nitride (BN) have been used to demonstrate biomolecule detection and analysis.³⁸¹⁻³⁸⁵ In these experiments, the molecules, suspended in an ionic solution, are driven by an electric field through a nanopore within a thin membrane while the ionic current is monitored to detect the translocation of molecules across the nanopore, which typically appears as reductions in current. Atomically thin 2D membranes are ideal for nanopore devices as they exhibit larger ionic currents compared to thicker silicon-based membranes^{381,382,385} and potential spatial sensitivity at the sub-nanometer scale for translocating molecules as only a small section of the molecule resides in the nanopore at a given time.³⁸⁵ Furthermore, monolayers of semiconducting transition metal dichalcogenides (TMDs) possess enhanced optical properties,³⁸⁶⁻³⁸⁸ a feature which could be further exploited for electrical and optical control of nanopores.

Among TMDs, monolayer tungsten disulfide (WS₂) has a direct bandgap of 2.1 eV³⁸⁹ and its photoluminescence (PL) emission is stronger than the well-studied MoS₂,^{388,390} which enables application of WS₂ monolayers in optoelectronic devices.³⁹¹ It

is also noteworthy that defects have been shown to modulate the PL signal of WS₂ monolayer flakes^{392,393} and can hence be used as a means to fine tune their optical response. One related property is the photo-oxidation of TMD monolayers in an oxidizing environment, like air and water.^{394,395} Introducing defects in the material can provide sites for light-facilitated oxidation and can be used to dynamically control defect size using optical excitation.

In this Letter, we demonstrate a class of optically active 2D nanopores in monolayer WS₂ membranes. We report WS₂ nanopore drilling using a focused electron beam and subsequent effects on PL spectra. We also demonstrate high ionic conductance and DNA translocations through these nanopores. Furthermore, during laser excitation of these nanopores at low power densities ($\lambda = 532$ nm, power density = 3 W/cm²), we note nanopore expansion at a rate of ~0.2-0.4 nm/s, potentially providing means to dynamically control nanopore dimensions with short light pulses.

Results and discussion

Figure 5.1.2.1 shows the material characterization of vapor-grown WS₂ triangular monolayers. Atomic force microscopy (AFM) of the flake (Figure 5.1.2.1b) shown in Figure 5.1.2.1a reveals a thickness of ~0.7 nm, which agrees with the reported thickness of monolayer WS₂.³⁹⁶ Using Raman spectroscopy, we observe the E' (353 cm⁻¹) and A₁' (418 cm⁻¹) modes of monolayer WS₂ as well as the Si peak from the substrate, centered at 521 cm⁻¹ (Figure 5.1.2.1c).³⁹⁶ The peak at 311 cm⁻¹ that is typically associated with

multilayer flakes is notably absent,³⁹⁷ thus confirming the presence of monolayers. Figure 5.1.2.1d is an aberration-corrected high-resolution scanning transmission electron microscope (AC-HRSTEM) image of a freestanding WS₂ monolayer suspended on a perforated carbon grid. The tungsten (bright white) and sulfur (gray) atoms are clearly visible. Selected-area electron diffraction (SAED) patterns (inset) also confirmed the expected hexagonal lattice of the 1H phase of WS₂ monolayers.

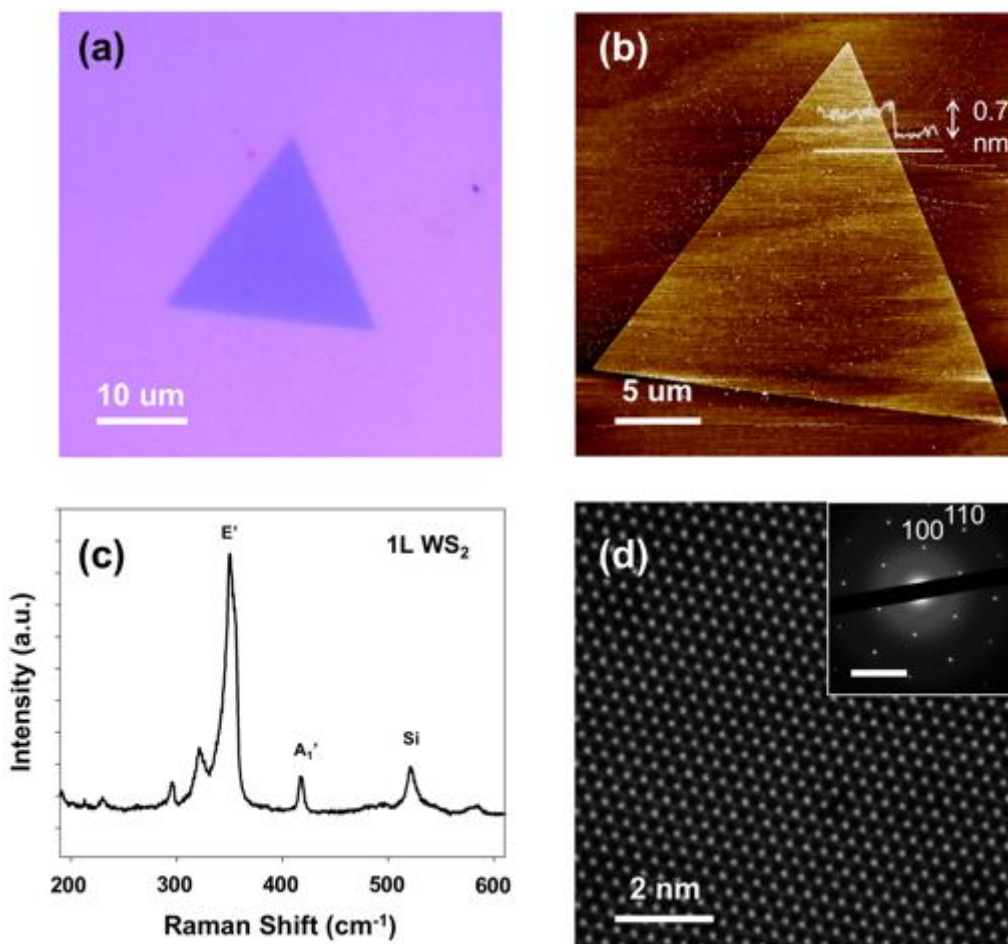


Figure 5.1.2.1. Characterization of WS₂ flakes. (a) Optical micrograph and (b) AFM scan of a monolayer WS₂ flake. The line profile in white indicates a thickness of 0.7 nm, which corresponds to a monolayer. (c) Raman spectrum of monolayer WS₂ flake with corresponding E' (356 cm⁻¹), A₁' (418 cm⁻¹), and Si (521 cm⁻¹) peaks. (d) Gaussian blur-filtered AC-HRSTEM lattice image taken at 80 kV. The inset is a SAED pattern with expected (100) and (110) diffraction spots.

We further characterize the WS₂ monolayers using PL spectroscopy. WS₂ flakes were suspended onto a perforated silicon nitride grid (DuraSiN DTM-25231) using a standard PMMA-based wet transfer procedure (Figure 5.1.2.2a) and PL spectral maps were obtained using a 532 nm laser excitation (Figure 5.1.2.2b). The PL spectra from various regions of the flake – suspended, supported edge and supported center - are plotted in Figure 5.1.2.2c. The PL signal exhibited 3 peaks: (i) the neutral exciton peak (X_0), which arises due to the radiative recombination of excitons across the bandgap,^{392,398,399} (ii) the charged trion peak (X_T), which comes from the recombination process requiring three charge carriers and as a result can arise due to charge doping^{330,386,400} or strain,⁴⁰¹ and (iii) defect peaks (X_D), which arise due to defect-induced midgap states that allow excitons to recombine at an energy lower than the bandgap.^{392,393} Lorentzian functions were used to fit the spectra for X_0 , X_T and X_D peaks. It was observed that the X_0 peak centered at ~2.02 eV red shifts (*i.e.*, PL wavelength increases) and decreases in intensity (or peak area) from the flake edge inwards until it becomes completely non-existent at the center of the flake. On the other hand, the X_T peak shifts from 1.98 eV to 1.94 eV (*i.e.*, red shifts) and the peak intensity decreases by 3 times from edge of the flake to inner region.³⁸⁶ The presence of the X_T peak lends the low energy tail in the spectra and likely appears due to the substrate-induced strain in the transferred flake.⁸⁰ The enhancement of the PL spectral intensity was observed between the suspended and the nearby supported region, which was measured as the ratio of the X_0 peak intensity (I_{sus}/I_{sup}), to be ~10-15 times, irrespective of the position of the suspended region on the monolayer (*i.e.* edge or center). This effect has previously been observed and quantified in suspended MoS₂ monolayers where the enhancement was ~2-4 times⁴⁰²

and was attributed to PL quenching caused by charge doping of the substrate in the supported regions. Similar effects have been observed in suspended WS_2 ³⁸⁶ but were not quantified, to the best of our knowledge.

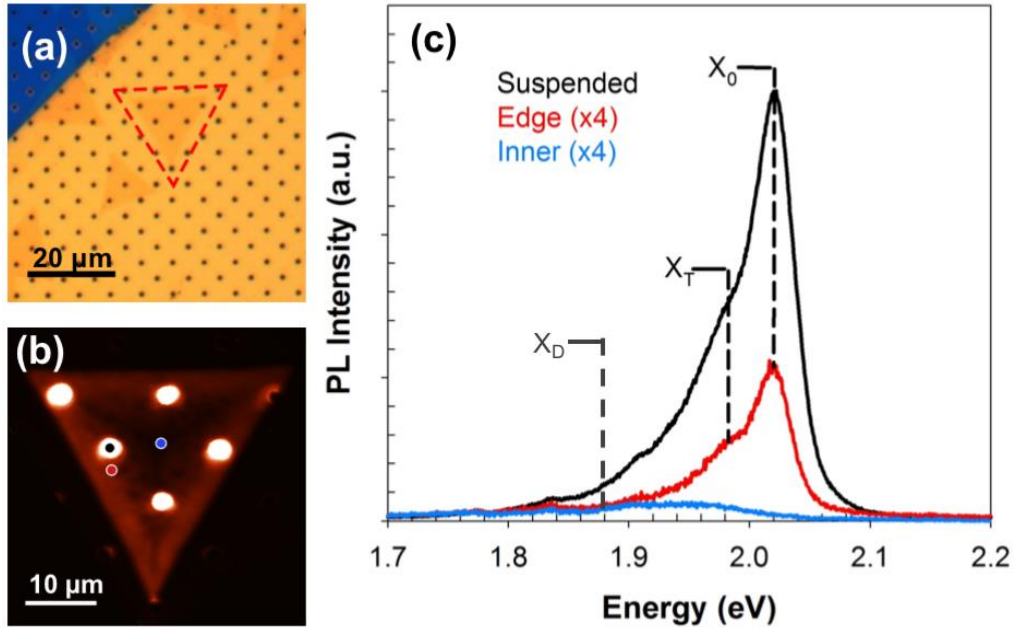


Figure 5.1.2.2. Photoluminescence study of monolayer WS_2 flakes. (a) Optical image of monolayer WS_2 flake on a perforated silicon nitride grid, outlined in red, and (b) the corresponding PL map with a 532 nm laser. PL spectra for suspended (black dot), supported edge (red dot) and supported center (blue dot) are plotted in (c). The neutral exciton peak, X_0 , at ~ 2.02 eV, trion peak, X_T , at ~ 1.98 eV and defect peak, X_D , at ~ 1.88 eV are shown with dotted lines. The edge (red) and center (blue) spectra are multiplied by a factor of 4 for better illustration.

Before drilling a nanopore in a suspended region of a WS_2 flake, the position of the suspended region must first be located in the TEM, and as a result the entire suspended region is exposed to electron beam (e-beam) doses on the order of $\sim 10^4$ - 10^5 e^-/nm^2 . It has been established that high energy e-beams can introduce lattice defects in TMDs (such as sulfur vacancies in MoS_2 ¹⁰⁶) and in other 2D materials.⁴⁰³ These defects can in turn cause changes in PL peak intensities due to trapped charge carriers, or introduce additional peaks as a result of the creation of midgap states.^{386,388,392,393} Thus, it

is advantageous to study the effects of e-beam exposure on the PL of suspended WS₂ monolayers during nanopore drilling.

We observe a change in the intensity of PL signals and formation of additional defect peaks due to imaging and nanopore drilling in STEM mode with different e-beam doses. Prior to imaging, the samples were subjected to rapid thermal annealing at 300°C for 90 mins in H₂/Ar in order to reduce any carbon contamination during drilling.⁴⁰³ PL maps of two different WS₂ flakes were obtained before (Figures 5.1.2.3a, 5.1.2.3d) and after e-beam drilling (Figure 5.1.2.3b – dose A = 2.6×10^5 e⁻/nm², Figure 3e – dose B = 5.5×10^4 e⁻/nm²) in the suspended region marked with a blue arrow. After undergoing 3-4 minutes of e-beam exposure (STEM imaging), 2-3 nanopores with diameters ~10 nm each were drilled in focused-spot mode in both membranes in close vicinity, as shown in the insets of Figures 5.1.2.3c and 5.1.2.3f. The nanopores were drilled close to each other (< 0.5 μm apart) to roughly differentiate between effects arising from beam exposure *versus* nanopore drilling, as we were limited by lateral PL resolution of 0.5 μm. As can be seen from Figures 5.1.2.3b and 5.1.2.3e, the beam exposure is clearly visible in the PL map as a darker region around the suspended region (outlined in yellow), with more widespread damage from dose A rather than from dose B.

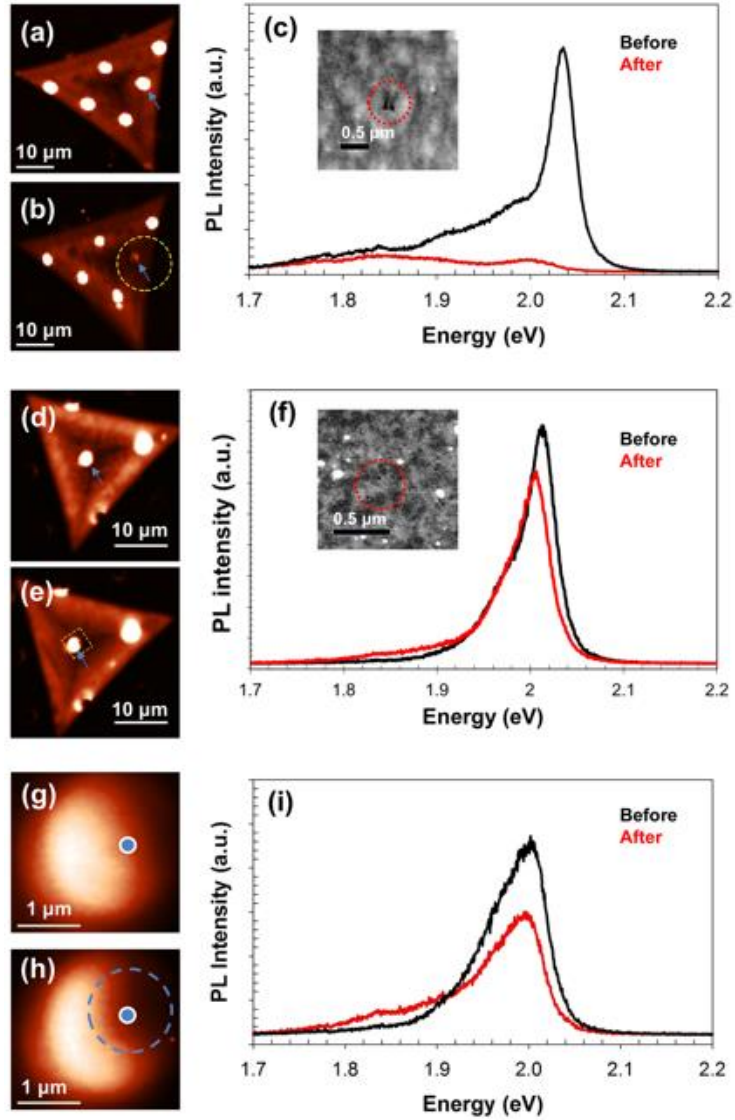


Figure 5.1.2.3. Change in PL due to beam exposure and nanopore drilling. PL intensity maps of a flake (a) before and (b) after STEM drilling with dose A (2.6×10^5 e⁻/nm²). Yellow dotted line in (b) shows the region damaged during STEM imaging. The region was viewed in STEM for ~3-4 min with two nanopores (diameters ~10 nm each) drilled in spot mode for 5 s. (c) PL of the suspended region, marked with blue arrows in (a-b), before and after STEM drilling. (inset) STEM image of the drilled nanopores. PL intensity maps of a flake (d) before and (e) after STEM drilling with dose B (5.5×10^4 e⁻/nm²); yellow dotted lines showing the e-beam damage. The region was viewed for ~3-4 min with three nanopores (diameter ≤ 10 nm each) drilled in spot mode for 3 s. (f) Corresponding PL of the same spot before and after STEM drilling on the suspended region marked with blue arrows in (d-e). (inset) STEM image of the nanopores. PL intensity maps of the zoomed-in suspended region of the flake shown in (d-e) before (g) and after (h) drilling showing nanopore-induced PL change in the area outlined in blue (R_{NP}). (i) PL of the R_{NP}, marked with a blue dot in (g-h), before and after drilling.

The PL spectrum of the suspended membrane shown in Figure 5.1.2.3c reveals that imaging with dose A resulted in the quenching of the X_0 (neutral exciton) peak, a ~ 26 -fold decrease of the X_T (charged trion) peak and a ~ 2 -fold increase of the X_D (defect) peak at ~ 1.85 eV. On the other hand, dose B (Figure 5.1.2.3f) led to almost no change of the X_0 and X_T peak intensities in addition to the formation of an additional X_D peak located at ~ 1.87 eV, which was initially absent for this flake. It should be noted that these spectra are obtained from the suspended region exposed only to the e-beam (R_{BE}) and not subjected to drilling (R_{NP}), which is studied next. These changes take place due to the e-beam bombardment damage that occurs during STEM imaging, which leads to sulfur vacancies and other defects with densities proportional to the e-beam dose.^{106,403}

To differentiate the effects due to beam exposure from those of nanopore drilling, we recorded PL maps of the suspended membrane near the nanopores, before (Figure 5.1.2.3g) and after (Figure 5.1.2.3h) drilling and found variations in the PL intensity across the monolayer membrane. Although the entire suspended region was exposed to the scanning beam during imaging in STEM mode, a darker region to the right of the membrane (R_{NP} ; outlined in blue; diameter ~ 0.6 μm) was observed where the nanopores were drilled while the left side of the membrane was relatively unaffected (R_{BE}). R_{NP} showed a 2-fold decrease in both the X_0 and X_T peak intensities and the formation of the X_D peak at ~ 1.88 eV (Figure 5.1.2.3i). The spectral weight percentage (*i.e.*, intensity percentage) of X_D differed in the two regions, with 10% for R_{BE} and 47% for R_{NP} , thus showing higher density of defects occurring near the nanopore. It was also observed that while the enhancement factor ($I_{\text{sus}}/I_{\text{sup}}$) remained ~ 12 for R_{BE} , R_{NP} had a reduced

enhancement factor of ~ 6 . The defects introduced due to the nanopore drilling in the vicinity of R_{NP} can provide sites for oxidation, which we investigate later in our report. It should be noted that the laser exposure from PL and Raman measurements was not seen to introduce additional defects. This was verified by letting the focused laser beam (power density = 4.4×10^4 W/cm²) illuminate suspended WS₂ regions (both with and without a nanopore) for at least 5 minutes. Raman measurements, from before and after exposure, also indicated no measurable change or shift in the WS₂ spectrum.

A schematic of a typical WS₂ nanopore device is shown in Figure 5.1.2.4a. 50-nm-thick suspended silicon nitride (SiN_x) membranes with dimension 50 μm x 50 μm were fabricated on 5 μm /500 μm SiO₂/Si wafers using optical lithography.^{382,404} A 200-500 nm diameter hole (area = 0.03 – 0.2 μm^2) was drilled in the SiN_x membrane using a focused ion beam (FIB) with a 10 pA, 30 kV Ga⁺ source, as illustrated in Figure 5.1.2.4b (inset). Monolayers of WS₂ were transferred onto the SiN_x membrane using either a Kapton tape-based micromanipulation positioning technique or a PMMA-based wet transfer procedure (see Methods). A successful transfer is shown in Figure 5.1.2.4b. Using the focused STEM probe with dose B, nanopores of diameters ranging from 2 to 8 nm were then drilled in the WS₂ membranes suspended over the FIB holes. AC-HRSTEM images of similarly drilled nanopores are illustrated in Figure 5.1.2.4c.

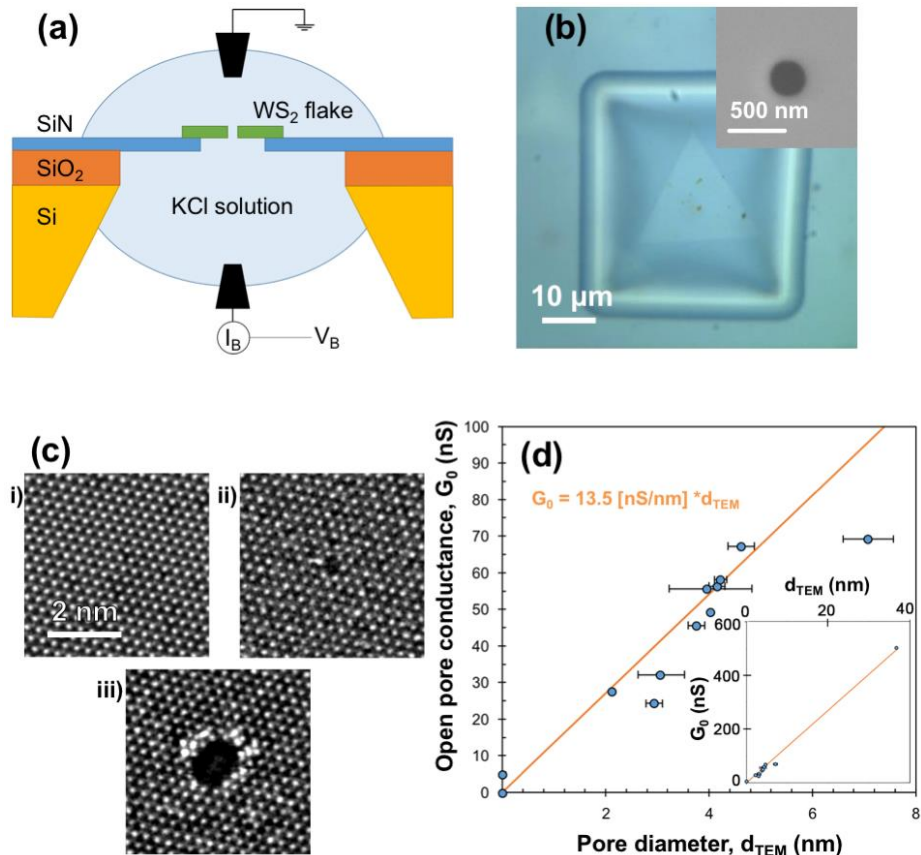


Figure 5.1.2.4. Fabrication and characterization of WS₂ nanopore devices. (a) Schematic of the nanopore device setup. The WS₂ flake (green) is suspended on a 200-500 nm FIB hole in a 50 nm thick and 50 μm x 50 μm dimensions SiN_x (deep blue) window, fabricated on a SiO₂/Si (orange/yellow) wafer. 1M or 3M KCl solution (light blue) is separated by the nanopore in the WS₂ flake and a bias voltage (V_B) is applied across the nanopore using Ag/AgCl electrodes (black) and the ionic current through the nanopore (I_B) is measured. (b) Optical image of a triangular WS₂ flake on a SiN_x window with FIB hole. (inset) An SEM image of a 300 nm FIB hole. (c) AC-HRSTEM image of (i) an undamaged suspended WS₂ membrane, (ii) a 0.3 nm nanopore and (iii) a 1.3 nm nanopore drilled with accelerating voltage 80kV. (d) Plot of open pore conductance of WS₂ nanopores with the corresponding nanopore diameter. Inset shows the plot over a larger d_{TEM} range. The solution conductivity was calculated by fitting the equation for 2D nanopores ($G_0 = \sigma d_{TEM}$) and found to be 13.5 ± 0.3 S/m. The nanopore diameter was calculated from the corresponding STEM image by defining a threshold for pixel intensities and selecting the pixels within that range in the vicinity of the pore in ImageJ software. This was repeated multiple times for a single pore and the standard deviation was taken as the measurement error. Standard deviations in the slope of I_B vs V_B plots for each nanopore was used as the error in open pore conductance, which are very small and lies within each data point area.

After loading onto a PDMS measurement cell, the nanopore device was wet using an ethanol:water (v/v 1:1) solution,³⁸¹ after which the electrolyte solution was introduced on both sides of the device. A bias voltage sweep (V_B) was applied across the membrane

and the ionic current (I_B) through the nanopore was monitored using a current amplifier in order to obtain the open pore conductance ($G_0 = I_B/V_B$). 1 M KCl solution was used as the electrolyte for most of our experiments, unless otherwise noted (see Methods). G_0 was plotted with the measured nanopore diameter (d_{TEM}) for several nanopore devices (see Figure 5.1.2.4d). By fitting the graph to a linear function, solution conductivity was calculated to be 13.5 ± 0.3 S/m, in good agreement with the measured conductivity of 11.8 S/m, using the conductance formula for 2D nanopores:

$$G_0 = \sigma d_{TEM}$$

where G_0 is the open pore conductance, σ is the calculated solution conductivity and d_{TEM} is the diameter of the nanopore measured from the corresponding STEM image.⁴⁰⁵

Open pore conductances for WS₂ nanopores with (i) $d_{TEM} = 4.4 \pm 0.9$ nm (pore A - red) and (ii) $d_{TEM} = 7.1 \pm 0.5$ nm (pore B - black) were obtained by cycling V_B between ± 200 mV (Figure 5a). It should be noted that 3 M and 1 M KCl solutions were used for pore A and pore B, respectively. The G_0 values thus obtained were 61.01 nS for pore A and 69.86 nS for pore B.

15 kbp double stranded DNA (10 ng/ μ l, random sequence) in buffered KCl solution was then introduced into the *cis* chamber and a constant V_B (400 mV for pore A and 200 mV for pore B) was applied to electrophoretically drive the DNA through the nanopore. The current traces hence obtained show DNA translocation events (see Figure 5.1.2.5b). We use the change in conductance ($\Delta G = \Delta I_B/V_B$) instead of change in ionic current to normalize our results. Scatter plots of (i) 1890 events and (ii) 2030 events were obtained from pores A and B, respectively, and the corresponding histograms of the event

depths (change in conductance or ΔG) and dwell time (duration of events) are plotted in Figure 5.1.2.5d. As pore diameters here are ~ 2 - 3 times larger than the diameter of dsDNA (~ 2.1 nm), we observe events that can be interpreted as DNA translocating in 3 possible orientations – unfolded, partially folded, and folded – each resulting in different current blockage levels (Figure 5.1.2.5c).⁴⁰⁶ Folded DNA translocation events in 3 M KCl have been reported in graphene and silicon nitride nanopores down to ~ 4.0 nm.^{385,406}

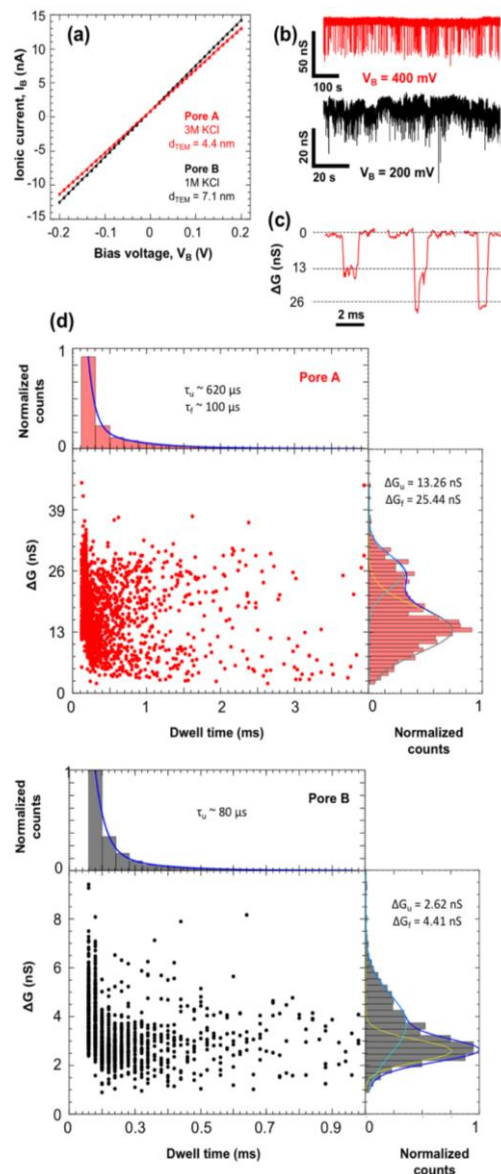


Figure 5.1.2.5. Double stranded DNA translocation through WS₂ nanopores. (a) Current-voltage measurement of WS₂ nanopores with diameters (d_{TEM}) of (i) 4.4 ± 0.9 nm (pore A in red) and (ii) 7.1 ± 0.5 nm (pore B in black) yielding an open pore conductances of 61.01 nS and 69.86 nS, respectively. (b) Ionic conductance time trace of DNA translocation events through the nanopore devices shown in (a) with 10 ng/ μ l 15 kbp dsDNA at $V_B = 400$ mV for pore A and $V_B = 200$ mV for pore B filtered at 10 kHz. (c) Zoomed-in events illustrating unfolded, partially folded and folded (left to right) DNA translocation events with the open pore conductance subtracted for pore A. (d) Scatter plots of change in conductance vs event duration for (i) 1890 events (pore A) and (ii) 2030 events (pore B). The histogram on the right shows the change in conductance fitted with two Gaussian curves for unfolded (ΔG_u , yellow) and folded events (ΔG_f , cyan). The histogram on the top shows the event duration or dwell time fitted with two exponential decay curves for unfolded (τ_u) and folded (τ_f) events. The τ_f was not obtained for pore B as we were limited by the sampling rate of the current amplifier.

As partially folded events may have various degrees of folding depending on the percentage of overlap, one distinct Gaussian distribution might not be representative of all the possible partially folded translocations. As a result, the event depth histograms were fitted to only two Gaussian curves which correspond to unfolded events (ΔG_u represented by the yellow curve) and folded events (ΔG_f represented by the cyan curve). Average change in conductances of (i) $\Delta G_u = 13.26$ nS and $\Delta G_f = 25.44$ nS for pore A, and (ii) $\Delta G_u = 2.62$ nS and $\Delta G_f = 4.41$ nS for pore B were obtained, yielding unfolded translocation blockage percentages ($\Delta G_u/G_0$) of $\sim 22\%$ and $\sim 4\%$ for pores A and B, respectively. These compare well with previously reported 2D nanopores.^{381–383} It is also common to fit the dwell time histogram to two exponential decay functions, one for unfolded events (τ_u) and one for folded events (τ_f).³⁸² In this case, we obtain time constants of (i) $\tau_u \sim 620$ μ s and $\tau_f \sim 100$ μ s for pore A and (ii) $\tau_u \sim 80$ μ s for pore B. τ_f was not obtained for pore B due to limitations in the sampling rate (50 kHz) of our current amplifier. High KCl concentration has been shown to reduce DNA-graphene interactions⁴⁰⁷ and lead to shorter dwell times for folded ds-DNA translocation events.³⁸⁵ It is likely that a similar mechanism is happening in pore A.

In addition to ionic current measurements in the dark, we also applied light to the nanopores to quantify the ionic current under illumination and explore the optical response of monolayer WS₂ nanopores in a biased ionic environment. The measurement setup is illustrated in Figure 5.1.2.6a. By means of a CMOS camera and a 4X objective lens (NA = 0.1), a 532 nm wavelength laser was monitored and focused on WS₂ nanopore devices mounted on a 3-axis micromanipulator stage. The power density of the laser was changed *via* a variable neutral density filter and by varying the laser driving current, both of which were calibrated using a power meter (see Methods).

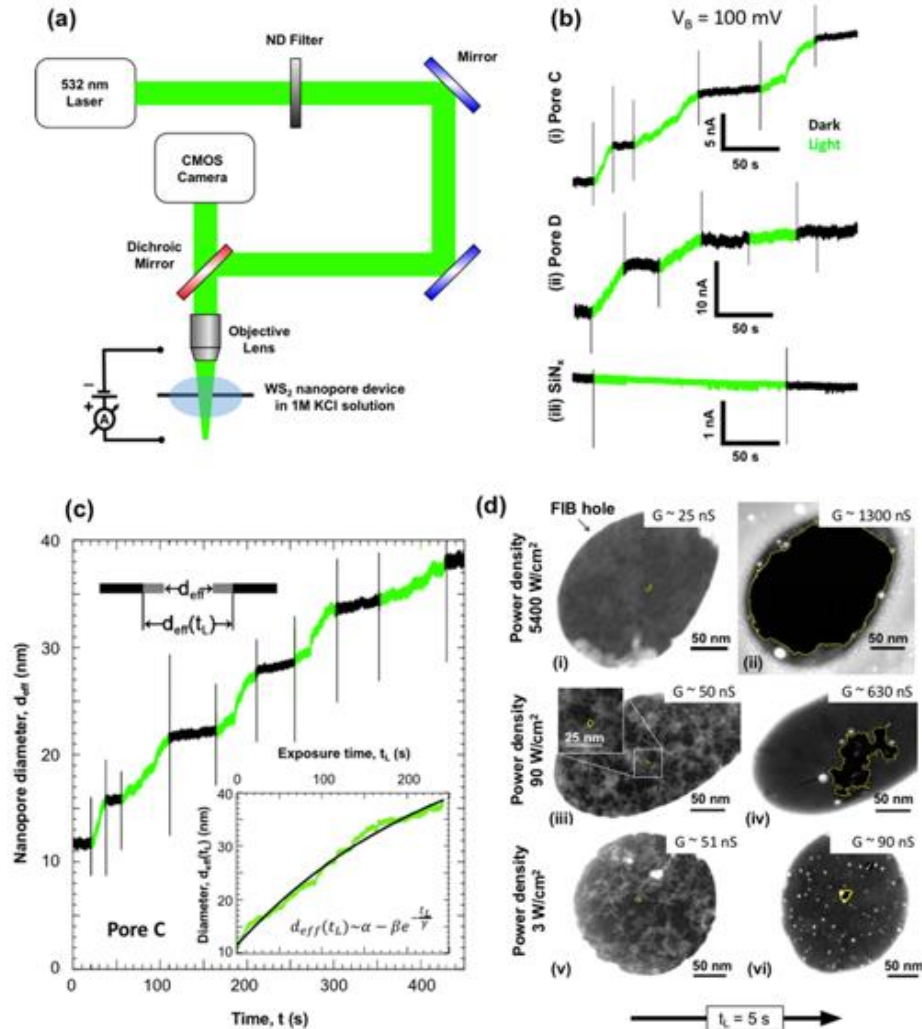


Figure 5.1.2.6. Optical activity of WS₂ nanopores in 1M KCl solution. (a) Schematic of the optical measurement setup. A 532 nm (green) laser is focused onto a nanopore device using an objective lens (4X) and 3-axis micromanipulator stage. The position of the laser and SiN_x window are monitored with a CMOS camera while its power is controlled through a variable neutral density filter and the laser driving voltage. All measurements were performed in 1M KCl solution. (b) Change in ionic current through WS₂ and SiN_x nanopores with laser exposure. Ionic current (I_B) measurements at $V_B = 100$ mV were obtained for two WS₂ nanopores of effective diameters (d_{eff}) of (i) 11.1 nm (pore C) and (ii) 43.2 nm (pore D), and a SiN_x nanopore with (iii) $d_{\text{eff}} = 4.8$ nm. Periods when the laser (power density = 3 W/cm²) is turned on (light) and off (dark) are represented in green and black, respectively. The spikes in I_B correspond to the capacitive noise from the switching the laser on or off. (c) Change in effective diameter of pore C with time. The effective diameter (d_{eff}) was plotted against the experiment time, t . The regions with the laser on (green) were extracted and concatenated into a single plot (inset) as a function of exposure time, t_L . The resulting exponential fit for the relation between effective nanopore diameter and laser exposure time is given by $\alpha = 55.1$ nm, $\beta = 43.5$ nm and $\gamma = 249.5$ s. An illustration of the expansion of the pore is shown on the top left. (d) STEM observation of the laser-induced expansion of nanopores. STEM images were obtained of WS₂ nanopores (outlined in yellow) with initial diameters (d_{TEM}) (i) 4.6, (iii) 4.0, and (v) 4.0 nm. Images after laser exposure ($t_L \sim 5$ s) to power densities of (ii) 5400, (iv) 90, and (vi) 3 W/cm² at $V_B = 0$ V shows expansion of pores. Corresponding conductance values before and after exposure are also provided.

In order to understand the effect of light on a WS₂ nanopore in an ionic solution, the pore conductance of multiple devices was measured as a function of laser exposure time. Here, we show results for a WS₂ nanopore (pore C) with an effective diameter ($d_{\text{eff}} = G/\sigma$) of 11.5 nm. As illustrated in Figure 5.1.2.6b (i), I_B was monitored at a constant $V_B = 100$ mV while the laser was turned on and off alternately with a constant power density of 3 W/cm². Before exposure, the pore conductance in the dark was stable over a period of 1 hour. However, during laser exposure, the I_B was seen to increase (green) and remained constant when the laser was turned off (black). This seemed to be an irreversible effect, resulting in ionic current time-traces consisting of a series of constant current periods (in the dark) connected by periods of increasing current (under laser illumination). Membrane charging cannot explain these observations, which would otherwise exhibit a return to the original conductance upon dissipation.⁴⁰⁸ We instead attribute it to a permanent physical expansion of the nanopore, confirmed by STEM imaging of nanopores, as discussed later on. A similar result was obtained for (ii) another

WS₂ nanopore (pore D - $d_{\text{eff}} = 43.2$ nm) under the same voltage and power density conditions. However, this was not the case for (iii) a SiN_x nanopore ($d_{\text{eff}} = 4.8$ nm), which showed no change in ionic current as a function of laser exposure at the same power density. This important control measurement demonstrates that solution evaporation and/or solution heating is also not the responsible mechanism for our observation, as either or both could cause a variation in ionic current regardless of the nanopore membrane material. It should be noted that enhancement of ionic current through a SiN_x nanopore has been reported previously, but at power densities ~ 6 orders of magnitude higher than what is used here.⁴⁰⁸

The observed nanopore expansion was further characterized by calculating the change in the effective nanopore diameter throughout the experiment for pore C (Figure 5.1.2.6c). The regions when the pore was exposed to light (green) were extracted and concatenated (Figure 6c inset) to help understand how d_{eff} changes with the laser exposure time (t_L). The d_{eff} vs. t_L plot was best fit empirically to an exponential trend:

$$d_{\text{eff}}(t_L) \sim \alpha - \beta e^{-\frac{t_L}{\gamma}}$$

where $\alpha = 55.1$ nm, $\beta = 43.6$ nm and $\gamma = 249.5$ s. The rate of expansion of the nanopore can then be calculated as:

$$\frac{d[d_{\text{eff}}(t_L)]}{dt_L} \sim \frac{\beta}{\gamma} e^{-\frac{t_L}{\gamma}}$$

where β/γ is the initial rate of expansion of pore. For pore C, this value was calculated to be 0.2 nm/s while for pore D it was 0.4 nm/s (see Supporting Information). The

approximate initial expansion rate was also calculated for other power densities by measuring the conductance change due to exposure of $t_L = 5$ s. It was seen that the expansion rate increased as the laser power density increased (see Supporting Information). It should be noted here that to ensure that the low $V_B = 100$ mV did not affect the nanopore, conductance was measured and seen to be constant for an hour in the dark. Nanopore illumination was also repeated with $V_B = 0$ V and conductance was measured in the dark after illumination, resulting in similar outcomes to those presented here.

To gain a better understanding of how nanopore expansion varies with power density, three nanopores were subjected to different power densities for $t_L = 5$ s and observed under STEM. In all cases, we measured the conductance before and after exposure. After the ionic measurement, the membrane was rinsed from the salt solution with water and annealed to allow for subsequent STEM imaging. Figure 5.1.2.6d shows STEM images of WS_2 nanopores with $d_{TEM} = 4.6$ nm (i) before and (ii) after being exposed to a power density 5400 W/cm^2 , $d_{TEM} = 4.0$ nm (iii) before and (iv) after being exposed to a power density of 90 W/cm^2 , and $d_{TEM} = 4.0$ nm (v) before and (vi) after being exposed to power density of 3 W/cm^2 . While the highest power density physically breaks the suspended membrane completely, the lower power densities gradually increases the pore size. This is also evident from the measured change in pore conductances, which increased by ~ 1275 nS for a power density of 5400 W/cm^2 , by ~ 592 nS for 90 W/cm^2 , and by ~ 39 nS for 3 W/cm^2 . It is possible in some cases to find other

pre-existing pores in the membranes that can further grow due to e-beam exposure during STEM imaging.

Even though we see irregular pore shape growth for large light intensities (90 W/cm²), we see steadier and more controlled expansion at lower light intensities (3 W/cm²) as shown in Figure 5.1.2.6d. By further optimization of this process, the use of controlled light pulses with controlled intensity and duration, it may be possible to make this process highly controllable and usable for applications. This is somewhat analogous to recently developed membrane electroporation protocols using voltage pulses.^{409–411} While these voltage pulses can break the membrane at high voltage and long durations, the procedure have been optimized for nanopore formation by fine control of the magnitude and duration of the pulses.

We also explored the impact of laser exposure on intact suspended WS₂ membranes containing no e-beam drilled nanopores. A rectifying curve is obtained initially with $G_0 = 2$ nS (corresponding to $d_{\text{eff}} = 0.2$ nm) possibly indicating the presence of intrinsic sub-nm pinholes in the membrane (see Supporting Information). Upon laser exposure (power density of 90 W/cm², $t_L = 15$ s), the conductance increased to 9 nS ($d_{\text{eff}} = 0.8$ nm). A further increase in power density (power density of 5400 W/cm², $t_L = 6$ s) did not increase the conductance or break the membrane. This seems to indicate that laser exposure might help form additional pathways for ionic flow if there are existing defects in the membranes. However, intentional e-beam damage used to create nanopores with exposed edges plays the dominant role in the further expansion of the nanopores upon

illumination, and the ionic current through it is the major contribution to the measured ionic current in nanopore devices.

Experiments were also conducted wherein suspended WS₂ membranes were exposed to STEM damage (dose = 1.1×10^4 e⁻/nm²) without nanopore drilling, and laser illumination (power density of 90 W/cm², t_L ~ 3 mins) was applied to see if nanopores can be formed. No appreciable change in conductance was observed, suggesting no perceptible expansion of e-beam induced defects from the applied dose. Further experiments are required to investigate the relation between e-beam dose, defect density and size, and the rate of defect formation and expansion in an ionic solution.

Based on our observations, we propose that e-beam induced defects of optimal size provide sites for photo-oxidation to take place in WS₂ membranes in an ionic solution, which generally occur at grain boundaries,^{394,395} leading to expansion of nanopores under laser illumination in KCl solution. Further studies are needed to explore the pore formation and expansion process in more detail and at the atomic scale using AC-HRSTEM characterization.

Conclusion

In summary, we present the demonstration of optically responsive WS₂ nanopore sensors for biomolecule analysis. We characterized our vapor grown WS₂ monolayers using Raman spectroscopy, AFM, TEM imaging, and PL spectroscopy. We showed that imaging and drilling of nanopores using a focused e-beam can introduce defects in

suspended WS₂ membranes, which appear as changes in the PL spectra. We determined a dose of 5.5×10^4 e⁻/nm² in STEM mode to be sufficient to drill a nanopore while adequately preserving the optical properties of WS₂ monolayers. Fabricated nanopore devices were then used to detect double-stranded DNA translocations. In contrast to SiN_x pores, the diameter of the WS₂ nanopore was optically expanded using a focused 532 nm laser, varying the rate of expansion as a function of incident optical power density. A rate of ~0.2-0.4 nm/s was obtained for a power density of 3 W/cm². We attribute this phenomenon to the photo-oxidation of nanopore edges in the ionic solution. We believe this initial study of WS₂ demonstrating electron beam induced effects on PL, DNA translocations through nanopores, and light-enabled pore expansion will aid future optoelectronic experiments on other optically-active TMD materials. Further studies may focus on understanding the detailed atomic mechanisms behind nanopore expansion in solution and using short laser pulses to potentially control nanopore edges at atomic scales.

Methods

Characterization. Monolayers of WS₂ were first selected through optical microscopy. AFM scans were obtained in a Bruker Dimension Icon operating in tapping mode. Raman spectroscopy and PL were performed in a NT-MDT NTEGRA Spectra with an excitation laser wavelength of 532 nm with spectral resolutions of 0.5 cm⁻¹ and 10⁻³ eV, respectively. TEM images and SAED patterns were taken in a JEOL JEM-2010F TEM operating at 200 kV. High-angle annular dark field (HAADF) AC-HRSTEM

images were obtained in FEI Titan G2 S/TEM operating at 80 kV. A Gaussian blur filter was applied to the AC-HRSTEM images using ImageJ software in order to reduce contrast from carbon contamination.

Nanopore device fabrication. WS₂ monolayers were separated from their SiO₂ growth substrate using a standard PMMA-based KOH wet etch at 75°C. After being washed in H₂O for at least 1 hour, the flakes were then transferred using one of two methods. The first method is a Kapton tape based method which utilizes a micromanipulator to position flakes onto previously described silicon nitride membranes.^{382,404} The other is a standard wet transfer in which flakes were scooped out onto SiN_x membranes (Figure 4a), dried, and left in acetone for 24 hours. The transfer yields obtained *via* micromanipulation and wet transfer were 60% and 80%, respectively. The slight variation of yield is mainly due to density of WS₂ monolayers used in each technique – micromanipulation for flakes grown at low density and wet transfer for flakes grown at high density. The devices were then washed with isopropanol and annealed at 300°C for 90 minutes in 5% H₂/95% Ar. Nanopores were drilled in the suspended WS₂ membranes using a 200 kV JEOL JEM-2010F TEM operating in STEM mode with a spot size of 1 nm and drilling time of 3-5s.

Ionic measurements. The nanopore device was mounted on a PDMS platform using Kwikcast sealant over an underlying channel for ionic fluid. The setup was then placed in a beaker containing ethanol:water (v/v 1:1) solution for at least 30 minutes. Bubbles were removed using a pipette every 10-minute interval. The platform was removed and the solution was carefully replaced with water, followed by the desired

ionic solution in the channel underneath (*trans* reservoir) and a drop on the top (*cis* reservoir). Ag/AgCl electrodes were used to perform ionic measurements with EPC-10 HEKA (sample rate = 50 kHz) amplifier. 1 M KCl (with 10 mM EDTA and 1 mM Tris; measured solution conductivity = 11.8 S/m, pH = 8.7) and 3 M KCl (with 30 mM EDTA and 3 mM Tris; measured solution conductivity = 30.2 S/m, pH = 7.8) solutions were prepared using DI water and the conductivity and pH were measured with Accumet XL-20 pH conductivity meter. Translocation data was analyzed using Pypore (<https://github.com/parkin/pypore>) and custom Python scripts.

Optical experiments. Samples were illuminated using a 532 nm (green) excitation laser (Laserglow Technologies) with a 5 mW power output. Power density was controlled by changing the laser driving current and *via* a variable neutral density filter (Thorlabs), and calibrated with a PHIR power meter located at the sample stage. All cables were kept electrically isolated or grounded to reduce any cross-talk. Alignment was performed by first focusing the laser on a white piece of paper and observing it using the CMOS camera. The laser spot was then centered and digitally marked in the image capture software window by changing the mirror orientations. This spot was then aligned to the nanopore device windows mounted on the micromanipulator stage with the laser beam turned off.

5.2 1H-MoS₂/1H-WS₂ heterostructure

By combining our efficient growth method for 1H-MoS₂ (section 4.1.1) and 1H-WS₂ (section 5.1.1), synthesis of 1H-MoS₂/1H-WS₂ heterostructures become possible (figure 5.2.1a). 1H-MoS₂ and 1H-WS₂ have different bandgaps (section 2.3.2), therefore heterostructures of both these materials is particularly interesting for any possible photoluminescence applications.^{14,412–415}

W is the harder to diffuse on the surface compared to Mo therefore the growth recipe follows predominantly the 1H-WS₂ recipe in section 5.1.1. A Si/SiO₂ chip is spin coated with a 2% sodium cholate growth promoter at 4000 rpm for 45 seconds, because sodium cholate is known to help promote the growth of both 1H-MoS₂ and 1H-WS₂.^{58,59,98,169,386} A micro-droplet of a 1:1 solution, combining a saturated aqueous solution of ammonium heptamolybdate (AHM) and a 3.1mM aqueous solution of ammonium metatungstate (AMT), is applied to the corners of the growth substrate. The AHM acts as the Mo feedstock, whereas the AMT acts as the W feedstock. The growth substrate is inserted into the center of the 1 inch CVD furnace, and a chip containing 25mg of S is positioned upstream at a distance of 17 cm from the growth substrate. The furnace is ramped up to 800 °C at a rate of 70 °C/min under a constant 500 sccm of N₂ gas, the S chip upstream will reach a temperature of 150 °C and start evaporating. After a 30 min growth time, the furnace is rapidly cooled and the growth substrate is retrieved. Many flakes have grown across the substrate, some are isolated monolayer single crystal 1H-MoS₂ flakes and others are isolated 1H-WS₂ flakes, however by carefully analyzing the substrate 1H-MoS₂/1H-WS₂ heterostructures can also be found (figure 5.2.1b).

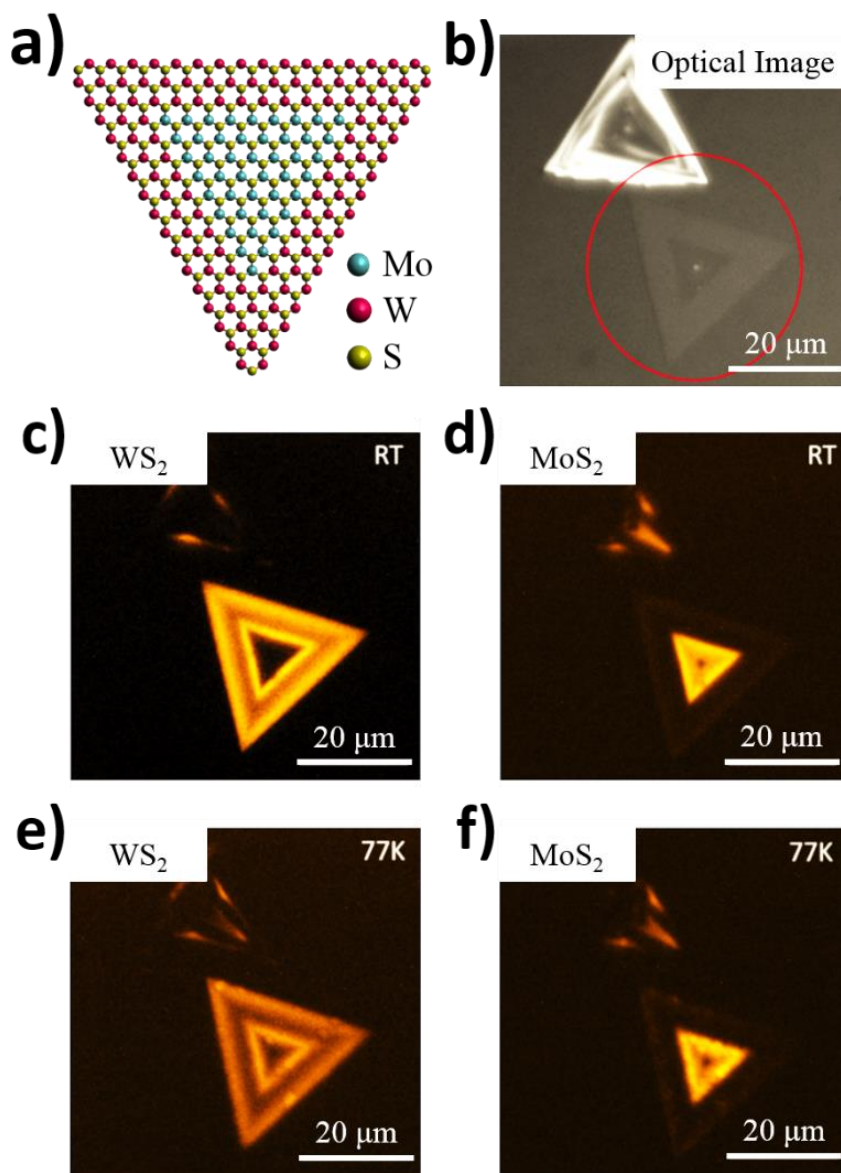


Figure 5.2.1. MoS₂WS₂ heterostructure. a) Ball and stick model of heterostructure. b) Optical micrograph of heterostructure. c,d,e,f) Photoluminescence of MoS₂ and WS₂ at various temperatures. Photoluminescence measurements were performed by Prof. Terrones group at PSU.

Photoluminescence measurements on the heterostructure at room temperature and low temperature reveal a clear distinction between both regions (figure 5.2.1cded). Monolayer 1H-MoS₂ and 1H-WS₂ have direct bandgaps at 1.84 eV and 1.97 eV respectively; the sharp emission of each region at their respective bandgap energies confirm the 1H-MoS₂/1H-WS₂ heterostructure.

5.3 1H-MoSe₂ and 1H-WSe₂

1H-MoSe₂ and 1H-WSe₂ are currently being explored by the scientific community due to their unique properties. 1H-WSe₂ is extremely enticing as it is the only known 2D TMD to be an intrinsic p-type semiconductor. The other known 2D p-type semiconductor is phosphorene which is notoriously unstable in air (see section 2.4). Therefore the successful synthesis of monolayer 1H-MoSe₂ and 1H-WSe₂ is the first step in enabling novel p/n junction devices utilizing undoped monolayer TMDs.

Monolayer 1H-MoSe₂ was grown by chemical vapor deposition (CVD). A 1% sodium cholate solution is spin coated at 4000 rpm for 45 seconds on a Si/SiO₂ growth substrate. Sodium cholate is a known growth promoter that helps with the diffusion of the Mo atoms on the Si/SiO₂ surface.^{59,98,169} Micro-droplets of a saturated aqueous solution of ammonium heptamolybdate (AHM) are applied to the corners of the growth substrate. The substrate is then inserted in the center of a 1inch CVD furnace and accompanied upstream by a selenium (Se) source. The Se source is placed at a distance of 14 cm from the growth substrate. The furnace is ramped up to 800 °C at a rate of 70 °C/min under a constant flow of 500 sccm of N₂ and 50 sccm H₂. The Se source reaches a temperature of 250 °C and start sublimating. After a 20 min growth, the furnace is rapidly cooled and 1H-MoSe₂ flakes have grown from the AHM droplets (figure 5.3.1a).

Monolayer 1H-WSe₂ was successfully grown by CVD. A 2% sodium cholate solution is spin coated at 4000 rpm for 45 seconds on a Si/SiO₂ growth substrate. The higher concentration of sodium cholate is due to the much higher weight and evaporating temperature W has in comparison to Mo, making it harder to diffuse W on the

surface.^{58,386} Large droplets of a 3.1mM aqueous solution of ammonium metatungstate (AMT) are applied to the substrate and the solution was spread around the substrate using a brush. We previously published this brushing technique for the growth of 1T'-WTe₂ (also discussed in section 6.2).⁵⁸ The substrate is then inserted into the center of the 1inch CVD furnace and accompanied upstream with the Se source at a distance of 13 cm from the growth substrate. The furnace is heated up to 750 °C at a rate of 70 °C/min under 350 sccm N₂ and 20 sccm H₂. The Se source reaches a temperature of 250 °C and start sublimating. After a 15 min growth time, the furnace is rapidly cooled. Figure 5.3.1b reveals 1H-WSe₂ flakes have grown across the substrate. The 1H-WSe₂ flakes were characterized by Raman spectroscopy (figure 5.3.1c). Using a red laser (633 nm) we were able to distinguish 3 peaks at 135 cm⁻¹, 258 cm⁻¹ and 394 cm⁻¹. These peaks are in agreement with reports on monolayer 1H-WSe₂ measured at room temperature with 633 nm.^{78,378,397} At a different laser wavelength, some of these peaks are not visible making 633 nm an ideal wavelength for observing the Raman modes of 1H-WSe₂. In monolayer 1H-WSe₂, the A_{1g} and E¹_{2g} peaks merge at 258 cm⁻¹.^{78,378,397} Our 258 cm⁻¹ peak has a small shoulder indicating 2 modes present under the peak, and the merging of both peaks confirms the monolayer height.

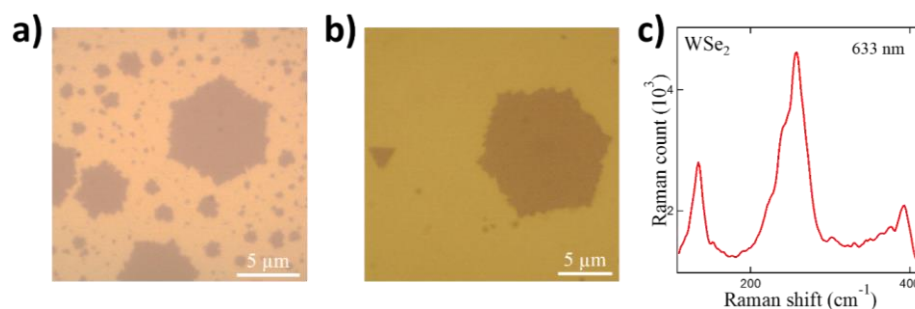


Figure 5.3.1. Characterization of the 1H-MSe₂. a) Optical micrograph of the CVD grown 1H-MoSe₂. b) Optical micrograph of the CVD grown 1H-WSe₂. c) Raman spectroscopy on the 1H-WSe₂ flakes.

CHAPTER VI.

1T'-MX₂, Unexplored Monolayer Materials

The 1H phase of transition metal dichalcogenides (TMDs) is the most studied phase of TMDs to date. Still, scientists are theoretically and experimentally beginning to explore alternate TMD phases. 1T'-TMDs are theoretically predicted to possess unique properties such as a 2D quantum spin hall effect. This has generated a large increase in scientific research on the 1T'-TMDs. However, experimentally, monolayer 1T'-TMDs are extremely challenging to achieve. In fact, they remained unexplored until recently due to the difficulty of synthesizing monolayer materials, and their high instability in air.

In this Chapter, I will detail how we successfully synthesized the first monolayer 1T'-molybdenum ditelluride (1T'-MoTe₂) and 1T'-tungsten ditelluride (1T'-WTe₂). We used graphene as a passivation layer to resolve its air instability. We then performed multiple characterization measurements, and achieved the first atomic resolution images of a monolayer 1T'-TMD. Our work on the synthesis of 1T'-TMDs has been highlighted in multiple press releases due to the high impact it has had in the field “beyond graphene”. Finally, I will discuss our work on the synthesis of an in-plane 1H/1T' heterostructure. We combined the growth method for 1H-TMDs with 1T'-TMDs to create a unique in-plane heterostructure of both phases. Characterization measurements revealed a buckling effect in the 1H region, and the atomic images at the 1H/1T' interface revealed a unique in-plane stitching of both phases.

6.1 1T'-MoTe₂

6.1.1 Monolayer single-crystal 1T'-MoTe₂ grown by chemical vapor deposition exhibits weak antilocalization effect

The results presented in this section have also appeared in the publication “Monolayer Single-Crystal 1T'-MoTe₂ Grown by Chemical Vapor Deposition Exhibits Weak Antilocalization Effect”, Carl H. Naylor, William M. Parkin, Jinglei Ping, Zhaoli Gao, Yu Ren Zhou, Youngkuk Kim, Frank Streller, Robert W. Carpick, Andrew M. Rappe, Marija Drndić, James M. Kikkawa, and A. T. Charlie Johnson, *Nano Letters*, 2016, 16 (7) pp 4297–4304.

Abstract

Growth of transition metal dichalcogenide (TMD) monolayers is of interest due to their unique electrical and optical properties. Films in the 2H and 1T phases have been widely studied but monolayers of some 1T'-TMDs are predicted to be large-gap quantum spin Hall insulators, suitable for innovative transistor structures that can be switched *via* a topological phase transition rather than conventional carrier depletion [Qian et al., *Science* 346, 1344–1347 (2014)]. Here we detail a reproducible method for chemical vapor deposition of monolayer, single-crystal flakes of 1T'-MoTe₂. Atomic force microscopy, Raman spectroscopy, X-ray photoelectron spectroscopy and transmission electron microscopy confirm the composition and structure of MoTe₂ flakes. Variable temperature magnetotransport

shows weak antilocalization at low temperatures, an effect seen in topological insulators and evidence of strong spin-orbit coupling. Our approach provides a pathway to systematic investigation of monolayer, single-crystal 1T'-MoTe₂ and implementation in next-generation nanoelectronic devices.

Two-dimensional transition-metal dichalcogenides (MX₂) have attracted great attention due to the broad set of material characteristics that can be accessed by varying the identity of the transition metal and chalcogenide atoms.^{35,41,43,45,416,417} The promise of MX₂ monolayer films for energy⁷² and other applications have been made apparent through investigations of their optical,^{44,418} electrical⁴⁴ and mechanical⁴¹⁹/tribological⁴²⁰ properties. Development of reproducible growth methods for high-quality monolayer MX₂ films is a key step in advancing basic and applied research into these materials. MX₂ materials can crystalize in different forms,⁴²¹ with the 2H phase of MoS₂ being most widely studied to date. Other structural phases, such as 1T and 1T', are of great interest and are being explored at a rapid pace. The monolayer 1T'-MX₂ compounds with molybdenum or tungsten as the transition metal are predicted to be large-gap quantum spin Hall (QSH) insulators,⁶¹ making them promising for applications in novel switching devices,⁶¹ spintronics, and quantum computation.^{113,114,422} One method to obtain 1T and 1T'-MX₂ is by phase transformation.⁴²³ Examples include transformation of MoS₂ from 2H to 1T by treatment with n-butyl lithium,⁶⁹ and conversion of MoTe₂ from 2H to 1T' by laser patterning.⁴²⁴ Computational studies suggest that it is possible to induce a transition from 2H to 1T' phase in MX₂ materials by application of stress,⁶⁸ but this

approach is complicated by the need to control the homogeneity of the strain across the sample. The metastable nature of 1T'-MoTe₂ makes direct growth by chemical vapor deposition (CVD) a challenge,⁴²⁵ but CVD growth of few-layer MoTe₂ in the 2H and 1T' phases was recently reported.^{425,426} There are as yet no reports of a reliable CVD growth method for monolayer, single-crystal, MoTe₂ in the 1T' phase, which would represent a critical step to enable systematic investigations of topological effects in this system.

Here we report direct CVD growth of single-crystal monolayer flakes of MoTe₂ in the 1T' phase along with associated measurements of key chemical, electrical and physical properties. X-ray photoelectron spectroscopy (XPS) was used to confirm that the chemical composition of the monolayer flakes corresponds to MoTe₂. Atomic force microscopy (AFM) revealed that the flakes are monolayer thickness, with minimal (< 5%) bilayer and multi-layer content. Raman spectroscopy, transmission electron microscopy (TEM) and aberration-corrected scanning TEM (ACSTEM) confirmed that the monolayer MoTe₂ flakes were single crystal and grown directly in the 1T' phase. TEM imaging and electron diffraction were used to identify a preferential crystal growth direction along the **b** vector axis. Finally, temperature dependent magneto-conductance measurements showed a weak antilocalization effect, which is observed in many topological insulators due to their strong spin-orbit coupling.⁴²⁷ These investigations set the stage for further explorations of monolayer MoTe₂ and its eventual application in next-generation electronic, sensor, and optoelectronic devices.

Monolayer MoTe₂ flakes were grown directly on a 300 nm SiO₂/Si substrate by CVD. First, a 1% sodium cholate solution, known to act as a growth promoter for

MoS₂,⁹⁸ is spin coated at 4000 rpm for 60 seconds onto the SiO₂ substrate. A droplet of a saturated solution of ammonium heptamolybdate in deionized (DI) water is deposited onto the substrate, providing the molybdenum feedstock (Fig. 6.1.1.1a). The substrate is placed in the center of a 1-inch CVD tube furnace, and 15 mg of solid tellurium is placed 5 cm upstream from the substrate (Fig. 6.1.1.1b). Growth occurs at atmospheric pressure in a flow of 400 sccm of nitrogen gas and 25 sccm of hydrogen (both 99.999% purity). The furnace temperature is ramped to 700 °C at a rate of 70 °C min⁻¹. While the Mo source and SiO₂ growth substrate reach 700 °C, the maximum temperature of the tellurium pellet is ~500 °C. After a 5-minute growth period, the furnace is opened, and the sample is rapidly cooled to room temperature in 1000 sccm flowing nitrogen.

After growth, the substrate is typically sparsely covered with monolayer MoTe₂ flakes that grow in a mm-scale “coffee ring” pattern around the location of the AHM droplet. In contrast to very regular triangular domains observed for MoS₂ grown by CVD,⁹⁵ MoTe₂ flakes are frequently rectangular in shape, as expected for oriented, single crystalline material, with typical dimensions of 3 x 10 μm (Fig. 6.1.1.1c). Two distinct growth regions are observed in the “coffee ring,” each with a different crystal growth shapes. In the inner part of the ring, the flakes are more dendritic in shape (polycrystalline), while in the outer part of the ring, the flakes are rectangular (single crystal). The crystal orientation can be determined from the shape of the flakes, as discussed below. These two different growth regions in the “coffee ring” suggest characteristics of the growth mechanism. The inner region of the “coffee ring” is closer to the Mo feedstock material (AHM). This region is expected to receive a larger Mo flux

compared to the outer part of the ring. In the outer part of the “coffee ring”, the nucleation density and relative flux ratio of Mo to Te atoms are apparently better optimized for growth of single-crystal 1T'-MoTe₂ flakes, with less perturbation from neighboring growth. In the inner region of the “coffee ring” the flux of Mo atoms is higher, resulting in denser growth and polycrystalline 1T'-MoTe₂ flakes. This growth mechanism is in agreement with other reports of CVD growth of MX₂ materials.^{98,169}

A second growth method provided larger areal density of monolayer MoTe₂ flakes. A 20 nm-thick rectangle of MoO₃ is deposited by thermal evaporation onto the growth substrate using a shadow mask. A 1% sodium cholate solution is spin coated onto the substrate at 4000 RPM for 60 seconds. The sample growth then proceeds as described above. Samples show a higher density of flakes (Fig. 6.1.1.1d), mostly with a star shape, in contrast to the rectangular single crystal flakes described previously. The growth region in this case is the entire area covered by Mo source material, which is on the order of 1-5 cm² in this experiment. This large-area growth method thus offers a path for future optimization of flake shape and surface coverage. Flakes from both growth methods were characterized as described below, and no significant differences were found. We found that growth of single-crystal monolayer flakes requires both the presence of the growth promoter and careful control of the quantity of molybdenum source material. If either of these parameters is outside of the ideal window, there will either be no growth or multi-layer crystallites will be formed.

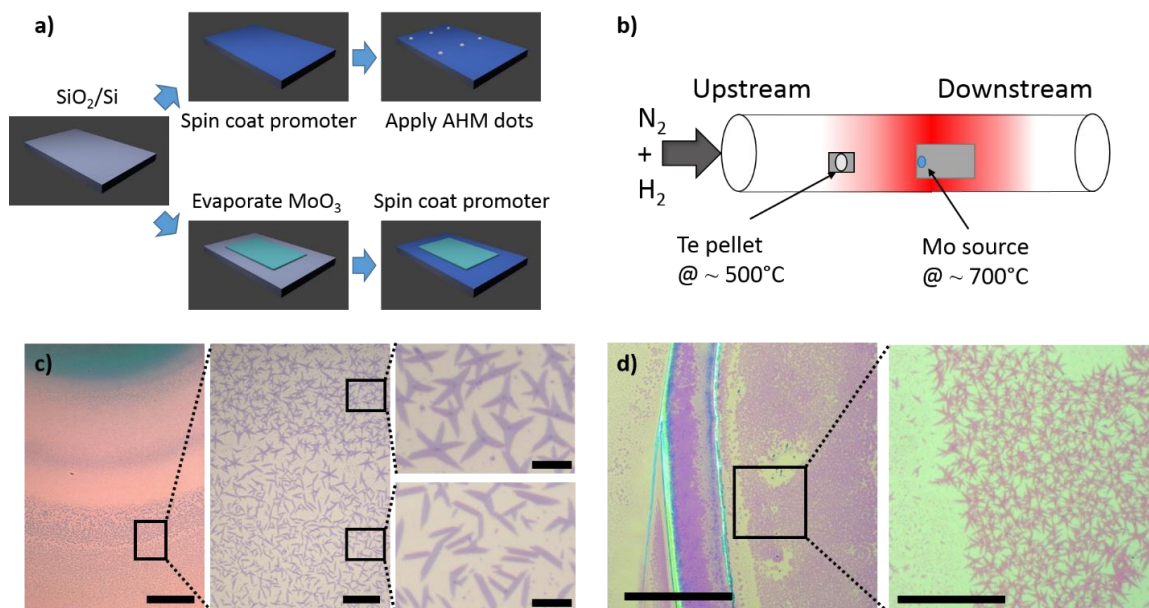


Figure 6.1.1.1. MoTe₂ growth. a) Process steps for droplet (above) and evaporation (below) methods. b) Schematic of the CVD growth setup. c) Optical micrograph displaying MoTe₂ flakes grown by the droplet method revealing “coffee ring” growth region. The inner region has polycrystalline flakes while the outer region has single crystal flakes. Scale bars are 200 μm, 40 μm and 10 μm, respectively. d) Optical micrograph displaying MoTe₂ flakes grown by the evaporation method. Scale bars are 200 μm and 40 μm, respectively.

XPS was used to determine the elemental and bond composition of the flakes. Peaks were observed at 572.1 eV, 582.5 eV, 227.7 eV and 231.0 eV, corresponding to the Te 3d_{5/2}, Te 3d_{3/2}, Mo 3d_{5/2} and Mo 3d_{3/2}, respectively (Figs. 6.1.1.2a-b).⁴²⁵ In group-6 TMDs, the 1T signal is typically downshifted by ~0.8 eV relative to the 2H phase,⁷⁰ and the peaks we observe show the expected downshift compared to the XPS spectrum for 2H-MoTe₂ reported by others.⁴²⁵ XPS is not sensitive to the difference between the 1T and 1T' structures.⁷⁰ Based on these data, the Te/Mo atomic ratio is measured to be 2.1, very close to the ideal value for MoTe₂. The full XPS spectrum and details as to how the stoichiometry was determined can be found in the Supplementary Information and Supplementary Fig. 1.

Raman spectroscopy with an excitation wavelength of 532 nm was performed to examine the vibrational modes of the MoTe₂ flakes. Raman peaks were observed at 112, 127, 161, 252, and 269 cm⁻¹ (Fig. 6.1.1.2c), corresponding to five Raman-active Ag modes of monolayer MoTe₂ in the 1T' phase predicted at 111.27, 125.69, 161.10, 254.58 and 269.22 cm⁻¹.⁴²⁸ The spectrum agrees well with previous reports of few layer MoTe₂ in the 1T' phase^{426,429} and it differs significantly from the experimental spectrum for the 2H and theoretical 1T phase.^{425,430,431} An additional predicted Raman-active mode⁴³⁰ at 80.41 cm⁻¹ is removed by the edge filter of the apparatus and is not expected to be observed. To our knowledge, this is the first experimental report of the peak at 269 cm⁻¹, which is expected to blueshift from 258 cm⁻¹ to 269 cm⁻¹ as the material is reduced from bulk to monolayer.⁴²⁹ Here, the peak is very distinct at 269 cm⁻¹, indicating the presence of monolayer 1T'-MoTe₂. Additionally, an unidentified peak at 188 cm⁻¹ was observed, in agreement with an earlier report.⁴²⁵ During Raman mapping measurements conducted in air, the flakes deteriorated over the course of a few hours, likely due to oxidation. To passivate the material, a sheet of monolayer CVD graphene was transferred over the sample immediately after growth and prior to taking Raman spectra, enabling the Raman mapping to be performed over many hours with no degradation of the material. The addition of the graphene layer did not affect the Raman modes (Supplementary Fig. 2). A Raman map of the amplitude of the 269 cm⁻¹ peak for a star-shaped MoTe₂ flake is shown in Fig. 6.1.1.2d. The map shows a slight intensity variation among the three segments of the flake (we confirmed that the peak position was fixed at 269 cm⁻¹ over the entire flake). This suggests that the different arms of the star are each monolayer 1T'-MoTe₂ but with different crystal orientations. The 188 cm⁻¹ intensity map (Fig. 6.1.1.2d)

reveals that this peak is active across the entire flake, which argues against a contamination effect and raises the question of which yet unidentified vibrational mode is associated with the peak at 188 cm^{-1} . AFM reveals a sample height of $\sim 0.8\text{ nm}$, as expected for monolayer MoTe_2 (Fig. 6.1.1.2e).^{426,431} The AFM image also shows the growth of a partial second layer of MoTe_2 near the center of the flake.

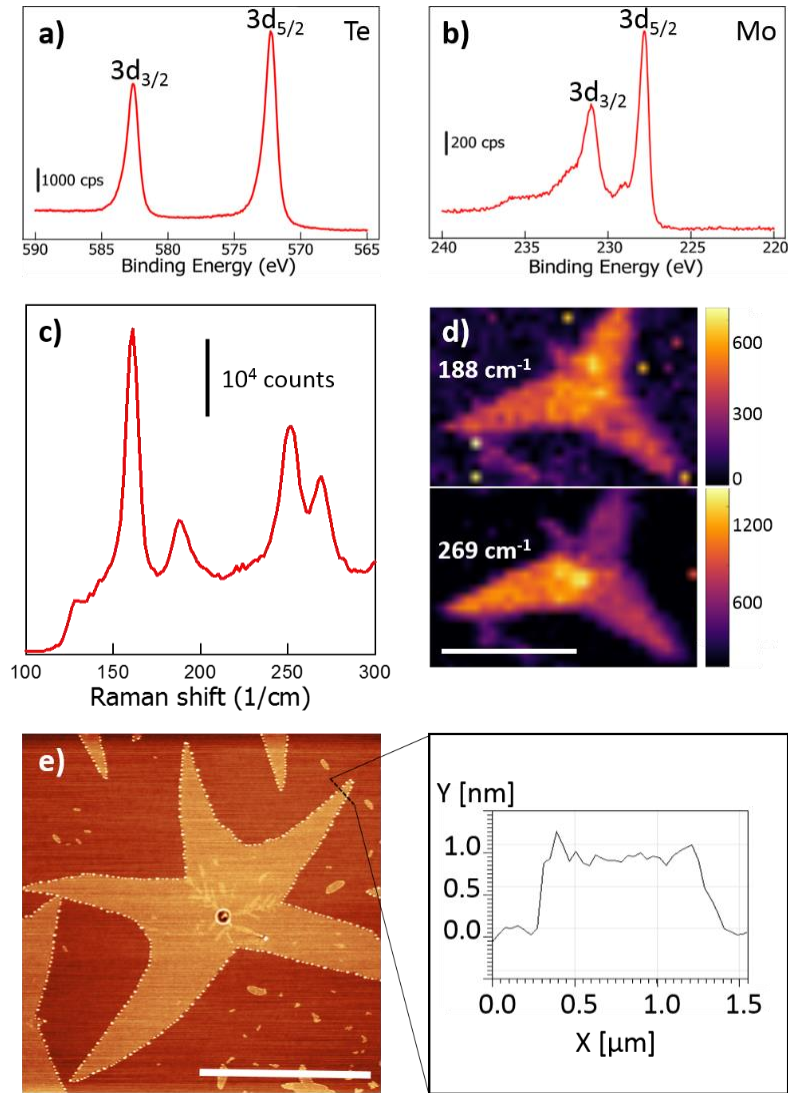


Figure 6.1.1.2. Characterization of MoTe_2 flakes by XPS and Raman spectroscopy. a) XPS spectrum showing $3d_{3/2}$ and $3d_{5/2}$ Te peaks. b) XPS spectrum showing $3d_{3/2}$ and $3d_{5/2}$ Mo peaks. c) Raman spectrum of MoTe_2 flake is consistent with monolayer $1T'$ - MoTe_2 . d) Raman mapping of the amplitude of the 188 and 269 cm^{-1} peaks. The scale bar is $10\text{ }\mu\text{m}$. e) AFM topographic image reveals

a clean surface with minimal bilayer content. The scale bar is 10 μm . The line scan indicates a thickness of 0.8 nm, as expected for monolayer material.

To transfer CVD-grown monolayer MoTe_2 flakes onto a new substrate, a procedure was developed where the SiO_2 interface layer was etched using hydrofluoric acid (HF). In this process, the sample is first spin coated with C4 PMMA (Microchem) at 3000 RPM for 60 seconds, and then the sample is carefully floated on top of a dilute HF solution (1:50 in DI water). The sample is gently pressed down so the solution covers the edges of the SiO_2 without covering the PMMA. The HF solution etches the SiO_2 beneath the MoTe_2 flakes until the PMMA/ MoTe_2 stack is released and floats on the solution. The sample is lifted using a polyethylene terephthalate (PET) sheet and transferred to multiple DI water baths to clean the sample. Finally the sample is picked up onto the desired substrate. The substrate is then put into an acetone bath for 3 minutes to dissolve the PMMA, rinsed in isopropanol for 1 minute, and dried using a N_2 gun.

The crystal structure of as-grown MoTe_2 flakes was determined using selected area electron diffraction (SAED) after the sample was transferred onto a holey-carbon TEM grid (Fig. 6.1.1.3a-b). A dark-field TEM (DF-TEM) image of rectangular MoTe_2 flake is shown in Fig. 6.1.1.3a (200 kV accelerating voltage); the inset shows the associated diffraction pattern. Both bulk and monolayer $1\text{T}'$ MoTe_2 belong to space group $\text{P}2_1/\text{m}$ (No. 11). The rectangular reciprocal lattice is characteristic of the $1\text{T}'$ phase, in contrast to the at least 3 fold symmetry expected for the 2H and 1T phases. The 2_1 screw axis is parallel to \mathbf{b} vector (Te zigzag chain direction) in $1\text{T}'$ - MoTe_2 , so the odd $(0k0)$ diffraction spots are forbidden, consistent with the observed SAED pattern. The SAED pattern shows excellent agreement with the simulated monolayer SAED pattern

(Supplementary Fig. 3). A selected-area aperture of effective size $\sim 1 \mu\text{m}$ was used, so the SAED pattern confirms that the MoTe_2 flakes are in the $1\text{T}'$ phase and shows the long-range order of the $1\text{T}'$ lattice. The $(0k0)$ axis in the SAED pattern (purple line in inset) corresponds to the \mathbf{b} vector direction in the real-space DF-TEM image. Therefore, the lattice is oriented such that the \mathbf{b} vector direction points along the long-axis of the rectangular flake. This was confirmed by lattice resolution images at higher magnifications and was consistent for each observed flake. To our knowledge, this is the first demonstration of oriented crystallite growth in this system.

In addition to single-crystal, rectangular monolayer MoTe_2 flakes, the growth procedure also produced polycrystalline flakes. The structure of one flake was analyzed by DF-TEM, where an aperture is used to select certain diffracted beams for image formation,^{95,432} and a tilt boundary with a crystal lattice rotation of $121.7^\circ \pm 0.5^\circ$ was identified, as shown in Supplementary Fig. 4. The measured boundary rotation, the SAED pattern at the boundary between the legs of the flake (Supplementary Fig. 4 center inset), and the DF-TEM image of the boundary indicate that the boundary lies along the (110) plane of one crystallite and the $(\bar{1}\bar{1}0)$ plane of the other, although grain boundaries were not imaged with atomic resolution. This particular rotation pattern was consistently observed in many polycrystalline flakes, implying that the legs of the polycrystalline flakes were grown at the same time and are not collisions of randomly oriented grains.

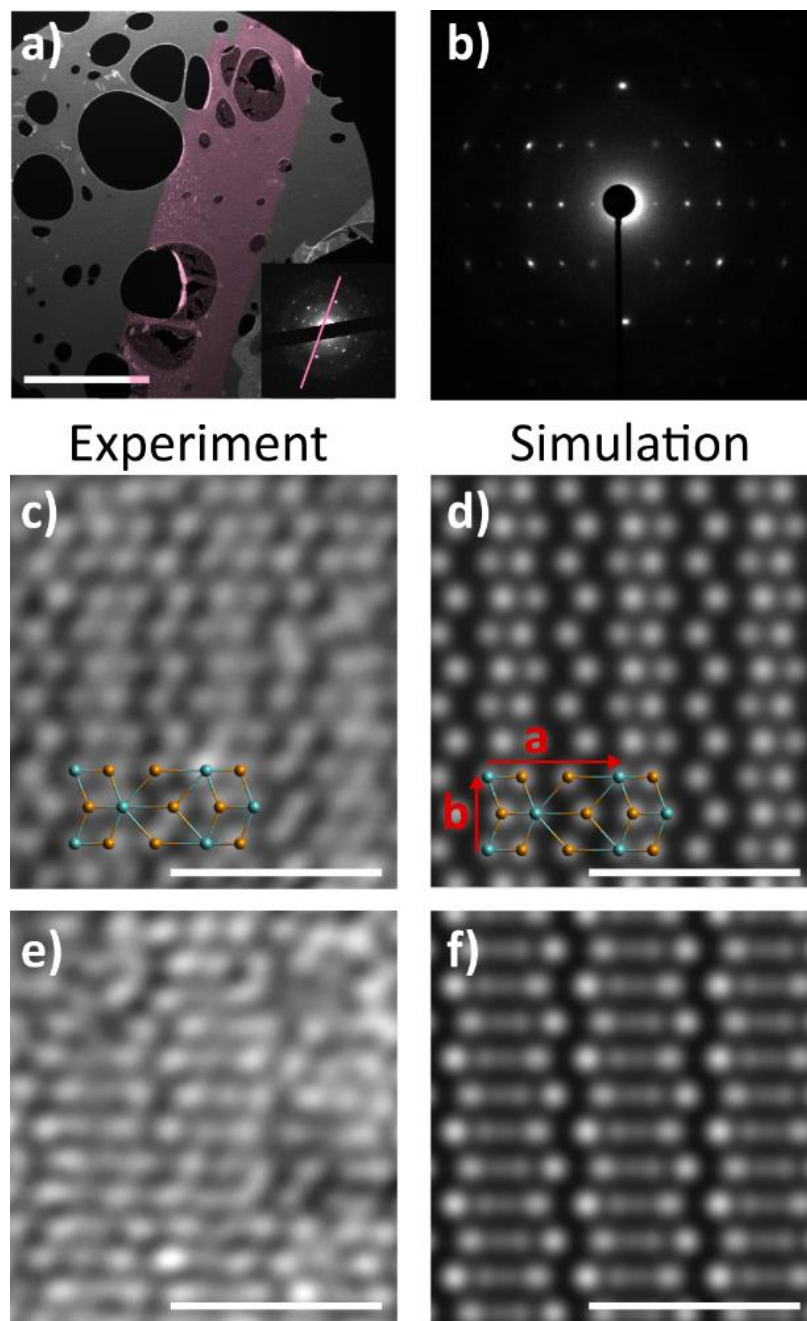


Figure 6.1.1.3. MoTe₂ TEM characterization. a) DF-TEM image (200 keV) of a single-crystal, rectangular MoTe₂ flake on a holey-carbon TEM grid. The scale bar is 2 μm . Inset: SAED pattern of the MoTe₂ flake at 200 kV, revealing a single crystal in the 1T' phase. The pink line indicates the direction of the (0k0) diffraction spots, corresponding to the b vector direction (Te zigzag chain direction) in the real-space, dark-field image. b) SAED pattern of a MoTe₂ flake at 80 kV, along the [001] zone axis (perpendicular to the monolayer flake), revealing a single crystal in the 1T' phase. c) High-angle annular dark field (HAADF) image taken with AC STEM revealing Mo and Te atoms in the monolayer 1T' configuration. The schematic overlay shows the rectangular unit cell and the location of the Mo (blue) and Te (orange) atoms. The scale bar is 1 nm. d) Multislice HAADF simulation of monolayer 1T'-MoTe₂, using lattice parameters $a = 6.33 \text{ \AA}$ and $b = 3.47 \text{ \AA}$.⁴³³ e) HAADF

image of a bilayer region. The scale bar is 1 nm. f) Multislice HAADF simulation of bilayer 1T'-MoTe₂.

To image the atomic structure of 1T'-MoTe₂, aberration-corrected, high-angle annular dark field (HAADF) images were taken in a JEOL 200CF (Fig. 6.1.1.3c and e) with a CEOS corrector for the STEM probe. The AC STEM was operated at 80 kV to reduce beam-induced displacements ('knock-on' damage), although damage occurred, as expected given the weak bonding in MoTe₂. The images were post-processed with a low-pass filter to remove high-frequency noise. The HAADF image in Fig. 6.1.1.3c clearly reveals the atomic structure expected for monolayer 1T'-MoTe₂, where atoms in one of the unit cells are labeled for comparison. The HAADF image shows excellent agreement with the monolayer ball-stick model and a multislice HAADF simulation⁴³⁴ of monolayer 1T'-MoTe₂ (Fig. 6.1.1.3d). The lattice constants are found to be $a = 6.34 \text{ \AA}$ and $b = 3.42 \text{ \AA}$, in excellent agreement with previous reports.^{61,433} In the images the Te atoms are slightly brighter than the Mo atoms, as expected since the HAADF intensity is proportional to the square of the atomic number for monolayer samples. The majority of each flake was monolayer, but small (~10 x 10 nm) double-layer regions were also found, as shown in Fig. 6.1.1.3e. The bi-layer HAADF image is in excellent agreement with the simulated image (Fig. 6.1.1.3f). The brightness in the double-layer regions is roughly twice that of the monolayer regions, in agreement with simulated images of mono and bi-layer regions (Supplementary Fig. 5). To our knowledge, this is the first report of atomic resolution images of monolayer 1T'-MoTe₂.

To further study the structural stability of monolayer 1T'-MoTe₂ on a SiO₂ substrate, we performed theoretical work using first-principles calculations. We first find

that the 1T'-MoTe₂ layer adheres to the SiO₂ substrate with binding energy of 65 meV per unit cell of MoTe₂, which is a typical van der Waals-type interaction. We also find that the energy barrier between 1T' and 2H increases from 1.73 eV/unit cell to 1.85 eV/unit cell on the SiO₂ substrate (Fig. 6.1.1.4). The 2H phase is slightly more stable on SiO₂, but the energy barrier between 1T' and 2H is similar with and without a substrate. So while a phase transformation from 1T' to 2H is possible if the right amount of energy is brought to the system, observing a phase transformation to 1T is unlikely as it would quickly revert back to the 1T' phase. Thus, the SiO₂ substrate is a good platform to study the 1T' phase of monolayer MoTe₂ and these computations support our hypothesis that monolayer MoTe₂ was grown directly in the 1T' phase.

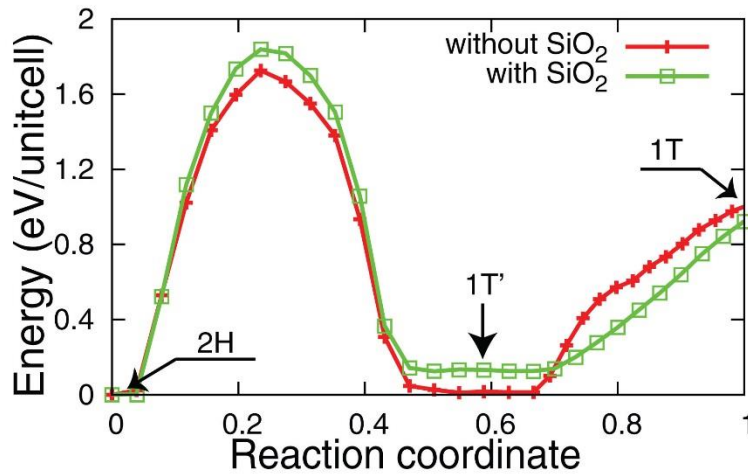


Figure 6.1.1.4. Stability computation using first-principles. Structural stability of monolayer transition metal MoTe₂ with and without a SiO₂ substrate.

For electrical measurements of monolayer MoTe₂, samples were transferred onto a 275nm SiO₂/Si substrate with pre-patterned set of Au electrodes made by electron beam lithography. In order to preferentially probe the properties of the material rather than grain boundaries, care was taken to create the sample from a region dominated by

rectangular single-crystal flakes rather than polycrystalline material. To minimize sample exposure to air, the transfer process was begun within minutes after growth and completed within 15-20 minutes. Each device contained five areas of interdigitated source and drain fingers (Fig. 6.1.1.5a). To ensure that multiple MoTe₂ flakes bridge the electrode pairs, the electrode areas are separated laterally to sample a large growth area (~0.5 mm x 0.5 mm), and the source-drain separation is 5 μm, smaller than the typical size of MoTe₂ flakes (10-20 μm). Two devices were measured to determine the effect of temperature and applied magnetic fields on the electrical properties.

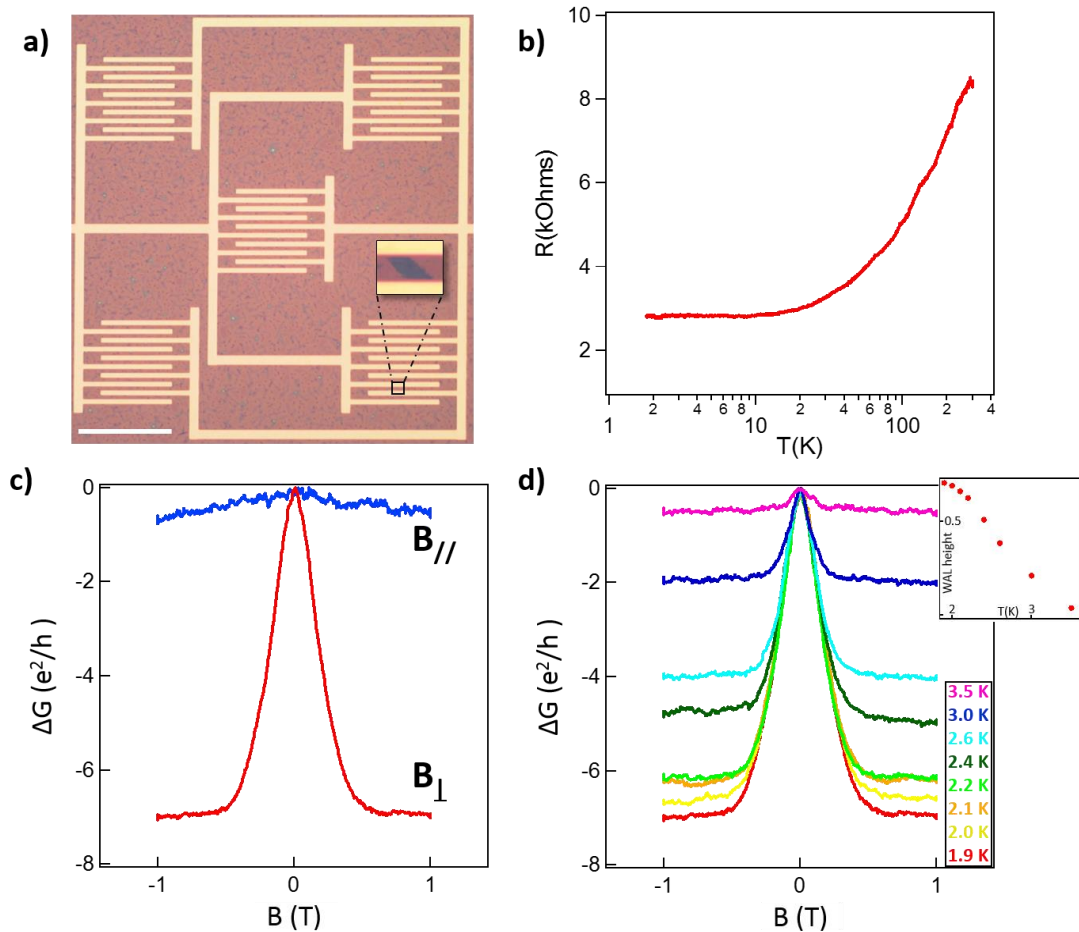


Figure 6.1.1.5. Electrical measurements of monolayer MoTe₂-1T'. a) Optical image of a device with MoTe₂ flakes contacted by electrodes. The scale bar is 100 μm. Inset: Magnified view of a flake

spanning the electrodes (Image contrast has been enhanced). b) Resistance versus temperature for monolayer 1T'-MoTe₂. c) Magnetoconductance for applied fields parallel (blue) and perpendicular (red) to the sample at T = 1.9 K. d) Magnetoconductance for temperatures from 1.9 K to 3.5 K showing that the weak antilocalization feature disappears at higher temperatures. Inset: WAL amplitude as a function of temperature.

The electrical resistance was monitored as the samples were cooled from 300 K to 1.9 K. One sample had decreasing resistance with decreasing temperature, clearly demonstrating metallic behavior (Fig. 6.1.1.5b). The resistance of the second sample generally increased with decreasing temperature, but nevertheless exhibited metallic behavior at low temperature as indicated by a positive slope of the reduced activation energy $-d(\ln R)/d(\ln T)$ on a log-log plot versus temperature (Supplementary Fig. 6b). Measurements of the anisotropic magnetoconductance at various temperatures were *quantitatively* similar in both shape and absolute size for both samples (Supplementary Fig. 6d), strongly suggesting that the difference in temperature-dependent resistance arises from a series contact resistance. At low temperature, both samples exhibited a weak anti-localization (WAL) cusp-like feature at zero magnetic field (Fig. 6.1.1.5c), which diminished with increasing temperature and could not be resolved for T > ~4K (Fig. 6.1.1.5d). The WAL effect is a signature of a metallic state in the presence of strong spin-orbit coupling^{427,435,436} and can be associated with either bulk or topological surface states. A similar effect was recently reported for few-layer samples of WTe₂ produced by mechanical exfoliation.⁶⁵ We varied the applied field angle in order to examine the residual isotropic magnetoconductance. The WAL cusp disappears when the field is applied parallel to the plane of the material (Fig. 6.1.1.5c), confirming the 2D nature of the WAL effect. Similar temperature and magnetic field dependence of the WAL cusp has been observed in topological insulator materials,^{65,427,437-440} and the data demonstrate

that these materials possess strong electronic spin-orbit effects that are essential for the emergence of nontrivial topological electronic states.

We report the growth of monolayer, single-crystal 1T'-MoTe₂ over large areas by chemical vapor deposition. XPS measurements confirm the expected stoichiometry for MoTe₂. AFM, Raman, TEM and ACSTEM measurements convincingly establish that the MoTe₂ material is of monolayer thickness, in the 1T' phase, and single crystal. We were able to orient the crystalline axes based on the shape of rectangular crystallites, and we identified a clear preferential crystal growth direction for the MoTe₂ flakes along the **b** vector axis. Low-temperature magnetoconductance measurements confirm the presence of a WAL cusp in monolayer MoTe₂. Thus, the structural and electronic ingredients necessary to realize topological surface states exist within this material. This advance in CVD growth and microscopic analysis paves the way for more detailed exploration of monolayer 1T'-MoTe₂, including its potential topological insulator properties and implementation in novel switching and sensor devices.

Methods

XPS. The chemistry of the near-surface region was investigated by XPS using a customized XPS spectrometer (VG Scienta AB, Uppsala, Sweden).⁴⁴¹ XPS analyses were performed using a monochromatic Al K α source (photon energy 1486.6 eV). The residual pressure in the analysis chamber was less than 1×10^{-8} Torr. The spectrometer was calibrated according to ISO 15472:2001 with an accuracy of ± 0.05 eV. Survey and high-

resolution spectra were acquired in constant-analyzer-energy mode with the pass energies of 200 and 100 eV, respectively. The spectra were processed using CasaXPS software (v.2.3.16, Casa Software Ltd., Wilmslow, Cheshire, U.K.). Background subtraction was performed using the Shirley–Sherwood method. The quantitative evaluation of the XPS data was based on integrating the intensity of the Mo 3d_{5/2} and Te 3d_{5/2} peaks by taking the atomic sensitivity factors for those signals into account. The atomic sensitivity factors used were 1.66 for the Mo 3d_{5/2} peak and 5.4 for the Te 3d_{5/2} peak.⁴⁴² The reference energies for Mo 3d_{5/2} and the Te 3d_{5/2} peaks are 227.7 and 572.1 eV, respectively.

ACSTEM. For AC-TEM imaging, MoTe₂ flakes were transferred onto a holey-carbon TEM grid using a PMMA-assisted transfer. AC-STEM of suspended MoTe₂ flakes was performed with a JEOL ARM 200CF equipped with a CEOS corrector. The TEM was operated at 80 kV to reduce knock-on damage. Images were acquired with a high-angle annular dark field detector. A low-pass filter was applied to the images to reduce noise. Selected-area electron diffraction patterns were acquired in TEM mode using a selected-area aperture with an effective size at the sample of ~1 μm.

HAADF simulations. QSTEM⁴³⁴ was used to perform multislice HAADF-STEM simulations. Microscope parameters for the 80 kV JEOL ARM 200CF were used for the simulation. These include C_s = 635 nm and C₅ = -55 μm. Other parameters used were C_c = 1 mm, dE = 0.5 eV, convergence angle = 20 mrad, HAADF detector inner angle = 70 mrad, HAADF detector outer angle = 200 mrad, defocus = -2 nm, brightness = 5 × 10⁸ A/cm²sr, and a dwell time of 1 μs. For each simulation, the simulation window size used was one unit cell, 6.33 Å × 3.469 Å with sampling 20 pix × 20 pix.

Structural Stability Simulations. To access the influence of SiO₂ on the stability of MoTe₂ single layer in 1T' phase, we performed first-principles calculations based on density functional theory (DFT). We use the Perdew-Burke-Ernzerhof-type generalized gradient approximation⁴⁴³ as implemented in the Quantum Espresso package.⁴⁴⁴ Norm-conserving, optimized, designed nonlocal pseudopotentials are generated using the Opium package.^{445,446} The energy barriers of MoTe₂ were calculated employing the nudged elastic band (NEB) approach as found in the Quantum Espresso package. The SiO₂ substrate was modeled using a slab geometry with four unit cells along (100) and a 3x1 supercell along (010) and (001) directions, respectively. The outer oxide atoms were passivated with hydrogen atoms. A 2x2 unitcell of MoTe₂ of 1T' phase was placed on a SiO₂ substrate, which induces a negligible strain on MoTe₂ and 15 % and 7 % artificial compressive strain on the SiO₂ substrate. The structure of substrate is fully optimized without MoTe₂ under strain then used throughout the energy barrier calculations of MoTe₂/SiO₂ system. The van der Waals interaction is described based on the semi-empirical dispersion-correction DFT (DFT-D) method.⁴⁴⁷

Electrical Measurements. Samples were loaded onto a rotating insert in a Quantum Design Physical Property Measurement System (PPMS). Temperature and magnetic field dependent electrical measurements were taken using a 1.0 mV source-drain bias using a Keithley 237 Source-Measure Unit. The angle of the magnetic field was calibrated first visually and then trimmed by nulling the WAL effect to determine the angle for B_{||}.

6.1.2 Intrinsic phonon bands in high quality monolayer T' molybdenum ditelluride

The results presented in this section have also appeared in the publication “Intrinsic phonon bands in high quality monolayer T' molybdenum ditelluride”, Shao-Yu Chen, Carl H. Naylor, Thomas Goldstein, A.T. Charlie Johnson, and Jun Yan, ACS Nano, 2017, 11 (1) pp 814–820.

Abstract

The topologically nontrivial and chemically functional distorted octahedral (T') transition metal dichalcogenides (TMDCs) are a type of layered semimetal that has attracted significant recent attention. However, the properties of monolayer (1L) T'-TMDC, a fundamental unit of system, is still largely unknown due to rapid sample degradation in air. Here we report that well-protected 1L CVD T'-MoTe₂ exhibits sharp and robust intrinsic Raman bands, with intensities about one order of magnitude stronger than those from bulk T'-MoTe₂. The high quality samples enabled us to reveal for the first time the set of all nine even-parity zone-center optical phonons, providing reliable fingerprints for the previously elusive crystal. By performing light polarization and crystal orientation resolved scattering analysis, we can effectively distinguish the intrinsic modes from Te-metalloid-like modes A (~122 cm⁻¹) and B (~141 cm⁻¹) which are related to the sample degradation. Our studies offer a powerful non-destructive method for assessing sample quality

and for monitoring sample degradation *in situ*, representing an important advance in understanding the fundamental properties of 1L- T' -TMDCs.

Molybdenum and tungsten based transition metal dichalcogenides (TMDCs) are a class of layered materials hosting versatile phases and polymorphs that exhibit fascinating physical, chemical and topological properties.^{35,61,66,88,423} Hexagonal (H) TMDCs such as $(\text{Mo,W})(\text{S,Se})_2$ are semiconductors with bandgaps ranging from visible to infrared, and distorted octahedral (T') TMDCs such as WTe_2 and MoTe_2 are semimetals that possess nontrivial electronic band topologies.^{61,66,448} As a layered material system these compounds and their intercalated products are being actively investigated for solid lubricant, catalyst, and super-capacitor applications.^{420,449–451} In the fundamental monolayer (1L) limit, H -TMDCs exhibit direct bandgap with coupled spin and valley physics,⁴⁵² and have been widely investigated for electrical, optoelectronic and valleytronic applications.^{42,44,453} In contrast 1L distorted octahedral (T') TMDCs, predicted to be two dimensional (2D) topological insulators,⁶¹ are much less studied experimentally.

It is of both fundamental and practical interest to develop a thorough understanding of T' -TMDC at the monolayer level. Since the prediction of the quantum spin Hall (QSH) effect in T' monolayer, several works have studied thin films^{429,454} (~10 nm thick) of T' - MoTe_2 and T' - WTe_2 to assess if the QSH gap is positive or negative, which is important for developing topological quantum computing devices using this system. Monolayer T' -TMDC can serve as a bottom-up starting point for understanding

multi-layered and intercalated T' -TMDCs, which have much higher electrical conductivity than their H counterparts, and could be more useful for solid state battery electrodes, electrochemical capacitors, and hydrogen evolution reactions.^{449,451}

As it turns out 1L- T' -TMDC is relatively challenging to work with due to rapid sample degradation in air.^{455,456} For this reason, several recent optical and electrical studies of the material system^{429,454,456} are limited to multi-layers; and despite recent efforts,^{150,151,457} a thorough Raman characterization of 1L- T' -TMDC is still lacking. Also, the sample degradation has led to confusion in distinguishing Raman bands intrinsic to T' -TMDC from those due to degradation products.^{424,458} In this paper, we show that well-protected 1L- T' -MoTe₂ exhibit sharp and robust intrinsic Raman bands, with intensities about one order of magnitude stronger than those from bulk T' -MoTe₂. The high quality samples enabled us to reveal for the first time the set of *all* nine even-parity zone-center optical phonons, representing a complete Raman characterization of a 1L- T' -TMDC. We also discovered that less well protected samples show coexistence of phonon spectra due to T' -MoTe₂ and its degradation products; the two types of Raman features exhibit drastically different symmetry properties, and can be unambiguously distinguished by light-polarization and crystal-angle resolved Raman tensor analysis. These experimental findings provide key insights into fundamental lattice dynamics of the crystal, and offer a powerful non-destructive means for assessing sample quality and for monitoring sample degradation *in situ*, paving way to topological transport investigations and to further understanding of the chemical and physical properties of T' -TMDCs. Our studies also clear up recent confusions on investigations of strain⁴⁵⁸ and laser⁴²⁴ induced H to T' phase

transition in MoTe₂ crystals, and show that care needs to be taken in distinguishing Raman features due to the phase transition and those due to sample degradation.

Results and Discussion

The 1L-*T'*-MoTe₂ studied in this paper is grown by chemical vapor deposition (CVD) on 300 nm SiO₂/Si substrate. The growth is achieved at 700°C with rapid thermal quench (See Methods for more details).⁵⁹ Figure 1a shows the optical image of a typical sample. The CVD grown 1L-*T'*-MoTe₂ flakes have a bamboo-leaf like shape; this elongated shape reflects the underlying atomic scale in-plane anisotropy due to spontaneous formation of zigzag Mo atomic chains as illustrated in Figure 1e. The step-height from substrate to the monolayer is about 0.8 nm as shown by atomic force microscope (AFM) measurements in Figure 6.1.2.1b, which is consistent with the 0.7-0.8 nm per layer thickness from previous studies.⁴²⁶ The crystal grows preferentially along the zigzag chains, which we denote as the *a*-axis. This can be seen from the transmission electron microscope (TEM) diffraction pattern (Figure 6.1.2.1d) of a sample transferred onto a holey-carbon TEM grid (Figure 6.1.2.1c): the rectangular reciprocal lattice is in accord with the rectangular real space unit cell (light blue rectangle in Figure 6.1.2.1e), from which we determine the in-plane unit vector lengths of the crystal to be $a = 3.42 \text{ \AA}$ $b = 6.34 \text{ \AA}$. For later description of the lattice vibrations we also show in Figure 6.1.2.1e the position of a mirror symmetry plane in the crystal (red horizontal line, perpendicular to the zigzag Mo atomic chain).

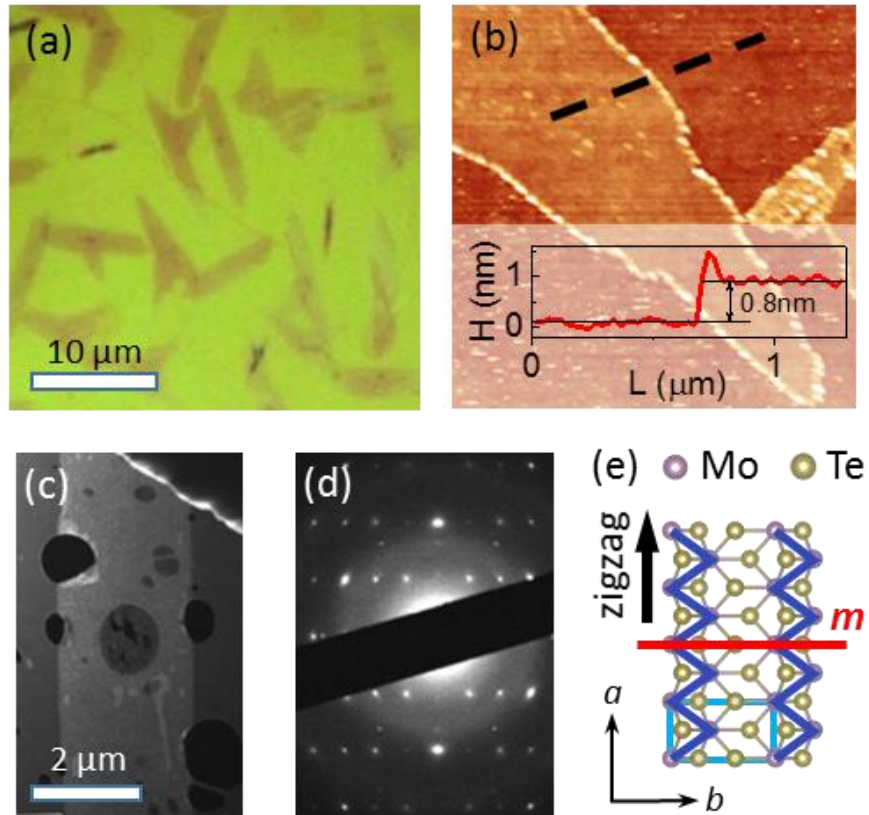


Figure 6.1.2.1. a) The optical microscope (OM) image of a typical sample. All bamboo-leaf like flakes on the image are 1L- T' -MoTe₂, and the small dark dots near center of the flakes are multilayer crystals. b) AFM image of a monolayer flake. The step height is 0.8 nm. c) Dark field TEM image of a 1L- T' -MoTe₂ flake transferred on top of holey carbon film. d) The selected-area electron diffraction image of a suspended 1L- T' -MoTe₂, exhibiting rectangular diffraction patterns. e) Schematic top view of the 1L- T' -MoTe₂ crystal. The a -axis is aligned with the zigzag direction. The Mo-Mo zigzag chains are highlighted by blue lines. The mirror plane which is perpendicular to zigzag chains is shown as a red line. The unit cell is denoted as a light-blue rectangle.

With the knowledge of the zigzag atomic chain direction, we proceed with Raman scattering measurements on the monolayer T' crystal, paying special attention to the angle between directions of the MoTe₂ a -axis and the light polarization. To protect the T' -MoTe₂, we cover the sample with CVD graphene (see Methods), whose Raman features⁴⁵⁹ have much higher energy than those in T' -MoTe₂. The sample is excited by a linearly polarized Nd:YAG laser at 532 nm, with the laser power kept below 200 μ W. We denote the angle between the incident light polarization and the crystal a -axis as θ (as

shown in Figure 6.1.2.2a), which can be continuously adjusted by rotating the laser polarization with a half waveplate. The scattered photons are directed through a set of half waveplate and linear polarizer in the collection path to select the co-linear (HH) or cross-linear (HV) component, which is subsequently dispersed by a triple spectrometer and detected with a liquid-nitrogen-cooled CCD camera.⁴⁶⁰ Throughout the light-polarization and crystal-angle resolved Raman measurements, the sample is mounted inside an optical cryostat pumped down to 3×10^{-6} torr.

Figure 6.1.2.2b compares typical room temperature spectra of 1L and bulk T' -MoTe₂ sample in the HH configuration at $\theta = 0^\circ$ using the same excitation power. The overall spectral shapes are similar below 200 cm^{-1} with the bulk Raman peaks slightly red-shifted due to interlayer coupling. Interestingly in contrast to studies of 1L- T' -WTe₂,^{150,151,457} the Raman peaks of our monolayer samples are intense and sharp, suggesting that our T' -MoTe₂ monolayers are of high crystalline quality.

In Figure 6.1.2.2c we selectively display the Raman spectra of 1L- T' -MoTe₂ in four different scattering configurations of HV and HH at $\theta = 0^\circ$ and 45° ; more detailed intensity angular dependences are plotted in Figure 6.1.2.3c. We observe in total nine zone-center optical phonons, including six ‘ m -modes’ (m^{85} , m^{113} , m^{128} , m^{164} , m^{253} and m^{270}) and three ‘ z -modes’ (z^{92} , z^{102} and z^{190}), where ‘ z ’ stands for the zigzag Mo atomic chain (black arrow in Figure 6.1.2.1e), and ‘ m ’ stands for the mirror plane perpendicular to the zigzag chain (red line in Figure 6.1.2.1e). The reason for this classification becomes clear in Figure 6.1.2.3 where we have plotted detailed angular dependence of Raman intensity in HH and HV together with the atomic displacements for corresponding

phonons. We observe that for the three ‘z-modes’ the vibrations are along the zigzag Mo atomic chain (a -axis), and that for the six ‘ m -modes’ the vibrations are in the mirror plane perpendicular to the zigzag chain direction (b - c plane).

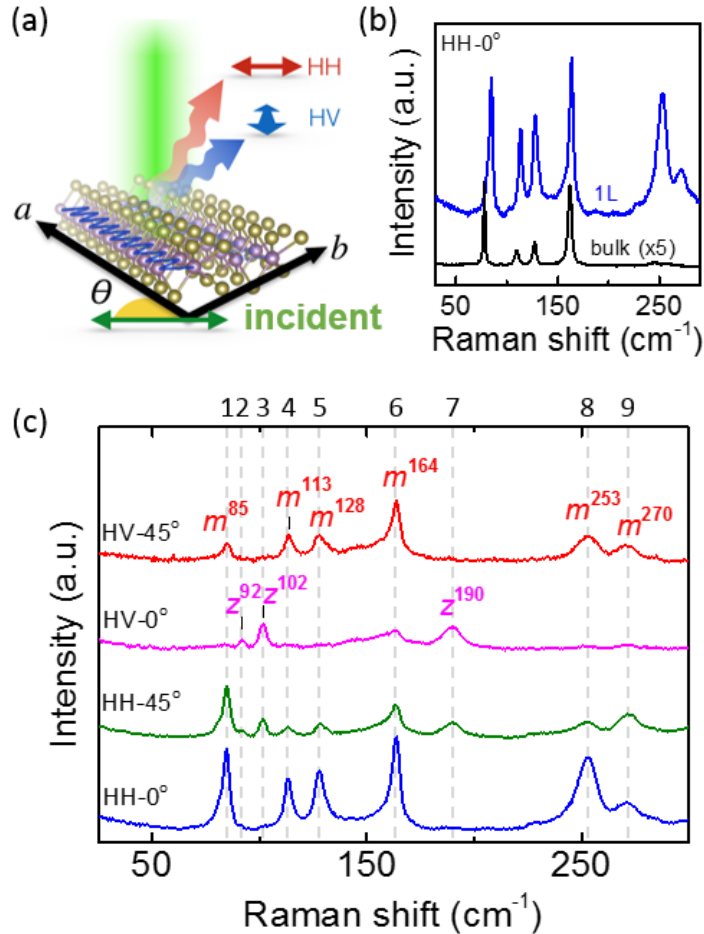


Figure 6.1.2.2. a) Schematics of light-polarization and crystal-orientation resolved Raman spectroscopy. The polarization of incident light (green arrow) is set at an angle θ with respect to the a -axis of the crystal. The scattered light is selectively collected in HH or HV configurations, corresponding to the detection of photons with co-linear or cross-linear polarization, respectively. b) Typical Raman spectra of 1L and bulk T' -MoTe₂ with $\theta = 0^\circ$ in HH configuration. c) The Raman spectra of 1L- T' -MoTe₂ detected with different combination of incident polarization angles and collection geometries. In HV configuration, the phonon modes are highly selective, showing 6 m -modes (m^{85} , m^{113} , m^{128} , m^{164} , m^{253} , m^{270}) at $\theta = 45^\circ$ and 3 z -modes (z^{92} , z^{102} , z^{190}) at $\theta = 0^\circ$.

The assignment and classification for the nine Raman bands can be understood from symmetry considerations. In Figure 6.1.2.3a we plot the top and side views of monolayer T' -MoTe₂ together with its unit cell and symmetry operations (the symbols are

consistent with the International Table for Crystallography).⁴⁶¹ The primitive unit cell, indicated as the shaded area, contains six atoms, resulting in 18 Brillouin zone center (Γ) phonons whose atomic displacements are illustrated in Figure 6.1.2.3c. Symmetry operations of the crystal include, in addition to translations, identity (E), inversion (i), mirror reflection (m), and a screw axis along the zigzag Mo chain (2^z_1) that form the C_{2h} group. Similar to the bulk T' -TMDC crystal with monoclinic stacking, 1L T' -MoTe₂ is centrosymmetric with its inversion centers inside the atomic layer (yellow dots in Figure 6.1.2.3a). For this reason, half of the 18 zone-center vibrations have even-parity and the other half have odd-parity. Since in crystals with inversion centers the even Raman-active and the odd infrared-active modes are mutually exclusive, the nine modes we observe are in fact, the maximum number of zone-center optical phonons that are allowed to appear in the Raman spectra.

Another important symmetry of 1L- T' -MoTe₂ is the mirror reflection operation (the mirrors are parallel to the b - c plane perpendicular to the zigzag direction; see red lines in Figure 6.1.2.1e and also Figure 6.1.2.3a). This mirror plane operation is shared by many T' -TMDC polytypes⁴⁶² and thus provides a generic way to categorize phonons as: m -modes, atomic vibrations in the mirror plane; and z -modes, atomic vibrations perpendicular to the mirror plane along the zigzag atomic chain. Because vibrations in a plane have twice degrees of freedom as compared with vibrations along a line, there are 12 m -modes and 6 z -modes among the 18 zone center phonons in 1L- T' -MoTe₂. Taking into account the inversion symmetry as discussed above, half of m - and half of z -modes have even parity, while the other half have odd parity. As a result, in monolayer T' -

MoTe₂, there are 3 Raman active z -modes and 6 Raman active m -modes. Our spectra shown in the Figure 6.1.2.2c display all 9 different modes, consistent with symmetry analysis and representing a complete Raman characterization of the zone-center optical phonons.

The mode assignment is further substantiated by the angular dependence of Raman intensity which is sensitive to the symmetry of phonon modes. The C_{2h} group has four irreducible representations (see Figure 6.1.2.3b) and the zone-center phonon representations are given by $3A_u + 6B_u + 6A_g + 3B_g$. Raman active z -modes are odd under m operation ($m = -1$) and are even under inversion operation ($i = 1$), resulting in the symmetry B_g . Raman active m -modes are even under both mirror reflection and inversion operation, resulting in the symmetry A_g . The theoretical angular dependence of Raman-active mode intensity is given by $I = A |\langle \epsilon_i | R^T \cdot \mathfrak{R} \cdot R | \epsilon_o \rangle|^2$, where A is a constant, ϵ_i and ϵ_o are polarizations of the incident and outgoing light respectively, \mathfrak{R} is the effective

Raman tensor linked to different symmetry (for m -modes $\mathfrak{R}_{A_g} = \begin{bmatrix} d & 0 & f \\ 0 & e & 0 \\ f & 0 & h \end{bmatrix}$, and for z -

modes $\mathfrak{R}_{B_g} = \begin{bmatrix} 0 & g & 0 \\ g & 0 & j \\ 0 & j & 0 \end{bmatrix}$),⁴⁶³ R is the in-plane (x - y plane) rotation matrix to determine

the angle between light polarization and a -axis given by

$$R = R_z = \begin{bmatrix} \cos(\theta) & -\sin(\theta) & 0 \\ \sin(\theta) & \cos(\theta) & 0 \\ 0 & 0 & 1 \end{bmatrix}. \text{ We let } \epsilon_i = \begin{bmatrix} 1 \\ 0 \\ 0 \end{bmatrix}, \text{ then } \epsilon_o \text{ equals } \begin{bmatrix} 0 \\ 1 \\ 0 \end{bmatrix} \text{ in HV and } \begin{bmatrix} 1 \\ 0 \\ 0 \end{bmatrix}$$

in HH. It is then straightforward to calculate the Raman intensity angular dependence for the z and m modes: $I_{HV}^z(\theta) \propto \cos^2(2\theta)$, $I_{HH}^z(\theta) \propto \sin^2(2\theta)$, $I_{HV}^m(\theta) \propto \sin^2(2\theta)$, and

$I_{HH}^m(\theta) \propto |d \cos^2\theta + e \sin^2\theta|^2$. This explains why the three z -modes in Figure 6.1.2.3c have the same angular dependence, while the six m -modes have the same angular dependence in HV but not in HH, since the latter depends on the phase difference between d and e in the effective Raman tensor \mathfrak{R}_{A_g} which are different for different lattice vibrations, and exhibits 2-fold, instead of 4-fold, symmetric patterns, reflecting the anisotropic phonon-specific interactions of T' -TMDC crystal.^{462,464,465} We note that the observed angular dependences here in the monolayer are exactly the same as those for the z -modes and m -modes in bulk T' -TMDC with either monoclinic or orthorhombic stacking,⁴⁶² attesting our previous statement that this classification of lattice vibrations in T' -TMDC crystals is very general.

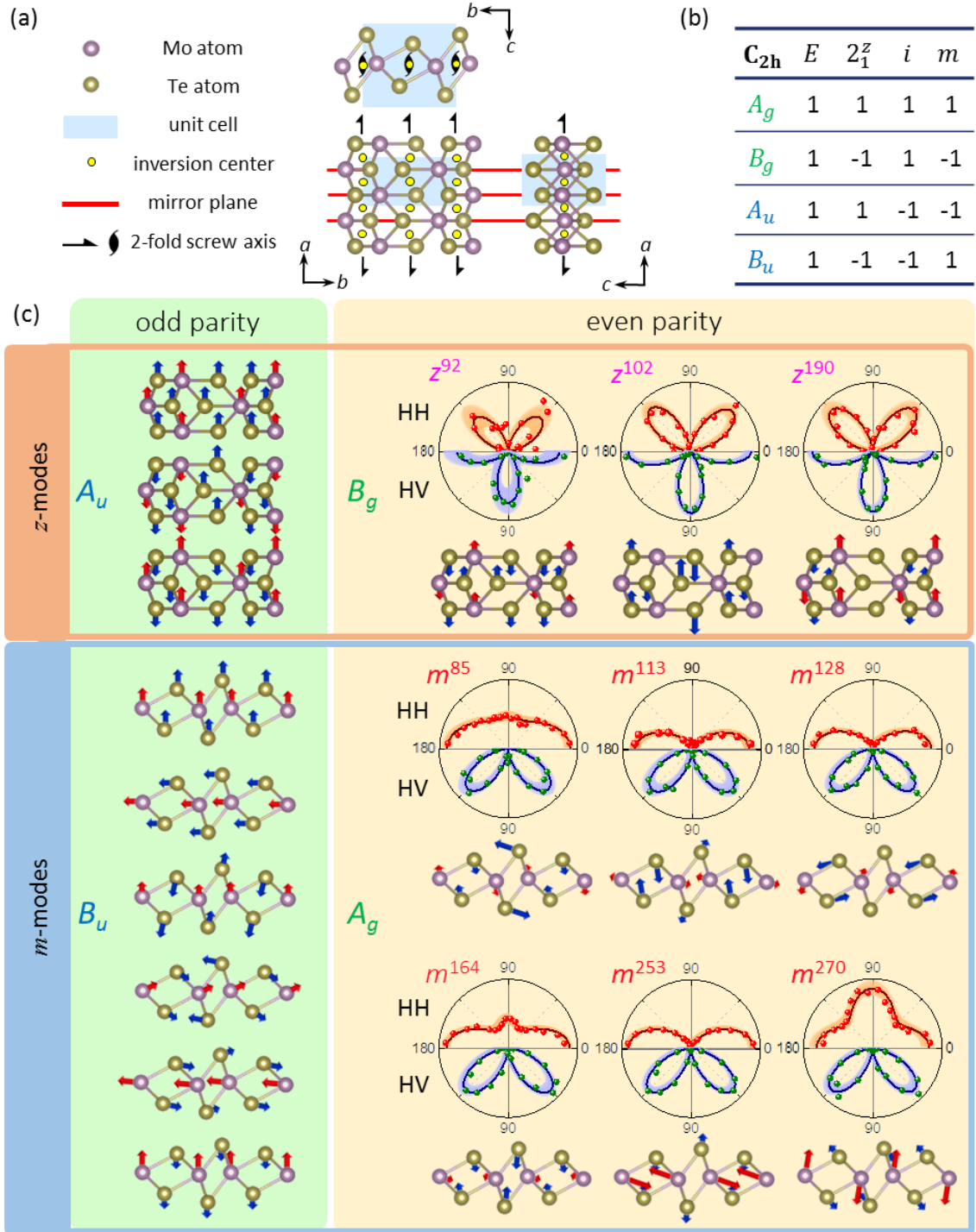


Figure 6.1.2.3. a) Top and side views of 1L- T' -MoTe₂ atomic arrangement. The unit cell and the symmetry operations are illustrated on top of the schematic drawings. b) Character table of the C_{2h} group. c) The schematics of all zone-center normal modes categorized into 4 groups with different symmetry: z -modes with odd parity belong to A_u symmetry; z -modes with even parity belong to B_g symmetry; m -modes with odd parity belong to B_u symmetry; and m -modes with even parity belong to A_g symmetry. The intensity angular dependences of the 9 Raman-active modes are plotted above the

corresponding lattice vibrations. The FWHM of each mode is included in the parentheses beside angular patterns.

The Raman data in Figures 6.1.2.2 & 6.1.2.3 are taken on flakes with the best quality. We have found that there is a correlation between optical contrast and sample quality: as can be seen in Figure 6.1.2.1a, the atomic flakes on the Si/SiO₂ substrate have similar shape but different darkness, and in general darker samples are of better quality. The variations of optical contrast and sample quality in certain areas on the silicon chip are likely due to non-uniform passivation from either water residue left during the transfer process (see Methods) or incomplete protection from CVD graphene that we use to cover the *T'*-MoTe₂ sample. There could be voids and cracks in the CVD graphene that were either innate from growth or created during the transfer process. In Figure 6.1.2.4 we show typical Raman spectra of four flakes with different optical contrast. Sample S1 is has ‘good’ contrast and the Raman features are similar to the data in Figure 6.1.2.2, indicating that it is well passivated; sample S4 is poorly passivated and has ‘poor’ contrast whose 1L-*T'*-MoTe₂ Raman features are almost gone, and instead, two intense new peaks (A to B) between 100 and 150 cm⁻¹ show up; meanwhile samples S2 and S3 are in-between with S2 displaying coexistence of Raman features from 1L-*T'*-MoTe₂ and from sample degradation. We note that our observation of the correlation between optical contrast and sample degradation is consistent with other investigations of air sensitive 2D materials in literature.^{457,466,467}

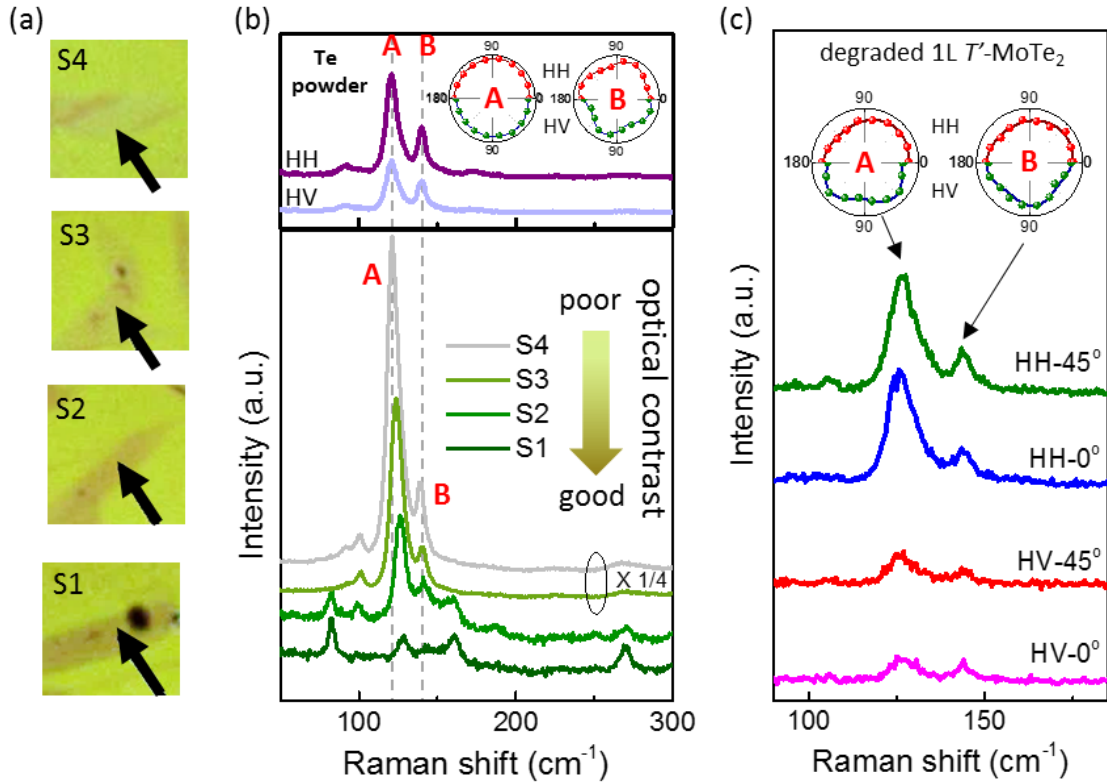


Figure 6.1.2.4. a) OM images of selected 1L- T' -MoTe₂ with different optical contrast: S1 to S4 from good to poor contrast. The arrows point to the positions where Raman spectra were collected. b) Lower panel: the Raman spectra for samples S1 to S4. The spectra are shifted vertically for clarity. The Raman spectra from Te powder are plotted for comparison in the upper panel. Insets show detailed angular dependence of Raman intensity in HH and HV for two prominent peaks A_1 and E of Te powder. c) The Raman spectra of the sample with poor contrast in HH or HV configuration with $\theta = 0^\circ$ and 45° . The angular dependences of intensity for peaks A and B of degraded 1L- T' -MoTe₂ are shown in the inset.

To understand the origin of these new peaks, we measured Raman spectra of tellurium powder (Sigma-Aldrich 99.997%); see the upper panel of Figure 6.1.2.4b. The Raman spectra of Te powder show two prominent modes A_1 and E (following the naming convention in crystalline Te),^{468,469} corresponding to the Te breathing vibration in the basal plane and asymmetric stretching vibration along the c -axis, respectively. These are similar to A and B modes we observed in sample S4, suggesting that Te metalloids are likely a by-product of MoTe₂ degradation. Note that there are some small energy differences between the Raman peaks in Te powder and degraded MoTe₂: peak A has

slightly higher energy in degraded MoTe₂ and redshifts from 128 cm⁻¹ in S2 to 122 cm⁻¹ in S4, approaching the 121 cm⁻¹ peak in Te powder, suggesting different Te cluster sizes in S2 to S4.^{470,471} We also note that this peak could overlap with the m¹²⁸ mode in 1L-*T'*-MoTe₂; however the former is typically much more intense. Meanwhile the Te-like side peak B (~142 cm⁻¹) is useful for monitoring sample quality, since 1L-*T'*-MoTe₂ is spectrally clean between 130 and 155 cm⁻¹.

To further confirm that the Raman peaks A and B are indeed due to sample degradation we collected polarization and angular dependent data similar to those in Figures 6.1.2.2&3. As can be seen in Figure 6.1.2.4c, the spectra taken on the degraded sample at $\theta = 0^\circ$ and 45° are almost identical in either HH or HV, in drastic contrast to intrinsic 1L-*T'*-MoTe₂ peaks in Fig. 6.1.2.2c. The detailed angular dependence of peaks A and B are shown in the top insets of Figure 4c; these are to be compared with the angular dependence of the *z*- and *m*-modes in Figure 6.1.2.3c, confirming that peaks A and B have very different symmetry properties. We also performed similar polarization-resolved measurements on the *A*₁ and *E* modes of Te powder as shown in the inset of the top panel in Figure 6.1.2.4b, which reflect the polycrystalline nature of the Te powder. The angular dependences of the two are similar, substantiating our speculation that the new peaks A and B in degraded *T'*-MoTe₂ are due to chemical reactions that generate clusters of Te metalloid.

To further understand the degradation rate of samples in different quality, we performed a set of controlled experiments using *in situ* Raman scattering to monitor sample degradation. Figures 5a and 5b show the time evolution of Raman spectra of a

‘good’ and a ‘poor’ sample. The spectra are recorded continuously in 30 seconds step for 5 minutes and the laser power is kept at 1mW focused to a spot size of about 1 μ m. In both samples, we observe increasing intensity of Te-like modes A and B as time goes but with different rates. For the ‘good’ sample, the intensity of Te-like modes grows while that of peaks due to 1L-*T'*-MoTe₂ decreases slowly. For the ‘poor’ sample, those 1L-*T'*-MoTe₂ modes disappear almost completely after the first 30 seconds; while the Te-like modes keep increasing and getting more and more intense, reaching more than twice the intensity of silicon peak in five minutes. As a controlled comparison, we also performed similar *in situ* Raman monitoring on a ‘good’ sample that was placed in the high vacuum pumped for a week at 3*10⁻⁶ torr. In this sample, no additional Te-like modes were seen in 5 minutes, indicating negligible degradation. We summarize in Figure 6.1.2.5c the evolution of the intensity ratio of mode A to the silicon phonon at 520 cm⁻¹ for the three *in situ* Raman measurements. For the ‘good’ sample the Te(A)/Si ratio increases slowly; for the ‘poor’ sample, the Te(A)/Si ratio increases rapidly and saturates after 4 minutes. As another evidence for sample degradation, we extracted the linewidth and intensity of the 1L-*T'*-MoTe₂ *m*⁸⁵ mode in Fig. 6.1.2.5a. The increase of FWHM from 3.4 to 4.6 cm⁻¹ in 5 minutes indicates the degradation of sample crystallinity, correlated with the intensity decrease which is consistent with previous degradation studies of air sensitive 2D materials.^{455,457,467}

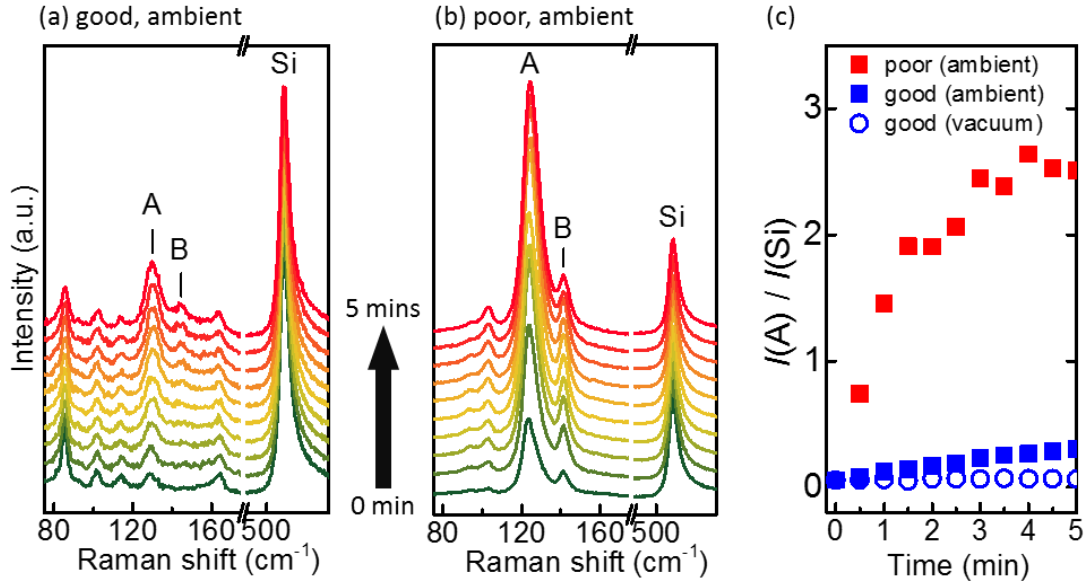


Figure 6.1.2.5. Spectral evolution of samples with a) good (similar to S1 in Figure 4a) and b) poor (similar to S4 in Figure 4a) optical contrast in ambient. The evolution of FWHM and intensity of m^{85} modes is extracted in the inset of Figure 5a, providing another evidence of sample degradation. c) The intensity ratio of peak A to the silicon mode plotted as a function of laser exposure time.

In literature laser irradiation has been used to induce phase transition between H - and T' - MoTe_2 to make ohmic homojunction contacts,⁴²⁴ where new Raman peaks at around 124 and 138 cm^{-1} have been attributed to T' - MoTe_2 (similar conclusions have been reached on a study of strain induced H to T' phase transition).⁴⁵⁸ We note that these peaks are quite similar to the Te metalloid Raman bands arising from sample degradation, raising questions regarding the final product of laser patterning and strain engineering in those samples.

Conclusion

In conclusion, the lattice dynamic of CVD 1L- T' - MoTe_2 is investigated by the polarization and crystal orientation resolved Raman spectroscopy. We observed the

complete set of Raman-active modes including 3 z -modes and 6 m -modes, providing non-destructive Raman fingerprints for high quality 1L T' -MoTe₂. By monitoring the intensity of Raman modes from sample degradation, we are able to quantitatively gauge the quality the 1L- T' -MoTe₂ crystal, which is important for developing electrochemical and/or topological devices using T' -MoTe₂. Moreover, our results provide a handy tool to determine the phase of MoTe₂, which is crucial for harnessing the versatile TMDC polytypes, such as metal-insulator transition and seamless homojunction physics.

Methods

Crystal growth. Monolayer T' -MoTe₂ flakes were grown by chemical vapor deposition. We first spin coat a 1% sodium cholate solution on 300 nm SiO₂/Si substrates at 4000 rpm for 60 s. The molybdenum feedstock is provided by a droplet of a saturated solution of ammonium heptamolybdate in deionized water deposited onto the substrate. The prepared substrate is subsequently positioned in the center of the furnace, with 15 mg of solid tellurium placed 5 cm upstream from the substrate. At atmospheric pressure in a flow of 400 sccm of nitrogen gas and 25 sccm of hydrogen (both 99.999% purity), the furnace temperature is ramped at a rate of 70 °C min⁻¹ to 700 °C. Meanwhile the temperature of the tellurium pellet is around 500 °C. After a 5 min growth period, the sample is rapidly cooled down to room temperature by flowing 1000 sccm nitrogen gas with the furnace lid open. Bulk T' -MoTe₂ crystals are grown *via* chemical vapor transport (CVT) method using bromine as the transport gas. The source materials, including Mo(99.9%), Te(99.997%), and TeBr₄(99.999%) powders, are placed in a fused

silica tube. Total amount of Mo and Te are kept in a stoichiometric 2:1 ratio with sufficient TeBr_4 to achieve a Br density of 3 mg/cm^3 . The tube is pump-purged with argon gas (99.999%) and sealed at low pressure prior to growth. The CVT growth is performed using a three-zone furnace, with the temperature setting of the reaction and growth zones at 1000 and 900 °C, respectively, for 100 h. At the end of the growth, the crystal is thermally quenched by a water bath.

Sample passivation. The graphene for passivating 1L- T' - MoTe_2 is firstly grown on a Cu foil substrate by CVD. It was then transferred off the Cu foil substrate by bubble transfer method with a NaOH solution and left afloat in a DI water bath. Following the growth of 1L- T' - MoTe_2 by CVD, the graphene is immediately transferred on top of the flakes to minimize degradation of the flakes from air. The 1L- T' - MoTe_2 is briefly dipped inside the DI water bath and the graphene is instantly pulled over the chip to cover the 1L- T' - MoTe_2 . The graphene/1L- T' - MoTe_2 stack is then immediately dried with N_2 gun. Through this quick passivation method, the 1L- T' - MoTe_2 flakes are in air and water for a handful of seconds which minimizes the degradation.

Transmission Electron Microscopy. The as grown 1L- T' - MoTe_2 flakes were transferred onto a commercial holey-carbon TEM grid using a typical wet transfer method. The TEM was performed with a JEOL ARM 200CF equipped with a CEOS corrector and a high-angle annular dark field detector. The operation voltage is kept below 80 kV to avoid sample damage. Selected-area electron diffraction patterns were acquired in TEM mode using an aperture with an effective size of $\sim 1 \text{ }\mu\text{m}$ at the sample.

6.2 1T'-WTe₂

6.2.1 Large-area synthesis of high-quality monolayer 1T'-WTe₂ flakes

The results presented in this section have also appeared in the publication “Large-area synthesis of high-quality monolayer 1T'-WTe₂ flakes”, Carl H. Naylor, William M. Parkin, Zhaoli Gao, Hojin Kang, Mehmet Noyan, Robert B. Wexler, Liang Z. Tan, Youngkuk Kim, Christopher E. Kehayias, Frank Streller, Yu Ren Zhou, Robert Carpick, Zhengtang Luo, Yung Woo Park, Andrew M. Rappe, Marija Drndić, James M. Kikkawa and A. T. Charlie Johnson, *2D Materials*, 2017, 4 021008. This work was highlighted in *Nature Nanotechnology* doi:10.1038/nnano.2017.37.

Abstract

Large-area growth of monolayer films of the transition metal dichalcogenides is of the utmost importance in this rapidly advancing research area. The mechanical exfoliation method offers high quality monolayer material but it is a problematic approach when applied to materials that are not air stable. One important example is 1T'-WTe₂, which in multilayer form is reported to possess a large non saturating magnetoresistance, pressure induced superconductivity, and a weak antilocalization effect, but electrical data for the monolayer is yet to be reported due to its rapid degradation in air. Here we report a reliable and reproducible large-area growth process for obtaining many monolayer 1T'-WTe₂ flakes. We confirmed the composition and structure of monolayer 1T'-WTe₂ flakes

using X-ray Photoelectron Spectroscopy, Energy-dispersive X-ray Spectroscopy, Atomic Force Microscopy, Raman spectroscopy and Aberration Corrected Transmission Electron Microscopy. We studied the time dependent degradation of monolayer 1T'-WTe₂ under ambient conditions, and we used first-principles calculations to identify reaction with oxygen as the degradation mechanism. Finally we investigated the electrical properties of monolayer 1T'-WTe₂ and found metallic conduction at low temperature along with a weak antilocalization effect that is evidence for strong spin-orbit coupling.

In the surge of research into the properties of two-dimensional materials “beyond graphene”, transition metal dichalcogenides (TMDs) have emerged as a platform for novel scientific discoveries and exploratory device concepts.^{35,39,41,43,45} TMDs, also known as MX₂ materials, in the monolayer form consist of a layer of metal atoms, such as molybdenum or tungsten, sandwiched between chalcogenide atoms, such as sulfur or selenium. The optical,⁴¹⁸ electrical,⁴⁴ mechanical⁷³ and tribological⁴²⁰ properties of these MX₂ materials have been widely studied in recent years, with numerous proposed applications⁷⁵ including energy storage⁷² and chemical sensors.⁷⁴ The majority of work to date has relied on mechanical micro-exfoliation to isolate flakes of high quality monolayer material but the yield for this method is typically very low, which makes comprehensive studies of monolayer MX₂ films difficult and tedious. Therefore there is an urgent need for the development of robust and reproducible methods to produce high quality, large-area monolayer MX₂ materials. Monolayer MX₂ films can be found in

different structural phases,⁷¹ which differ in the arrangement of the top layer of chalcogenide atoms with respect to the bottom layer (figure 6.2.1.1(a)). MX_2 materials frequently grow in the highly symmetric 1H phase where the top layer of chalcogenide atoms is aligned with the bottom layer. 1H-MoS₂, the most commonly studied 1H material to this point, is a semiconductor which can be incorporated into field effect transistor (FET) devices with high on/off ratio, reasonable values of carrier mobility, and a band gap that is tuned by the number of atomic layers.^{48,472} In the 1T phase, the top layer of chalcogenide atoms is shifted with respect to the bottom layer so that as viewed normal to the plane, the chalcogenide atoms form a hexagon around the metal atom. The 1T phase of MoS₂ has been accessed experimentally through chemical transformation induced by n-butyllithium.^{69,423,473} While 1H-MoS₂ is a semiconductor, 1T-MoS₂ is metallic, so lateral heterostructures of monolayer 1H/1T MoS₂ are attractive candidates for developing low contact resistance devices.⁶⁹ The 1T' phase is a distorted 1T phase where the chalcogenide atoms have distanced themselves from their hexagonal position around the metal atom. The 1T' phase can be easily recognized and differentiated from the 1T phase by the presence of isolated zigzag chains of chalcogenide atoms that run vertically in figure 1a.

The 1T' phase of TMDs has recently attracted great attention due to the prediction that they support topological electronic states.⁶¹ For most of the MX_2 materials, it has been predicted that the 1H phase is the energetic ground state, and that transitions from the 1H to the 1T' phase can be induced by strain.⁶⁸ One exception is WTe₂, where the 1T' phase is predicted to be the ground state. Bulk crystals of 1T'-MoTe₂ and 1T'-WTe₂ have

been grown, and exfoliation has been used to produce few-layer films, but monolayer films are rarely reported using this approach.^{65,456,457} There are reports of a large non-saturating magnetoresistance,⁴⁷⁴ the appearance of weak antilocalization,⁶⁵ and pressure induced superconductivity⁶⁰ in *few-layer* 1T'-WTe₂, which is relatively stable under ambient conditions for films of six or more layers. However, since it is difficult to obtain monolayer flakes with reproducible properties by exfoliation, and because both 1T'-MoTe₂ and 1T'-WTe₂ are highly unstable under ambient conditions, there are to date very few studies of the properties of monolayer flakes. Recently we reported growth of monolayer single-crystal flakes of 1T'-MoTe₂ by chemical vapour deposition (CVD) with good surface coverage, which enabled an extensive study of 1T'-MoTe₂ in the monolayer form.⁵⁹ This was followed with a study on the absorption dichroism in monolayer 1T'-MoTe₂.⁴⁵⁵ Recently a group has shown that growth of 1T'-WTe₂ in monolayer form is possible by CVD⁴⁷⁵ but there remains a need for careful investigation of the properties of monolayer flakes as well as a deeper understanding of the process of degradation under ambient conditions.

Here we present a facile, reproducible approach for growth of large, monolayer single crystal 1T'-WTe₂ flakes by CVD with a surface coverage of ~ 20 %. Monolayer 1T'-WTe₂ flakes degrade within minutes under ambient conditions, but we found that by minimizing the handling time and passivating the samples with CVD-grown graphene, we were able to characterize monolayer flakes of 1T'-WTe₂. The chemical composition of the films was determined using X-ray photoelectron spectroscopy (XPS), and Atomic Force Microscopy (AFM) was used to confirm that the flakes were of monolayer height.

Raman mapping was used to study the vibrational modes of monolayer and bilayer 1T'-WTe₂, with the results being in excellent agreement with theoretically predicted phonon frequencies. Aberration Corrected Scanning Transmission Electron Microscopy (ACSTEM) was used to determine that the WTe₂ films were in the 1T' structural phase. Because the growth method produces a high density of monolayer 1T'-WTe₂ flakes compared to the exfoliation method, we were able to study the degradation of the material in air. We explored degradation mechanisms by using density functional theory calculations and concluded that the films oxidize quickly in ambient. We obtained the first electrical results on monolayer 1T'-WTe₂, finding a weak antilocalization effect at low temperature, which is consistent with the presence of strong spin-orbit coupling. This work creates a pathway towards the use of 1T'-WTe₂ for integrated device structures whose operation relies on control of topological states and phases.

Growth process

The CVD process for monolayer 1T'-WTe₂ flakes relies on deposition of W-feedstock material and a growth promoter⁵⁹ onto the growth substrate, followed by exposure to tellurium metal vapour at a temperature of 650 °C (a furnace schematic is shown in figure 6.2.1.1(b)). We developed two different methods for achieving monolayer 1T'-WTe₂ flakes on a Si/SiO₂ substrate, which differ only in the method used to apply the W source material (figures 6.2.1.1(c-d)). The first approach used a 5 nm thermal evaporation of WO₃ (figure 6.2.1.1(c)), while in the second a large droplet of

ammonia metatungstate was spread over a large fraction of the substrate (figure 6.2.1.1(d)). The second process was the most efficient, enabling dense growth of large ($\sim 50 \mu\text{m}$) monolayer single crystal and polycrystalline $1\text{T}'\text{-WTe}_2$ flakes across a $2 \text{ cm} \times 3 \text{ cm}$ Si/SiO_2 substrate (figure 6.2.1.1(d)). Monolayer flakes grown by both methods showed identical physical and chemical properties. In the higher magnification optical images of figure 6.2.1.1(d), the top image shows regions of larger polycrystalline flakes that grew close to the initial source material, while monolayer single crystal flakes are seen further away from the initial ammonia metatungstate source. This suggests that the growth mechanism is similar to other TMDs such as $1\text{T}'\text{-MoTe}_2$ ⁵⁹ and 1H-MoS_2 ^{98,169} where the ratio of atoms is suitable for growth of monolayer single crystal flakes.

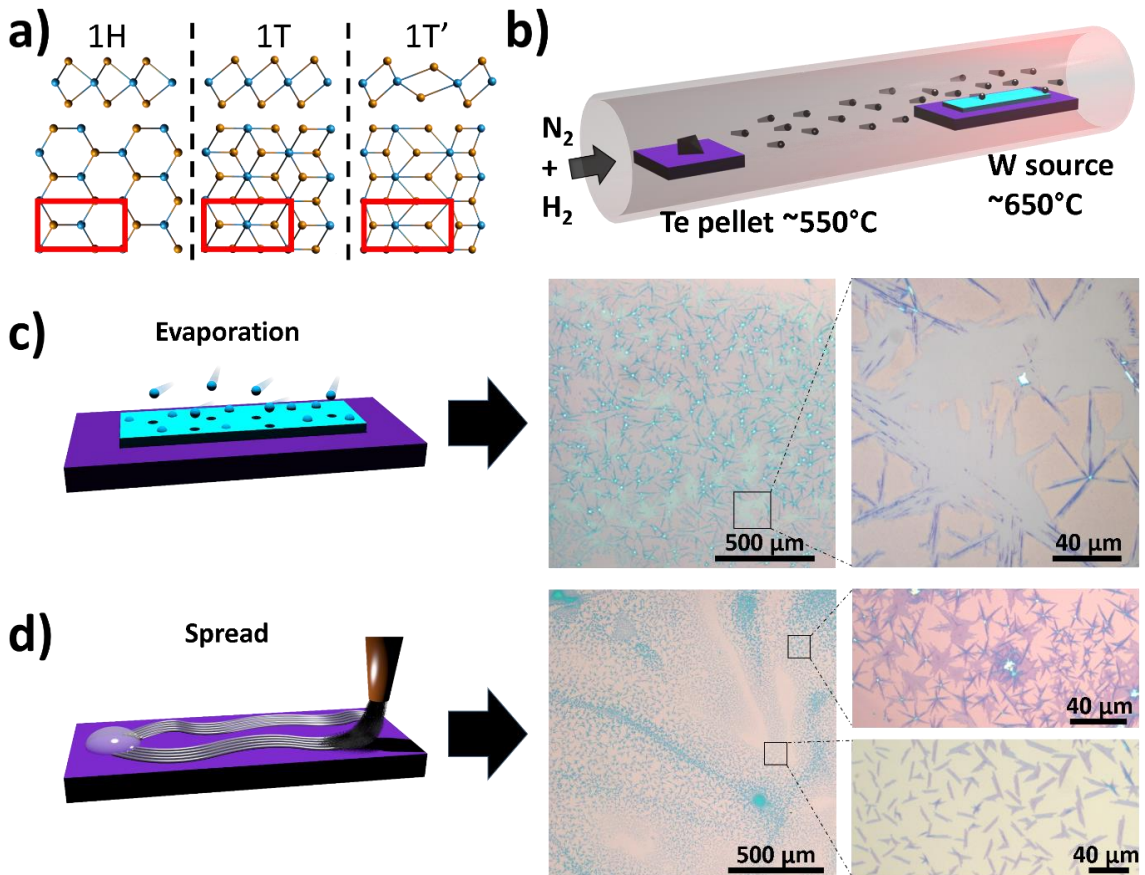


Figure 6.2.1.1. 1T'-WTe₂ growth. a) Ball and stick diagrams for the 1H, 1T and 1T' phases of WTe₂. b) Schematic of the growth process. c) Optical micrograph of 1T'-WTe₂ flakes grown by the evaporation method. Monolayer 1T'-WTe₂ material appears as light gray “webs” on the growth substrate. Darker multilayer regions are also observed. d) Optical micrograph of 1T'-WTe₂ flakes grown by the spread method.

Characterization of monolayer 1T'-WTe₂ flakes

XPS and Energy Dispersive X-ray Spectroscopy (EDS) were used to determine the elemental and bond composition of the 1T'-WTe₂ flakes. Peaks in the X-ray photoelectron spectrum were observed at 573.0, 583.4, 243.7, 256.3 eV, corresponding to the Te 3d_{5/2}, Te 3d_{3/2}, W 4d_{5/2}, and W 4d_{3/2} signals, respectively (figure 6.2.1.2(a)). These results are comparable to previous reports of XPS on exfoliated flakes of 1T'-WTe₂.⁴⁵⁶ On the basis of these data, the Te/W atomic ratio was found to be 2.04, very close to the expected value for 1T'-WTe₂. The full XPS spectrum and details as to how the stoichiometry was determined can be found in the Supporting Information and figure S1. The EDS results can be found in figure S2; they indicate a stoichiometry of 1:2, in good agreement with the XPS analysis. Atomic force microscopy (AFM) was performed on the flakes, revealing a height of roughly 1 nm (figure 6.2.1.2(b)) as expected for monolayers, and in agreement with previous reports on exfoliated 1T'-WTe₂ flakes.^{150,457} Flakes grown through this method are predominantly monolayer thickness, but occasionally small bilayer regions are found on the edges of the flakes as seen in figures 6.2.1.2(b-c).

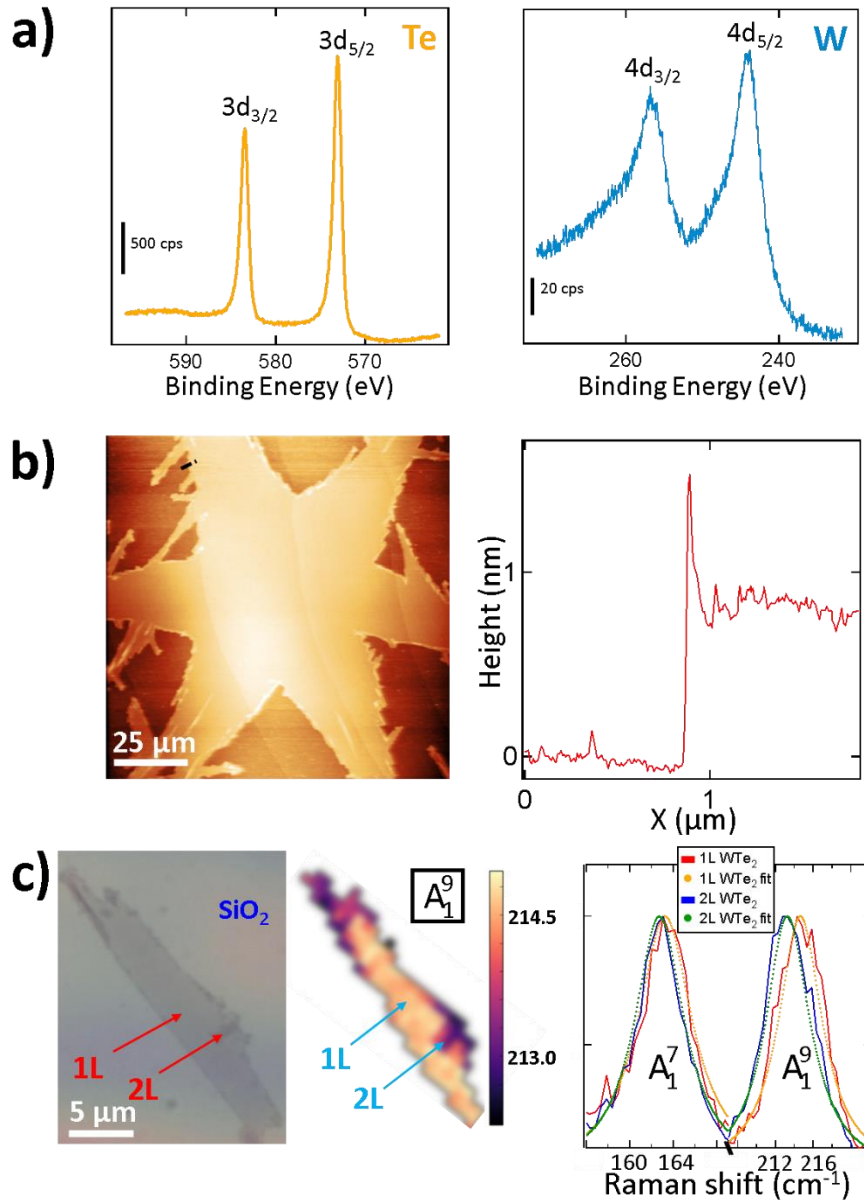


Figure 6.2.1.2. 1T'-WTe₂ characterization. a) XPS spectrum showing binding energies characteristic of 3d_{3/2} and 3d_{5/2} electron orbitals for Te, and the 4d_{3/2} and 4d_{5/2} orbitals for W. b) AFM image of a large 1T'-WTe₂ monolayer flake. AFM line scan shows that the flake height is ~ 0.8 nm, as expected for monolayer material. c) (left) Optical image of a 1T'-WTe₂ flake containing both monolayer and bilayer regions. (middle) Raman mapping of the A₁⁹ peak position of 1T'-WTe₂ flake showing the difference in peak position between monolayer and bilayer. (right) The Raman spectrum shows that the A₁⁷ peak for bilayer 1T'-WTe₂ is close to that for the monolayer, while the A₁⁹ peak is shifted by ~ 1.5 cm⁻¹.

Raman mapping was performed on a 1T'-WTe₂ flake that was predominantly monolayer but with small bilayer regions on the edges (figure 6.2.1.2(c)) in order to study

the effect of this thickness change on the phonon modes. The flake was encapsulated with large-area graphene to avoid degradation during the measurements. Two main Raman peaks were observed: the in-plane $A_{7_1}^7$ peak, and the $A_{9_1}^9$ peak, which contains both in-plane and out-of-plane vibrations.⁴⁵⁷ For the monolayer region, the $A_{7_1}^7$ and $A_{9_1}^9$ peaks were observed at 163.2 cm^{-1} and 214.7 cm^{-1} , respectively. For the bilayer region the $A_{7_1}^7$ peak was at 162.7 cm^{-1} , while the $A_{9_1}^9$ was shifted to 213.2 cm^{-1} (figure 6.2.1.2(c)). All of these peak positions are red-shifted by $\sim 1\text{ cm}^{-1}$ compared to previously reported values,^{65,150,151,457} but the separation between the $A_{7_1}^7$ and $A_{9_1}^9$ peaks is in good agreement with these earlier works. To explain this observation, we used density functional theory to compute the frequencies of the Raman-active phonon modes before and after introduction of a graphene capping layer. For uncapped monolayer $1T'$ -WTe₂ we calculate the position of the $A_{7_1}^7$ and $A_{9_1}^9$ peaks at 161.54 cm^{-1} and 211.36 cm^{-1} respectively. With the addition of graphene, the peaks show a small red shift to 159.95 cm^{-1} and 208.35 cm^{-1} . These calculated values are in good agreement with the measurements, and the calculation also explains the slight red shift in our data compared to earlier reports, which we attribute to the presence of the graphene capping layer. Using the same approach, we also studied the evolution of the Raman-active phonon modes as a function of layer number. We find that the $A_{9_1}^9$ should redshift from 211.36 cm^{-1} for monolayer material to 209.53 cm^{-1} for bulk, in agreement with our measurements and previous DFT studies.^{150,457}

Monolayer and few-layer $1T'$ -WTe₂ flakes are unstable under atmosphere as well as transmission electron microscopy (TEM) irradiation, so the $1T'$ -WTe₂ flakes were

encapsulated between graphene monolayers (figure 6.2.1.3(a)) to reduce damage during transfer and TEM imaging.^{476,477} (Details regarding the fabrication of the heterostructure stack can be found in the method section.) The intensity in high-angle annular dark field (HAADF) images is proportional to the square of the atomic number (Z) so the two graphene ($Z_C = 6$) layers surrounding the $1T'$ -WTe₂ monolayer ($Z_W = 74$, $Z_{Te} = 52$) are effectively invisible, making this graphene/MX₂/graphene structure ideal for further studies on unstable materials. To determine the lattice parameters and image the atomic structure of monolayer $1T'$ -WTe₂, selected-area electron diffraction (SAED) images and HAADF images were obtained using a JEOL 200CF (figure 6.2.1.3(c)) equipped with a CEOS corrector for the ACSTEM probe. The ACSTEM was operated at 60 kV to reduce beam-induced displacements of atoms from the lattice, although damage was observed at high magnifications after as little as one exposure. The symmetry of the graphene lattice is different from that of $1T'$ -WTe₂, so the two diffraction patterns are readily distinguished. Figure 6.2.1.3(b) is the SAED image of the graphene/ $1T'$ -WTe₂/graphene heterostructure, where the graphene diffraction spots are highlighted in blue and the $1T'$ -WTe₂ spots in pink. The SAED pattern for $1T'$ -WTe₂ matches the simulated SAED pattern in figure S3. Calibrating the SAED pattern using the graphene diffraction spots ($\bar{a}_{[10\bar{1}0]} = \frac{\sqrt{3} \times 2.46 \text{ \AA}}{2} = 4.692 \text{ nm}^{-1}$),⁴⁷⁸ we measure the lattice constants for $1T'$ -WTe₂ to be $a = 3.49 \text{ \AA}$ and $b = 6.32 \text{ \AA}$, in excellent agreement with previous reports.⁴³³ The single crystal domain size is measured to be on the order of 10-20 μm^2 . Figure 6.2.1.3(c) is an HAADF image of the monolayer $1T'$ -WTe₂ that shows excellent agreement with the simulated HAADF image in figure 6.2.1.3(d).

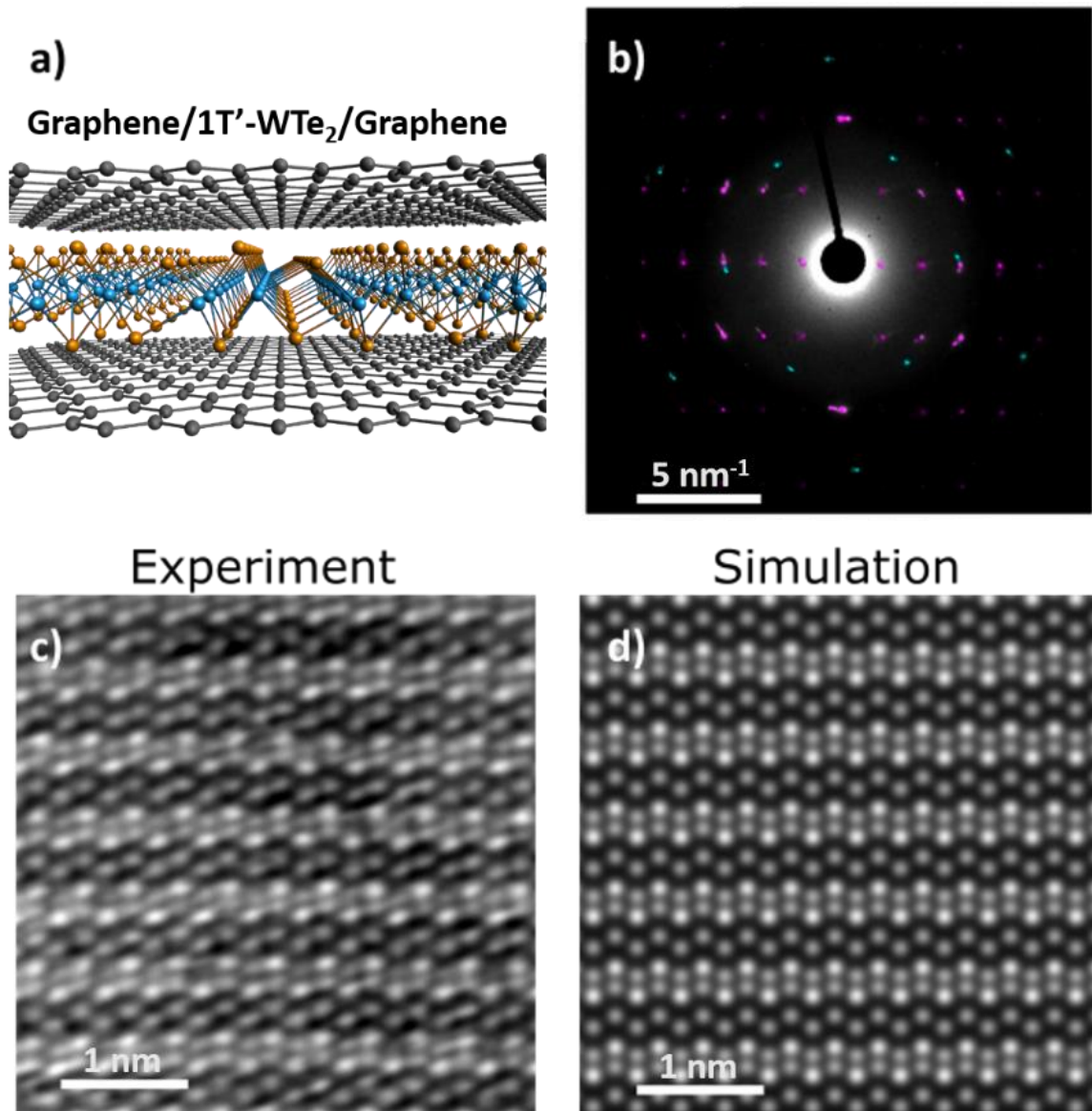


Figure 6.2.1.3. TEM characterization of 1T'-WTe₂. a) Ball and stick model of the graphene-WTe₂-graphene stack used for TEM imaging. b) Inverted SAED pattern of the graphene-WTe₂-graphene stack at 60 kV accelerating voltage. False colour has been added to distinguish between the 1T'-WTe₂ (pink) and graphene (blue) diffraction spots. c) High angle annular dark field (HAADF) image of monolayer 1T'-WTe₂ at 60 kV accelerating voltage. d) Simulated HAADF image of monolayer 1T'-WTe₂ using quantitative image simulation in transmission electron microscopy (QSTEM)⁴³⁴ with lattice parameters $a = 6.282 \text{ \AA}$ and $b = 3.496 \text{ \AA}$.⁴³³

Degradation of monolayer 1T'-WTe₂ under ambient conditions

Bi-layer 1T'-WTe₂ is reported to be unstable under ambient conditions, as evidenced by a decay in the Raman signal intensity over the course of several hours.⁴⁵⁷ If bi-layer samples decay in hours, one might expect that monolayer samples decay much more quickly. To date, however, careful study of the stability of monolayer 1T'-WTe₂ flakes has been problematic due to their rapid degradation and the low yield of the exfoliation method. Due to the relatively high coverage of monolayer 1T'-WTe₂ flakes that is characteristic of our CVD growth process, we were able to observe the decaying of the monolayer flake through multiple experimental approaches. We first studied degradation of the material through measurements of the image contrast in optical micrographs, defined as $[I_{FL} - I_{SUB}]/I_{SUB}$, where I_{FL} and I_{SUB} are the image intensity of the flake and the background oxidized silicon substrate, respectively (figure 6.2.1.4(a)). A sample of monolayer flakes was removed from the growth furnace and immediately transported to an optical microscope where it was left under ambient conditions for 3 days (figure 6.2.1.4(a)). The optical contrast of the flake against the substrate was observed to decrease rapidly over time, suggesting that the flake underwent a chemical reaction with room air. After 30 minutes the optical contrast saturated at a low level, implying that the chemical reaction terminated.

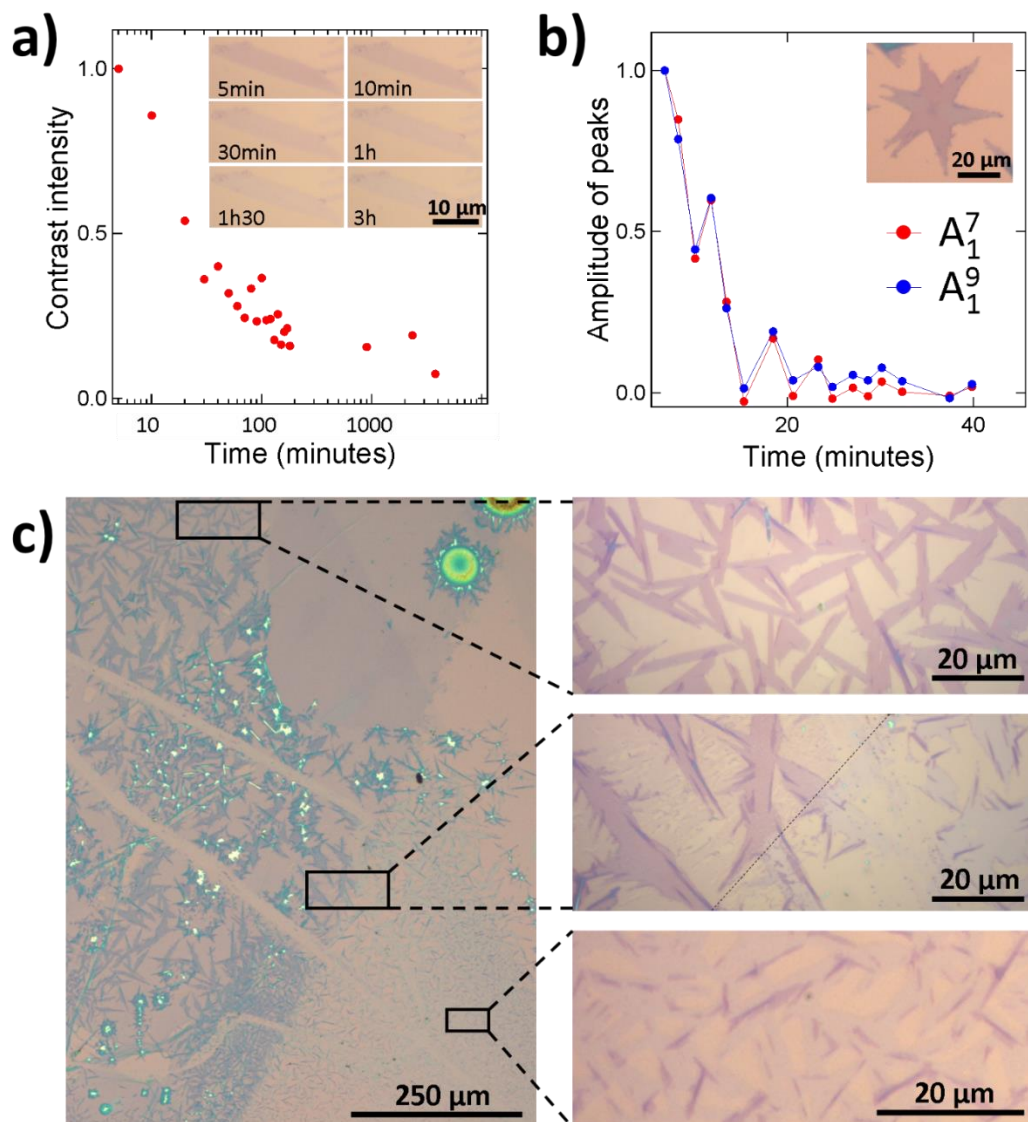


Figure 6.2.1.4. Degradation of 1T'-WTe₂ in air. a) Time dependence of the optical contrast of a 1T'-WTe₂ flake ("FL") compared to the SiO₂/Si substrate ("SUB"). Contrast is defined as $[I_{FL} - I_{SUB}]/I_{SUB}$. Inset: Representative optical images of the decaying flake. b) Plot showing the decrease over time of the amplitude of A₁⁷ and A₁⁹ Raman peaks of monolayer 1T'-WTe₂. Inset: Optical micrograph of the 1T'-WTe₂ flake used for the Raman measurements. c) Optical microscope image after graphene transfer shows that there is a clear difference in the optical contrast of flakes exposed to air (lower right portion of image) compared to flakes passivated by graphene.

We studied the amplitude of the A₁⁷ and A₁⁹ peaks in the Raman spectrum of uncapped monolayer 1T'-WTe₂ flakes left exposed to air (figure 6.2.1.4(b)). We first performed a scan on an as-prepared monolayer 1T'-WTe₂ flake, and each scan at later times was conducted on a new, unmeasured flake in order to avoid the confounding

influence of damage to the material caused by exposure to the Raman laser. Through this approach, we were able to study how exposure to room air affects the A_1^7 and A_1^9 Raman peaks of monolayer 1T'-WTe₂. The peak amplitudes decreased in a nearly identical manner, with a strong (~ 50%) reduction within a few minutes, and the peaks essentially disappeared after 30 minutes, in rough agreement with the optical contrast data of figure 6.2.1.4(a). To our knowledge this is first reported study of the decay of monolayer 1T'-WTe₂ flakes under ambient using Raman spectroscopy. The results clearly indicate that monolayer 1T'-WTe₂ flakes decay within tens of minutes when left unprotected under ambient conditions.

We discovered that degradation of monolayer 1T'-WTe₂ could be avoided by transferring a sheet of graphene onto the substrate immediately after growth. The graphene-capped samples were stable for days, which enabled Raman mapping measurements, as illustrated in figure 6.2.1.2(c). Figure 6.2.1.4(c) is an optical image taken 12 hours after a sample of monolayer 1T'-WTe₂ flakes was partially capped with graphene. The top zoomed-in image shows that for monolayer flakes under graphene, the optical contrast against the oxidized silicon substrate remained very strong and was comparable to that observed for flakes immediately after growth. The bottom image is a portion of the sample where uncapped monolayer flakes were exposed to air for several hours. These flakes showed very low optical contrast, which is typical of degraded material, in agreement with figure 6.2.1.4(a). The middle image is of the region near the boundary of the graphene sheet. Some flakes in this region were half exposed to air, and the optical contrast of exposed regions was very different from that where the material

was covered by the graphene overlayer. This image highlights the degradation of 1T'-WTe₂ flakes in air and the utility of graphene as a passivation layer. Based on these measurements, we hypothesized that the films were damaged by reacting with a component molecule of the air.

Investigation of instability using density functional theory calculations

We explored possible degradation mechanisms by using density functional theory calculations to study the adsorption of H₂(g), O₂(g), and H₂O(g) on monolayer 1T'-WTe₂ as the first is present during synthesis and the latter two are ubiquitous. Figure 6.2.1.5(a) shows two perspectives of the 1T'-WTe₂ (001) surface. The thickness of the monolayer under vacuum is 4.22 Å. The Te atomic layer lies on top of the layer of W atoms, which can have one of two geometries: small and large W₃ triangles. In an oxygenated environment, 1T'-WTe₂ favors the dissociative adsorption of O₂(g), with the equilibrium structure at 0 K shown in figure 6.2.1.5(b). The adsorption process in the figure is highly exothermic ($\Delta E_{\text{ads}} = -3.60$ eV/O₂) and the adsorption location shown is greatly favored over other locations. Therefore surface oxidation by O₂(g) is expected under experimental conditions of ambient O₂(g) pressure and temperature. When O₂(g) dissociates, one O atom binds directly atop a W atom in the sublayer. The other O atom displaces Te from a small W₃ site, thus forming a W₃O subunit. This site is favored over the large W₃ triangle for dissociative O₂ adsorption because it provides three-fold coordination for one of the O atoms. The displaced Te atom rises slightly off the surface (figure 6.2.1.5(c)), increasing

the thickness of the monolayer from 4.22 Å to 5.12 Å. Therefore, this calculation suggests that 1T'-WTe₂ is highly susceptible to oxidation, which leads to structural degradation via displacement of Te. We find that oxygen chemisorption transfers intensity in the Raman spectrum from the A₁⁷ and A₁⁹ peaks to new modes in the Raman spectrum associated with the vibration of W-O bonds. We calculated Raman frequencies of 322.82 cm⁻¹, 389.19 cm⁻¹ for in-plane oxygen vibrations, and a mode at 500.03 cm⁻¹ with predominantly oxygen out-of-plane vibrations.

We also investigated the possibility that H₂(g), present during synthesis, could passivate the surface. We find, however, that H₂(g) prefers physisorption over dissociative chemisorption (figure S4(a)). This process is slightly exothermic with $\Delta E_{\text{ads}} = -0.07$ eV/ H₂, and the thickness of the monolayer is unaffected by H₂(g) adsorption. The surface greatly prefers oxidation to hydrogenation.

Finally, we considered the competition between O₂(g) and H₂O(g) as surface oxidizing agents (see Supporting Information). Unlike O₂(g), H₂O(g) prefers associative adsorption at Te sites. Figure S4(b) shows that H₂O(g) weakly interacts with the surface by forming van der Waals bonds between H and Te, with no effect on the thickness of the monolayer. Adsorption is spontaneous ($\Delta E_{\text{ads}} = -0.27$ eV/ H₂O) but the energetics are far less favorable than for dissociative O₂(g) adsorption. Therefore, O₂(g) is a much more potent surface oxidizer than H₂O(g). Based on these considerations, we conclude that 1T'-WTe₂ monolayer films degrade under ambient through oxidation, leading to the changes in optical contrast and the Raman spectrum that are discussed above.

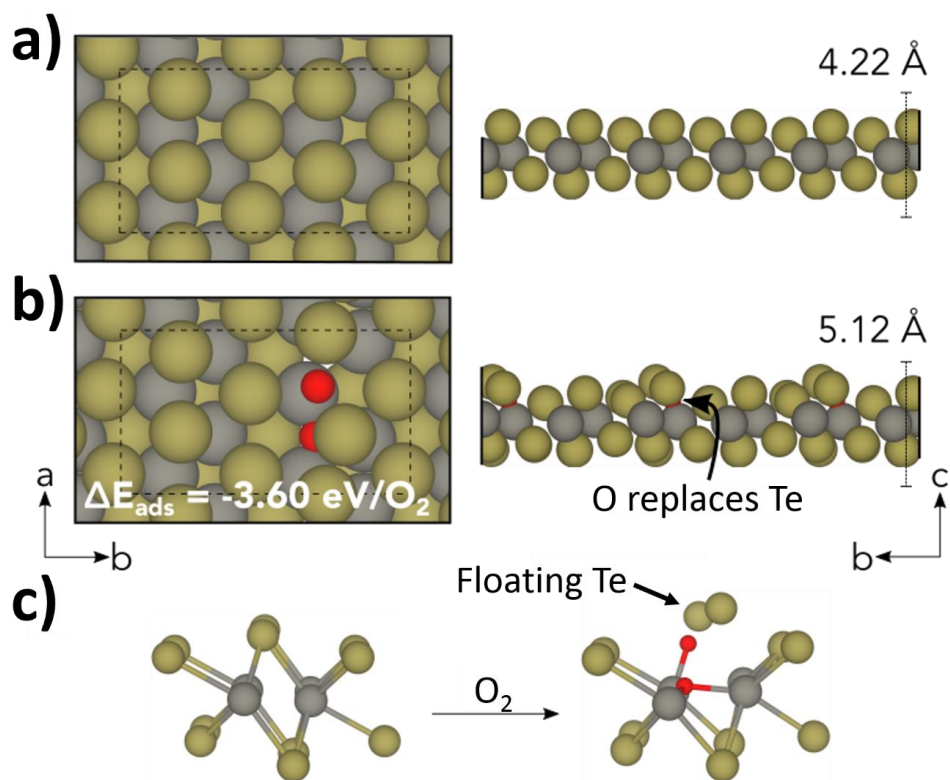


Figure 6.2.1.5. Surface structure of monolayer 1T'-WTe₂(001). a) Under vacuum. b) In the presence O₂. c) Te displacement due to O₂ molecules. The W, Te and O atoms are coloured grey, green and red respectively.

Semimetallic nature of monolayer 1T'-WTe₂

First-principles calculations were performed to confirm the semimetallic nature of monolayer 1T'-WTe₂. As shown in figure S5, the Fermi level overlaps with the conduction and valance bands, forming electron and hole pockets near the Γ point. Nonetheless, since the bulk energy gap is well developed throughout the entire Brillouin zone, separating the conduction and valance bands, the time-reversal invariant Z_2 topological phase⁴²² can be evaluated using the all the states from 1st to n^{th} bands, where n is the electron filling. We find the Z_2 topological invariant is nontrivial, as reported in a

previous study.⁶¹ The semimetallic nature of WTe₂ obstructs disentanglement of the helical edge states of the nontrivial topological phase and the bulk metallic states. Nonetheless, the quantum spin Hall effect in WTe₂ could potentially be observed by applying an external electric field or strain, which would induce a band gap and isolate the surface edge states from the bulk states.⁶¹

Devices for transport measurements on single monolayer flakes were fabricated by electron beam lithography with minimal material degradation due to air exposure. Details of the fabrication process are provided in the Methods section. Care was taken to define the contact pattern so that the electrical leads to a particular monolayer flake would not be short-circuited by other 1T'-WTe₂ flakes on the substrate (figure 6.2.1.6(a)). The monolayer 1T'-WTe₂ material was kept passivated by a PMMA layer, with only brief exposure to air. After fabrication, we carried out low temperature magnetoresistance measurements under high vacuum. Once the electrical measurements were completed, Raman spectroscopy was performed on the flake to confirm its monolayer thickness.

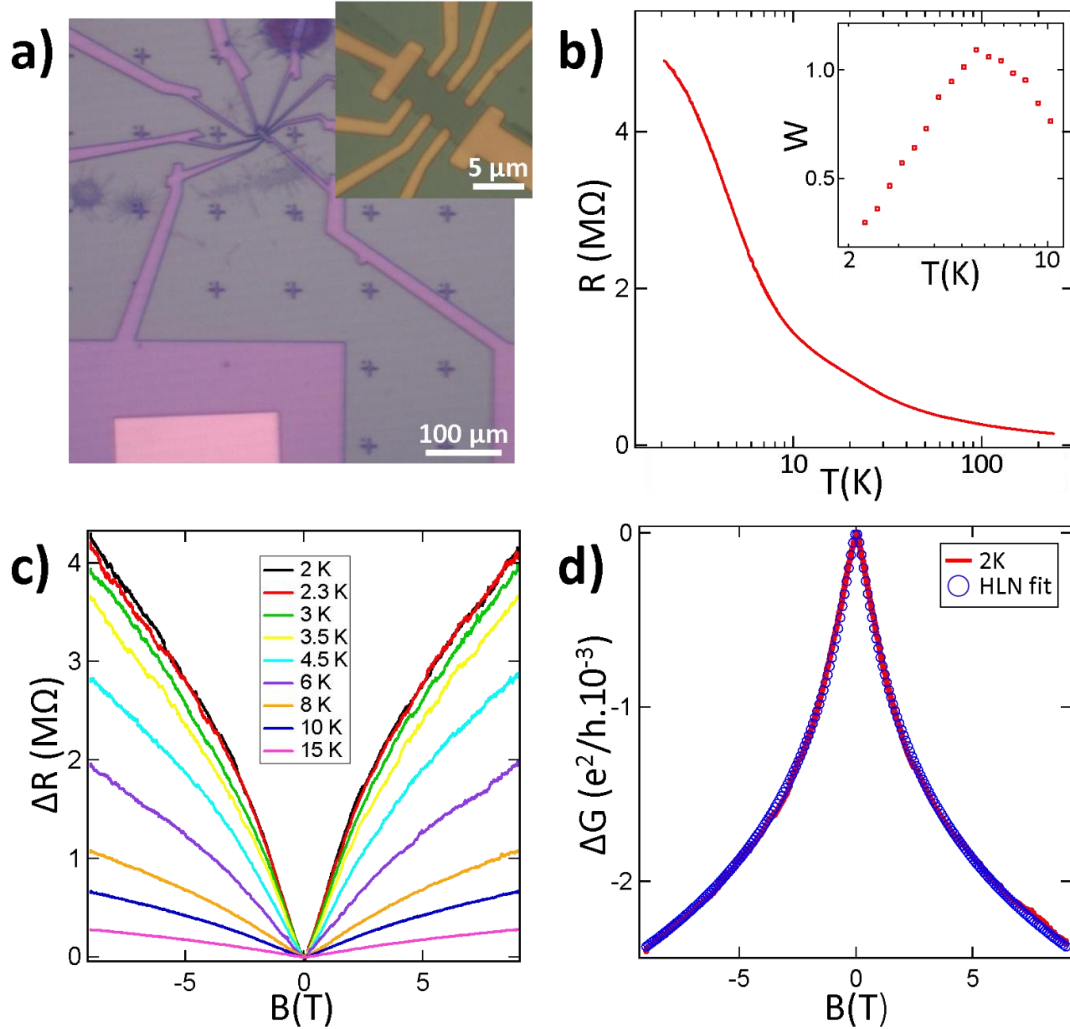


Figure 6.2.1.6. Electrical data of monolayer 1T'-WTe₂. a) Optical image showing the device structure with a visible window through the PMMA coating to the contact electrode. Inset: Optical micrograph of the monolayer 1T'-WTe₂ flake device. b) Resistance vs temperature behavior of the device. Inset: Reduced activation energy as a function of temperature showing metallic behavior. c) Magnetoresistance for different temperatures, showing the appearance of the weak antilocalization cusp. d) Magnetoconductance measurement at 2K (red curve), fitted with Hikami-Larkin-Nagaoka (HLN) theory (blue circle). The results show excellent agreement between the data and the fit.

We monitored the sample resistance in a 4-probe measurement configuration as the sample was slowly warmed from 2 K to 300 K (figure 6.2.1.6(b)). The insert of the figure shows the reduced activation energy $W = -d(\ln R)/d(\ln T)$ as a function of temperature revealing a positive slope at low temperature, indicating metallic behavior.⁴⁷⁹ To our knowledge, these are the first measurements of monolayer 1T'-WTe₂ showing this

property. The sample magnetoresistance showed a cusp-like weak antilocalization (WAL) feature that became more pronounced and narrower at low temperature. The WAL effect can be associated with either bulk or topological states and its appearance here indicates that spin-orbit coupling is sufficiently strong that the spin orbit scattering length is much less than the phase scattering length.^{427,435,480,481} WAL has been observed in multilayer 1T'-WTe₂⁶⁵ but until now has not been reported in monolayer devices, presumably because of their air sensitivity. The measured sample magnetoconductance was fitted with the Hikami-Larkin-Nagaoka (HLN) equation in the limit of strong spin orbit coupling, $\sigma(B) - \sigma(0) = -\alpha \frac{e^2}{\pi h} \left[\Psi \left(\frac{1}{2} + \frac{B_\phi}{B} \right) - \ln \left(\frac{B_\phi}{B} \right) \right]$,⁴⁸² where Ψ is the digamma function, and $B_\phi = \frac{\hbar}{4e l_\phi^2}$ with l_ϕ the phase coherence length (figure 6.2.1.6(d)). Agreement for all temperatures was excellent with the inferred phase coherence length ranging from 40 nm at 2 K to 22 nm at 15 K. The parameter α indicates the number of conduction channels, and is of order unity in topological insulators.^{65,427,435,439,440,483} In our measurements we found nearly 100% magnetoresistance at 2 K but HLN analysis yielded $\alpha \ll 1$ due to the high channel resistance (far exceeding the resistance quantum), indicating diffusive transport and no contribution from ballistic channels. We note, however, that we assumed conduction in the flake was uniform across its area when converting conductance into conductivity, and that the value of α would be systematically underrepresented if conduction actually occurred through a path significantly less wide than the flake width. Through these electrical results we conclude that monolayer 1T'-WTe₂ possesses a strong spin orbit coupling effect, a first step toward realizing topological electronic states.

Conclusion

We have demonstrated a facile and reproducible growth method for achieving monolayer $1T'$ -WTe₂ flakes. Samples were carefully characterized using XPS, Raman spectroscopy, AFM and ACSTEM to confirm their atomic composition and structural configuration. We demonstrated the use of a graphene overlayer to passivate the material and avoid degradation under ambient. Degradation occurs rapidly (minutes) and is most likely driven by a reaction with oxygen gas, as we demonstrated computationally. Finally we presented the first electrical data on monolayer $1T'$ -WTe₂. A WAL effect appears at low temperature and is well fit by the HLN equation in the limit of strong spin orbit coupling. The approach presented here provides a pathway to further study of topological electronic states in this two-dimensional material.

Methods

CVD Growth of $1T'$ -WTe₂. First a growth promoter of 2% sodium cholate in DI water was spin-coated onto the growth substrate at 4000 rpm for 60 seconds. Then several 100 μ L droplets of a 3.1 mM solution of ammonia metatungstate were applied and spread gently across the chip using a brush with micrometer-diameter wires. The growth substrate was placed in the center of the CVD furnace, and a second chip containing 25 mg of tellurium was placed 5 cm upstream from the growth substrate (see figure 6.2.1.1(b) for a schematic of the growth system). The chamber was flushed for 5 min under a flow of 350 sccm of N₂ and 22 sscm of H₂, and then the furnace temperature

was increased to 650 °C at a rate of 70 °C min⁻¹. The growth substrate containing the W source material reached the furnace temperature of 650 °C, while the upstream tellurium material reached 550 °C and started to sublime. The furnace was held at 650 °C for a 6 min film growth period, and the furnace was then rapidly cooled under the same gas flows. The growth substrate was retrieved, and large amounts of monolayer 1T'-WTe₂ flakes were found to have grown all across the substrate.

XPS. The chemistry of the near-surface region was investigated by XPS using a customized XPS spectrometer (VG Scienta AB, Uppsala, Sweden).⁴⁴¹ XPS analyses were performed using a monochromatic Al K α source (photon energy 1486.6 eV). The residual pressure in the analysis chamber was less than 1×10^{-8} Torr. The spectrometer was calibrated according to ISO 15472:2001 with an accuracy of ± 0.05 eV. Survey and high-resolution spectra were acquired in constant-analyzer-energy mode with the pass energies of 200 and 100 eV, respectively. The spectra were processed using CasaXPS software (v.2.3.16, Casa Software Ltd., Wilmslow, Cheshire, U.K.). Background subtraction was performed using the Shirley–Sherwood method. Examples of XPS analysis performed with this spectrometer can be found in references.^{484,485} The quantitative evaluation of the XPS data was based on integrating the intensity of the W 4d_{5/2} and Te 3d_{5/2} peaks by taking the atomic sensitivity factors for those signals into account. The atomic sensitivity factors used were 2.6 for the Mo 3d_{5/2} peak and 5.4 for the Te 3d_{5/2} peak.⁴²⁷ The reference energies for W 4d_{5/2} and the Te 3d_{5/2} peaks are 243.7 and 573.0 eV, respectively.

Graphene/MX2/Graphene. Monolayer graphene was grown by CVD following the recipe discussed in the following paragraph. Two pieces of graphene were transferred by the bubble transfer method and left floating in deionized (DI) water. The first sheet of graphene was transferred onto a TEM grid and dried, while the second graphene sample was left in the water bath for later use. The PMMA layer used in the transfer process of the first graphene sheet was dissolved with acetone, followed by isopropanol (IPA). We then grew monolayer 1T'-WTe₂ flakes by CVD, and once the growth was completed, the substrate was removed from the furnace and immediately covered with the second graphene sheet and dried. Through this method the 1T'-WTe₂ experienced minimal exposure to air. The PMMA/graphene/1T'-WTe₂ stack on the SiO₂/Si growth substrate was then released using a diluted HF solution of 1:25 and quickly washed in 2 DI water baths before being transferred onto the first graphene sheet on the TEM grid. Acetone was then used to dissolve the PMMA followed by IPA. We were then left with a graphene/1T'-WTe₂/graphene heterostructure on a TEM grid (figure 6.2.1.3(a)). The sample was stable in this configuration and could be transported to the ACSTEM for high resolution imaging.

Graphene growth. Graphene synthesis was carried out in a low-pressure CVD furnace (OTF-1200X-4-C4-SL-UL, MTI Corp.). Cu foils (Alfa Aesar Item #46365) were cleaned with 5.4% HNO₃ for 40 seconds and two DI water baths for 2 min, and then blown dry with N₂ gas. The reaction chamber was pumped to a base pressure of ~ 50 mTorr. The Cu growth substrate was annealed at 1020 °C for 30 minutes under a gas flow of 500 sccm Ar and 80 sccm H₂. Monolayer graphene was then grown using

methane as a carbon source at a flow rate of 5 sccm for 5 mins and then 10 sccm for 15 mins. The reactor was subsequently cooled to room temperature rapidly under a flow of 80 sccm H₂ and 10 sccm CH₄.

Structural Stability calculations. Density functional theory calculations were carried out using the QUANTUM ESPRESSO code.⁴⁴⁴ Designed, optimized, norm-conserving pseudopotentials⁴⁴⁶ were used to soften the valence electron wavefunctions and ionic potentials of W and Te. Fully relativistic pseudopotentials were generated using the OPIUM code.⁴⁴⁵ Pseudopotentials for H and O were generated with neutral reference electronic configurations. The reference electronic configurations of W and Te were $5s^25p^65d^06s^0$ (W⁴⁺) and $5s^24d^{10}5p^4$ (Te²⁻) respectively. An augmentation operator was applied to the *s* potential of the W pseudopotential to improve transferability with less positive oxidation states of W. The Kohn-Sham orbitals were expanded in a plane wave basis with an energy cutoff of 50 Ry. The generalized gradient approximation (GGA) of Perdew, Burke, and Ernzerhof⁴⁴³ was used to calculate the electron exchange and correlation energy. Calculations were spin polarized along the *z*-axis to allow for a proper treatment of electron spin. A Gaussian smearing of 0.005 Ry was used to improve electronic convergence. We also included Grimme's semiempirical DFT-D2 method⁴⁸⁶ to treat van der Waals interactions for physisorption and chemisorption. The 8×12×1 *k*-points of the Brillouin zone were sampled using Monkhorst-Pack scheme⁴⁸⁷ to obtain self-consistent charge density for the monolayer. Bulk WTe₂ has an orthorhombic crystal structure in space group Pmn2₁ (no. 31). It exhibits W₃Te₆ layers along the *z*-axis separated by 3.42 Å. We model monolayer WTe₂ by increasing the interlayer separation

to approximately 24 Å. The lattice constants (with the exception of c) and ionic positions were relaxed until the total energy and force changed by less than 1×10^{-8} Ry and 1×10^{-6} Ry/Bohr respectively. The threshold for self-consistent field (SCF) convergence was 1×10^{-10} Ry. The relaxed lattice constants, $a = 3.54$ Å and $b = 6.23$ Å, are in good agreement with literature x-ray diffraction (XRD) measurements, $a = 3.50$ Å and $b = 6.34$ Å. In order to model a wider array of adsorption geometries, we use a 2×2 surface unit cell. Both associative and dissociative adsorption were considered for $\text{H}_2(\text{g})$ and $\text{H}_2\text{O}(\text{g})$. Only dissociative adsorption was considered for $\text{O}_2(\text{g})$ given that DFT significantly overestimates its binding energy due to the self-interaction error of electrons in the exchange term. Adsorption geometries were calculated by relaxing the ionic positions of the monolayer and adsorbates until the total energy and force reached convergence thresholds of 1×10^{-4} Ry and 1×10^{-3} Ry/Bohr respectively. The convergence threshold for SCF calculations was slightly increased to 1×10^{-6} Ry. Milder thresholds allowed for a computationally efficient yet thorough investigation of adsorption locations.

6.3 1H /1T' heterostructures

6.3.1 Synthesis and physical properties of monolayer transition metal dichalcogenide 1H/1T' heterostructures

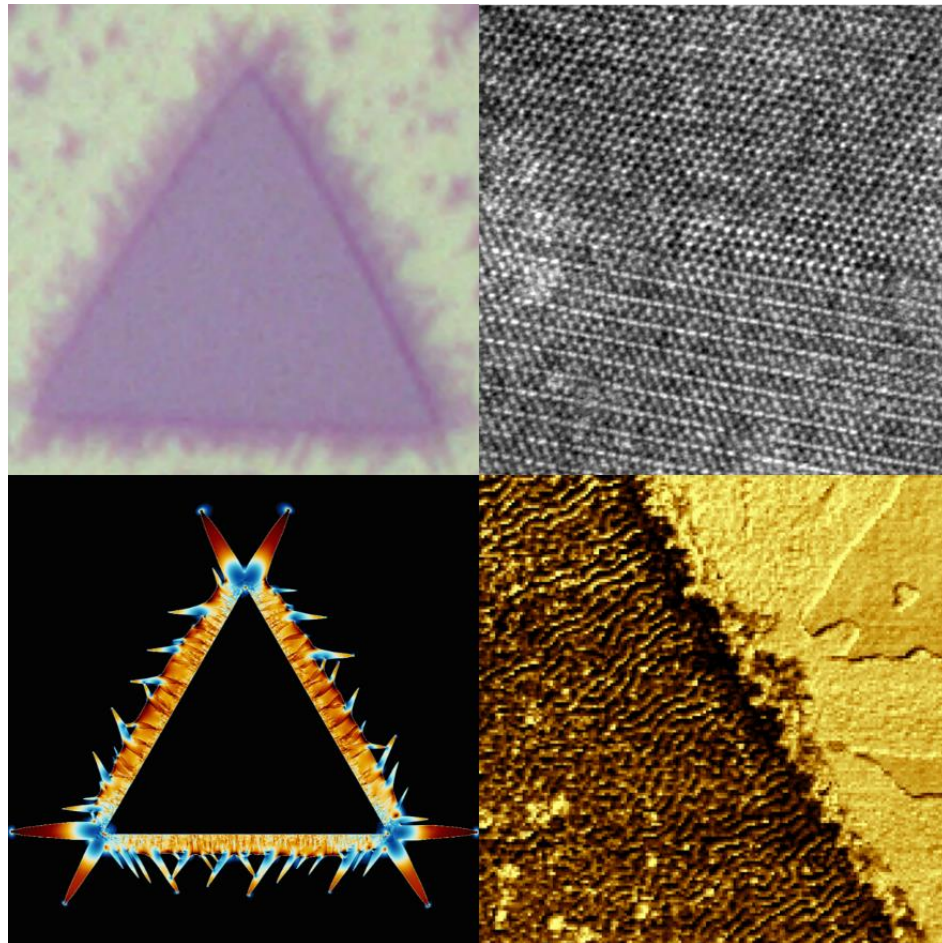
The results presented in this section is currently being prepared for the publication “Synthesis and physical properties of monolayer transition metal dichalcogenide 1H /1T' heterostructures”, Carl H. Naylor, William M. Parkin, Zhaoli Gao, Joel Berry, Songsong Zhou, Qicheng Zhang, John B. McClimon, Liang Z. Tan, Christopher E. Kehayias, Mengqiang Zhao, Ram S. Gona, Robert W. Carpick, Andrew M. Rappe, David J. Srolovitz, Marija Drndic, A.T. Charlie Johnson.

Abstract

Heterostructures of transition metal dichalcogenides (TMDs) offer the attractive prospect of combining distinct physical properties derived from different TMD structures. Here we report direct chemical vapor deposition of in-plane monolayer heterostructures based on 1H-MoS₂ and 1T'-MoTe₂. The large lattice mismatch between these materials led to intriguing phenomena at their interface. Atomic force microscopy indicated buckling in the 1H region. Tip-enhanced Raman spectroscopy showed mode structure consistent with Te substitution in the 1H region during 1T'-MoTe₂ growth. This was confirmed by atomic resolution transmission electron microscopy, which also revealed an atomically-stitched, dislocation-free 1H/1T' interface. Theoretical modeling revealed that both the

buckling and absence of interfacial misfit dislocations were explained by Te substitution into the 1H region. Phase field simulations predicted 1T' morphologies with spike-shaped islands at specific orientations consistent with experiments. Electrical measurements across the heterostructure confirmed its electrical continuity. This work demonstrates the feasibility of dislocation-free stitching of two different atomic configurations and a pathway towards direct synthesis of monolayer TMD heterostructures of different phases.

TOC:



Over the past decade the study of novel two-dimensional materials “beyond graphene”, such as metal carbides (“Mxenes”), layered perovskites, and black phosphorus, has grown rapidly.^{34,38} Transition metal dichalcogenides (TMDs) have emerged as a leading platform to broaden the set of available materials and associated material properties.^{35–37,44} TMDs consist of metal atoms (e.g. Mo, W) sandwiched between chalcogen atoms (S, Se or Te). In the monolayer form, TMDs can assume various atomic configurations known as the 1H, 1T and 1T’ phases (Figure 6.3.1.1a).^{61,67–69,71} In the 1H phase, the top layer of chalcogen atoms is aligned with the bottom layer. In the 1T phase, the top layer of chalcogen atoms is shifted with respect to the bottom layer so that the chalcogen atoms form a hexagon around the metal atom when viewed along a direction normal to the plane. The 1T’ phase can be visualized as a distorted 1T structure that results in the isolation of a chain of chalcogen atoms. The large variety of atomic combinations and structural phases that characterize the TMD materials family leads to a large number of different materials with diverse physical and chemical properties.

There are two primary methods to produce TMDs in monolayer form: mechanical or liquid exfoliation from the bulk and synthesis by chemical vapor deposition (CVD). Mechanical exfoliation relies on the use of an adhesive tape to repeatedly peel apart the layers of a bulk crystal until a monolayer region is achieved.²⁵ This technique yields high quality monolayer material but very low surface coverage, making the method tedious and ill-suited for scalable manufacturing. Liquid exfoliation relies on polymers and sonication to dissociate bulk crystals into thin flakes. It yields many monolayer regions,¹³⁶ but the technique usually leads to undesirable surface contamination and

structural distortion or damage. Synthesis by CVD relies on solid and/or vapor precursors to directly grow monolayer TMD flakes on a substrate. The method is very reproducible and yields large amounts of high quality monolayer TMDs.^{59,74,98,140}

Of all the TMDs, 1H-MoS₂ and 1H-WSe₂ are the most widely synthesized and studied to date.^{41,48,77,95,192} They are semiconductors with high on/off ratios, reasonable mobility values, large photoluminescence, and energy band gaps whose size is tuned by the thickness of the flake.²¹ Monolayer 1H-MoS₂ can be transformed into 1T-MoS₂ through chemical treatment with n-butyllithium. This approach was used to convert parts of an exfoliated 1H-MoS₂ flake to 1T-MoS₂ to create a 1H-MoS₂/1T-MoS₂ heterostructure.⁶⁹ However this method is complicated by the fact that 1T-MoS₂ is very unstable in air, while n-butyllithium is pyrophoric. As an alternative, groups have reported phase transformations of small regions of an exfoliated 1H-MoS₂ flake by rhenium intercalation and thermal annealing in an electron microscope.¹¹² Other groups have also reported laser-enabled phase patterning of few-layer exfoliated MoTe₂ flakes to yield 1H/1T' heterostructures.⁶⁷ To date, no group has reported the synthesis of in-plane heterostructures of monolayer TMDs of different atomic configuration.

1T'-MoTe₂ and 1T'-WTe₂ are semimetals that are theoretically predicted and experimentally observed to exhibit fascinating properties such as Weyl semimetal behavior,⁶⁶ superconductivity,⁶⁰ large non-saturating magnetoresistance,⁵⁵ quantum spin hall effect,⁶¹ and weak antilocalization at low temperature.^{58,59} These properties have motivated multiple efforts towards synthesis of monolayer TMDs in the 1T' phase. We previously reported the growth of high quality monolayer 1T'-MoTe₂ and 1T'-WTe₂,

along with measurements and analysis of their physical properties.^{58,59} These materials degrade rapidly in air but passivation techniques can be used to stabilize the materials and enable more detailed property measurements. Other groups have also reported the synthesis of monolayer 1T'-MX₂ materials with observations of optical dichroism and superconductivity.^{475,488}

In this work, we report successful direct synthesis of monolayer 1H/1T' in-plane, atomically "stitched" heterostructures by combining growth techniques for monolayer 1H-MoS₂ and 1T'-MoTe₂. We successfully stabilized the heterostructure flakes by passivation with large-area CVD graphene. X-ray Photoelectron Spectroscopy (XPS) was used to confirm the chemical composition of the sample. Tip enhanced Raman spectroscopy (TERS) demonstrated the distinction between the 1H and 1T' regions. The observed Raman modes matched theoretical predictions based on Density Functional Perturbation Theory (DFPT)⁴⁸⁹ and hinted at the substitution of Te for S in the 1H-MoS₂ region. Atomic force microscopy (AFM) measurements showed that the heterostructure flakes were of monolayer height with a buckled topography in the 1H-MoS₂ region. We performed DFPT simulations that revealed a buckling mechanism due primarily to Te substitution in the 1H-MoS₂ region as well as a proposed growth mechanism that both correlate with our observations. Aberration corrected scanning transmission electron microscopy (ACSTEM) was used to image the 1H and 1T' atomic configurations within a monolayer flake as well as the stitching structure at the interface. ACSTEM images also confirmed the presence of significant Te substitution in the 1H-MoS₂ region. Finally, we used electron beam lithography to electrically contact the 1H/1T' in both regions of a

single heterostructure flake and show that the 1H-MoS₂ remained semiconducting in the presence of the buckled interface as well as the Te atom substitutions. This study reveals an alternative pathway to the creation of in-plane TMD heterostructures and should motivate further work towards the intriguing prospect of combining the relatively unexplored electrical properties of 1T' TMDs with those of the more studied 1H TMDs.

CVD synthesis of 1H/1T' in-plane heterostructures

Synthesis of monolayer 1H/1T' heterostructures by chemical vapor deposition (CVD) was accomplished through a two-step process based on ammonium heptamolybdate (AHM) and vapors from sulfur and tellurium powders as precursor materials (Figure 6.3.1.1b). We began by growing single crystal 1H-MoS₂ flakes, and then switched the furnace conditions to allow for growth of 1T'-MoTe₂ single crystal flakes, some of which nucleated at 1H-MoS₂ edges to form an atomically stitched heterophase interface (Figure 6.3.1.1c). Details of the growth method can be found in the Methods section. Figure 1d includes a photograph showing a “coffee ring” of material that has grown around the original AHM droplet. At higher magnification (Figure 6.3.1.1d) many 1H triangular flakes are seen with 1T' needles growing around the flake to give a 1H/1T' in-plane heterostructure.

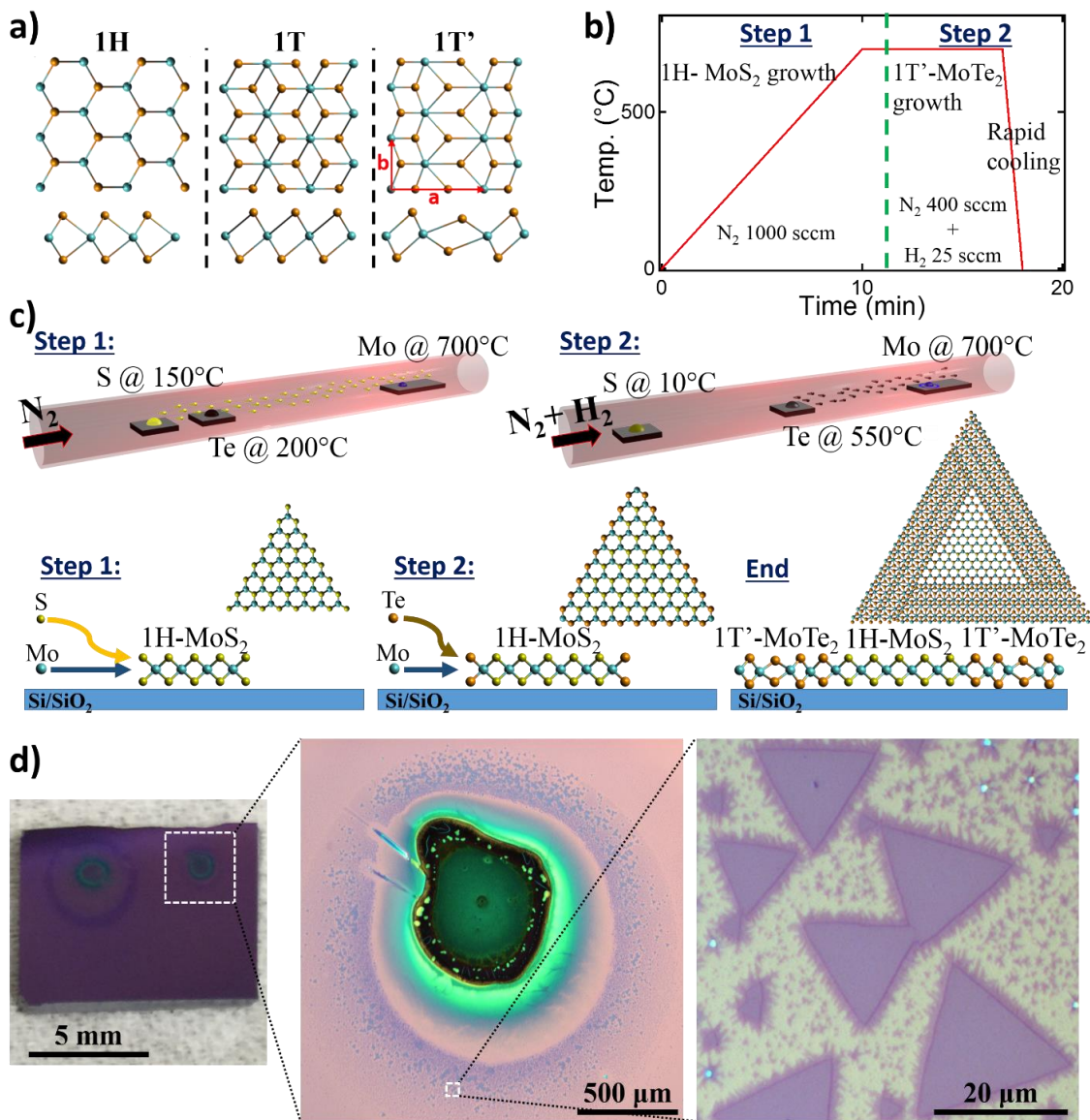


Figure 6.3.1.1. 1H/1T' growth. a) Ball and stick diagrams for the 1H, 1T and 1T' phases of monolayer metal dichalcogenides (transition metal in blue and chalcogen in orange). b) Flow graph of the two-step growth process. c) Schematic of the growth setup and process. d) Optical micrographs of 1H/1T' flakes under increasing magnification.

Characterization of 1H/1T' Heterostructures

XPS was performed on the 1H/1T' heterostructures to confirm their composition (Figure 6.3.1.2a). We identify the MoX₂ (3d_{5/2}, 3d_{3/2}) peaks, as well as peaks for Te

($3d_{5/2}$, $3d_{3/2}$) and S ($2s$, $2p_{3/2}$, $2p_{1/2}$). The XPS results confirm the presence of Mo, S, and Te atoms in the flakes, however it is difficult to determine the exact stoichiometry of a particular flake due to the high areal density of $1T'$ - MoTe_2 flakes that also form on the substrate (Figure 6.3.1.1d) and the large spot size of the XPS beam (1 x 3 mm). We also identify the presence of MoO_3 and MoO_2 ($3d_{5/2}$, $3d_{3/2}$) peaks in the XPS spectrum for regions containing only flake material (i.e., heterostructures and $1T'$ - MoTe_2). The presence of these MoO_x compounds is ascribed to the reaction of $1T'$ - MoTe_2 with O_2 from the air, in agreement with previous reports,^{58,59,490,491} and confirming the need to passivate the $1H/1T'$ heterostructure for further studies.

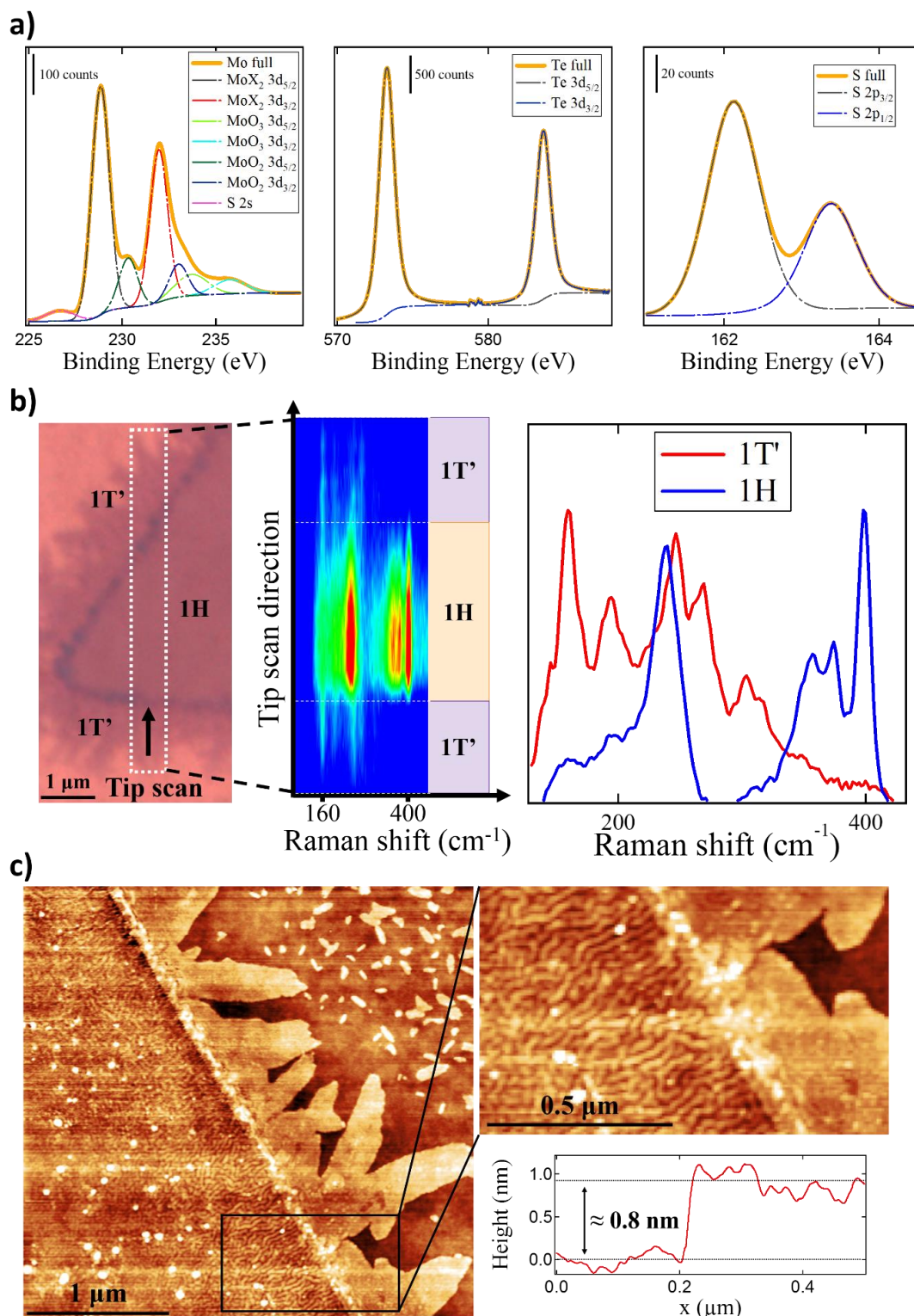


Figure 6.3.1.2. Characterization of 1H/1T' heterostructure flakes. a) X-ray photoelectron spectroscopy (XPS) data revealing the presence Mo, S and Te compounds in the flake. b) Tip-enhanced Raman spectroscopy results show clear differences between the 1H and 1T' regions. c)

AFM of a 1H/1T' flakes indicate monolayer height and the presence of wrinkles indicative of buckling of the 1H region.

Tip-enhanced Raman spectroscopy (TERS) was used to study the vibrational spectrum of different regions of the heterostructure and provide further insight into their chemical composition. Since 1T'-MoTe₂ decays rapidly in air, we passivated the heterostructure sample with a CVD-grown graphene sheet before conducting TERS measurements, with the TERS results shown in Figure 6.3.1.2b. The tip scan line begins in a 1T' region, moves through a 1H region and then moves into a region of 1T'. The three regions are clearly observed in the TERS results, enabling analysis of the Raman-active modes in each region. In the 1T' region (beginning and end of the scan line) we identify five vibrational modes, at 160 cm⁻¹, 190 cm⁻¹, 248 cm⁻¹, 269 cm⁻¹, and 300 cm⁻¹, where the last is due to the Si substrate.⁴⁹² The other four peaks in the spectrum are the Raman-active A_g modes of monolayer 1T'-MoTe₂, and the measured values are in excellent agreement with previous reports on monolayer 1T'-MoTe₂ and with theoretical predictions.^{59,430,490} The 269 cm⁻¹ peak is confirmation of the monolayer form of the 1T'-MoTe₂ region, because this spectral line is expected to shift for multi-layer material, towards a value of 258 cm⁻¹ for the bulk.⁴²⁹

In the center of the flake (the 1H region), we identified 4 vibrational modes at 240 cm⁻¹, 359 cm⁻¹, 372 cm⁻¹ and 400 cm⁻¹. Stoichiometric 1H-MoS₂ is known to exhibit two peaks, E¹_{2g} and A_{1g}. We performed calculations based on DFPT and found modes at 376 cm⁻¹ and 395 cm⁻¹, consistent with previous reports.^{77,191} These two vibrational modes occur at frequencies very similar to the observed modes at 372 cm⁻¹ and 400 cm⁻¹, suggesting the presence of 1H-MoS₂ in the 1H region of the heterostructure flakes. To

explain the other two modes in the TERS spectrum (240 cm^{-1} and 359 cm^{-1}), we performed DFPT simulations on $1\text{H-MoS}_{2(1-x)}\text{Te}_{2x}$ for $x=0.5$ and found that both E_{2g}^1 and A_{1g} modes redshift, as expected for substitution of S with the more massive Te atoms. The E_{2g} mode redshifts from 376 cm^{-1} to 340 cm^{-1} , while the A_{1g} mode shifts dramatically from 395 cm^{-1} to 217 cm^{-1} . These two modes characteristic of $1\text{H-MoS}_{2(1-x)}\text{Te}_{2x}$ closely match the 359 cm^{-1} and 240 cm^{-1} modes observed for the 1H region in the heterostructure. We also note from Figure 6.3.1.2b that the intensity of the A_{1g} 400 cm^{-1} is close to the 240 cm^{-1} and the E_{2g} 372 cm^{-1} matches the 359 cm^{-1} , consistent with this assignment. Based on these observations, we propose a model for heterostructure growth, where the triangular region was first grown as 1H-MoS₂ but then during the growth of the 1T'-MoTe₂ region, Te atoms insert into some S sites, converting nanoscale regions of the triangle into 1H-MoS₂/1H-MoSTe structures. These TERS results confirm the 1H/1T' nature of the heterostructure flakes and the identity of the 1T'-MoTe₂ material, and they also suggest the existence of Te substitution for S in the triangular 1H-MoS₂ region.

Atomic force microscopy (AFM) was used to investigate the height and structure of the heterostructure flakes (Figure 6.3.1.2c). We measured a height of approximately 0.8 nm at the edge of the flake, consistent with monolayer material, and also noticed small multilayer regions along some sections of the 1H/1T' interface. This indicates that growth of 1T'-MoTe₂ occurred at the 1H-MoS₂ edge, preferentially in-plane but also to some extent in the out-of-plane direction. We also observed wrinkles at the interface between the 1H and 1T' regions, which ran perpendicular to the 1H/1T' interface and extended into the 1H region for roughly 500 nm.

The observation of a buckled 1H phase and a flat 1T' phase near the interface is surprising when compared to the behavior expected upon joining perfect 1H-MoS₂ and 1T'-MoTe₂ crystals along their short unit cell direction (*b*) with no compositional mixing. The equilibrium lattice constants, $b_{1\text{H-MoS}_2} = 3.183 \text{ \AA}$ and $b_{1\text{T}'\text{-MoTe}_2} = 3.455 \text{ \AA}$,⁶⁸ indicate that a very large lattice misfit strain, $\varepsilon_0 \approx 8.55\%$, is associated with such an interface. The 1H side would be under tension and the 1T' side under compression; therefore buckling should be expected in the 1T' domains, rather than in the 1H domains.

The observed behavior (buckling of the 1H domain) can be understood as the result of 2D compositional mixing between chalcogen species rather than 1D interfacial misfit strain. DFT-based calculations indicate that 1H-MoS_{2(1-x)}Te_{2x} is a solid solution above $\sim 230^\circ\text{C}$ for all *x*.⁴⁹³ There is therefore a thermodynamic driving force for Te atoms to substitute into S lattice sites in 1H-MoS₂ during growth. The presence of Te in the 1H phase, at increasing levels near the interface, is consistent with the TERS results above and is confirmed by TEM imaging and analysis (Figure 6.3.1.3e and discussion below).

Within the 1H lattice, substitutional Te atoms generate a significant biaxial compressive strain, $\varepsilon_{Te} \approx 0.115x$, where *x* is Te composition in MoS_{2(1-x)}Te_{2x}.⁴⁹³ This strain appears to be the cause of the buckling observed within the 1H phase domains. The amount of Te required to produce the wrinkle amplitude *A* and wavelength λ determined from the AFM images (Figure 6.3.1.2c) can be estimated from a simple one-dimensional geometric analysis. The strain relieved by a sinusoidal buckling profile is $\varepsilon_b = (L-L_0)/L_0 \approx (\pi A/\lambda)^2$, where *L* is the arc length of the 1D profile over a lateral distance *L*₀ (assuming $2\pi A \ll \lambda$). The measured average values of $A \approx 0.4 \text{ nm}$ and $\lambda \approx 25 \text{ nm}$ give $\varepsilon_b \approx 0.25\%$.

Equating ε_b with ε_{Te} , which amounts to assuming that the observed buckling relieves all Te induced misfit strain, and solving for the Te composition suggests that 2% ($x \simeq 0.02$) of the S atoms are replaced by Te atoms within the 500 nm (l_0) wide region of the 1H phase where buckling is observed.

Furthermore, a quasi-2D buckling analysis indicates that the width of the buckled region, $l_0 = 500$ nm, is much too large to be caused by interfacial misfit strain alone. Compressive stress localized to the edge of a free 2D sheet induces 1D wrinkles that decay away from the edge of the sheet over a length scale $l_0 \simeq 0.23\lambda$.⁴⁹⁴ For $\lambda \simeq 25$ nm, the predicted $l_0 \simeq 6$ nm, much less than the observed value of 500 nm. The wrinkling morphology is also generally 2D/herringbone-like away from the interface, which is consistent with equi-biaxial compression induced by Te substitution as opposed to uniaxial compression induced by 1D interfacial misfit. The 1D buckling near the interface could result from 1H/1T' interfacial misfit and/or from bulk Te substitution if the 1H/1T' interface is free to displace along its normal (traction-free boundary). A change in buckling wavelength near the interface would be expected in the former case, but no such change is resolvable in the AFM images. We therefore conclude that the observed buckling is a result of thermodynamically-driven, but kinetically-limited, Te substitution within the 1H phase leading to biaxial compressive strain in this region.

ACSTEM

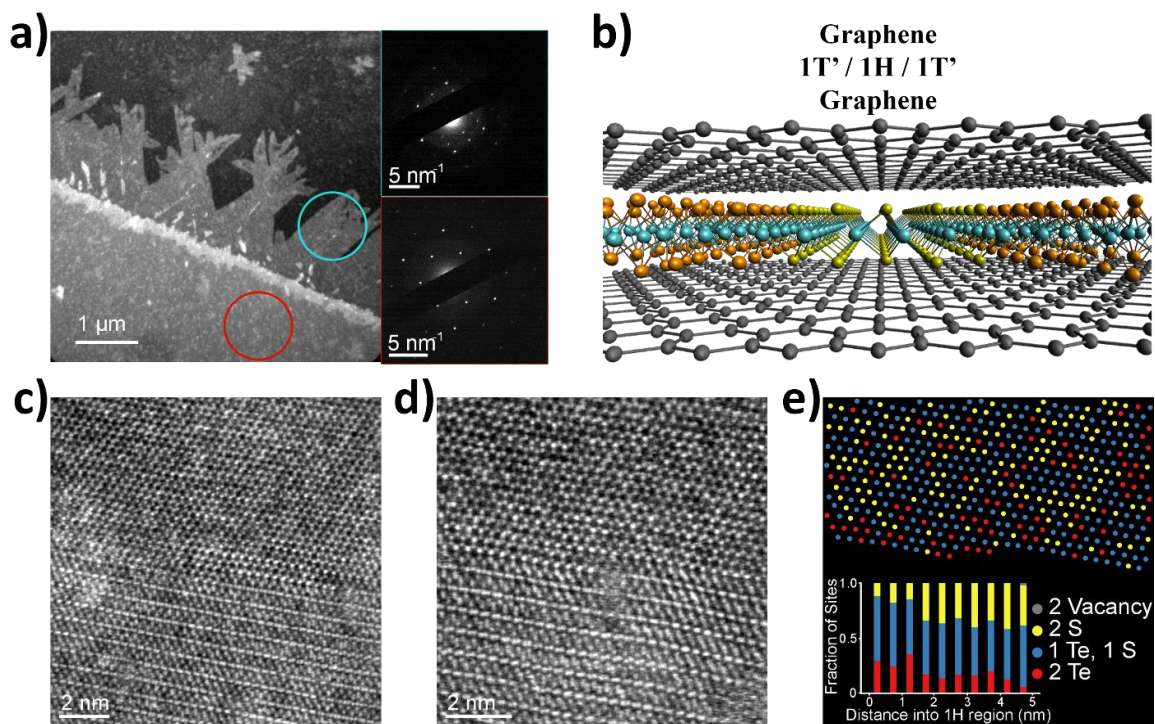


Figure 6.3.1.3. Characterization by Transmission Electron Microscopy (TEM). a) Dark-field TEM micrograph of the interface between a 1H region (bottom) and 1T' region (top) of a flake on a TEM carbon grid. The top-right image shows selected area electron diffraction (SAED) pattern from the circled 1T' region, and the bottom-right image shows a SAED pattern from the circled 1H region. b) Schematic of graphene encapsulating a 1H/1T' heterostructure used for aberration-corrected scanning TEM measurements. c,d) Aberration-corrected high angle annular dark field (HAADF) images of the interface between 1H and 1T'. e) Sulfur sites in the MoS₂ region in d) labeled with number of tellurium substitutions estimated using the intensity of the site in the HAADF image. Inset is the occurrence of each substitution type as a function of distance from the boundary.

Figure 6.3.1.3a shows a dark-field TEM (DF) image of the interface between the 1H and 1T' regions of a heterostructure flake. The selected-area electron diffraction pattern of the 1T' region showed that the 1T'-MoTe₂ flakes grew fastest along the direction of the Te zigzag chain (i.e., the shorter [010] direction of the unit cell), resulting in a rectangular morphology with the long axis along the [010] crystal direction, consistent with our earlier report on CVD growth of 1T'-MoTe₂.⁵⁹ SAED also was used to determine that the edges of the 1H region were oriented along its zigzag [110]

direction, and that the [010] direction in the 1T'-MoTe₂ flakes is oriented at 60° and 120° from parallel to the interface.

Due to the unstable nature of 1T'-MoTe₂, we encapsulated the heterostructure between two sheets of graphene for atomic resolution TEM imaging (details can be found in the method section). The graphene sheets isolated the heterostructure (Figure 6.3.1.3b) and prevented air from oxidizing the 1T' material as observed in previous reports.⁵⁸ This structure was then transferred onto a TEM grid for ACSTEM imaging.

Aberration corrected high angle annular dark field STEM (HAADF) images show, however, that the orientation of the rectangular 1T'-MoTe₂ regions away from the boundary of the heterostructure does not directly reflect the atomic stitching at the interface. Atomic resolution images (Figure 6.3.1.3c and 6.3.1.3d) of the 1H-1T' interface show that the stitching mainly consists of the zigzag edges of the 1H region stitched to the Te zigzag chain edges of the 1T'-MoTe₂ so that the [010] 1T' direction is parallel to the interface. This edge stitching is not represented in the lower magnification dark field image (Figure 6.3.1.3a) that shows 1T'-MoTe₂ flakes grown at 60° and 120° from parallel to the interface, indicating that the edge of the 1H parent is *not* atomically smooth. Any interface rotation into or out of the edge of the 1H triangle will expose zigzag MoS₂ edges at 60° or 120° from parallel to the edge. 1T'-MoTe₂ domains seeded on these rotated 1H edges will have their fast-growing [010] axes pointed at 60° or 120° from parallel to the edge of the 1H parent, and thus the presence of these two different 1T' rotational variants dominate the features far from the interface.

The HAADF images also showed Te substitution near the interface. HAADF images are mass contrast, with intensity proportional to atomic number ($Z_S = 16$, $Z_{Mo} = 42$, $Z_{Te} = 52$), so it is straightforward to distinguish the S and Mo sublattices as well as Te substitutions at sulfur sites. Figure 6.3.1.3e shows the S_2 sites in a 1H region near the interface labeled with the number of Te substitutions, based on the HAADF intensity (see supplement figure S2). The heterostructure growth introduced both single and double Te substitutions in the 1H region, especially near the interface, in agreement with our TERS measurements.

In the absence of S-Te mixing near the 1H/1T' interface, the large misfit between the two lattices, $\epsilon_0 \simeq 8.55\%$, would be expected to result in a large density of misfit dislocations along the interface. A dislocation spacing $s_0 = b/\epsilon_0 \simeq 4\text{nm}$, where b is the magnitude of the Burgers vector (equal to the lattice parameter b), would be required to accommodate this strain in the absence of 1T' buckling. Misfit dislocations are not visible along the interface in the TEM images shown in Figures 6.3.1.3c and 6.3.1.3d, each of which spans $\sim 10\text{-}13\text{ nm}$. This indicates that $s_0 > 13\text{ nm}$ and that misfit strain is relieved by other means. The previously discussed S-Te mixing along the flake edges accounts for this strain relief and the observed lack of dislocations as described in the following paragraph.

Interfacial misfit decreases nearly linearly with increasing Te composition in the 1H phase, as $\epsilon_0 \simeq 0.1125 (0.76-x)$ (assuming $x = 1$ on the 1T' side of the interface).⁴⁹³ Analysis of the Te composition from TEM images indicates that $x \simeq 0.50\text{-}0.75$ in the 1H phase near the interface (Figure 6.3.1.3e). Analysis of 1H and 1T' lattice parameters from

TEM images similarly indicates that $x \approx 0.51-0.75$ and $x \approx 0.69-0.94$ in the 1H and 1T' phases, respectively, near the interface (see Figure 6.3.1.4a). These bounds are obtained by equating the measured lattice parameters a and b in each phase (see Figure 6.3.1.4) to that corresponding to the equilibrium a or b at a given Te composition x .⁴⁹³ Interfacial misfit strain is greatly reduced at these compositions, to $\varepsilon_0 \lesssim 0.6\%$. The minimum misfit dislocation spacing correspondingly increases to $s_0 \gtrsim 55$ nm, which is consistent with the observation of well-stitched, dislocation-free interfaces in the 10-13 nm wide TEM images.

Modulations of Te composition in the 1H phase may also result from thermodynamically-driven phase separation into Te-rich and Te-poor phases upon quenching below $T \lesssim 230^\circ\text{C}$.⁴⁹³ Without knowledge of S and Te transport rates in this temperature range, it is unclear whether such phase separation is kinetically feasible. The small magnitude and relative spatial uniformity of 1H phase buckling are consistent with the presence of a broad, homogeneous Te-poor phase resulting from phase separation. Observations of small 1H phase subdomains on the T' side of the interface are also consistent with the formation of a phase separated Te-rich 1H phase near the initial interface, followed by incomplete transformation of this region to 1T'.

Growth morphology

The needle-like growth morphology of the 1T' domains differs from the more compact second phase growth morphologies observed in other lateral TMD

heterostructures such as MoS₂/WS₂^{14,495} and MoSe₂/WSe₂.²⁴⁴ In these systems both phases are 1H crystals with nearly identical lattice parameters and thus no elastic misfit. One therefore expects continued step-wise growth from the triangular flakes of the first phase, with little to no change in the growth morphology of the second phase.

Isolated single crystal 1T'-MoTe₂ flakes have been observed to grow with elongated, rectangular, needle-like shapes in which the short (*b*) unit cell direction is aligned with the long edge of the flake.^{59,490} We have calculated the edge energies along the *a* and *b* directions in 1T'-MoTe₂ using DFT and find that the *b* edge has lower energy ($\lesssim 200$ meV/Å) than the *a* edge (~ 270 meV/Å) [See Supporting Information]. This anisotropy indicates that the lowest energy crystal shapes will be rectangular and elongated in the *b* direction as observed in experiments. This edge energy anisotropy likely plays an important role in generating the needle-like patterns observed in the present system. One added constraint is that 1T' nucleation initially occurs at the edge of the parent 1H flake. Coherency across the interface dictates only three possible 1T' orientations (with *b* parallel to or at 60° or 120° from parallel to the flake edge, see Figure 6.3.1.4b) due to the lower (rectangular) symmetry of the 1T' crystal. These are precisely the needle orientations observed in the present system (see Figure 6.3.1.3). Such a morphology may therefore result from simple geometric constraints and edge energy anisotropy alone.

We emphasize that a second constraint in heterostructure growth, elastic (heteroepitaxial) coupling between phases, can independently control growth morphology. Our analysis of interfacial composition (see Figure 6.3.1.4a) indicates that a

nonzero misfit strain persists between the 1H and 1T' domains. This strain may significantly influence 1T' growth, but it is unclear which type of morphology should result. We have therefore performed continuum phase field elastic simulations of the nucleation and growth of 1T' domains that are bound to an elastically misfitting parent 1H crystal. The model describes how 1T' domains form and evolve to minimize elastic misfit energy during displacive 1H \rightarrow 1T' structural transformations,⁴⁹⁶ (see the Supporting Information for more details).

Figure 6.3.1.4b shows a representative morphology from a growth simulation at the misfit strain corresponding to $x=0.75$ and 0.94 on the 1H and 1T' sides of the interface, respectively (as inferred from the TEM-derived lattice parameters corresponding to the shaded gray regions in Figure 6.3.1.4a). Needle morphologies very similar to those seen in the experiments appear, with needles composed of the two 1T' variant orientations at 60° or 120° from parallel to each flake edge. A strip composed predominantly of the third variant orientation is also observed along the inner portion of each edge, consistent with the observed [010] alignment of the 1H and 1T' lattices across the interface. A relatively uniform, compact triangular growth morphology is obtained in the absence of elastic misfit or when the misfit strain is shear-dominant rather than dilatation-dominant (see the Supporting Information). These results demonstrate that elastic misfit alone can induce needle-like 1T' growth morphologies, even in the absence of anisotropic edge energies and growth rates. At the estimated misfit strain and computed edge anisotropy level of the present system, we expect that both effects drive the observed needle-like growth morphologies.

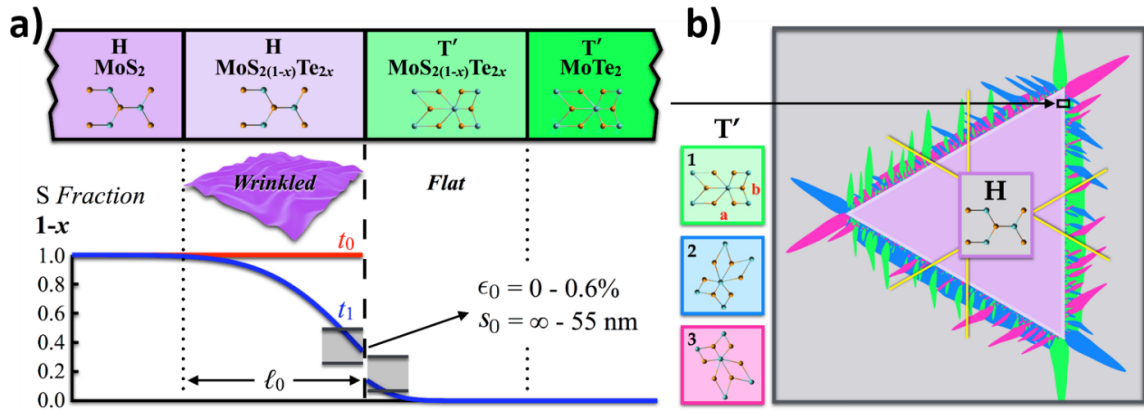


Figure 6.3.1.4. Effects of the composition, elastic misfit strain, and out-of-plane bending on the interface structure and growth morphology. a) Schematic of compositional domains and variation of sulfur composition ($1 - x$) near the 1H/1T' interface. Configurations are shown at the end of 1H-MoS₂ growth (t_0 , red line) and at the end of 1T'-MoTe₂ growth (t_1 , blue lines). Bounds (gray shaded areas) are those inferred from TEM-derived lattice parameters. The indicated ranges of misfit strain ϵ_0 and equilibrium dislocation spacing $s_0 = b/\epsilon_0$ are those computed based on the shaded gray compositional bounds. b) Simulated 1T' growth/transformation morphology at the misfit strain corresponding to $x = 0.75$ and 0.94 on the 1H and 1T' sides of the interface. The color scheme employed for the T' domains is shown on the left. Yellow lines are oriented at 60° and 120° from parallel to each edge.

Electrical

Field effect transistor (FET) devices were made using electron beam lithography to study the electrical properties of the heterostructure. The 1H /1T' flake was first etched into a rectangle to create a 1T' /1H /1T' device, and four contacts were patterned, as shown in Figure 6.3.1.5a. The device was immediately inserted in a vacuum probe station, and electrical data was collected under a pressure of 10^{-7} Torr. We created 15 separate devices on one growth substrate, and we collected useful electrical data from five of them. The electrical responses of all five devices were comparable, and care was taken to determine that there were no gate leaks, thus confirming that the measured responses were due to the monolayer device structure. Figure 6.3.1.5a is an optical

micrograph of a device, taken after all electrical measurements were completed. The lack of optical contrast for parts of the $1T'$ - MoTe_2 region (away from the contact) indicates that this small region had oxidized.^{58,59,490}

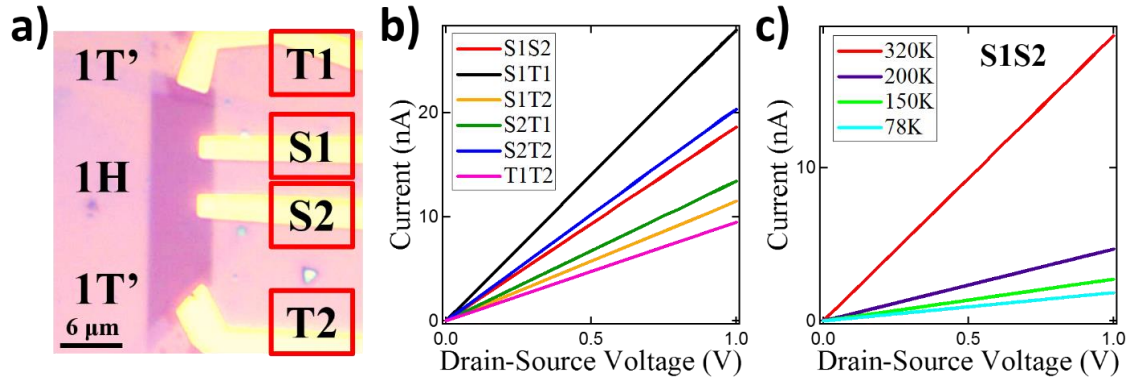


Figure 6.3.1.5. Electrical responses from the $1T'/1H/1T'$ structure. **a)** Optical micrograph of a $1T'/1H/1T'$ device. **b)** Current-bias voltage (I-V) characteristics for different contact pairs, measured at room temperature with $V_g = 20\text{V}$. **c)** I-V characteristic at different temperatures for the $1H\text{-MoS}_2$ region (S1-S2 contact pair), with $V_g = 20\text{V}$.

Figure 6.3.1.5b reveals the electrical responses through all possible connections and highlights that the $1T'$ contacts have survived and are electronically stitched to the $1H$ region. Higher current was observed through the $1T'$ contacts in all of the samples. A high off-state current was observed in our three terminal measurements; consistent with Te doping in the $1H$ region. Figure 6.3.1.5c shows the electrical responses at various temperatures through the $1H$ region with a 20V applied back gate bias. The decrease in current with decreasing temperature indicates a semiconducting material, therefore even with the buckling and the Te substitutions in the $1H\text{-MoS}_2$ triangles, the structure remained a semiconductor. To our knowledge, these are the first reported electrical responses of an in plane monolayer $1T'/1H$ heterostructure grown by CVD.

Conclusion

We have developed an approach for synthesis of in-plane 1H/1T' monolayer TMD heterostructures. The data indicate that there was Te substitution along the periphery of the 1H-MoS₂ region that caused this area to buckle. The chemical composition and atomic structure of the heterostructure flakes were confirmed by XPS, tip-enhanced Raman spectroscopy, AFM, and ACSTEM, with the interpretation guided by DFPT simulations. Continued growth under MoTe₂ growth conditions produced three distinct 1T'-MoTe₂ variants that were atomically stitched to the 1H-MoS₂ phase, as confirmed through ACSTEM images; no misfit dislocations were observed along the interface. Electrical measurements confirmed that the 1H region maintained its semiconducting properties. However it is desirable to reduce the amount of Te substitution in the 1H region in order to maintain the high quality n-type semiconducting properties of the 1H-MoS₂. This work provides a pathway to in-depth investigations of synthesis of TMD heterostructures combining different phases and possible effects occurring at the in-plane interface of monolayer semiconductors and topological insulators.

Methods

CVD synthesis of 1H/1T' heterostructures. The Si/SiO₂ growth substrate was prepared by spin coating a growth promoter of 1% sodium cholate at 3000 rpm for 60 seconds. Sodium cholate is known to act as a growth promoter for 1H-MoS₂ and 1T'-

MoTe₂.^{59,98,169} A micro-droplet of a saturated solution of ammonium heptamolybdate (AHM) was deposited onto the substrate to provide the molybdenum feedstock. The chip was then inserted into the center of a CVD furnace, with two source chips placed upstream, one chip with 25 mg of sulfur and the second with 25mg of tellurium. The sulfur (tellurium) source was placed 18 cm (15 cm) from the growth substrate. The CVD furnace was then heated to 700°C at a rate of 70°C/min under a constant flow of 1000 sccm N₂. The S chip reached a temperature of 150°C and started to sublime, while the Te pellet was at 200°C, well below its sublimation temperature of 550°C (figure 1c, step1). After 12 minutes of 1H-MoS₂ growth we used a magnetic system to slide the Te substrate closer to the growth substrate, where it rose in temperature to 550°C and began to sublime. We used the same system to slide the sulfur substrate away so that it rapidly cooled, and we adjusted the gas flow to 25 sccm H₂ and 400 sccm of N₂ (figure 6.3.1.1c, step2). After a 5 minute growth time, the furnace was rapidly cooled and the substrate retrieved.

XPS. The sample was transferred to the XPS loadlock and pumped down within 20 min of growth to minimize sample oxidation. Measurements were performed in the constant analyzer energy mode using a customized XPS spectrometer with a monochromatized Al K α source.⁴⁴¹ The XPS spectrometer was calibrated in accordance with ISO 15472:2001 to an accuracy of better than ± 0.05 eV for the 100 eV pass energy used for the high resolution spectra and the 200 eV pass energy used for the survey spectra. High resolution spectra were fit with peak shapes composed of a convolution of Gaussian and Lorentzian functions superimposed atop a Shirley-Sherwood

background.⁴⁹⁷ Synthetic peaks were constrained to have appropriate intensity ratios for spin-orbit split states and the same FWHM, with the exception of the Mo 3d components for MoO₃. High resolution spectra revealed the presence of charging due to the thickness of the SiO_x layer on the Si substrate. This effect was corrected for all high resolution spectra by shifting the aliphatic carbon peak, which was the most intense component of the C1s spectra, to 285.0 eV.⁴⁹⁸ Mo 3d high resolution spectra were fit with seven components: S 2s at 226.65±0.02 eV, Mo 3d^{5/2} from Te_xMo_yS_z at 228.85±0.02 eV, MoO₂ 3d^{5/2} at 230.31±0.01 eV, Te_xMo_yS_z 3d^{3/2} at 231.98±0.03 eV, MoO₂ 3d^{3/2} at 233.04±0.04 eV, MoO₃ 3d^{5/2} at 233.74±0.04 eV, and MoO₃ 3d^{3/2} at 235.92±0.16 eV.^{499,500} Te 3d spectra were fit with two components: Te 3d^{5/2} from Te_xMo_yS_z at 573.26±0.01 eV and Te_xMo_yS_z 3d^{3/2} at 583.65±0.02 eV. S 2p spectra were fit with two components: 2p^{3/2} from Te_xMo_yS_z at 162.15±0.03 eV, and Te_xMo_yS_z 2p^{1/2} at 163.36±0.02 eV.

Selected Area Electron Diffraction (SAED). The SAED patterns were taken in a JEOL 2100 operated at 200 kV. The heterostructure flakes were transferred onto a TEM carbon grid using a previously described HF transfer process.⁵⁹

Aberration corrected HAADF imaging was performed with a JOEL ARM 200CF with a corrector on the STEM probe and operated at 80 kV. The flakes were encapsulated between two graphene layers and transferred onto a holey carbon grid to slow oxidation outside of the TEM⁵⁹ and electron-beam induced damage in the TEM, as the graphene is effectively invisible on MoS₂/MoTe₂ in the mass contrast HAADF images (Figure 6.3.1.3b).⁴⁷⁷

CHAPTER VII.

Summary, Future Work and Conclusion

7.1 Summary of 1H-MX₂ materials

The field “beyond graphene” began with the study of an exfoliated 1H-MoS₂ flake. Scientists quickly realized the immense potential exfoliated monolayer 1H-MoS₂ has to offer, which led to a surge in research on 1H-MX₂ materials. There is a real need for the synthesis of high quality, large area, monolayer, 1H-MX₂ materials to satisfy the demands of educational and industrial research.

In Chapters 4 and 5, we demonstrated the synthesis by chemical vapor deposition (CVD) of large area, monolayer, single crystal flakes of 1H-MoS₂, 1H-WS₂, 1H-MoSe₂ and 1H-WSe₂ (figure 7.1.1). The high quality of these flakes has been demonstrated by the large amount of research/publications currently being achieved with these materials. Under the 1H atomic configuration, these transition metal dichalcogenides (TMDs) are predominantly n-type semiconductors apart from 1H-WSe₂ which is p-type. They possess reasonable values of mobility and high on/off ratios which makes them promising candidates for an alternative to Si in the semiconducting industry. They have a bandgap dependent of the number of layers and possess strong photoluminescence when they are in the monolayer form.

We incorporated these TMDs into multiple applications. We patterned the growth of 1H-MoS₂. By controlling the location of the Mo seed, we can predetermine the exact

growth location of a 1H-MoS₂ flake. This is a scalable growth technique for potential large scale manufacturing. We incorporated the 1H-MoS₂ into a scalable biosensor for opioid detection. Opioid overdose accounts for over 30,000 deaths a year in the United States, and there are over 250 million prescriptions of opioids handed out a year (roughly equivalent to one prescription per adult in the United States).^{6,7} There is an urgent need to further understand the interactions opioids have with our health, and this sensor is a first step in the understanding these mechanisms. We evaluated and understood the large electrical responses observed in a 1H-MoS₂ vapor sensor. We uncovered that the responses were not only due to the changes of intrinsic resistivity in the 1H-MoS₂ but also from the Au/1H-MoS₂ contact. This work highlights the importance of contacts with TMDs and that passivation of these contacts is a requirement. We manufactured a universal biosensor utilizing hBN films. By incorporating a monolayer of hBN on top of a material, chemical functionalization becomes dependent solely on hBN and not the underlying material. This technique leads to high device survival rate and optimum sensor responses. We manufactured scalable flexible 1H-MoS₂ devices. Flexible devices are attractive for obvious reasons, and incorporating novel TMDs onto such substrates is a first step into wearable sensors. Finally, we reported some of the work currently being done by our collaborators on the synthesized 1H-MoS₂.

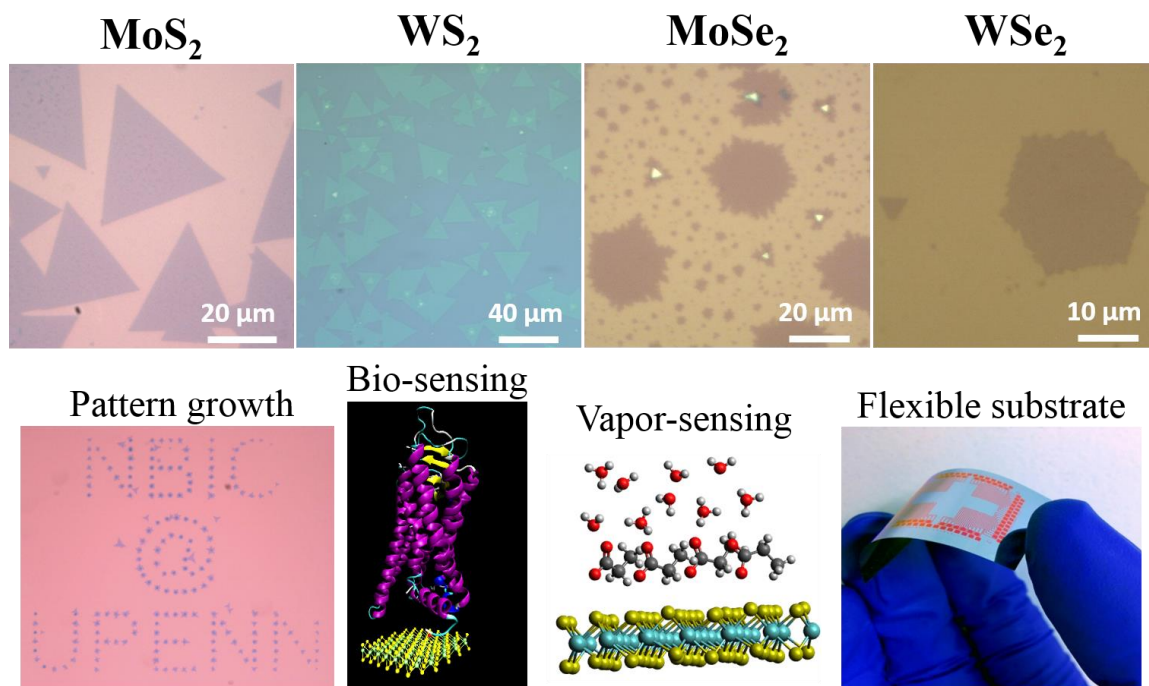


Figure 7.1.1. Summary of 1H-MX₂.

7.2 Summary of 1T'-MX₂ materials

The 1T' atomic configuration is a very attractive phase due to the theoretical prediction of large-gap quantum spin hall insulators in 1T'-MX₂. 2D topological insulators are attractive materials for potential applications in quantum computing because of the topologically protected conductive region. The 1T'-MX₂ materials could also be suitable for innovative transistor structures that can be switched *via* a topological phase transition rather than conventional carrier depletion. For these reasons, 1T'-MX₂ materials are very promising 2D TMDs. However 1T'-MX₂ are notoriously unstable in air and phase transformation from 1H to 1T' proves challenging.

In Chapter 6, we reported the first direct synthesis of monolayer 1T'-MX₂ materials with the growth of 1T'-MoTe₂ and 1T'-WTe₂ (figure 7.2.1). These materials are very unstable in air, however by utilizing sheets of graphene we were able to passivate the material and perform lengthy characterizations. Aberration corrected transmission electron microscopy images revealed the first images of the 1T' phase, with a clear distinction of the isolated chain of chalcogen atoms the signature of 1T'-MX₂ materials. Electrical measurements performed on 1T'-MX₂ revealed a weak antilocalization effect at low temperature, indicative of a strong spin-orbit coupling effect that is essential for emergence of non-trivial states.

We believe that our highly successful growth technique for producing monolayer 1T'-MX₂ materials will pave the way for further studies on this promising and exciting phase of TMDs with potential applications in quantum computing.

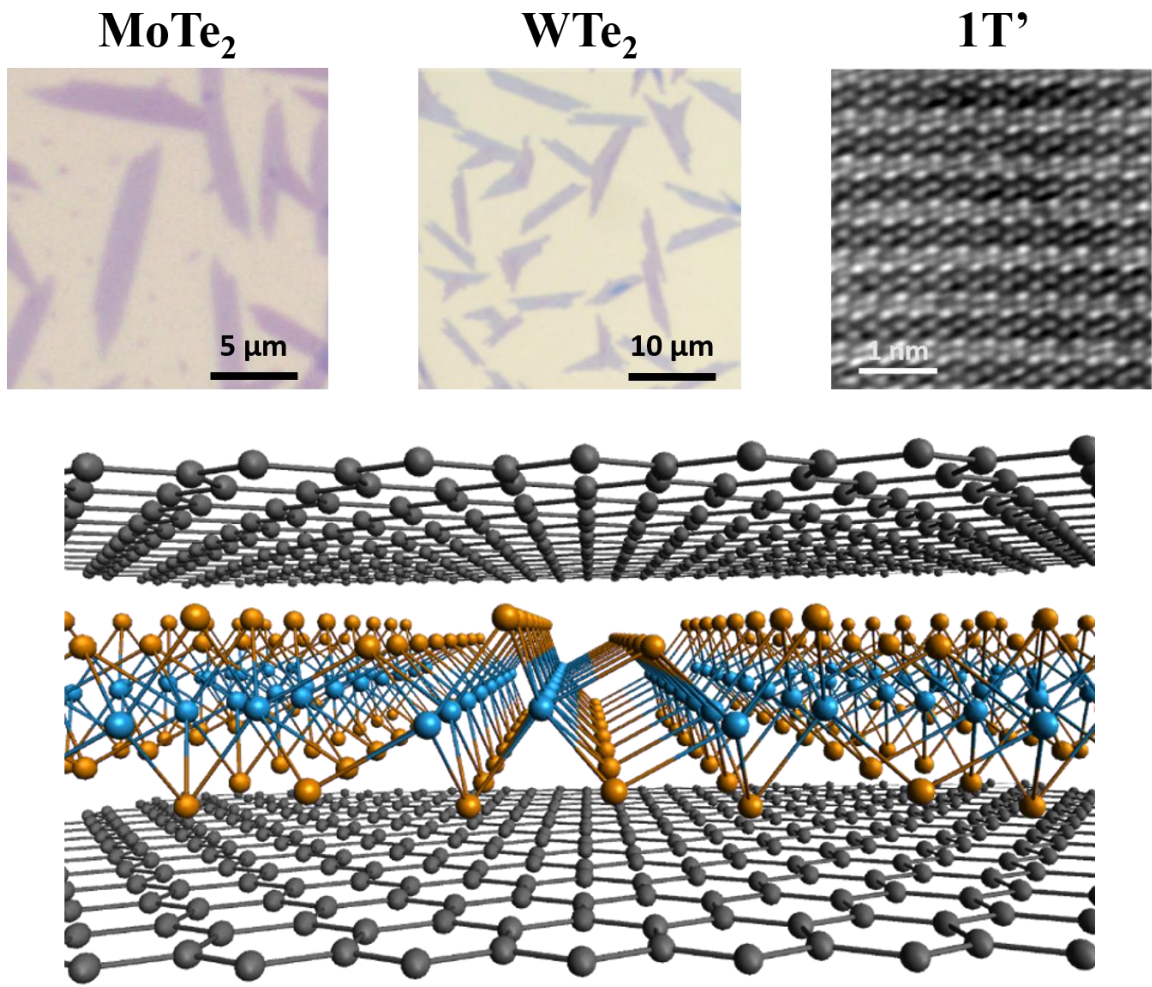


Figure 7.2.1. Summary of 1T'-MX₂.

7.3 Summary of TMD heterostructures

Heterostructures of different TMDs are an exciting area in the field “beyond graphene”. They offer the possibility of combining various properties of TMDs creating a unique material.

In Chapters 5 and 6, we reported the synthesis of in-plane monolayer heterostructures of TMDs. We demonstrated the growth of 1H-MoS₂/1H-WS₂, these TMDs exhibit the same 1H atomic configuration and have minimal lattice mismatch. They have different bandgap energy values so one could choose which material fluoresces by controlling the incident light wavelength. We reported the growth of in-plane 1H/1T' heterostructures. The in-plane synthesis of different atomic configurations heterostructures lead to a wrinkling/buckling in the 1H region. ACTEM images of the interface revealed a dislocation free in-plane stitching of both phases (figure 7.3.1).

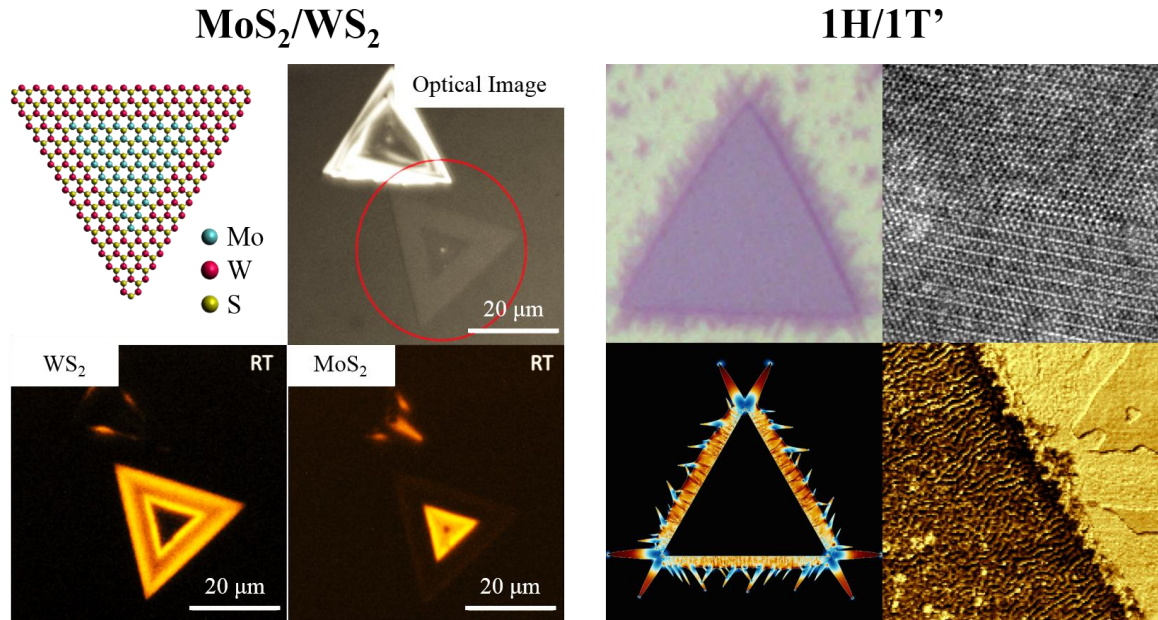


Figure 7.3.1. Summary of TMD heterostructures.

7.4 Future work and conclusion

Currently, we are exploring alternative heterostructures. P-type semiconductor 1H-WSe₂ in a 1H-WSe₂/1T'-WTe₂ heterostructure. Initial results seem to reveal that the in-plane heterostructure consists of 1 H-WSe₂ core and 1T'-WTe₂ peripheral. Observation using an optical microscope show the 1T'-WTe₂ region has decayed within 20 minutes (figure 7.4.1).

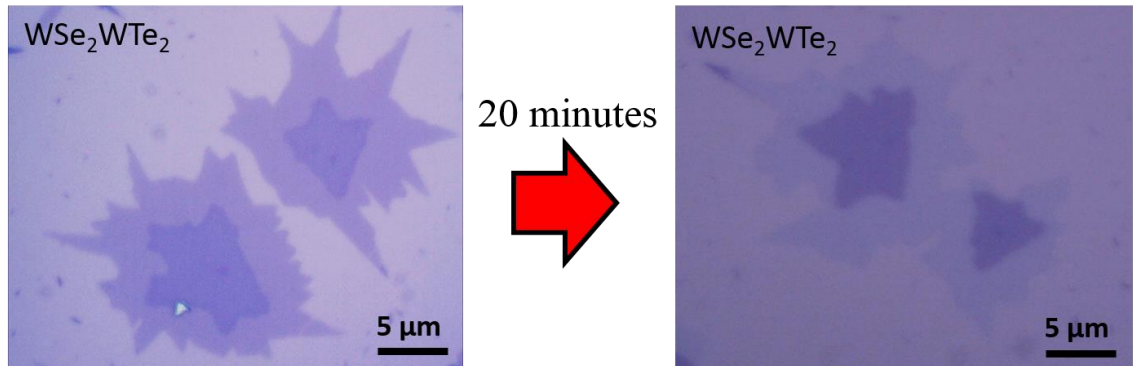


Figure 7.4.1. 1H-WSe₂/1T'-WTe₂ heterostructure.

Other potential heterostructures include 1H-WSe₂/1H-MoS₂ (figure 7.4.2). 1H-WSe₂ is a p-type semiconductor and 1H-MoS₂ is an n-type semiconductor, therefore an in-plane heterostructure of both these TMDs would yield a monolayer p/n junction. The p/n junctions are vital for photovoltaic and light emitting technologies. A brief operating schematic of solar cell with a p/n junction can be seen in figure 7.4.2. A photon brings sufficient energy to excite an electron into the conduction band creating an electron/hole pair. The electron and hole will split by moving to the lower, more favorable energy state, which generates a potential difference between the p-type and n-type regions. Synthesizing large area, high quality monolayer 1H-WSe₂/1H-MoS₂ heterostructures would be a first step towards efficient 2D solar cells and light emitting technologies.

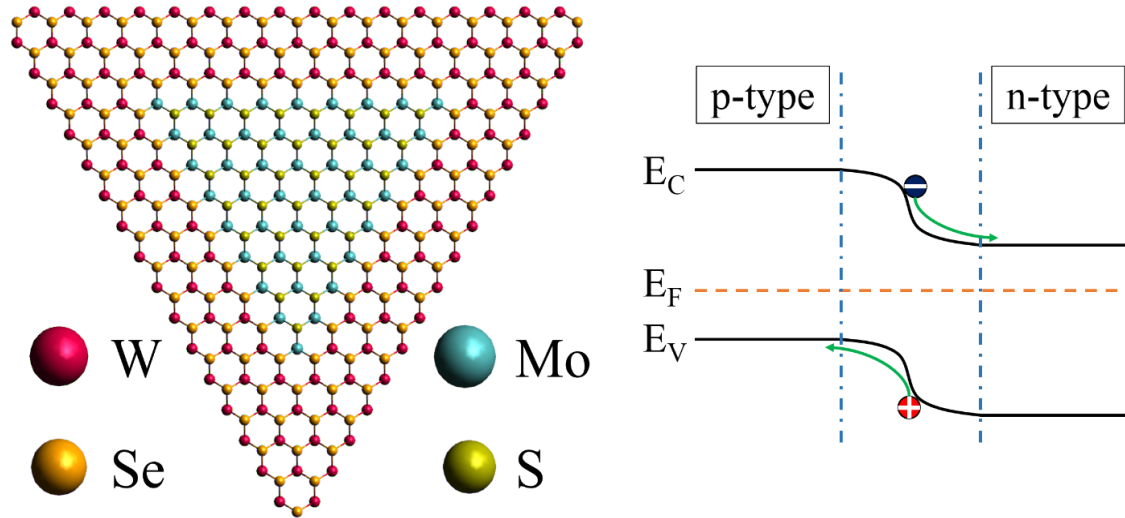


Figure 7.4.2. 1H-WSe₂/1H-MoS₂ heterostructures, a p/n junction.

Scientists are beginning to explore the exciting properties of different metal group TMDs. We will start experimenting with the synthesis of monolayer 1T-TaS₂ with Ta belonging to the group 7 (figure 7.4.3). 1T-TaS₂ is one of few TMDs that can be synthesized in the 1T phase.

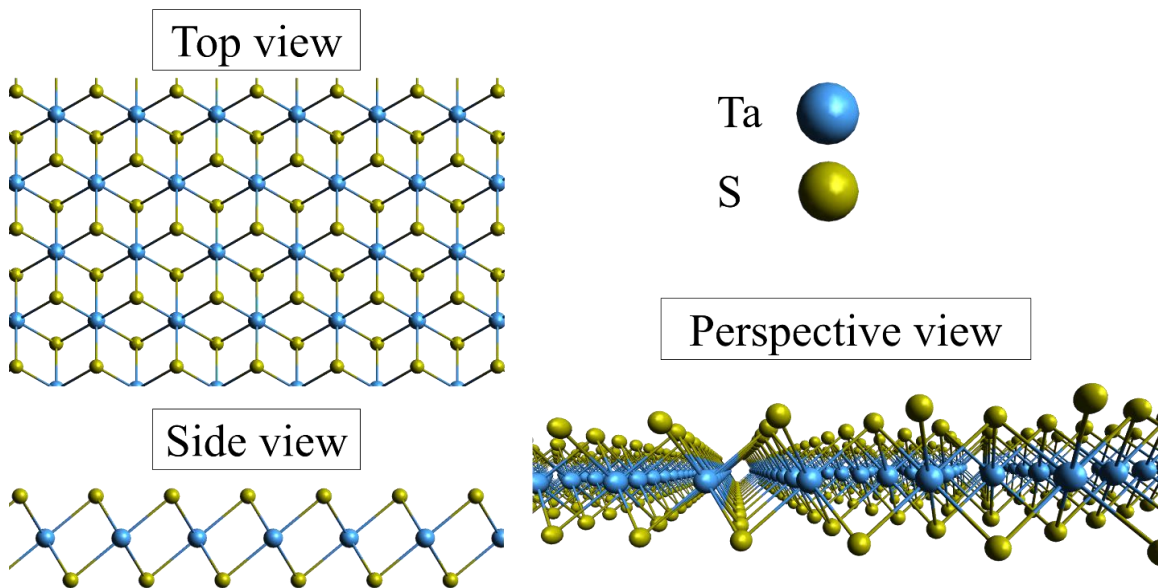


Figure 7.4.3. 1T-TaS₂.

In order for TMDs to have an immense impact in today's society, scientists first have to overcome a few challenges, for instance, the synthesis of high quality monolayer sheets to enable scalable fabrication, and solve the instability in air of some TMDs. Though challenging, these hurdles are not limiting; scientists are steps away from discovering solutions.

Throughout this thesis, we have demonstrated the recent advances in state of the art synthesis of 2D nanomaterials. The wide combination of metals and chalcogen atoms that yield a TMD combined with the variances in atomic configuration produce a vast amount of nanomaterials that all possess unique properties (e.g. semiconductors and topological insulators). Each TMD has its own specificity and possible application ranging from biosensing to quantum computing (figure 7.4.4). TMDs are at a young age and scientists are only just beginning to see the immense potential TMDs have to offer (figure 7.4.5). The large quantity of properties that are accessible with TMDs coupled with the wide variety of applications is why TMDs are the leading candidate in the field “beyond graphene”.

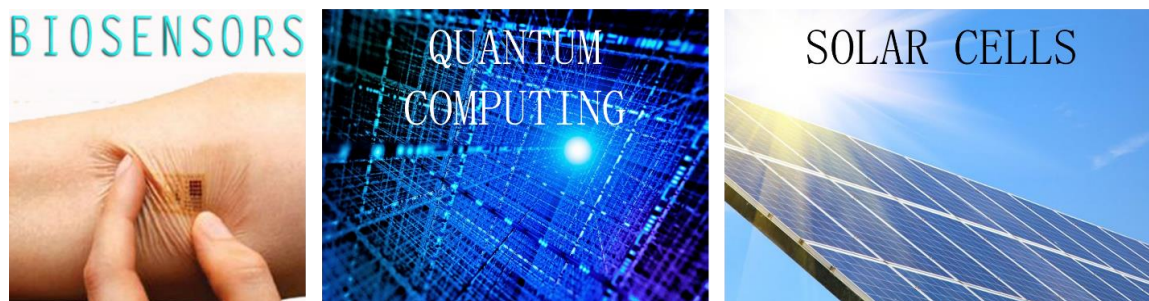


Figure 7.4.4. Potential applications with TMDs.

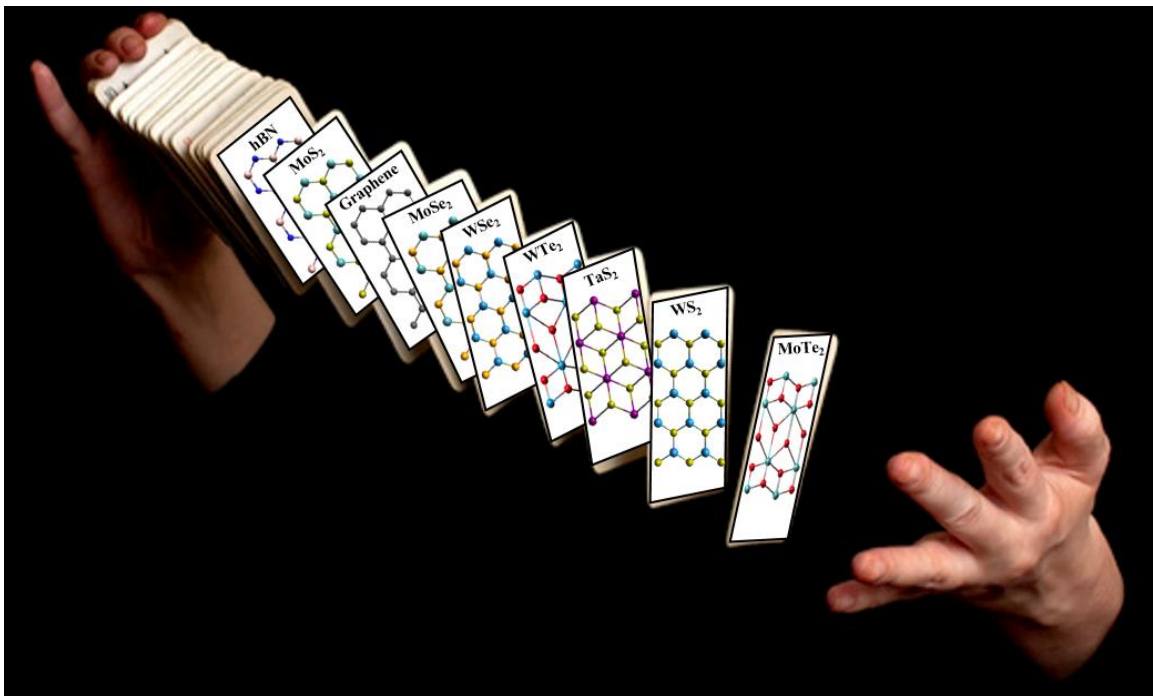


Figure 7.4.5. TMDs.

BIBLIOGRAPHY

1. Lee, C. *et al.* Measurement of the elastic properties and intrinsic strength of monolayer graphene. *Science* **321**, 385–388 (2008).
2. Lee, G. *et al.* High-Strength chemical-vapor deposited graphene and grain boundaries. *Science* **340**, 1073–1077 (2013).
3. Pinto, A. M. *et al.* Graphene-based materials biocompatibility: a review. *Colloids Surf. B* **111**, 188–202 (2013).
4. Novoselov, K. S. *et al.* Two-dimensional gas of massless Dirac fermions in graphene. *Nature* **438**, 197–200 (2005).
5. Novoselov, K. S. *et al.* Room-temperature quantum hall effect in graphene. *Science* **315**, 1379 (2007).
6. Rudd, R. A. *et al.* Increases in drug and opioid-involved overdose deaths - United States , 2010 - 2015. *MMWR* **65**, 1445–1452 (2016).
7. Bohnert, A. S. B. *et al.* and Association between opioid prescribing patterns and opioid overdose-related deaths. *JAMA* **305**, 1315–1321 (2011).
8. Kittel, C. Introduction to solid state physics (8th Edition). *Wiley* (2005).
9. Ashcroft, N. W. & Mermin, N. D. Solid state physics. *Brooks/Cole* (1976).
10. Hu, H. The nature and behavior of grain boundaries. *Plenum Press* (1972).
11. Hu, S. *et al.* Grain boundary segregation of impurities during polycrystalline colloidal crystallization. *Cryst. Growth Des.* **15**, 5685–5692 (2015).
12. Lin, P. *et al.* Influence of grain boundary character distribution on sensitization and intergranular corrosion of alloy 600. *Scrpita Metallurgica et Materiala* **33**, 1387–1392 (1995).
13. Han, G. H. *et al.* Continuous growth of hexagonal graphene and boron nitride in-plane heterostructures by atmospheric pressure chemical vapor deposition. *ACS Nano* **7**, 10129–10138 (2013).
14. Gong, Y. *et al.* Vertical and in-plane heterostructures from WS₂/MoS₂ monolayers. *Nat. Mat.* **13**, 1135–1142 (2014).
15. Wang, W. *et al.* Measurement of the cleavage energy of graphite. *Nat. Commun.* **6**, 1–7 (2015).
16. Meek, J. M. & Craggs, J. D. Electrical breakdown of gases. *Wiley* (1978).
17. Griffiths, D. J. Introduction to quantum mechanics (2nd Edition). *Pearson Prentice Hall* (2004).
18. Kittel, C. & Kroemer, H. Thermal physics (2nd Edition). *Freeman* (1980).
19. Kronig, R. de L. & Penney, W. G. The Kronig Penney model: a single lecture illustrating the band structure of solids. *Chem. Educator* **1**, 1–10 (1996).
20. <http://lampx.tugraz.at/~hadley/ss1/KronigPenney/KronigPenney.php>.
21. Zhu, J. *et al.* Thickness-dependent bandgap tunable molybdenum disulfide films for optoelectronics. *RSC Adv.* **6**, 110604 (2016).
22. Mouras, S. *et al.* Synthesis of first stage graphite intercalation compounds with fluorides. *Rev. Chim. Miner.* **24**, 572 (1987)
23. Cooper, D. R. *et al.* Experimental review of graphene. *ISRN Condensed Matter Physics* **2012**, 501686 (2012).
24. Warner, J. H. *et al.* Atomic structure of ABC rhombohedral stacked trilayer graphene. *ACS Nano* **6**, 5680–5686 (2012).
25. Novoselov, K. S. *et al.* Two-dimensional atomic crystals. *Proc. Natl Acad. Sci.* **102**, 10451–10453 (2005).
26. Geim, A. K. Graphene: status and prospects. *Science* **324**, 1530–1534 (2009).
27. Briggs, B. D. *et al.* Electromechanical robustness of monolayer graphene with extreme bending. *Appl. Phys. Lett.* **97**, 223102 (2010).
28. Wallace, P. R. The band theory of graphite. *Phys. Rev.* **71**, 622–634 (1947).
29. Reich, S. *et al.* Tight-binding description of graphene. *Phys. Rev. B* **66**, 035412 (2002).
30. Bolotin, K. I. *et al.* Temperature-dependent transport in suspended graphene. *Phys. Rev. Lett.* **101**, 096802 (2008).
31. Kretinin, A. V. *et al.* Electronic properties of graphene encapsulated with different two-

- dimensional atomic crystals. *Nano Lett.* **14**, 3270–3276 (2014).
32. Chen, J. *et al.* Intrinsic and extrinsic performance limits of graphene devices on SiO₂. *Nat. Nanotech.* **3**, 206–209 (2008).
 33. Dean, C. R. *et al.* Boron nitride substrates for high-quality graphene electronics. *Nat. Nanotech.* **5**, 722–726 (2010).
 34. Bhimanapati, G. R. *et al.* Recent advances in two-dimensional materials beyond graphene. *ACS Nano* **9**, 11509–11539 (2015).
 35. Chhowalla, M. *et al.* The chemistry of two-dimensional layered transition metal dichalcogenide nanosheets. *Nat. Chem.* **5**, 263–275 (2013).
 36. Robinson, D. S. *et al.* Beyond graphene: progress in novel two-dimensional materials and van der Waals solids. *Annu. Rev. Mater. Res.* **45**, 1–27 (2015).
 37. Duan, X. *et al.* Two-dimensional transition metal dichalcogenides as atomically thin semiconductors: opportunities and challenges. *Chem. Soc. Rev.* **44**, 8859–8876 (2015).
 38. Geim, A. K. & Grigorieva, I. V. Van der Waals heterostructures. *Nature* **499**, 419–425 (2013).
 39. Gupta, A. *et al.* Recent development in 2D materials beyond graphene. *Prog. Mater. Sci.* **73**, 44–126 (2015).
 40. Mas-Balleste, R. *et al.* 2D materials: to graphene and beyond. *Nanoscale* **3**, 20 (2011).
 41. Mak, K. F. *et al.* Atomically thin MoS₂: a new direct-gap semiconductor. *Phys. Rev. Lett.* **105**, 136805 (2010).
 42. Mak, K. F. & Shan, J. Photonics and optoelectronics of 2D semiconductor transition metal dichalcogenides. *Nat. Photonics* **10**, 216–226 (2016).
 43. Tan, C. & Zhang, H. Two-dimensional transition metal dichalcogenide nanosheet-based composites. *Chem. Soc. Rev.* **44**, 2713–2731 (2015).
 44. Wang, Q. H. *et al.* Electronics and optoelectronics of two-dimensional transition metal dichalcogenides. *Nat. Nanotech.* **7**, 699–712 (2012).
 45. Zhang, H. Ultrathin two-dimensional nanomaterials. *ACS Nano* **9**, 9451–9469 (2015).
 46. Hoffman, D. M. *et al.* Optical properties of pyrolytic boron nitride in the energy range 0.05–10 eV. *Phys. Rev. B* **30**, 6051–6056 (1984).
 47. Kobayashi, Y. *et al.* Hexagonal boron nitride grown by MOVPE. *J. Cryst. Growth* **310**, 5044 (2008).
 48. Cui, X. *et al.* Multi-terminal transport measurements of MoS₂ using a van der Waals heterostructure device platform. *Nat. Nanotech.* **10**, 534–540 (2015).
 49. Doganov, R. A. *et al.* Transport properties of pristine few-layer black phosphorus in an inert atmosphere. *Nat. Commun.* **6**, 6647 (2015).
 50. Kim, S. M. *et al.* Synthesis of patched or stacked graphene and hBN flakes: a route to hybrid structure discovery. *Nano Lett.* **13**, 933–941 (2013).
 51. Shanmugam, M. *et al.* 2D layered insulator hexagonal boron nitride enabled surface passivation in dye sensitized solar cells. *Nanoscale* **5**, 11275 (2013).
 52. Dean, C. R. *et al.* Multicomponent fractional quantum Hall effect in graphene. *Nat. Phys.* **7**, 693–696 (2011).
 53. Gannett, W. *et al.* Boron nitride substrates for high mobility chemical vapor deposited graphene. *Appl. Phys. Lett.* **98**, 242105 (2011).
 54. Spalvins, T. J. Lubrication with sputtered MoS₂ films: principles, operation, limitations. *Mater. Engin. Performance* **1**, 347–351 (1992).
 55. Ali, M. N. *et al.* Large, non-saturating magnetoresistance in WTe₂. *Nature* **514**, 205–208 (2014).
 56. Cao, T. *et al.* Valley-selective circular dichroism of monolayer molybdenum disulphide. *Nat. Commun.* **3**, 885–887 (2012).
 57. Lopez-sanchez, O. *et al.* Ultrasensitive photodetectors based on monolayer MoS₂. *Nat. Nanotech.* **8**, 497–501 (2013).
 58. Naylor, C. H. *et al.* Large-area synthesis of high-quality monolayer 1T'-WTe₂ flakes. *2D Mater.* **4**, 021008 (2017).
 59. Naylor, C. H. *et al.* Monolayer single-crystal 1T'-MoTe₂ grown by chemical vapor deposition exhibits weak antilocalization effect. *Nano Lett.* **16**, 4297 (2016).
 60. Pan, X.-C. *et al.* Pressure-driven dome-shaped superconductivity and electronic structural evolution

- in tungsten ditelluride. *Nat. Commun.* **6**, 7805 (2015).
61. Qian, X. *et al.* Quantum spin Hall effect in two-dimensional transition metal dichalcogenides. *Science* **346**, 1344–1347 (2014).
 62. Radisavljevic, B. *et al.* Single-layer MoS₂ transistors. *Nat. Nanotech.* **6**, 147–150 (2011).
 63. Splendiani, A. *et al.* Emerging photoluminescence in monolayer MoS₂. *Nano Lett.* **10**, 1271 (2010).
 64. Sundaram, R. S. *et al.* Electroluminescence in single layer MoS₂. *Nano Lett.* **13**, 1416 (2013).
 65. Wang, L. *et al.* Tuning magnetotransport in a compensated semimetal at the atomic scale. *Nat. Commun.* **6**, 8892 (2015).
 66. Soluyanov, A. A. *et al.* Type-II Weyl semimetals. *Nature* **527**, 495–498 (2015).
 67. Cho, S. *et al.* Phase patterning for ohmic homojunction contact in MoTe₂. *Science* **349**, 625 (2015).
 68. Duerloo, K.-A. N. *et al.* Structural phase transitions in two-dimensional Mo- and W-dichalcogenide monolayers. *Nat. Commun.* **5**, 1–9 (2014).
 69. Kappera, R. *et al.* Phase-engineered low-resistance contacts for ultrathin MoS₂ transistors. *Nat. Mater.* **13**, 1128–1134 (2014).
 70. Voiry, D. *et al.* Phase engineering of transition metal dichalcogenides. *Chem. Soc. Rev.* **44**, 2702–2712 (2015).
 71. Wilson, J. A. & Yoffe, A. D. The transition metal dichalcogenides discussion and interpretation of the observed optical, electrical and structural properties. *Adv. Phys.* **18**, 193–335 (1969).
 72. Li, H. *et al.* Emerging energy applications of two-dimensional layered transition metal dichalcogenides. *Nano Energy* **18**, 293–305 (2015).
 73. Li, H. *et al.* Optoelectronic crystal of artificial atoms in strain-textured molybdenum disulphide. *Nat. Commun.* **6**, 7381 (2015).
 74. Naylor, C. H. *et al.* Scalable production of molybdenum disulfide based biosensors. *ACS Nano* **10**, 6173–6179 (2016).
 75. Tedstone, A. A. *et al.* Synthesis, properties, and applications of transition metal-doped layered transition metal dichalcogenides. *Chem. Mater.* **28**, 1965–1974 (2016).
 76. Berkdemir, A. *et al.* Identification of individual and few layers of WS₂ using Raman spectroscopy. *Sci. Rep.* **3**, 1755 (2013).
 77. Lee, C. *et al.* Anomalous lattice vibrations of single- and few-layer MoS₂. *ACS Nano* **4**, 2695–2700 (2010).
 78. Tonndorf, P. *et al.* Photoluminescence emission and Raman response of monolayer MoS₂, MoSe₂, and WSe₂. *Opt. Express* **21**, 4908–4916 (2013).
 79. Chakraborty, B. *et al.* Symmetry-dependent phonon renormalization in monolayer MoS₂ transistor. *Phys. Rev. B* **85**, 161403 (2012).
 80. Conley, H. J. *et al.* Bandgap engineering of strained monolayer and bilayer MoS₂. *Nano Lett.* **13**, 3626–3630 (2013).
 81. Gong, C. *et al.* Band alignment of two-dimensional transition metal dichalcogenides: application in tunnel field effect transistors. *Appl. Phys. Lett.* **103**, 053513 (2013).
 82. Espejo, C. *et al.* Band structure tunability in MoS₂ under interlayer compression : A DFT and GW study. *Phys. Rev. B* **87**, 245114 (2013).
 83. Kuc, A. *et al.* Influence of quantum confinement on the electronic structure of the transition metal sulfide TS₂. *Phys. Rev. B* **83**, 245213 (2011).
 84. Li, T. *et al.* Electronic properties of MoS₂ nanoparticles. *J. Phys. Chem C.* **111**, 16192 (2007).
 85. Mak, K. F. *et al.* Control of valley polarization in monolayer MoS₂ by optical helicity. *Nat. Nanotech.* **7**, 494–498 (2012).
 86. Zeng, H. *et al.* Valley polarization in MoS₂ monolayers by optical pumping. *Nat. Nanotech.* **7**, 490–493 (2012).
 87. Wu, S. *et al.* Electrical tuning of valley magnetic moment through symmetry control in bilayer MoS₂. *Nat. Phys.* **9**, 149–153 (2013).
 88. Xu, X. *et al.* Spin and pseudospins in layered transition metal dichalcogenides. *Nat. Phys.* **10**, 343–350 (2014).
 89. Yuan, H. *et al.* Zeeman-type spin splitting controlled by an electric field. *Nat. Phys.* **9**, 563–569 (2013).
 90. Fang, H. *et al.* High-performance single layered WSe₂ p-FETs with chemically doped contacts.

- Nano Lett.* **12**, 3788–3792 (2012).
91. Liu, Y. *et al.* Large area growth and electrical properties of p-type WSe₂ atomic layers. *Nano Lett.* **15**, 709–713 (2015).
 92. Kanazawa, T. *et al.* Few-layer HfS₂ transistors. *Sci. rep.* **6**, 22277 (2016).
 93. Ma, N. & Jena, D. Charge scattering and mobility in atomically thin semiconductors. *Phys. Rev. X.* **4**, 011043 (2014).
 94. Wu, W. *et al.* High mobility and high on/off ratio field-effect transistors based on chemical vapor deposited single-crystal MoS₂ grains. *Appl. Phys. Lett.* **102**, 142106 (2013).
 95. van der Zande, A. M. *et al.* Grains and grain boundaries in highly crystalline monolayer molybdenum disulphide. *Nat. Mater.* **12**, 554–561 (2013).
 96. Ben, Z. *et al.* Bandgap inhomogeneity of MoS₂ monolayer on epitaxial graphene bilayer in van der Waals p-n junction. *Carbon* **110**, 396–403 (2016).
 97. Danda, G. *et al.* Monolayer WS₂ nanopores for DNA translocation with light-adjustable sizes. *ACS Nano* **11**, 1937–1945 (2017).
 98. Han, G. H. *et al.* Seeded growth of highly crystalline molybdenum disulphide monolayers at controlled locations. *Nat. Commun.* **6**, 6128 (2015).
 99. Henck, H. *et al.* Electrolytic phototransistor based on graphene-MoS₂ van der Waals p-n heterojunction with tunable photoresponse. *Appl. Phys. Lett.* **109**, 113103 (2016).
 100. Yi, F. *et al.* Optomechanical enhancement of doubly resonant 2D optical nonlinearity. *Nano Lett.* **16**, 1931–1636 (2016).
 101. Lee, B. *et al.* Fano resonance and spectrally modified photoluminescence enhancement in monolayer MoS₂ integrated with plasmonic nanoantenna array. *Nano Lett.* **15**, 3646–3653 (2015).
 102. Liu, W. *et al.* Strong exciton–plasmon coupling in MoS₂ coupled with plasmonic lattice. *Nano Lett.* **16**, 1262–1269 (2016).
 103. Martinez, L. M. *et al.* MoS₂ based dual input logic AND gate. *AIP Adv.* **6**, 125041 (2016).
 104. Mlack, J. T. *et al.* Transfer of monolayer TMD WS₂ and Raman study of substrate effects. *Sci. Rep.* **7**, 43037 (2017).
 105. Madauss, L. *et al.* Defect engineering of single- and few-layer MoS₂ by swift heavy ion irradiation. *2D Mater.* **4**, 015034 (2016).
 106. Parkin, W. M. *et al.* Raman shifts in electron-irradiated monolayer MoS₂. *ACS Nano* **10**, 4134–4142 (2016).
 107. Pierucci, D. *et al.* Band alignment and minigaps in monolayer MoS₂-Graphene van der Waals heterostructures. *Nano Lett.* **16**, 4054–4061 (2016).
 108. Pierucci, D. *et al.* Tunable doping in hydrogenated single layered molybdenum disulfide. *ACS Nano* **11**, 1755–1761 (2017).
 109. Pierucci, D. *et al.* Large area molybdenum disulphide-epitaxial graphene vertical van der Waals heterostructures. *Sci. Rep.* **6**, 26656 (2016).
 110. Reed, J. C. *et al.* Photothermal characterization of MoS₂ emission coupled to a microdisk cavity. *Appl. Phys. Lett.* **109**, 193109 (2016).
 111. Serrano, W. *et al.* Facile fabrication of a ultraviolet tunable MoS₂/p-Si junction diode. *Appl. Phys. Lett.* **106**, 193504 (2015).
 112. Lin, Y. *et al.* Atomic mechanism of the semiconducting-to-metallic phase transition in single-layered MoS₂. *Nat. Nanotech.* **9**, 391–396 (2014).
 113. Kane, C. L. & Mele, E. J. Quantum spin Hall effect in graphene. *Phys. Rev. Lett.* **95**, 226801 (2005).
 114. Kane, C. L. & Mele, E. J. Z₂ topological order and the quantum spin Hall effect. *Phys. Rev. Lett.* **95**, 146802 (2005).
 115. Wu, C. *et al.* Helical liquid and the edge of quantum spin Hall systems. *Phys. Rev. Lett.* **96**, 106401 (2006).
 116. Kim, J. *et al.* Observation of tunable band gap and anisotropic Dirac semimetal state in black phosphorus. *Science* **349**, 723–726 (2015).
 117. Li, L. *et al.* Black phosphorus field-effect transistors. *Nat. Nanotech.* **9**, 372–377 (2014).
 118. Lee, S. *et al.* Anisotropic in-plane thermal conductivity of black phosphorus nanoribbons at

- temperatures higher than 100K. *Nat. Commun.* **6**, 8573 (2015).
119. Tian, Z. *et al.* Two-dimensional SnS: a phosphorene analogue with strong in-plane electronic anisotropy. *ACS Nano* **11**, 2219 (2017).
 120. Carvalho, A. *et al.* Phosphorene: from theory to applications. *Nat. Rev. Mater.* **1**, 16061 (2016).
 121. Wang, Y. *et al.* Degradation of black phosphorus: a real-time ^{31}P NMR study. *2D Mater.* **3**, 035025 (2016).
 122. <http://substance-en.etsmtl.ca/black-phosphorus-the-new-semiconductor-in-town/>.
 123. Naguib, M. *et al.* Two-dimensional nanocrystals produced by exfoliation of Ti_3AlC_2 . *Adv. Mater.* **23**, 4248–4253 (2011).
 124. Naguib, M. *et al.* Two-dimensional transition metal carbides. *ACS Nano* **6**, 1322–1331 (2012).
 125. Halim, J. *et al.* X-ray photoelectron spectroscopy of select multi-layered transition metal carbides (MXenes). *Appl. Surf. Sci.* **362**, 406–417 (2016).
 126. Harris, K. J. *et al.* Direct measurement of surface termination groups and their connectivity in the 2D MXene V_2CT_x using NMR spectroscopy. *J. Phys. Chem. C* **119**, 13713–13720 (2015).
 127. Barsoum, M. W. The $\text{M}_{N+1}\text{AX}_N$ phases: a new class of solids: thermodynamically stable nanolaminates. *Prog. Solid State Chem.* **28**, 201–281 (2000).
 128. Anasori, B. *et al.* 2D metal carbides and nitrides (MXenes) for energy storage. *Nat. Rev. Mater.* **2**, 16098 (2017).
 129. Ma, Z. *et al.* Tunable band structures of heterostructured bilayers with transition-metal dichalcogenide and MXene monolayer. *J. Phys. Chem. C* **118**, 5593–5599 (2014).
 130. Chen, J. *et al.* CO_2 and temperature dual responsive "Smart" MXene phases. *Chem. Commun.* **51**, 314–317 (2015).
 131. Mashtalir, O. *et al.* Dye adsorption and decomposition on two-dimensional titanium carbide in aqueous media. *J. Mater. Chem. A* **2**, 14334–14338 (2014).
 132. Ren, C. E. *et al.* Charge- and size-selective ion sieving through $\text{Ti}_3\text{C}_2\text{T}_x$ MXene membranes. *J. Phys. Chem. Lett.* **6**, 4026–4031 (2015).
 133. <http://onlinelibrary.wiley.com/doi/10.1002/adma.201470041/epdf>.
 134. "Graphene pioneers bag Nobel prize", Institute of Physics, UK. 5 October 2010.
 135. Zan, R. *et al.* Atomic structure of graphene and h-BN layers and their interactions with metals. *Advances in graphene science*, 639–663 (2013).
 136. Coleman, J. N. *et al.* Two-dimensional nanosheets produced by liquid exfoliation of layered materials. *Science* **331**, 568, (2011).
 137. Cho, A. Y. & Arthur, J. R. Molecular beam epitaxy. *Prog. Solid State Chem.* **10**, 157 (1975).
 138. <http://en.rusnano.com/portfolio/companies/semiteq>
 139. Bae, S. *et al.* Roll-to-roll production of 30-inch graphene films for transparent electrodes. *Nat. Nanotech.* **5**, 574–578 (2010).
 140. Kang, K. *et al.* High-mobility three-atom-thick semiconducting films with wafer-scale homogeneity. *Nature* **520**, 656–660 (2015).
 141. Sachs, R. *et al.* Direct comparison of graphene devices before and after transfer to different substrates. *Appl. Phys. Lett.* **104**, 033103 (2014).
 142. <http://www.brukerafmprobes.com/p-3365-nchv.aspx>.
 143. Garcia, R. Attractive and repulsive tip-sample interaction regimes in tapping-mode atomic force microscopy. *Phys. Rev. B* **60**, 4961–4967 (1999).
 144. <http://www.horiba.com/scientific/products/raman-spectroscopy/raman-academy/raman-faqs/what-laser-wavelengths-are-used-for-raman-spectroscopy/>.
 145. Dresselhaus, M. S. *et al.* Perspectives on carbon nanotubes and graphene Raman spectroscopy. *Nano Lett.* **10**, 751–758 (2010).
 146. Ferrari, A. C. *et al.* Raman spectrum of graphene and graphene layers. *Phys. Rev. Lett.* **97**, 187401 (2006).
 147. Ferrari, A. C. Raman spectroscopy of graphene and graphite: disorder, electron–phonon coupling, doping and nonadiabatic effects. *Solid State Commun.* **143**, 47–57 (2007).
 148. Frank, O. *et al.* Raman 2D-band splitting in graphene: theory and experiment. *ACS Nano* **5**, 2231–2239 (2011).
 149. Malard, L. M. *et al.* Raman spectroscopy in graphene. *Phys. Rep.* **473**, 51–87 (2009).

150. Jiang, Y. C. *et al.* Raman fingerprint for semi-metal WTe₂ evolving from bulk to monolayer. *Sci. Rep.* **6**, 19624 (2016).
151. Lee, J. *et al.* Single- and few-layer WTe₂ and their suspended nanostructures: Raman signatures and nanomechanical resonances. *Nanoscale* **8**, 7854 (2016).
152. Rose, H. H. Historical aspects of aberration correction. *J. Electron Microsc.* **58**, 77–85 (2009).
153. Smith, D. J. Development of aberration-corrected electron microscopy. *Microsc. Microanal.* **14**, 2 (2008).
154. Liu, W. *et al.* Electrical contacts to individual SWCNTs: a review. *Beilstein J. Nanotechnol.* **5**, 2202–2215 (2014).
155. Pellegrini, B. Properties of silicon-metal contacts versus metal work-function, silicon impurity concentration and bias voltage. *J. Phys. D: Appl. Phys.* **9**, 55 (1976).
156. Liu, W. *et al.* The impact of Cr adhesion layer on CNFET electrical characteristics. *Nanotechnology* **27**, 1 (2015).
157. Illarionov, Y. Y. *et al.* The role of charge trapping in MoS₂/SiO₂ and MoS₂/hBN field-effect transistors. *2D Mater.* **3**, 035004 (2016)
158. Kalon, G. *et al.* The role of charge traps in inducing hysteresis: capacitance–voltage measurements on top gated bilayer graphene. *Appl. Phys. Lett.* **99**, 083109 (2011).
159. Shi, Y. *et al.* Effects of traps on charge storage characteristics in metal-oxide-semiconductor memory structures based on silicon nanocrystals. *J. Appl. Phys.* **84**, 2358 (1998).
160. Schwierz, F. Graphene transistors. *Nat. Nanotech.* **5**, 487–496 (2010).
161. George, A. S. *et al.* Wafer scale synthesis and high resolution structural characterization of atomically thin MoS₂ layers. *Adv. Funct. Mater.* **24**, 7461–7466 (2014).
162. Wu, W. *et al.* High mobility and high on/off ratio field-effect transistors based on chemical vapor deposited single-crystal MoS₂ grains. *Appl. Phys. Lett.* **102**, 142106 (2013).
163. Perera, M. M. *et al.* Improved carrier mobility in few-layer MoS₂ field-effect transistors with ionic-liquid gating. *ACS Nano* **7**, 4449–4458 (2013).
164. Wang, J. *et al.* High mobility MoS₂ transistor with low Schottky barrier contact by using atomic thick h-BN as a tunneling layer. *Adv. Mater.* **28**, 8302–8308 (2016).
165. Banica, F.-G. Chemical sensors and biosensors: fundamentals and applications. *Wiley* (2012).
166. Gesztelyi, R. *et al.* The Hill equation and the origin of quantitative pharmacology. *Arch. Hist. Exact. Sci.* **66**, 427–438 (2012).
167. Heck, H. A. Statistical theory of cooperative binding to proteins. The Hill equation and the binding potential. *J. Am. Chem. Soc.* **93**, 23–29 (1971).
168. Stefan, M. I. & Nove, N. Le. Cooperative binding. *PLoS One* **9**, 2–7 (2013).
169. Ling, X. *et al.* Role of the seeding promoter in MoS₂ growth by chemical vapor deposition. *Nano Lett.* **14**, 464–472 (2014).
170. Lanzillo, N. A. *et al.* Temperature-dependent phonon shifts in monolayer MoS₂. *Appl. Phys. Lett.* **103**, 093102 (2013).
171. Oh, H. M. *et al.* Photochemical reaction in monolayer MoS₂ via correlated photoluminescence, Raman spectroscopy, and atomic force microscopy. *ACS Nano* **10**, 5230–5236 (2016).
172. Bean, K. E. Anisotropic etching of Silicon. *IEEE Trans. Electron Devices* **25**, 1185–1193 (1978).
173. Bao, W. *et al.* High mobility ambipolar MoS₂ field-effect transistors: substrate and dielectric effects. *Appl. Phys. Lett.* **102**, 042104 (2013).
174. Chang, H. *et al.* High-performance, highly bendable MoS₂ transistors with high -k dielectrics for flexible low-power. *ACS Nano* **7**, 5446–5452 (2013).
175. Jariwala, D. *et al.* Gate-tunable carbon nanotube-MoS₂ heterojunction p-n diode. *Proc. Natl. Acad. Sci U.S.A.* **110**, 18076–18080 (2013).
176. Salvatore, G. A. *et al.* Fabrication and transfer of flexible few-layers MoS₂ thin film transistors to any arbitrary substrate. *ACS Nano* **7**, 8809–8815 (2013).
177. Radisavljevic, B. *et al.* Integrated circuits and logic operations based on single-layer MoS₂. *ACS Nano* **5**, 9934–9938 (2011).
178. Jariwala, D. *et al.* Emerging device applications for two-dimensional transition metal dichalcogenides. *ACS Nano* **8**, 1102–1120 (2014).
179. Yu, W. J. *et al.* Highly efficient gate-tunable photocurrent generation in vertical heterostructures of

- layered materials. *Nat. Nanotech.* **8**, 952–958 (2013).
180. Zhang, W. *et al.* High-gain phototransistors based on a CVD MoS₂ monolayer. *Adv. Mater.* **25**, 3456–3461 (2013).
 181. Zhan, Y. *et al.* Large-area vapor-phase growth and characterization of MoS₂ atomic layers on a SiO₂ substrate. *Small* **8**, 966–971 (2012).
 182. Liu, K. -K. *et al.* Growth of large-area and highly crystalline MoS₂ thin layers on insulating substrates. *Nano Lett.* **12**, 1538–1544 (2012).
 183. Lee, Y. *et al.* Synthesis and transfer of single-layer transition metal disulfides on diverse surfaces. *Nano Lett.* **13**, 1852–1857 (2013).
 184. Lee, Y. *et al.* Synthesis of large-area MoS₂ atomic layers with chemical vapor deposition. *Adv. Mater.* **24**, 2320–2325 (2012).
 185. Najmaei, S. *et al.* Vapour phase growth and grain boundary structure of molybdenum disulphide atomic layers. *Nat. Mater.* **12**, 754–759 (2013).
 186. Nam, H. *et al.* MoS₂ transistors fabricated via of few-layer MoS₂ flakes into large-area arrays. *ACS Nano* **7**, 5870–5881 (2013).
 187. Park, W. *et al.* Photoelectron spectroscopic imaging and device applications of large-area patternable single-layer MoS₂ synthesized by chemical vapor deposition. *ACS Nano* **8**, 4961–4968 (2014).
 188. Li, H. *et al.* Controlled synthesis of topological insulator nanoplate arrays on mica. *J. Am. Chem. Soc.* **134**, 6132–6135 (2012).
 189. Wienold, J. *et al.* Structural investigation of the thermal decomposition of ammonium heptamolybdate by in situ XAFS and XRD. *Eur. J. Inorg. Chem.* **2003**, 1058–1071 (2003).
 190. Hanadi, Z. M. *et al.* The thermal decomposition of ammonium heptamolybdate. *Thermochim. Acta* **45**, 221–232 (1981).
 191. Li, H. *et al.* From bulk to monolayer MoS₂: evolution of Raman scattering. *Adv. Funct. Mater.* **22**, 1385–1390 (2012).
 192. Radisavljevic, B. *et al.* Single-layer MoS₂ transistors. *Nat. Nanotech.* **6**, 147–150 (2011).
 193. Gong, C. *et al.* Metal contacts on physical vapor deposited monolayer MoS₂. *ACS Nano* **7**, 11350–11357 (2013).
 194. Shi, H. *et al.* Exciton dynamics in suspended monolayer and few-layer MoS₂ 2D crystals. *ACS Nano* **7**, 1072–1080 (2013).
 195. He, K. *et al.* Experimental demonstration of continuous electronic structure tuning via strain in atomically thin MoS₂. *Nano Lett.* **13**, 2931–2936 (2013).
 196. Brivio, J. *et al.* Ripples and layers in ultrathin MoS₂ membranes. *Nano Lett.* **11**, 5148–5153 (2011).
 197. Ping, J. & Fuhrer, M. S. Layer number and stacking sequence imaging of few-layer graphene by transmission electron microscopy. *Nano Lett.* **12**, 4635–4641 (2012).
 198. Yang, W. *et al.* Carbon nanomaterials in biosensors: should you use nanotubes or graphene? *Angew. Chem. Int. Ed.* **49**, 2114–2138 (2010).
 199. Choi, Y. *et al.* Single-molecule lysozyme dynamics monitored by an electronic circuit. *Science* **335**, 319–324 (2012).
 200. Lerner, M. B. *et al.* Hybrids of a genetically engineered antibody and a carbon nanotube transistor for detection of prostate cancer biomarkers. *ACS Nano* **6**, 5143–5149 (2012).
 201. Lerner, M. B. *et al.* Scalable production of highly sensitive nanosensors based on graphene functionalized with a designed g protein-coupled receptor. *Nano Lett.* **14**, 2709–2714 (2014).
 202. Nam, H. *et al.* Fabrication and comparison of MoS₂ and WSe₂ field-effect transistor biosensors. *J. Vac. Sci. Technol. B.* **33**, 06FG01 (2016).
 203. Sarkar, D. *et al.* MoS₂ field-effect transistor for next-generation label-free biosensors. *ACS Nano* **8**, 3992–4003 (2014).
 204. Jiang, K. *et al.* Protein immobilization on carbon nanotubes via a two-step process of diimide-activated amidation. *J. Mater. Chem.* **14**, 37–39 (2004).
 205. Kodali, V. K. *et al.* Nonperturbative chemical modification of graphene for protein micropatterning. *Langmuir* **27**, 863–865 (2011).
 206. Lerner, M. B. *et al.* Biosensors and bioelectronics detecting lyme disease using antibody-functionalized single-walled carbon nanotube transistors. *Biosens. Bioelectron.* **45**, 163–167

- (2013).
207. Goldsmith, B. R. *et al.* Biomimetic chemical sensors using nanoelectronic readout of olfactory receptor proteins. *ACS Nano* **5**, 5408–5416 (2011).
 208. Graff, R. A. *et al.* Synthesis of nickel - nitrilotriacetic acid coupled single-walled carbon nanotubes for directed self-assembly with polyhistidine-tagged proteins. *Chem. Mater.* **20**, 1824–1829 (2008).
 209. Lu, Y. *et al.* Graphene-protein bioelectronic devices with wavelength-dependent photoresponse. *Appl. Phys. Lett.* **100**, 033110 (2012).
 210. Wang, L. *et al.* Specific and reversible immobilization of NadH oxidase on functionalized carbon nanotubes. *J. Biotechnol.* **150**, 57–63 (2010).
 211. Lerner, M. B. *et al.* Toward Quantifying the Electrostatic Transduction Mechanism in Carbon Nanotube Molecular Sensors. *J. Am. Chem. Soc.* **134**, 14318–14321 (2012).
 212. Choi, Y. *et al.* Dissecting single-molecule signal transduction in carbon nanotube circuits with protein engineering. *Nano Lett.* **13**, 625–631 (2013).
 213. Gao, N. *et al.* General strategy for biodetection in high ionic strength solutions using transistor-based nanoelectronic sensors. *Nano Lett.* **15**, 2143–2148 (2015).
 214. Ping, J. *et al.* Biosensors and bioelectronics quantifying the effect of ionic screening with protein-decorated graphene transistors. *Biosens. Bioelectron.* **89**, 689–692 (2017).
 215. Sorgenfrei, S. *et al.* Debye screening in single-molecule carbon nanotube field-effect sensors. *Nano Lett.* **11**, 3739–3743 (2011).
 216. Zhao, X. *et al.* Characterization of a computationally designed water-soluble human μ -opioid receptor variant using available structural information. *Anesthesiology* **121**, 866–875 (2014).
 217. Perez-Aguilar, J. M. *et al.* A computationally designed water-soluble variant of a g-protein-coupled receptor: the human mu opioid receptor. *PLoS One* **8**, e66009 (2013).
 218. Schmidt, H. *et al.* Transport properties of monolayer MoS₂ grown by chemical vapor deposition. *Nano Lett.* **14**, 1909–1913 (2014).
 219. Mouri, S. *et al.* Tunable photoluminescence of monolayer MoS₂ via chemical doping. *Nano Lett.* **13**, 5944–5948 (2013).
 220. Liu, B. *et al.* High-performance chemical sensing using Schottky-contacted chemical vapor deposition grown monolayer MoS₂ transistors. *ACS Nano* **8**, 5304–5314 (2014).
 221. Perkins, F. K. *et al.* Chemical vapor sensing with monolayer MoS₂. *Nano Lett.* **13**, 668–673(2013).
 222. Bernardi, M. *et al.* Extraordinary sunlight absorption and one nanometer thick photovoltaics using two-dimensional monolayer materials. *Nano Lett.* **13**, 3664–3670 (2013).
 223. Tsai, M. *et al.* Monolayer MoS₂ heterojunction solar cells. *ACS Nano* **8**, 8317–8322 (2014).
 224. Roy, K. *et al.* Graphene – MoS₂ hybrid structures for multifunctional photoresponsive memory devices. *Nat. Nanotechn.* **8**, 826–830 (2013).
 225. Mak, K. F. *et al.* The valley Hall effect in MoS₂ transistors. *Science* **344**, 1489–1492 (2014).
 226. Late, D. J. *et al.* Hysteresis in single-layer MoS₂ field effect transistors. *ACS Nano* **6**, 5635–5641 (2012).
 227. Bertolazzi, S. *et al.* Nonvolatile memory cells based on MoS₂/graphene heterostructures. *ACS Nano* **7**, 3246–3252 (2013).
 228. Wang, L. *et al.* Biosensor for label-free sensitive detection of cancer marker proteins in solution. *Small* **10**, 1101–1105 (2014).
 229. Tahir, M. N. *et al.* Overcoming the insolubility of molybdenum disulfide nanoparticles through a high degree of sidewall functionalization using polymeric chelating ligands. *Angew. Chem. Int. Ed.* **45**, 4809–4815 (2006).
 230. McCarthy, P. J. *et al.* Inner complex chelates. I. Analogs of bisacetylacetonediethylenediimine and its metal chelates^{1,2}. *J. Am. Chem. Soc.* **77**, 5820–5824 (1955).
 231. Shelnut, J. A. *et al.* Nonplanar porphyrins and their significance in proteins. *Chem. Soc. Rev.* **27**, 31–41 (1998).
 232. Bayburt, T. H. & Sligar, S. G. Membrane protein assembly into Nanodiscs. *FEBS Lett.* **584**, 1721–1727 (2010).
 233. Frederickson, R. C. Enkephalin pentapeptides-a review of current evidence for a physiological role in vertebrate neurotransmission. *Life Sci.* **21**, 23–42 (1977).
 234. Emmerson, P. J. *et al.* Binding affinity and selectivity of opioids at mu, delta and kappa receptors in

- monkey brain membranes. *J. Pharmacol. Exp. Ther.* **271**, 1630–1637 (1994).
235. Geim, A. K. & Novoselov, K. S. The rise of graphene. *Nat. Mater.* **6**, 183–191 (2007).
236. Li, X. & Zhu, H. Two-dimensional MoS₂: properties, preparation, and applications. *J. Materiomics* **1**, 33–44 (2015).
237. Subbaiah, Y. P. V. *et al.* Atomically thin MoS₂: a versatile nongraphene 2D material. *Adv. Funct. Mater.* **26**, 2046–2069 (2016).
238. Ataca, C. *et al.* Mechanical and electronic properties of MoS₂ nanoribbons and their defects. *J. Phys. Chem. C* **115**, 3934–3941 (2011).
239. Castellanos-gomez, A. *et al.* Elastic properties of freely suspended MoS₂ nanosheets. *Adv. Mater.* **24**, 772–775 (2012).
240. Castellanos-gomez, A. *et al.* Mechanical properties of freely suspended semiconducting graphene-like layers based on MoS₂. *Nanoscale Res. Lett.* **7**, 223 (2012).
241. Jiang, J. *et al.* Molecular dynamics simulations of single-layer molybdenum disulphide (MoS₂): Stillinger-Weber parametrization, mechanical properties, and thermal conductivity. *J. Appl. Phys.* **114**, 064307 (2013).
242. Lembke, D. *et al.* Single-layer MoS₂ electronics. *Acc. Chem. Res.* **48**, 100–110 (2015).
243. Wang, X. *et al.* Controlled synthesis of highly crystalline MoS₂ flakes by chemical vapor deposition. *J. Am. Chem. Soc.* **135**, 5304–5307 (2013).
244. Huang, C. *et al.* Lateral heterojunctions within monolayer MoSe₂–WSe₂ semiconductors. *Nat. Mater.* **13**, 1096–1101 (2014).
245. Zhang, X. *et al.* Synthesis of lateral heterostructures of semiconducting atomic layers. *Nano Lett.* **15**, 410–415 (2015).
246. Zhang, Y. *et al.* Controlled growth of high-quality monolayer WS₂ layers on sapphire. *ACS Nano* **7**, 8963–8971 (2013).
247. Yue, Q. *et al.* Adsorption of gas molecules on monolayer MoS₂ and effect of applied electric field. *Nanoscale Res. Lett.* **8**, 425 (2013).
248. Kybert, N. J. *et al.* Differentiation of complex vapor mixtures using versatile DNA-carbon nanotube chemical sensor arrays. *ACS Nano* **7**, 2800–2807 (2013).
249. Sano, K. *et al.* Large variability of contact resistance in Au/Cr/MoS₂ system and its suppression by Cr thinning. *Jpn J. Appl. Phys.* **55**, 036501 (2016).
250. Lee, J. *et al.* Two dimensional layered MoS₂ biosensors enable highly sensitive detection of biomolecules. *Sci. Rep.* **4**, 7352 (2014).
251. Yang, Y. *et al.* Graphene based materials for biomedical applications. *Biochem. Pharmacol.* **16**, 365–373 (2013).
252. Haes, A. J. & Duyne, R. P. Van. A nanoscale optical biosensor: sensitivity and selectivity of an approach based on the localized surface plasmon resonance spectroscopy of triangular silver nanoparticles. *J. Am. Chem. Soc.* **124**, 10596–10604 (2002).
253. Katz, E. & Willner, I. Probing biomolecular interactions at conductive and semiconductive surfaces by impedance spectroscopy: routes to impedimetric immunosensors, DNA-sensors, and enzyme biosensors. *Electroanalysis* **15**, 913–947 (2003).
254. Shao, Y. *et al.* Graphene based electrochemical sensors and biosensors: a review. *Electroanalysis* **22**, 1027–1036 (2010).
255. Wu, L. *et al.* Highly sensitive graphene biosensors based on surface plasmon resonance. *Opt. Express* **18**, 14395–14400 (2010).
256. Ghosh, S. *et al.* Effect of 1-pyrene carboxylic-acid functionalization of graphene on its capacitive energy storage. *J. Phys. Chem. C* **116**, 20688–20693 (2012).
257. Ping, J. *et al.* Scalable production of high-sensitivity, label-free DNA biosensors based on back-gated graphene field effect transistors. *ACS Nano* **10**, 8700–8704 (2016).
258. Akinwande, D. *et al.* Two-dimensional flexible nanoelectronics. *Nat. Commun.* **5**, 5678 (2014).
259. Navick, X. *et al.* Fabrication of ultra-low radioactivity detector holders for Edelweiss-II. *Nucl. Instrum. Methods, Phys. Res. A* **520**, 189–192 (2004).
260. Gao, Z. *et al.* Scalable production of sensor arrays based on high-mobility hybrid graphene field effect transistors. *ACS Appl. Mater. Interfaces* **8**, 27546–27552 (2016).
261. Zhang, Y. *et al.* Electronic structure, surface doping, and optical response in epitaxial WSe₂ thin

- films. *Nano Lett.* **16**, 2485–2491 (2016).
262. Britnell, L. *et al.* Strong light-matter interactions in heterostructures of atomically thin films. *Science* **340**, 1311–1314 (2013).
263. Chang, Y. *et al.* Monolayer MoSe₂ grown by chemical vapor deposition for fast photodetection. *ACS Nano* **8**, 8582–8590 (2014).
264. Britnell, L. *et al.* Field-effect tunneling transistor based on vertical graphene heterostructures. *Science* **335**, 947–950 (2012).
265. Li, M. *et al.* Heterostructures based on two-dimensional layered materials and their potential applications. *Biochem. Pharmacol.* **19**, 322–335 (2016).
266. Sediri, H. *et al.* Atomically sharp interface in an h-BN-epitaxial graphene van der Waals heterostructure. *Sci. Rep.* **5**, 16465 (2015).
267. Zhang, W. *et al.* Ultrahigh-gain photodetectors based on atomically thin graphene-MoS₂ heterostructures. *Sci. Rep.* **4**, 3826 (2014).
268. Koma, A. Van der Waals epitaxy for highly lattice-mismatched systems. *J. of Cryst. Growth* **202**, 236–241 (1999).
269. Diaz, H. C. *et al.* Interface properties of CVD grown graphene transferred onto MoS₂(0001). *Nanoscale* **6**, 1071–1078 (2014).
270. Chen, K. *et al.* Electronic properties of MoS₂-WS₂ heterostructures synthesized with two-step lateral epitaxial strategy. *ACS Nano* **9**, 9868–9876 (2015).
271. Chiu, M. *et al.* Determination of band alignment in the single-layer MoS₂/WS₂ heterojunction. *Nat. Commun.* **6**, 7666 (2015).
272. Alidoust, N. *et al.* Observation of monolayer valence band spin-orbit effect and induced quantum well states in MoX₂. *Nat. Commun.* **5**, 4673 (2014).
273. Kam, K. K. & Parkinson, B. A. Detailed photocurrent spectroscopy of the semiconducting group VIB transition metal dichalcogenides. *J. Phys. Chem* **86**, 463–467 (1982).
274. Jin, W. *et al.* Direct measurement of the thickness-dependent electronic band structure of MoS₂ using angle-resolved photoemission spectroscopy. *Phys. Rev. Lett.* **111**, 106801 (2013).
275. Ray, S. C. Structure and optical properties of molybdenum disulphide (MoS₂) thin film deposited by the dip technique. *J. Mater. Sci. Lett.* **19**, 803–804 (2000).
276. Ji, Q. *et al.* Chemical vapour deposition of group-VIB metal dichalcogenide monolayers: engineered substrates from amorphous to single crystalline. *Chem. Soc. Rev.* **44**, 2587–2602 (2015).
277. Eda, G. *et al.* Photoluminescence from chemically exfoliated MoS₂. *Nano Lett.* **11**, 5111–5116 (2011).
278. Wang, S. *et al.* All chemical vapor deposition growth of MoS₂:h-BN vertical van der Waals heterostructures. *ACS Nano* **9**, 5246–5254 (2015).
279. Zhou, K. *et al.* Raman modes of MoS₂ used as fingerprint of van der Waals interactions in 2-D crystal-based heterostructures. *ACS Nano* **8**, 9914–9924 (2014).
280. Liu, K. *et al.* Elastic properties of chemical-vapor-deposited monolayer MoS₂, WS₂, and their bilayer heterostructures. *Nano Lett.* **14**, 5097–5103 (2014).
281. Shim, G. W. Large-area single-layer MoSe₂ and its van der Waals heterostructures. *ACS Nano* **8**, 6655–6662 (2014).
282. Li, L. *et al.* Raman shift and electrical properties of MoS₂ bilayer on boron nitride substrate. *Nanotechnology* **26**, 295702 (2015).
283. Ni, Z. H. *et al.* Raman spectroscopy of epitaxial graphene on a SiC substrate. *Phys. Rev. B.* **77**, 115416 (2008).
284. Girifalco, L. A. & Lad, R. A. Energy of cohesion, compressibility, and the potential energy functions of the graphite system. *J. Chem. Phys.* **25**, 693 (1956).
285. Palser, A. H. R. Interlayer interactions in graphite and carbon nanotubes. *Phys. Chem. Chem. Phys.* **1**, 4459–4464 (1999).
286. Moon, P. & Koshino, M. Electronic properties of graphene/hexagonal-boron-nitride moire superlattice. *Phys. Rev. B* **90**, 155406 (2014).
287. Wang, Z. *et al.* Electronic structure of twisted bilayers of graphene/MoS₂ and MoS₂/MoS₂. *J. Phys. Chem. C* **119**, 4752–4758 (2015).
288. Coletti, C. *et al.* Large area quasi-free standing monolayer graphene on 3C-SiC(111). *Appl. Phys.*

- Lett.* **99**, 081904 (2011).
289. Emtsev, K. V *et al.* Interaction, growth, and ordering of epitaxial graphene on SiC{0001} surfaces: a comparative photoelectron spectroscopy study. *Phys. Rev. B.* **77**, 155303 (2008).
 290. Ouerghi, A. *et al.* Large-area and high-quality epitaxial graphene on off-axis SiC Wafers. *ACS Nano* **6**, 6075–6082 (2012).
 291. Landemark, E. *et al.* Core-level spectroscopy of the clean Si(001) surface: charge transfer within asymmetric dimers of the 2*1 and c(4*2) reconstruction. *Phys. Rev. Lett.* **69**, 1588–1591 (1992).
 292. Riedl, C. *et al.* Structural and electronic properties of epitaxial graphene on SiC(0001): a review of growth, characterization, transfer doping and hydrogen intercalation. *J. Phys D: Appl. Phys.* **43**, 374009 (2010).
 293. Silly, M. G. *et al.* Electronic and structural properties of graphene-based metal-semiconducting heterostructures engineered by silicon intercalation. *Carbon* **76**, 27–39 (2014).
 294. Mattila, S. *et al.* Core level spectroscopy of MoS₂. *Surf. Sci.* **600**, 5168–5175 (2006).
 295. Kim, I. S. *et al.* Influence of stoichiometry on the optical and electrical properties of chemical vapor deposition derived MoS₂. *ACS Nano* **8**, 10551–10558 (2014).
 296. Zhou, W. *et al.* Intrinsic structural defects in monolayer molybdenum disulfide. *Nano Lett.* **13**, 2615–2622 (2013).
 297. Addou, R. *et al.* Impurities and electronic property variations of natural MoS₂ crystal surfaces. *ACS Nano* **9**, 9124–9133 (2015).
 298. Baker, M. A. *et al.* XPS investigation of preferential sputtering of S from MoS₂ and determination of MoS_x stoichiometry from Mo and S peak positions. *App. Surf. Sci.* **150**, 255–262 (1999).
 299. Fleischauer, P. D. & Lince, J. R. A comparison of oxidation and oxygen substitution in MoS₂ solid film lubricants. *Tribol. Int.* **32**, 627–636 (2000).
 300. Levasseur, A. *et al.* X-ray photoelectron spectroscopy: a powerful tool for a better characterization of thin film materials. *Bull. Mater. Sci.* **22**, 607–614 (1999).
 301. Yin, Z. *et al.* Preparation of MoS₂–MoO₃ hybrid nanomaterials for light-emitting diodes. *Angewandte* **53**, 12768–12773 (2014).
 302. Yeh, J. J. & Lindau, I. Atomic subshell photoionization cross sections and asymmetry parameters: 1 ≤ X ≤ 103. *At. Data Nucl. Data Tables* **32**, 1 (1985).
 303. Liu, X. *et al.* Rotationally commensurate growth of MoS₂ on epitaxial graphene. *ACS Nano* **10**, 1067–1075 (2016).
 304. Kang, J. *et al.* Computational study of metal contacts to monolayer transition-metal dichalcogenide semiconductors. *Phys. Rev. X* **4**, 031005 (2014).
 305. Lee, C. *et al.* Atomically thin p–n junctions with van der Waals heterointerfaces. *Nat. Nanotech.* **9**, 676–681 (2014).
 306. Bostwick, A. *et al.* Quasiparticle dynamics in graphene. *Nat. Phys.* **3**, 36–40 (2007).
 307. Yeh, P. *et al.* Direct measurement of the tunable electronic structure of bilayer MoS₂ by interlayer twist. *Nano Lett.* **16**, 953–959 (2016).
 308. Brumme, T. *et al.* First-principles theory of field-effect doping in transition-metal dichalcogenides: structural properties, electronic structure, Hall coefficient, and electrical conductivity. *Phys. Rev. B.* **91**, 155436 (2015).
 309. Jin, W. *et al.* Tuning the electronic structure of monolayer graphene/MoS₂ van der Waals heterostructures via interlayer twist. *Phys. Rev. B.* **92**, 201409 (2015).
 310. Miwa, J. A. *et al.* Van der Waals epitaxy of heterostructures in ultrahigh vacuum. *ACS Nano* **9**, 6502–6510 (2015).
 311. Voloshina, E. N. *et al.* Electronic structure and imaging contrast of graphene moire on metals. *Sci. Rep.* **3**, 1072 (2013).
 312. Pletikoscic, I. *et al.* Dirac cones and minigaps for graphene on Ir(111). *Phys. Rev. Lett.* **102**, 056808 (2009).
 313. Walter, A. L. *et al.* Electronic structure of graphene on single-crystal copper substrates. *Phys. Rev. B* **84**, 195443 (2011).
 314. Busse, C. *et al.* Graphene on Ir (111): physisorption with chemical modulation. *Phys. Rev. Lett.* **107**, 036101 (2011).
 315. Sutter, P. *et al.* Graphene on Pt (111): growth and substrate interaction. *Phys. Rev. B* **80**, 245411

- (2009).
316. Wang, B. *et al.* Coupling epitaxy, chemical bonding, and work function at local scale in transition metal-supported graphene. *ACS Nano* **4**, 5773–5782 (2010).
 317. Alfe, D. *et al.* Fine tuning of graphene-metal adhesion by surface alloying. *Sci. Rep.* **3**, 2430 (2013).
 318. Voloshina, E. N. *et al.* Graphene on Rh (111): scanning tunneling and atomic force microscopies studies. *Appl. Phys. Lett.* **100**, 241606 (2012).
 319. Moritz, W. *et al.* Structure determination of the coincidence phase of graphene on Ru (0001). *Phys. Rev. Lett.* **104**, 136102 (2010).
 320. Pacile, D. *et al.* Artificially lattice-mismatched graphene/metal interface : graphene/Ni/Ir(111). *Phys. Rev. B* **87**, 035420 (2013).
 321. Shikin, A. M. *et al.* Induced spin–orbit splitting in graphene: the role of atomic number of the intercalated metal and π -d hybridization. *New J. Phys* **15**, 013014 (2013).
 322. Papagno, M. *et al.* Hybridization of graphene and a Ag monolayer supported on Re(0001). *Phys. Rev. B* **88**, 235430 (2013).
 323. Diaz, H. C. *et al.* Direct observation of interlayer hybridization and dirac relativistic carriers in graphene/MoS₂ van der Waals heterostructures. *Nano Lett.* **15**, 1135–1140 (2015).
 324. Rutter, G. M. *et al.* Scattering and interference in epitaxial graphene. *Science* **317**, 219–222 (2007).
 325. Ponomarenko, L. A. *et al.* Cloning of Dirac fermions in graphene superlattices. *Nature* **497**, 594–597 (2013).
 326. Yankowitz, M. *et al.* Emergence of superlattice Dirac points in graphene on hexagonal boron nitride. *Nat. Phys.* **8**, 382–386 (2012).
 327. Park, C. *et al.* Anisotropic behaviours of massless Dirac fermions in graphene under periodic potentials. *Nat. Phys.* **4**, 213–217 (2008).
 328. Fogler, M. M. *et al.* High-temperature superfluidity with indirect excitons in van der Waals heterostructures. *Nat. Commun.* **5**, 4555 (2014).
 329. Withers, F. *et al.* Light-emitting diodes by band-structure engineering in van der Waals heterostructures. *Nat. Mater.* **14**, 301–306 (2015).
 330. Chernikov, A. *et al.* Exciton Binding Energy and Nonhydrogenic Rydberg Series in Monolayer WS₂. *Phys. Rev. Lett.* **113**, 076802 (2014).
 331. Ugeda, M. M. *et al.* Giant bandgap renormalization and excitonic effects in a monolayer transition metal dichalcogenide semiconductor. *Nat. Mater.* **13**, 1091–1095 (2014).
 332. He, K. *et al.* Tightly bound excitons in monolayer WSe₂. *Phys. Rev. Lett.* **113**, 026803 (2014).
 333. Ye, Z. *et al.* Probing the excitonic dark states in single-layer tungsten disulphide. *Nature* **513**, 214–218 (2014).
 334. Zhang, C. *et al.* Absorption of light by excitons and trions in monolayers of metal dichalcogenide MoS₂: experiments and theory. *Phys. Rev. B* **89**, 205436 (2014).
 335. Robert, C. *et al.* Exciton radiative lifetime in transition metal dichalcogenide monolayers. *Phys. Rev. B* **93**, 205423 (2016).
 336. Ross, J. S. *et al.* Electrical control of neutral and charged excitons in a monolayer semiconductor. *Nat. Commun.* **4**, 1474 (2013).
 337. Mak, K. F. *et al.* Tightly bound trions in monolayer MoS₂. *Nat. Mater.* **12**, 207–211 (2013).
 338. Li, Z. *et al.* Active Light Control of the MoS₂ monolayer exciton binding energy. *ACS Nano* **9**, 10158–10164 (2015).
 339. Liu, X. *et al.* Strong light-matter coupling in two-dimensional atomic crystals. *Nat. Photonics* **9**, 30–34 (2015).
 340. Wang, S. *et al.* Coherent coupling of WS₂ monolayers with metallic photonic nanostructures at room temperature. *Nano Lett.* **16**, 4368–4374 (2016).
 341. Gan, X. *et al.* Controlling the spontaneous emission rate of monolayer MoS₂ in a photonic crystal nanocavity. *Appl. Phys. Lett.* **103**, 181119 (2013).
 342. Butun, S. *et al.* Enhanced light emission from large-area monolayer MoS₂ using plasmonic nanodisc arrays. *Nano Lett.* **15**, 2700–2704 (2015).
 343. Sobhani, A. *et al.* Enhancing the photocurrent and photoluminescence of single crystal monolayer MoS₂ with resonant plasmonic nanoshells. *Appl. Phys. Lett.* **104**, 031112 (2014).

344. Zhao, W. *et al.* Exciton–plasmon coupling and electromagnetically induced transparency in monolayer semiconductors hybridized with Ag nanoparticles. *Adv. Mater.* **28**, 2709–2715 (2016).
345. Dufferwiel, S. *et al.* Exciton–polaritons in van der Waals heterostructures embedded in tunable microcavities. *Nat. Commun.* **6**, 8579 (2015).
346. Wang, Z. *et al.* Giant photoluminescence enhancement in tungsten-diselenide-gold plasmonic hybrid structures. *Nat. Commun.* **7**, 11283 (2016).
347. Wu, S. *et al.* Monolayer semiconductor nanocavity lasers with ultralow thresholds. *Nature* **520**, 69–72 (2015).
348. Auguie, B. & Barnes, W. L. Collective resonances in gold nanoparticle arrays. *Phys. Rev. Lett.* **101**, 143902 (2008).
349. Zou, S. *et al.* Silver nanoparticle array structures that produce remarkably narrow plasmon lineshapes. *J. Chem. Phys.* **120**, 10871 (2004).
350. Gao, S. *et al.* Dynamical excitonic effects in doped two-dimensional semiconductors. *Nano Lett.* **16**, 5568–5573 (2016).
351. Chernikov, A. *et al.* Electrical tuning of exciton binding energies in monolayer WS₂. *Phys. Rev. Lett.* **115**, 126802 (2015).
352. Seyler, K. L. *et al.* Electrical control of second-harmonic generation in a WSe₂ monolayer transistor. *Nat. Nanotech.* **10**, 407–411 (2015).
353. Sun, L. *et al.* Resolving parity and order of Fabry–Perot modes in semiconductor nanostructure waveguides and lasers: Young’s interference experiment revisited. *Nano Lett.* **14**, 6564 (2014).
354. Combescot, M. Trion oscillator strength. *Solid State Comm.* **128**, 273–277 (2003).
355. Schmitt-Rink, S. *et al.* Linear and nonlinear optical properties of semiconductor quantum wells. *Adv. Phys.* **38**, 89 (1989).
356. Yin, X. *et al.* Edge nonlinear optics on a MoS₂ atomic monolayer. *Science* **344**, 488–491 (2014).
357. Mai, C. *et al.* Exciton valley relaxation in a single layer of WS₂ measured by ultrafast spectroscopy. *Phys. Rev. B* **90**, 041414(R) (2014).
358. Malard, L. M. *et al.* Observation of intense second harmonic generation from MoS₂ atomic crystals. *Phys. Rev. B* **87**, 201401(R) (2013).
359. Li, Y. *et al.* Probing symmetry properties of few-layer MoS₂ and h-BN by optical second-harmonic generation. *Nano Lett.* **13**, 3329–3333 (2013).
360. Hsu, W. -T. *et al.* Second harmonic generation from artificially stacked transition metal dichalcogenide twisted bilayers. *ACS Nano* **8**, 2951–2958 (2014).
361. Kumar, N. *et al.* Second harmonic microscopy of monolayer MoS₂. *Phys. Rev. B* **87**, 161403 (2013).
362. Engel, M. *et al.* Light-matter interaction in microcavity-controlled graphene transistor. *Nat. Commun.* **3**, 906 (2012).
363. Furchi, M. *et al.* Microcavity-integrated graphene photodetector. *Nano Lett.* **12**, 2773–2777 (2012).
364. Lee, J. *et al.* Giant nonlinear response from plasmonic metasurfaces coupled to intersubband transitions. *Nature* **511**, 65–69 (2014).
365. Gan, X. *et al.* Controlling the spontaneous emission rate of monolayer MoS₂ in a photonic crystal nanocavity. *Appl. Phys. Lett.* **103**, 181119 (2013).
366. Schwarz, S. *et al.* Two-dimensional metal–chalcogenide films in tunable optical microcavities. *Nano Lett.* **14**, 7003–7008 (2014).
367. Rodriguez, A. *et al.* X² and X³ harmonic generation at a critical power in inhomogeneous doubly resonant cavities. *Opt. Express* **15**, 7303–7318 (2007).
368. Ou, Z. Y. & Kimble, H. J. Enhanced conversion efficiency for harmonic generation with double resonance. *Opt. Express* **18**, 1053–1055 (1993).
369. Ashkin, A. *et al.* Resonant optical second harmonic generation and mixing. *IEEE J. Quantum Electron.* **2**, 109–124 (1966).
370. Bi, Z. -F. *et al.* High-efficiency second-harmonic generation in doubly-resonant X² microring resonators. *Opt. Express* **20**, 7526–7543 (2012).
371. Simonneau, C. *et al.* Second-harmonic generation in a doubly resonant semiconductor microcavity. *Opt. Express* **22**, 1775–1777 (1997).
372. Yeh, P. *Optical Waves in Layered Media*. Wiley, Vol. 95 (1988).

373. Ren, M. & Li, Z. Enhanced nonlinear frequency conversion in defective nonlinear photonic crystals with designed polarization distribution. *J. Opt. Soc. Am. B* **27**, 1551–1560 (2010).
374. Berger, V. Second-harmonic generation in monolithic cavities. *J. Opt. Soc. Am. B* **14**, 1351–1360 (1997).
375. Liscidini, M. & Andreani, L. C. Second-harmonic generation in doubly resonant microcavities with periodic dielectric mirrors. *Phys. Rev. E* **73**, 016613 (2006).
376. Yi, F. *et al.* Plasmonically enhanced thermomechanical detection of infrared radiation. *Nano Lett.* **13**, 1638–1643 (2013).
377. Ren, M. *et al.* Enhanced second-harmonic generation from metal-integrated semiconductor nanowires via highly confined whispering gallery modes. *Nat. Commun.* **5**, 5432 (2014).
378. Zeng, H. *et al.* Optical signature of symmetry variations and spin-valley coupling in atomically tungsten dichalcogenides. *Sci. Rep.* **3**, 1608 (2013).
379. Huang, X. *et al.* Quantitative analysis of temperature dependence of raman shift of monolayer WS₂. *Sci. Rep.* **6**, 32236 (2016).
380. Shi, W. *et al.* Raman and photoluminescence spectra of two-dimensional nanocrystallites of monolayer WS₂ and WSe₂. *2D Mater.* **3**, 025016 (2016).
381. Liu, K. *et al.* Atomically thin molybdenum disulfide nanopores with high sensitivity for DNA translocation. *ACS Nano* **8**, 2504–2511 (2014).
382. Merchant, C. A. *et al.* DNA translocation through graphene. *Nano Lett.* **10**, 2915–2921 (2010).
383. Zhou, Z. *et al.* DNA translocation through hydrophilic nanopore in hexagonal boron nitride. *Sci. Rep.* **3**, 3287 (2013).
384. Feng, J. *et al.* Single-layer MoS₂ nanopores as nanopower generators. *Nature* **536**, 197–200 (2016).
385. Garaj, S. *et al.* Molecule-hugging graphene nanopores. *Proc. Natl. Acad. Sci. U.S.A.* **110**, 12192–12196 (2013).
386. Kim, M. S. *et al.* Biexciton emission from edges and grain boundaries of triangular WS₂ monolayers. *ACS Nano* **10**, 2399–2405 (2016).
387. Gutierrez, H. R. *et al.* Extraordinary room-temperature photoluminescence in triangular WS₂ monolayers. *Nano Lett.* **13**, 3447–3454 (2013).
388. Peimyoo, N. *et al.* Nonblinking, intense two-dimensional light emitter: monolayer WS₂ triangles. *ACS Nano* **7**, 10985–10994 (2013).
389. Beal, A. R. *et al.* Excitons in 2H-WSe₂ and 3R-WS₂. *J. Phys. C: Solid State Phys.* **9**, 2459 (1976).
390. Yuan, L. & Huang, L. Exciton dynamics and annihilation in WS₂ 2D semiconductors. *Nanoscale* **7**, 7402–7408 (2015).
391. Jo, S. *et al.* Mono- and bilayer WS₂ light-emitting transistors. *Nano Lett.* **14**, 2019–2025 (2014).
392. Chow, P. K. *et al.* Defect-induced photoluminescence in monolayer semiconducting transition metal dichalcogenides. *ACS Nano* **9**, 1520–1527 (2015).
393. Tongay, S. *et al.* Defects activated photoluminescence in two-dimensional semiconductors: interplay between bound, charged, and free excitons. *Sci. Rep.* **3**, 02657 (2013).
394. Gao, J. *et al.* Aging of transition metal dichalcogenide monolayers. *ACS Nano* **10**, 2628 (2016).
395. Ahn, S. *et al.* Prevention of transition metal dichalcogenide photodegradation by encapsulation with h-BN layers. *ACS Nano* **10**, 8973–8979 (2016).
396. Su, L. *et al.* Effects of substrate type and material-substrate bonding on high-temperature behavior of monolayer WS₂. *Nano Res.* **8**, 2686–2697 (2015).
397. Zhao, W. *et al.* Lattice dynamics in mono- and few-layer sheets of WS₂ and WSe₂. *Nanoscale* **5**, 9677–9683 (2013).
398. Zhao, W. *et al.* Evolution of electronic structure in atomically thin sheets of WS₂ and WSe₂. *ACS Nano* **7**, 791–797 (2013).
399. Wang, Y. *et al.* Morphological and structural evolution of WS₂ nanosheets irradiated with an electron beam. *Phys. Chem. Chem. Phys.* **17**, 2678–2685 (2014).
400. Plechinger, G. *et al.* Identification of excitons, trions and biexcitons in single-layer WS₂. *Phys. Status Solidi RRL* **9**, 457–461 (2015).
401. Wang, Y. *et al.* Strain-induced direct–indirect bandgap transition and phonon modulation in monolayer WS₂. *Nano Res.* **8**, 2562–2572 (2015).
402. Scheuschner, N. *et al.* Photoluminescence of freestanding single- and few-layer MoS₂. *Phys. Rev.*

- B: Condens. Matter Mater. Phys.* **89**, 125406 (2014).
403. Puster, M. *et al.* Toward sensitive graphene nanoribbon-nanopore devices by preventing electron beam-induced damage. *ACS Nano* **7**, 11283–11289 (2013).
404. Venta, K. E. *et al.* Gold nanorod translocations and charge measurement through solid-state nanopores. *Nano Lett.* **14**, 5358–5364 (2014).
405. Schneider, G. F. *et al.* DNA translocation through graphene nanopores. *Nano Lett.* **10**, 3163 (2010).
406. Mihovilovic, M. *et al.* Statistics of DNA capture by a solid-state nanopore. *Phys. Rev. Lett.* **110**, 028102 (2013).
407. Garaj, S. *et al.* Graphene as a subnanometre trans-electrode membrane. *Nature* **467**, 190–193 (2010).
408. Di Fiori, N. *et al.* Optoelectronic control of surface charge and translocation dynamics in solid-state nanopores. *Nat. Nanotech.* **8**, 946–951 (2013).
409. Kuan, A. T. *et al.* Electrical pulse fabrication of graphene nanopores in electrolyte solution. *Appl. Phys. Lett.* **106**, 203109 (2017).
410. Kwok, H. *et al.* Nanopore fabrication by controlled dielectric breakdown. *PLoS One* **9**, e92880 (2014).
411. Yanagi, I. *et al.* Fabricating nanopores with diameters of sub-1 nm to 3 nm using multilevel pulse-voltage injection. *Sci. Rep.* **4**, 05000 (2014).
412. Kosmider, K. & Fernandez-Rossier, J. Electronic properties of the MoS₂-WS₂ heterojunction. *Phys. Rev. B* **87**, 075451 (2013).
413. Komsa, H. *et al.* Electronic structures and optical properties of realistic transition metal dichalcogenide heterostructures from first principles. *Phys. Rev. B* **88**, 085318 (2013).
414. Yu, Y. *et al.* Equally efficient interlayer exciton relaxation and improved absorption in epitaxial and nonepitaxial MoS₂/WS₂ heterostructures. *Nano Lett.* **15**, 486–491 (2015).
415. Tongay, S. *et al.* Tuning interlayer coupling in large-area heterostructures with CVD-grown MoS₂ and WS₂ monolayers. *Nano Lett.* **14**, 3185–3190 (2014).
416. Han, S. A. *et al.* Synthesis, properties and potential applications of two-dimensional transition metal dichalcogenides. *Nano Converg.* **2**, 17 (2015).
417. Huang, X. *et al.* Metal dichalcogenide nanosheets: preparation, properties and applications. *Chem. Soc. Rev.* **42**, 1934–1946 (2013).
418. Lee, B. *et al.* Fano resonance and spectrally modified photoluminescence enhancement in monolayer MoS₂ integrated with plasmonic nanoantenna array. *Nano Lett.* **15**, 3646–3653 (2015).
419. Feng, J. *et al.* Strain-engineered artificial atom as a broad-spectrum solar energy funnel. *Nat. Photonics* **6**, 866–872 (2012).
420. Lee, C. *et al.* Frictional characteristics of atomically thin sheets. *Science* **328**, 76–80 (2010).
421. Wilson, J. A. & Yoffe, A. D. Transition metal dichalcogenides discussion and interpretation of the observed optical, electrical and structural properties. *Adv. Phys.* **18**, 193–335 (1969).
422. Hasan, M. Z. & Kane, C. L. *Colloquium*: Topological insulators. *Rev. Mod. Phys.* **82**, 3045–3067 (2010).
423. Voiry, D. & Chhowalla, M. Phase engineering of transition metal dichalcogenides. *Chem. Soc. Rev.* **44**, 2702–2712 (2015).
424. Cho, S. *et al.* Phase patterning for ohmic homojunction contact in MoTe₂. *Science* **349**, 625 (2015).
425. Zhou, L. *et al.* Large-area synthesis of high-quality uniform few-layer MoTe₂. *J. Am. Chem. Soc.* **137**, 11892–11895 (2015).
426. Park, J. *et al.* Phase-engineered synthesis of centimeter-scale 1T⁻ and 2H- molybdenum ditelluride thin films. *ACS Nano* **9**, 6548–6554 (2015).
427. Bao, L. *et al.* Weak anti-localization and quantum oscillations of surface states in topological insulator Bi₂Se₂Te. *Sci. Rep.* **2**, 1–7 (2012).
428. Kan, M. *et al.* Phase stability and Raman vibration of the molybdenum ditelluride (MoTe₂) monolayer. *Phys. Chem. Chem. Phys.* **17**, 14866–14871 (2015).
429. Keum, D. H. *et al.* Bandgap opening in few-layered monoclinic MoTe₂. *Nat. Phys.* **11**, 482–486 (2015).
430. Kan, M. *et al.* Phase stability and raman vibration of molybdenum ditelluride (MoTe₂). *Phys. Chem. Chem. Phys.* **17**, 14866–14871 (2015).

431. Yang, J. *et al.* Robust Excitons and Trions. *ACS Nano* **9**, 6603–6609 (2015).
432. Huang, P. Y. *et al.* Grains and grain boundaries in single-layer graphene atomic patchwork quilts. *Nature* **469**, 389–392 (2011).
433. Brown, B. E. The crystal structures of WTe₂ and high-temperature MoTe₂. *Acta Crystallogr.* **20**, 268–274 (1966).
434. Koch, C. Determination of core structure periodicity and point defect density along dislocations. *Dissertation* (2002).
435. Chen, J. *et al.* Gate-voltage control of chemical potential and weak antilocalization in Bi₂Se₃. *Phys. Rev. Lett.* **105**, 176602 (2010).
436. Fu, L. *et al.* Topological insulators in three dimensions. *Phys. Rev. Lett.* **98**, 1–4 (2007).
437. Cha, J. J. *et al.* Weak antilocalization in Bi₂(Se_xTe_{1-x}) nanoribbons and nanoplates. *Nano Lett.* **12**, 1107–1111 (2012).
438. Chen, J. *et al.* Gate-voltage control of chemical potential and weak antilocalization in Bi₂Se₃. *Phys. Rev. Lett.* **105**, 176602 (2010).
439. He, H. *et al.* Impurity effect on weak antilocalization in the topological insulator Bi₂Te₃. *Phys. Rev. Lett.* **106**, 166805 (2011).
440. Liu, M. *et al.* Crossover between weak antilocalization and weak localization in a magnetically doped topological insulator. *Phys. Rev. Lett.* **108**, 036805 (2012).
441. Mangolini, F. *et al.* Angle-resolved environmental X-ray photoelectron spectroscopy: a new laboratory setup for photoemission studies at pressures up to 0.4 Torr. *Rev. Sci. Instrum.* **83**, 093112 (2012).
442. Wagner, C. D. *et al.* Empirical atomic sensitivity factors for quantitative analysis by electron spectroscopy for chemical analysis. *Surf. Interface Anal.* **3**, 211–225 (1981).
443. Perdew, J. P. *et al.* Generalized Gradient Approximation Made Simple. *Phys. Rev. Lett.* **77**, 3865–3868 (1996).
444. Giannozzi, P. *et al.* QUANTUM ESPRESSO: a modular and open-source software project for quantum simulations of materials. *J. Phys.: Condens. Matter* **21**, 395502 (2009).
445. Ramer, N. J. & Rappe, A. M. Designed nonlocal pseudopotentials for enhanced transferability. *Phys. Rev. B: Condens. Matter Mater. Phys.* **59**, 12471 (1999).
446. Rappe, A. M. *et al.* Optimized pseudopotentials. *Phys. Rev. B* **41**, 1227–1230 (1990).
447. Steffen, C. *et al.* TmoleX-a graphical user interface for TURBOMOLE. *J. Comput. Chem.* **31**, 2967–2970 (2010).
448. Sun, Y. *et al.* Prediction of Weyl semimetal in orthorhombic MoTe₂. *Phys. Rev. B: Condens. Matter Mater. Phys.* **92**, 161107 (2015).
449. Acerce, M. *et al.* Metallic 1T phase MoS₂ nanosheets as supercapacitor electrode materials. *Nat. Nanotech.* **10**, 313–318 (2015).
450. Tenne, R. *et al.* Hollow nanoparticles of WS₂ as potential solid-state lubricants. *Nature* **675**, 791–793 (2006).
451. Voiry, D. *et al.* Enhanced catalytic activity in strained chemically exfoliated WS₂ nanosheets for hydrogen evolution. *Nat. Mater.* **12**, 850–855 (2013).
452. Xiao, D. *et al.* Coupled spin and valley physics in monolayers of MoS₂ and other group-VI dichalcogenides. *Phys. Rev. Lett.* **108**, 196802 (2012).
453. Schaibley, J. R. *et al.* Valleytronics in 2D materials. *Nat. Rev. Mater.* **1**, 16055 (2016).
454. Zheng, F. *et al.* On the quantum spin Hall gap of monolayer 1T'-WTe₂. *Adv. Mater.* **28**, 4845–4851 (2016).
455. Han, G. H. *et al.* Absorption dichroism of monolayer 1T'-MoTe₂ in visible range. *2D Mater.* **3**, 031010 (2016).
456. Lee, C. *et al.* Tungsten ditelluride: a layered semimetal. *Sci. Rep.* **5**, 10013 (2015).
457. Kim, Y. *et al.* Anomalous Raman scattering and lattice dynamics in mono- and few-layer WTe₂. *Nanoscale* **8**, 2309–2316 (2016).
458. Song, S. *et al.* Room temperature semiconductor – metal transition of MoTe₂ thin films engineered by strain. *Nano Lett.* **16**, 188–193 (2016).
459. Yan, J. *et al.* Raman scattering and tunable electron – phonon coupling in single layer graphene. *Solid State Commun.* **143**, 39–43 (2007).

460. Goldstein, T. *et al.* Raman scattering and anomalous Stokes – anti-Stokes ratio in MoTe₂ atomic layers. *Sci. Rep.* **6**, 28024 (2016).
461. Hahn, T. *International Tables for Crystallography, Vol. A: Space Group Symmetry*, 5th ed.; Springer: Berlin, Germany, 2002.
462. Chen, S., *et al.* Activation of new Raman modes by inversion symmetry breaking in Type II Weyl semimetal candidate T'-MoTe₂. *Nano Lett.* **16**, 5852–5860 (2016).
463. Loudon, R. The Raman effect in crystals. *Adv. Phys.* **13**, 423–482 (1964).
464. Ling, X. *et al.* Anisotropic electron-photon and electron-phonon interactions in black phosphorus. *Nano Lett.* **16**, 2260–2267 (2016).
465. Ribeiro, H. B. *et al.* Unusual angular dependence of the Raman response in black phosphorus. *ACS Nano* **9**, 4270–4276 (2015).
466. Kim, J. *et al.* Toward air-stable multilayer phosphorene thin-films and transistors. *Sci. Rep.* **5**, 8989 (2015).
467. Ye, F. *et al.* Environmental instability and degradation of single- and few-layer WTe₂ nanosheets in ambient conditions. *Small* **12**, 5802–5808 (2016).
468. Pine, A. S. & Dresselhaus, G. Raman spectra and lattice dynamics of tellurium. *Phys. Rev. B - Condens. Matter Mater. Phys.* **4**, 356–371 (1971).
469. Martin, R. M. *et al.* Intermolecular bonding and lattice dynamics of Se and Te. *Phys. Rev. B* **13**, 1383–1395 (1976).
470. Wang, S. *et al.* Synthesis, characterization and optical properties of flower-like tellurium. *CrystEngComm.* **12**, 166 (2010).
471. Campbell, I. H. & Fauchet, P. M. The effects of microcrystal size and shape on the one phonon Raman spectra of crystalline semiconductors. *Solid State Commun.* **58**, 739–741 (1986).
472. Chu, T. *et al.* Electrically tunable bandgaps in bilayer MoS₂. *Nano Lett.* **15**, 8000–8007 (2015).
473. Eda, G. *et al.* Coherent atomic and electronic heterostructures of single-layer MoS₂. *ACS Nano* **6**, 7311–7317 (2012).
474. Ali, M. N. *et al.* Large, non-saturating magnetoresistance in WTe₂. *Nature* **514**, 205–208 (2014).
475. Zhou, J. *et al.* Large-area and high-quality 2D transition metal telluride. *Adv. Mater.* **29**, 1603471 (2017).
476. Algara-siller, G. *et al.* The pristine atomic structure of MoS₂ monolayer protected from electron radiation damage by graphene. *Appl. Phys. Lett.* **103**, 203107 (2017).
477. Zan, R. *et al.* Control of radiation damage in MoS₂ by graphene encapsulation. *ACS Nano* **7**, 10167–10174 (2013).
478. Elias, D. C. *et al.* Control of graphene's properties by reversible hydrogenation: evidence for graphene. *Science* **323**, 610–614 (2009).
479. Vora, P. M. *et al.* Correlating magnetotransport and diamagnetism of sp²-bonded carbon networks through the metal-insulator transition. *Phys. Rev. B* **84**, 155114 (2011).
480. Fu, L. *et al.* Topological insulators in three dimensions. *Phys. Rev. Lett.* **98**, 106803 (2007).
481. Garate, I. & Glazman, L. Weak localization and antilocalization in topological insulator thin films with coherent bulk-surface coupling. *Phys. Rev. B* **86**, 035422 (2012).
482. Hikami, S. *et al.* Spin-orbit interaction and magnetoresistance in the two dimensional random system. *Prog. Theor. Phys.* **63**, 707–710 (1980).
483. Cha, J. J. *et al.* Weak antilocalization in Bi₂(Se_xTe_{1-x})₃ nanoribbons and nanoplates. *Nano Lett.* **12**, 1107–1111 (2012).
484. Streller, F. *et al.* Novel metal silicide thin films by design via controlled solid-state diffusion. *Chem. Mater.* **27**, 4247–4253 (2015).
485. Streller, F. *et al.* Valence band control of metal silicide films via stoichiometry. *J. Phys. Chem. Lett.* **7**, 2573–2578 (2016).
486. Steffen, C. *et al.* TmoleX-a graphical user interface for TURBOMOLE. *J. Comput. Chem.* **31**, 2967–2970 (2010).
487. Monkhorst, H. J. & Pack, J. D. Special points for Brillouin-zone integrations. *Phys. Rev. B* **13**, 5188 (1976).
488. Han, G. H. *et al.* Absorption dichroism of monolayer 1T'-MoTe₂ in visible range. *2D Mater.* **3**, 031010 (2016).

489. Baroni, S. *et al.* Phonons and related crystal properties from density-functional perturbation theory. *Rev. Mod. Phys.* **73**, 515 (2001).
490. Chen, S. *et al.* Intrinsic phonon bands in high-quality monolayer T' molybdenum ditelluride. *ACS Nano* **11**, 814–820 (2017).
491. Kim, Y. *et al.* Anomalous lattice dynamics of mono-, bi-, and tri-layer WTe₂. *Nanoscale* **8**, 2309 (2016).
492. Khorasaninejad, M. *et al.* Enhanced first-order Raman scattering from arrays of vertical Silicon nanowires. *Nanotechnology* **23**, 275706 (2012).
493. Kang, J. *et al.* Monolayer semiconducting transition metal dichalcogenide alloys: stability and band bowing. *J. Appl. Phys.* **113**, 143703 (2013).
494. Shenoy, V. B. *et al.* Edge-stress-induced warping of graphene sheets and nanoribbons. *Phys. Rev. Lett.* **101**, 245501 (2008).
495. Bogaert, K. *et al.* Diffusion-mediated synthesis of MoS₂/WS₂ lateral heterostructures. *Nano Lett.* **16**, 5129 (2016).
496. Berry, J. *et al.* Dynamic phase engineering of bendable transition metal dichalcogenide monolayers. *Nano Lett.* Article ASAP (2017).
497. Shirley, D. A. High-resolution X-ray photoemission spectrum of the valence bands of gold. *Phys. Rev. B* **5**, 4709 (1972).
498. Moulder, J. F. & Chastain, J. Handbook of X-ray photoelectron spectroscopy: a reference book of standard spectra for identification and interpretation of XPS data; Perkin-Elmer Corporation, Physical Electronics Division (1992).
499. Laursen, A. B., *et al.* MoS₂—an integrated protective and active layer on n⁺ p-Si for solar H₂ evolution. *Phys. Chem. Chem. Phys.* **15**, 20000 (2013).
500. Ueno, K. & Fukushima, K. Changes in structure and chemical composition of α -MoTe₂ and β -MoTe₂ during heating in vacuum conditions. *Appl. Phys. Express* **8**, 095201 (2015).